

ÉCOLE DOCTORALE DES SCIENCES CHIMIQUES

Institut de science et d'ingénierie supramoléculaires

THÈSE présentée par :

Alessandro BERTUCCI

soutenue le : **20 Mars 2015**

pour obtenir le grade de : **Docteur de l'université de Strasbourg**

Discipline/ Spécialité : Chimie

**Hybrid organic-inorganic interfaces for
biomedical applications**

THÈSE dirigée par :

[Mme DE COLA Luisa]
[M. CORRADINI Roberto]

Professeur, Université de Strasbourg
Professeur, Università di Parma

RAPPORTEURS :

[M. PRODI Luca]
[M. BISCARINI Fabio]

Professeur, Università di Bologna
Professeur, Università di Modena e Reggio Emilia

AUTRES MEMBRES DU JURY :

[M. BIANCO Alberto]
[Mme TEULADE-FICHOUE Marie-Paule]

Directeur de Recherche, CNRS (DR2)
Directeur de Recherche, CNRS Institut Curie

UNIVERSITÀ DEGLI STUDI DI PARMA

Dottorato di ricerca in Scienze Chimiche

Ciclo XXVII

Hybrid organic-inorganic interfaces for biomedical applications

Coordinatore:

Chiar.mo Prof. Roberto Cammi

Tutor:

Chiar.mo Prof. Roberto Corradini (Università di Parma)

Chiar.ma Prof. Luisa De Cola (Université de Strasbourg)

Dottorando: Alessandro Bertucci

Daß diese Wirkung aber nötig sei, dies würde jeder am sichersten, durch Intuition, nachempfinden, wenn er einmal, sei es auch im Traume, in eine althellenische Existenz sich zurückversetzt fühlte: im Wandeln unter hohen ionischen Säulengängen, aufwärtsblickend zu einem Horizont, der durch reine und edle Linien abgeschnitten ist, neben sich Widerspiegelungen seiner verklärten Gestalt in leuchtendem Marmor, rings um sich feierlich schreitende oder zart bewegte Menschen, mit harmonisch tönenden Lauten und rhythmischer Gebärdensprache – würde er nicht, bei diesem fortwährenden Einströmen der Schönheit, zu Apollo die Hand erhebend ausrufen müssen: »Seliges Volk der Hellenen! Wie groß muß unter euch Dionysus sein, wenn der delische Gott solche Zauber für nötig hält, um euren dithyrambischen Wahnsinn zu heilen!« – Einem so Gestimmten dürfte aber ein greiser Athener, mit dem erhabenen Auge des Äschylus zu ihm aufblickend, entgegen: »Sage aber auch dies, du wunderlicher Fremdling: wieviel mußte dies Volk leiden, um so schön werden zu können!«

[Friedrich Nietzsche,
Die Geburt der Tragödie aus dem Geiste der Musik, 1872]

Table of contents

Résumé	1
1. Introduction	25
1.1. Nanotechnology and nanomedicine	25
1.2. Hybrid bioorganic-inorganic structures	30
1.3. Zeolite-L for biomedical applications	33
1.4. Mesoporous silica nanoparticles and their applications in nanomedicine	38
1.5. Peptide Nucleic Acid (PNA)	43
1.6. Nanostructures and PNA in analytical techniques for DNA detection	46
1.7. Aim of the thesis	50
2. Making the tools: synthesis and characterization of zeolite-L, mesoporous silica nanoparticles and Peptide nucleic acid	61
2.1. Synthesis and characterization of Zeolite-L	61
2.2. Guest molecule loading	65
2.3. Functionalization of the zeolite outer surface	68
2.4. Synthesis and characterization of mesoporous silica nanoparticles	69
2.5. Surface functionalization and cargo loading	72
2.6. Synthesis and characterization of Peptide Nucleic Acid	73
2.7. Experimental section	77
3. Multifunctional zeolite-L nanocontainers for DNA and drug delivery into living cells	82
3.1. DNA transfection: technologies and challenges	82
3.2. DNA-modified Zeolite-L crystals: preparation and analysis	86
3.3. Synthesis and functionalization of microzeolite-L	87
3.4. DAPI controlled delivery from DNA-modified microzeolite-L	89
3.5. Intracellular DAPI and DNA release by microzeolite-L	90
3.6. Synthesis and functionalization of nanozeolite-L	92
3.7. Cellular uptake of DNA-(DXP)-modified nanozeolite-L	93
3.8. Intracellular DAPI and DNA release by nanozeolite-L	95
3.9. Fate of the particles and released DNA: sub-cellular localization	100
3.10. Conclusion	101
3.11. Experimental section	101
4. Intracellular delivery of Peptide Nucleic Acid and organic molecules using zeolite-L nanocarriers	109
4.1. Cellular delivery of Peptide Nucleic Acid	110
4.2. Material preparation and characterization	112
4.3. In vitro Experiments on HeLa cells	115
4.4. Delivery of DAPI as a model drug	118
4.5. Fabrication of antimir-PNA-Zeolites	119
4.6. Cationic antimir-PNA-zeolites: synthesis and cellular uptake	121
4.7. PNA-gated multifunctional zeolite nanocarriers for miRNA-responsive controlled drug delivery	126
4.8. Conclusion	132
4.9. Experimental section	132

5. Mesoporous silica nanoparticles for simultaneous delivery of temozolomide and microRNA-targeting PNA in glioma cancer treatment	141
5.1 MicroRNAs as gene therapy targets	141
5.2 Synthesis and characterization of MSNPs	144
5.3 Multi-functionalization of MSNPs	145
5.4 Cellular uptake studies	147
5.5 In vitro viability tests on C6 glioma cell line	148
5.6 Effects of PNA-MSNPs on miR-221	150
5.7 Effects of PNA-TMZ-MSNPs on apoptosis of glioma T98G cells	151
5.8 Conclusion	155
5.9 Experimental section	155
6. Biodegradable hybrid core/shell silica nanospheres for protein encapsulation and intracellular delivery	163
6.1 Protein encapsulation and intracellular delivery	163
6.2 Core/shell capsules fabrication and characterization	166
6.3 Breaking the shell: kinetics and delivery properties	170
6.4 Live cell distribution	177
6.5 Intracellular delivery: anticancer activity	183
6.6 Conclusion	187
6.7 Experimental section	187
7. PNA-modified photonic crystal fibers as label-free DNA biosensors for the detection of single-point genetic mutations	197
7.1 Photonic crystal fibers for sensing applications	197
7.2 Fabrication of PNA-modified Photonic Crystal Fibers	201
7.3 Nanoparticle-enhanced DNA detection	204
7.4 Conclusion	207
7.5 Experimental section	208
8. Detection of unamplified genomic DNA by a PNA modified photonic crystal fiber optofluidic system	214
8.1 PNA-functionalized Large Mode Area Photonic Crystal Fibers	215
8.2 Optical detection of genomic DNA and statistics analysis	217
8.3 Finite element method simulation	221
8.4 Conclusion	223
8.5 Experimental section	224
9. Tweezer-like Dual-Pyrene PNA as fluorescent switching probe for selective nucleic acid detection	230
9.1 Molecular probes for analytical nucleic acid recognition	230
9.2 Design and Synthesis of a double-pyrene-modified PNA monomer	235
9.3 Studies on fluorescence properties	241
9.4 Synthesis of a PNA-based switching probe	243
9.5 Detection of target nucleic acid by fluorescence emission switching	246
9.6 Studies on stability of PNA(py-py):DNA duplexes	251
9.7 Conclusion	252
9.8 Experimental section	252

10. Instrumental techniques	
10.1. Scanning electron microscopy (SEM)	265
10.2 Transmission electron microscopy (TEM)	267
10.3 Dynamic light scattering (DLS)	268
10.4 Zeta potential	270
10.5 Confocal Microscopy	272
10.6 Electrospray-Mass Spectrometry (ESI-MS)	274
10.7 Electrostatic Trap “Orbitrap”	275
11. Summary	279
Acknowledgments	284
Curriculum Vitae	288

Résumé

Le développement de matériaux hybrides, obtenus par combinaison de matériaux inorganiques avec des molécules organiques, a ouvert une nouvelle voie au développement de systèmes innovants possédant des architectures complexes et des fonctions particulièrement intéressantes^[1-3]. Les futures générations de matériaux hybrides trouveront certainement des applications dans de nombreux domaines, de l'optique à l'électronique en passant par la biologie et la médecine^[4]. Cette approche offre l'avantage de modifier les parties inorganique et organique pour éventuellement réaliser des systèmes multifonctionnels *ad hoc*. Ce concept est très intéressant lorsque des biomolécules sont couplées à des matériaux spécifiques permettant le développement d'outils ayant des propriétés uniques pour des applications biomédicales, à l'interface entre la chimie des matériaux et la biologie. Dans ce contexte, ce travail de thèse s'est concentré sur le développement de nouveaux types de matériaux hybrides bio-fonctionnels pour des applications dans des domaines tels que les nanotechnologies, la nanomédecine et la biodétection.

Les nanotechnologies sont un domaine en pleine expansion qui tend à développer des matériaux fonctionnels de l'ordre du nanomètre (1 à 100 nm) et ayant des propriétés électroniques, optiques ou encore magnétiques uniques^[5-7]. La taille, la forme, la composition chimique ainsi que l'organisation à l'échelle nanoscopique sont des paramètres critiques à considérer lors de l'étude des propriétés des nanomatériaux et de leurs interactions avec leur environnement. Le concept général du projet consiste en la synthèse ou l'assemblage du matériau inorganique dans une composition, une forme et une taille bien définies tandis que des propriétés supplémentaires pourront être introduites *via* notamment la modification de la surface du matériau. Les nanoparticules sont particulièrement intéressantes pour des applications biomédicales car leur taille est comparable à celle de nombreuses variétés de biomolécules. De plus, leur taille est de plusieurs ordres de magnitude plus petite que les cellules eucaryotes. Ces propriétés permettent au matériau d'avoir des interactions spécifiques avec des biomolécules mais aussi une internalisation facile dans les cellules^[8-10]. De plus, certains de ces matériaux peuvent être développés avec des composés biocompatibles. L'aspect le plus intéressant est que plusieurs molécules peuvent être combinées sur un seul type de nanoparticule. De nombreuses fonctions peuvent ainsi être introduites sur le même système, permettant ainsi de combiner une grande quantité de composés dans un espace confiné. Cette approche rend possible l'utilisation de la chimie couche à couche pour

fonctionnaliser des nanomatériaux à des fins biomédicales ^[11,12]. Parmi les différentes classes de nanoobjets, les nanocontainers semblent être très intéressants pour des applications en médecine. Cet intérêt s'explique par leur faculté à encapsuler un large panel de molécules comme des protéines, enzymes, peptides, principes actifs ou encore des molécules fluorescentes ^[13-16]. La molécule ainsi encapsulée est protégée des dégradations chimiques et biologiques, mais aussi de possibles interactions non désirées avec l'environnement *in vivo* ou *in vitro*. De plus, ces nanocontainers peuvent permettre une libération contrôlée et durable de la molécule ^[17-18]. Enfin, une modification de surface est aussi possible permettant de créer des outils multifonctionnels capables de servir à des fins de diagnostic, d'imagerie et de traitement ^[19-21]

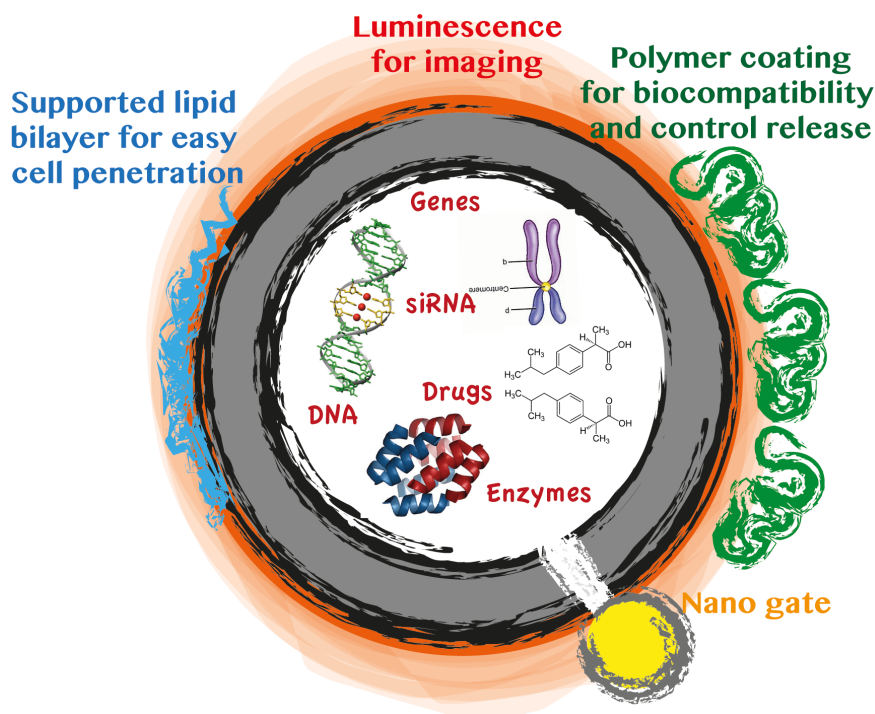


Fig. 1 Représentation schématique d'une nanoparticule poreuse adaptée aux applications biomédicales. Les cavités sont remplies de molécules hôtes. La surface est modifiée afin d'optimiser la biocompatibilité. Les pores peuvent être conçus de telle sorte que le relargage du cargo se produit de manière contrôlée. Image provenant de H. Luelf, A. Devaux, E.A. Prasetyanto, L. De Cola, *Porous nanomaterials for biomedical applications*, in *Organic Nanomaterials: Synthesis, Characterization, and Device Applications*, Wiley, 2013, Ch. 22. Copyright © 2013 John Wiley & Sons, Inc. All rights reserved.

Un design précis des nanosystèmes, pour les rendre capables d'apporter des molécules bioactives à l'intérieur de cellules vivantes, est un objectif intéressant. La reconnaissance de séquences moléculaires spécifiques par des analogues d'oligonucléotides comme les acides nucléiques peptidiques (ANP), ou la transfection d'acides nucléiques fonctionnels (plasmide

d'ADN ou siRNA) devient accessible par cette stratégie. La première partie des travaux de cette thèse montre donc le premier exemple de l'utilisation de cristaux de zéolite-L comme nanovecteurs multifonctionnels capables de transporter à la fois des molécules organiques mais aussi de l'ANP ou de l'ADN dans des cellules vivantes, permettant de construire des matériaux hybrides et/ou des plateformes de transport. La zéolite-L est un exemple de la classe des matériaux poreux à base d'aluminosilicate appelé zéolite. C'est une zéolite synthétique possédant une symétrie hexagonale [22]. La structure est construite de sorte à ce qu'un système de « tunnels » unidimensionnels (formés par des pores) soit parallèle à l'axe c. L'entrée des pores, qui correspond aussi au diamètre le plus petit du pore est de 0.71 nm. La taille la plus grande du pore est de 1.26 nm et la longueur d'une unité est de 0.75 nm (Fig. 2). Le contrôle de la taille, de la morphologie et de l'aspect sont obtenus par la modification des conditions opératoires, même à une échelle nanoscopique. Pour utiliser la zéolite-L comme matériaux fonctionnel, les cristaux peuvent être fonctionnalisés par l'introduction de différents groupes fonctionnels à la surface du cristal, mais aussi par l'introduction des différentes molécules hôtes à l'intérieur des pores [23-24].

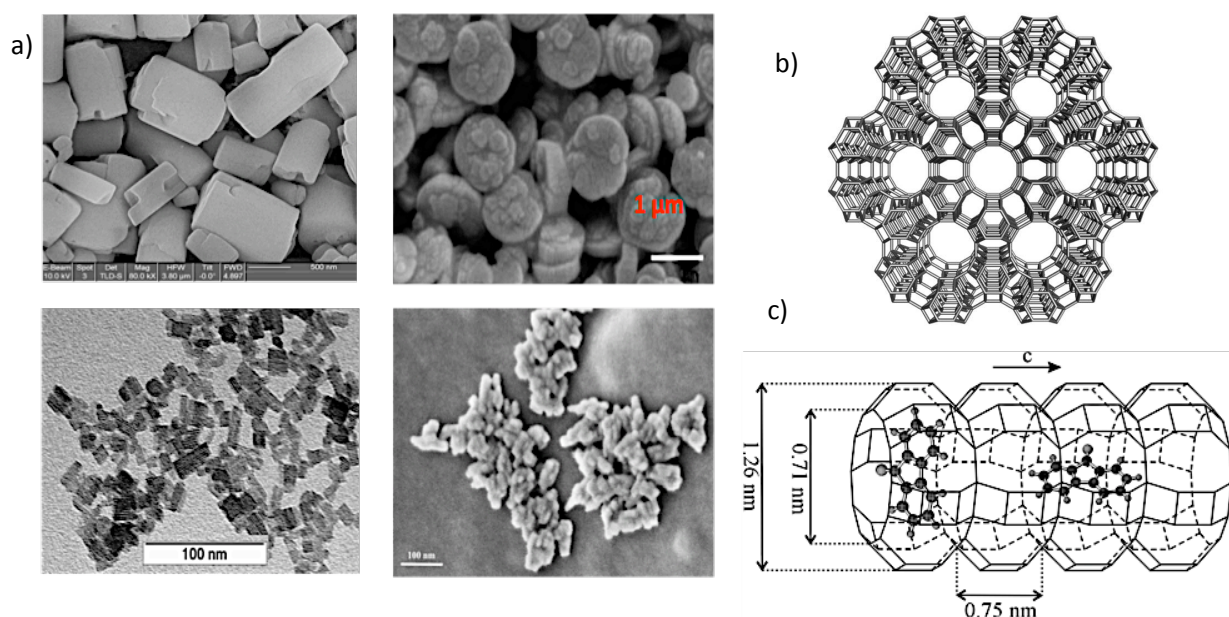


Fig. 2: a) Exemples de différentes morphologies de zéolite-L synthétique; b) Vue d'une zéolite-L selon l'axe c. Les pores sont orientés de manière hexagonale; c) Représentation d'un « tunnel » montrant le diamètre à l'entrée, le diamètre et la longueur.

En détail, des nanocristaux de zéolite-L ont été fonctionnalisés de manière covalente par de l'ANP à la surface et une molécule fluorescente à l'intérieur des pores permettant à la fois de suivre les cristaux et aussi d'étudier les propriétés de relargage à l'intérieur des cellules. Les ANP sont des analogues d'oligonucléotides où le squelette sucres-phosphate est remplacé par

Les expérimentations cellulaires ont été menées sur des cellules humaines du cancer de l'utérus (HeLa). Une internalisation très rapide des zéolites fonctionnalisées avec de l'APN a été observée. Après seulement un temps d'incubation d'une heure, une importante concentration de particule a pu être observée à l'intérieur des cellules par microscopie confocale (Fig. 4, gauche, A-C). L'augmentation du temps d'incubation permet d'augmenter considérablement la concentration de molécule à l'intérieur des cellules (Fig 4, gauche, G-I). Dans les différents cas, la distribution des particules est la même dans tout le cytoplasme. En tenant compte que l'ANP possède une très mauvaise aptitude à franchir la barrière cellulaire, cette approche se montre comme une voie simple et directe pour l'introduire à l'intérieur des cellules. La possibilité de combiner l'activité de l'oligonucléotide avec un principe actif qui pourrait être libéré de la zéolite après dégradation de la couche de PLL a aussi été étudiée. Du DAPI a été utilisé comme molécule modèle car un signal de luminescence est émis après migration dans le noyau cellulaire, là où les nanoparticules ne peuvent pas entrer. Des expérimentations sur des cellules ont montré qu'après 4 heures d'incubation, une quantité non négligeable de DAPI a pu être observée dans le noyau. En effet, la libération du DAPI peut avoir lieu car le PLL a été dégradé et donc les pores sont maintenant ouverts permettant au DAPI de sortir de la zéolite. Ce relargage est plus important lorsque le temps d'incubation a été augmenté jusqu'à 24h, les noyaux sont alors totalement marqués (Fig. 4, droite).

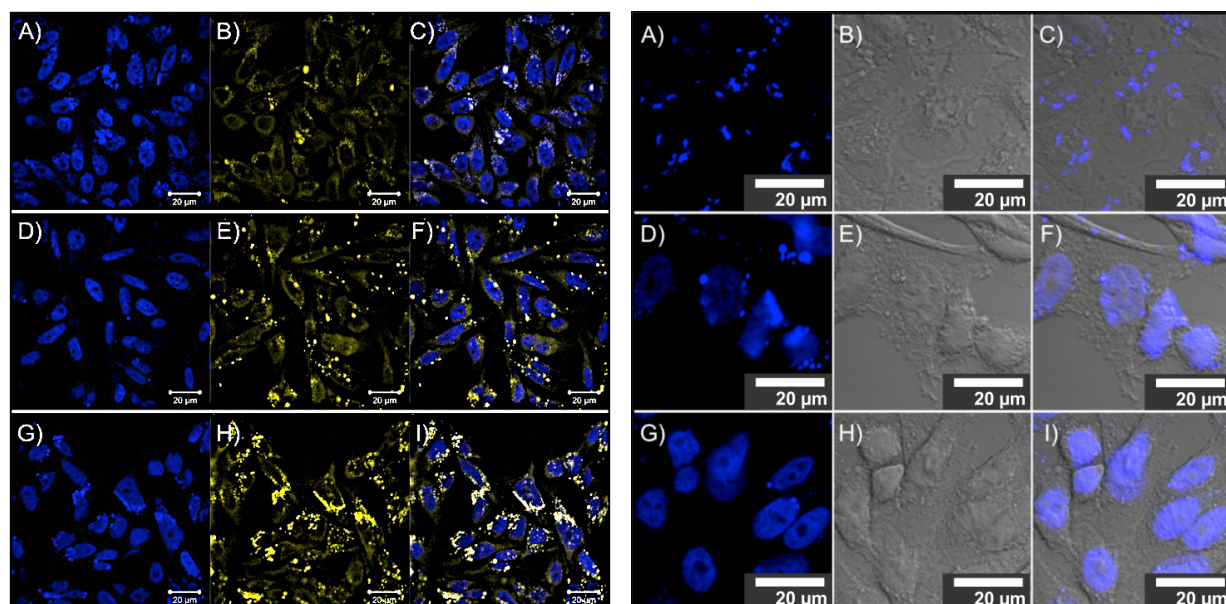


Fig. 4: Gauche) microscopie confocale de cellules HeLa incubées avec PLL-PNA-DXP-zeolites pendant 1 heure (A, B, C), 4 heures (D, E, F) et 24 heures (G, H, I). A, D, G) le noyau est marqué par du DAPI; B, E, H) le signal jaune du DXP permet de localiser les nanoparticules dans la cellule; C, F, I) superposition. Droite) images des cellules incubées avec PLL-PNA-DAPI-zeolites pendant 1 heure (A, B, C), 4 heures (D, E, F) et 24 heures (G, H, I). Le signal bleu est toujours le DAPI.

Ces résultats montrent que cette voie permet d'introduire des séquences spécifiques d'APN dans les cellules combiné à une libération de principes actifs. Nous avons aussi réalisé un système en utilisant des séquences d'ANP ciblant des microARN spécifiques impliqués dans la prolifération de certaines tumeurs (en particulier, le miR-210 et le miR-221). Une plateforme similaire fonctionnalisée avec des ANP cationiques, qui n'exigent pas l'utilisation de PLL pour améliorer l'internalisation cellulaire, a aussi été envisagée. Tous ces nanosystèmes devront être testés par des expérimentations biologiques *ad hoc*.

En utilisant une approche similaire, il a été aussi démontré que des zéolites remplies avec une petite molécule modèle et possédant des oligonucléotides d'ADN adsorbés par interactions électrostatiques peuvent être utilisées pour faire de la transfection. Plus particulièrement, il a été montré une libération simultanée de DAPI et d'ADN (marqué par une molécule de cyanine5 (Cy5) émettant dans le rouge). Pour la première fois, des expérimentations cellulaires spécifiques ont été effectuées pour suivre la cinétique de libération des deux molécules dans les cellules et pour localiser les nanocontainers par microscopie confocale. Les deux émissions, bleu et rouge, peuvent être suivies indépendamment l'une de l'autre donnant ainsi des informations sur le devenir des composants à l'intérieur de la cellule. En détail, une molécule fluorescente soluble dans l'eau (le DAPI) a été introduite dans un premier temps à l'intérieur des pores de la zéolite. La surface du matériau, fortement chargée négativement, a été fonctionnalisée avec du (3-aminopropyl)triéthoxysilane (APTES) permettant d'avoir des charges positives à la surface pour favoriser une interaction électrostatique entre l'ADN et la surface des particules. Le nouveau matériau a été caractérisé par SEM, DLS, potentiel zeta et par microscopie confocale, permettant de localiser au même temps le signal du DAPI (à l'intérieur des pores) et de l'ADN (sur la surface).

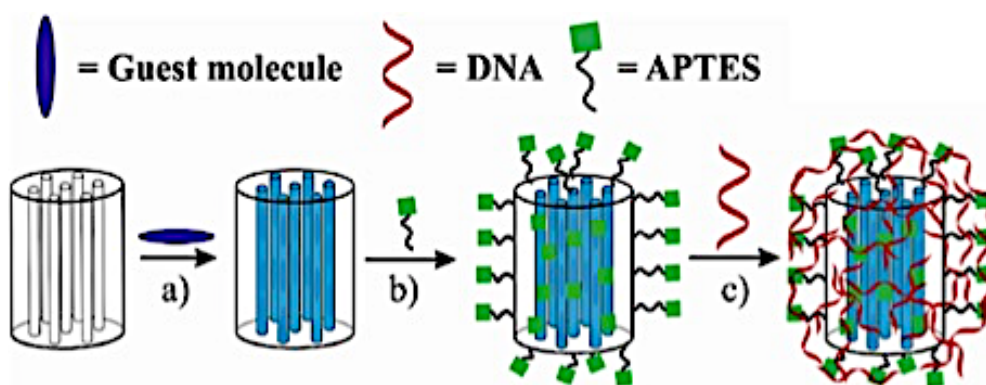


Fig. 5 Plan représentant les étapes de fonctionnalisation pour obtenir le matériau zéolite final rempli de DAPI et modifié par de l'ADN adsorbé sur la surface.

La quantité d'ADN sur la surface de la zéolite a été déterminée par une méthode UV-Vis^[30], fournissant une valeur de 8,6 nmol d'ADN par mg de zéolite. Nous avons aussi observé que l'introduction de l'ADN sur la particule permet de fermer les pores de la zéolite empêchant la libération des molécules présentes à l'intérieur. Une fois l'ADN détaché de la particule, les pores sont alors ré-ouverts permettant le relargage de la molécule hôte. De ce fait, nous avons étudié le relargage simultané d'ADN et de DAPI par microscopie confocale. De plus, les filaments d'actine ont été marqués avec de l'Alexa Fluor® 568 Phalloïdin après fixation des cellules, car son émission ne se superpose pas avec les émissions du DAPI et de Cy5. Les résultats sont montrés dans la figure 5. Après 1 heure, quelques particules sont internalisées et l'ADN est toujours fixé à la surface des particules, car les émissions du DAPI et de Cy5 sont superposées (Figure 6A-D). La captation des particules augmente après 4 heures d'incubation et un premier marquage du noyau, due à un relargage du DAPI dans la particule, est observé (Figure 6E-H). Cela est possible après le détachement de l'ADN de la surface des zéolites (voir le signal rouge diffus par le cytoplasme, Fig. 6G), permettant d'ouvrir les pores et donc de libérer le DAPI emmagasiné dans la zéolite. Après 24h, nous avons pu observer une intense fluorescence du DAPI dans le noyau ainsi qu'un fort signal de l'ADN dans le cytoplasme (Figure 6I-L).

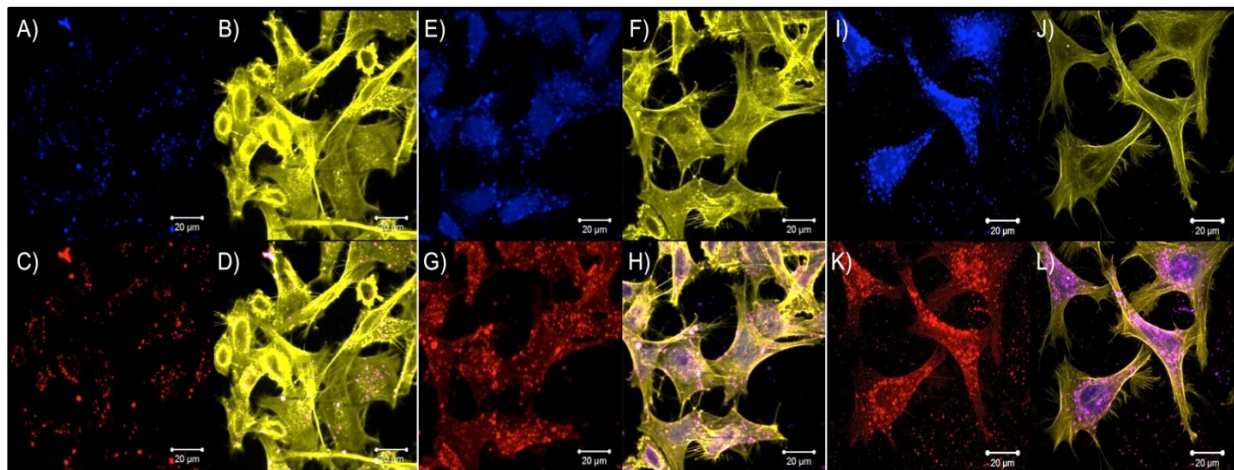


Fig. 6 Imagerie confocale montrant l'internalisation de zeolite-L remplie de DAPI et modifiée par de l'AND par des cellules HeLa. A-D) 1 heure d'incubation; E-H) 4 heures d'incubation; I-L) 24 heures d'incubation. A, E, I) fluorescence du DAPI; B, F, J) émission d'Alexa Fluor® 568 Phalloïdin; C, G, K) fluorescence du Cy5-ADN; D, H, L) superposition.

Dans les expériences décrites ci-dessus, l'augmentation de la concentration en DAPI dans le noyau et de l'ADN dans le cytoplasme sont obtenus par deux mécanismes indépendants : dans

un premier temps le DAPI et l'ADN sont continuellement relargués de la zéolite, ce qui conduit à augmenter leur concentration au fil du temps. Mais d'un autre côté, à cause de temps d'incubation différents, la concentration en particule augmente à l'intérieur de la cellule [31] et, par conséquent, un accroissement de la concentration de l'ADN et du DAPI dans la cellule est observé. Ainsi, une étude plus poussée a été menée pour comprendre la cinétique de relargage. La concentration en particule à l'intérieur des cellules a été maintenant constante pendant plus de 72h. Un relargage lent de DAPI et d'ADN de la zéolite est observé et ensuite un fort signal provenant du DAPI (dans le noyau) et de l'ADN (dans le cytoplasme) a pu être observé après 24, 48 et 72 heures d'incubation, ceci montrant les propriétés de relargage du système. Comme montré avec d'autres types de particule, nous nous attendions à observer une accumulation des cristaux dans les lysosomes [32-34]. Pour montrer cette hypothèse, nous avons marqué le lysosome après 72h avec une molécule fluorescente verte Lysotracker Green DND-26 et avons cherché la superposition de cette émission avec le DAPI résiduel venant des particules.

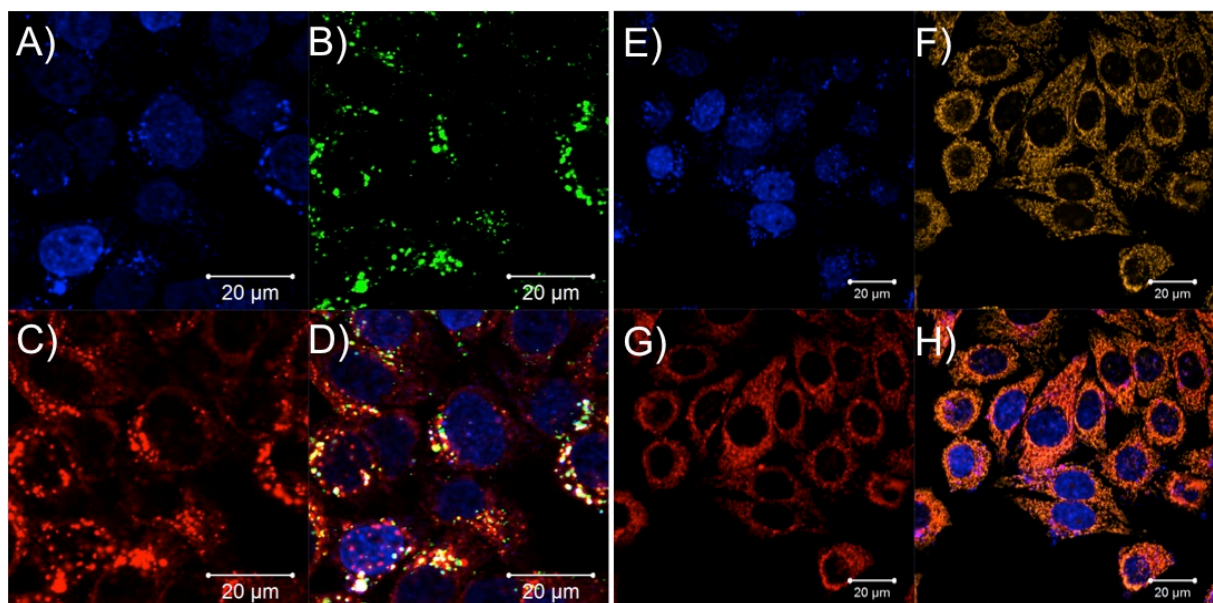


Fig. 7 Imagerie confocale montrant la localisation des particules dans le lysosome (A – D) et de l'ADN dans les mitochondries (E – H). A, E) émission du DAPI; B) marqueur du Lysosome; F) marqueur des Mitochondries; C, G) Fluorescence de Cy5; D, H) superposition.

Les figures 7A-D montrent clairement une très bonne superposition des 2 signaux (coefficient de co-localisation = 0.86). Ceci tend à prouver que les particules s'accumulent dans les lysosomes. Nous avons déterminé aussi la localisation intra cellulaire de l'ADN libéré. Comme montré dans des expérimentations *in vitro* rapportées dans la littérature, l'ADN tend à

migrer vers les mitochondries ^[35-36] et ainsi nous avons étudié s'il était possible d'observer la même tendance pour notre système. Ainsi, nous avons marqué les mitochondries avec un marqueur émettant dans le jaune-orange MitoTracker Orange, comme montré dans les figures 7E-H. Une très bonne superposition (coefficient de co-localisation = 0.91) du signal de l'ADN avec celui du marqueur des mitochondries a été observée, prouvant qu'après le détachement de la zéolite, l'ADN migre dans la mitochondrie. Ainsi, notre système multifonctionnel pourrait devenir un prototype pour le développement d'une nouvelle classe de particule pour le relargage simultané d'oligonucléotides et de molécules organiques. La combinaison d'un plasmide d'ADN ou de SiARN avec un principe actif pourrait être particulièrement intéressante pour le traitement de différents types de cancer.

Toujours dans le domaine de la nanomédecine, une partie de ce travail de thèse a été menée pour développer des nanoparticules de silice mésoporeuses (MSNPs) multifonctionnelles. Des récentes avancées pour la synthèse de nanoparticules à base silice mésoporeuse ont montré qu'il est possible de contrôler la taille des particules, la morphologie, la porosité ainsi que la stabilité chimique. Cela rend les matrices à base de silice très attractives pour une grande variété d'applications en nanotechnologie, surtout pour des applications en drug delivery, thérapie génique, ou encore imagerie ^[34,37-38]. Les matériaux de silice mésoporeux, composés d'une structure poreuse avec des centaines de pores vides (mésopores), sont capables d'absorber/encapsuler des quantités relativement importantes de molécules bioactives. Des propriétés uniques, comme une grande surface, un important volume de pore, la possibilité de contrôler la taille des pores et aussi leur bonne stabilité thermique et chimique, les rendent attractives pour des applications de "drug delivery".

Ici, les MSNPs, qui ont une taille d'environ 100 nm de diamètre, sont synthétisés par une voie sol-gel utilisant un surfactant comme agent pour la formation des pores ^[39]. Un marqueur fluorescent (Cyanine 5) a été introduit directement dans la structure en silice des nanoparticules lors de la synthèse. Le nouveau matériau a été complètement caractérisé par SEM, TEM, SAXS, potentiel zeta et microscopie par fluorescence (les images SEM et TEM images sont reportés en Fig. 8).

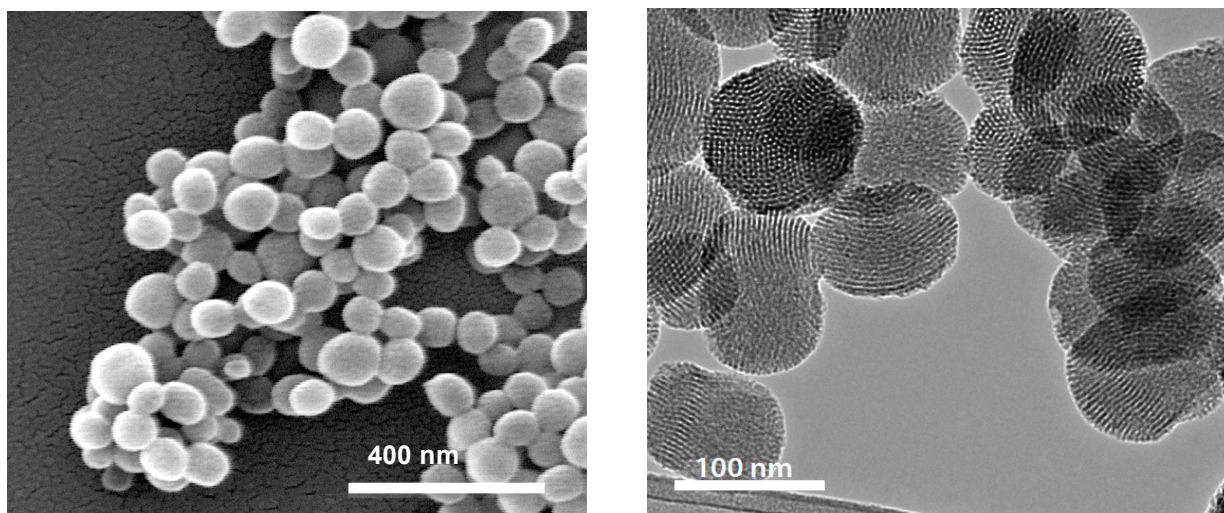


Figure 8. Gauche) image SEM des MSNPs ; droite) image TEM qui montre le système de pores à l'intérieur.

Ces MSNPs ont été utilisées comme système pour combiner l'administration d'un principe actif et une thérapie génique et ainsi traiter des tumeurs cérébrales grâce à un effet synergique des deux mécanismes. Après l'enlèvement du surfactant et ainsi la formation des pores vides, la Temozolomide (TMZ), médicament généralement utilisé pour traiter les tumeurs au cerveau ^[40], a été introduit à l'intérieur des pores. Une séquence d'ANP cationique (8R-ANP221, conjuguée avec huit unités d'arginine) ciblant le miR-221, dont la surexpression est impliquée dans la prolifération de différents types de tumeurs ^[41-43], a été adsorbée à la surface fonctionnalisée des nanoparticules.

Le miR-221 est impliqué dans la régulation de plusieurs gènes clés pour le métabolisme cellulaire, parmi lesquels l'ARNm $p27^{kip1}$ qui semble être l'un des plus intéressants. En effet, la protéine correspondante est un élément régulateur capable de moduler l'activité du complexe cycline-CDK, et donc la progression du cycle cellulaire ^[44]. Le knock-down de ce miR-221 peut potentiellement déclencher la régulation du $p27^{kip1}$ à la hausse ^[45]. Il a été également montré que la down-régulation du miR-221 permet la sensibilisation des gliomes au traitement avec la temozolomide. Ceci permet d'envisager une stratégie médicale où la thérapie génique et l'administration de l'agent de chimiothérapie pourraient être couplées ^[46]. La procédure complète de la synthèse du nano système est décrite en détails dans la Figure 9. La charge en temozolomide (environ 17% en masse) ainsi que l'adsorption d'APN sur la surface de la particule (environ 15 $\mu\text{g}/\text{mg}$ MSNPs) ont été déterminées par spectroscopie UV-Vis.

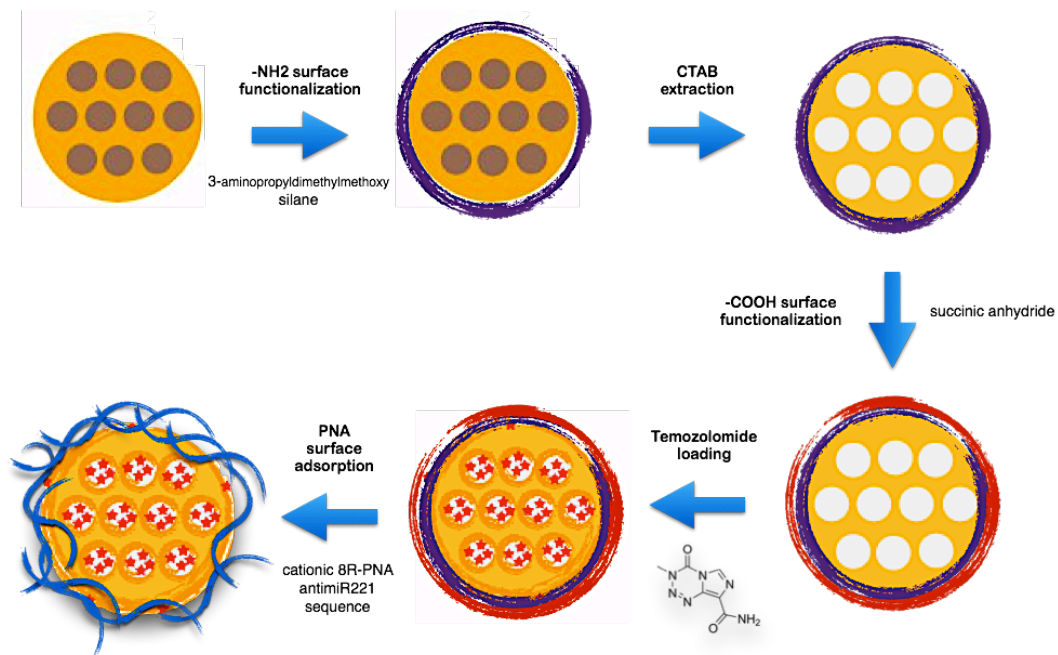


Fig. 9 Représentation schématique des étapes de fonctionnalisation permettant l'accès au matériau final.

Le suivi du signal du fluorophore Cy5, intégré à la structure des MSNPs par microscopie confocale ainsi que le z-stack après 1, 4 et 24h ont permis de vérifier l'internalisation des nanoparticules dans le cytoplasme des cellules gliales. Des tests de viabilité ont été menés pour déterminer l'activité cytotoxique du nano système sur les cellules cancéreuses C6, qui constituent une espèce très représentée dans les tumeurs cérébrales. Une diminution significative de la viabilité cellulaire a été obtenue pour les cellules traitées avec le système ANP-TMZ-MSNPs, jusqu'à environ 20% après 48h d'incubation (échantillon de contrôle : 88%). Devant ces résultats préliminaires encourageants, d'autres expérimentations biologiques sur l'apoptose cellulaire et la diminution de la biodisponibilité du miR-221 ont été menées sur une lignée cellulaire humaine gliale T98G.

Les résultats obtenus montrent que, tout d'abord, l'ANP relâché de la surface des MSNPs est encore parfaitement capable de cibler le miR-221 complémentaire. La très petite différence obtenue par rapport à l'ANP de contrôle est attribuée à la libération retardée de l'ANP de la surface des nanoparticules (Fig. 10A). Les expérimentations menées sur les cellules à également montré l'induction d'apoptose grâce au nano système. Ainsi, nous avons démontrés qu'un effet thérapeutique peut être sensiblement amélioré (Fig. 10B).

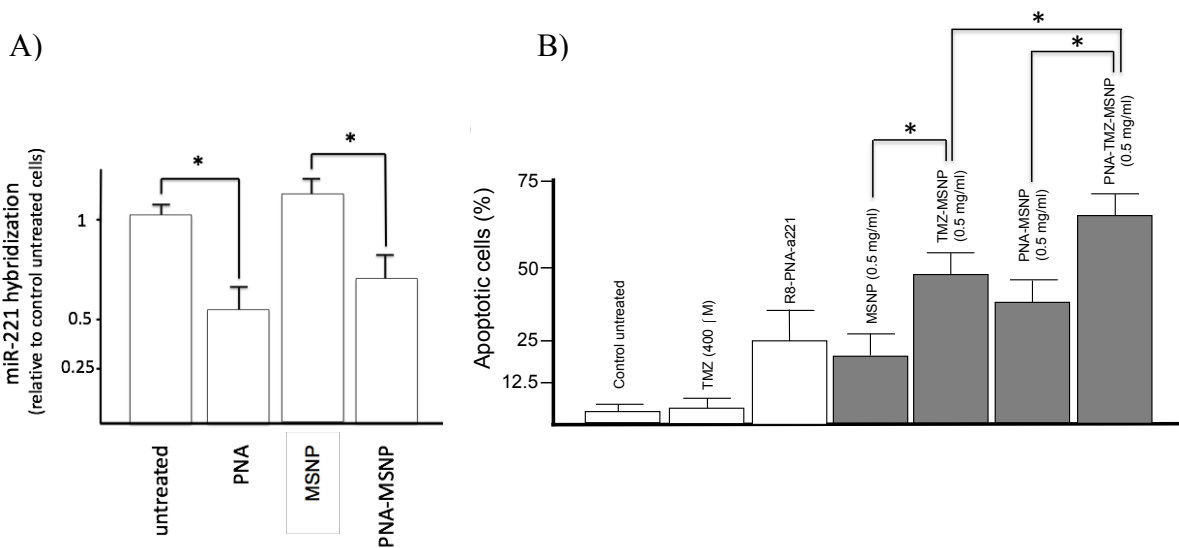


Fig. 10 A) Niveaux de miR-221 dans les cellules T98G traitées avec ANP-MSNPs. Les cellules ont été cultivées pendant 48h en présence de 0.25 mg/ml MSNPs, 0.25 mg/ml ANP-MSNPs et 1 μ M 8R-ANP221 ; ensuite l'ARN a été extrait et qRT-PCR a été menée à identifier le niveau du miR-221. B) Graphique de synthèse comprenant l'induction d'apoptose obtenue en traitant les cellules T98G en différentes conditions, qui montre l'effet amélioré fourni par le système ANP-TMZ-MSNP.

Ceci met en évidence la possibilité réelle d'exploiter la combinaison d'un relargage durable d'un principe actif par une plateforme mésoporeuse avec une approche basée sur la thérapie génique, en particulier pour traiter une tumeur agressive comme le glioblastome.

Une approche basée sur les nanotechnologies à architectures complexes a aussi été étudiée pour la réalisation d'une nanoparticule hybride organique/inorganique qui permettrait d'encapsuler des enzymes dans une matrice de silice biodégradable. L'encapsulation de macromolécules bioactives avec des matrices inorganiques est actuellement un sujet brûlant car cela permet de protéger des espèces fragiles et sensibles à un environnement extérieur pour d'éventuelles applications dans le domaine de la biotechnologie^[47-50].

L'administration de protéines dans des cellules vivantes pour différentes applications constitue en effet un objectif important à cause de nombreuses contraintes comme la difficulté pour certaines espèces de franchir la membrane cellulaire, la fragilité des enzymes qui conduit à leur dégradation ou encore leur trop grande toxicité pour être injectés directement *in vivo*. Ainsi, l'objectif de ce projet consiste à créer un nouveau système où un effet positif serait obtenu grâce à l'encapsulation de protéines dans une paroi protectrice tout en augmentant les propriétés d'internalisation dans les cellules vivantes.

En détails, différentes protéines (Cytochrome C, Green Fluorescent Protein, Human TRAIL Apo2, Onconase) ont été encapsulées par une technique de micro émulsion inverse avec une coque hybride de silice dégradable, contenant des ponts disulfures dans sa structure. La

présence de ces ponts disulfures rend la paroi dégradable vis-à-vis de stimulus comme l'action d'agents réducteurs (présents, par exemple, dans le cytoplasme des cellules, et à hautes concentrations dans les cellules tumorales), permettant ainsi le relargage de la protéine suite à la rupture de la coquille. Des mesures par SEM ont montré la formation de nanoparticules sphériques bien définies d'une taille allant de 50 à 100 nm et l'analyse au TEM a permis de visualiser la structure core/shell des nanoparticules.

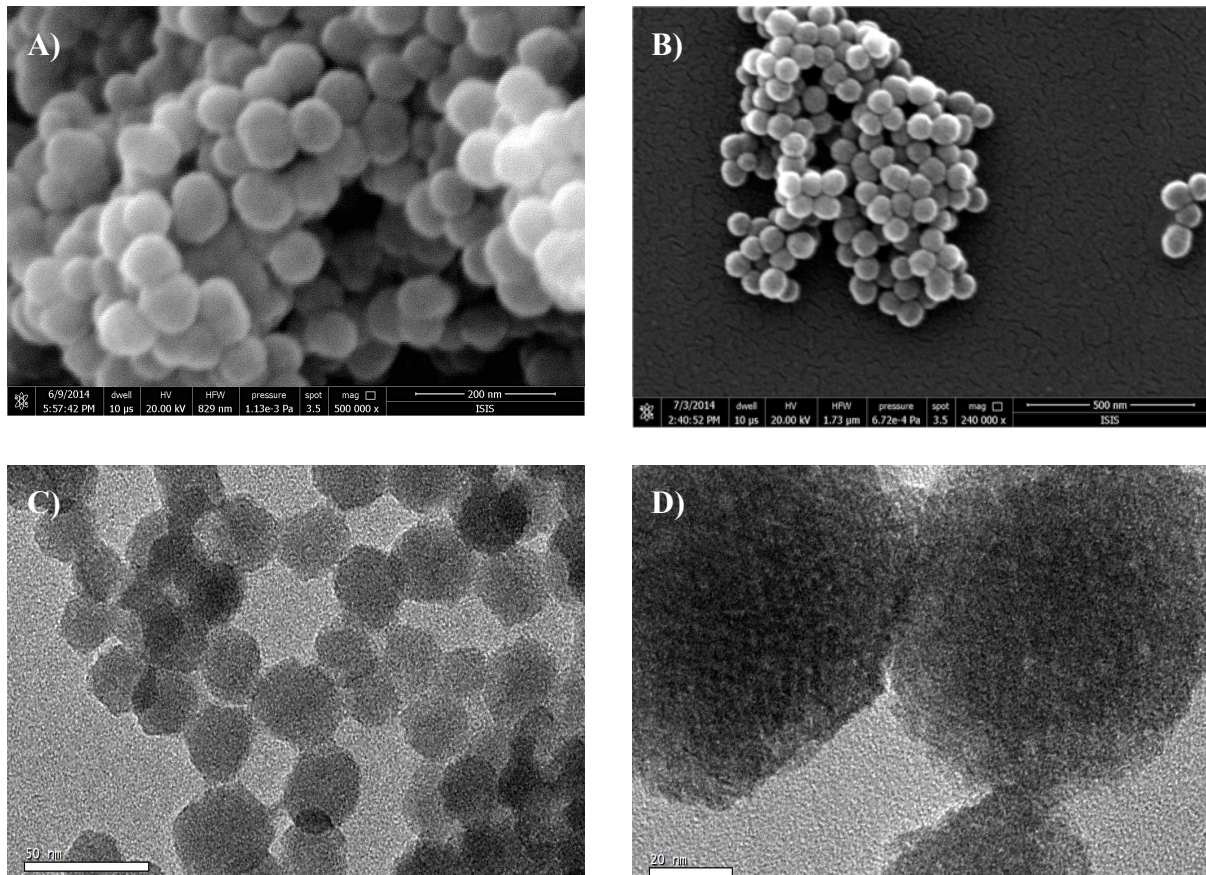


Fig. 11 A) Image SEM des nano capsules contenant molécules de Cytochrome C ; B) image SEM de nano capsules contenant de la GFP; C) Image TEM des nano capsules contenant le Cytochrome C ; D) HR-TEM montrant la structure core/shell des nano sphères.

Pour étudier la dégradation de la paroi de silice et le relargage de la protéine, des particules hybrides contenant du Cytochrome ont été incubées avec différents agents réducteurs. Le surnageant a été analysé par spectroscopie UV-Vis pour montrer la présence de l'enzyme libéré dans la solution. Pour comparer les résultats, le même Cytochrome C a été encapsulé dans une coquille ne contenant pas de ponts disulfure (seulement de la silice) et traité de la même façon avec des agents réducteurs. La Figure 12B montre clairement que l'enzyme est relâché seulement dans le cas des nanoparticules dégradables. Parallèlement, le phénomène de

dégradation de la coquille en environnement réducteur a été étudié via TEM, comme reporté en Figure 12C et 12D.

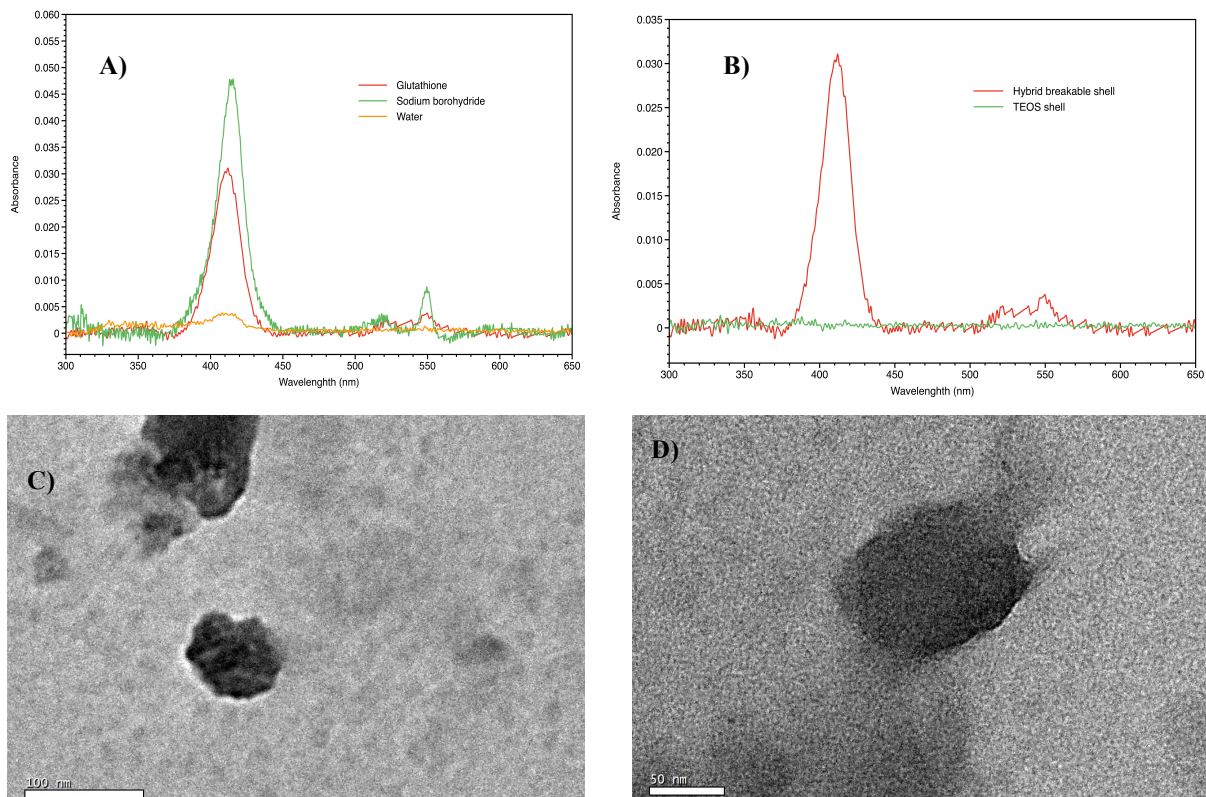


Fig. 12. A) Spectre UV-Vis du surnageant après traitement des particules dégradables contenant Cytochrome C avec respectivement NaBH_4 , glutathion et seulement de l'eau; B) spectre UV-Vis du surnageant après traitement avec du glutathion pour les particules à paroi dégradables et non dégradables; C) Image TEM qui montre dynamiquement la destruction de la coquille hybride; D) Une particule totalement déformée après l'action de l'agent réducteur.

Pour montrer qu'une fois les protéines libérées, elles possèdent encore leur activité enzymatique, TRAIL Apo2 Ligand et Onconase (des espèces très cytotoxiques qui présentent une bonne activité anti-tumorale^[51,52]) ont été encapsulées dans la nanoparticule dégradables et incubées avec des cellules cancéreuses de mammifère. Les tests de viabilité cellulaires ont effectivement montré une diminution drastique de la quantité de cellules lorsque celles-ci sont traitées avec le matériau dégradables. Aucun effet cytotoxique n'a pu être observé sur les cellules (comparé à l'échantillon de référence) pour la même protéine mais cette fois encapsulée dans une nanoparticule de pure silice. Ces résultats donnent des indications intéressantes concernant la dégradation de la particule, le relargage des protéines encapsulées dans les cellules, mais surtout sur la conservation de l'activité enzymatique. Afin d'investiguer et, si possible, visualiser le phénomène de rupture de la coque et le relargage du

cargo dans les cellules, des expérimentations par microscopie confocale ont été menées en suivant le signal en fluorescence de GFP encapsulée lors de l'incubation avec les cellules. De façon intéressante, après 24h d'incubation, nous avons pu constater qu'un signal vert diffus se trouve dans le cytoplasme, en combinaison avec de plus grands agrégats qui indiquent, très probablement, la présence de nanoparticules intactes. Donc, pour mieux investiguer la distribution de l'émission en fluorescence dans les cellules, des mesures de co-localisation ont été menées en marquant les lysosomes avec un marqueur spécifique, pour étudier la superposition de ce signal avec celui de la GFP.

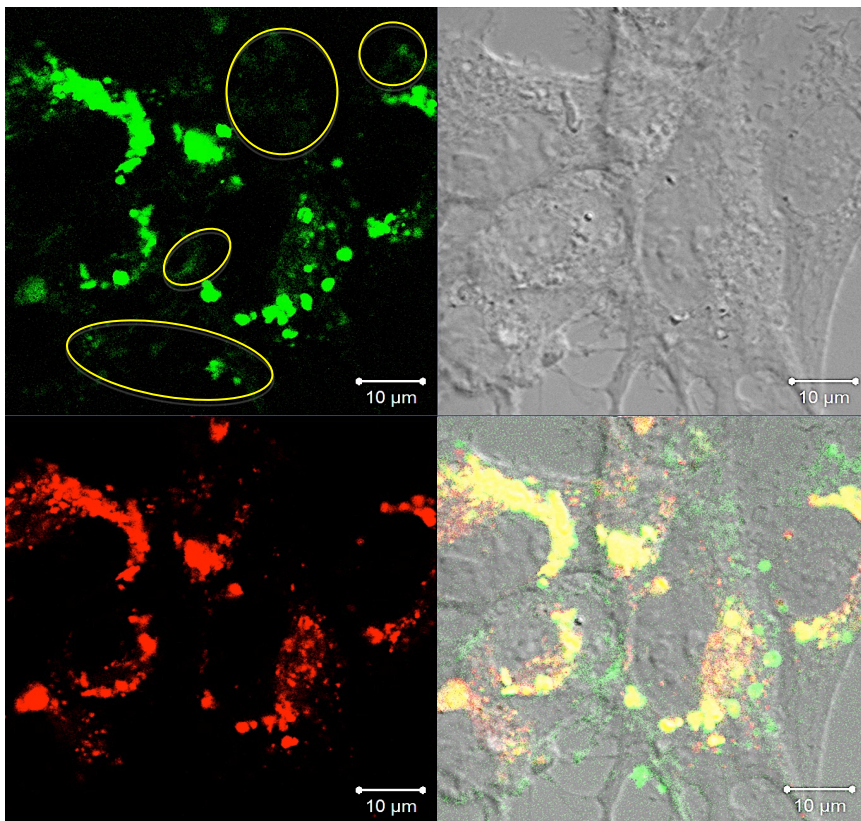


Fig. 13 Imagerie confocale montrant la localisation des particules dans les cellules C6 gliome. A) Signal fluorescent de la GFP ; B) Image *brightfield* ; C) marquage des lysosomes ; D) superposition. Les cercles jaunes dans le panneau A soulignent le signal GFP qui n'est pas co-localisé.

Comme montré en Figure 13, la majeure partie des gros agrégats semble localisée dans les lysosomes, suggérant que ce signal est celui de la GFP encore encapsulée dans des coques intactes piégées dans le lysosome. Ce qui est intéressant est le fait que l'émission verte de la GFP est aussi enregistrée comme un signal diffus dans certaines régions du cytoplasme, sans aucune co-localisation spécifique avec les lysosomes (voir les zones entourées en jaune en

Fig. 13A et les régions vertes en Fig. 13D). Cette émission diffuse peut être considérée comme une bonne indication de la présence de GFP qui a été effectivement relâchée des particules et des lysosomes après la dégradation de la coquille protectrice, et qui s'est diffusée ensuite dans le cytoplasme. En raison des propriétés décrites précédemment, le système hybride proposé pourrait avoir des applications biomédicales afin de traiter des maladies qui sont causées par un manque ou une pénurie de certaines enzymes.

Néanmoins, les interfaces hybrides organiques-inorganiques n'ont pas seulement pris de l'importance pour le développement de nanomatériaux multifonctionnels, mais ils jouent un rôle de plus en plus important en chimie analytique et en biodétection. De nombreux systèmes utilisant plusieurs techniques de transduction ont été développés, ceci en couplant un matériau avec des biomolécules pour détecter des cibles spécifiques^[53-56]. Ceci est essentiellement vrai pour la détection ultrasensible d'ADN. La partie organique permettant la détection (ANP, oligonucléotides d'ADN, 'DNAzyme', 'molecular beacons') doit être attachée à un bon système de transduction permettant une reconnaissance et une détection spécifique de la séquence d'ADN désirée. En particulier, les systèmes de biodétection optiques sont à présent très étudiés et le domaine de la « biophotonique » semble être très prometteur pour le développement de nouvelles techniques rapides et peu onéreuses pour le diagnostic médical. Les détecteurs à base de fibre optique représentent une nouvelle plateforme offrant l'avantage d'être petits et flexibles. Les fibres à cristaux photoniques (PCFs) ont la particularité unique de présenter une section transversale définie par une série de « trous d'air » qui sont appropriés pour une fonctionnalisation interne^[57-60]. Ces trous sont également utilisés en tant que canaux pour de la microfluidique, ce qui permet de réaliser l'infiltration des échantillons et d'obtenir une modulation du spectre de la lumière transmise, cette dernière étant induite par la liaison que forme l'analyte avec la surface interne modifiée. La détection réalisée dans ces fibres exploite les queues évanescentes du champ électromagnétique des modes assistés : plus la taille de la fraction de ce champ qui se propage en tant qu'onde évanescente est grande, plus l'interaction avec les échantillons placés dans les trous ou absorbés sur la surface du capillaire PCF est forte. De plus, un réseau de Bragg inscrit dans ces fibres laisse l'opérateur travailler en mode réflexion. Cela va permettre (à partir du moment où la longueur d'onde de la lumière réfléchie dépend de l'indice de réfraction effectif n_{eff}) d'obtenir une sensibilité ainsi qu'une technique de lecture du signal standardisée dans la région infrarouge. L'intérieur des canaux a été donc fonctionnalisé de manière covalente par une séquence d'ANP ciblant de l'ADN ayant une mutation impliquée dans la fibrose kystique. Une solution d'ADN contenant la mutation a été introduite dans les canaux du capillaire permettant ainsi une interaction avec

le fragment d'ANP attaché sur la surface des canaux. Une amplification du signal optique a été enfin obtenue grâce à l'addition finale d'une nanoparticule d'or fonctionnalisée avec un oligonucléotide ciblant la région de l'ADN analysé à flanc de celle hybridée avec l'ANP (Fig. 14).

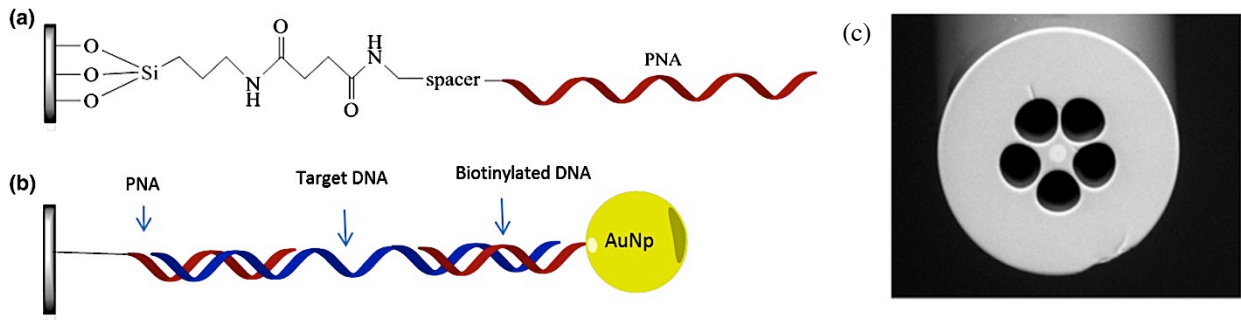


Fig. 14. a) Représentation de l'introduction de la séquence d'ANP à l'intérieur à la surface des canaux; b) vue schématique du système sandwich utilisé pour la détection d'ADN; c) image SEM du PCF 5-trou utilisé pour ce travail.

Les mesures expérimentales ont montré un net décalage de la longueur d'onde du signal réfléchi par le réseau de Bragg en analysant une solution d'ADN à 100 nM ; de plus, des mesures de fluorescence ont confirmées la formation de l'hybride dans les canaux. Des mesures successives ont permis d'obtenir un signal reproductible, suggérant qu'il est possible de réutiliser le détecteur. Des mesures ont aussi été effectuées en utilisant une solution d'ADN à 100 nM possédant une seule base 'mismatch', correspondant au gène naturel sain, et les résultats ont montré une forte sélectivité du détecteur seulement envers la cible mutée (Fig. 15).

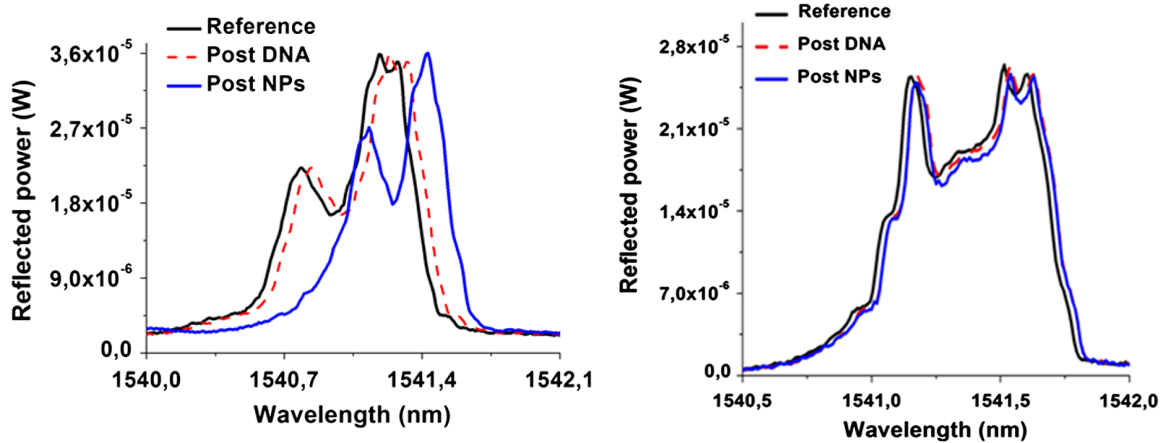


Fig. 15 Gauche) Mesure spectrale enregistrée après le processus d'hybridation en utilisant une solution 100 nM d'ADN complémentaire (ligne rouge) et après l'infiltration des nanoparticules d'or (ligne bleue). Un clair déplacement a été obtenu, dans l'ordre de 0.27 nm. Droite) La même mesure effectuée en utilisant une solution 100 nM d'ADN « single-mismatch ».

Devant ces résultats prometteurs, une approche similaire a ensuite été utilisée pour effectuer la détection ultrasensible d'ADN génomique. Les technologies utilisées de nos jours pour analyser l'ADN génomique se basent généralement sur l'utilisation de séquences marquées spécifiques, en combinaison avec une amplification par une réaction en chaîne par polymérase (PCR). Une méthode de détection directe qui ne nécessiterait pas l'utilisation de PCR et de marquage permettrait une analyse plus rapide, économique et simple de petite quantité d'ADN. Nous avons montré que le système basé sur l'utilisation des fibres à cristaux photoniques permet de détecter de l'ADN à très faible concentration sans utiliser de PCR et de marqueur. Des PCF, contenant 60 micro-canaux et un réseau de Bragg ont été fonctionnalisés avec une séquence d'ANP détectant le soja modifié génétiquement « Roundup Ready » (RR). Le soja RR a été choisi comme modèle pour sa pertinence en analyse agroalimentaire mais aussi car les échantillons d'ADN de la séquence ciblée sont sans ambiguïtés et disponibles comme matériau certifié. Les fibres ont été utilisées encore comme un moyen de détection d'ADN en mesurant le déplacement de la longueur d'onde de la lumière réfléchie. L'amplification du signal optique a été obtenue en utilisant des nanoparticules d'or recouvertes de streptavidine et d'oligonucléotides ciblant aussi une région de l'ADN génomique analysé, en suivant un schéma de type « sandwich » pour faire la détection. Des échantillons contenant différents pourcentages d'ADN modifié génétiquement (0%, 0,1%, 1% et 10% de soja GMO) ont été analysés. Les résultats ont révélé que d'un point de vue statistique, une détection significative de la cible d'ADN à faible concentration, faible pourcentage et très faible volume d'échantillon a été obtenue. Après un traitement statistique,

nous avons montré que ce système est capable de différencier significativement les échantillons de 0%, 1% et 10%. De plus, d'après nos données, la concentration minimum d'ADN cible qui a été possible de détecter est de 0,3 ng/mL, correspondant à 410 zM.

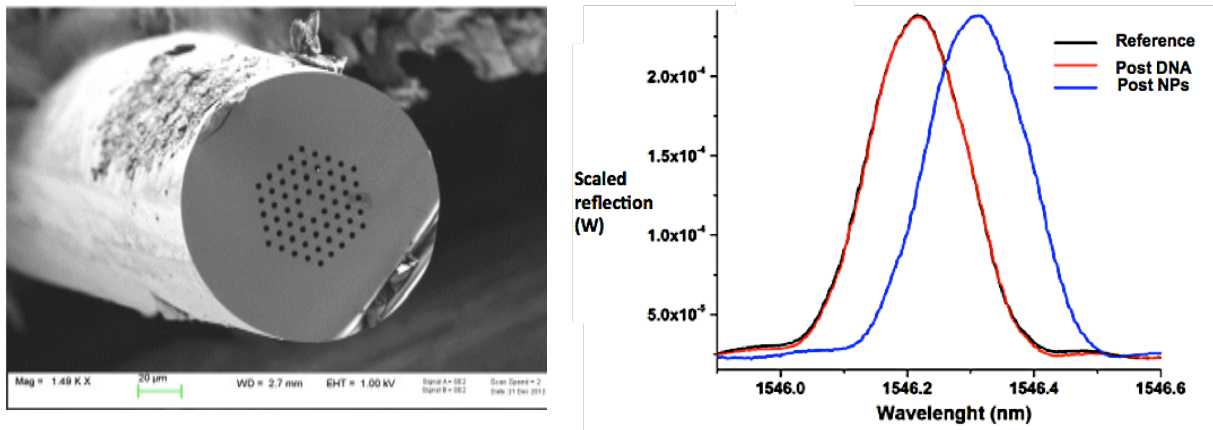


Fig. 16 Gauche) Image SEM de la fibre optique LMA-10 utilisé dans cette étude, montrant la géométrie hexagonale de ses 60 micro-canaux; Droite) Décalage de la longueur d'onde dans le mode réflexion (i) avant (noir), (ii) après ADN (rouge), et (iii) après introduction des nanoparticules d'or (bleu), en utilisant un échantillon contenant 10% d'ADN génomique, donnant un décalage moyen de 0,08 nm (RSD 27%).

Des simulations théoriques de la fibre optique (basé sur la méthode des éléments finis) semblent en accord avec la formation d'une couche de matériau organique avec une épaisseur moyenne de 39 nm pour le plus grand pourcentage (10% of soja RR) analysé. Ceci est en accord avec la déposition moyenne de plus d'une couche de matériau nanoparticule/streptavidine à la surface de la fibre. Cela est aussi consistant au regard de l'augmentation de la sensibilité observée lors de la détection d'ADN génomique avec d'autres techniques utilisant un schéma similaire de captation de nanoparticules d'or [61-62]. Cette technologie pourrait être très intéressante pour la réalisation d'instruments de mesure portables capables d'effectuer les analyses sur site et avec de très faibles concentrations d'échantillon, en mettant à profit le nombre très important d'outils et de processus développés de nos jours dans les technologies de la communication et de l'information.

Le ciblage de séquences d'ADN ou d'ARN spécifiques peut être aussi accompli en solution en utilisant des structures d'acides nucléiques adaptées chimiquement. La création des sondes moléculaires exploitent ainsi la reconnaissance sélective de séquences cibles pour fournir une réponse analytique [63-65].

En particulier, les excellentes propriétés d'hybridation combinées à leur stabilité chimique et biologique élevées, font des oligomères d'ANP de bons candidats pour la réalisation de sondes spécifiques pour des applications de diagnostics. L'ossature de l'ANP peut servir de modèle pour la conception de nouveaux composés capables d'effectuer la reconnaissance d'acides nucléiques et ensuite de la détection, en exploitant l'introduction de modifications chimiques appropriées à la structure de base ^[66,67]. Une partie de ce travail a donc été dédié à la réalisation d'une sonde à base d'ANP, qui est synthétisée de manière à introduire deux groupes pyrène sur la même unité monomère, dans une nouvelle géométrie de type pince. Le système de détection est donc basé sur la commutation excimère-monomère des unités de pyrène. L'hybridation de la sonde avec sa séquence cible produit un changement du signal d'émission utilisable comme signal de détection.

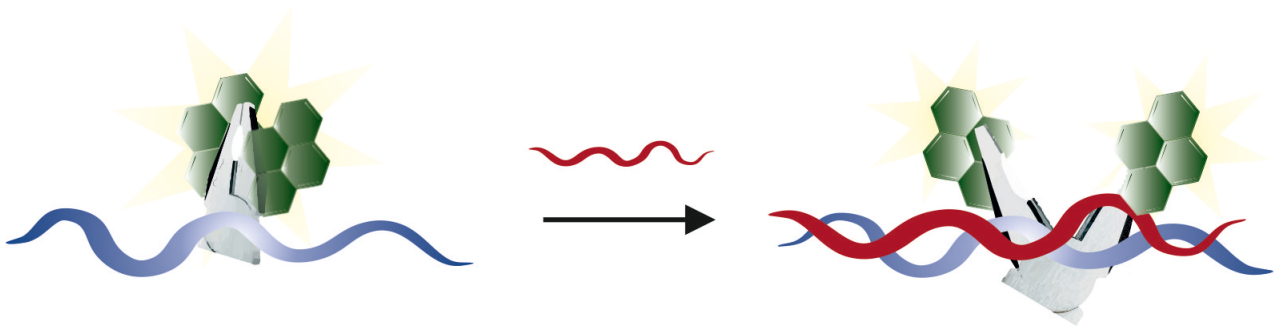


Fig. 17 Schéma du système proposé. La sonde ANP a une conformation initiale qui permet à deux unités de pyrène d'interagir donnant l'émission typique de la forme excimère (à gauche); après l'hybridation avec la séquence cible (brin rouge), les deux branches de pyrène sont forcées à s'ouvrir, résultant en l'émission de l'espèce monomère (à droite), fournissant ainsi un mécanisme adapté à des fins de détection.

Des études préliminaires ont été conduites sur l'unité monomérique d'ANP modifié, où l'introduction du premier pyrène est effectué sur la base nucléotidique. Le deuxième pyrène est attaché au squelette de l'ANP modifié grâce une chaîne de lysine. Les propriétés de fluorescence de cette unité ont démontré que les unités de pyrène sont effectivement capable d'interagir entre elles, ouvrant la possibilité de réaliser une vraie sonde de commutation ANP, dont les performances fluorescentes finales pourrait être appropriées et efficaces pour la détection de l'acide nucléique cible spécifique. En particulier, la séquence cible de la sonde est celle du miR-221, qui, comme déjà mentionné précédemment, est impliquée dans la prolifération de diverse formes des tumeurs et donc particulièrement intéressant du point de vue du diagnostic. Après la synthèse en phase solide de la sonde modifiée, les études sur les propriétés fluorescentes du système ont mis en évidence que le phénomène d'hybridation avec

la séquence cible complémentaire est en effet capable de déclencher la commutation du spectre d'émission de la sonde, donnant un signal clair de détection (Fig. 18).

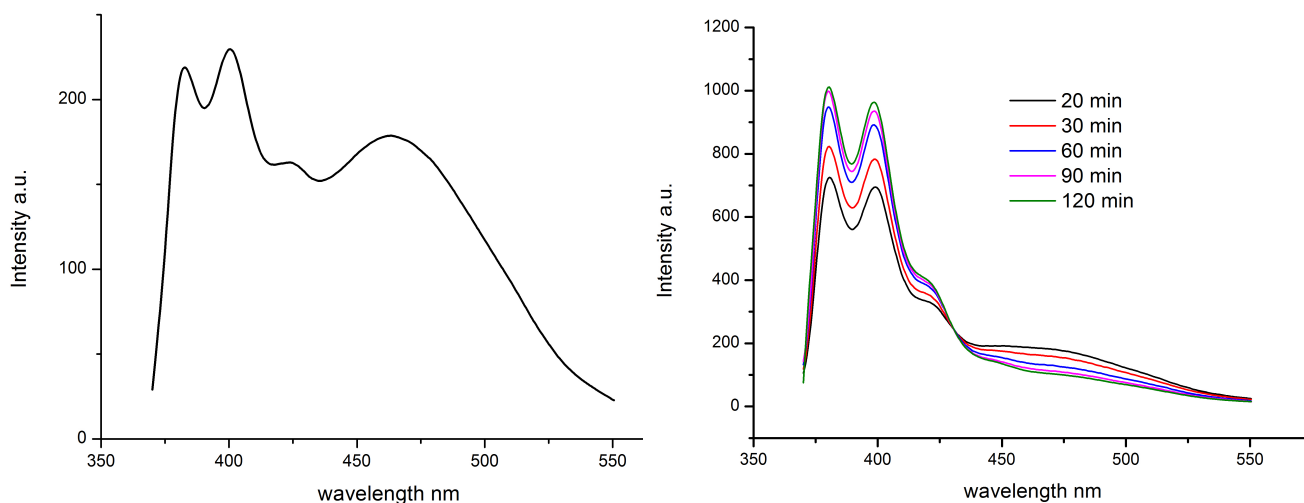


Fig. 18 Gauche) Spectre d'émission en fluorescence d'une solution aqueuse de la sonde ANP, avant l'addition de l'ADN cible, montrant la bande d'émission typique de l'excimère ; droite) Effet provoqué sur le spectre par l'addition d'un brin d'ADN mimant le miR-221, qui cause la chute drastique de la bande de l'excimère, en faveur d'une augmentation du signal du monomère de pyrène.

La synthèse de la sonde ainsi conçue met également en évidence la possibilité de créer des molécules complexes multifonctionnelles et en particulier d'introduire des modifications multiples sur une structure d'ANP pour combiner un système de détection moléculaire avec les excellentes propriétés chimiques et biologiques de l'ANP, afin d'avoir des outils avancés dans le domaine de l'imagerie et du diagnostic.

Références

- [1] C. Sanchez, B. Julian, P. Belleville, M. Popall, *J. Mater. Chem.* **2005**, *15*, 3559-3592
- [2] P. Judeinstein, C. Sanchez, *J. Mater. Chem.* **1996**, *6*, 511-525
- [3] C. Sanchez, P. Belleville, M. Popall, L. Nicole, *Chem. Soc. Rev.* **2011**, *40*, 696-753
- [4] C. Sanchez, K.J. Shea, S. Kitagawa, *Chem. Soc. Rev.* **2011**, *40*, 471-472.
- [5] P.K. Jain, X. Huang, I.H. El-Sayed, M.A. El-Sayed, *Account. Chem. Res.* **2008**, *41*, 1578-1586
- [6] A.H. Lu, E.L. Salabas, F. Schuth, *Angew. Chem. Int. Ed.* **2007**, *46*, 1222-1244.
- [7] A.M. Smith, S.M. Nie, *Acc. Chem. Res.* **2010**, *43*, 190-200.
- [8] K.M. Taylor-Pashow, J. Della Rocca, R.C. Huxford, W. Lin, *Chem Commun.* **2010**, *46*, 5832-5849.
- [9] F. Caruso, T. Hyeon, V.M. Rotello, *Chem. Soc. Rev.* **2012**, *41*, 2537-2538.
- [10] A. Albanese, P.S. Tang, W.C. Chan, *Annu. Rev. Biomed. Engin.* **2012**, *14*, 1-16.

- [11] H. Luelf, A. Devaux, E.A. Prasetyanto, L. De Cola, *Porous nanomaterials for biomedical applications, in Organic Nanomaterials: Synthesis, Characterization, and Device Applications*, Wiley, **2013**, Ch. 22.
- [12] Y. Yan, G.K. Such, A.P. Johnston, H. Lomas, F. Caruso, *ACS nano* **2011**, *5*, 4252-4257.
- [13] Moller, S.M., and Bein, T., *Science*, **333**, 297-298, **2011**.
- [14] Mackowiak, S., Schmidt, A., Weiss, V., Argyo, C., von Schirnding, C., Bein, T., Bräuchle, C., *Nano Lett.* **13**, 2576-2583, **2013**
- [15] Dobay, M., Schmidt, A., Mendoza, E., Bein, T., Rädler, J., *Nano Lett.* **13**, 1047-1052, **2013**
- [16] Schloßbauer, A., Sauer, A., Cauda, V., Schmidt, A., Engelke, H., Rothbauer, U., Zolghadr, K., Leonhardt, H., Bräuchle, C., Bein, T., *Adv. Healthcare Mater.* **1**, 316-320, **2012**.
- [17] S. Mura, J. Nicolas, P. Couvreur, *Nat. Mater.* **2013**, *12*, 991-1003.
- [18] S. Ganta, H. Devalapally, A. Shahiwala, M. Amiji, *J. Control. Release* **2008**, *126*, 187-204.
- [19] A. Verma, F. Stellacci, *Small* **2010**, *6*, 12-21.
- [20] I. Slowing, B.G. Trewyn, V.S.Y. Lin, *J. Am. Chem. Soc.* **2006**, *128*, 14792-14793.
- [21] J. Kim, Y. Piao, T. Hyeon, *Chem. Soc. Rev.* **2009**, *38*(2), 372-390.
- [22] A. Ruiz, D. Bruehwiler, T. Ban, G. Calzaferri, *Monatshefte fuer Chemie* **2005**, *136*, 77.89
- [23] C.A. Strassert, M. Otter, R.Q. Albuquerque, A. Höne, Y. Vida, B. Maier, L. De Cola, *Angew. Chem. Int. Ed.* **2009**, *48*, 7928-7931.
- [24] M. Busby, H. Kerschbaumer, G. Calzaferri, L. De Cola, *Adv. Mater.* **2008**, *20*, 1614-1618.
- [25] P. E. Nielsen, M. Egholm, R. H. Berg, O. Buchardt, *Science* **1991**, *254*, 1497-1500.
- [26] B. Hyrup, P. E. Nielsen, *Bioorgan. Med. Chem.* **1996**, *4*, 5-23.
- [27] U. Koppelhus, P. E. Nielsen, *Adv. Drug. Deliver. Rev.* **2003**, *55*, 267-280.
- [28] H. J. P. Ryser, W. Shen, *P. Natl. Acad. Sci. USA* **1978**, *75*, 3867-3870.
- [29] G. Calzaferri, S. Huber, H. Maas, C. Minkowski, *Angew. Chem. Int. Ed.* **2003**, *42*, 3732-3758
- [30] E. Climent, R. Martinez-Manez, F. Sancenon, M. D. Marcos, J. Soto, A. Maquieira, P. Amoros, *Angew. Chem. Int. Ed.* **2010**, *122*, 7439-7441;
- [31] A. Salvati, A. Christoffer, T. dos Santos, J. Varela, P. Pinto, I. Lynch, K. A. Dawson, *Nanomedicine* **2011**, *7*, 818-826
- [32] Laskar, M. Ghosh, S. I. Khattak, W. Li, X.-M. Yuan, *Nanomedicine* **2012**, *7*, 705-717.
- [33] F. Wang, L. Yu, M. P. Monopoli, P. Sandin, E. Mahon, A. Salvati, K. A. Dawson, *Nanomedicine* **2013**, *9*, 1159-1168
- [34] Z. Li, J.C. Barnes, A. Bosoy, J.F. Stoddart, J.I. Zink, *Chem. Soc. Rev.* **2012**, *41*, 2590-2605.
- [35] N. Ibrahim, H. Handa, A. Cosset, M. Koulintchenko, Y. Konstantinov, R. N. Lightowlers, A. Dietrich, F. Weber-Lotfi, *Pharm. Res.* **2011**, *28*, 2871-2872
- [36] V. P. Torchilin, B. A. Khaw, V. Weissig, *Somat. Cell Mol. Genet.* **2002**, *27*, 49-64
- [37] I. I. Slowing, B. G. Trewyn, S. Giri, V. S.-Y Lin, *Adv. Funct. Mat.* **2007**, *17*, 1225-1236.
- [38] I. I. Slowing, J. L. Vivero-Escoto, C. W. Wu, V. S.-Y Lin, *Adv. Drug Delivery Rev.*, **2008**, 1278-1288,
- [39] C.T. Kresge, M.E. Leonowicz, W.J. Roth, J.C. Vartuli, J.S. Beck, *Nature*, **1992**, *359*, 710-712
- [40] H.S. Friedman, T. Kerby, H. Calvert, *Clin. Cancer Res.* **2000**, *6*, 2585-2597.
- [41] E. Brognara, E. Fabbri, E. Bazzoli, G. Montagner, C. Ghimenton, A. Echer, C. Cantù, A. Manicardi, N. Bianchi, A. Finotti, G. Breveglieri, M. Borgatti, R. Corradini, V. Bezzeri, G. Cabrini, R. Gambari, *J. Neuro-Oncol.* **2014**, *118*, 18-29
- [42] J. Zhang, L. Han, Y. Ge, X. Zhou, A. Zhang, C. Zhang, Y. Zhong, Y. You, P. Pu, C. Kang, *Int. J. Oncol.* **2010**, 913-920
- [43] J. K. Kim, K. Choi, M. Lee, M. Jo, S. Kim. *Biomaterials* **2012**, *33*, 207-217
- [44] A. Borriello, V. Cucciola, A. Oliva, V. Zappia, F. Della Ragione, *Cell Cycle* **2007**, *6*, 1053-1061.
- [45] J.K. Gillies, I.A. Lorimer, *Cell Cycle* **2007**, *6*, 2005.
- [46] L. Chen, J. Zhang, L. Han, A. Zhang, C. Zhang, Y. Zheng, *et al. Oncol. Reports* **2012**, *27*, 854.
- [47] L. Betancor, H. R. Luckarift, *Trends Biotechnol.* **2008**, *26*, 566-572.
- [48] L. M. Ellerby, C. R. Nishida, F. Nishida, S. A. Yamanaka, B. Dunn, J. S. Valentine, J. I. Zink, *Science* **1992**, *255*, 1113-1115.
- [49] D. Ma, M. Li, A. J. Patil, S. Mann, *Adv. Mater.* **2004**, *16*, 1838-1841.
- [50] A. Cao, Z. Ye, Z. Cai, E. Dong, X. Yang, G. Liu, X. Deng, Y. Wang, S. Yang, H. Wang, M. Wu, Y. Liu, *Angew. Chem. Int. Ed.* **2010**, *49*, 3022-3025.
- [51] M.S. Iordanov, O.P. Ryabinina, J. Wong, T.H. Dinh, D.L. Newton, S.M. Rybak, B.E. Magun, *Cancer Res.* **2000**, *60*, 1983-1994.
- [52] R. Koschny, H. Walczak, T.M. Ganten, *J. Mol. Med.* **2007**, *85*, 923-935.
- [53] L. Nicu, T. Leichlé, *J. Appl. Phys.* **2008**, 104
- [54] J. N. Anker, W. P. Hall, O. Lyandres, N. C. Shah, J. Zhao, R. P. Van Duyne, *Nature Materials* **7**, 442 - 453 (**2008**)
- [55] J. Wang, *Biosens. Bioelectr.* **1998**, *13*, 757-762

- [56] W. Zhao, J. Xu, H. Chen, *Chem. Rev.* **2014** DOI: 10.1021/cr500100j
- [57] J. C. Knight, *Nature* **2003**, *424*, 847-851.
- [58] L. Rindorf, J.B. Jensen, M. Dufva, L.H. Pedersen, O. Bang, *Optics Express* **2006**, *14*, 8224-8231.
- [59] E. Coscelli, M. Sozzi, F. Poli, D. Passaro, A. Cucinotta, S. Selleri, R. Corradini, R. Marchelli, *IEEE J. Sel. Top Quant.* **2010**, *16*, 967-972.
- [60] Corradini, R.; Selleri, S. Photonic Crystal Fiber for Physical, Chemical and Biological Sensing **2010**, 80-84 in "Photonic Cystal Fibers for Physical, Chemical and Biological Sensing" Prisco, M.; Cutolo, A.; Cusano, A. Eds. Bentham Publisher
- [61] R. D'Agata, R. Corradini, C. ferretti, L. Zanolì, M. Gatti, R. Marchelli, G. Spoto, *Biosens. Bioelectron.* **2010**, *25*, 2095-2100
- [62] R. D'Agata, G. Breveglieri, L. Zanolì, M. Borgatti, G. Spoto, R. Gambari. *Anal. Chem.* **2011** *83*, 8711–8717.
- [63] B. Juskowiak, *Anal. Bioanal. Chem.* **2011**, *399*, 3157-3176.
- [64] A.Z. Wang, O.C. Farokhzad, *J. Nucl. Med.* **2014**, *55*, 353-356.
- [65] J. Liu, Z. Cao, Y. Lu, *Chem. Rev.* **2009**, *109*, 1948-1998.
- [66] A. Tonelli, T. Tedeschi, A. Germini, S. Sforza, R. Corradini, M.C. Medici, *et al. Mol. BioSystems* **2011**, *7*, 1684-1692.
- [67] F. Totsingan, T. Tedeschi, S. Sforza, R. Corradini, R. Marchelli, *Chirality* **2009**, *21*, 245-253.

1

Introduction

Abstract

This chapter will introduce general concepts as background and state-of-the-art relatively to the topics of the research work presented throughout this thesis. At the beginning, an overview about nanotechnology and nanomedicine will be provided, underlining the potentiality of nanocontainers. A brief summary on hybrid bioorganic-inorganic materials and the strategies offered by combining the chemistry of materials with that of biomolecules will be then given. A special focus will be given to Zeolite-L and mesoporous silica nanoparticles as selected platforms of this thesis. Since large part of the work has been dedicated to peptide nucleic acids (PNAs), a description of these molecules and of their applications in biomedicine and diagnostics will also be included. Finally, an overview on the analytical strategies and techniques currently implemented for nucleic acid detection will be presented.

1.1 Nanotechnology and nanomedicine

Nanotechnology represents nowadays one of the most active fields of research, dealing with the development of nanometer sized (1 to 100 nm) functional materials showing unique electronic, optical, magnetic and biological properties.^[1-6] Among others, nanomedicine is indeed one of the fastest growing areas in nanotechnology and is supposed to revolutionize healthcare and medicine through novel advanced diagnostic and therapeutic tools. Chemistry fosters advances in nanomedicine, providing suitable materials as well as state-of-the-art biochemical and analytical techniques. Various nanostructured materials have been synthesized for diverse medical applications, including biomedical imaging, biosensing, diagnostics and therapy, their size-dependent physical properties playing important roles in the interaction with biological systems.^[7-10]

It has been shown that for nanoparticles, the size, shape, and of course the chemical composition as well as the organization at the nanoscale are key parameters to allow for controlling their properties and to manipulate and tune the interaction with their environment

(e.g. cytotoxicity). A huge variety of components such as semiconductors, metals, metal oxides, as well as polymers, lipids or other organic molecules may be used to produce functional nanosystems. The general design principle is based on synthesizing or assembling the components into the desired composition, shape, and size while further properties can be introduced by surface modifications.^[11]

A wide variety of nanostructured materials have been described in the literature such as gold and silver nanoparticles,^[2,12] quantum dots,^[13] magnetic nanoparticles,^[14] carbon nanotubes,^[15] silica-based nanomaterials,^[16] titania nanoparticles,^[17] liposomes,^[18] and soft polymer nanoparticles^[19] just to cite the most common ones. A very general scheme summarizing the materials, their properties and their applications is reported in Figure 1.1.

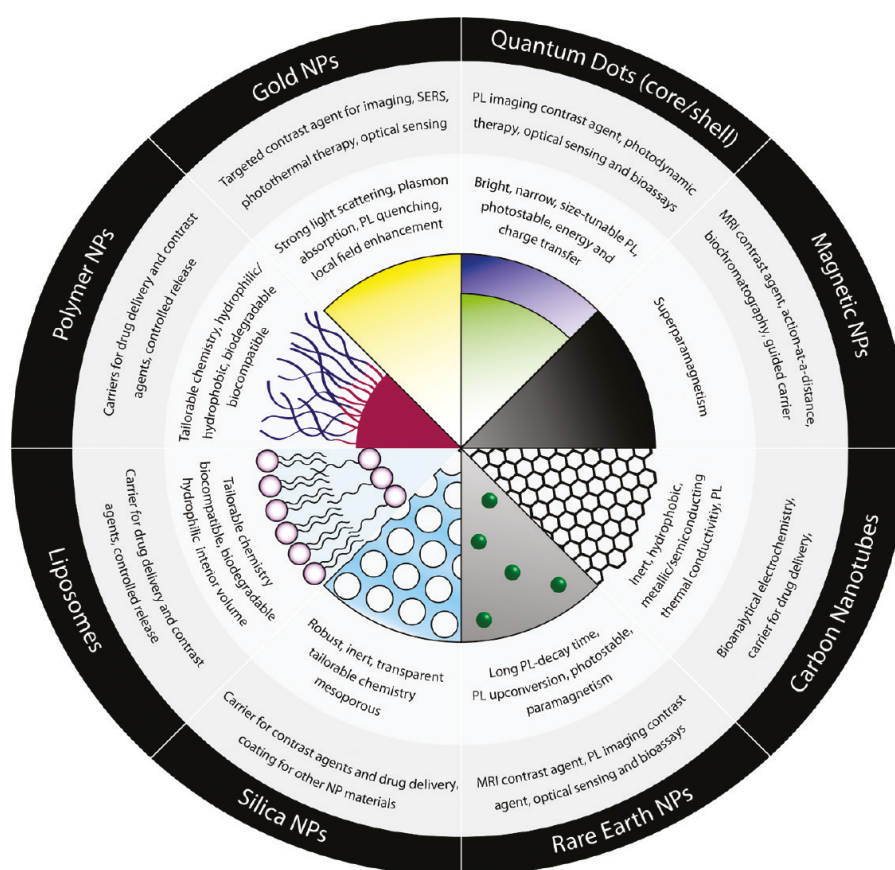


Fig. 1.1 Selected nanoparticle (NP) materials, their properties of interest, and prominent biological applications. Reprinted with permission from W.R. Algar, D.E. Prasuhn, M.H. Stewart, T.L. Jennings, J.B. Blanco-Canosa, P.E. Dawson, I.L. Medintz, *Bioconjugate Chem.* **2011**, *22*, 825-858. Copyright (2011) American Chemical Society.

One of the strategic advantages of nanomaterials for biomedical applications is their vast modification possibilities: many nanostructured materials can be used as platforms in which

several functions can be combined in a single type of nanoparticle and a high density of desired components may be assembled and organized at the nanometer scale. In many cases, these structures still retain efficient solubility and colloidal properties for use in complex environments (e.g. blood, tissues, etc.), leading to a huge range of possibilities for sensing, imaging, and targeting.^[20-21]

The versatility of nanoparticle-based platforms with respect to possible modification is indeed associated with a large surface to volume ratio. Differently from the extremely small surface to volume ratio of bulk materials, nanomaterials provide bigger values that can be effectively controlled through the size of the material. Such a property is vitally important for optimizing drug payloads and tuning the interactions with the surrounding environment.

The shape of nanomaterials also plays a direct role in their function in biological systems. Nanoparticles can be synthesized into structures with a myriad of shapes and sizes based on variable synthetic conditions. A wide overview of state-of-the-art material synthesis has been provided by Mirkin and his coworkers.^[22] The shape of nanomaterials has indeed a direct effect on how they respond *in vitro* and *in vivo*.^[23-24] Several groups have explored how cellular uptake is influenced by shape and, for instance, it has been shown that in studies with sub-100 nm nanoparticles, spheres show an appreciable advantage over rods and other shapes with respect to cell uptake.^[25-26] Furthermore, it has been recently observed that the *in vivo* biodistribution and clearance behavior of silica nanoparticles depends strongly on their aspect ratio.^[27] In addition, within a given geometric shape, the size of these structures strongly affects the uptake and the accumulation in the body. For spherical gold nanoparticles, silica nanoparticles, single-walled carbon nanotubes, and quantum dots, a 50 nm diameter is the right choice to maximize the rate of uptake and intracellular concentration in some types of mammalian cells.^[28-30] In addition to size, surface charge is also an important parameter involved in the biological behavior of the nanomaterial. Compared with nanoparticles with a neutral or negative charge, positively charged nanoparticles are internalized at a faster rate,^[31-32] on account of the slightly negative charge of the cellular membrane, and of the influence of the electrostatic interactions in the uptake process.^[26,33-34] A representative scheme of the possible pathways involved in the cellular uptake process in relationship with the properties of the particles is depicted in Figure 1.2.

It is worth mentioning that in presence of serum or other biological environments, the nanoparticle surface is quickly covered by a corona made up of different proteins, so that the cell uptake is also strongly affected, if not totally driven by the corona composition.^[35-36] The formation of a protein corona is for example involved in the cellular uptake of

negatively charged DNA-coated nanoparticles.^[37]

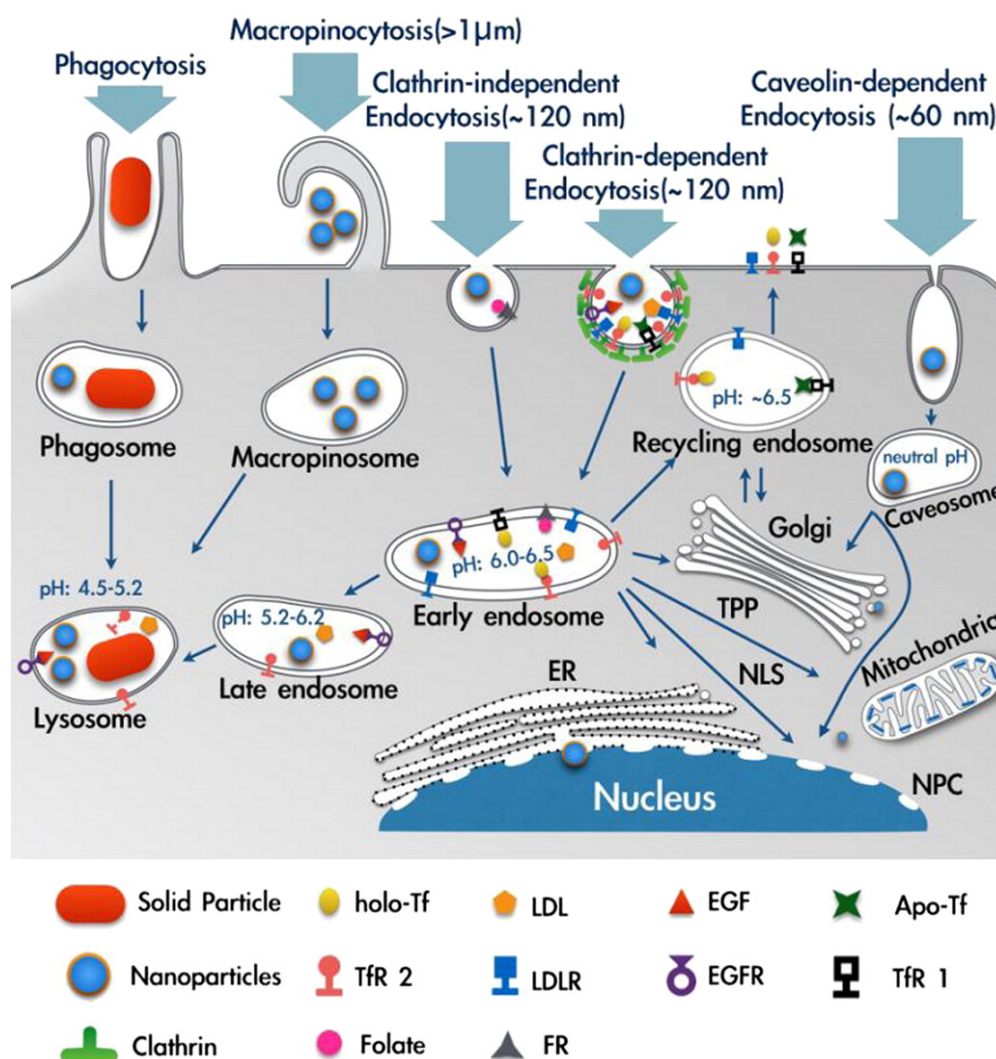


Fig. 1.2 Illustration of possible cellular internalization pathways (phagocytosis, macropinocytosis, clathrin-dependent endocytosis, clathrin-independent endocytosis, and caveolae-dependent endocytosis). The fate of internalized cargo and localization to subcellular compartments are also depicted. ER: endoplasmic reticulum, NLS: nuclear localization signal, NPC: nuclear pore complex, TPP: triphenylphosphonium cation. Reprinted from *J. Control. Release*, 190, B. Yameen, W.I. Choi, C. Vilos, A. Swami, J. Shi, O.C. Farokhzad, Insight into nanoparticle cellular uptake and intracellular targeting, 485-499. Copyright (2014), with permission from Elsevier.

Nanoparticles have been also identified as potent tools for drug delivery, which still remains a crucial aspect of medicine to be improved for therapies for a range of human diseases.^[38] It has been shown that nanoparticles are extremely promising for improving drug efficacy through their ability to protect the often fragile or water insoluble medicine, carrying the drug molecules into the cells and release them in a sustainable manner. In such a context, the so-called nanocontainers are worth to be pointed out as powerful tools for nanomedical applications.^[39] A major advantage of these materials is their ability to entrap a large variety

of guest species such as proteins, enzymes, peptides, hormones, metabolites, DNA, complexes, metal clusters, or other types of molecules.^[40-43] The encapsulation indeed protects the guest species from chemical or biological degradation as well as from possible unwanted interactions with the biological environment. Furthermore, since many drugs or biomacromolecules have poor cellular uptake or poor solubility, the use of proper nanocontainers might improve their properties, since they can be modified on the outer surface with different functional groups, e.g. cell penetrating or solubilizing ones.^[44-45]

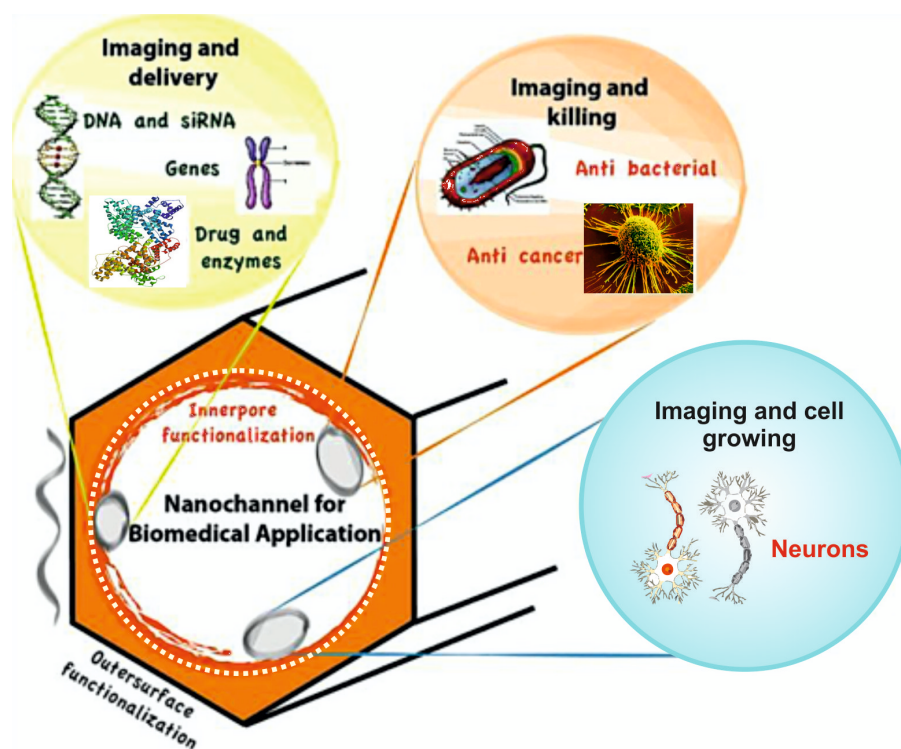


Fig. 1.3 Schematic illustration of multifunctional nanocontainers and their potential bioapplications.

It is also possible to modify the surfaces of nanocontainers with ligands for specific receptors in order to target specific cell types or, after cellular uptake, specific organelles or compartments of the cell.^[46-47] A wide variety of nanocontainers has been described in the literature such as polymer based micelles or vesicles,^[48] liposomes,^[49] metal-organic frameworks (MOFs),^[50] carbon nanotubes,^[51] classical zeolites or zeolite-like materials^[52] mesoporous silica or organosilicates.^[53-54] Among the others, this thesis will especially focus on the use of zeolite-L crystals and mesoporous silica nanoparticles (MSNPs), as described in the following sections.

As discussed by far, the concept of introducing multiple functionalities on the same nanoparticle becomes indeed a striking strategy when nanomaterials are no longer either “imaging” or “therapeutic” systems, but combinations of both, which merge the unique

properties of the material with those of the drug payload and other functionalities. To describe this unique feature, scientists have developed the term “theranostics” (therapeutics + diagnostics). The potential advantages of theranostics have been exploited for the progress of nanomedicine, and specific applications have been reported by several authors.^[55-58] Among the others, a significant and outstanding branch of research in this field is based on the development of hybrid multilayered organic-inorganic materials in which an inorganic nanosized platform is coupled with a bioorganic moiety, e.g. nucleic acids and proteins, providing unique systems with exceptional crossed properties that can be exploited for example for gene therapy, transfection or targeted enzymatic delivery.

1.2 Hybrid bioorganic-inorganic structures

The strategies offered by combining material chemistry together with organic molecules, in order to fabricate hybrid networks with unique properties at the interface, have paved the way to innovative composites showing complex architectures and interesting peculiar functions. There is no doubt that, by playing with both inorganic and organic chemistry, new generations of hybrid materials will provide revolutionary applications.^[59-60]

This concept becomes even more interesting when biomolecules constitute the organic moiety coupled with specific materials, since powerful tools with exceptional properties could be developed for biomedical applications. Bionanotechnology can be thus defined as a field representing all facets of research at the intersection of biology and nanomaterials and is generally characterized by two main goals. The first goal focuses on utilizing the inherent structural, specific recognition, or catalytic properties of biomolecules to assemble composite nanoscale materials or devices with novel properties. One of the most visible example of this is the use of nucleic acid structures to control the placement and organization of nanoparticles in order to create complex and bio-inspired functional structures.^[61-62] The second goal focuses indeed on utilizing the unique properties of nanomaterials within the context of nanomedicine. This thesis will expand and emphasize the latter approach, of which one of the best examples is offered by the coupling of nanosized materials and nucleic acids. For instance, RNA interference (RNAi) for personalized medicine is a hot topic for which a huge variety of nanovectors have been proposed in order to achieve transport and delivery to tissues and within cells. These carriers include lipid-based, polymer-based and many inorganic-based nanomaterial platforms that integrate various functionalities to compact, deliver, and release nucleic acids, and enhance gene silencing on specific targets. The intracellular delivery of Small interfering RNA, siRNA, for anticancer purposes has

been, for instance, efficiently achieved by using mesoporous silica nanoparticles (MSNPs) as showed by Zink and Nel.^[63-64] MSNPs represent indeed a versatile and powerful platform to be used in combination with nucleic acids, and further explanations will be given in the following paragraph. Among other possible options, Yu *et al.* have recently proposed functionalized large pore MSNPs for gene delivery and controlled release,^[65] whilst hollow MSNPs for target drug/siRNA co-delivery have been described by Zhao *et al.*^[66] Lipid-based systems have been exploited by Anderson and Langer for a potent siRNA delivery to nonhuman primates,^[67] and a full overview on the use of liposomes as siRNA nanocarriers has been provided by Lopez-Berestein.^[68]

Quantum dots have also been presented as suitable and powerful RNA carriers,^[69] as well as magnetic iron oxide^[70] and gold nanoparticles.^[71] Gold nanoparticles have been proposed by several authors as ideal substrates for the realization of DNA-modified hybrid systems: the so-called spherical nucleic acids developed by Mirkin's group represent a well-known example (Fig. 1.4).^[72]

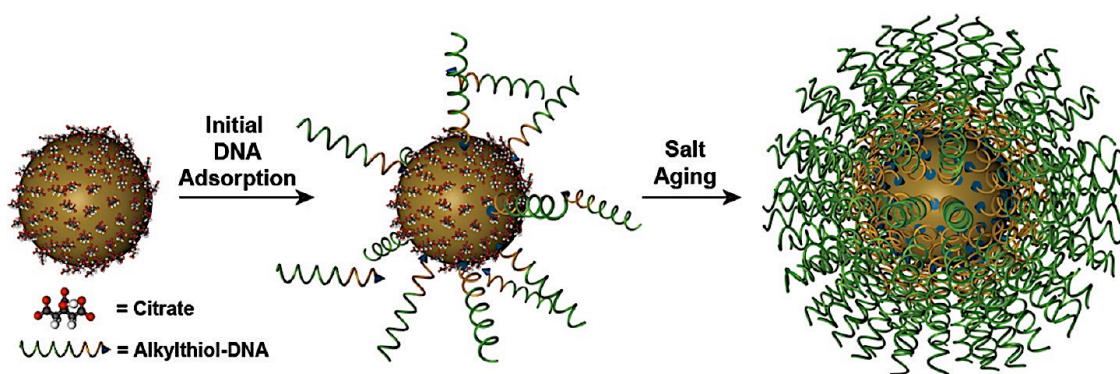


Fig. 1.4 Synthesis of spherical nucleic acids (SNA). Citrate-stabilized gold nanoparticles are incubated with alkylthiol-functionalized oligonucleotides in water to form a low-density monolayer. By incubating the nanoparticles in aqueous solutions with successively higher concentrations of salt and surfactants, a high-density SNA shell is formed. Reprinted with permission from J.I. Cutler, E. Auyeung, C.A. Mirkin, *J. Am. Chem. Soc.* **2012**, *134*, 1376-1391. Copyright (2012) American Chemical Society.

DNA-functionalized gold nanoparticles have also found a broad range of applications in the biosensing field, having been used in Surface Plasmon Resonance (SPR),^[73] colorimetric assays^[74] or electrochemical techniques.^[75] In this context, functionalized AuNps will be described throughout Chapter 7 and 8 as necessary tools for ultra-sensitive PCR-free genomic DNA detection, although a full overview on the optical and plasmonic properties is beyond the scope of this thesis, since only the refractive index of the particles has been considered in the detection scheme proposed.

Carbon nanotubes have gained as well more and more attention in the past years in the bio-nano community and some nice example of coupling with biomolecules have been showed:

for instance the use as plasmid DNA delivery vectors^[76] or as platforms to bind proteins^[77] have been covered.

Proteins are biomacromolecules of undoubted value for a myriad of biotechnological applications, and the realization of hybrid protein-inorganic nanomaterials is a fascinating challenge towards various and innovative goals. Encapsulation of proteins within nanostructures has been studied for different purposes, for instance from the construction of silica shells to protect and enhance the fluorescent properties of Green Fluorescent Protein (GFP)^[78] to the entrapment of diverse proteins in carbon nanotubes as biomedical devices.^[79] Mesoporous silica particles have been also used to incorporate proteins and enzymes, as investigated by Caruso, who studied the best parameters for an efficient enzyme immobilization in porous silica spheres,^[80] or Lin *et al.* who showed the intracellular delivery of membrane-impermeable proteins.^[81] The delivery of selected proteins anyhow still remains a challenge and the need for biocompatible, efficient, and safe vectors will be highlighted in Chapter 6. Protein substrates can be otherwise used as organic scaffolds to build up hybrid structures and composites, as in the case of the beautiful hybrid nanoflowers presented by Zare *et al.* (Fig. 1.5).^[82]

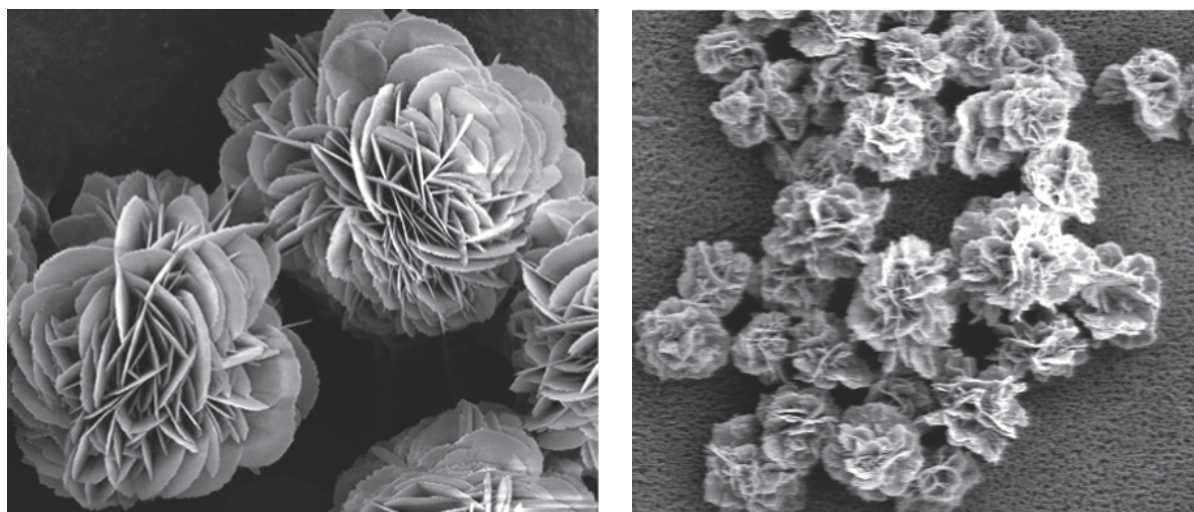


Fig. 1.5 SEM images of hybrid $\text{Cu}_3(\text{PO}_4)_2 \cdot 3\text{H}_2\text{O}$ /protein nanoflowers. Left image shows nanoflowers obtained using laccase, right one by using carbonic anhydrase. Reprinted by permission from Macmillan Publishers Ltd: Nature Nanotechnology, advance online publication, 3 June 2012, doi:10.1038/nnano.2012.80. J. Ge, J. Lei, R.N. Zare, *Nat. Nanotechnol.* **2012**, 7, 428-432.

Eventually, it is worth mentioning that also antibodies interfaced with different materials have been broadly and extensively utilized for the fabrication of selective and sensitive biosensors and microarrays. Works by De Cola *et al.* on bio-conjugated fluorescent zeolite nanocrystals as labels in protein microarrays,^[83] or by Hall *et al.* based on Localized Surface

Plasmon Resonance (LSPR) biosensors signal enhancement using nanoparticle-antibody conjugates^[84] represent two explicative examples in this broad field of research.

1.3 Zeolite-L for biomedical applications

Zeolites are porous crystalline aluminosilicate featuring defined channels and cavities.

Up to date, there are more than 200 different zeolite framework-types identified and Zeolite-L is one representative of them. Zeolites-L are characterized by hexagonal symmetry and show an anionic framework completed by charge-compensating cations. The crystals consist of so-called cancrinite cages (ϵ cages), which are piled up and interconnected to form a one-dimensional channel system running parallel to the cylinder c-axis for the whole length (Figure 1.6). The pore opening, and thus the smallest channel diameter, is 7.1 Å. The largest channel diameter is 1.26 nm and the unit cell length is 7.5 Å. The channels are oriented in a hexagonal manner and the center-to-center distance of two adjacent channels is 1.8 nm. Due to the presence of aluminum atoms in the zeolite framework, a net negative charge is showed, which needs to be compensated by charge-balancing cations, generally sodium and potassium.

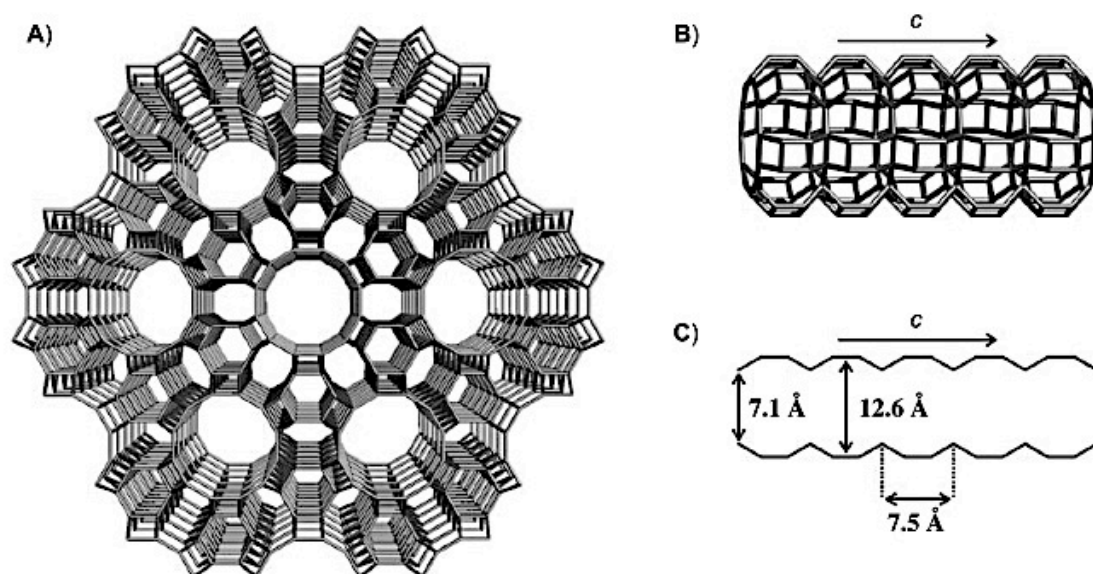


Fig. 1.6 A) Zeolite-L framework projected along the c-axis; B) side view of the main channel; C) its dimensions. Adapted from G. Calzaferri, S. Huber, H. Maas, C. Minkowski, *Angew. Chem. Int. Ed.* **2003**, *42*, 3732-3758. Copyright © 2003 WILEY-VCH Verlag GmbH & Co. KGaA, Weinheim

These cations may however be easily replaced by other ones or even by different positively charged species, such as dyes or biologically active molecules.^[85-86] Water molecules are also part of the structure and are reported to behave like an intracrystalline liquid. The

stoichiometry of zeolite L with monovalent cations M is $(M)_9[Al_9Si_{27}O_{72}] \cdot n H_2O$, where n equals 21 in fully hydrated materials and 16 at about 20 % relative humidity.^[87]

A big potentiality of zeolites-L resides also in the possibility of tuning the size and the morphology according to the requirements of a given application. Starting from a standard routine protocol, the crystal shape and aspect ratio can be controlled by changing the ratio between the precursors as well as other synthesis parameters, such as the type of silica source, solvents, temperature, and crystallization with or without stirring. A wide range of different zeolite crystals from nano-sized cylinders to micro-sized flat discs can be obtained varying these conditions,^[87-88] as will be discussed further in Chapter 2.

In order to use zeolite-L crystals as functional nanomaterials, they can be tailor modified by introducing functional groups at different levels. In particular, it has been shown that the internal channel system as well as the pore openings and the external surface can be functionalized independently from each other,^[89] which can be used to design very specific crystals for every application. The channels of a zeolite-L are capable of hosting a variety of guest molecules. This entrapment preserves the guest from a direct contact with the external environment, and can lead to increased thermal or chemical stabilities as well as avoiding undesired reactions or interactions. Interestingly, it has been shown that guests incorporated into the channel system of zeolite-L can form unique one-dimensional arrangements with very special properties that cannot be otherwise seen in solution or in solid state.^[90-92] This unique orientation of dye molecules has been investigated in detail with regard to specific optical and magnetic properties.^[93-95] Further details on the insertion of dye molecules into the pore system of zeolite-L will be given in Chapter 2.

A second important component of a zeolite-L crystal is the pore opening, since it represents the interface between the interior and the exterior of a crystal, and indeed plays a very important role in the loading and release of guest molecules. Control on the leakage of the entrapped molecules and of the interfaces between internal/external surface can be achieved by using proper stopper molecules. A traditional stopcock consists of a long tail, which shows a high affinity for the pore system and can be inserted into the channels, and a bulky head group, which is not able to enter the pore system and thus blocks the pores.^[96-98] Additionally, a second strategy considers a proper functionalization with molecules big enough to act as stoppers (even biomolecules, as described Chapter 4) and that can be slowly detached from the outer surface allowing for the payload release.^[99] Functional stopper molecules can be used as molecular valves that open and close the pores under certain conditions,^[100-102] and engineering gated systems able to release the cargo only upon a

precise stimulus is indeed a challenge towards smart and selective nanocarriers for targeted-release of drugs. The external surface eventually plays a crucial role for biological applications since it is directly in contact with the surrounding and determines how the materials will interact with it. The external surface can be tailored and functionalized by grafting functional molecules onto it. Depending on the final goal, diverse molecules for improving the biocompatibility or dispersability,^[103-105] for enabling targeting of biomolecules, bacteria or cells,^[106-107] or for introducing chemical, luminescent, magnetic or radioactive^[108] labels, can be attached to the surface. Further details about possible different surface modifications will be discussed in Chapter 2.

Zeolites have traditionally found application in catalysis and in the study of energetic and photophysical processes in an entrapping environment, but their special properties have indeed captured scientists' attention also towards their use in the biotechnology field.

Amongst the earlier examples exploiting the possibility of loading the zeolites with guest species, zeolite Y has been proposed as scaffold in combination with the use of Gd(III) for magnetic resonance imaging MRI applications by Bresinka et al. in 1994.^[109] They have shown that Gd(III) can undergo exchange with sodium in NaY-zeolites forming the so-called "Gadolite", which is used as a positive oral contrast agent for MRI. The stability of the material has been evaluated under different pH conditions, as well its relaxivity as aqueous suspension.

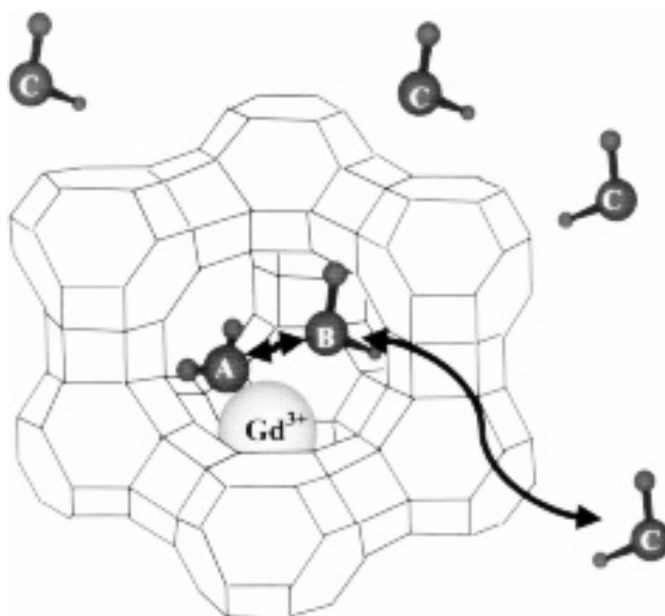


Fig. 1.7 Schematic representation of the “two-step” model considered for the relaxivity in aqueous suspensions of Gd³⁺-loaded zeolite Y. “A” represents a water molecule coordinated to Gd³⁺, “B” an intra-framework water molecule not coordinated to Gd³⁺ and “C” bulk water molecules. Reprinted with permission from C. Platas-Iglesias, L. Vander Elst, W. Zhou, R.N. Muller, C.F. Geraldes, T. Maschmeyer, J.A. Peters, *Chem.-Eur. J.* **2002**, 8, 5121-5131. Copyright © 2002 WILEY-VCH Verlag GmbH & Co. KGaA, Weinheim.

Further studies on the same systems have been then carried out by Csajbók *et al.*^[110] and Platas-Iglesias *et al.*^[111] to reveal the mechanism causing the enhanced MRI contrast effect, as reported in Figure 1.7.

Zeolite-L crystals have been then exploited for imaging applications and in 2008 the first example of a dual-probe imaging system (optical and magnetic) has been reported.^[39] The channels of nanometer sized (about 30 nm) zeolite-L crystals were loaded with the fluorescent dye pyronine, which could be used as the optical unit. In a second step the outer surface was modified with a highly stable Gadolinium(III) complex acting as the unit for magnetic imaging.^[39] Imaging can also be done using radioisotopes by scintillation methods (PET, Positron Emission Tomography). A pioneer strategy in this field based on radiolabeling of nanozeolites has been developed by De Cola's group, which also reported, for the first time, experiments on the *in vivo* biodistribution.^[112] Zeolite-L crystals were filled with the positively charged γ -emitter $^{111}\text{In}^{3+}$. In order to avoid leakage of the indium into the media, the channels were blocked with stopcock molecules. A final coating with PEG chains to increase biocompatibility and prolong circulatory time was eventually done. The designed system is shown in Figure 1.8.

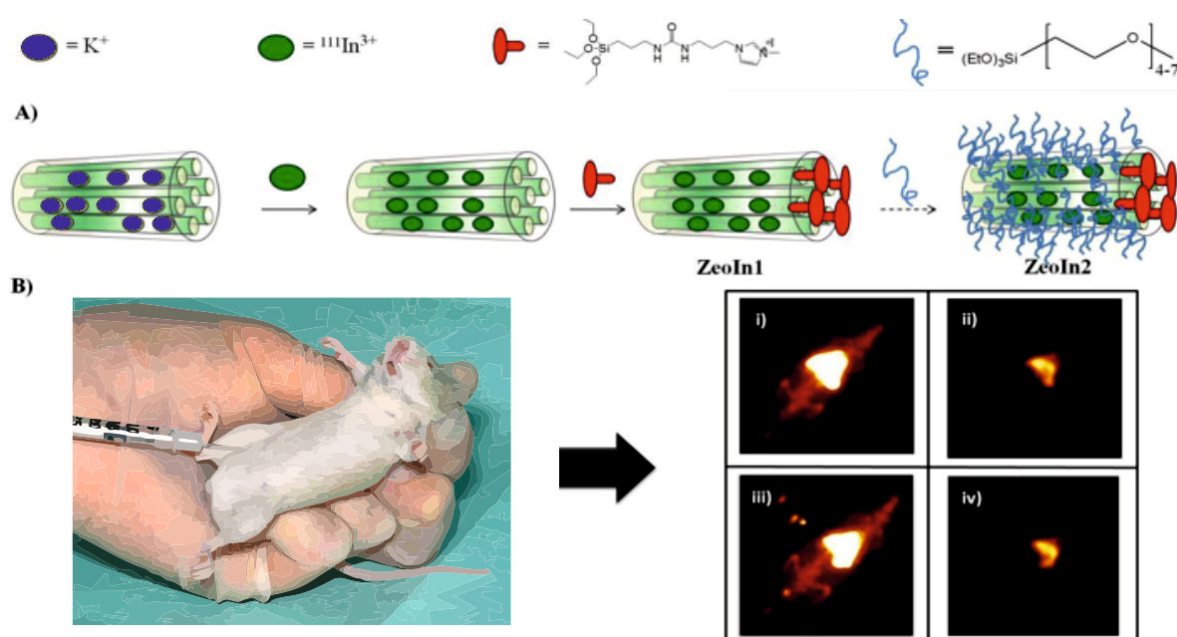


Fig. 1.8 A) Schematic picture of multifunctionalization of a zeolite-L crystal; B) Two-dimensional static scintigraphic images obtained 70 min after injection of the zeolites. *ZeoIn1* injected into rat 1 in i) high and ii) low contrast. *ZeoIn2* injected into rat 2 in iii) high and iv) low contrast.

The same group then showed the possibility to move towards a theranostic approach using small zeolites featuring different functionalities that are able to target, label, and photoinactivate pathogenic and antibiotic-resistant bacteria.^[113] In detail, a green

hydrophobic perylene diimide dye (DXP) was inserted into the pores of zeolite-L nanocrystals to label the cells. The outer surface was then functionalized with a silicon phthalocyanine photosensitizer able to produce toxic singlet oxygen upon irradiation with red light. Additionally, the outer surface was further functionalized with amine groups, which are protonated in physiological conditions and bind electrostatically to the negatively charged membrane of the bacteria. A schematic view of the functional nanosystem and of its components is reported in figure 1.9. After the binding of the particles to the bacteria, confirmed by the green fluorescence of the dye entrapped in the crystals, the particles can be irradiated with red light to trigger the production of singlet oxygen, which then efficiently kills the bacteria.

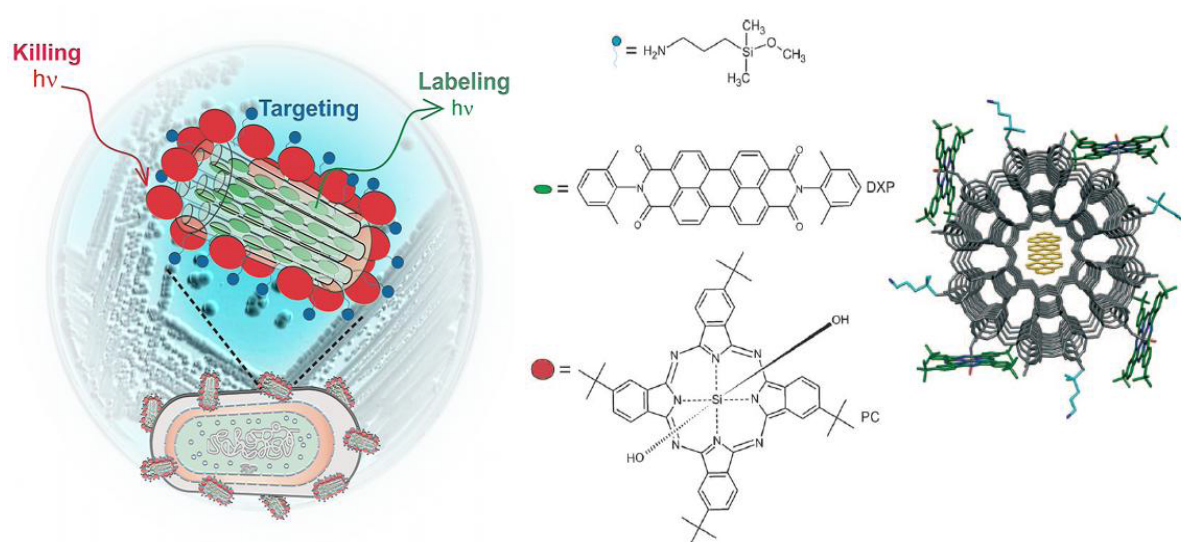


Fig. 1.9 Left: schematic picture of a multifunctional nanomaterial based on zeolite-L that can target, label, and kill bacteria. Middle: molecular components used for the fabrication of this nanomaterial. Right: Scheme showing a top view of one channel of zeolite-L loaded with the dye (DXP) and functionalized with targeting groups (3-aminopropyl-dimethyl-methoxysilane) and killing agent (singlet oxygen producing silicon phthalocyanine) bound to the outer surface. Adapted from H. Luelf, A. Devaux, E.A. Prasetyanto, L. De Cola, Porous nanomaterials for biomedical applications, in *Organic Nanomaterials: Synthesis, Characterization, and Device Applications*, Wiley, **2013**, Ch. 22.

Indeed it is also imaginable to release the guest molecules loaded into the zeolite pores, thus leading to drug delivery applications. On this account, not many examples have been reported so far and this field still has to be fully explored. Among the proposed strategies, Arruebo *et al.* reported a magnetic triggered drug delivery system based on magnetite and FAU zeolites containing doxorubicin, and *in vitro* experiments have shown that this system is able to store and release remarkable amounts of the drug.^[114] A slightly different approach to drug-release from loaded zeolites has been reported by Fatouros *et al.*, who have applied a

combination of experiments and theoretical modeling to verify the potential use of zeolite BEA as drug delivery vector.^[115] Eventually, Rimoli et al. proposed synthetic zeolites-X and -A as nanocarriers for the sustained release of ketoprofen as model drug, studying how the release profile changes depending on the pH conditions.^[116]

Last but not least, it has been shown that zeolite nanocrystals can also be used as external tools to self-assemble living systems, on account of their interaction with them. The self-assembly was achieved by using nonpathogenic *E. coli* and microzeolite-L crystals: *E. coli* bacteria showing a negatively charged outer membrane and zeolites amine-functionalized only at the channel entrances were demonstrated to give birth to self-assembled hybrid structures with two bacteria kept united by a container junction,^[117] as shown in Figure 1.10.

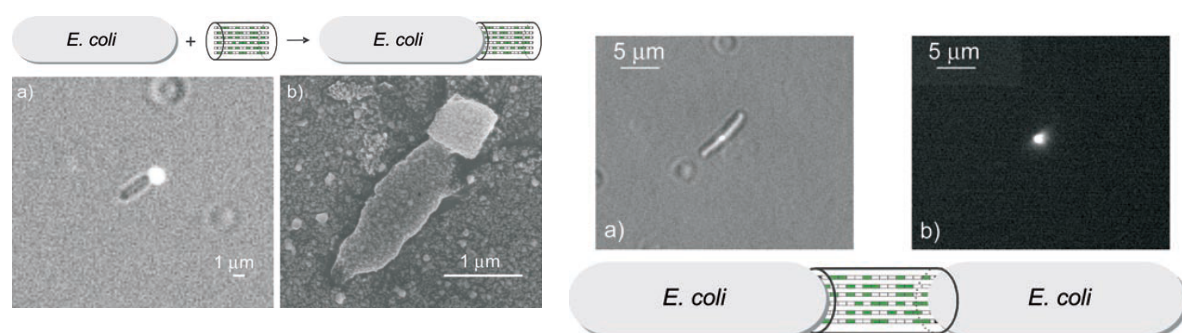


Fig. 1.10 Left) 1:1 zeolite-L/bacteria assembly. a) Optical microscope image taken upon irradiation with white and blue light; b) SEM image of the assembly after evaporation of the solvent and coating with silver. Right) Self-assembly of two bacteria by using a zeolite-L crystal as junction. a) Optical image taken upon white and blue light irradiation; b) Irradiation of the same sample with blue light. The fluorescence of the dye filled junction is monitored. Adapted from Z. Popović, M. Otter, G. Calzaferri, L. De Cola, *Angew. Chem. Int. Ed.* 2007, 46, 6188-6191. Copyright © 2007 WILEY-VCH Verlag GmbH & Co. KGaA, Weinheim.

1.4 Mesoporous silica nanoparticles and their application in nanomedicine

Since the first report using MCM-41 type mesoporous silica nanoparticles (MSNPs) as drug delivery system in 2001,^[118] the last decade has witnessed an exponential increase in research on biomedical application of MSNPs. The design of biocompatible and multifunctional MSNPs is still one of the hottest topics in nanobiotechnology and nanomedicine. As nanocarriers, MSNPs with unique mesoporous structure have been explored as effective drug delivery systems for a variety of therapeutic agents to fight against various kinds of diseases. Possessing a high surface area-to-volume ratio allows for increased surface functionalization, while still maintaining great porosity, which enables the inorganic platforms to house appreciable amounts of payload without destabilization of the silica framework.^[119-121] The possibility of introducing diverse and multi-functionalities to

develop highly engineered MSNPs has convinced scientists about their unprecedented advantages and potentialities among the possible nanosystems, especially for cancer therapy.^[122-124] Figure 1.11 gives a schematic summary of some of the typical species used in combination with the MSNP carrier.

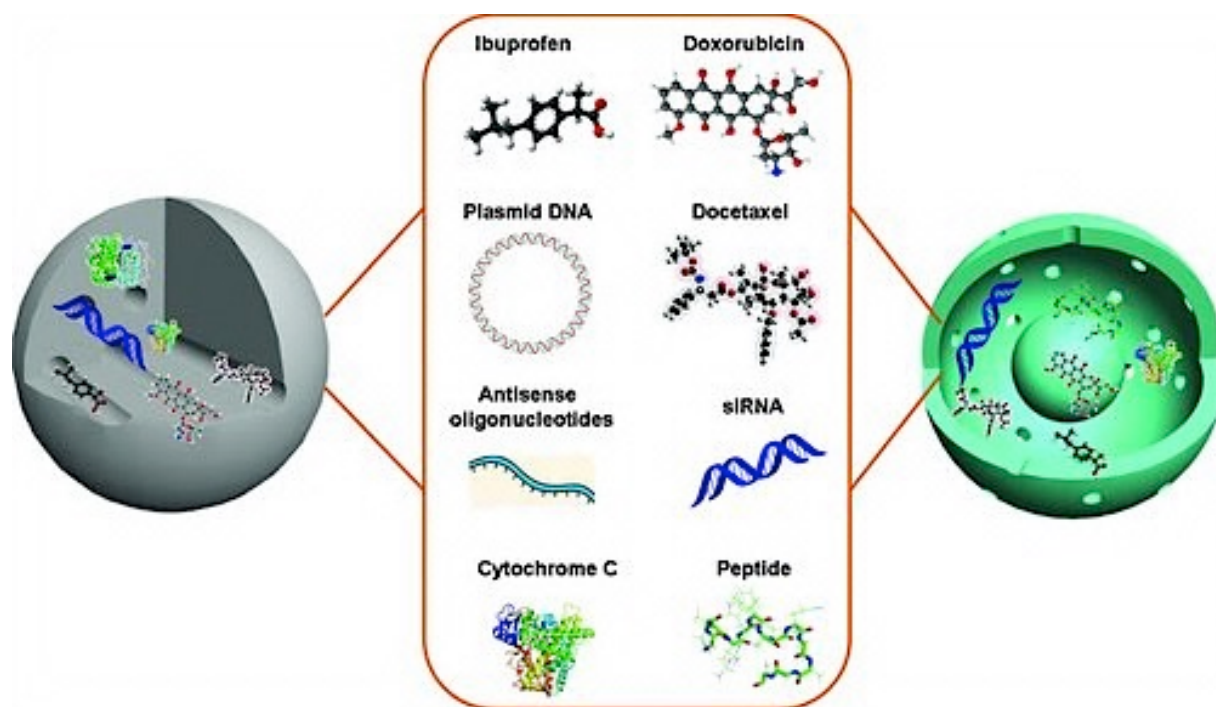


Fig. 1.11 Mesoporous silica nanoparticles as versatile drug delivery systems for a variety of therapeutic agents including pharmaceutical drugs (ibuprofen, doxorubicin, docetaxel, exc.), therapeutic genes (plasmid DNA, antisense oligonucleotides, and siRNA), and therapeutic proteins and peptides. Reprinted with permission from F. Tang, L. Li, D. Chen, *Adv. Mater.* **2012** *24*, 1504-1534. Copyright © 2012 WILEY-VCH Verlag GmbH & Co. KGaA, Weinheim

Generally speaking, a base-catalyzed sol-gel process is employed to produce silica nanoparticles with sizes suitable for biomedical applications. This process is in particular utilized to form the silica network, while the presence of templating micelles of surfactant is required to create the pores. Then, the ease of introducing various organic functional groups, either through covalent bonding or electrostatic interactions, provides high level of versatility and many mechanized features to the mesoporous silica materials. The strategies used for the synthesis of the material and those exploited to perform the designed surface functionalization will be discussed in details in Chapter 2. Beyond the wide range of possibilities offered by the chemical species attached to the particle surface, the other crucial property that makes mesoporous silica materials such powerful tools for drug delivery applications is their ability to encapsulate different types of cargo molecules within their pore channels. The encapsulation process may protect many therapeutic agents from

enzymatic degradation or any unwanted interaction with the external environment. The use of MSNPs as drug containers also endow a sustainable release of the therapeutic agent over time into cells, which may be more efficient than the normal pharmacokinetics of the free drug.^[125] Before MSNPs can be effectively applied as drug delivery systems, their cellular uptake and cytotoxic properties have to be investigated. Cellular uptake of the MSNPs and their good biocompatibility was confirmed with both healthy and cancer cell lines.^[126-128] Several research groups have demonstrated that cell uptake and cellular toxicity of the MSNPs may depend on the particle's size, shape, surface charge and functional groups.^[129-132] Cell staining experiments in conjunction with fluorescently labeled MSNPs allow the study of the cellular uptake mechanisms and the particle location inside the cells. Small MSNPs (< 200–300 nm) are normally taken up by cells via endocytotic pathway, which consists of the particle interacting with the cell surface, cell membrane invagination and pinching off.^[119,130-134] The nanoparticles upon uptake are located inside the endosomes, before fusing with the lysosomes. The MSNPs usually end up inside these acidic (pH \sim 4.5) organelles in cells (see Figure 1.12).^[135-137]

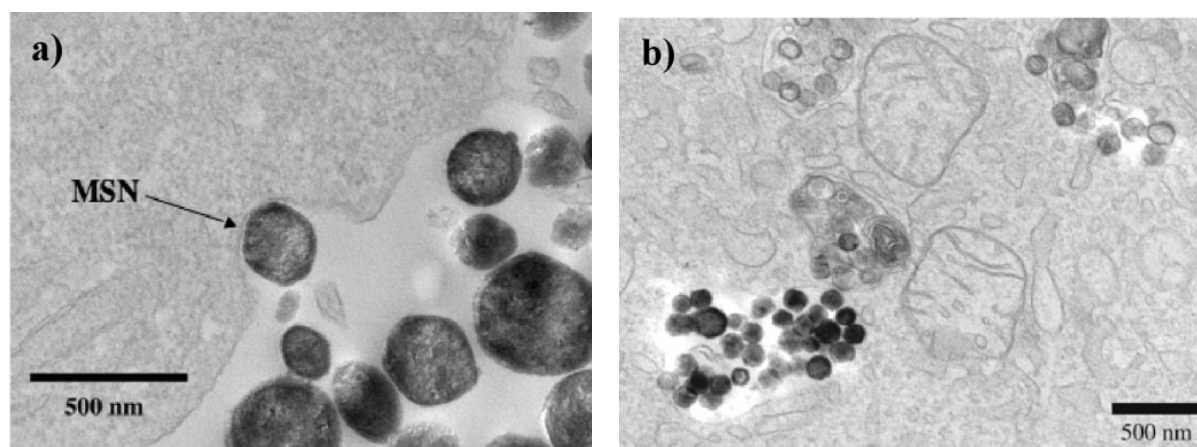


Fig. 1.12 Transmission electron microscopy images of HeLa cells set in contact with MSNPs. A) A single particle entering through the cell membrane; B) MSNPs trapped in vesicles inside the cells. Reprinted with permission from I.I. Slowing, B.G. Trewyn, S. Giri, V.S.Y. Lin, *Adv. Funct. Mater.* **2007**, *17*, 1225-1236. Copyright © 2007 WILEY-VCH Verlag GmbH & Co. KGaA, Weinheim.

The payload can be released into these vesicles and then diffusing in the cytoplasm, alternatively it has also been shown that functionalized MSNPs can lead to an endosomal rupture and escape, which enables the membrane impermeable cargos such as hydrophilic drugs, DNA and siRNA molecules to be released and travel to their effective sites.^[130,138-140] The drug delivery properties of MSNPs rely on the large pore capacity of the mesoporous material, which can improve the storage and release of both various hydrophobic and

hydrophilic anti-cancer drugs, offering a sustainable delivery when internalized in the cells. This is indeed of great importance especially for hydrophobic species because the effectiveness of such drugs may be hampered by their low solubility in water. Once incorporated in the pores, the cargo molecules do not escape easily into water when MSNPs are dissolved in an aqueous environment, which reduces the leakiness of the delivery system, allowing more drugs to reach their therapeutic target. Among the others, the MSNP-mediated doxorubicin delivery to live cells has been extensively investigated and several applications are covered in the literature.^[141-143] For instance, very recently Hakeem *et al.* reported natural chitosan end-capped MSNPs as novel, dual stimuli, responsive nanocarriers for controlled anticancer drug delivery. The chitosan nanovalves tightly close the pores of the MSNPs to control premature cargo release under physiological conditions, but respond to lysozyme and acidic media to release the trapped doxorubicin into the cells (see Figure 1.13).^[144]

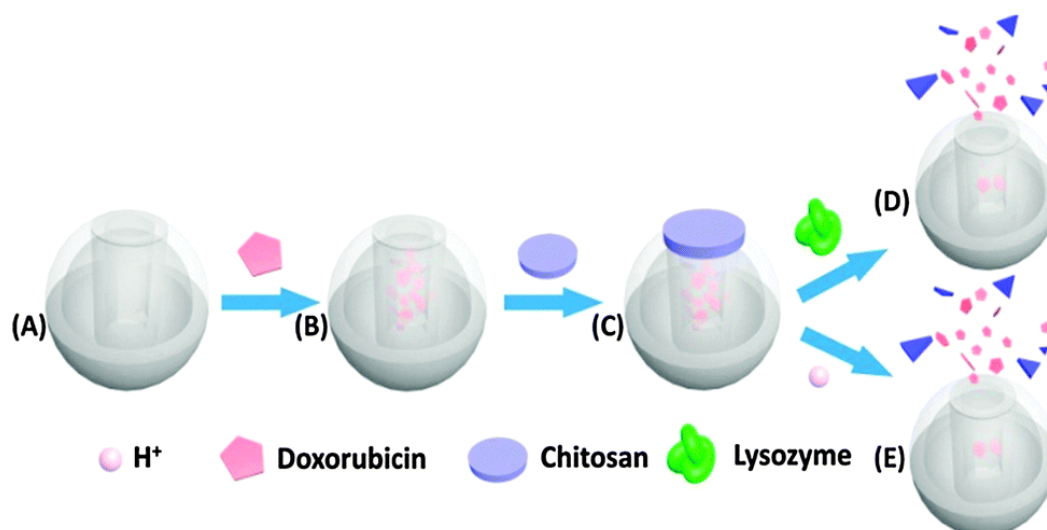


Fig. 1.13 Schematic illustration of the dual stimuli-responsive nanocarriers based on MSNPs for smart anticancer drug delivery. Doxorubicin is loaded into the pores, after which a coating of chitosan is applied and used to trigger the drug release upon its degradation caused by lysozyme activity or pH change. Reproduced from A. Hakeem, R. Duan, F. Zahid, C. Dong, B. Wang, F. Hong, *et al. Chem. Commun.* **2014**, *50*, 13268-13271 with permission of The Royal Society of Chemistry.

The properties of MSNPs as carriers for the hydrophobic drug Ibuprofen have been as well deeply studied.^[145-147] *In vitro* applications of MSNPs to deliver anti-cancer drugs such as camptothecin (CPT)^[148] and paclitaxel (Taxol)^[149] to human cancer cells have been also proposed. MSNPs have been used to deliver CPT anticancer drugs *in vivo* into human xenografts in mice and suppress the tumor growth.^[150] In another study, engineered MSNPs

with PEI-PEG copolymer coating were used for delivering doxorubicin on a KB-31 xenografted tumor model.^[151]

MSNPs can be successfully used also for delivering nucleic acids, such as DNAs and siRNA for gene therapy purposes.^[138,152-153] The advantage of using MSNP-based gene delivery systems is that they allow both the binding of nucleic acid molecules on the outer surface of the particles and the incorporation of small therapeutic agents inside the pore channels, enabling the synergistic dual delivery of nucleic acids and drugs.^[154-155] One way of using MSNPs as a plasmid DNA delivery vehicle has involved the surface grafting of second generation (G2) PAMAM dendrimers.^[156] Polyethyleneimine (PEI) coated MSNPs have also been used to deliver siRNA and DNA constructs.^[157-159] In a dual delivery design, the co-delivery of doxorubicin and the p-glycoprotein (Pgp) siRNA, which shuts down the Pgp expression to a drug-resistant cancer cell line (KB-V1 cells), resulted in a significantly and improved cell killing.^[160] A simplified scheme summarizing the concept of this work is reported in Figure 1.14.

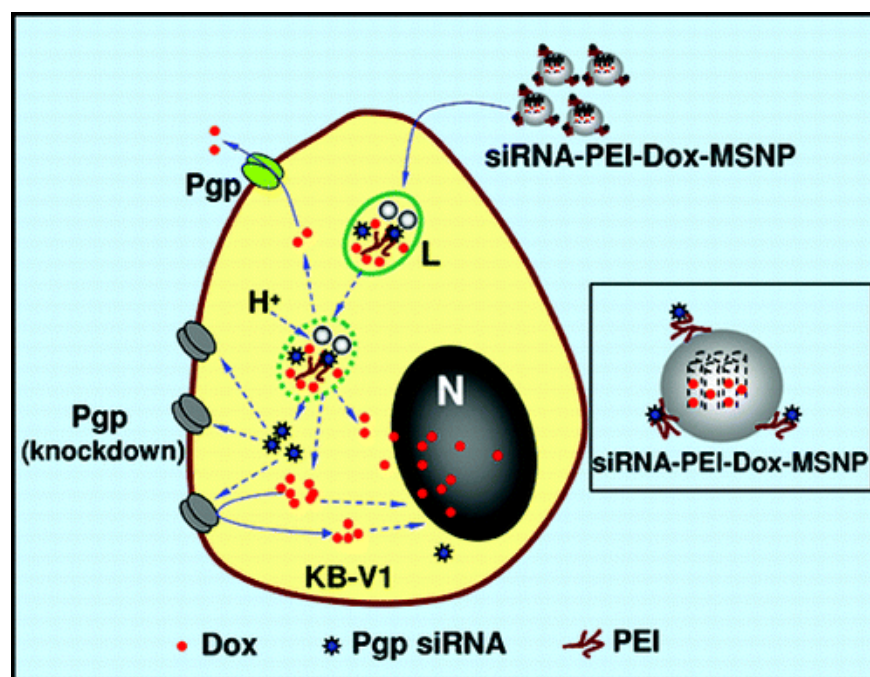


Fig. 1.14 Schematic illustration showing siRNA-PEI-Dox-MSNPs and their use to overcome drug resistance in KB-V1 cells. Selected siRNA strands targeting the Pgp cause its knockdown, which leads to a more efficient effect of the delivered doxorubicin in a synergistic pathway. Reprinted with permission from H. Meng, M. Liang, T. Xia, Z. Li, Z. Ji, I.J. Zink, A.E. Nel, *ACS Nano* 2010, 4, 4539-4550. Copyright (YEAR) American Chemical Society."

Co-delivery of Doxorubicin and a Bcl-2 siRNA by MSNPs has been also demonstrated to enhance the efficacy of chemotherapy in multidrug-resistant cancer cells.^[161] So far, however, the use of MSNPs in combination with unnatural nucleic acids as PNA or LNA has

not been yet reported, which may lead to interesting results thanks to the high targeting properties of these probes.

Unique attempts have been made in using MSNPs as suitable tools for the entrapment of proteins and their potential intracellular delivery.^[162] Lin's group showed the use of MSNPs with larger pores to encapsulate the membrane-impermeable cytochrome C and to deliver it efficiently to HeLa cells.^[163] Caruso *et al.* reported how a variety of enzymes could be encapsulated in mesoporous silica spheres by immobilizing them in the particles, and by subsequently depositing multilayered thin shells by a layer-by-layer technique.^[164] Several efforts have been made on the development of highly mechanized MSNPs bearing molecular moieties that can provide a control over the pore opening and thus a triggered cargo release. Engineered structure presenting supramolecular nanovalves, nanoimpellers, or nanopistons have been reported.^[165-170] a detailed overview on these systems is however beyond the scope of this thesis. In Chapter 5, a first example of multifunctional MSNPs carriers loaded with an antibraincancer drug and carrying PNA probes targeting a specific microRNA involved in tumor proliferation and drug resistance will be displayed, from material preparation and characterization to *in vitro* experiments on human cell lines.

1.5 Peptide nucleic acid (PNA)

DNA and RNA have been mainly used in several applications in bio-nanotechnology, as components or as targets. However, other special classes of nucleic acids have been synthesized over the past decades as DNA mimics, in which the essential features of natural DNA, such as the presence of nucleobases able to perform Watson-Crick-like base pairing, were maintained, but different structural features have been introduced either at the backbone or at the nucleobase level. Among the others, Peptide Nucleic Acids (PNAs) are DNA oligonucleotide analogs in which the negatively charged sugar-phosphate backbone is replaced by a neutral polyamide backbone made of *N*-(2-aminoethyl)glycine units.^[171] PNAs are considered extremely promising tools due to their unique properties, since they can bind complementary DNA or RNA sequences following standard Watson-Crick rules,^[172] but, due to the lack of electrostatic repulsion, PNA/DNA and PNA/RNA complexes have improved thermal stability when compared to DNA/DNA and DNA/RNA duplexes.^[173]

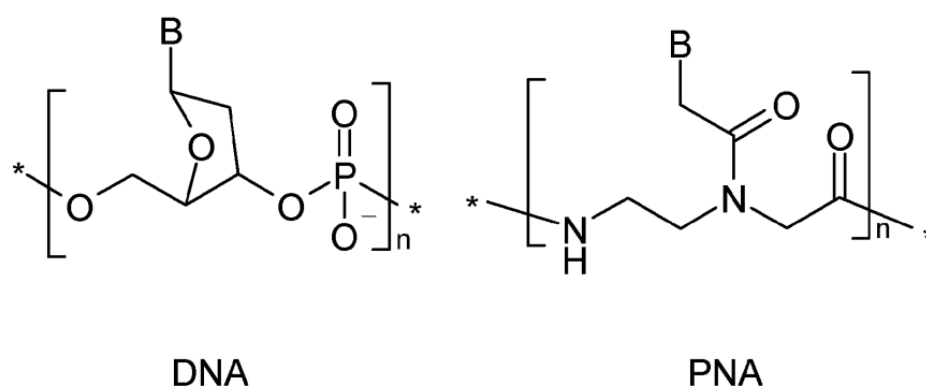


Fig. 1.15 Comparison between natural sugar-phosphate DNA backbone (left) and artificial synthetic peptide-like PNA (right). Letter “B” in the structures stands for one of the nucleobases.

This very high affinity for the DNA targets is very important for improving the performances in many applications devoted to DNA recognition.^[174-176] Another key feature of PNA probes relies on their selectivity: a single base-pairing mismatch in PNA/DNA duplexes is more destabilizing than in DNA/DNA complexes of the same length. Moreover, since the increased affinity makes it possible to obtain stable PNA-DNA and PNA-RNA complexes even with short PNA probes (10-mer or less), as compared to DNA probes, the possibility of using short sequences favors an even improved selectivity, which in some applications allows for an easy detection of single-point mutations and single nucleotide polymorphisms.^[177-178] It is worth to notice that PNA/DNA hybridization is less destabilized by the presence of organic solvents, and is less sensitive to the presence of salts, which are instead necessary to attenuate electrostatic repulsions in DNA duplexes. Actually, PNA/DNA binding can be efficiently achieved even under very low salt concentrations, a useful condition that promotes the destabilization of RNA and DNA secondary structures, resulting in a better access to target sequences.^[179] Low ionic strength conditions are for instance essential when targeting a double-stranded DNA, in order to disfavor DNA-DNA duplex formation, and to allow PNA probes to invade the double helix, displacing the homologous DNA strand. The relative independence of PNA performances with respect to the environment makes them ideal tools for more robust analytical procedures, especially in the case of the analysis of complex matrices such as biological fluids.^[180] Furthermore, an essential property of PNAs that is extremely useful in many biomedical applications is their biological stability to both nucleases and peptidases, since their artificial synthetic backbone prevents recognition by natural enzymes, making them highly persistent in biological fluids.^[181] Furthermore, the PNA scaffold may serve as a model for the design of novel molecules able to perform nucleic acid target recognition. Many modifications of the basic

PNAs have been proposed in the past years, in order to improve their performances and tune their properties. Several reviews have covered the literature concerning possible chemical modifications of the PNA structure.^[182-184] In figure 1.16, an example of a backbone-modified PNA bearing lysine side chains is reported; the presence of three adjacent chiral monomers (chiral box) was shown to highly improve the sequence selectivity of PNA, both in terms of direction control (antiparallel vs parallel binding) and single-mismatch recognition.^[185] Base modifications, as well backbone chemical transformations have been successfully exploited to improve the DNA recognition process by PNAs.^[186] Modification of adenine and thymine residues with pseudo-complementary bases 2-6-diaminopurine and 2-thiouracil,^[187] and introduction of chiral elements into the PNA backbone are two examples of this approach.^[185,188] The introduction of different functional groups with different charges/polarity/flexibility has been extensively described in the literature,^[189] and special modifications aiming at improving solubility and biological properties as cellular internalization will be furthermore presented in Chapter 4 of this thesis.

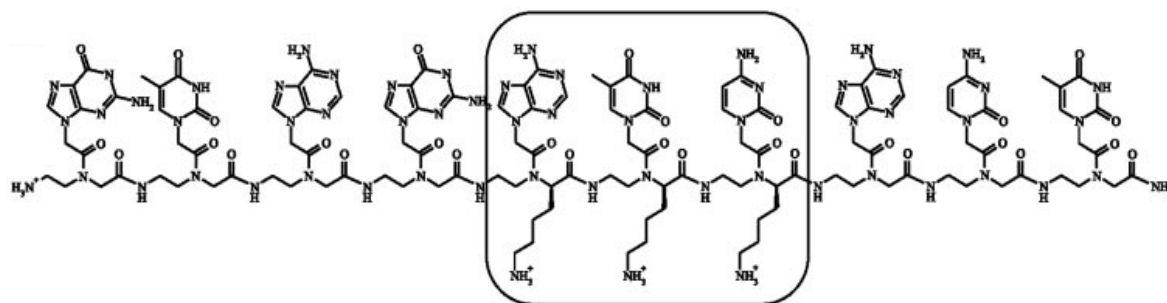


Fig. 1.16 Example of a modified PNA in which a chiral motif made of D-Lysine moieties has been inserted in the backbone. The presence of the new amine group in the lysine tail allows also for further functionalization steps. Adapted from V. Menchise, G. De Simone, T. Tedeschi, R. Corradini, S., Sforza, R. Marchelli, D. Capasso, M. Saviano, C. Pedone, *Proc. Nat. Acad. Sci.* **2003**, *100*, 12021-12026. Copyright © 2003, The National Academy of Sciences

On account of all the properties described above, PNAs have become important candidates for biological applications in diagnostics and gene therapy. Two strategies are basically involved in using PNAs as drug candidates, namely the anti-gene and the antisense approaches. In anti-gene strategy, PNA sequences are designed to recognize and hybridize complementary sequences in a particular gene, interfering with its transcription.^[190] PNAs are capable of arresting transcriptional processes by virtue of their ability to form a stable PNA:DNA:PNA triplex structure leading to a strand invasion complex (with displacement of one DNA strand) when challenging dsDNA. Macadangdang *et al.* showed, for example, the targeting of MDR1 gene to reduce drug resistance in cells,^[191] while Tonelli *et al.*

demonstrated antitumor activity in Rhabdomyosarcomas and transcriptional block by PNA anti-gene therapy.^[192]

Alternatively, in the case of antisense strategy, the PNA probe is designed to recognize and hybridize to complementary sequences of mRNA (or miRNA), in order to inhibit its translation or cause its degradation. Several papers have been published on this topic, for instance reporting the inhibition of staphylococcus aureus gene expression and growth using antisense PNAs,^[193] or targeting of mRNA for the diagnosis and treatment of acute lung injury.^[194] Strong evidences of miRNA targeting for the modulation of gene expression have been reported, among the others, by Corradini's and Gambari's groups^[195-196] and by Gait's group.^[197-198]

In diagnostics, PNAs have been utilized as analytical tools in a variety of sensing techniques, including microarrays,^[199-200] electrochemical-based,^[201-202] SPR,^[203-204] fluorescence in situ hybridization (FISH),^[205-206] and many others.^[207]

1.6 Nanostructures and PNA in Analytical techniques for DNA detection

The extraordinary effort in the sequencing of living organism genome constantly opens up new roads for the use of genetic information and offers possible new targets as specific markers in the analysis of samples of biological origin. This process calls for the development of new techniques and protocols for a simpler, faster, and cheaper detection of target nucleic acids to be used in different areas.

Most of the currently available methodologies to detect DNA sequences rely on the recognition capabilities of nucleic acids themselves and, thus, are based on the hybridization reaction between a probe oligonucleotide showing a specific sequence and the counterpart present in the DNA target. Most of the above methods need the amplification of the target species as a consequence of the very reduced amount of DNA material often available and detect the duplex formation by using labels and transducers able to generate a detectable signal upon the hybridization event. The polymerase chain reaction (PCR) is still the most common technique used to amplify a target DNA sequence; it is able to amplify a single piece of DNA up to several orders of magnitude higher, duplicating millions copies of a specific DNA sequence. Real-time PCR is currently the golden standard protocol for quantitative DNA detection. The PCR amplification is such an established procedure since it enhances both the specificity and the sensitivity of the method, by increasing the target

concentration. Once the PCR reaction is accomplished, the analytical detection method can be based on different techniques and literature is full of various examples based on optical^[208-210] and electrochemical^[211-213] techniques. An example is reported in Figure 1.17, showing an optical detection approach based on the use of gold nanorods.

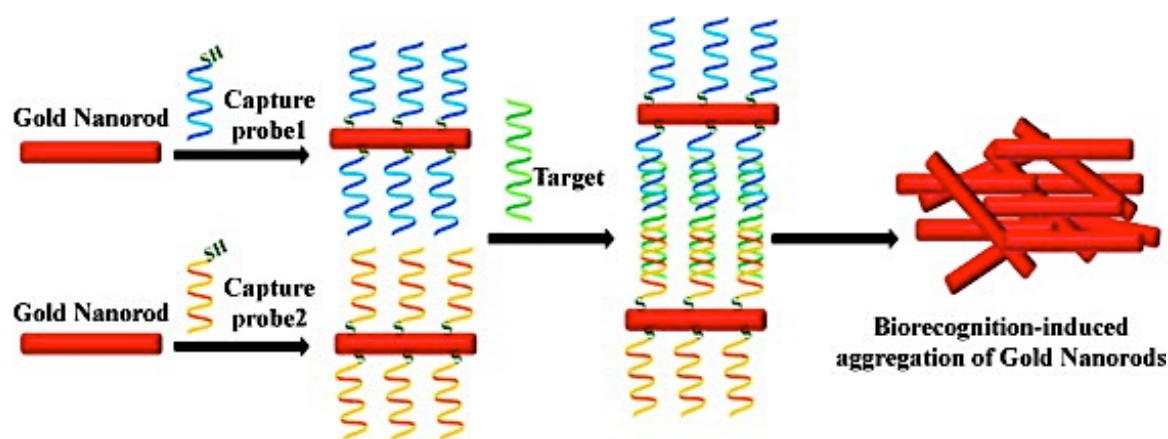


Fig. 1.17 Representation of DNA hybridization detection scheme with gold nanorods. Specific target recognition induces aggregation of gold nanorods, modulating the optical response. Reprinted from Parab, H. J., Jung, C., Lee, J. H., & Park, H. G. (2010). A gold nanorod-based optical DNA biosensor for the diagnosis of pathogens. *Biosensors and Bioelectronics*, 26(2), 667-673. Copyright (2010), with permission from Elsevier.

Among others, a very interesting and promising platform towards cheaper point-of-care diagnostics is the one developed on paper-based substrates, which has been implemented by various authors.^[214-215]

Nevertheless, PCR-based techniques still show drawbacks, the main being the need of trained personnel and careful control of the reaction conditions, laboratory equipment and reagent storage in order to avoid false positive and false negative results; furthermore PCR shows difficulty in amplifying large target DNA molecules (more than about 10000 bases) and the possible amplification of DNA sequences different from the target ones resulting in non-specific signals.

This is the reason why a growing sector in the DNA sensing field is now focusing on the opportunity given by the direct analysis of non-amplified genomic DNA, which turns out to be an excellent cost-effective alternative that can be achieved by using ultrasensitive DNA detection methods, reducing the extra labor and costs derived from the amplification step.

The enhanced sensitivity required when non-amplified genomic DNA constitutes the target of the analysis has prompted efforts directed towards the identification of novel strategies, leading to the combination of advanced materials with specific detection tools.

Advanced materials play different roles in the ultrasensitive PCR-free detection and nanostructures as metallic nanoparticles have been widely investigated for their optical and conductive properties.^[216-217]

Optical and electrochemical detection devices are among the most widely investigated for the analysis of non-amplified nucleic acids. In particular, optical detection has long been a powerful tool since it possesses some unique advantages over other analytical methods, e.g. the light beam produces much less interference to biological events, optical signal is immune to electromagnetic interferences, and optical labels are safe and easy to handle when compared with classical radioactive ones. Colorimetric assays have been extensively used since the seminal work from Mirkin's group in 1996, based on gold nanoparticles assembly driven by DNA hybridization.^[218-220] Fluorescent assays have been as well commonly utilized and examples of approaches based on molecular beacons,^[221-222] advanced structured nanomaterials,^[223-225] and electrochemiluminescence^[226] have been reported.

Electrochemical sensors show as well great promises due to their capability to provide efficient signal transduction and precise DNA recognition at a relatively low cost. A broad range of designs for various electrochemical devices is nowadays available and the advent of nanotechnology has drastically improved the fabrication of highly sensitive and specific electrochemical sensors.^[227]

Nanomaterials can be used in various aspects of the detection system including capture probes, reporting molecules, electrode fabrication, and electrode coatings.^[228] These materials offer improved biocompatibility, additional binding sites, and high signal intensities via enhanced electrical properties; nanofabrication allows also for miniaturization of the system, increasing sensitivity and reducing sample consumption.

Electrochemical sensors relying on the use of gold nanoparticles,^[229-230] silicon nanowires,^[231-232] carbon nanotubes,^[233-234] and graphene platforms^[235-236] are few examples among the huge variety of possibilities investigated in this field.

The key process in DNA sensing is the molecular recognition of DNA or RNA via Watson-Crick base pairing with a chemosensor probe, normally consisting of a nucleic acid tract complementary to that to be detected. Probe selection, surface structure and architecture are also key parameters in the enhanced sensitivity detection of non-amplified DNA, since some of the physical processes which can be exploited to generate the analytical signal are strongly dependent on them. For the generation of strong and reliable signals, an advantage is offered indeed by specifically designed probes such as PNAs, whose chemical and biological properties, as described in the previous chapter, make them particularly suited for

ultrasensitive detection. Using Surface Plasmon Resonance imaging (SPRi), a powerful label-free method for real-time monitoring of the biomolecular recognition events happening at a surface level,^[237-238] Spoto and coworkers developed sandwich-like systems based on PNA and oligonucleotide-functionalized gold nanoparticles to achieve a significant signal enhancement.^[180,217] Detection of single point mutation using non-amplified DNA was achieved, enabling to directly analyze mutant DNA connected to thalassemia in blood samples (Fig. 1.18).^[180]

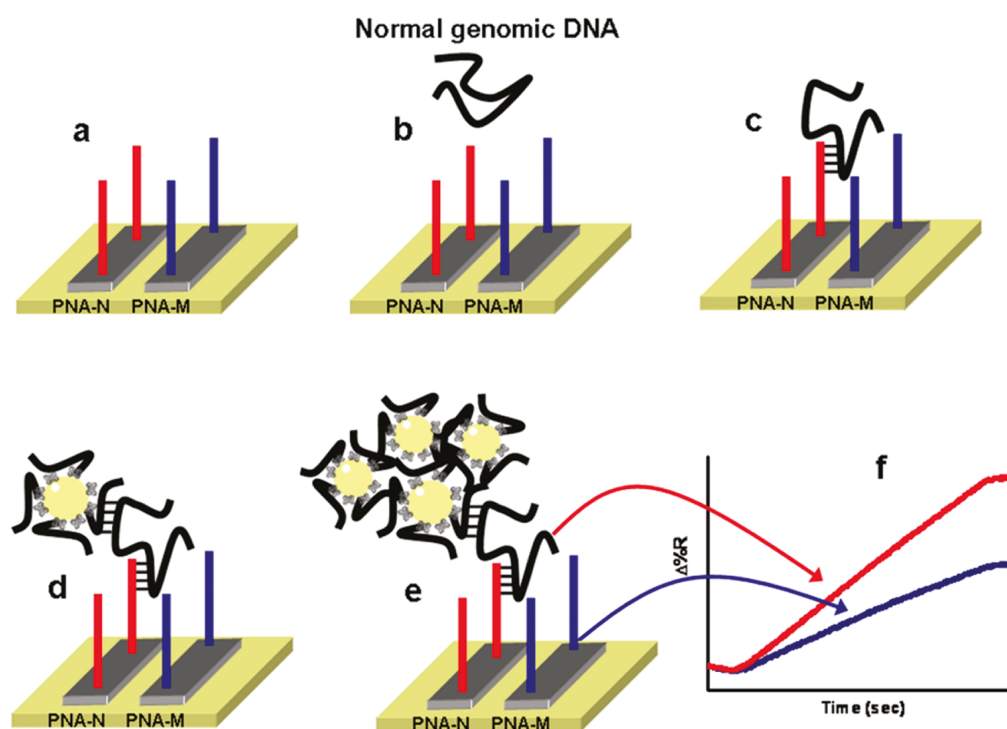


Fig. 1.18 Schematic description of the nanoparticle-enhanced SPR strategy used to detect a normal β^N/β^N , a heterozygous β^{9}/β^N , and a homozygous β^{9}/β^{9} genomic DNA. In order to simplify the pictorial representation only specifically adsorbed DNA is shown. Nonspecifically adsorbed DNA is also present on the surface and contributes to generate the SPR-detected signal. PNA-N and PNA-M probes specifically recognize the normal β -globin and the mutated β^{9} -globin genomic sequences, respectively. Reprinted with permission from R. D'Agata, G. Breveglieri, L.M. Zanoli, M. Borgatti, G. Spoto, R. Gambari, *Anal. Chem.* **2011**, 83, 8711-8717. Copyright (2011) American Chemical Society.

Thus, the combination of advanced nanotechnological and biotechnological tools, together with ICT capabilities, allows for envisaging that new sensor technologies with improved performances and easy-to-use accessibility might be developed and brought to the commercial level in the near future, thus leading to more easily handle DNA-based tests in many fields, including biomedical monitoring, forensic science, and food analysis.^[239]

1.7. Aim of the thesis

The aim of this thesis is to develop novel hybrid organic-inorganic materials and interfaces for biomedical applications. Structured materials as zeolite-L, mesoporous silica nanoparticles, and photonic crystal fibers are designed in combination with nucleic acid moieties (PNA and DNA), drug molecules, and proteins. This strategy offers the possibility of producing unique platforms with peculiar features at the interface, ranging applications from diagnostics to therapeutics. The thesis is divided in 10 chapters:

Chapter 1 gives a general introduction on the main topic this thesis is based on, i.e. nanomaterials and nanomedicine, Peptide nucleic acids, and nucleic acid detection.

Chapter 2 introduces general concepts and experimental techniques, which have been used throughout this thesis. The zeolite synthesis, loading, and functionalization are discussed, as well for MSNPs. The synthesis and characterization of PNA is eventually presented.

Chapter 3 investigates the possibility of using zeolite-L nanoparticles as DNA oligonucleotide carriers for a simultaneous release of the oligonucleotide and a model drug, which has been incorporated in the zeolite pores.

Chapter 4 shows the use of zeolite-L as a platform to develop novel PN-zeolite concrete hybrids to overcome the low cellular uptake of PNAs, demonstrating also the ability of the carriers to deliver the guest molecules incorporated.

Chapter 5 then moves to a direct therapeutic application based on the use of MSNPs loaded with a chemotherapy agent and carrying anti-miR PNA probes, in order to treat glioblastoma by a synergistic combination of gene therapy and sustained drug administration.

Chapter 6 shows how it is possible to overcome the limit of typical inorganic nanomaterials moving towards the realization of hybrid biodegradable organosilica shells used for encapsulating and releasing proteins and enzymes. The shell is built up directly around a bunch of proteins, thus maintaining a nanometer sized biocompatible nature.

Chapter 7 opens the section dedicated to ultra-sensitive nucleic acid detection, presenting the use of PNA-functionalized photonic crystal fibers (PCFs) in combination with modified gold nanoparticles as novel devices able to discriminate between the mutated DNA target sequences involved in cystic fibrosis development and the wild type differing only for a single point mutation.

Chapter 8 brings the same PCF-based detection scheme to a higher goal, showing the possibility of performing PCR-free analysis of genomic DNA with ultra-small consumption of the sample, detecting the target DNA tract at pg/mL concentrations.

Chapter 9 shows that the PNA probe can be thought not only as the recognition element, but also as the reporter moiety at the same time, presenting the synthesis of a pyrene-modified PNA switching probe able to indicate the presence of the target sequences thanks to the change of the fluorescent properties upon hybridization.

Chapter 10 describes the principles of the main instrumental techniques used throughout this thesis.

As can be seen by the strong interdisciplinarity of the work, the thesis has been carried out in two different laboratories: in the group of Prof. Roberto Corradini at the University of Parma, and in the group of Prof. Luisa De Cola at ISIS, Université de Strasbourg, thanks to the support of the Italian scholarship provided by the Ministry for Education, University, and Research (MIUR), and of the French Embassy in Italy through the MAE grant for the scientific cooperation between France and Italy.

REFERENCES

- [1] S. Eustis, M.A. El-Sayed, *Chem. Soc. Rev.*, **2006**, *35*, 209-217.
- [2] M.C. Daniel, D. Astruc, *Chem. Rev.* **2004**, *104*, 293-346.
- [3] A.M. Smith, S.M. Nie, *Acc. Chem. Res.* **2010**, *43*, 190-200.
- [4] J. Shi, A.R. Votruba, O.C. Farokhzad, R. Langer, *Nano Lett.* **2010**, *10*, 3223-3230.
- [5] F. Zhao, Y. Zhao, Y. Liu, X. Chang, C. Chen, Y. Zhao, *Small*, **2011**, *7*, 1322-1337.
- [6] F Tang, L Li, D Chen, *Adv. Mater.* **2012**, *24*, 1504-1534.
- [7] T.L. Doane, C. Burda, *Chem. Soc. Rev.* **2012**, *41*, 2885-2911.
- [8] B. Y. S. Kim, J. T. Rutka and W. C. W. Chan, *N. Engl. J. Med.* **2010**, *363*, 2434-2443
- [9] T. Lammers, S. Aime, W.E. Hennink, G. Storm, F. Kiessling, *Acc. Chem. Res.* **2011**, *44*, 1029-1038.
- [10] K. Riehemann, S.W. Schneider, T.A. Luger, B. Godin, M. Ferrari, H. Fuchs, *Angewandte Chemie Int. Ed.*, **2009**, *48*, 872-897.
- [11] W.R. Algar, D.E. Prasuhn, M.H. Stewart, T.L. Jennings, J.B. Blanco-Canosa, P.E. Dawson, I.L. Medintz, *Bioconjugate Chem.* **2011**, *22*, 825-858.
- [12] Y. Sun, Y. Xia, *Science* **2002**, *298*, 2176-2179.
- [13] W.K. Leutwyler, S.L. Bürgi, H. Burgl, *Science* **1996**, *271*, 933-937.
- [14] A. Lu, E.E. Salabas, F. Schüth, *Angew. Chem. Int. Ed.* **2007**, *46*, 1222-1244.
- [15] T.W. Ebbesen, P.M. Ajayan, *Nature* **1992**, *358*, 220-222.
- [16] F. Tang, L. Li, D. Chen, *Adv. Mater.* **2012**, *24*, 1504-1534.
- [17] M. Niederberger, *Accounts Chem. Res.* **2007**, *40*, 793-800.
- [18] A. Samad, Y. Sultana, M. Aqil, *Curr. Drug Deliver.* **2007**, *4*, 297-305.
- [19] J.P. Rao, K.E. Geckeler, *Progr. Polym. Sci.* **2011**, *36*, 887-913.
- [20] M. De, P.S. Ghosh, V.M. Rotello, *Adv. Mat.* **2008**, *20*, 4225-4241.
- [21] K. Saha, A. Bajaj, B. Duncan, V.M. Rotello, *Small* **2011**, *7*, 1903-1918.
- [22] M. R. Jones, K. D. Osberg, R. J. MacFarlane, M. R. Langille, C. A. Mirkin, *Chem. Rev.* **2011**, *111*, 3736-3827.

- [23] B. Yameen, W.I. Choi, C. Vilos, A. Swami, J. Shi, O.C. Farokhzad, *J. Control. Release* **2014**, *190*, 485-499.
- [24] A. Albanese, P.S. Tang, W.C. Chan, *Annu. Rev. Biomed. Eng.* **2012**, *14*, 1-16.
- [25] Y. Qiu, Y. Liu, L. Wang, L. Xu, R. Bai, Y. Ji, X. Wu, Y. Zhao, Y. Li, C. Chen *Biomaterials*, **2010**, *31*, 7606-7619.
- [26] B.D. Chithrani, A.A. Ghazani, W.C. Chan, *Nano letters*, **2006**, *6*, 662-668.
- [27] X. Huang, L. Li, T. Liu, N. Hao, H. Liu, D. Chen, F. Tang, *ACS Nano*, **2011**, *5*, 5390-5399.
- [28] B.D. Chithrani, W.C. Chan, *Nano Letters*, **2007**, *7*, 1542-1550.
- [29] F. Lu, S. Wu, Y. Hung, C.Y. Mou, *Small*, **2009**, *5*, 1408-1413.
- [30] H. Jin, D.A. Heller, R. Sharma, M.S. Strano, *ACS Nano*, **2009**, *3*, 149-158.
- [31] D.L Thorek, A. Tsourkas, *Biomaterials*, **2008**, *29*, 3583-3590.
- [32] R.R. Arvizo, O.R. Miranda, M.A. Thompson, C.M. Pabelick, R. Bhattacharya, J.D. Robertson, P. Mukherjee, *Nano letters*, **2010**, *10*, 2543-2548.
- [33] J. Wang, S. Tian, R.A. Petros, M.E. Napier, J.M. DeSimone, *J. Am. Chem. Soc.* **2010**, *132*, 11306-11313.
- [34] A. Verma, F. Stellacci, *Small* **2010**, *6*, 12-21.
- [35] M. Lundqvist, J. Stigler, G. Elia, I. Lynch, T. Cedervall, K.A. Dawson, *PNAS*, **2010**, *105*, 14265-14270.
- [36] M.P. Monopoli, D. Walczyk, A. Campbell, G. Elia, I. Lynch, F. Baldelli Bombelli, K.A. Dawson, *J. Am. Chem. Soc.* **2011**, *133*, 2525-2534.
- [37] D.A. Giljohann, D.S. Seferos, P.C. Patel, J.E. Millstone, N.L. Rosi, C.A. Mirkin, *Nano letters*, **2007**, *7*, 3818-3821.
- [38] B. P. Timko, K. Whitehead, W. Gao, D. S. Kohane, O. Farokhzad, D. Anderson, R. Langer, *Annu. Rev. Mater. Res.* **2011**, *41*, 1-20.
- [39] H. Luelf, A. Devaux, E.A. Prasetyanto, L. De Cola, Porous nanomaterials for biomedical applications, in *Organic Nanomaterials: Synthesis, Characterization, and Device Applications*, Wiley, **2013**, Ch. 22.
- [40] K. Moller, T. Bein, *Science* **2011**, *333*, 297-298.
- [41] S. Mackowiak, A. Schmidt, V. Weiss, C. Argyo, C. von Schirnding, T. Bein, C. Bräuchle, *Nano Lett.* **2013**, *13*, 2576-2583.
- [42] A. Schloßbauer, A. Sauer, V. Cauda, A. Schmidt, H. Engelke, U. Rothbauer, K. Zolghadr, H. Leonhardt, C. Bräuchle, T. Bein, *Adv. Healthcare Mater.* **2012**, *1*, 316-320.
- [43] M. Dobay, A. Schmidt, E. Mendoza, T. Bein, J. Rädler. *Nano Lett.* **2013**, *13*, 1047-1052.
- [44] G.B. Sukhorukov, A.L. Rogach, B. Zebli, A.G. Skirtach, K. Kohler, A.A. Antipov, N. Gaponik, A.S. Susha, M. Winterhalter, W.J. Parak, *Small* **2005**, *1*, 194-200.
- [45] E.S Olson, T. Jiang, T.A. Aguilera, Q.T. Nguyen, Q.T. Ellies, M. Scadeng, R.Y. Tsien, *PNAS*, **2010**, *107*, 4311-4316.
- [46] V.A. Kickhoefer, M. Han, S. Raval-Fernandes, M.J. Poderycki, R.J. Moniz, D. Vaccari, L-H. Rome, *ACS Nano*, **2008**, *3*, 27-36.
- [47] D.P. Ferris, J. Lu, C. Gothard, R. Yanes, C.R. Thomas, J.C. Olsen, J. Zink, *Small* **2011**, *7*, 1816-1826.
- [48] C.J.F. Rijcken, O. Soga, W.E. Henink, C.F. von Nostrum, *J. Controlled Release* **2007**, *120*, 131-148.
- [49] A. Schroeder, D.A. Heller, M.M. Winslow, J.E. Dahlman, G.W. Pratt, R. Langer, D.G. Anderson, *Nature Reviews Cancer*, **2011**, *12*, 39-50.
- [50] O.M. Yaghi, M. O'Keeffe, N.W. Ockwig, H.K. Chae, *Nature* **2003**, *423*, 705-714.
- [51] S.R. Ji, C. Liu, B. Zhang, F. Yang, J. Xu, J. Long, X.J. Yu, *Biochimica et Biophysica Acta* **2010**, *1806*, 29-35.

- [52] G. Calzaferri, A. Devaux, *Manipulation of energy transfer processes in the channels of zeolite L*, in *Supramolecular Effects in Photochemical and Photophysical Processes*. John Wiley & Sons, Inc. New Jersey, **2011**.
- [53] I.I. Slowing, B.G. Trewyn, S. Giri, V.Y. Lin, *Adv. Funct. Mat.* **2007**, *17*, 1225-1236.
- [54] Z. Li, J.C. Barnes, A. Bosoy, J.F. Stoddart, J. Zink, *Chem. Soc. Rev.* **2011**, *41*, 2590-2605.
- [55] S. S. Kelkar, T. M. Reineke, *Bioconjugate Chem.* **2011**, *22*, 1879–1903.
- [56] T. Lammers, S. Aime, W. E. Hennink, G. Storm, F. Kiessling, *Acc. Chem. Res.* **2011**, *4*, 1114-1122.
- [57] M. E. Gindy, R. K. Prud'homme, *Expert Opin. Drug Delivery* **2009**, *6*, 865–878.
- [58] M.W. Ambrogio, C.R. Thomas, Y.L. Zhao, J.I. Zink, J.F. Stoddart, *Acc. Chem. Res.* **2011**, *44*, 903-913.
- [59] C. Sanchez, B. Julian, P. Belleville, M. Popall, *J. Mater. Chem.* **2005**, *15*, 3559-3592.
- [60] C. Sanchez, P. Belleville, M. Popall, L. Nicole, *Chem. Soc. Rev.* **2011**, *40*(2), 696-753.
- [61] R. Macfarlane, B. Lee, M.R. Jones, N. Harris, G.C. Schatz, C.A. Mirkin, *Science* **2011**, *334*, 204-208.
- [62] A. Kuzyk, R. Schreiber, Z. Fan, G. Pardatscher, E.M. Roller, A. Högele, T. Liedl, *Nature* **2012**, *483*, 311-314.
- [63] H. Meng, M. Liong, T. Xia, Z. Li, Z. Ji, J. Zink, A.E. Nel, *ACS nano* **2010**, *4*, 4539-4550.
- [64] H. Meng, W.X. Mai, H. Zhang, M. Xue, T. Xia, S. Lin, J. Zink, A.E. Nel, *ACS nano* **2013**, *7*, 994-1005.
- [65] S.B. Hartono, N.T. Phuoc, M. Yu, Z. Jia, M.J. Monteiro, S. Qiao, C. Yu, *J. Mater. Chem. B* **2014**, *2*, 718-726.
- [66] X. Ma, Y. Zhao, K.W. Ng, Y. Zhao, *Chem-Eur. J.* **2013**, *19*, 15593-15603.
- [67] Y. Dong, K.T. Love, J.R. Dorkin, S. Sirirungruang, Y. Zhang, D. Chen, R. Bogorad, H. Yin, Y. Chen, A. Vegas, C. Alabi, G. Sahai, K. Olejnik, W. Wang, A. Schroeder, A. Lytton-Jean, D. Siegwart, R. Langer, D.G. Anderson, *PNAS* **2014**, *111*, 3955-3960.
- [68] B. Ozpolat, A.K. Sood, G. Lopez-Berestein, *Adv. Drug Deliver. Rev.* **2014**, *66*, 110-116.
- [69] C.E. Probst, P. Zrazhevskiy, V. Bagalkot, X. Gao, *Adv. Drug Deliver. Rev.* **2013**, *65*, 703-718.
- [70] S. Jiang, A.A. Eltoukhy, K.T. Love, R. Langer, D.G. Anderson, *Nano letters* **2013**, *13*, 1059-1064.
- [71] Y. Ding, Z. Jiang, K. Saha, C.S. Kim, S.T. Kim, R.F. Landis, V.M. Rotello, *Mol. Ther.* **2014**, *22*, 1075-1083.
- [72] J.I. Cutler, E. Auyeung, C.A. Mirkin, *J. Am. Chem. Soc.* **2012**, *134*, 1376-1391.
- [73] L.M. Zanolli, R. D'Agata, G. Spoto, *Anal. Bioanal. Chem.* **2012**, *402*, 1759-1771.
- [74] R. Verdoold, R. Gill, F. Ungureanu, R. Molenaar, R.P. Kooyman, *Biosens. Bioelectron.* **2011**, *27*, 77-81.
- [75] H. Dong, Z. Zhu, J. Ju, F. Yan, *Biosens. Bioelectron.* **2012**, *33*, 228-232.
- [76] C. Geyik, S. Evran, S. Timur, A. Telefoncu, *Biotechnol. Progr.* **2014**, *30*, 224-232.
- [77] C. Ge, J. Du, L. Zhao, L. Wang, Y. Liu, D., Li, C. Chen, *PNAS* **2011**, *108*, 16968-16973.
- [78] A. Cao, Z. Ye, Z. Cai, E. Dong, X. Yang, G. Liu, Y. Liu, *Angewandte Chemie Int. Ed.* **2010**, *49*, 3022-3025.
- [79] Y. Kang, Q. Wang, Y.C. Liu, J.W. Shen, T. Wu, *J. Phys. Chem. B* **2010**, *114*, 2869-2875.
- [80] Y. Wang, F. Caruso, *Chem. Mat.* **2005**, *17*, 953-961.
- [81] I.I. Slowing, B.G. Trewyn, V.S.Y. Lin, *J. Am. Chem. Soc.* **2007**, *129*, 8845-8849.
- [82] J. Ge, J. Lei, R.N. Zare, *Nature nanotechnology* **2012**, *7*, 428-432.

- [83] Z. Li, G. Luppi, A. Geiger, H.P. Josel, L. De Cola, *Small* **2011**, *7*, 3193-3201.
- [84] W.P. Hall, S.N. Ngatia, R.P. Van Duyne, *J. Phys. Chem. C* **2011**, *115*, 1410-1414.
- [85] G. Calzaferri, S. Huber, H. Maas, C. Minkowski, *Angew. Chem. Int. Ed.* **2003**, *42*, 3732-3758.
- [86] A. Z. Ruiz, H. Li, G. Calzaferri, *Angewandte Chemie* **2006**, *118*, 5408-5413.
- [87] A.Z. Ruiz, D. Brühwiler, T. Ban, G. Calzaferri, *Monatshefte für Chemie/Chemical Monthly* **2005**, *136*, 77-89.
- [88] S. Megelski, G. Calzaferri, *Adv. Funct. Mater.* **2001**, *11*, 277-286.
- [89] M. Busby, H. Kerschbaumer, G. Calzaferri, *Adv. Mater.* **2008**, *20*, 1614-1618.
- [90] M. Busby, A. Devaux, C. Blum, V. Subramaniam, G. Calzaferri, L. De Cola, *J. Phys. Chem. C* **2011**, *115*, 5974-5988.
- [91] H. Maas, A. Khatyr, G. Calzaferri, *Micropor. Mesopor. Mat.* **2003**, *65*, 233-242.
- [92] S. Megelski, A. Lieb, M. Pauchard, A. Drechsler, S. Glaus, C. Debus, A. Meixner, G. Calzaferri, *J. Phys. Chem. B* **2001**, *105*, 25-35.
- [93] G. Calzaferri, M. Pauchard, H. Maas, S. Huber, A. Khatyr, T. Schaafsma, *J. Mater. Chem.* **2002**, *12*, 1-13.
- [94] S. Ramachandra, K.C. Schuermann, F. Cucinotta, G. Calzaferri, L. De Cola, *Small* **2011**, *7*, 1488-1494.
- [95] R.N. Mahato, H. Lülfi, M.H. Siekman, S.P. Kersten, P.A. Bobbert, M.P. de Jong, L. De Cola, W.G. van der Wiel, *Science* **2013**, *341*, 257-260.
- [96] H. Maas, G. Calzaferri, *Angew. Chem. Int. Ed.* **2002**, *41*, 2284-2288.
- [97] D. Brühwiler, G. Calzaferri, *Comptes Rendus Chimie* **2005**, *8*, 391-398.
- [98] I. López-Duarte, L.Q. Dieu, I. Dolamic, M. Martínez-Díaz, T. Torres, G. Calzaferri, D. Brühwiler, *Chem-Eur. J.* **2011**, *17*, 1855-1862.
- [99] E. Climent, R. Martínez-Mañez, F. Sancenón, M.D. Marcos, J. Soto, A. Maquieira, P. Amorós, *Angewandte Chemie* **2010**, *122*, 7439-7441.
- [100] H. Meng, M. Xue, T. Xia, Y.L. Zhao, F. Tamanoi, J.F. Stoddart, J.I. Zink, A.E. Nel, *J. Am. Chem. Soc.* **2010**, *132*, 12690-12697.
- [101] C.R. Thomas, D.P. Ferris, J.H. Lee, E. Choi, M.C. Cho, E.S. Kim, J.F. Stoddart, J.S. Shin, J. Cheon, J.I. Zink, *J. Am. Chem. Soc.* **2010**, *132*, 10623-10625.
- [102] M. Vallet-Regi, F. Balas, D. Arcos, *Angew. Chem. Int. Ed.* **2007**, *46*, 7548-7558.
- [103] A.A. Bruns, J. Vider, H. Ow, E. Herz, O. Penate-Medina, M. Baumgart, S.M. Larson, U. Wiesner, M. Bradbury, *Nano Lett.* **2009**, *18*, 442-448.
- [104] J. Lu, Z. Li, J.I. Zink, F. Tamanoi, *Nanomed-Nanotechnol.* **2012**, *8*, 212-220.
- [105] H.J. Metz, G. Calzaferri, A. Devaux, S. Suarez, A. Kunzmann, *U.S. Patent No. 7,655,300*. Washington, DC: U.S. Patent and Trademark Office **2010**.
- [106] G. Qi, L. Li, F. Yu, H. Wang, H. ACS *Appl. Mater. Interf.* **2013**, *5*, 10874-10881.
- [107] J. Rosenholm, C. Sahlgren, M. Lindén, *J. Mater. Chem.* **2010**, *20*, 2707-2713.
- [108] B.G. Trewyn, I.I. Slowing, S. Giri, H.T. Chen, V.S.Y. Lin, *Acc. Chem. Res.* **2007**, *40*, 846-853.
- [109] I. Bresinska, K.J.J. Balkus, *J. Phys. Chem.* **1994**, *98*, 12989-12994.
- [110] E. Csajbók, I. Bányai, L. Vander Elst, R.N. Muller, W. Zhou, J.A. Peters, *Chem.-Eur. J.* **2005**, *11*, 4799-4807.
- [111] C. Platas-Iglesias, L. Vander Elst, W. Zhou, R.N. Muller, C.F. Geraldes, T. Maschmeyer, J.A. Peters, *Chem.-Eur. J.* **2002**, *8*, 5121-5131.
- [112] M.M. Tsotsalas, K. Kopka, G. Luppi, S. Wagner, M.P. Law, M. Schäfers, L. De Cola, *ACS Nano* **2009**, *4*, 342-348.
- [113] C.A. Strassert, M. Otter, R.Q. Albuquerque, A. Höne, Y. Vida, B. Maier, L. De Cola, *Angew. Chem. Int. Ed.* **2009**, *48*, 7928-7931.
- [114] M. Arruebo, R. Fernandez-Pacheco, S. Irusta, J. Arbiol, M.R. Ibarra, J. Santamaria, *Nanotech.* **2006**, *17*, 4057-4064.

- [115] D.G. Fatouros, D. Douroumis, V. Nikolakis, S. Ntais, A.M. Moschovi, V. Trivedi, P.A. Cox, *J. Mater. Chem.* **2011**, *21*, 7789-7794.
- [116] M. Rimoli, M.R. Rabaioli, D. Melisi, A. Curcio, S. Mondello, R. Mirabelli, E. Abignente, *J. Biomed. Mater. Res. Part A* **2008**, *87*, 156-164.
- [117] Z. Popović, M. Otter, G. Calzaferri, L. De Cola, *Angew. Chem. Int. Ed.* **2007**, *46*, 6188-6191.
- [118] M. Vallet-Regí, A. Rámila, R. P. del Real, J. Pérez-Pariente, *Chem. Mater.* **2001**, *13*, 308-311.
- [119] J.L. Vivero-Escoto, I.I. Slowing, B.G. Trewyn, V. S.-Y. Lin, *Small* **2010**, *6*, 1952–1967
- [120] M. Liong, J. Lu, M. Kovichich, T. Xia, S. G. Ruehm, A. E. Nel, F. Tamanoi, J. I. Zink, *ACS Nano* **2008**, *2*, 889–896.
- [121] K. K. Coti, M. E. Belowich, M. Liong, M. W. Ambrogio, Y. A. Lau, H. A. Khatib, J. I. Zink, N. M. Khashab and J. F. Stoddart, *Nanoscale* **2009**, *1*, 16–39.
- [122] Z. Li, J.C. Barnes, A. Bosoy, J.F. Stoddart, J.I. Zink, *Chem. Soc. Rev.* **2012**, *41*, 2590-2605.
- [123] F. Tang, L. Li, D. Chen, *Adv. Mater.* **2012** *24*, 1504-1534.
- [124] Q. He, J. Shi, *J. Mater. Chem.* **2011**, *21*, 5845-5855.
- [125] X. Li, Q. He, J. Shi, *ACS nano* **2014**, *8*, 1309-1320.
- [126] Q. Fu, G. V.-R. Rao, L. K. Ista, Y. Wu, B. P. Andrzejewski, L. A. Sklar, T. L. Ward, G. P. Lopez, *Adv. Mater.* **2003**, *15*, 1262–1266.
- [127] S. P. Hudson, R. F. Padera, R. Langer, D. S. Kohane, *Biomaterials* **2008**, *29*, 4045–4055.
- [128] D. R. Radu, C. Y. Lai, K. Jeftinija, E. W. Rowe, S. Jeftinija, V. S.-Y. Lin, *J. Am. Chem. Soc.* **2004**, *126*, 13216–13217.
- [129] S. H. Wu, Y. Hung, C. Y. Mou, *Chem. Commun.* **2011**, *47*, 9972–9985.
- [130] I. Slowing, B.G. Trewyn, V.S.Y. Lin, *J. Am. Chem. Soc.* **2006**, *128*, 14792-14793.
- [131] X. Huang, X. Teng, D. Chen, F. Tang, J. He, *Biomaterials* **2010**, *31*, 438-448.
- [132] H. Meng, S. Yang, Z. Li, T. Xia, J. Chen, Z. Ji, H. Zhang, *et al. ACS Nano* **2011**, *5*, 4434-4447.
- [133] B.G. Trewyn, S. Giri, I.I. Slowing, V.S.Y. Lin, *Chem. Commun.* **2007**, *31*, 3236-3245.
- [134] I.I. Slowing, B.G. Trewyn, S. Giri, V.S.Y. Lin, *Adv. Funct. Mater.* **2007**, *17*, 1225-1236.
- [135] C.H. Lee, S.H. Cheng, I. Huang, J.S. Souris, C.S. Yang, C.Y. Mou, L.W. Lo, *Angew. Chem.* **2010**, *122*, 8390-8395.
- [136] J. Lu, M. Liong, J.I. Zink, F. Tamanoi, *Small* **2007**, *3*, 1341-1346.
- [137] H. Meng, M. Liong, T. Xia, Z. Li, Z. Ji, J.I. Zink, A.E. Nel, *ACS Nano* **2010**, *4*, 4539-455.
- [138] I.I. Slowing, J.L. Vivero-Escoto, C.W. Wu, V.S.Y. Lin, *Adv. Drug Deliver. Rev.* **2008**, *60*, 1278-1288.
- [139] J.M. Rosenholm, E. Peuhu, J.E. Eriksson, C. Sahlgren, M. Lindén, *Nano Lett.* **2009**, *9*, 3308-3311.
- [140] Q. Zhang, F. Liu, K.T. Nguyen, X. Ma, X. Wang, B. Xing, Y. Zhao, *Adv. Funct. Mater.* **2012**, *22*, 5144-5156.
- [141] Y. Gao, Y. Chen, X. Ji, X. He, Q. Yin, Z. Zhang, Y. Li, *ACS Nano* **2011**, *5*, 9788-9798.
- [142] X. Hu, X. Hao, Y. Wu, J. Zhang, X. Zhang, P.C. Wang, X.J. Liang, *J. Mater. Chem. B* **2013**, *1*, 1109-1118.
- [143] N. Singh, A. Karambelkar, L. Gu, K. Lin, J.S. Miller, C.S. Chen, M.J. Sailor, S.N. Bhatia, *J. Am. Chem. Soc.* **2011**, *133*, 19582-19585.

- [144] A. Hakeem, R. Duan, F. Zahid, C. Dong, B. Wang, F. Hong, *et al. Chem. Commun.* **2014**, *50*, 13268-13271.
- [145] J. Andersson, J. Rosenholm, S. Areva, M. Linden, *Chem. Mater.* **2004**, *16*, 4160–4167.
- [146] B. Munoz, A. Ramila, J. Perez-Pariente, I. Diaz, M. Vallet-Regi, *Chem. Mater.* **2003**, *15*, 500–503.
- [147] M. Manzano, V. Aina, C. O. Arean, F. Balas, V. Cauda, M. R. Colilla, M. Delgado, M. Vallet-Regi, *Chem. Eng. J.* **2008**, *137*, 30–37.
- [148] J. Lu, M. Liong, J. I. Zink, F. Tamanoi, *Small* **2007**, *3*, 1341–1346.
- [149] J. Lu, M. Liong, S. Sherman, T. Xia, M. Kovoichich, A. E. Nel, J. I. Zink, F. Tamanoi, *NanoBiotechnology* **2007**, *3*, 89–95.
- [150] J. Lu, M. Liong, Z. Li, J. I. Zink, F. Tamanoi, *Small* **2010**, *6*, 1794–1805.
- [151] H. Meng, M. Xue, T. Xia, Z. Ji, D. Tarn, J. I. Zink, A. E. Nel, *ACS Nano* **2011**, *5*, 4131–4144.
- [152] M.H. Kim, H. Na, Y.K. Kim, S.R. Ryoo, H.S. Cho, K.E. Lee, D.H. Min, *ACS Nano* **2011**, *5*, 3568-3576.
- [153] F. Torney, B.G. Trewyn, V.S.Y. Lin, K. Wang, *Nat. Nanotech.* **2007**, *2*, 295-300.
- [154] H. Meng, W.X. Mai, H. Zhang, M. Xue, T. Xia, S. Lin, X. Wanh, Y. Zhao, Z. Ji, J.I. Zink, A.E. Nel, *ACS Nano* **2013**, *7*, 994-1005.
- [155] X. Ma, Y. Zhao, K. Ng, Y. Zhao, *Chem.-Eur. J.* **2013**, *19*, 15593-15603.
- [156] D. R. Radu, C. Y. Lai, K. Jeftinija, E. W. Rowe, S. Jeftinija, V. S.-Y. Lin, *J. Am. Chem. Soc.* **2004**, *126*, 13216–13217.
- [157] J. Shen, H.C. Kim, H. Su, F. Wang, J. Wolfram, D. Kirui, H. Shen, *Theranostics* **2014**, *4*, 487-497.
- [158] T. Xia, M. Kovoichich, M. Liong, H. Meng, S. Kabehie, S. George, J.I. Zink, A.E. Nel, *ACS Nano* **2009**, *3*, 3273-3286.
- [159] X. Li, Y. Chen, M. Wang, Y. Ma, W. Xia, H. Gu, *Biomaterials* **2013**, *34*, 1391-1401.
- [160] H. Meng, M. Liong, T. Xia, Z. Li, Z. Ji, J.I. Zink, A.E. Nel, *ACS Nano* **2010**, *4*, 4539-4550.
- [161] A.M. Chen, M. Zhang, D. Wei, D. Stueber, O. Taratula, T. Minko, H. He, *Small* **2009**, *5*, 2673-2677.
- [162] C.H. Lee, T.S. Lin, C.Y. Mou, *Nano Today* **2009**, *4*, 165-179.
- [163] I.I. Slowing, B.G. Trewyn, V.S.Y. Lin, *J. Am. Chem. Soc.* **2007**, *129*, 8845-8849.
- [164] Y. Wang, F. Caruso, *Chem. Mater.* **2005**, *17*, 953-961.
- [165] S. Angelos, E. Choi, F. Vogtle, L. De Cola, J. I. Zink, *J. Phys. Chem. C* **2007**, *111*, 6589–6592.
- [166] N. Liu, D. R. Dunphy, P. Atanassov, S. D. Bunge, Z. Chen, G. P. Lopez, T. J. Boyle, C. J. Brinker, *Nano Lett.* **2004**, *4*, 551–554.
- [167] T. D. Nguyen, H. R. Tseng, P. C. Celestre, A. H. Flood, Y. Liu, J. F. Stoddart, J. I. Zink, *Proc. Natl. Acad. Sci. USA* **2005**, *102*, 10029–10034.
- [168] C. Wang, Z. Li, D. Cao, Y.L. Zhao, J.W. Gaines, O.A. Bozdemir, J.F. Stoddart, *Angew. Chem. Int. Ed.* **2012**, *51*, 5460-5465.
- [169] M.W. Ambrogio, C.R. Thomas, Y. Zhao, J.I. Zink, J.F. Stoddart, *Acc. Chem. Res.* **2011**, *44*, 903-913.
- [170] Y. Zhao, Z. Li, S. Kabehie, Y. Y. Botros, J. F. Stoddart, J. I. Zink, *J. Am. Chem. Soc.* **2010**, *132*, 13016–13025.
- [171] P.E. Nielsen, M. Egholm, R.H. Berg, O. Buchardt, *Science* **1991**, *254*, 1497–1500
- [172] M. Egholm, O. Buchardt, L. Christensen, C. Behrens, S.M. Freier, D.A. Driver, R.H. Berg, S.K. Kim, B. Norden, P.E. Nielsen, *Nature* **1993**, *365*, 566–568.
- [173] T. Ratilainen, A. Holm'en, E. Tuite, P.E. Nielsen, B. Nord'en, *Biochem.* **2000**, *39*, 7781–7791.

- [174] B. Cai, S. Wang, L. Huang, Y. Ning, Z. Zhang, G.J. Zhang, *ACS nano* **2014**, *8*, 2632-2638.
- [175] A. Singer, M. Wanunu, W. Morrison, H. Kuhn, M. Frank-Kamenetskii, A. Meller, *Nano letters* **2010**, *10*, 738-742.
- [176] H.U. Khan, M.E. Roberts, O. Johnson, R. Förch, W. Knoll, Z. Bao, *Adv. Mater.* **2010**, *22*, 4452-4456.
- [177] B. Ren, J.M. Zhou, M. Komiyama, *Nucleic Acids Res.* **2004**, *32*, e42.
- [178] B.S. Gaylord, M.R. Massie, S.C. Feinstein, G.C. Bazan, *PNAS* **2005**, *102*, 34-39.
- [179] S. Tomac, M. Sarkar, T. Ratilainen, P. Wittung, P.E. Nielsen, B. Nordén, A. Gräslund, *J. Am. Chem. Soc.* **1996**, *118*, 5544-5552.
- [180] R. D'Agata, G. Breveglieri, L.M. Zanolli, M. Borgatti, G. Spoto, R. Gambari, *Anal. Chem.* **2011**, *83*, 8711-8717.
- [181] V.A. Demidov, V.N. Potaman, M.D. Frank-Kamenetskii, M. Egholm, O. Buchardt, S.H. Sonnichsen, P.E. Nielsen, *Biochem. Pharm.* **1994**, *48*, 1310-1313.
- [182] B. Falkiewicz, *Acta Biochim. Pol.* **1999**, 100646, 509-529.
- [183] J. Micklefield, *Curr. Med. Chem.* **2001**, *8*, 1157-1179.
- [184] R. Corradini, S. Sforza, T. Tedeschi, F. Totsingan, A. Manicardi, R. Marchelli, *Curr. Topics Med. Chem.* **2011**, *11*, 1535-1554.
- [185] V. Menchise, G. De Simone, T. Tedeschi, R. Corradini, S., Sforza, R. Marchelli, D. Capasso, M. Saviano, C. Pedone, *Proc. Nat. Acad. Sci.* **2003**, *100*, 12021-12026.
- [186] A. Bertucci, A. Manicardi, R. Corradini, *Advanced Molecular Probes for Sequence-Specific DNA Recognition, in: Detection of non-amplified Genomic DNA*, Springer, Dordrecht, The Netherlands **2012**
- [187] I.G. Panyutin, I.V. Panyutin, V.V. Demidov, *Anal. Biochem.* **2007**, *362*, 145-147.
- [188] T. Tedeschi, S. Sforza, R. Corradini, R. Marchelli, *Tetrahedron letters* **2005**, *46*, 8395-8399.
- [189] E. Rozners, *J. Nucl. Acids* **2012**.
- [190] K. Kaihatsu, K.E. Huffman, D.R. Corey, *Biochem.* **2004**, *43*, 14340-14347.
- [191] B. Macadangdang, N. Zhang, P.E. Lund, A.H. Marple, M. Okabe, M.M. Gottesman, C. Kimchi-Sarfaty, *PloS one* **2011**, *6*, e17981.
- [192] R. Tonelli, A. McIntyre, C. Camerin, Z.S. Walters, K. Di Leo, J. Self *et al.* *Clin. Cancer. Res.* **2012**, *18*, 796-807.
- [193] N. Nekhotiaeva, S.K. Awasthi, P.E. Nielsen, L. Good, *Mol. Ther.* **2004**, *10*, 652-659.
- [194] R. Shrestha, Y. Shen, K.A. Pollack, J.S.A. Taylor, K.L. Wooley, *Bioconjugate Chem.* **2012**, *23*, 574-585.
- [195] E. Brognara, E. Fabbri, E. Bazzoli, G. Montagner, C. Ghimenton, A. Eccher *et al.* *J. neuro-oncol.* **2014**, *118*, 19-28.
- [196] A. Manicardi, E. Fabbri, T. Tedeschi, S. Sforza, N. Bianchi, E. Brognara *et al.* *ChemBioChem* **2012**, *13*, 1327-1337.
- [197] M.M. Fabani, C. Abreu-Goodger, D. Williams, P.A. Lyons, A.G. Torres, K.G. Smith, M.J. Gait, E. Vigorito, *Nucleic acids Res.* **2010**, gkq160.
- [198] A.G. Torres, M.M. Fabani, E. Vigorito, D. Williams, N. Al-Obaidi, F. Wojciechowski, M.J. Gait, *Nucleic acids Res.* **2012**, *40*, 2152-2167.
- [199] H.F. Arlinghaus, M. Schröder, J.C. Feldner, O. Brandt, J.D. Hoheisel, D. Lipinsky, *Appl. Surf. Sci.* **2004**, *231*, 392-396.
- [200] O. Brandt, J.D. Hoheisel, *TRENDS in Biotechnology* **2004**, *22*, 617-622.
- [201] J.B. Raof, R. Ojani, S.M. Golabi, E. Hamidi-Asl, M.S. Hejazi, *Sensor Actuat. B-Chem.* **2011**, *157*, 195-201.
- [202] S. Jampasa, W. Wonsawat, N. Rodthongkum, W. Siangproh, P. Yanatatsaneejit, T. Vilaivan, O. Chailapakul, *Biosens. Bioelectron.* **2014**, *54*, 428-434.

- [203] R. D'Agata, G. Spoto, *Artif. DNA PNA XNA* **2012**, *3*, 45-52.
- [204] T. Endo, K. Kerman, N. Nagatani, Y. Takamura, E. Tamiya, *Anal. Chem.* **2005**, *77*, 6976-6984.
- [205] I.K. Oliveira, G.W. Procop, D. Wilson, J. Coull, H. Stender, *J. Clin Microbiol.* **2002**, *40*, 247-251.
- [206] R.S. Santos, N. Guimarães, P. Madureira, N.F. Azevedo, *J. Biotech.* **2014**, *187*, 16-24.
- [207] C. Briones, M. Moreno, *Anal. Bioanal. Chem.* **2012**, *402*, 3071-3089.
- [208] H.J. Parab, C. Jung, J.H. Lee, H.G. Park, *Biosens. Bioelectron.* **2010**, *26*, 667-673.
- [209] M.L. Ermini, S. Mariani, S. Scarano, D. Campa, R. Barale, M. Minunni, *Anal. Bioanal. Chem.* **2013**, *405*, 985-993.
- [210] E. Sharon, R. Freeman, I. Willner, *Anal. Chem.* **2010**, *82*, 7073-7077.
- [211] X. Chen, Y.H. Lin, J. Li, L.S. Lin, G.N. Chen, H.H. Yang, *Chem. Comm.* **2011**, *47*, 12116-12118.
- [212] T.G. Drummond, M.G. Hill, J.K. Barton, *Nature biotech.* **2003**, *21*, 1192-1199.
- [213] S.K. Jha, R. Chand, D. Han, Y. Jang, G.S. Ra, J.S. Kim, Y.S. Kim, *Lab on a Chip* **2012**, *12*, 4455-4464.
- [214] A.C. Araújo, Y. Song, J. Lundeberg, P.L. Ståhl, H. Brumer III, *Anal. Chem.* **2012**, *84*, 3311-3317.
- [215] A.W. Martinez, S.T. Phillips, G.M. Whitesides, *Anal. Chem.* **2009**, *82*, 3-10.
- [216] R. Stine, J.T. Robinson, P.E. Sheehan, C.R. Tamanaha, *Adv. Mater.* **2010**, *22*, 5297-5300.
- [217] R. D'Agata, R. Corradini, C. Ferretti, L. Zanolli, M. Gatti, R. Marchelli, G. Spoto, *Biosens. Bioelectron.* **2010**, *25*, 2095-2100.
- [218] C.A. Mirkin, R.L. Letsinger, R.C. Mucic, J.J. Storhoff, *Nature* **1996**, *382*, 607-609.
- [219] J.J. Storhoff, C.A. Mirkin, *Chem. Rev.* **1999**, *99*, 1849-1862.
- [220] D. LI, C. Fan, *Optical detection on Non-amplified Genomic DNA*, in: *Detection of non-amplified Genomic DNA*, Springer, Dordrecht, The Netherlands **2012**.
- [221] M. You, C.J. Yang, W. Tan, *Molecular Beacons for Detection of Single-Nucleotide Polymorphisms*, in: *Molecular Beacons*, Springer Berlin Heidelberg, **2013**.
- [222] K. Wang, Z. Tang, C.J. Yang, Y. Kim, X. Fang, W. Li, W. Tan, *Angew. Chem. Int. Ed.* **2009**, *48*, 856-870.
- [223] J. Yan, M.C. Estévez, J.E. Smith, K. Wang, X. He, L. Wang, W. Tan, *Nano Today* **2007**, *2*, 44-50.
- [224] Y. Gao, W.L. Stanford, W.C. Chan, *Small* **2011**, *7*, 137-146.
- [225] Z. Gao, A. Agarwal, A.D. Trigg, N. Singh, C. Fang, C. Tung, J. Kong, *Anal. Chem.* **2007**, *79*, 3291-3297.
- [226] R. Duan, X. Zhou, D. Xing, *Anal. Chem.* **2010**, *82*, 3099-3103.
- [227] E. Alipour, M.H. Pournaghi-Azar, M. Parvizi, S.M. Golabi, M.S. Hejazi, *Electrochimica Acta* **2011**, *56*, 1925-1931.
- [228] S. Marín, A. Merkoçi, *Electrochemical detection of DNA using nanomaterial based sensors*, in: *Detection of non-amplified Genomic DNA*, Springer, Dordrecht, The Netherlands **2012**.
- [229] J.M. Nam, S.I. Stoeva, C.A. Mirkin, *J. Am. Chem. Soc.* **2004**, *126*, 5932-5933.
- [230] Y.S. Ang, L.Y.L. Yung, *ACS nano* **2012**, *6*, 8815-8823.
- [231] A. Gao, N. Lu, P. Dai, T. Li, H. Pei, X. Gao, C. Fan, *Nano letters* **2011**, *11*, 3974-3978.
- [232] P. Xie, Q. Xiong, Y. Fang, Q. Qing, C.M. Lieber, *Nature nanotech.* **2012**, *7*, 119-125.
- [233] Y. Weizmann, D.M. Chenoweth, T.M. Swager, *J. Am. Chem. Soc.* **2011**, *133*, 3238-3241.
- [234] S. Sorgenfrei, C.Y. Chiu, R.L. Gonzalez Jr, Y. Yu, P. Kim, C. Nuckolls, K.L. Shepard, K. L. *Nature nanotech.* **2011**, *6*, 126-132.

- [235] R. Stine, J.T. Robinson, P.E. Sheehan, C.R. Tamanaha, *Adv. Mater.* **2010**, *22*, 5297-5300.
- [236] L. Zhu, L. Luo, Z. Wang, *Z. Biosens. Bioelectron.* **2012**, *35*, 507-511.
- [237] K. Tamada, F. Nakamura, M. Ito, X. Li, A. Baba, *Plasmonics* **2007**, *2*, 185-191.
- [238] T.T. Goodrich, H.J. Lee, R.M. Corn, *J. Am. Chem. Soc.* **2004**, *126*, 4086-4087.
- [239] S. Sforza, R. Corradini, T. Tedeschi, R. Marchelli, *Chem. Soc. Rev.* **2011**, *40*, 221-23.

2

Making the tools: synthesis and characterization of zeolite-L, mesoporous silica nanoparticles and Peptide nucleic acid

Abstract

This chapter describes how the key building blocks of this thesis have been realized. First, the synthesis of zeolite L in different sizes and aspect ratios is presented, focusing in particular on cylindrical zeolite-L crystals. A general overview on the approaches followed for the insertion of guest molecules and for the functionalization of the external surface is reported. Subsequently, synthetic procedures and functionalization strategies are also described for mesoporous silica nanoparticles. Finally, the synthetic routes used for the synthesis of Peptide Nucleic Acid are presented as well as the typical characterization procedures.

2.1 Synthesis and characterization of Zeolite-L

One of the main features of Zeolite-L crystals is that it is possible to tune the synthetic conditions in order to have materials of different sizes, shape, and aspect ratio. The applications of the diverse formats vary from designing artificial photonic antenna systems^[1] to applying zeolite-L crystals as functional materials in self-assembled arrangements^[1-2] and biomedical applications.^[3-7] By changing the synthetic parameters (e.g. composition of the synthesis gel, temperature, aging time, dynamic or static conditions) the crystal morphology (from cylindrical to disc-shaped) and the final size (from 30 nm to about 10000 nm) can be tailored tuned (See Figure 2.1.).^[8]

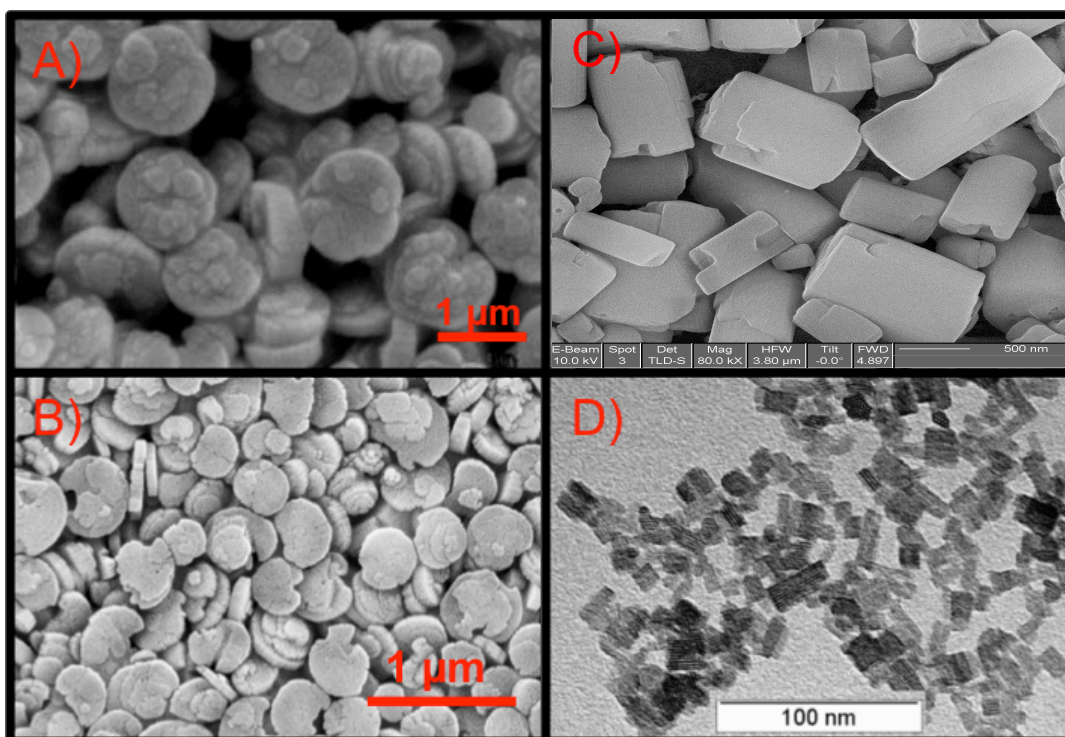


Figure 2.1. Zeolite-L crystals in different sizes and shapes. A) SEM picture of disc shaped micrometer sized zeolite-L crystals; B) SEM image of smaller disc shaped crystals; C) SEM image of cylindrical zeolite-L crystals of c.a. 1 μm ; D) TEM picture of nanometer sized cylindrical zeolites-L.

Zeolite-L crystals are synthesized using a hydrothermal condition from gels containing an aluminum and a silicon source, and the necessary counter cations (see figure 2.2.). Upon mixing of these two sources, the hydrothermal synthesis is carried out at high temperatures in either static or dynamic conditions depending on the final desired aspect ratio, using Teflon vessels and an oven equipped with a rotating unit.

Details about the synthesis conditions of specific zeolite-L crystals used throughout this thesis are reported in the experimental section at the end of this Chapter. After aging, crystals are always washed several times with deionized water till the supernatant shows neutral pH. After drying, the crystals are analyzed by means of powder x-ray diffraction (XRD), to prove their crystallinity, by dynamic light scattering (DLS) to determine the dynamic radius and zeta potential measurements for their external overall charge, by scanning electron microscopy (SEM) and transmission electron microscopy (TEM) for determining their size, monodispersity, morphology, shape. All these techniques have been used to characterize the synthesized crystals, and with the exception of XRD, a general overview on their principles is reported in Chapter 10.

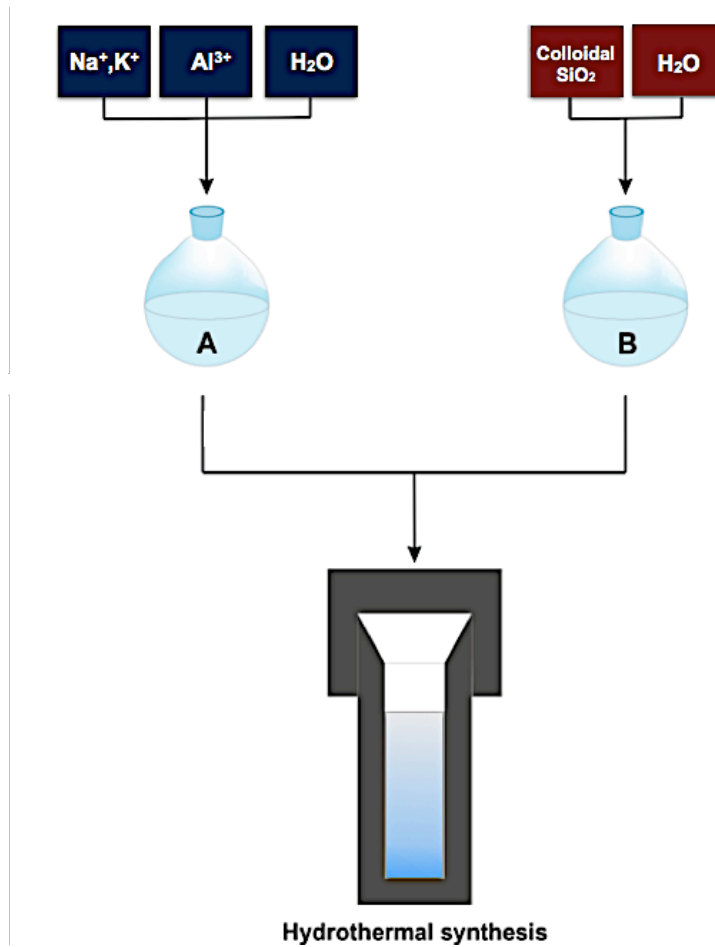
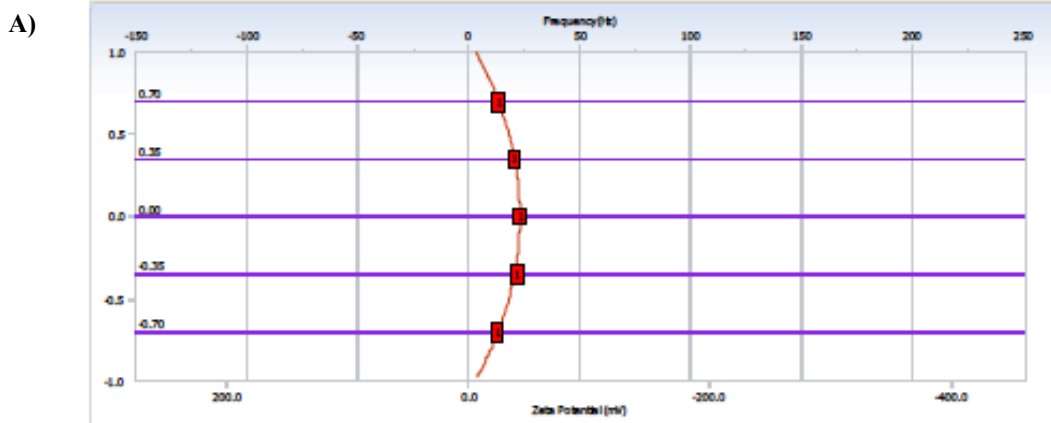


Figure 2.2. Schematic representation of zeolite-L hydrothermal synthesis.

The zeta-potential measurement gives an immediate and a good indication on the material and eventually on the functionalization of the surface. Since of the presence of free hydroxyl-groups on the outer crystal surface, the crystals show a net negative charge and the zeta potential of non-functionalized zeolite-L crystals is typically found around -35 mV. In Figure 2.3 the typical zeta potential plots obtained for zeolite-L are reported.



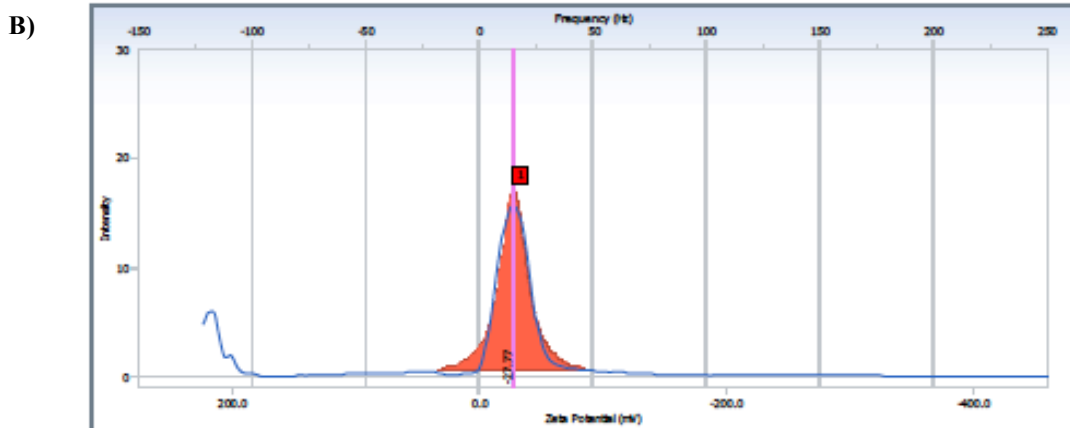


Figure 2.3 A) Electro osmotic flow showing the movement of the particles under the applied electric field; B) Mobility distribution plot revealing the net surface charge of the particles.

Dynamic light scattering is then utilized to investigate the size and the dispersity of the obtained zeolite crystals. Even though some materials are far from spherical shape some indication on the dynamic radius is still possible. Some better information on the morphology, size and shape of the prepared material is obtained with SEM and TEM. With the microscopy techniques we can indeed directly visualize the material at high resolution and observe the porous structure of the crystals. Representative DLS graphs and SEM/TEM pictures of cylindrical micrometer and nanometer sized zeolite-L crystals are shown in Figure 2.4 and 2.5.

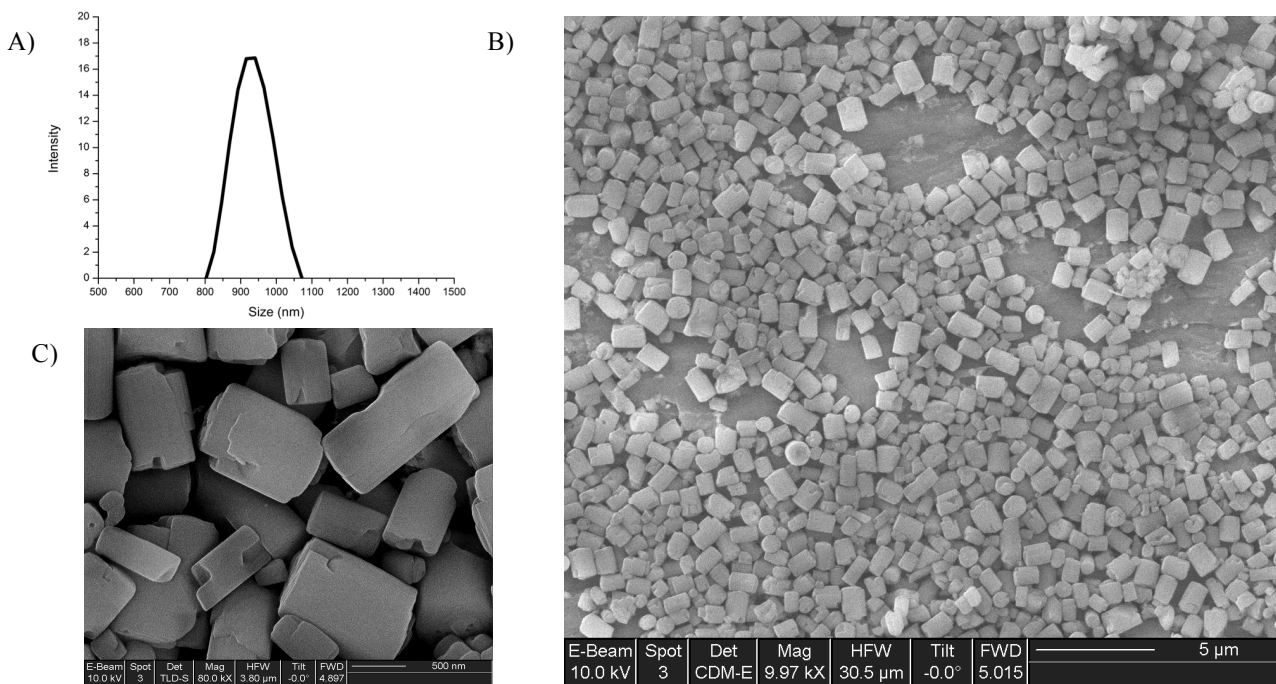


Figure 2.4 A) DLS size distribution graph for microzeolites-L; B) SEM picture of the zeolite micro-cylinders; C) SEM zoomed view of few particles.

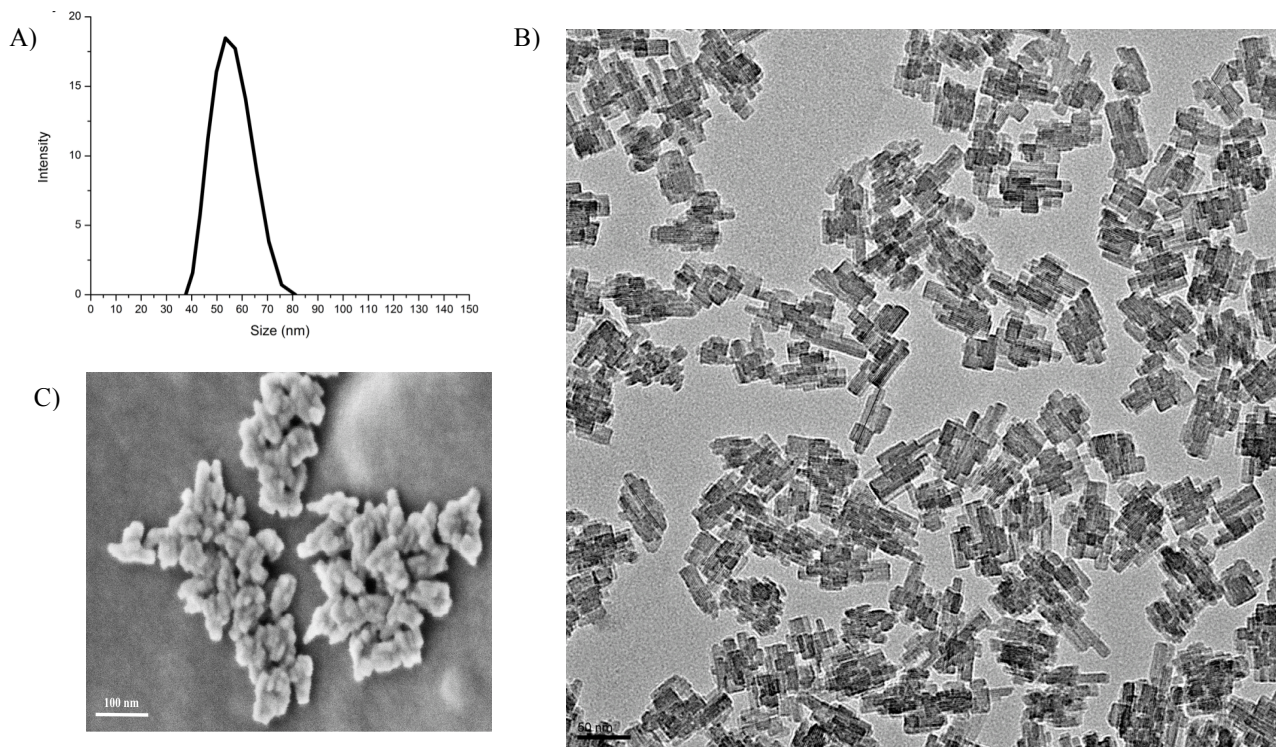


Figure 2.5 A) DLS size distribution graph; B) TEM picture; C) SEM image of cylindrical zeolite nanocrystals.

2.2 Guest molecules loading

The loading of zeolite-L crystals, inserting desired guest molecules into the channels, can be done in different ways, i.e. by ion exchange (for cationic guest species), by insertion from the gas phase (if the guest molecules undergoes sublimation without degrading), by crystallization inclusion,^[9] or by *in situ* synthesis in the channel system.^[10] This thesis exclusively focuses on the guest insertion either by cation exchange or from the gas phase.

Four different cation sites (A, B, C, D) have been reported in the zeolite framework. Site A is located in the center of the double six-ring unit, B is in the center of the cancrinite cage, C lies midway between the centers of two adjacent ϵ cages, and D is inside the main channel near the wall of the eight-ring (see Figure 2.6 for a better understanding). Cations in the D position are actually the ones that undergo exchange with other cationic species. Dehydrated zeolite-L has an additional cation site placed between two adjacent sites A (see Figure 2.6).^[11]

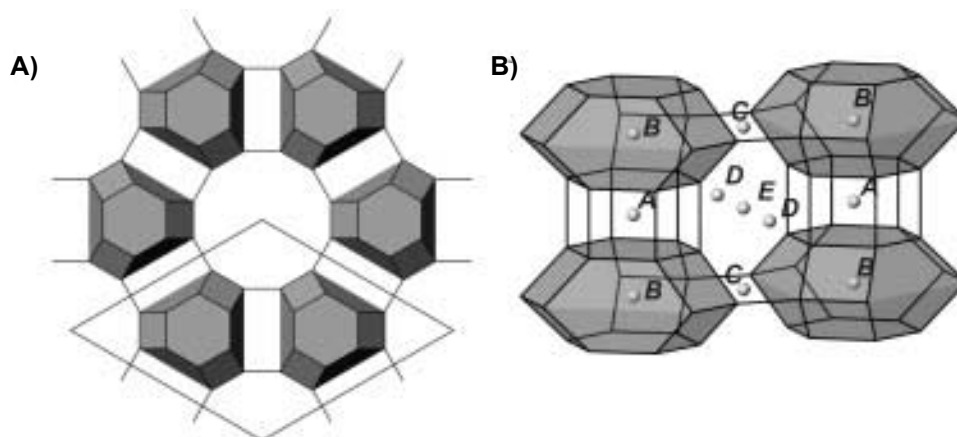


Figure 2.6 A) Projection of the zeolite-L framework along c axis, with the cancrinite cages highlighted as polyhedra;; B) section showing the different cationic positions A to E. Adapted from G. Calzaferri, S. Huber, H. Maas, C. Minkowski, *Angew. Chem. Int. Ed.* **2003**, *42*, 3732-3758. Copyright © 2003 WILEY-VCH Verlag GmbH & Co. KGaA, Weinheim

Insertion via cation exchange is thus done replacing the counter balancing cations (generally K^+) with the guest molecules. Therefore the zeolites are usually dispersed in an aqueous solution of cationic guest molecule, which simply allows for the counter cations to be replaced by the new guest species (see Experimental section). When varying the insertion time, the temperature, or the guest concentration in solution, the loading value can be also regulated.

The insertion of neutral molecules follows instead a slightly different approach. In this strategy, the water molecules adsorbed in the zeolite channels are replaced by the guest species. Because the zeolite has a high affinity for water, the adsorption sites in the channels are occupied and have to be emptied first by drying the zeolite. In a second step, neutral dye molecules can be inserted accordingly to a solid–gas equilibrium.^[11] Therefore the zeolites are mixed together with the guest molecules in a custom made glass ampoule and dried under high vacuum. Then the glass ampoule is sealed and the dye insertion is done at high temperatures, determined by the sublimation temperature of the molecules to be inserted, for usually 2-3 days. After insertion has occurred, the dye molecules only adsorbed on the zeolite surface are removed with several washing steps.

Once the insertion has been achieved, a fundamental parameter that must be considered is the effective amount of guest molecules inserted, defined as the loading value of the zeolite. This number can be furnished as milligram guest molecules per gram zeolite or, which is more common, as a loading parameter p , which is defined as the number of molecules per site available. The

number of sites is thus expressed as the number of unit cells in a given amount of zeolite, divided by the number of unit cells one guest molecule occupies (See equation 2.1).^[12]

$$N_s = \frac{m_z}{2880 \frac{g}{mol}} * \frac{1}{s} \quad \text{Eq. 2.1}$$

where m_z is the amount of zeolite-L in gram, 2880 g/mol is the molecular weight of one unit cell and s is the number of unit cells one guest molecule occupies.

The loading parameter is finally expressed as the ratio between the sites occupied (N_D) by guest molecules and the total number of sites available (N_S), as shown in equation 2.2.

$$p = \frac{N_D}{N_S} \quad \text{Eq. 2.2}$$

The loading value can be determined experimentally by means of thermogravimetric analysis (TGA), which allows for determining first the percentage (in mass units) of loading, from which one can calculate to loading parameter p .

An exemplificative thermogravimetric curve for DXP loaded zeolite L crystals is shown in figure 2.7.

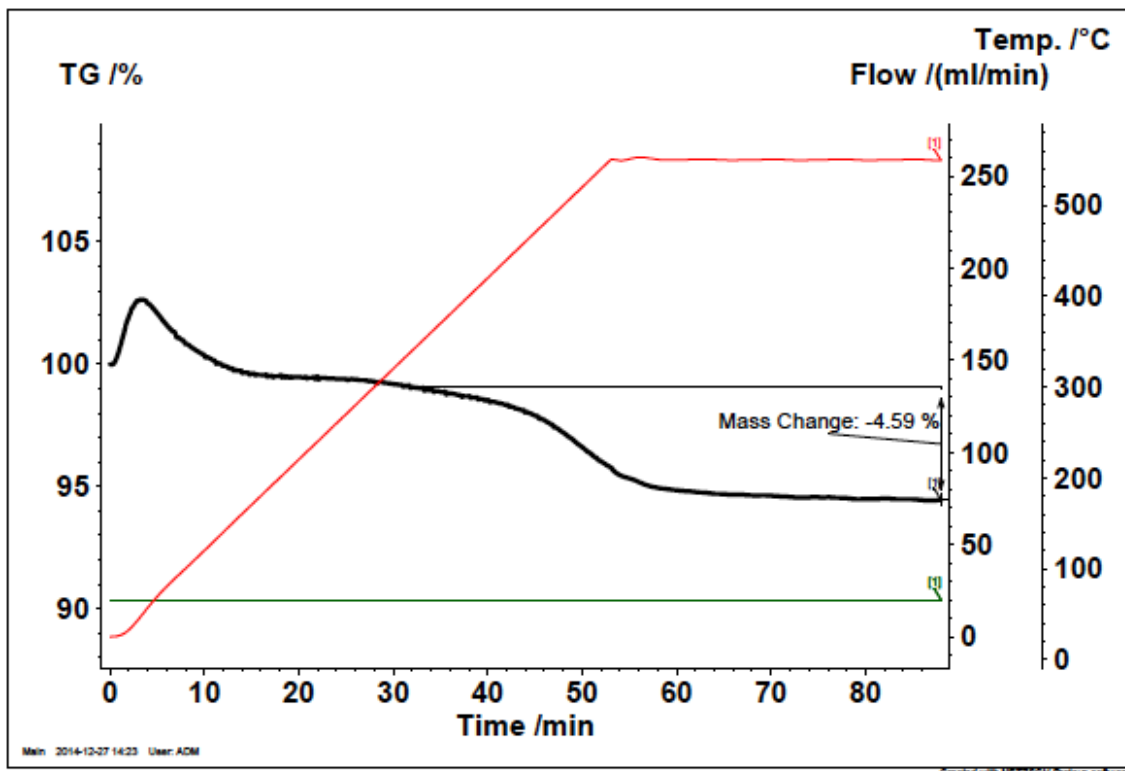


Figure 2.7 A typical thermogravimetric analysis curve obtained for dye loaded zeolite-L crystals.

The black curve shows the mass loss upon heating under N₂/O₂ atmosphere, while the red curve shows the temperature gradient. The initial weight loss occurring at low temperatures is due to evaporation of water molecules from the zeolite-L surface and channels. At higher temperatures (above 250 °C) a fast weight loss can be observed due to the loss of the guest organic molecules, and the signal reaches a plateau after these latter have been completely removed from the zeolites. An alternative strategy relies on the analysis based on the so-called HF test.^[13] This implicates that the zeolite matrix is dissolved in hydrofluoric acid and the guest concentration in solution is usually determined by means of UV/Vis absorption spectroscopy using the typical absorption bands of the guest. An example of this approach, although used to quantify the amount of an organic compound bound to the zeolite surface and not inserted into the pores, will be shown in Chapter 4.

2.3 Functionalization of the zeolite outer surface

The modification of the external surface is indeed one of the key aspects while designing and synthesizing the novel functional material, since it is the part of a zeolite crystal that is directly in contact with the surrounding environment.

Functionalization of the external surface can be done either by electrostatic interaction exploiting the net negative charge of zeolite-L surface, or by grafting the desired species in a covalent way to the surface by means of standard silane chemistry.^[14] The electrostatic interaction-based strategy exploits molecules possessing positive charges able to interact with the negatively charged zeolite surface, but an inverse approach is also possible if a negatively charged molecule must be attached, which means the surface can be modified with positively charged groups in a first step and then functionalized with the negative species in a second step (see Chapter 3 for an exemplificative application of this strategy).

The second possibility is based on the binding of functional groups covalently to the surface, which is usually done by silane chemistry using the desired derivative. In this case, the zeolites are mostly dispersed in alcoholic medium or toluene, and after the silane reagent and a catalyst, mostly triethylamine, have been added, the silane derivative covalently bound to the free hydroxyl groups on the zeolite surface (see Figure 2.8). Purification is then performed washing the zeolites a couple times with a good solvent for the silane.

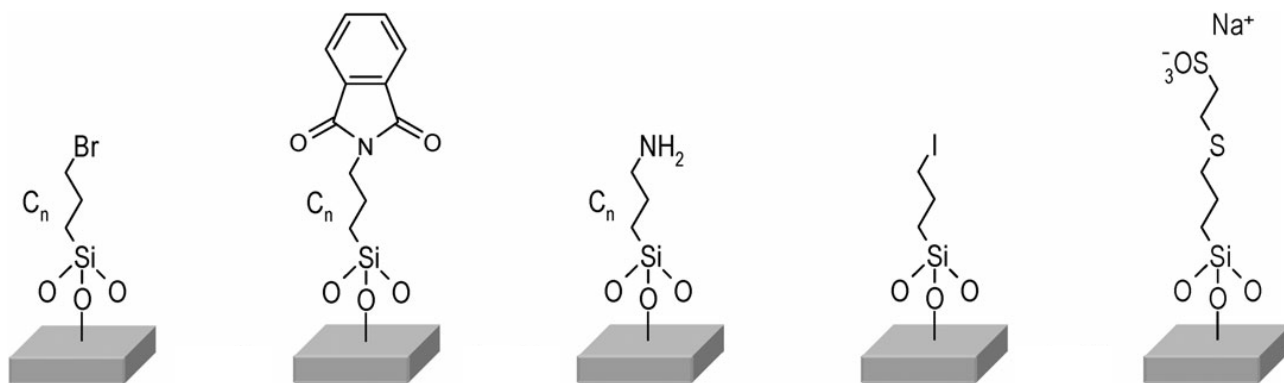
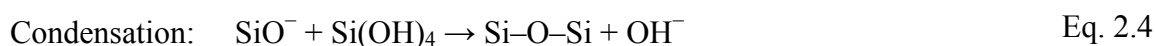
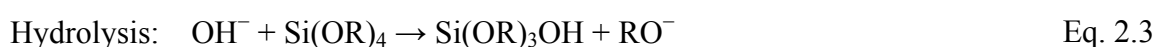


Figure 2.8 Some examples of the possible surface modification obtained using silane chemistry. Adapted from C. Haensch, S. Hoepfner, U.S. Schubert, *Chem. Soc. Rev.* **2010**, *39*, 2323-2334, with permission of The Royal Society of Chemistry.

The number of groups attached to the surface can be then evaluated following different strategies, depending indeed on the nature of the surface functionalities. If the groups are accessible by UV/Vis spectroscopy, quantification can be done by spectroscopy measuring the absorbance of a known amount of the functionalized zeolite (see Chapter 4), otherwise chemical methods as the ninhydrin test for amine groups can be thought as suitable ways. IR is also a valuable tool to establish if the reaction has occurred and in some cases XPS can reveal the functionalization and give quantitative information. Eventually, quantification can also be achieved by thermogravimetric analysis monitoring the weight loss when there are no interferences due to the presence of guest molecules in the channels.

2.4 Synthesis and characterization of Mesoporous silica nanoparticles

Mesoporous silica nanoparticles (MSNPs) differ from zeolite crystal for being amorphous materials totally made of silica. Different synthetic conditions may lead to the realization of diverse platform formats, e.g. different sizes of the whole particle and of the single pores, while the final shape is usually a spherical one. A base-catalyzed sol-gel process has been developed to produce silica nanoparticles with sizes suitable for biomedical applications. This sol-gel process is based on the use of organosilane precursors (TMOS, TEOS, etc.), which, by means of hydrolysis and condensation reactions,^[15]



lead to the formation of a new colloidal phase (sol). The small colloidal particles then condense into the gel phase.^[16-17] For example, the Stöber process has been widely applied for the preparation of monodispersed silica nanoparticles between 50 and 2000 nm size, following the ammonia-catalyzed hydrolysis of tetraethylorthosilicate (TEOS) in a water-alcohol solution.^[16] Then, micelles formed by a cationic surfactant are used in order to direct the silicate source to condense around the micellar template into ordered silica networks. In a typical synthesis of the 100 nm MCM-41 type mesoporous silica nanoparticles, the silica source, tetraethylorthosilicate (TEOS), is added into a heated basic aqueous solution of the templating surfactant, commonly cetyltrimethylammonium bromide (CTAB). 100 nm diameter nanoparticles are formed through base-catalyzed sol-gel condensation around the hexagonally packed micelle structures.^[18-19] After removing the templating agent from the mesopores in acidic alcohol to decrease the interactions between the surfactant and the silica frame, particles spherical in shape, roughly 100 nm in diameter, and containing 2D-hexagonally arranged pores 2–3 nm in diameter are obtained.^[20]

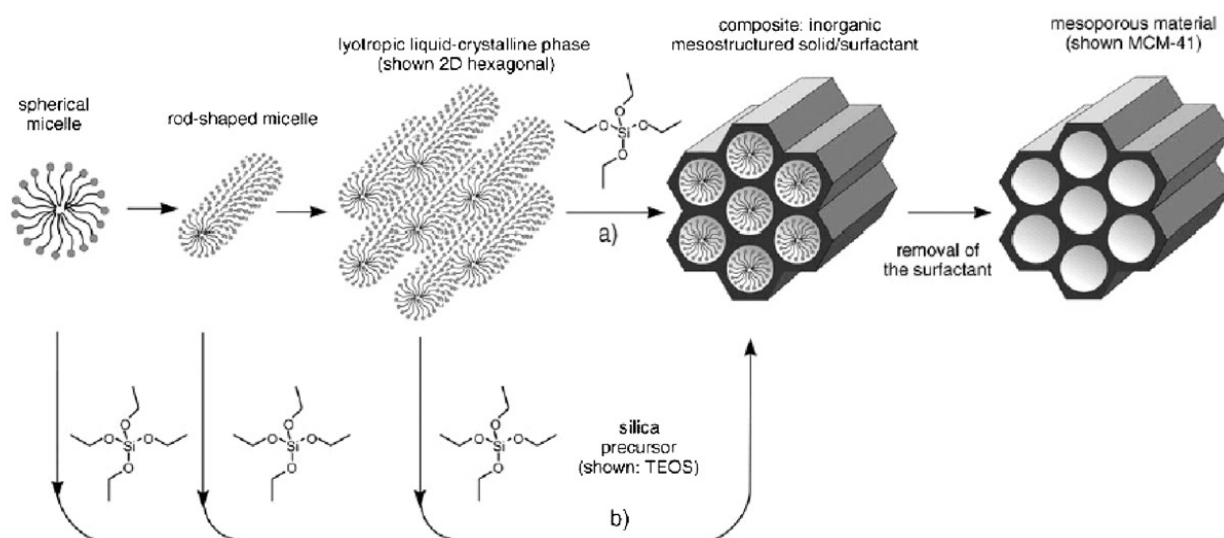


Fig. 2.9 Scheme of synthesis of MSNPs with CTAB surfactant micelles as template. Adapted from F. Tang, L. Li, D. Chen, *Adv. Mater.* **2012**, *24*, 1504-1534. Copyright © 2012 WILEY-VCH Verlag GmbH & Co. KGaA, Weinheim

As in the case of zeolite-L, the characterization of the synthesized material can be done in different ways. Dynamic light scattering can be used once again to monitor the size distribution of the particles, and especially SEM and TEM are utilized to visualize the particles and to check size, shape and, by means of HR-TEM, the porous inner structure. The porosity can then be measured by

nitrogen adsorption. Therefore the amount of nitrogen adsorbed inside the pores is measured to determine the pore volume, the pore size, or the surface area of the crystals.

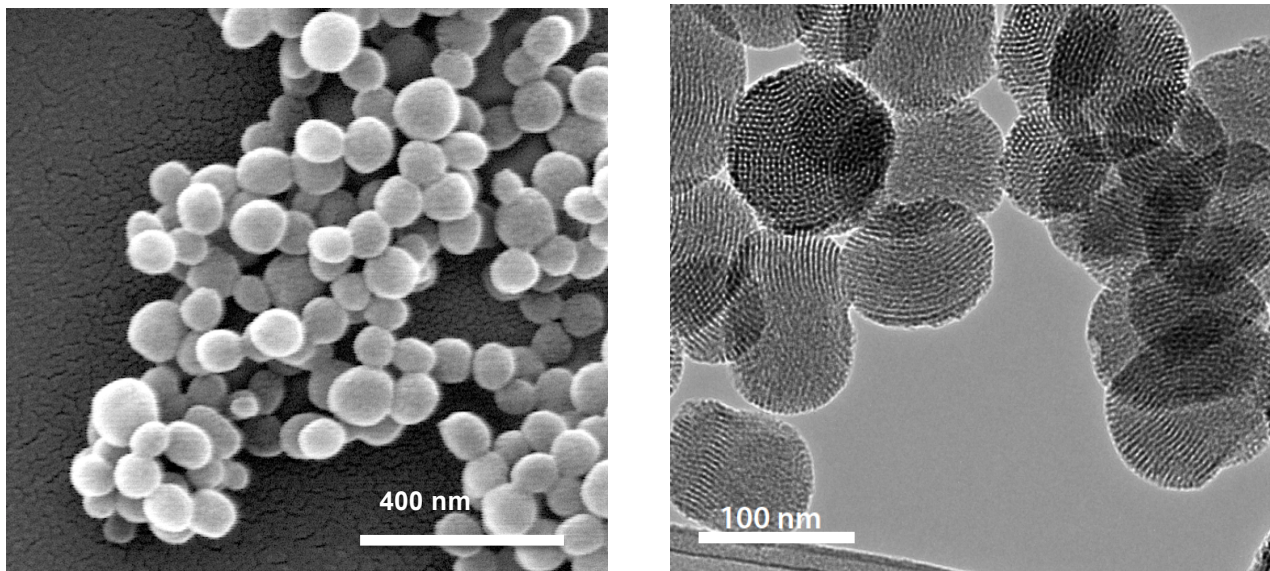


Fig. 2.10 Left) SEM image of the MSNPs right after surfactant-templated synthesis; right) HR-TEM image of MSNPs after extraction of the CTAB, revealing the porous pattern.

Additionally, small-angle X-ray scattering (SAXS) is an instrumental technique usually applied for the characterization of MSNPs. SAXS relies on the elastic scattering of X-rays by a sample which is nanostructured, recording the scattered light at very low angles (typically $0.1 - 10^\circ$). This low angular range is useful since can especially give information, among the others, on the peculiar distances of partially ordered materials and on the pore sizes.^[21-22] Thus, once recorded the SAXS spectrum, one can identify the porous structure of a nanoparticle by comparing the scattering peaks with the pattern belonging to a specific geometry. This has been done, for instance, for 100 nm sized MSNPs, to check the presence of the typical 2D hexagonal lattice of channels. The SAXS graph is reported in Figure 2.11, which shows three clear diffraction peaks that are indexed to this specific porous geometry.

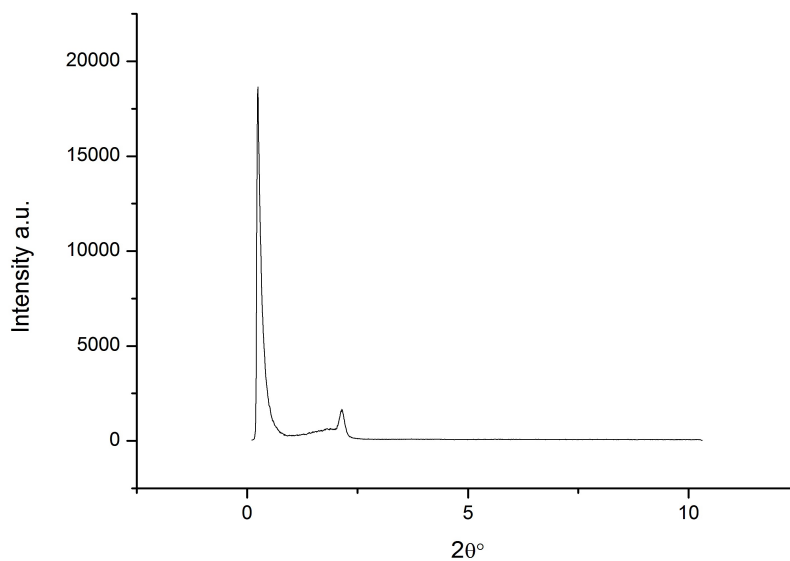


Fig. 2.11 SAXS pattern of MSNPs after removal of the templating surfactant. The peak distribution is typical of a 2D-hexagonal pore distribution.

2.5 Surface functionalization and cargo loading

The ease of introducing various organic functional groups, either through covalent bonding or electrostatic interactions, provides high level of flexibility and many addressable features to the mesoporous silica materials. As in the case of zeolite, the high versatility of the material with respect to several possible modifications is a crucial aspect towards the fabrication of advanced functional structures. The covalent attachment of functional groups usually involves introducing organic structures in the form of silanes, which can be attached using co-condensation or post-synthetic grafting methods.^[23] The co-condensation procedure allows the hydrolysis of the functional silanes while the particles are on the way of forming, therefore the guest molecules are incorporated into the resulting silica frameworks. This is, for instance, a very useful procedure to embed a selected dye directly into the silica scaffold, leading to the formation of fluorescent MSNPs through a one-pot step (see Chapter 5). In contrast, post-synthetic grafting introduces the functional groups mainly to the exposed silica surface after the MSNPs are formed. The same silane chemistry seen for the zeolite is applicable to the case of MSNPs. Since the pore of MSNPs are more accessible than the zeolite ones, one should consider that the first step of surface functionalization must be performed while the surfactant is still in the pores, thus preventing an unwanted additional functionalization of the inner channels. Besides covalent attachment, functional moieties can also be added to the MSNPs through electrostatic interactions, either taking advantage of the negative charges from the free SiO^- groups on the particle's surface or modifying

the surface in a more complex desired way. For example, cationic polymers (such as polyethyleneimine) can be electrostatically adsorbed onto the silica nanoparticles to provide nucleic acid binding properties.^[24-25] In Chapter 5, an example of a combination of co-condensation, covalent functionalization, and electrostatic adsorption on the same nanoparticle will be shown. The functionalization steps can be checked, as in the case of zeolites, by means of instrumental techniques (IR, zeta potential to monitor the changes in the net surface charge, DLS to observe modifications in the average size, UV-Vis spectroscopy to control the attachment of specific species by analyzing the resulting supernatant), or chemical methods, e.g. ninhydrin test, to check the presence of specific groups.

The other crucial property that makes mesoporous silica materials such powerful tools for drug delivery applications is their ability to encapsulate different types of cargo molecules within their pore channels, since in this class of material the pore diameter can reach several nanometers. The encapsulation process may protect many therapeutic agents from biological or chemical degradation, or any unwanted interaction with the external environment. The particles are usually loaded by soaking them in a drug solution, and the interactions between the cargo molecules and the particle include hydrogen bonding and electrostatic interactions. When cationic drugs are used, the loading process easily takes place thanks to the electrostatic interaction between the guest molecules and the negatively charged walls of the pores^[26-27]; neutral and smaller guest molecules might require a slightly more complex strategy to enhance the loading percentage, as the impregnation method discussed in Chapter 5. However it is important to note that differently from zeolites the charge inside the pore and outside is the same and therefore unspecific binding on the surface is more likely to occur. To prevent the surface functionalization with the molecules that should be entrapped in the channels, different strategies can be applied. For example the surface can be functionalized with orthogonal groups before the template (micelles), which blocks the channels, is removed. After the coating, the template removal will allow the penetration and the selective adsorption of the molecules inside the porous structure. As for the zeolite case, an evaluation of the loading value can be achieved for instance by TGA (taking into account the presence of additional organic sources), or by UV-Vis spectroscopy either dissolving the material in HF or by analyzing the supernatant recovered after the soaking procedure.

2.6 Synthesis and characterization of Peptide Nucleic Acid

The PNA oligomer synthesis follows well-established synthetic procedures derived from peptide synthesis, which are mainly based on solid phase methodologies. The widespread strategies utilized

in peptide synthesis involve the *tert*-butyloxycarbonyl (Boc) and the 9-Fluorenyl-methyloxycarbonyl (Fmoc) protecting groups.

In figure 2.12, a general scheme for the synthesis of PNA oligomers on solid-phase is reported. The elongation of the sequence initiates by deprotecting the N-terminus of the first anchored monomer to the resin, and by coupling to it the following *N*-protected monomer. The coupling reactions are carried out with proper coupling reagents such as *N,N,N',N'*-tetramethyl-*O*-(1*H*-benzotriazol-1-yl)uronium hexafluorophosphate (HBTU) or 1-[Bis(dimethylamino)methylene]-1*H*-1,2,3-triazolo[4,5-*b*]pyridinium 3-oxid hexafluorophosphate (HATU).^[28] The exocyclic amine groups present on cytosine, adenine and guanine may interfere with the synthesis and therefore need to be protected with semi-permanent groups orthogonal to the main N-terminal protecting group. Capping of unreacted amine group at the end of the coupling step is usually carried out in order to block the truncated chain and prevent the growth of unwanted side strands. In PNA synthesis, this capping step is usually performed using a mild capping reagent, *N*¹-benzyloxycarbonyl-*N*³-methylimidazolium triflate, or a diluted mixture of acetic anhydride and pyridine in NMP, followed by piperidine washes (not suitable for Fmoc chemistry) to avoid the undesired acetylation of guanine²⁶.^[26] Once the synthesis of the PNA sequence is done, the chain is detached from the resin, and the protecting groups of the bases are usually simultaneously removed during this step. If necessary, the deprotection of bases and the cleavage from the resin can be also performed in different steps.

When following the Boc strategy, the solid phase is usually made of a methylbenzhydryl amine (MBHA) derivatized polymer (polystyrene, or, more recently, PEG-based platforms as in the modern ChemMatrix® resin), in which the first PNA monomer is linked via an amide bond. The amine groups of the nucleobases are protected as benzyloxycarbonyl derivatives (Cbz), this protecting group combination being often defined as the Boc/Cbz strategy. The Boc group is deprotected in acidic conditions with trifluoroacetic acid (TFA), and the final cleavage of PNA from the resin, with simultaneous deprotection of the amine groups in the nucleobases, is carried out with HF or, more often, with a mixture of trifluoroacetic and trifluoromethanesulphonic acids (TFA/TFMSA).

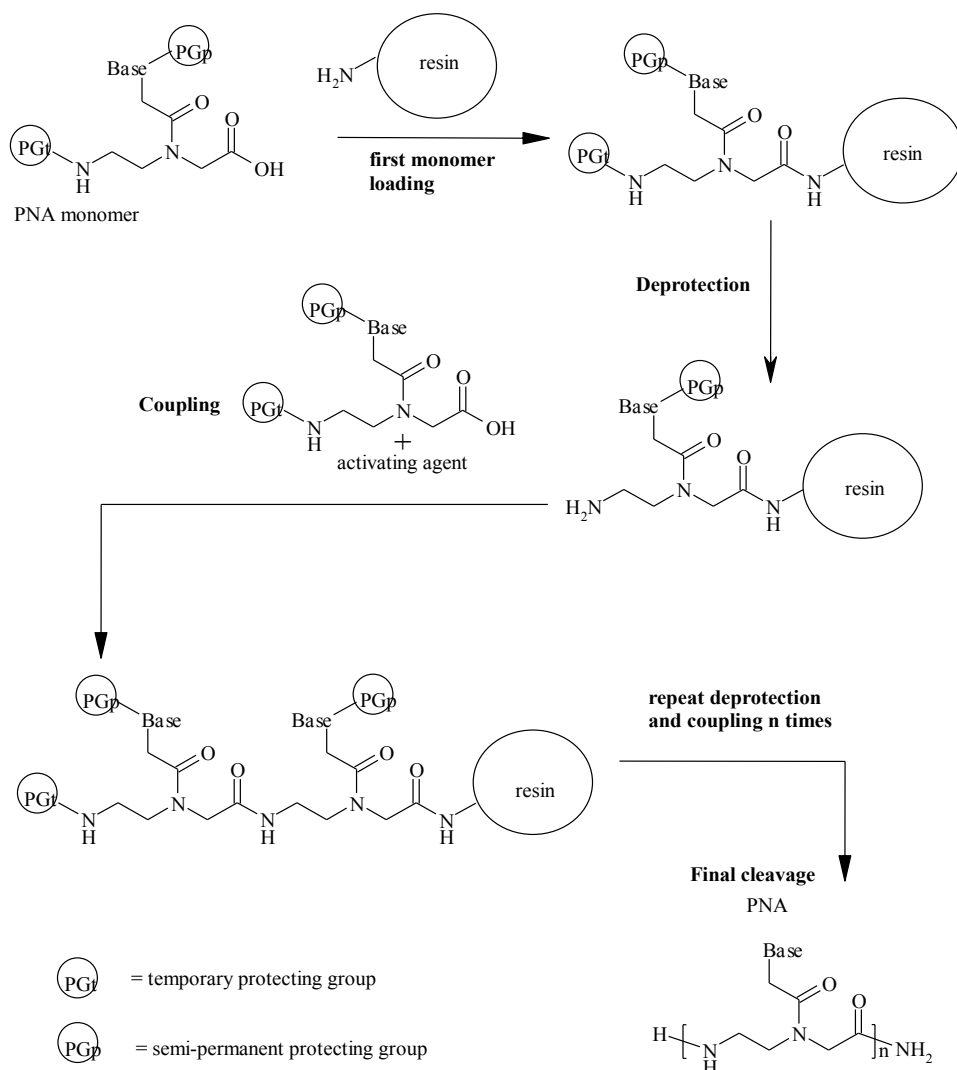


Figure 2.12 Schematic procedure for solid phase PNA synthesis.

The Fmoc protecting group follows instead a different chemistry and undergoes deprotection under mild basic conditions with piperidine. This makes it compatible with resin linkers, such as MBHA-Rink amide or chlorotriyl groups, which can be cleaved under less acidic conditions (TFA). Commercial available Fmoc monomers are currently protected on nucleobases with the benzhydryloxycarbonyl (Bhoc) groups, which can be easily removed by TFA during the cleavage step. Possible alternative chemical strategies for PNA synthesis have been reviewed by Corradini *et al.*^[29] The solid phase procedure also allows for the synthesis of PNA-peptide conjugates that can easily be assembled following the same strategy for both the PNA and the peptide moieties, taking into account the nature of the selected aminoacidic residues to rationalize the ideal and proper combination of protecting groups. An example of this strategy will be unfolded in Chapter 5 when presenting cationic PNA sequences obtained by conjugating the PNA chain to a series of arginine

units; other examples from the literature will be reported in Chapter 4 among the strategies thought to improve the cellular uptake properties of PNA. Eventually, other residues may be linked to PNAs during solid-phase synthesis, the most common being biotin (for immunoaffinity binding with streptavidin)^[30-31] and fluorescein (for fluorescent studies).^[32-33]

Once the final PNA chain is synthesized and cleaved from the resin, a purification step is carried out by means of RP-HPLC, which allows for separating the truncated sequences from the desired one (see next Chapters for experimental details). Finally, the characterization of the pure product is performed by ESI-MS, which gives the typical multi-charged mass peaks that are used to univocally identify the PNA by its molecular weight. An example of a PNA mass spectrum is shown in Figure 2.13, where it is clear the presence of the multi-charged peak distribution.

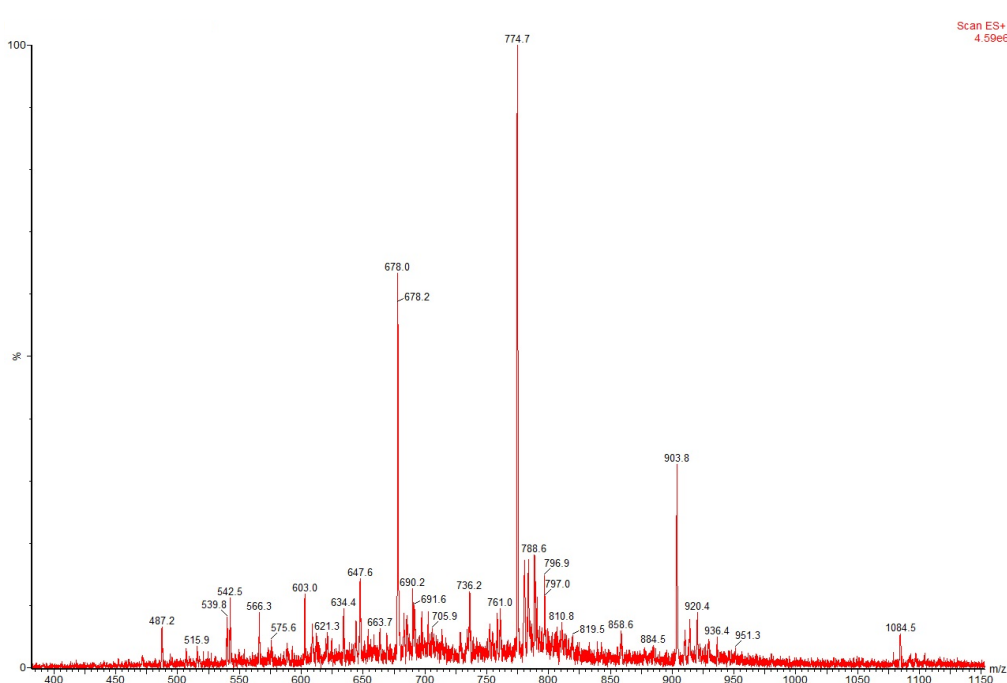


Figure 2.13 ESI-MS spectrum of a 15-mer PNA conjugated with eight arginine residues (see Chapter 5).

The purified PNAs are then eventually quantified by UV-Vis spectroscopy by UV absorbance using the following $\epsilon_{260} \text{ M}^{-1} \text{ cm}^{-1}$ for the nucleobases: T 8600, C 6600, A 13700, G 11700. This allows for quantifying the final product and evaluating the yield of the synthesis.

2.7 Experimental section

Zeolite Synthesis

Nanozeolite-L

Preparation of the silica dispersion: 15.00 g Aerosil OX-50 were added slowly to 35.00 g doubly distilled water and dispersed 8 minutes by using an Ultra Turrax disperser (IKA T18 Basic, 18000 rpm). After that, the dispersion was kept for 1 hour at room temperature and re-dispersed for 8 minutes before use. Preparation of the aluminum solution (Solution A): 4.84 g KOH were dissolved in 20.00 g doubly distilled water. Then 1.56 g Al(OH)₃ were added to the solution and it was refluxed until a clear solution was obtained. Preparation of solution B: 7.23 g KOH were dissolved in 21.68 g doubly distilled water and 40.06 of the silica dispersion were added. Finally, solution A was quickly added to solution B and the mixture was stirred at room temperature until the solution became turbid. Crystallization was then done at 170 °C for 6 hours at 40 rpm.

Microzeolite-L

6.22 g KOH were added to 44.00 g doubly distilled water and fully dissolved. Then, 1.16 g Al was added to the solution, which was refluxed until the Al resulted fully dissolved. After cooling to room temperature, the amount of lost water was added. Subsequently, this solution was quickly added to 28.68 g of Ludox HS-40 and vigorously stirred for about 2 minutes. Finally, the highly viscous suspension was transferred to a Teflon vessel and aging was done for 3 days at 175 °C. Then, the vessel was cooled to room temperature and zeolites were washed with doubly distilled water until the supernatant showed a neutral pH.

Dye loading

Gas-Phase insertion

DXP loading

DXP was inserted from the gas phase at 300 °C. Therefore, 0.5 mg DXP was mixed with 100 mg zeolite-L in a glass ampoule to achieve a loading of around 7% ($n_{\text{dye}}/n_{\text{site}}$). The ampoule was dehydrated at about 4.0×10^{-6} mbar for 12 hours and sealed. Insertion was then done at 300 °C for 24 hours. Afterwards, the zeolite-L crystals were washed with n-butanol until the supernatant showed no more fluorescence, and the zeolites were finally dried in vacuum.

Cation exchange

DAPI loading

Zeolite particles (150 mg), were dispersed in 15 ml of a 0.3 mM aqueous solution of DAPI and stirred overnight at 50°C. The zeolites were recovered by centrifugation and washed with water until the supernatant did not show any fluorescence. TG-analysis then showed a loading value of around 0.97 mg DAPI/ 100 mg zeolites.

Oxazine 170 loading

Zeolite-L nanocrystals (200 mg) were dispersed in a 0.01 mmol solution of oxazine170 perchlorate in water and stirred overnight at reflux. The fluorescent zeolites were then recovered by centrifugation, washing the solid residue with water until the supernatant resulted completely UV transparent. After TG-analysis, a value of about 2 mg of oxazine per 100 mg of zeolites was found.

MSNPs synthesis

100 nm MSNPs

Cetyl trimethylammonium bromide (CTAB) (0.5 g) was dissolved in water (240 mL) containing 1.75 mL of NaOH 2M. The solution was then heated up to 80°C and stirred vigorously. Meanwhile, TEOS (2.5 mL) was dissolved in absolute ethanol (3 mL). This second solution was then added to the former CTAB flask and the final mixture was stirred overnight at 80°C. The particles were then recovered by centrifugation and washed several times with water.

100 nm red emissive MSNPs

Cetyl trimethylammonium bromide (CTAB) (0.5 g) was dissolved in water (240 mL) containing 1.75 mL of NaOH 2M. The solution was then heated up to 80°C and stirred vigorously. Meanwhile, TEOS (2.5 mL) was dissolved in absolute ethanol (3 mL), adding 50 mL of APTES and 0.1 mg of Cyanine 5-NHS ester dye (NHS-Cy5). This second solution was then added to the former CTAB flask and the final mixture was stirred overnight at 80°C. The particles were then recovered by centrifugation and washed several times with water.

PNA synthesis

The synthesis of the different specific PNA sequences will be reported in the experimental sections of the corresponding Chapters.

REFERENCES

- [1] G. Calzaferri, R. Meallet-Renault, D. Bruehwiler, R. Pansu, I. Dolamic, T. Dienel, P. Adler, H. Li, A. Kunzmann, *ChemPhysChem* **2011**, *12*, 580-594.
- [2] M. Becker, L. De Cola, A. Studer, *J. Mater. Chem. C* **2013**, *1*, 3287-329.
- [3] B. Schulte, M. Tsotsalas, M. Becker, A. Studer, L. De Cola, *Angew. Chem. Int. Ed.* **2010**, *49*, 6881-6884.
- [4] J. El-Gindi, K. Benson, L. De Cola, H.J. Galla, N.S. Kehr, *Angew. Chem. Int. Ed.* **2012**, *51*, 3716-3720.
- [5] M.M. Tsotsalas, K. Kopka, G. Luppi, S. Wagner, M.P. Law, M. Schaefer, L. De Cola, *ACS Nano* **2010**, *4*, 342-348.
- [6] M.M. Tsotsalas, M. Busbu, E. Gianolo, S. Aime, L. De Cola, *Chem. Mater.* **2008**, *20*, 5888-5893.
- [7] C.A. Strassert, M. Otter, R.Q. Albuquerque, A. Hone, Y. Vida, B. Maier, L. De Cola, *Angew. Chem. Int. Ed.* **2009**, *48*, 7928-7931.
- [8] A. Zabala Ruiz, D. Bruehwiler, T. Ban, G. Calzaferri, *Monatshefte fuer Chemie* **2005**, *136*, 77-89.
- [9] M. Ganschow, G. Schulz-Ekloff, M. Wark, M. Wendschuh-Josties, D. Wöhrle, *J. Mater. Chem.* **2001**, *11*, 1823.
- [10] P. Lainé, M. Lanz, G. Calzaferri, *Inorg. Chem.* **1996**, *35*, 3514.
- [11] G. Calzaferri, S. Huber, H. Maas, C. Minkowski, *Angew. Chem. Int. Ed.* **2003**, *42*, 3732-3758.
- [12] B. Hennessy, S. Megelski, C. Marcolli, V. Shklover, C. Bärlocher, G. Calzaferri, *J. Phys. Chem. B* **1999**, *103*, 3340-3351.
- [13] S.A. Johnson, E.S. Brigham, P.J. Ollivier, T.E. Mallouk, *Chem. Mater.* **1997**, *9*, 2448-2458.
- [14] C. Haensch, S. Hoepfener, U.S. Schubert, *Chem. Soc. Rev.* **2010**, *39*, 2323-2334.
- [15] F. Hoffmann, M. Cornelius, J. Morell, M. Fröba, *Angew. Chem. Int. Ed.* **2006**, *45*, 3216-3251.
- [16] C. J. Brinker, G. W. Scherer, Academic Press, Inc., San Diego, **1990**.
- [17] W. Stober, A. Fink, E. Bohn, *J. Colloid. Interface Sci.* **1968**, *26*, 62-69.
- [18] K. K. Coti, M. E. Belowich, M. Liong, M. W. Ambrogio, Y. A. Lau, H. A. Khatib, J. I. Zink, N. M. Khashab, J. F. Stoddart, *Nanoscale* **2009**, *1*, 16-39.
- [19] S. H. Wu, Y. Hung, C. Y. Mou, *Chem. Commun.* **2011**, *47*, 9972-9985.
- [20] F. Tang, L. Li, D. Chen, *Adv. Mater.* **2012**, *24*, 1504-1534.
- [21] L.A. Feigin, D.I. Svergun, G. W. Taylor (Ed.). New York: Plenum Press. **1987**.
- [22] H.D. Bale, P.W. Schmidt, *Phys. Rev. Lett.* **1984**, *53*, 596.
- [23] M. H. Lim, A. Stein, *Chem. Mater.* **1999**, *11*, 3285-3295.
- [24] C. Hom, J. Lu, M. Liong, H. Luo, Z. Li, J. I. Zink, F. Tamanoi, *Small* **2010**, *6*, 1185-1190.
- [25] T. Xia, M. Kovoichich, M. Liong, H. Meng, S. Kabehie, S. George, J. I. Zink, A. E. Nel, *ACS Nano* **2009**, *3*, 3273-3286.
- [26] H. Meng, M. Liong, T. Xia, Z. Li, Z. Ji, J.I. Zink, A.E. Nel, *ACS nano* **2010**, *4*, 4539-4550.
- [27] A. Chen, M. Zhang, D. Wei, D. Stueber, O. Taratula, T. Minko, H. He, *Small* **2009**, *5*, 2673-2677.
- [28] T. Koch, H.F. Hansen, P. Andersen, T. Larsen, H.G. Batz, K. Otteson, H. Orum, *J. Pept. Res.* **1997**, *49*, 80.
- [29] R. Corradini, S. Sforza, T. Tedeschi, R. Marchelli, "Peptide nucleic acids (PNAs) and their analogs: synthesis and applications" in "Seminars in Organic Synthesis- XXVIII Summer School A. Corbella"- Società Chimica Italiana, **2003** Pages 41-70. ISBN 88-86208-27-8.
- [30] F. Höök, A. Ray, B. Nordén, B. Kasemo, *Langmuir* **2001**, *17*, 8305-8312.
- [31] U. Koppelhus, P.E. Nielsen, *Adv. Drug Deliver. Rev.* **2003**, *55*, 267-280.

- [32] C. Wang, P.F. Ren, X.J. Huang, J. Wu, Z.K. Xu, *Chem. Commun.* **2011**, 47, 3930-3932.
- [33] B. Sahu, I. Sacui, S. Rapireddy, K.J. Zanotti, R. Bahal, B.A. Armitage, D.H. Ly, *J. Org. Chem.* **2011**, 76, 5614-5627.

3

Multifunctional zeolite-L nanocontainers for DNA and drug delivery into living cells

Abstract

The design and synthesis of multifunctional nanomaterials could lead to relevant applications for biomedical purposes. This chapter describes a first example of using zeolite-L crystals as multifunctional nanocontainers to simultaneously deliver DNA oligonucleotides and organic molecules into living cells. Multifunctional zeolites-L in nanometer and micrometer scales are prepared by filling the pore system with guest molecules, their surface is functionalized with positively charge groups, and DNA is adsorbed electrostatically on them. We demonstrate the cellular uptake of the system, and the release kinetics of DNA and of the guest molecules into living cells, which proves the multi-delivery ability of the system. The localization of all the components in different cellular compartments is also investigated. The system is proposed as a novel class of nanoparticles for drug delivery and gene therapy.

H. Lülfi, A. Bertucci, D. Septiadi, R. Corradini, L. De Cola, Multifunctional inorganic nanocontainers for DNA and drug delivery into living cells, *Chem-Eur. J.* **2014**, *20*, 10900-10904.

3.1 DNA transfection: technologies and challenges

The past several years have witnessed the evolution of gene medicine from an experimental technology into a viable strategy for developing therapeutics for a wide range of human disorders and for reprogramming the genic expressions of cells. Numerous DNA or DNA-like species including plasmids containing transgenes, oligonucleotides, aptamers, ribozymes, DNAzymes, and small interfering RNAs have been investigated to control disease progression and to manipulate living organism by gene knock-out or knock-in. A major hurdle, however, still resides in the low efficiency of the DNA transfection systems, which is crucial for the success of DNA as a pharmaceutical or a basic research tool. Efficiency of transfection is dependent on both the

efficiency of DNA delivery (i.e., fraction of DNA molecules getting into the nucleus) and the efficiency of DNA expression (i.e., fraction of nuclear DNA molecules that undergo transcription).^[1] Additionally, transfection efficiencies *in vitro* and *in vivo* do not always have a real correlation, making translation of positive results in cell culture into animals even more difficult.^[2-3] Therefore, the challenge of DNA delivery is to develop a system that is both highly efficient in delivery/expression and applicable to basic research as well as clinical settings. Currently, because of their highly evolved and specialized components, viral systems are by far the most effective means of DNA transfection, enabling to achieve high efficiencies for both delivery and expression. The wide commercial availability of recombinant virus-based vectors for DNA delivery and the fact that more than 70% of gene therapy clinical trials carried out so far have used modified viruses is a consistent proof of this.^[4-5] Although they have substantially advanced the field of gene therapy, several limitations are still associated with viral vectors, including carcinogenesis,^[6] immunogenicity,^[7] limited DNA packaging capacity,^[8] and difficulty of vector production.^[9] Non-viral gene therapy has the potential to address many of these limitations, particularly with respect to safety. For example, synthetic ‘vehicles’ tend to have lower immunogenicity than viral vectors, and patients do not have pre-existing immunity, as is the case with some viral systems. Non-viral vectors also have the potential to deliver larger genetic payloads and are typically easier to synthesize than viral ones. Furthermore, the toxicity and immunogenicity of viral systems also hamper their routine use in basic research laboratories. For these reasons, non-viral systems, especially synthetic DNA delivery systems, have become increasingly desirable in both basic research laboratories and clinical settings.^[10-12] The direct injection of naked DNA into a cell is perhaps the most conceptually simple and straightforward approach to gene delivery. One drawback of this tactic, however, is that microinjection can be achieved only one cell at a time, which limits its use to applications in which individual cell manipulation is desired and possible, such as producing transgenic organisms. Though relatively efficient, the method is also rather slow and laborious and therefore neither appropriate for research with large numbers of cells nor practical for DNA delivery *in vivo*. The injection of naked DNA alone or in combination with physical methods^[13] such as gene gun,^[14-15] electroporation,^[16-17] hydrodynamic delivery,^[18] sonoporation,^[19] and magnetofection^[20] has been proposed in this context.

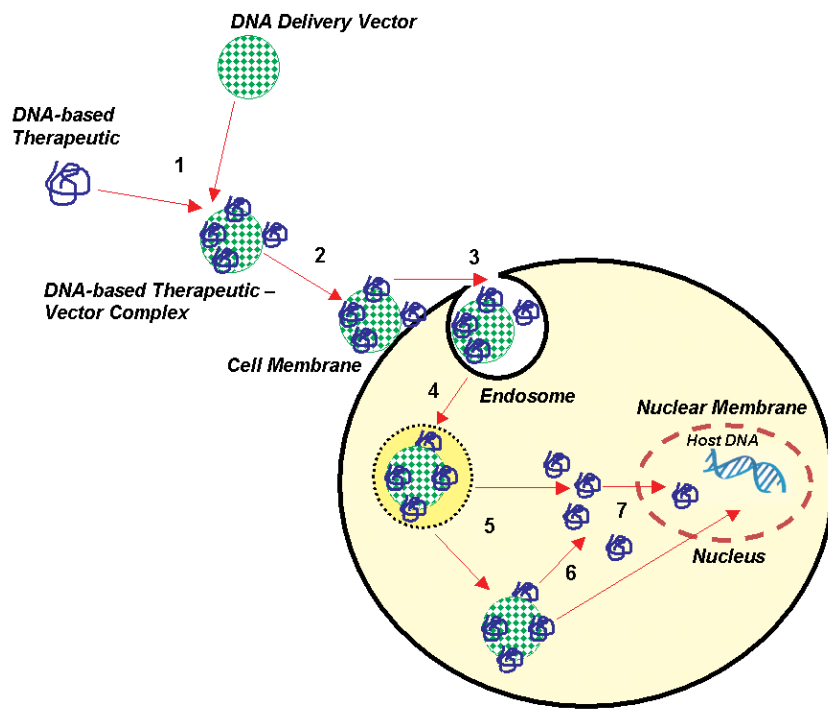


Fig. 3.1 Schematic generalized representation of delivery of a DNA-based therapeutic using a transfection vector. (1) Formation of the complex between DNA and the vector; (2) interaction of DNA-based therapeutic-vector complex with cell membrane; (3) cellular internalization via receptor- or non-receptor-mediated endocytosis pathways; (4) endosomal breakdown; (5) cytoplasmic release of DNA-vector complex or DNA-based therapeutic alone (cytoplasm is the site of action for antisense oligonucleotides, aptamer, ribozymes, DNAzymes, and cytoplasmic plasmid DNA expression systems); (6) dissociation of DNA-based therapeutic from the vector; (7) nuclear translocation of DNA (Nucleus is the site of action for transgenes in plasmids for gene therapy, and antigene oligonucleotides). Springer, S.D. Patil, D.G. Rhodes, D.J. Burgess, DNA-based therapeutics and DNA delivery systems: A comprehensive review, *The AAPS journal* **2005**, 7, E61-E77. Copyright © 2005, American Association of Pharmaceutical Scientists, with kind permission from Springer Science and Business Media.

Nevertheless, the strategy that has been investigated the most, for its undeniable potentialities, is the one based on chemical methods, material chemistry and nanotechnology, which is arguably the easiest, most versatile, most effective, and most desirable for the DNA delivery methods. The general principle of a chemical approach is based on complex formation between positively charged species (usually polymers) and negatively charged DNA molecules. The earliest chemical methods for DNA delivery were introduced in the late 1950s. These techniques used high salt concentration and polycationic proteins to enhance nucleic acid entry into the cells.^[21] Cationic polymers constitute indeed one of the most used non-viral DNA vectors, since their attractiveness for their immense chemical diversity and their potential for functionalization. Examples of polymeric DNA vectors are poly-L-lysine (PLL) and polyethylenimine (PEI). Numerous modified variants of PLL with enhanced gene delivery properties have been reported.^[22-26] One example includes PLL covered with the hydrophilic polymer PEG, which is designed to minimize nonspecific interaction with serum components and thereby increase circulation time.^[27] PEI and its variants are also among the most studied polymeric materials for gene delivery. Intravenous injection of PEI-DNA

polyplexes in mice has been observed to afford gene transfection in the lungs,^[28] and block copolymers of PEG and PEI for improved stability and biocompatibility,^[29-30] as well as degradable disulphide-crosslinked PEIs for reduced toxicity have been investigated.^[31]

Lipid-based vectors are also worth to be cited, and notably is the development of the cationic lipid Lipofectin in 1987, which is one of the first systems used *in vivo* and currently still an applied system for laboratory research.^[32] Literature is full of examples of several variants of lipid-based systems,^[33-36] and especially the use of liposomes has shown very worthy results.^[37-40]

Other approaches have been proposed by using different peptides and proteins as DNA delivery platforms.^[41-44] Furthermore, dendrimers like polyamidoamine (PAMAM) have been studied as suitable carriers, since they show well-defined structures and architectures capable to pack the DNA and deliver it into the cells.^[45-47]

Recently, the advent of nanotechnology has had a big impact on designing transfection vectors and the use of different nanoparticles as DNA carriers has become very popular. Several works deal with soft, cationic, polymeric nanoparticles, where the general concept of electrostatically binding the negatively charged DNA to a positively charged carrier has been maintained.^[48-51]

When going from soft to “hard” nanoparticles, gold nanoparticles are among the most popular ones,^[52-55] but also superparamagnetic iron oxide nanoparticles have been reported as suitable DNA carrier systems,^[56-58] nanorods and nanotubes have also been investigated for the same purposes.^[59-62] In all of the above reported examples the particles behave merely as vehicles, without further functions after the DNA is finally desorbed from the surface. Thus, the use of porous materials opens fascinating ways for enabling to introduce a multifunctionality to the carrier, with an internal part and an external surface which can be loaded with different molecules; with this approach e.g. a drug might be released from the pores of a material and DNA can be delivered on the surface to provide a synergistic effect.

An increasing number of publications report the use of mesoporous silica nanoparticles (MSNP) as DNA carriers and it has been shown that they can be used to transfer high amounts of plasmid DNA into HeLa,^[63-64] HEK293T^[65] cells, or plant cells.^[66] Recently, for instance, Zhou *et al.* proposed the use of DNA-gated MSNPs for multiple delivery,^[67] while Kim *et al.* showed the synthesis and application in gene delivery of MSNPs with ultralarge pores.^[68]

However, the number of papers reporting the use of multivalent porous materials as DNA carriers is still barely exploited in some *in vitro* experiments^[69] and *in vivo* examples are not yet published. Above that, the fate of the nanoparticles in the cells or the kinetics of the DNA release has not been deeply studied and no data are reported about a simultaneous DNA and drug delivery from the same transfection system.

Furthermore, the application of zeolite crystals as DNA transfection systems has not been reported so far. The work described in this chapter represents, to the best of our knowledge, the first example of the use of zeolites for DNA delivery into living cells. Thanks to the porous nature of these materials, the loading of selected molecules into the crystal channels and their subsequent release was demonstrated to be also possible at the same time. This work deeply investigates the kinetics of the fluorescent labeled DNA and the fluorescent drug-mimicking molecule upon their release from the zeolite directly inside living cells. We have followed in real time their migration into the cells, and evidenced the final fate and distribution of the different components of the nanosystem (DNA oligonucleotide, payload dye, zeolite particle) inside the living cells, showing the localization in different cellular compartments.

3.2 DNA-modified Zeolite-L crystals: preparation and analysis

The synthetic and functionalization pathway of the multilayered particles is depicted in figure 3.3. Zeolite crystals of two different sizes, c.a. 50 nm (nanozeolite-L) and c.a. 1 μm (microzeolite-L), have been synthesized as described in Chapter 2. A full characterization has been carried out by Scanning electron microscopy (SEM), Transmission electron microscopy (TEM), Dynamic Light Scattering (DLS) and Zeta potential measurements. In a subsequent step, the zeolite pores have been filled with the guest molecules, as the neutral green fluorescent dye *N,N'*-bis(2,6-dimethylphenyl)perylene-3,4,9,10-tetracarboxylic diimide (DXP) or the nucleus stain 4',6-diamidino-2-phenylindole (DAPI), which is entrapped in its cationic form. The dye loading is then determined by thermogravimetric analysis (TGA).

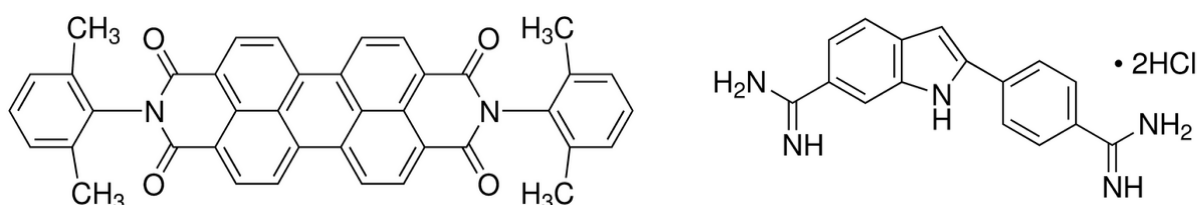


Fig. 3.2 DXP (left) and DAPI (right) molecular structures.

The surface of the zeolite is strongly negative due to the presence of -OH groups. In order to electrostatically bind DNA to the zeolites, the surface of the crystals must be positively charged; this was obtained by functionalization with (3-aminopropyl)triethoxysilane (APTES). The amine-modified zeolites thus obtained are indeed partially protonated in physiological conditions leading to a positively charged particle surface. The presence of the NH₂ groups was confirmed by zeta

potential measurement (+2.58 mV) and positive ninhydrin test. The modified surface can then electrostatically anchor the DNA oligonucleotide strands (5'-GCAACAGTGAAGGAAAGCC-3') to the particles.

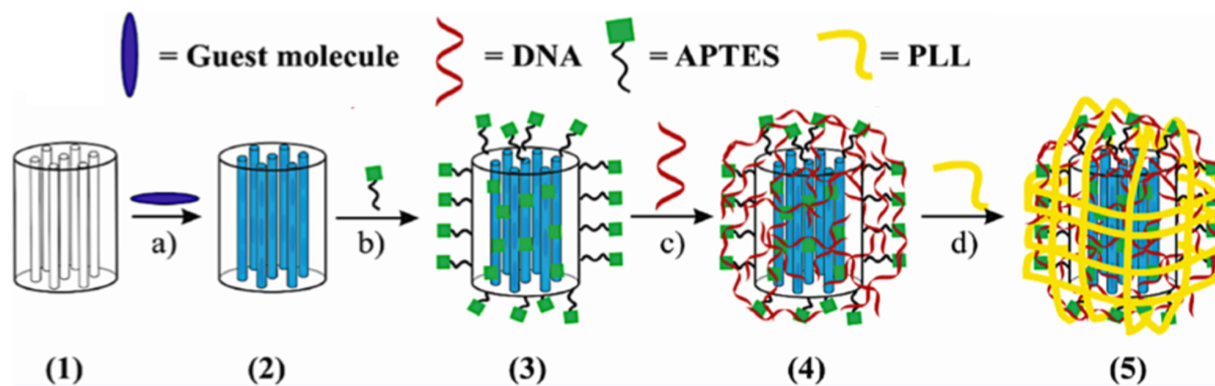


Fig. 3.3 Preparation and characterization of the designed particles. (1) Empty zeolites, (2) pores filled with guests. (3) NH₂ functionalization, (4) DNA functionalization, (5) PLL coating.

Upon DNA binding to the zeolites, the successful attachment was checked by zeta potential measurements (-17.04 mV) and by Confocal Microscopy, verifying the perfect overlap of the emission signals of the labeled DNA on the surface and of the dye caged in the pores.

Quantification of the DNA bound to the zeolites surface was achieved following literature methodology,^[70] and will be described more detailed in the following paragraphs for each system (microzeolites and nanozeolites).

For kinetics studies and for increasing cellular uptake, a thin layer of degradable PLL can also be eventually electrostatically adsorbed onto the DNA-modified zeolites, leading to overall positively charged particles and allowing for protection of the oligonucleotide in the extracellular environment.

3.3 Synthesis and functionalization of microzeolite-L

Cylinder-shaped microzeolites of size around 1 μm were synthesized as reported in Chapter 2. The obtained crystals have been then characterized by means of SEM and DLS.

The crystals were filled with DAPI by cationic exchange in water solution. Their functionalization with APTES and coating with the DNA was performed accordingly to the scheme reported in figure 3.3. The amount of DNA bound to the crystal surface was then quantified by UV-Vis spectroscopy, using a Cyanine 3-labeled DNA. Seven solutions containing each 1 mg of NH₂ functionalized zeolites were incubated with different concentrated solutions of labeled DNA (0.5 mL PBS buffer, 37 °C, 30 min). The particles were then removed by centrifugation and the amount of DNA

adsorbed to the particles was quantified by means of the characteristic UV/Vis absorption of the cyanine 3 (Cy3), calculating the difference between the DNA concentration in the supernatant before and after adsorption.

To precisely calculate DNA loading, a calibration curve of standard solutions of labeled DNA at different concentrations in the range 0.1 μM - 3 μM (5 levels, $n=3$) was built up, monitoring the absorbance value of Cy3 at 550 nm, by UV-Vis Spectroscopy. The linear model was checked by Mandel test and the final equation used was $A = 0.1923[\text{DNA}]$.

A linear increase of DNA binding to the microzeolite-L particles with increasing DNA concentrations was observed until a plateau was reached at a concentration of 15 nmol DNA per 0.5 mL PBS. At this working concentration, about 7.8 nmol DNA were bound to 1 mg of microzeolites, and a further increase in DNA concentration did not lead to an increased binding as shown in Figure 3.4.

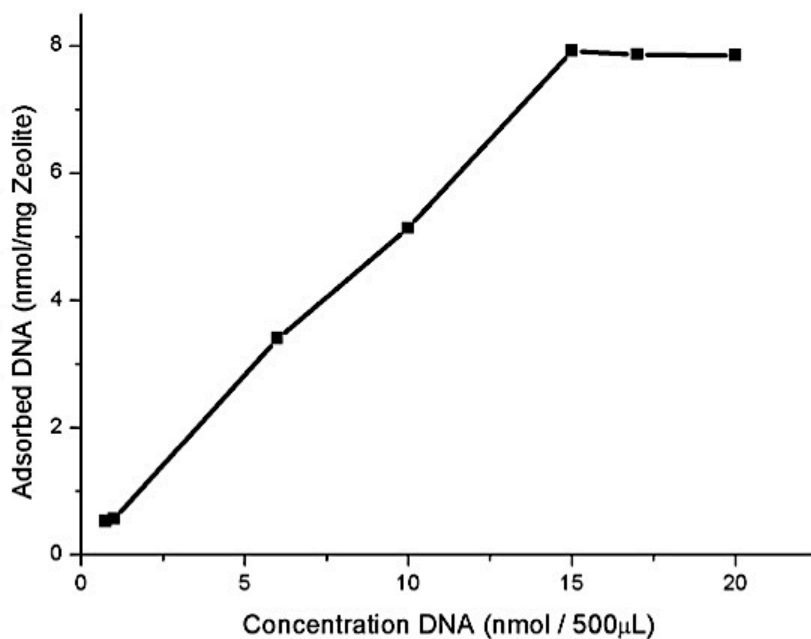


Fig. 3.4 Amount of DNA bound to 1 mg of microzeolite-L as a function of the DNA concentration in the incubating solution.

It is also possible to express the loading value as the number of DNA molecules attached to a single zeolite crystal and an amount of around 8.3×10^6 DNA molecules per microzeolite-L particle has been calculated. Further details and precise calculations are listed in the experimental part at the end of this chapter.

3.4 DAPI controlled delivery from DNA-modified microzeolite-L

The electrostatic adsorption of DNA to the surface of the crystals leads to a nearly complete closing of the pores, causing an inhibition of DAPI release; this release would however spontaneously take place when the DNA-zeolite adduct is immersed in a salted medium, due to cationic exchange. This concept has been already demonstrated for MSNPs,^[70] but it can also work for zeolites. The strategy of exploiting the formation of DNA/DNA duplexes was used to partially detach the DNA from the particles at a faster rate than the normal anionic exchange. This has been done by firstly filling the channels with DAPI and covering the zeolites with DNA, as described early on. The DNA-modified zeolites were then dispersed in PBS and incubated with a DNA oligonucleotide full complementary to the sequence adsorbed on the zeolites. Upon recognition of the complementary strand, the DNA anchored to the surface is partially desorbed, and the DAPI can be released in the solution. Centrifugation of the dispersion, and quantification of the fluorescence obtained from the supernatant, allowed the evaluation of the DAPI in solution. The results are summarized in figure 3.5 showing the DAPI concentration in the supernatant after its release.

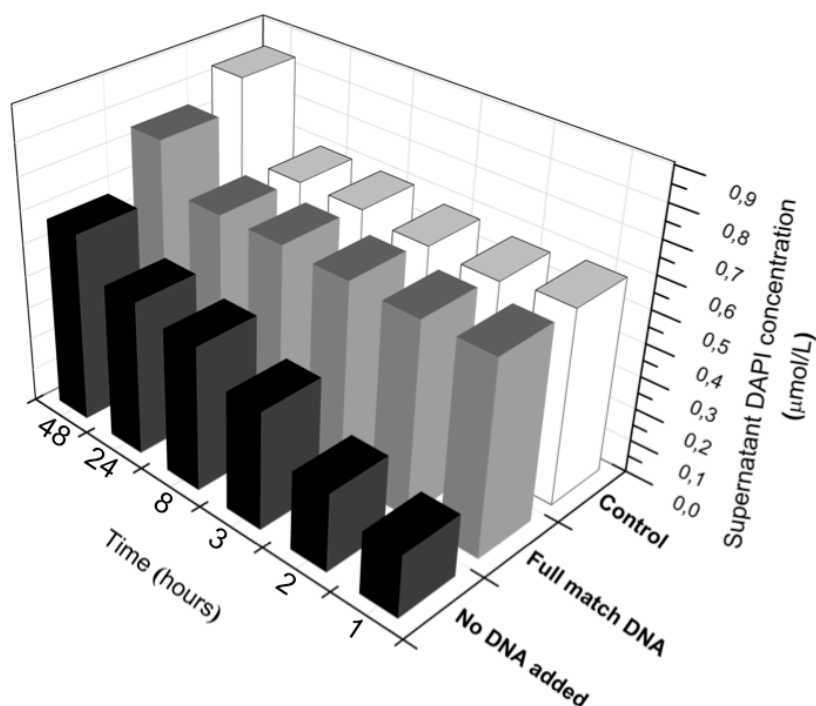


Fig. 3.5 Graphical summary of the leaking experiments to confirm the stimuli-responsive release of DAPI from DNA-functionalized zeolite-L.

In order to have a clear understanding of this process, different experiments were performed as follows:

(1) - Control Experiment. NH_2 -functionalized zeolites (1 mg) loaded with DAPI were dispersed in PBS (2 mL).

Aliquots of the supernatant were collected after 1, 2, 3, 8, 24, and 48 hours. This experiment was performed to define the fastest release (white bars in figure 3.5).

(2) - DNA-functionalized zeolites (1 mg) loaded with DAPI were dispersed in PBS (2 mL). Aliquots of the supernatant were collected after the same times as above. A very slow DAPI release was observed (black bars).

(3) - DNA-functionalized zeolites (1 mg) loaded with DAPI were dispersed in PBS containing a full match DNA sequence (5'-GCTTTCCTTCACTGTTGC-3'). Aliquots of the supernatant were collected after the above mentioned times. The addition of the full match DNA led to a DNA/DNA duplex formation, which triggers the unwrapping of the DNA from the particles. A relatively faster DAPI release was observed.

Quantification of DAPI in solution was made by fluorescence spectroscopy ($\lambda_{exc} = 350$ nm, $\lambda_{em} = 439$ nm), by means of a calibration curve built up in the operative range (4 levels, $n=3$). The linear model was validated by Mandel test and the final equation used was $y = 142395x$.

This leaking test gives a proof that the zeolite-based DNA carrier system can also act as a stimulus responsive pore-closing/pore-opening platform, which may be indeed very useful for tuning the release properties for specific and targeted therapeutics applications. The DAPI release observed also in the absence of the complementary DNA strands can be attributed to the slow detachment of DNA from the particles, due to the exchange with anions from the medium; these results were further confirmed by the cellular experiments described in the following paragraph.

3.5 Intracellular DAPI and DNA release by microzeolite-L

The cellular uptake of DNA-(DAPI)-functionalized microzeolites and the DNA and DAPI release from the particles were studied by confocal microscopy.

Due to their large dimensions and their negative charge, the particles were coated with a thin layer of PLL, which is commonly used to enhance nanoparticle uptake.^[71-73] Additionally, this coating acts as a protective layer for the adsorbed DNA, and assures the integrity of the system until it is internalized into the cells. Due to its biodegradability, the PLL coating is then degraded inside the cells, which uncovers the DNA layer and allows for its release.^[74-75] Cell experiments were done by using human cervical cancer cells (HeLa) (approximately 50000 cells per well), and incubation was done for 1, 4 and 24 hours using a particle concentration of 0.01 mg/mL. After incubation, the cells were fixed, washed with PBS and the actin filaments were stained with Alexa Fluor® 568 Phalloidin. A Cyanine 5-labeled DNA (Cy5-DNA) was used, because its red emission does not overlap with the yellow fluorescent actin stain or the blue DAPI fluorescence. The results are shown in figure 3.6.

From the confocal micrograph, it is possible to notice that after 1 hour of incubation only very few particles are uptaken by the cells, which is confirmed by recording z-stacks (figure 3.6 M). From the perfect overlap of the DAPI and Cy5 signals, it can be concluded that the DNA is indeed still bound to the particles after the cellular internalization.

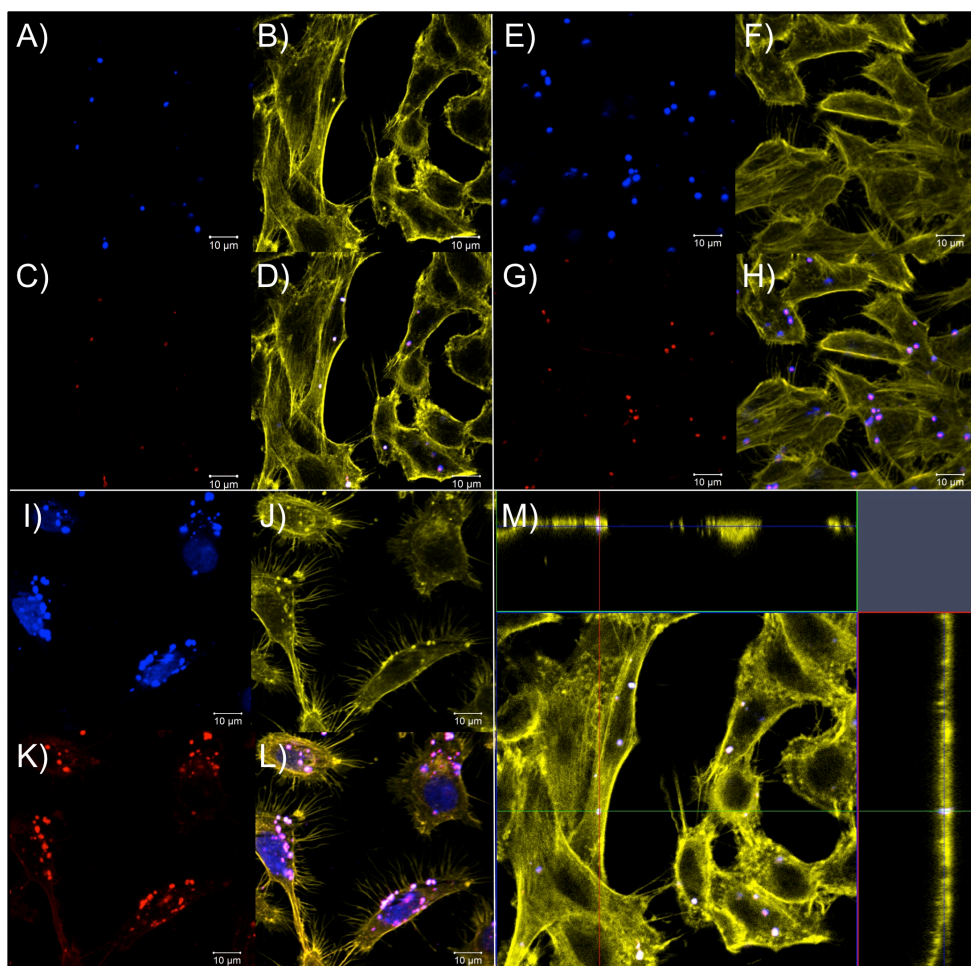


Fig. 3.6 Confocal micrographs displaying the cell uptake of DNA-(DAPI)-modified microzeolites-L. A to D: 1 hour incubation; E to H: 4 hours incubation; I to L: 24 hours incubation. M: z-stack after 1 hour incubation. A, E, I: DAPI emission; B, F, J: Alexa Fluor® 568 Phalloidin fluorescence; C, G, K: Cy5 emission; D, H, L: merged. Excitation wavelength: 405 (DAPI), 514 (Alexa) and 633 nm (Cy5).

After 4 hours, a slightly higher amount of particles were internalized, but the total number was still very small. The Cy5 signal still was associated only with the particle spots (co-localization of the DAPI and Cy5 signal), and no DAPI fluorescence was indeed recorded in the nucleus.

The number of particles uptaken by the cells was further increased after 24 hours and a light pale red staining of the cytoplasm could be observed, which can be ascribed to the detachment of very small amounts of DNA from the zeolite surface, probably due to the (slow) exchange with positively charged species present in the cellular environment. A sufficient amount of DAPI was

released from the pores, and was able to stain the nucleus, providing a recordable blue signal. However, the majority of DAPI was still present inside the zeolites, and most of DNA was bound to them, as inferred from the very bright co-localized blue and red spots in figure 3.6I and K. In view of achieving better and more interesting results for the behavior of the system *in vitro*, the work was then focused on the use of nanosized zeolite crystals.

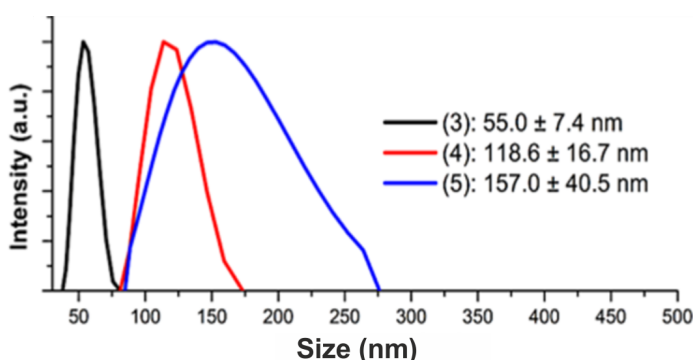
3.6 Synthesis and functionalization of nanozeolite-L

Nanozeolites in the size range 50-60 nm were prepared following a literature procedure³ and details of their synthesis are reported in Chapter 2.

The particles have been characterized by means of DLS, SEM, and TEM (see Chapter 2)

After the isolation of the nanocrystals, the pores were filled either with the water soluble DAPI nucleus stain or with the hydrophobic green fluorescent DXP.

In order to electrostatically bind DNA to the zeolites, the surface of crystals has been functionalized with APTES, as already discussed for the microzeolites. A zeta potential shift from - 33.59 mV to +2.58 mV was observed upon functionalization. The presence of the -NH₂ groups was further confirmed by a positive ninhydrin test. The modified surface was then used to electrostatically bind to the DNA oligonucleotides, which was achieved by dispersing the amine-functionalized nanozeolites (1 mg) in a solution of DNA in PBS buffer (15 nmol / 0.5 mL). Incubation was done at 37 °C for 30 min and the particles were washed with deionized water before cellular experiments. Upon DNA binding to the nanozeolites, the zeta potential decreases to a value of -17.04 mV and the particle size increases from about 55 nm to 120 nm, which is a first proof of a successful DNA attachment.



Sample	Zeta potential (mV) in PBS
(1) and (2)	- 33.59
(3)	+ 2. 58
(4)	- 17.04
(5)	+ 28.28

Fig. 3.7 Left) Size distribution by DLS of A) amine-functionalized nanozeolites (black curve), B) DNA- functionalized nanozeolites (red curve), C) DNA- and PLL-coated nanozeolites (blue curve). Right) Zeta potentials of every preparation step. Numbers from 1 to 5 refer to the functionalization steps depicted in figure 3.3.

To have an additional proof that the DNA was electrostatically bound to the zeolites, the zeolite channels were loaded with the green fluorescent DXP dye and a red-emitting Cy5-DNA was used.

After interaction of the zeolites with the DNA, the fluorescent emission of the particles was analyzed by confocal microscopy, and a perfect overlap of both green and red emissions was observed, confirming the co-localization of the DNA with the particles.

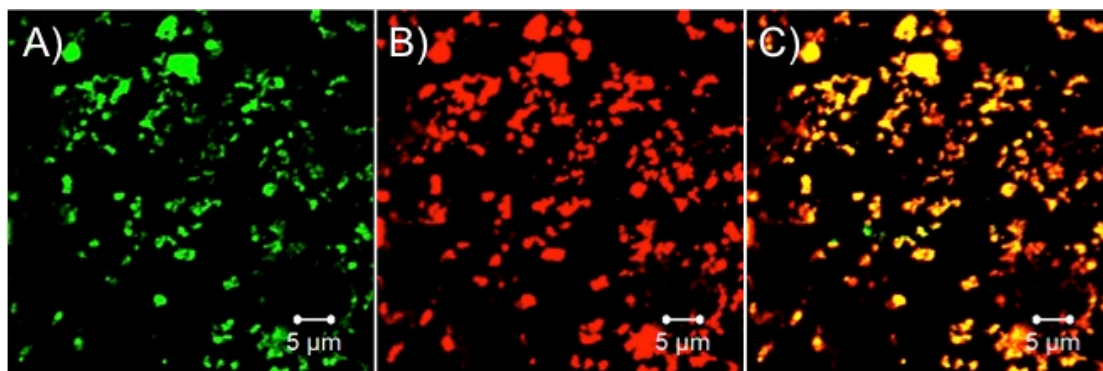


Fig. 3.8 Confirmation of DNA binding by signal overlap of DXP and Cy5. A) DXP signal; B) Cy5 signal; C) overlap. The sample was excited at 514 (DXP) and 633 nm (Cy5).

Quantification of the DNA bound to the zeolites surface was achieved following the same method already described for the microzeolites. A number of 8.6 nmol DNA per mg of nanozeolites has been calculated, which is in accordance to previously published results for mesoporous silica nanoparticles, MSNPs.^[70] This DNA amount corresponds to a binding of about 1360 molecules per nanozeolite-L (see experimental section for all the details).

In a last additional step, a fraction of the DNA-functionalized zeolites was coated with PLL by treatment for 1 hour in an aqueous solution of the polymer. An increase in particle size (from about 120 to 160 nm) and a positive zeta potential of the particles (+28.28 mV) was observed. The PLL has a double function: (i) to change the overall charge of the zeolite, facilitating the cell internalization, (ii) to protect the oligonucleotide, but then to degrade slowly inside the cell allowing slow release of the zeolite cargo.

3.7 Cellular uptake of DNA-(DXP)-modified nanozeolite-L

The very poor uptake seen in the case of the uncoated microzeolite-L crystals could be greatly improved by using nanozeolite-L particles. The same cell experiments described above were thus performed with these particles. DXP was first used as label, since is not able to leak out of the zeolites due to its insolubility in water, in order to gather information on the exact localization of the zeolites independently from the binding to DNA. This allowed for carrying out an independent kinetics study of the DNA release whilst monitoring the particle uptake and localization by using

the DXP signal. A very high particle uptake was registered with this system (without PLL), thus the particles were not subsequently coated with PLL. No actin stain was used in this experiment, because of the emission overlap with DXP. DAPI staining for the visualization of the cell nuclei was done after cell fixation. Additionally, the uptake of the particles was proved by recording z-stacks after 24 hours. The results are shown in figure 3.9.

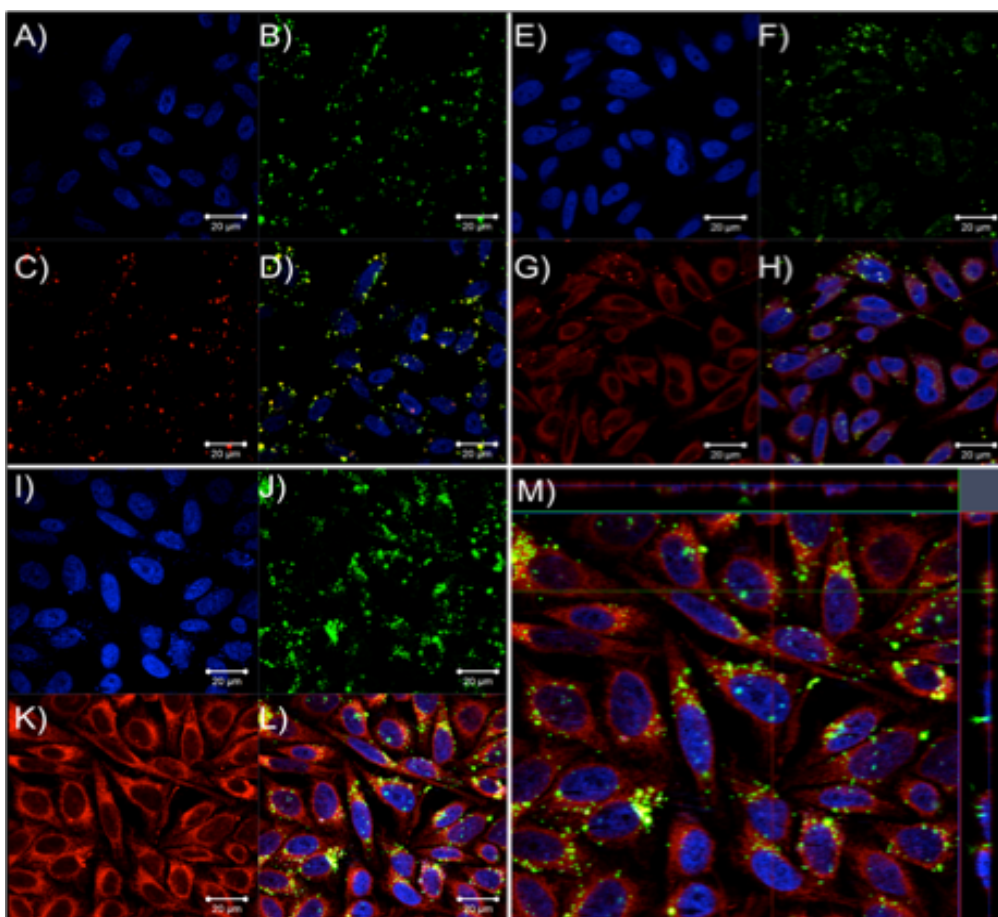


Fig. 3.9 Confocal micrographs showing the uptake of DNA-(DXP)-modified nanozeolite-L particles. A to D: 1 hour incubation; E to H: 4 hours incubation; I to L: 24 hours incubation. M: z-stack after 24 hour incubation. A, E, I: DAPI emission from stained nuclei; B, F, J: DXP fluorescence (zeolites); C, G, K: Cy5 emission (labeled DNA); D, H, L: overlay.

Already after 1 hour of incubation, a significant amount of particles was uptaken by the cells. As it can be seen from the overlap of the DXP and Cy5 emission signals, the DNA is still bound to the particles (See figure 3.9B and C). After 4 hours of incubation the intracellular particle concentration was further increased. At this time, a first red diffused staining of the cytoplasm could be seen, which could be ascribed to small amounts of DNA detached from some of the particles inside the cells. However, a big part of the DNA was still located at the particle surface, which is confirmed by the overlap of the DXP and Cy5 signal. The DNA detachment resulted greatly enhanced for an

incubation time of 24 hours, which led to the bright red emission diffused in the cytoplasm. At the same time, the particle concentration in the cells was increased, due to the constant incubation with medium containing the particle dispersion, thus also leading to a higher amount of unbound DNA in the cytoplasm.

3.8 Intracellular DAPI and DNA release by nanozeolite-L

The simultaneous DNA and DAPI release from the nanozeolite-L carriers has been investigated by confocal microscopy. Actin filaments were also stained with Alexa Fluor® 568 Phalloidin after cell fixation, since its emission does not overlap with DAPI or Cy5. The results are shown in figure 3.10.

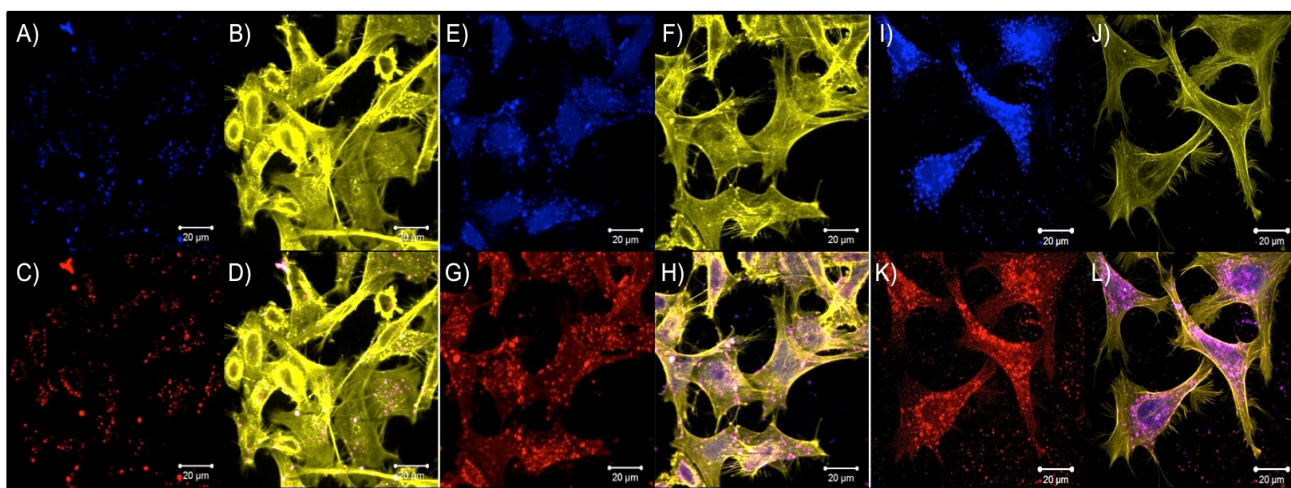


Fig. 3.10 Confocal micrographs showing the uptake and intracellular behavior of DNA-(DAPI)-modified nanozeolite-L in HeLa cells. A to D: 1 hour incubation; E to H: 4 hours incubation. I to L: 24 hours incubation. A, E, I: DAPI fluorescence. B, F, J: Alexa Fluor® 568 Phalloidin emission. C, G, K: Cy5 fluorescence. D, H, L: overlay.

After 1 hour of incubation, a discrete amount of particles was uptaken and the DNA was still bound at the particle surface, as proved by the overlap of the DAPI and Cy5 emissions (Figure 3.10A to D). The particle uptake was further increased after 4 hours of incubation and a pale blue staining of the cell nuclei, due to small amounts of DAPI leaking from the pores, was obtained (Figure 3.10E to H). After 24 hours of incubation, a strong DAPI fluorescence emission coming from the nucleus and a bright DNA signal in the cytoplasm (Figure 3.10I to L) could be clearly seen. Particle internalization was proven by recording z-stacks (Figure 3.11) of the cells and, even though the overall charge of the system was negative, the functionalized nanozeolites were efficiently uptaken by HeLa cells.

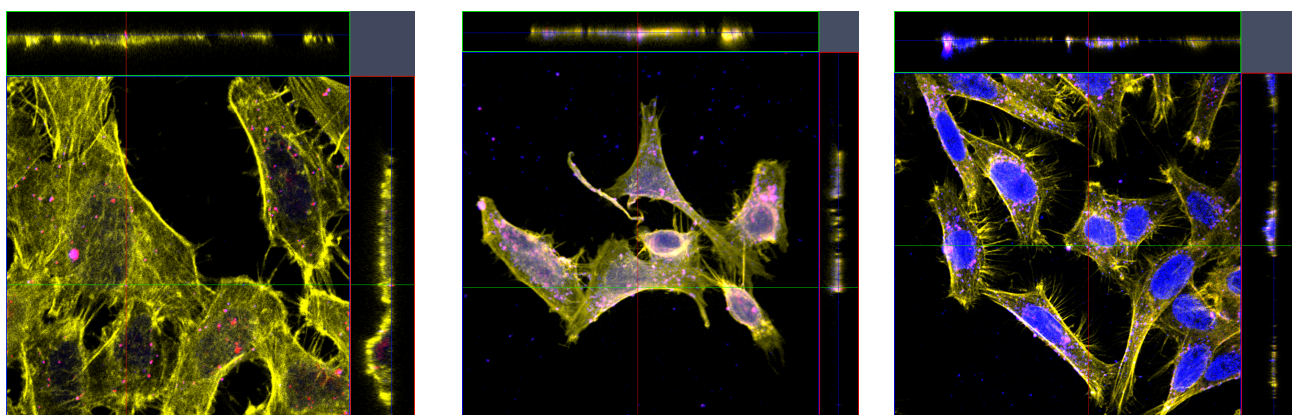


Fig. 3.11 Z-stacks of HeLa cells after 1 hour incubation (left), 4 hour incubation (middle), 24 hour incubation (right) with DNA-(DAPI)-modified nanozeolite-L.

Additionally, a cell viability study after 24 hours incubation showed negligible toxicity of the system, as shown in figure 3.12. For experimental details of the viability study, see the experimental part at the end of this chapter.

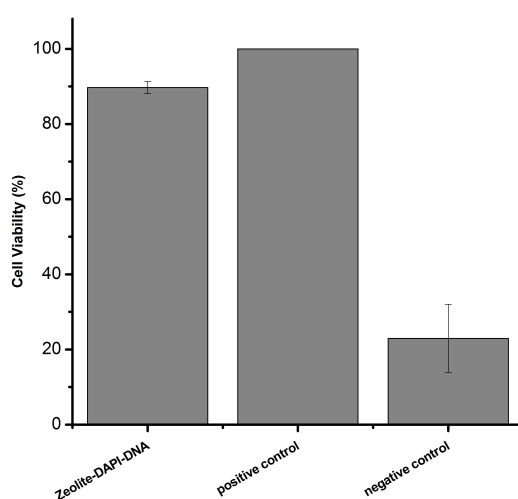


Fig. 3.12 Viability of HeLa cells upon treatment with DNA-modified nanozeolites. Positive control: untreated cells, negative control: 30% DMSO.

Even though the multifunctional system could already be considered as a carrier for drug and DNA delivery, a deep analysis of the cell uptake after short incubation times (see e.g. Figure 3.10A-D) showed that the amount of zeolites inside the cells was actually quite low. Under these conditions, the kinetics of release of DNA or DAI cannot be evaluated properly, since the increasing concentrations of DAPI in the nucleus and DNA in the cytoplasm are determined by two independent mechanisms. On the one hand the DAPI and DNA are continuously released from the

zeolites, which leads to increasing concentration of those in the nucleus and cytoplasm. On the other hand, due to the different incubation times, the intracellular particle concentration increases, most probably linearly,^[76] leading to increasing concentrations of DNA and DAPI within the cells. In order to have a better understanding of the release kinetics, and despite the cell proliferation paths that reduce the number of zeolites in each cell, the intracellular particle concentration was kept constant and the release after 1 hour of incubation was monitored. The DNA-functionalized particles were therefore covered with a thin layer of PLL, to efficiently increase cell uptake. The incubation time was thus reduced to 1 hour and a concentration of 0.01 mg/mL of zeolites was employed. After incubation the cells were extensively washed with PBS buffer to remove loosely bound zeolites from the cell surfaces. Then the cells were cultured and live-cell imaging was done directly after incubation, at time: 1 hour, 2 hours, 4 hours, 6 hours, 24 hours, 48 hours and 72 hours to follow the DAPI and DNA signals. The results are summarized in figure 3.13. Particle internalization was proved by recording z-stacks after 1 hour of incubation (Figure 3.14).

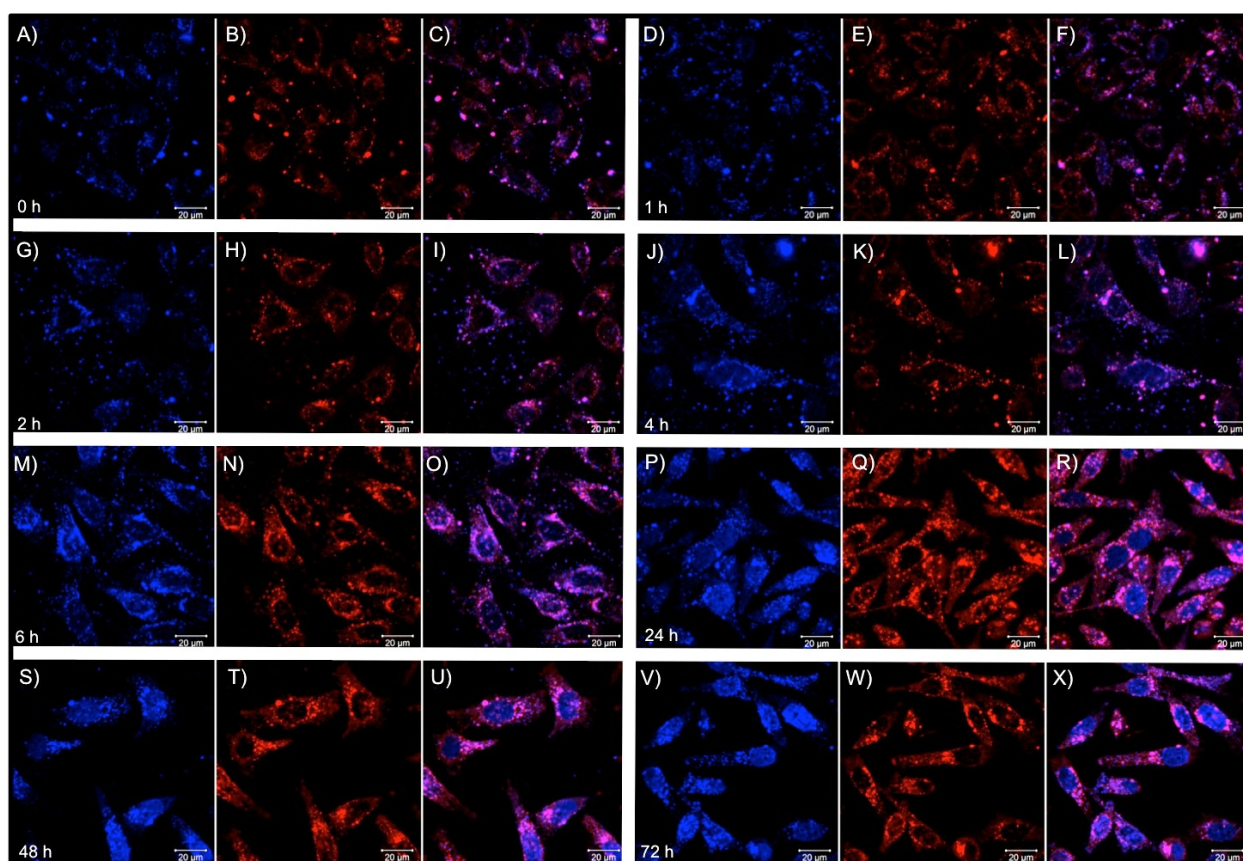


Fig. 3.13 Confocal microscopy images showing the kinetics of DAPI and DNA release from PLL covered nanozeolite-L in HeLa cells. The cells were incubated and imaging was done directly after incubation (A, B, C); after 1 hour (D, E, F); after 2 hours (G, H, I); after 4 hours (J, K, L); after 6 hours (M, N, O); after 24 hours (P, Q, R); after 48 hours (S, T, U) and after 72 hours (V, W, X). Left image: DAPI fluorescence; middle image: Cy5 emission; right image: Overlay. Excitation = 405 and 633 nm for DAPI and Cy5 respectively. Emissions were recorded with a DAPI emission filter and a Cy5 emission filter, respectively.

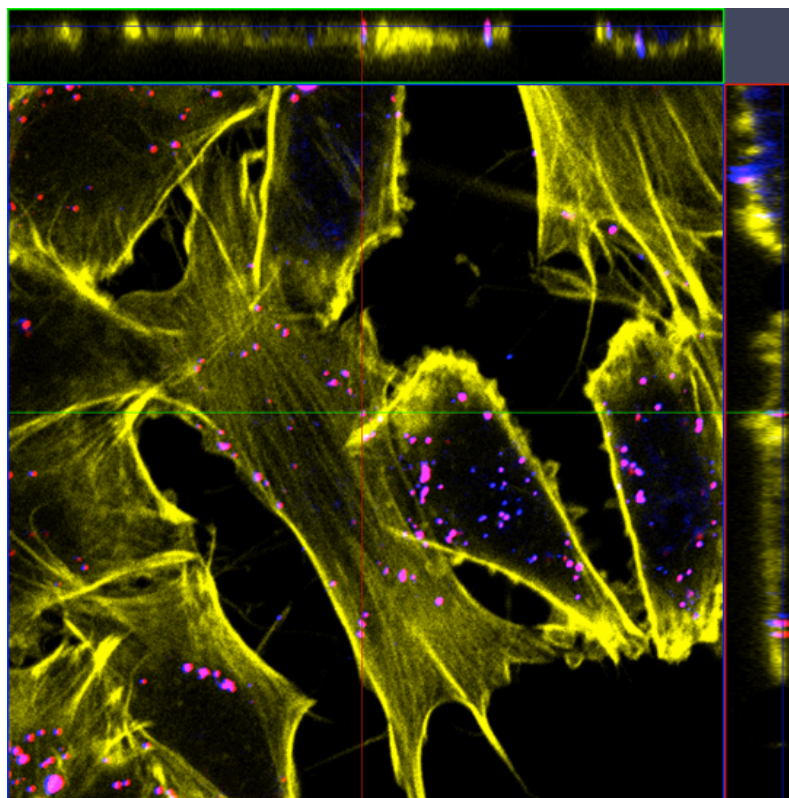


Fig 3.14 Z-stack of PLL-coated DNA(DAPI)-nanozeolites after 1 hour incubation, showing cellular uptake.

To determine the effect of the PLL coating on the DAPI and DNA release kinetics, the cells were also incubated with DNA-functionalized particles, in the absence of PLL, and a concentration ten times higher, of 0.1 mg/mL, was used to achieve a sufficient uptake already after 1 hour (Figure 3.15).

In both experiments a rather large amount of particles uptaken by the cells was observed, which allowed for studying the kinetics. However is worth to note that even though a tenfold lower particle concentration was employed for the PLL-coated particles, the uptake looked similar or even slightly higher compared to the uncoated (no PLL) zeolites. Both samples showed a slow release of DAPI and DNA from the zeolites, however the PLL coated system indicated that DAPI requires at least 4 hours (Figure 3.13J, K, L) to be clearly observed into the nucleus. This time delay is related to the PLL degradation time inside the cell.^[77] For the uncoated particles, a pale nucleus staining already after 1 hour of incubation could be noticed. Both the DAPI and the DNA signals (in the cytoplasm) could be followed by confocal microscopy and images were recorded after 24, 48 and 72 hours (see Figure 3.13 and 3.15). Keeping in mind that cell division occurs after 24 hours, a decrease of the particle number to about half was expected for each division.

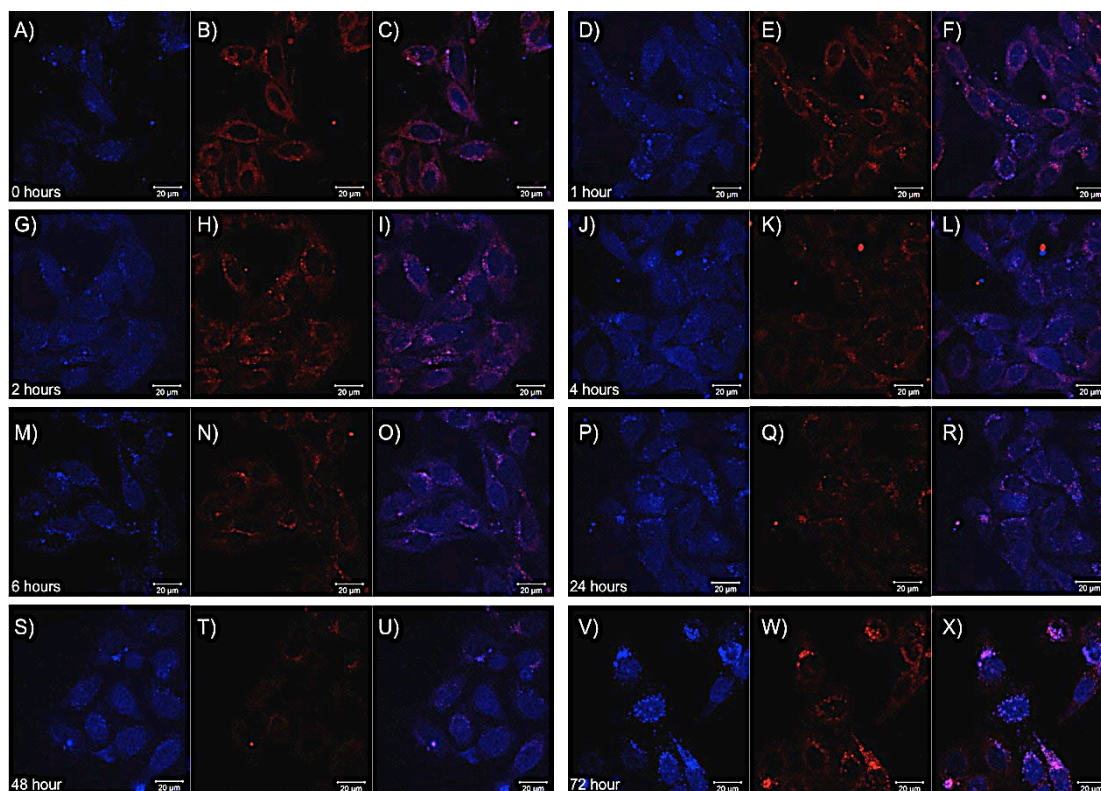


Fig. 3.15 Confocal micrographs showing the kinetics of DAPI and DNA release from nanozeolite-L (No PLL coating). Incubation was done for 1 hour followed by an extensive washing with PBS buffer to remove surface adsorbed particles. The cells were incubated and imaging was done directly after incubation (A, B, C); after 1 hour (D, E, F); after 2 hours (G, H, I); after 4 hours (J, K, L); after 6 hours (M, N, O); after 24 hours (P, Q, R); after 48 hours (S, T, U) and after 72 hours (V, W, X). Left image: DAPI signal; middle image: Cy5 signal; right image: Overlay. Excitation = 405 and 633 nm. Emission was recorded with a DAPI emission filter and a Cy5 emission filter.

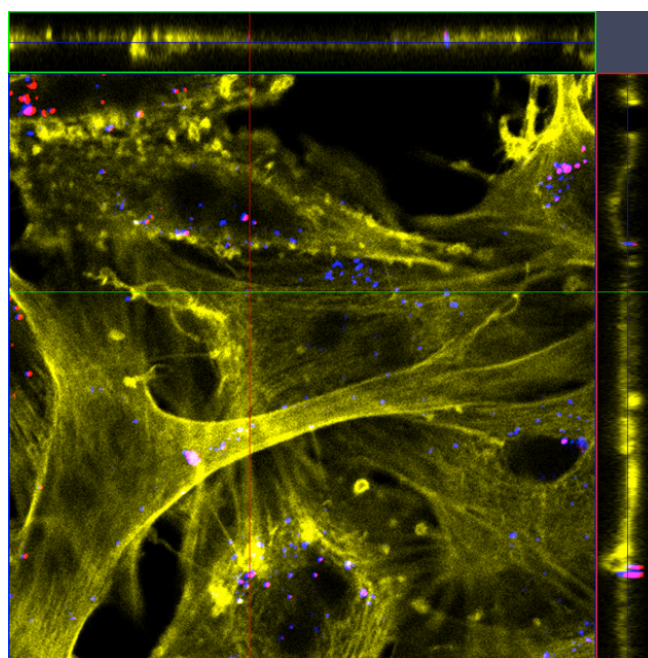


Fig. 3.16 Z-stack of zeolites (No PLL) after 1 hour incubation.

3.9 Fate of the particles and released DNA: sub-cellular localization

As reported for a variety of particles, zeolite crystals were expected to end up and accumulate in the lysosomes.^[76-79] To test this hypothesis, in HeLa cells treated with DNA(DAPI) zeolites-L system, the lysosomes were labeled after 72 hours with the green fluorescent dye LysoTracker Green DND-26 and the overlap of this emission with the residual extra-nuclear DAPI fluorescence from the particles was checked. As shown in figure 3.17A-D, both signals resulted very well overlapping (co-localization coefficient = 0.86), which proved the accumulation of the particles in the lysosomes.

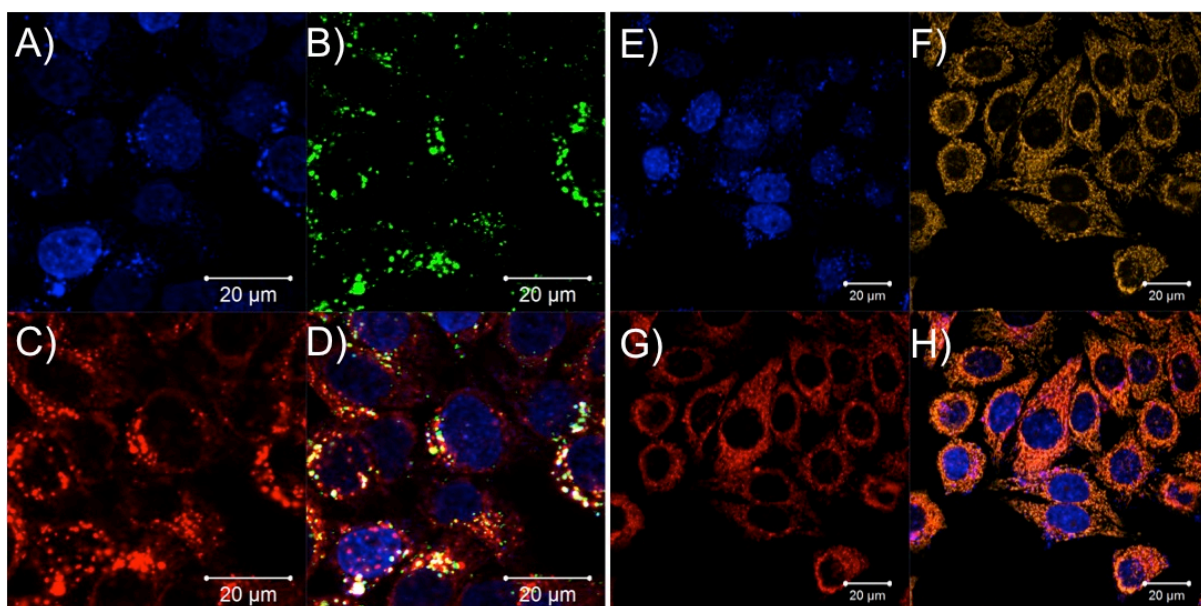


Fig. 3.17 72 hours confocal micrographs showing the localization of the particles in the lysosomes (A-D) and the released DNA in the mitochondria (E-H) of HeLa cells. A, E: DAPI signal. B: lysosome stain. F: mitochondria stain. C, G: Cy5-DNA signal; D, H: Overlay. Excitation was performed at 405 nm, 543 nm and 633 nm.

On the other hand, the intracellular localization of the desorbed DNA was determined. As reported in some *in vitro* experiments, a transfected DNA may tend to migrate to the mitochondria^[80-81] and therefore the same behavior was checked to occur also in our system. The mitochondria were labeled with the yellow-orange emissive dye MitoTracker Orange CMTMRos, as shown in figure 3.17E-H. A very good overlap (co-localization coefficient = 0.91) of the DNA signal with the mitochondria stain could be seen, which proved that also in our case, after release from the zeolites, the DNA tend to migrate and accumulate into the mitochondria.

3.10 Conclusion

The DNA and model drug (DAPI) release system based on zeolite-L particles has been presented as a powerful tool for a multi-delivery in living cells. The uptake has been shown significantly improved by using nanozeolite-L particles vs larger micrometer-sized particles, and the presence of a polycation such as PLL has been demonstrated able to play an important role for the internalization pathway. The PLL-coated DNA zeolites are of great interest since it is possible to delay the release of the oligonucleotide as well as of the molecules entrapped in the nanocontainers. The PLL layer could as well protect more labile and more fragile molecules from degradation, before reaching the target. It has been also shown that it is possible to follow the fate of each component and to localize every species in different compartments of the cell, which is important for a better comprehension of processes occurring in living organisms. Due to the negligible toxicity of the system, the presented multifunctional system may be a prototype for the development of a new class of particles for the simultaneous delivery of nucleic acids and drugs. Plasmid DNA, as well as SiRNA can be used for gene therapy, which is of a particular interest for cancer therapy. The use of the multifunctional zeolite nanocrystals can be indeed envisaged also for these *in vivo* applications.

3.11 Experimental section

Amine functionalization and DNA binding

Zeolite particles (100 mg) were dispersed in toluene (10 mL) by sonication. APTES (50 μ L, 0.2 mmol) was added to the suspension in presence of a catalytic amount of TEA and the mixture was stirred at room temperature overnight. The zeolites were then washed with ethanol (3 x 15 mL) and dried in vacuum.

NH₂-functionalized zeolites (1 mg) were dispersed in a solution of 15 nmol DNA in 0.5 mL PBS buffer. Incubation was done for 30 min at 37 °C and the zeolites were recovered by centrifugation (30 min, 14000 rpm) using an Eppendorf centrifuge.

Poly-L-lysine coating

The zeolites were dispersed in a 1% (*wt/wt*) aqueous PLL solution and incubated for 1 hour. The zeolites were recovered by centrifugation and washed twice with deionized water.

Quantification of the DNA binding to microzeolite-L

NH₂-modified microzeolite-L crystals (1mg) were incubated in different concentrated Cy3-labeled DNA solutions in PBS buffer. The particles were incubated for 30 min at 37 °C and then removed by centrifugation. Quantification was then done by subtracting the DNA concentration in the supernatant and from the initial DNA concentration. A calibration curve was used for quantification. The final curve (5 levels, n = 3 for each level) was $y = 0.1923x$ and the significance of the linear model has been confirmed by Mandel test.

Calculation of the number of DNA molecules binding to one single microzeolite-L particle

Zeolite-L dimensions: diameter = 1000 nm
 radius = 500 nm
 length = 1000 nm
 mass = 0.001 g

Number of parallel channels:

$$n_{ch} = \frac{(r)(r)^2\pi}{|a|^2 \sin 60} = \frac{\pi}{2\sqrt{3}} \left(\frac{2r}{|a|}\right)^2 \text{ with} \quad (1)$$

a: primitive vector perpendicular to the c-axis

r: zeolite-L diameter radius in nm

Equation (1) can be approximated as

$$n_{ch} = 1.104 r^2 \quad (2)$$

Thus a zeolite-L with a radius of 500 nm obtains about 276000 parallel channels.

Number (mol) of unit cells in one crystal:

$$N_{ch} = n_{ch} \left(\frac{1}{N_A |c|}\right) \text{ with} \quad (3)$$

l: length of zeolite crystal

|c|: primitive c-vector (0.75 nm)

Thus a zeolite L crystal with a length of 1000 nm has 6.011E-16 mol unit cells.

Weight of one crystal:

$$m_{Zeo} = N_{ch} M_{u.c.} \text{ with} \quad (4)$$

M_{u.c.} being the molecular weight of one unit cell (2880 g/mol)

Thus the weight of one zeolite-L crystal is about 1.76E-12 g.

Number of crystals in 1 mg:

$$N_{Zeo} = \frac{\text{Sample mass}}{m_{Zeo}} \quad (5)$$

Thus in 1 mg of zeolites there are 5.68x10⁸ single crystals.

DNA absorbed on 5.68x10⁸ zeolite-L particles (1 mg): 8 nmol

Thus the weight of one zeolite-L crystal is about 2.64E-16 g.

Number of crystals in 1 mg:

$$N_{\text{Zeo}} = \frac{\text{Sample mass}}{m_{\text{Zeo}}} \quad (5)$$

Thus in 1 mg of zeolites there are 3.8×10^{12} single crystals.

DNA absorbed on 3.8×10^{12} zeolite-L crystals (1 mg): 8.6 nmol

DNA molecules on one zeolite crystal:

$$\frac{8.6 \times 10^{-9} \times 6.022 \times 10^{23}}{3.8 \times 10^{12}} = 1362$$

Cell Culture

HeLa cells were cultured inside media which contain 88 % Dulbecco's Modified Eagle Medium (DMEM), 10 % Fetal Bovine Serum, 1 % Penicillin-Streptomycin and 1 % L-Glutamine 200mM, under 37°C and 5% of CO₂, conditioning for 48 hours until 70 to 80 % cell confluency was reached. Subsequently, the cells were washed twice with Phosphate Buffer Solution and treated with trypsin. Then, approximately 50,000 cells were reseeded on the monolayer glass cover slip inside 6 well plate culture dish. New culture media (2 ml) were added gently and the cells were grown overnight.

Cell viability study

Cell viability was measured by an automatic cell counter CASY (Roche Innovatis AG, Bielefeld, Germany). 50,000 cells were grown in 2 ml of culture media inside 6 well plates at 37°C, 5 % CO₂ environment for 24 hours. Culture media were removed and replaced by solution containing 0.01 mg/ml of zeolites-DAPI-DNA, followed by cell incubation. After 24 hours of incubation, the culture media were removed to an eppendorf tube and 0.5 ml of trypsin were added. In order to detach the cell from the surface of the plate, cells were incubated for the next 10 minutes. Subsequently, 1.5 ml of new culture media were added to neutralize trypsin. Cell suspension, together with the first solution collected, were removed into 10 ml eppendorf tube and centrifuged at 1000 rpm for 5 minutes. Supernatant was removed and cell palates were suspended into 1 ml of new culture media. 200 µl of the cell suspension was dissolved in 10 ml of CASY solution and measurement was performed. To add negative control experiment, the exact same procedure was

performed by incubating cells in 50% of ethanol in culture media while for positive control, cells were incubated only with culture media.

REFERENCES

- [1] D. Luo, W.M. Saltzman, *Nature biotech.* **2000**, *18*, 33-37.
- [2] A. Fasbender, J. Zabner, B.G. Zeiher, M.J. Welsh, *Gene Ther.* **1997**, *4*, 1173-1180.
- [3] H. Matsui, L.G. Johnson, S.H. Randell, R.C. Boucher, *J. Biol. Chem.* **1997**, *272*, 1117-1126.
- [4] M.A. Kay, *Nature Rev. Genet* **2011**, *12*, 316-328.
- [5] F. Mingozzi, K.A. High, *Nature Rev. Genet.* **2011**, *12*, 341-355.
- [6] C. Baum, O. Kustikova, U. Modlich, Z. Li, B. Fehse, *Hum. Gene Ther.* **2006**, *17*, 253-263.
- [7] N. Bessis, F.J. Garcia Cozar, M.C. Boissier, *Gene Ther.* **2004**, *11*, S10-S17.
- [8] C.E. Thomas, A. Ehrhardt, M.A. Kay, *Nature Rev. Genet.* **2003**, *4*, 346-358.
- [9] D. Bouard, D. Alazard-Dany, F.L. Cosset, *Br. J. Pharmacol.* **2009**, *157*, 153-165.
- [10] H. Yin, R.L. Kanasty, A.A. Eltoukhy, A.J. Vegas, J.R. Dorkin, D.G. Anderson, *Nature Rev. Genet.* **2014**, *15*, 541-555.
- [11] T. Niidome, L. Huang, *Gene Ther.* **2002**, *9*, 1647-1652.
- [12] S.D. Patil, D.G. Rhodes, D.J. Burgess, *The AAPS journal* **2005**, *7*, E61-E77.
- [13] S. Mehier-Humbert, R.H. Guy, *Adv. Drug Deliv. Rev.* **2005**, *57*, 733-753.
- [14] E.F. Fynan, R.G. Webster, D.H. Fuller, J.R. Haynes, J.C. Santoro, *PNAS* **1993**, *90*, 11478-82.
- [15] A. Porgador, K.R. Irvine, A. Iwasaki, B.H. Barber, N.P. Restifo, R.N. Germain, *J. Exp. Med.* **1998**, *188*, 1075-1082.
- [16] J.M. McMahon, E. Signori, K.E. Wells, V.M. Fazio, D.J. Wells, *Gene Ther.* **2001**, *8*, 1264-1270.
- [17] D.J. Wells, *Gene Ther.* **2004**, *11*, 1363-1369.
- [18] B.L. Hodges, R.K. Scheule, *Exp. Opin. Biol. Ther.* **2003**, *3*, 911-918.
- [19] C.M. Newman, T. Bettinger, *Gene Ther.* **2007**, *14*, 465-475.
- [20] C. Plank, U. Schillinger, F. Scherer, C. Bergemann, J.S. Rémy, F. Krötz, J. Rosenecker, *Biol. Chem.* **2003**, *384*, 737-747.
- [21] P.L. Felgner, *Adv. Drug Deliv. Rev.* **1990**, *5*, 163-187.
- [22] H. Gonzalez, S.J. Hwang, M.E. Davis, *Bioconj. Chem.* **1999**, *10*, 1068-1074.
- [23] M. Hiersch, M. Rimann, V. Panagiotopoulou, E. Ozturk, T. Biedermann, M. Textor, T.C. Luhmann, H. Hall, *Biomater.* **2013**, *34*, 4173-4182.
- [24] J.J. Xiang, J.Q. Tang, S.G. Zhu, X. Nie, H. Lu, S. Shen, X. Li, K. Tang, M. Zhou, G.J. Li, *J. Gene Med.* **2003**, *5*, 803-817.
- [25] D. Zhou, C. Li, Y. Hu, H. Zhou, J. Chen, Z. Zhang; T. Guo, *J. Mater. Chem.* **2012**, *22*, 10743-10751.
- [26] D. Kwoh, C.C. Coffin, C.P. Lollo, J. Jovenal, M.G. Banaszczyk, P. Mullen, A. Phillips, A. Amini, J. Fabrycki, R.M. Bartholomew, *et al. BBA-Gene Struct. Expr.* **1999**, *1444*, 171-190.
- [27] F. Alexis, E. Pridgen, L.K. Molnar, O.C. Farokhzad, *Mol. Pharm.* **2008**, *5*, 505-515.
- [28] D. Goula, C. Benoist, S. Mantero, G. Merlo, G. Levi, B.A. Demeneix, *Gene Ther.* **1998**, *5*, 1291-1295.
- [29] H. Petersen, P.M. Fechner, A.L. Martin, K. Kunath, S. Stolnik, C.J. Roberts, D. Fischer, M.C. Davies, T. Kissel, *Bioconjug. Chem.* **2002**, *13*, 845-854.
- [30] H.K. Nguyen, P. Lemieux, S.V. Vinogradov, C.L. Gebhart, N. Guerin, G. Paradis, A.V. Kabanov, *Gene Ther.* **2000**, *7*, 126-138.
- [31] M. Breunig, U. Lungwitz, R. Liebl, A. Goepferich, *Proc. Natl. Acad. Sci. USA* **2007**, *104*, 14454-14459.

- [32] P.L. Felgner, T.R. Gadek, M. Holm, R. Roman, H.W. Chan, M. Wenz, M. Danielsen, *Proc. Natl. Acad. Sci. USA* **1987**, *84*, 7413-7417.
- [33] M.C. Pedroso de Lima, S. Simões, P. Pires, H. Faneca, N. Düzgüneş, *Adv. Drug Del. Rev.* **2001**, *47*, 277-294.
- [34] W. Li, F.C. Szoka Jr, *Pharm. Res.* **2007**, *24*, 438-449.
- [35] K. Rombouts, T.F. Martens, E. Zagato, J. Demeester, S.C. De Smedt, K. Braeckmans, K. Remaut, *Mol. Pharm.* **2014**, *11*, 1359-1368.
- [36] K.K. Ewert, H.M. Evans, A. Zidovska, N.F. Bouxsein, A. Ahmad, C.R. Safinya, *J. Am. Chem. Soc.* **2006**, *128*, 3998-4006.
- [37] V.P. Torchilin, T.S. Levchenko, R. Rammohan, N. Volodina, B. *Proc. Natl. Acad. Sci. USA* **2003**, *100*, 1972-1977.
- [38] D.A. Balazs, W.T. Godbey, *J. Drug. Del.* **2011**, Article ID 326497.
- [39] H. Li, L. Piao, B. Yu, B.C. Yung, W. Zhang, P.G. Wang, R.J. Lee, *Biomater.* **2011**, *32*, 6614-6620.
- [40] J. Schäfer, S. Höbel, U. Bakowsky, A. Aigner, *Biomater.* **2010**, *31*, 6892-6900.
- [41] E. Kleemann, M. Neu, N. Jekel, L. Fink, T. Schmehl, T. Gessler, T. Kissel, *J. Control. Rel.* **2005**, *109*, 299-316.
- [42] A. Aris, A. Villaverde, *Biochem. Bioph. Res. Comm.* **2000**, *278*, 455-461.
- [43] F. Simeoni, M.C. Morris, F. Heitz, G. Divita, *Nucleic acids Res.* **2003**, *31*, 2717-2724.
- [44] Y. Huang, *Adv. Drug Deliv. Rev.* **2013**, *65*, 1299-1315.
- [45] J.F. Kukowska-Latallo, A.U. Bielinska, J. Johnson, R. Splindler, D.A. Tomalia, J.R. Baker, *Proc. Natl. Acad. Sci. USA* **1996**, *93*, 4897-4902.
- [46] D. Luo, K. Haverstick, N. Belcheva, E. Han, W.M. Saltzman, *Macromol.* **2002**, *35*, 3456-3462.
- [47] X. Liu, J. Wu, M. Yamine, J. Zhou, P. Posocco, S. Viel, L. Peng, *Bioconj. Chem.* **2011**, *22*, 2461-2473.
- [48] S. Mahor, E. Collin, B.C. Dash, A. Pandit, *Curr. Drug Deliv.* **2011**, *8*, 354-362.
- [49] V.P. Torchilin, *Biopolymers* **2008**, *90*, 604-610.
- [50] Q. Wang, X. Zhuang, J. Mu, Z.B. Deng, H. Jiang, L. Zhang, H.G. Zhang, *Nature Comm.* **2013**, *4*, 1867.
- [51] M. Elsabahy, K.L. Wooley, *Chem. Soc. Rev.* **2012**, *41*, 2545-2561.
- [52] A. Elbakry, E.C. Wurster, A. Zaky, R. Liebl, E. Schindler, P. Bauer-Kreisel, M. Breunig, *Small* **2012**, *8*, 3847-3856.
- [53] J.H. Kim, J.H. Yeom, J.J. Ko, M.S. Han, K. Lee, S.Y. Na, J. Bae, *J. Biotech.* **2011**, *155*, 287-292.
- [54] K.C. Bahadur, B. Thapa, N. Bhattarai, *Nanotechn. Rev.* **2014**, *3*, 269-280.
- [55] D. Pissuwan, T. Niidome, M.B. Cortie, *J. Control. Rel.* **2011**, *149*, 65-71.
- [56] S.C. McBain, H. Yiu, A. El Haj, J. Dobson, *J. Mater. Chem.* **2007**, *17*, 2561-2565.
- [57] K.C.F. Leung, C.P. Chak, S.F. Lee, J.M. Lai, X.M. Zhu, Y.X.J. Wang, C. Cheng, *Chem. Comm.* **2013**, *49*, 549-551.
- [58] S. Jiang, A.A. Eltoukhy, K.T. Love, R. Langer, D. Anderson, *Nano letters* **2013**, *13*, 1059-1064.
- [59] A.K. Salem, P.C. Searson, K.W. Leong, *Nature Mater.* **2003**, *2*, 668-671.
- [60] A. Wijaya, S.B. Schaffer, I.G. Pallares, K. Hamad-Schifferli, *ACS Nano* **2008**, *3*, 80-86.
- [61] D. Pantarotto, R. Singh, D. McCarthy, M. Erhardt, J.P. Briand, M. Prato, A. Bianco, *Angew. Chem.* **2004**, *116*, 5354-5358.
- [62] J.E. Nazhad Dolatabadi, Y. Omid, D. Losic, *Curr. Nanosci.* **2011**, *7*, 297-314.
- [63] M. Kar, N. Tiwari, M. Tiwari, M. Lahiri, S.S. Gupta, *Part. Part. Syst. Char.* **2013**, *30*, 166-179.
- [64] D.R. Radu, C.Y. Lai, K. Jeftinija, E.W. Rowe, S. Jeftinija, V.S.Y. Lin, *J. Am. Chem. Soc.* **2004**, *126*, 13216-13217.

- [65] D. Brevet, O. Hocine, A. Delalande, L. Raehm, C. Charnay, P. Midoux, C. Pichon, *Int. J. Pharm.* **2014**, *471*, 197-205.
- [66] F. Torney, B.G. Trewyn, V.S.Y. Lin, K. Wang, *Nature Nanotech.* **2007**, *2*, 295-300.
- [67] S. Zhou, X. Du, F. Cui, X. Zhang, *Small* **2014**, *10*, 980-988.
- [68] M. Kim, H. Na, Y. Kim, S.R. Ryoo, H.S. Cho, K.E. Lee, H. Jeon, R. Ryoo, D. Min, *ACS Nano* **2011**, *5*, 3568-76.
- [69] I.I. Slowing, J.L. Vivero-Escoto, C.W. Wu, V.S.Y. Lin, *Adv. Drug Deliv. Rev.* **2008**, *60*, 1278-1288.
- [70] E. Climent, R. Martínez-Máñez, F. Sancenón, M.D. Marcos, J. Soto, A. Maquieira, P. Amorós, *Angewandte Chemie* **2010**, *122*, 7439-7441.
- [71] Z. Li, C. Shuai, X. Li, J. Xiang, G. Li, *J. Biomed. Mater. Res. A* **2013**, *101*, 2846-2850.
- [72] T. Lühmann, M. Rimann, A.G. Bittermann, H. Hall, *Bioconj. Chem.* **2008**, *19*, 1907-1916.
- [73] H.D. Singh, G. Wang, H. Uludag, L.D. Unsworth, *Acta Biomater.* **2010**, *6*, 4277-4284.
- [74] K. Ren, J. Ji, J. Shen, *Bioconj. Chem.* **2006**, *17*, 77-83.
- [75] K. Ren, J. Ji, J. Shen, *Biomater.* **2006**, *27*, 1152-1159.
- [76] A. Salvati, A. Christoffer, T. dos Santos, J. Varela, P. Pinto, I. Lynch, K. A. Dawson, *Nanomedicine* **2011**, *7*, 818-826.
- [77] M. Westwood, D. Roberts, R Parker, *Carbohyd. Polym.* **2011**, *84*, 960-969.
- [78] A. Laskar, M. Ghosh, S. I. Khattak, W. Li, X.-M. Yuan, *Nanomedicine* **2012**, *7*, 705-717
- [79] F. Wang, L. Yu, M. P. Monopoli, P. Sandin, E. Mahon, A. Salvati, K. A. Dawson, *Nanomedicine* **2013**, *9*, 1159-1168.
- [80] N. Ibrahim, H. Handa, A. Cosset, M. Koulintchenko, Y. Konstantinov, R. N. Lightowers, A. Dietrich, F. Weber-Lotfi, *Pharm. Res.* **2011**, *28*, 2871-2872.
- [81] V. P. Torchilin, B. A. Khaw, V. Weissig, *Somat. Cell Mol. Genet.* **2002**, *27*, 49-64.
- [82] J.B. Jensen, L.H. Pedersen, P.E. Hoiby, L.B. Nielsen, T.P. Hansen, J.R. Folkenberg, J. Riishede, D. Noordegraaf, K. Nielsen, A. Carlsen, A. Bjarklev, *Opt. Lett.* **2004**, *29*, 1974-1976.

4

Intracellular delivery of Peptide Nucleic Acid and organic molecules using zeolite-L nanocarriers

Abstract

The manufacture of multifunctional nanosystems that can carry into live cells peptide nucleic acids able to target specific nucleic acid species represents an important step towards the development of highly selective tools for potential personalized therapeutics based on gene expression control. This chapter describes a very first example of the use of zeolite nanocrystals as multifunctional nanocarriers to deliver simultaneously PNA and organic molecules into living cells. Hybrid PNA-Zeolite-L nanocrystals are obtained by covalently anchoring the PNA probes onto the surface, while the channel system is filled with fluorescent guest molecules. The cellular uptake of the PNA-Zeolite-L nanoparticles is significantly increased coating the whole system with a thin layer of biodegradable poly-L-lysine. The delivery of DAPI as a model drug molecule, inserted into the zeolite pores, is also demonstrated to occur in the cells, proving the multifunctional ability of the system. These zeolite nanosystem are eventually designed carrying PNA probes to target specific microRNA (miRNA) sequences, whose antisense knockdown might be used for arresting tumor proliferation. PNA-zeolite-L nanoparticles bearing cationic-modified PNA probes for miRNA targeting are also fabricated and their use for specific *in vitro* experiments is envisaged. The last paragraph eventually reports preliminary results on the manufacture of PNA-gated multifunctional zeolite nanocarriers for miRNA-responsive controlled drug delivery, in view of potential smart delivery platforms releasing the payload only when in presence of the target miRNA.

A. Bertucci, H. Lülfi, D. Septiadi, A. Manicardi, R. Corradini, L. De Cola, Intracellular delivery of Peptide Nucleic Acid and organic molecules using zeolite-L nanocrystals, *Adv. Health. Mat.*, **2014**, 3, 1812-1817

4.1 Cellular delivery of Peptide Nucleic Acid

The chemical and biological properties of PNAs have been already pointed out in the dedicated section in the Introduction (Chapter 1, 1.5) of this thesis. It has been highlighted how all its qualities make PNA an extremely powerful tool for antisense- and antigene-based biomedical applications.

Nevertheless, the widespread use of PNA as an experimental and therapeutic regulator for gene expression *in vitro* and *in vivo* has been hampered so far by its poor cell membrane permeability and its low cellular uptake. In the past decades, several efforts have been made to overcome this limitation and different strategies have been investigated to provide a more efficient internalization. Early on, first attempts have been made for the cellular delivery of unmodified PNAs, and physical techniques as microinjection and electroporation have been exploited.^[1-3] However, as already discussed for similar approaches for DNA delivery, laborious laboratory techniques and hurdles to transfer the same technology to real clinical samples have made these protocols not be considered as ideal ones.^[4] Chemical approaches have thus been mostly investigated and implemented for the biological delivery of PNA. Indeed, one of the most suitable strategies has relied on conferring higher cell permeability to the PNA molecule itself, introducing several modifications directly at the molecular structure level.^[5] A possible approach to enhance PNA cell uptake has been based on the direct modification of the PNA backbone.^[6-9] For example, C5-arginine-modified PNAs were successfully tested to enter K526 cells and to inhibit the activity of the target miRNA-210.^[10] Aminomethylene-modification has been also reported by Mitra *et al.* as a feasible candidate to improve PNA cellular uptake.^[11] The same group of Ganesh has recently reported that also the introduction of pendant chiral C γ -(alkylideneamino/guanidino) cationic sidechains to PNA backbone can influence the hybridization properties and cellular uptake.^[12] The strategy based on modifying the γ -position of the backbone had been also suggested by Danith Ly and co-workers.^[13-14] An alternative very popular approach used to increase membrane permeability is based on the conjugation of PNA sequences with cellular uptake-enhancing moieties. For instance, the conjugation of PNAs with cell penetrating peptides (CPP) has been widely proposed as an optimal solution for cell experiments.^[15-19] Gait *et al.* successfully proposed, for instance, CPP-PNAs as inhibitors of HIV-1 Tat-dependent trans-activation in cells.^[20] CPP-PNA-based microRNA inhibitors have been shown to elicit anti-inflammatory effects in microglia cells by Brown and Yin.^[21]

More recently, Cordier *et al.* investigated cell uptake and antisense activity of a tridecamer PNA that targets the HIV-1 polypurine tract sequence, delivered using the arginine-rich (R/W)₉ peptide (RRWRRRWR).^[22] However, a drawback of such a strategy is that the PNA–CPP conjugates

internalized by cells could be retained in the endosome/lysosome compartments, drastically reducing the actual available amount of free active PNA.^[23-25]

PNAs can also be conjugated with other molecular species, including lipophilic moieties,^[26-28] adamantyl,^[29] terpyridine,^[30] or flavin groups.^[23]

The general growing interest for nanotechnology has led also to development of prototypes of nanoparticle-based platforms to enhance the intracellular delivery of PNA. Very recently, first examples of using polymeric soft nanoparticles as PNA carriers have been reported in the literature. Fang *et al.* reported an approach based on cationic shell-cross-linked knedel-like nanoparticles (see Figure 4.1).^[31]

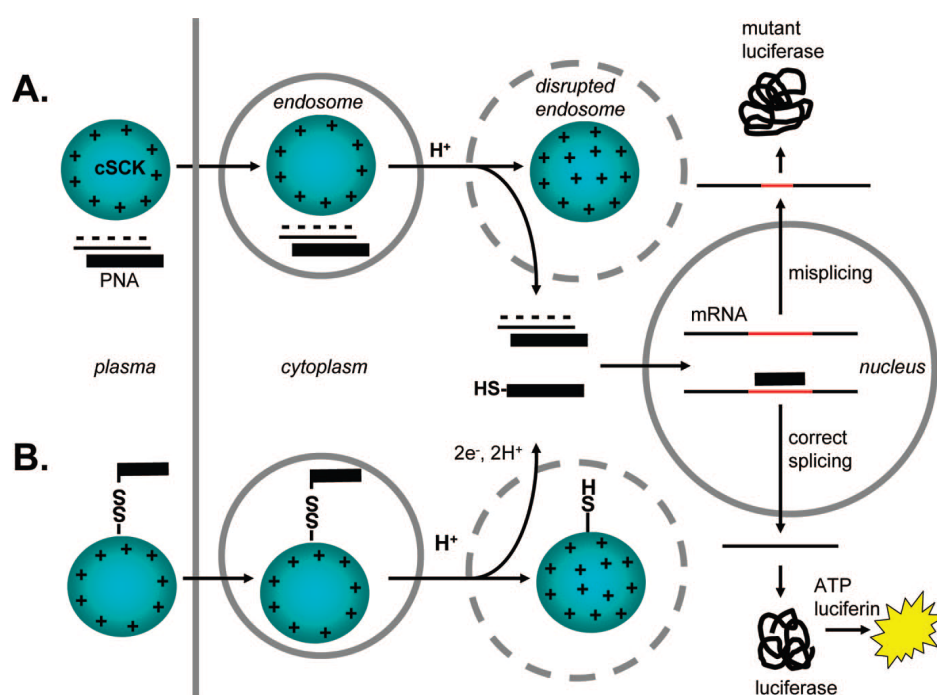


Fig. 4.1 Strategies for the development of electrostatic and covalent-based nanoparticle agents for transfection of PNA. (A) Electrostatic system. (B) Bioreductively cleavable covalent system. In case A, the cationic shell facilitates the electrostatic binding of PNA-ODN duplexes. The remaining basic groups act as a proton sponge that acquires additional protons and counterions, causing disruption of the endosome and delivery of the probes, which are made for targeting specific mRNAs. In case B, disruption of the endosome exposes the particles to reducing agents which cleave the disulfide bond and cause the release of the splice-correcting PNA. Reprinted with permission from H. Fang, K. Zhang, G. Shen, K. L. Wooley, J.S.A. Taylor, *Mol. Pharm.* **2009**, *6*, 615–626. Copyright (YEAR) American Chemical Society.

This is, together with the work of McNeer *et al.*^[32] presenting the use of biodegradable poly(lactic-co-glycolic acid) (PLGA) nanoparticles as delivery platforms for PNA oligonucleotides, one of the few examples in literature in which nanoparticles, more precisely soft polymeric, were thought as tools to facilitate PNA cellular uptake.

Anstaett *et al.* showed a first example of PNA-gold nanoparticle composites, but no biological applications are yet reported.^[33]

Carbon-based nanostructured materials have been recently explored as possible suitable carriers for PNAs, and a pioneering work on *in vitro* targeting with PNA probes coupled to nano graphene oxide particles has been published by Ryoo *et al.*^[34] However, there are no reports so far on using inorganic porous nanoparticles as possible carriers for the PNA delivery *in vitro* or *in vivo*. Especially silica-based nanoparticles can provide an optimal substrate due to their useful chemical and biological properties, which have been already presented in the previous chapters. Using porous nanomaterials would allow also for introducing further functions to the system, e.g. inserting a releasable payload in the pores, and thus for manufacturing tailor made multifunctional nanoparticles.

Binding of the PNA probes to the selected inorganic platform can be achieved considering two main feasible strategies. On one hand, one could think to covalently link the probes to the particles to fabricate a hybrid composite, on the other to adsorb the PNA on the material surface to have species that can be detached and released. Indeed, zeolite-L crystals, which have been presented in the previous chapter as efficient transfection tools, are suitable candidates to be used as nanopatform for the PNA delivery as well.

Herein, the first example of using porous nanozeolites as multifunctional PNA and drug delivery system is reported, demonstrating the ability to deliver high amounts of both a model drug and PNA to live cells.

4.2 Material preparation and characterization

Zeolite-L crystals of 60 nm were synthesized according to a literature protocol^[35] and characterized by SEM, TEM, DLS, and zeta potential measurements.

The zeolites were obtained as monodisperse single cylindrical crystals and showed a negative zeta potential of -34.05 mV (in PBS buffer). In the next steps, the pores were filled with the desired guest organic molecules and PNA probes were covalently attached to the outer surface, following a layer-by-layer approach.

The crystal channels were firstly loaded either with DAPI by cationic exchange (see experimental section) or with DXP by gas phase insertion, then the outer particle surface was functionalized with (3-aminopropyl)triethoxysilane (APTES). The functionalization was confirmed by a zeta potential shift from negative to $+15.70$ mV and by a positive ninhydrin test. Subsequently, the amine groups were converted into carboxylic acid functions, as confirmed by a new zeta potential shift to -37.37 mV. Eventually, the carboxylic moieties were converted into NHS-ester groups and the PNA probes H-(AEEA)₂-CTTTCCTTCACTGTT-NH₂ (AEEA = 2-(2-aminoethoxy)ethoxyacetyl spacer) were

covalently bound via acyl coupling reactions. The PNA sequence used throughout this study is full complementary to a DNA sequence bearing a single point mutation (W1282X) implicated in human Cystic Fibrosis disease,^[36] and represents a good example in view of possible further biomedical purposes. After PNA attachment, the remaining NHS esters were quenched with ethanolamine and the zeta potential of the final PNA-functionalized particles was found to be -10.21 mV. The final overall negative zeta potential is a crucial parameter in view of coating the particles with a thin layer of poly-L-lysine (PLL), which is a cell uptake-enhancing cationic polymer in physiological media. A schematic representation of the material preparation is shown in Figure 4.2.

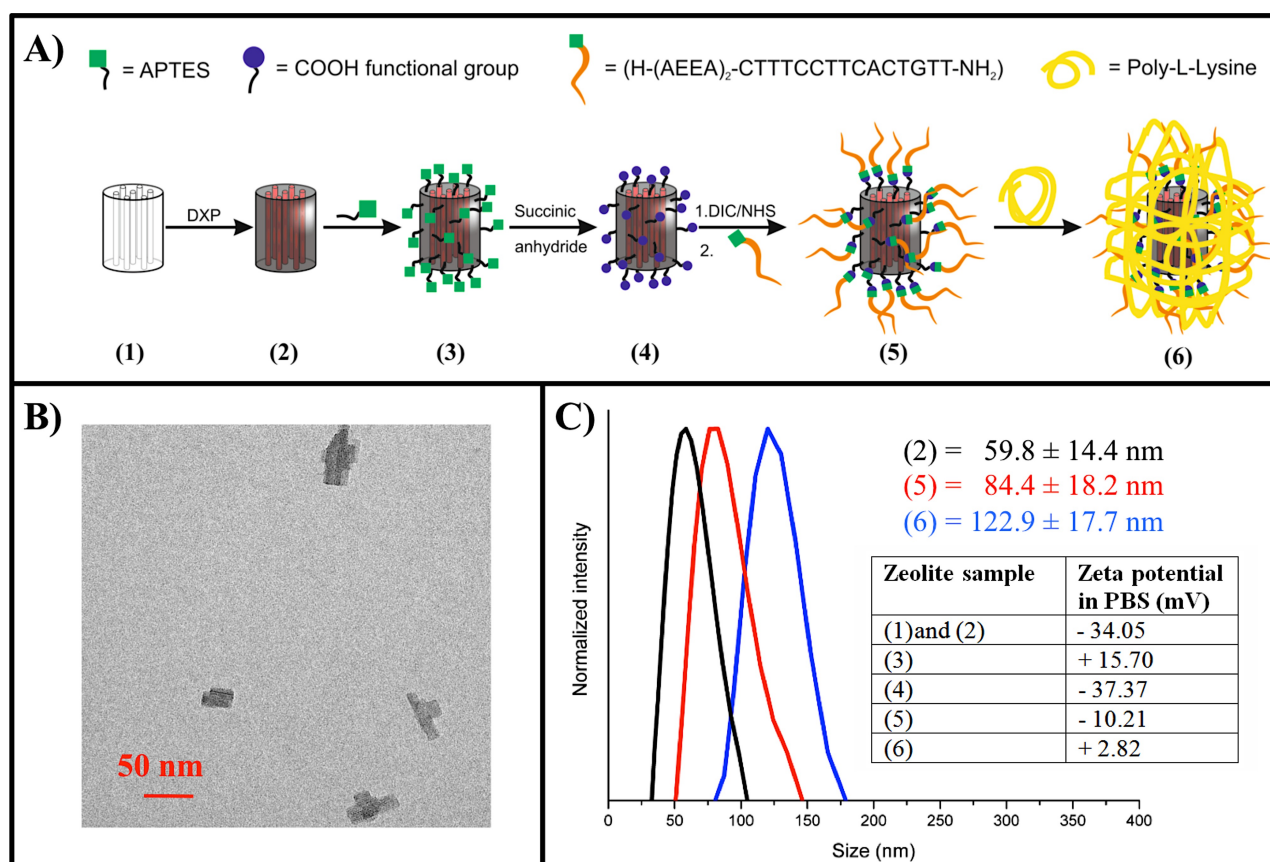


Fig. 4.2 A) Schematic representation of the synthetic pathway for preparing PNA-zeolite-L nanoparticles; B) TEM image of zeolite-L nanocrystals, C) DLS measurement showing the size distribution of diverse functionalized particles; Table inset: Zeta-potential values obtained after each functionalization step.

After the PLL final coating, the positive zeta potential was observed stable after 24 hours, and the average size of the particle (123 nm) with a very low data dispersion (14% RSD) confirmed that no significant aggregation was present at this stage.

To further prove the successful functionalization of the zeolite-L crystals with PNA, a hybridization test with a Cy3-labeled full-complementary DNA oligonucleotide was carried out, which led to a zeta potential shift to -24.80 mV. Additionally, confocal microscopy was used to assess the co-

localization of the Cy3 label (full-complementary DNA hybridized to PNA) and the fluorescent label (DAPI) entrapped in the zeolite-L pores (Figure 4.3).

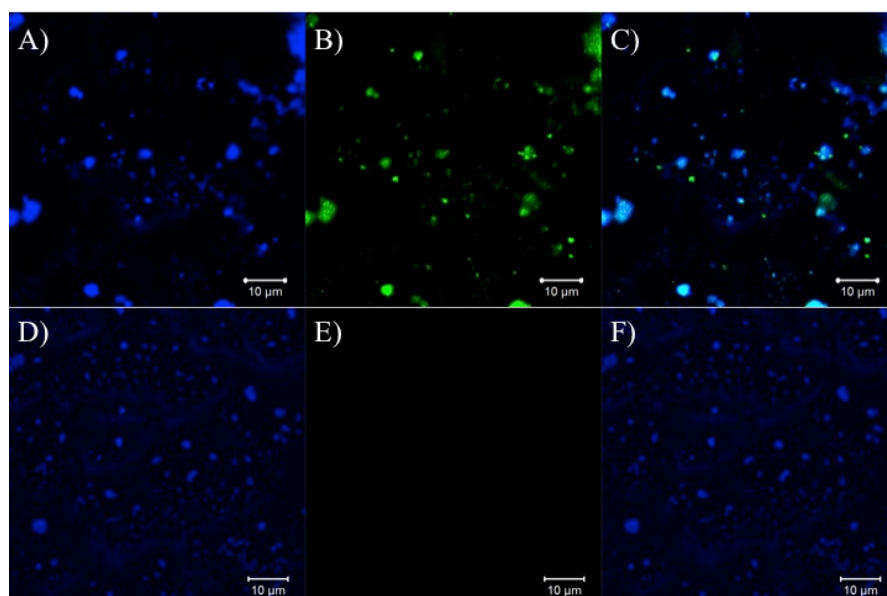


Fig. 4.3 Images A-C: Confocal micrograph of PNA functionalized zeolites hybridized with full complementary Cy3-labeled DNA Oligonucleotide. A): DAPI signal (blue); B): Cy3 signal (green color); C): Merged. Images D-F: control samples (naked zeolites incubated with the same Cy3-DNA). The images are recorded by using the same parameters as for A, B and C. Excitation was done at 405 nm (DAPI) and 543 nm (Cy3).

The number of PNA units attached to a single zeolite-L crystal was then determined. Therefore a PNA labeled with a fluorescent dye (TAMRA) was used for quantification by means of UV/Vis spectroscopy after the PNA-functionalized particles had been totally dissolved in hydrofluoric acid (HF). About 150 PNA molecules were found attached to the surface of a single zeolite-L nanocrystal. Detailed calculations are reported in the experimental section.

For antisense purposes, it is crucial that the PNA probes maintain their biological activity even when anchored to the zeolites. Thus, it was necessary to verify that the PNA retains its DNA/RNA-hybridization behavior when attached to the zeolites. PNA-zeolite-L particles were therefore incubated with 3 different Cy-3 labeled DNA strands: a full match, a single mismatch, and a 3-mismatch oligonucleotide (sequences are reported in Table 4.1). The particles were then washed and dissolved in HF, and UV/Vis spectroscopy was applied to determine the DNA concentration in the solution. A clear difference in DNA binding was observed depending on the sequence, as reported in Figure 4.4. The highest amount of DNA bound to the PNA-zeolites was obtained when a fully complementary DNA strand was used. The introduction of one mismatch in the DNA led to a significant reduction of binding and finally no signal was observed with a 3-mismatch DNA strand. These results confirmed that PNA retains its sequence selectivity, following the Watson-

Crick base pairing scheme, also when covalently anchored to the surface of zeolite-L. This is indeed crucial in view of possible antisense applications *in vitro* and *in vivo*.

Table 4.1 Sequences of DNA-Oligonucleotide used for the hybridization tests.

DNA-Oligo	Sequence
DNA Full Match	Cy3-AACAGTGAAGGAAAG
DNA single mismatch	Cy3-AACAGTGGAGGAAAG
DNA 3-mismatches	Cy3-AAGAGTGGAGGGAAG

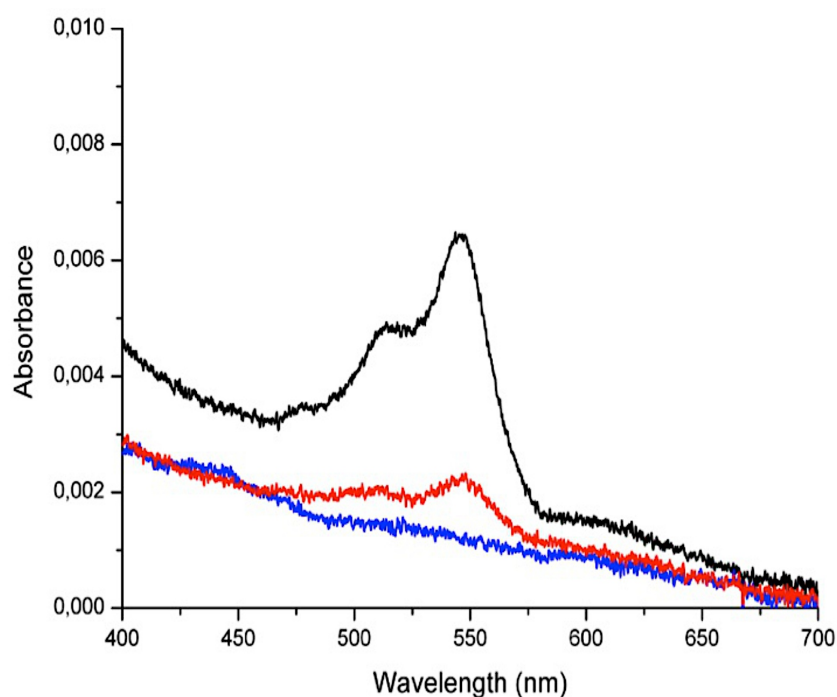


Figure 4.4 UV/Vis spectra of dissolved PNA-zeolite particles after hybridization with 3 different DNA strands. Black line: Full-match DNA strand; Red line: single mismatch DNA strand; Blue line: 3-mismatch DNA strand.

4.3 *In vitro* Experiments on HeLa cells

To track the nanozeolites by fluorescence microscopy, the particles were filled with the green fluorescent DXP, chosen because of its insolubility in aqueous media, which prevents its release from the pores. The nanocontainers were then covalently functionalized with PNA and further coated with PLL to improve cell uptake, as shown in figure 3.3. Indeed, it has been shown that the molecular corona surrounding nanoparticles plays a significant role during the uptake process,^[37-38] thus biocompatible polymers can be used to increase the cellular uptake of nanoparticles.^[39-42] PLL represents indeed a good candidate.^[43] Besides the total biocompatibility, it is also

biodegradable^[44,45] and therefore does not affect the overall activity of the system. PLL coating was confirmed by a zeta potential shift to +2.82 mV, and a size increase to about 120 nm, as confirmed by DLS measurements (Figure 4.2).

Cell experiments were carried out on human cervical cancer cells (HeLa) (50000 cells per well). Incubation was done for 1, 4, and 24 hours using a particle concentration of 0.01 mg/mL. After incubation, the cells were washed, fixed, and analysed by confocal microscopy. Figure 3.6 shows confocal micrographs after the above cited incubation time.

A very fast uptake of the PNA-functionalized zeolites was indeed obtained and already after an incubation time of 1 hour a high particle concentration could be detected inside the cells, as shown in Figure 4.5 (A-C). The actual particle uptake was confirmed by recording z-stacks after 1 hour of incubation (Figure 4.6A).

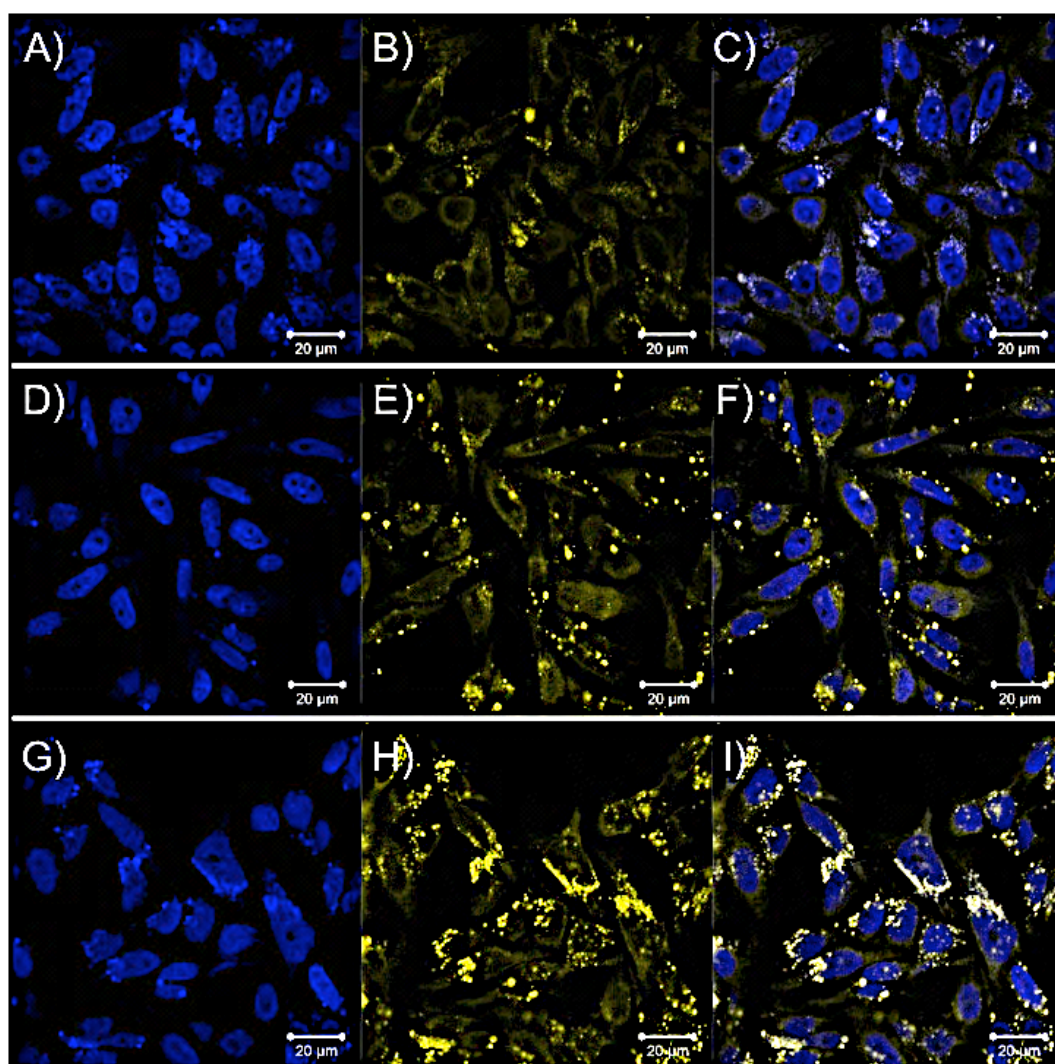


Figure 4.5 Confocal micrographs of HeLa Cells incubated with a 0.01 mg/ml dispersion of PLL-PNA-DXP-functionalized zeolites for 1 hour (A, B, C), 4 hours (D, E, F) and 24 hours (G, H, I). A, D, G) fluorescent image of cell nuclei stained with DAPI; B, E, H) fluorescent image of DXP, showing the presence of the nanoparticles inside cells; C, F, I) overlay of the previous pictures.

An increase in incubation time then led to even higher particle concentrations inside the cells, and after 24 hours a very high particle concentration could be observed (Figure 4.5G-I). In all cases, the particles looked equally distributed in the cytoplasm without entering the nucleus. Taking into account that PNA is very poor cell membrane permeable, this approach presents a very simple and straightforward way to efficiently deliver PNA into living cells.

To prove that the PNA-zeolite-L system is not toxic, a cell-viability test was carried out under the same conditions described above (see also experimental section). The final viability results are reported in a graph in figure 4.6B, which clearly states that HeLa cells are still viable after 24 hours of incubation with the PNA hybrid particles.

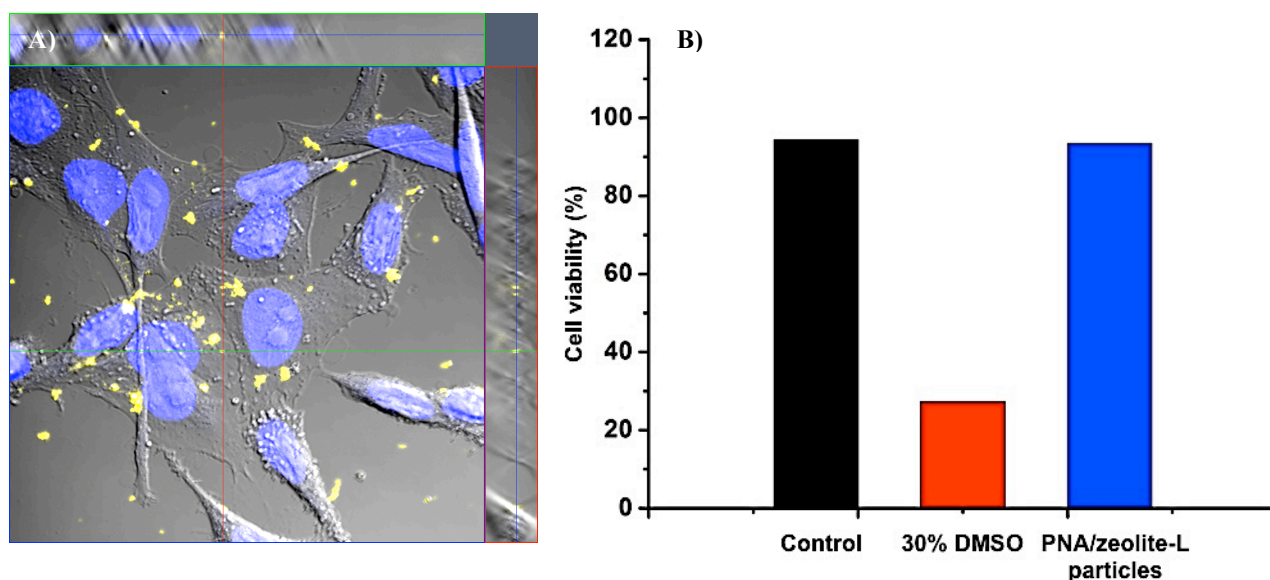


Fig. 4.6 A) Orthogonal view of cells taken by Z-stack acquisition, showing the localization of PNA-zeolites in the cytoplasm. B) Cell Viability study of zeolite-PNA towards HeLa cells and its comparison to the negative (30% DMSO inside culture media) and positive (without anything) control. The working concentration for zeolite-PNA is 0.01 mg/ml and the incubation was performed for 24 hours.

In order to demonstrate that the PNA-zeolites are internalized without destruction of the oligonucleotide and that the PNA units are still covalently bound to the nanocontainers after internalization, a fluorescence colocalization experiment was performed. A PNA sequence labeled with the yellow fluorescent TAMRA (H-TAMRA-(D-Lys)-GTAGATGA-NH₂) was attached to the surface of the zeolites, in this case filled with deep red fluorescent oxazine 170 in the pores. The use of oxazine 170 as label for the nanocontainers has been dictated by the need for having an emission color (deep red) that does not overlap with TAMRA (yellow) or DAPI (blue), which was used to stain the cell nuclei. Again, the particles were coated with PLL and cell experiments were done as described above, incubating the cells over 24 hours. The different fluorescent labels have been then

localized using different excitation wavelengths. As can be seen in figure 4.7, the emitting zeolites, red, and the labeled PNA, displayed in green, showed an identical pattern, and the co-localization proves that the PNA is still bound to the zeolites after cell internalization and PLL degradation. Additionally, the images show that the nanomaterials are distributed in the cytoplasm with pattern similar to that of PLL-PNA-DXP (Figure 4.5), with no particles observed inside the nucleus.

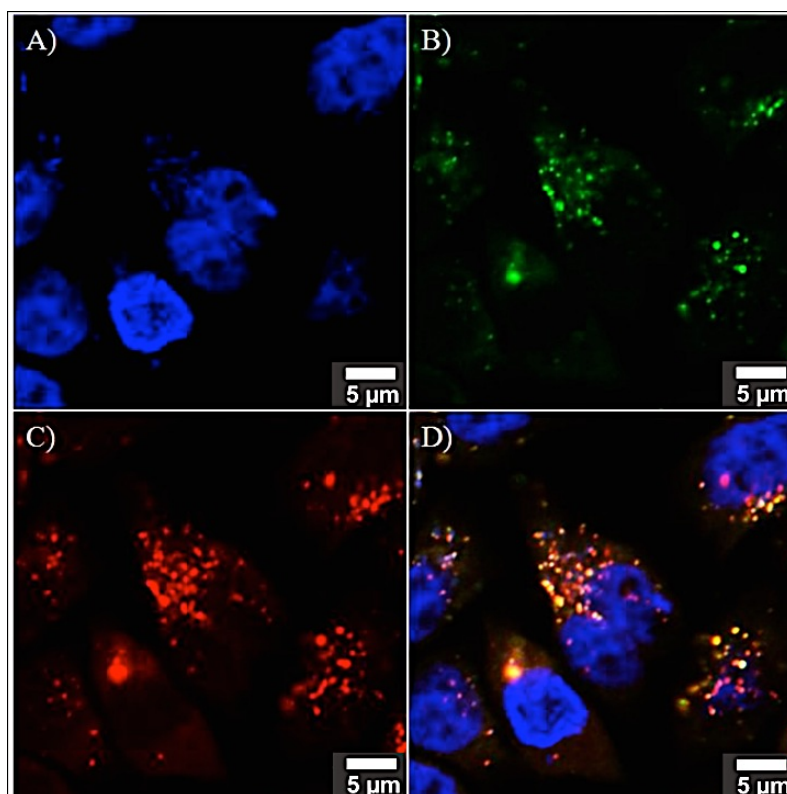


Fig. 4.7 Confocal micrographs of HeLa Cells treated with (TAMRA)-PNA-Oxazine-zeolites after 24 hours of incubation using a 0.01 mg/ml concentration of the dispersion. A) fluorescent image of cell nuclei stained with DAPI; B) fluorescent image of TAMRA, showing the position of the labeled PNA probes; C) fluorescent image of oxazine 170. D) overlay of the previous pictures to prove co-localization of the PNA and the zeolites. Excitation was performed at 405 nm (DAPI), 543 nm (TAMRA) and 633 nm (Oxazine 170).

4.4 Delivery of DAPI as a model drug

Once confirmed that the PNA-nanocontainers can be efficiently internalized and no degradation of the covalent bond occurs, the possibility to combine the oligonucleotide activities with a guest molecule that can be released from the zeolites after degradation of the PLL was investigated. DAPI has been selected as a model drug, since its fluorescence can be easily detected and after the release it will migrate into the nucleus, where the particles cannot enter. DAPI was inserted into the zeolite channels by cationic exchange and the filled crystals were functionalized as described previously. The DAPI loading was determined by thermogravimetric analysis to be 16% $n_{\text{dye}}/n_{\text{site}}$. Cell experiments have been carried out under the same conditions of the other samples as already described. After incubating the cells for 1 hour (figure 4.8 A-C), as expected, it was possible to

observe the internalization of the particles, but no release of DAPI was detected, since the nucleus appeared unstained and the blue emission was registered only coming from the zeolites. This can be indeed ascribed to the PLL coating which prevents the diffusion of the DAPI from the zeolite pores and which has relatively slow kinetics of degradation inside the cells.^[46]

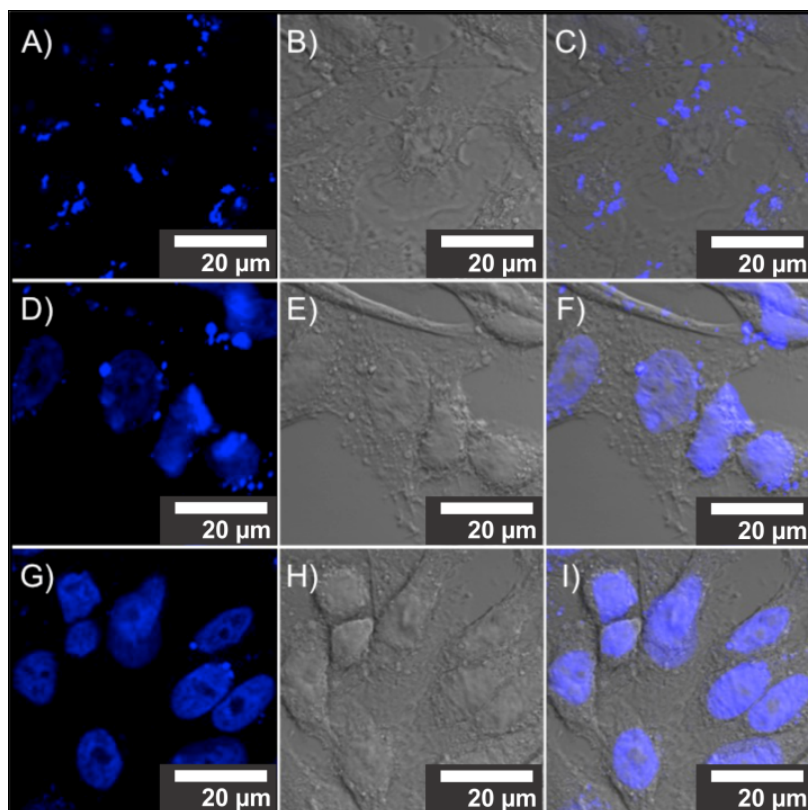


Fig. 4.8 Confocal micrographs of HeLa cells incubated with a 0.01 mg/ml dispersion of PLL-PNA-DAPI-functionalized zeolites for 1 hour (A-C), 4 hours (D-F), 24 hours (G-I). A, D, G) Fluorescent image recorded monitoring DAPI signal; B, E, H) Bright field image; C, F, I) overlay of the previous ones.

After 4 hours of incubation, a notable amount of DAPI could be found in the nucleus (See Figure 4.8 D-F). Indeed a first release of DAPI occurred at this time, since the PLL underwent degradation, which caused the opening of the channels and allowed for the leakage of the guest DAPI into the cell. The release resulted further increased when the incubation time was prolonged to 24 hours (Figure 4.8 G-I). It is worth noticing that also the number of particles which are internalized is time dependent, thus the final delivery of DAPI is the result of the increase in concentration of the uptaken particles as well as the slow release of the fluorophore from the pores.

4.5 Fabrication of anti-miR-PNA-Zeolites

After the properties of the generic PNA-zeolite conjugates had been deeply studied, hybrid particles suitable for being applied towards real biomedical applications were fabricated. In particular, an

antisense approach for gene therapy constitutes the ideal goal of the hybrid nanosystem when using specific sequences of PNA. First promising examples of antisense activity in live cells carried on by nucleic acid-nanoparticles composites have been recently reported in the literature,^[47-49] hence a similar effect is envisaged for the PNA-zeolite system as well.

An exceptionally growing interest is now focusing on microRNAs (miRNAs or miRs), which are short non-coding RNA molecules that act as gene regulators by repressing translation or by inducing the cleavage of target mRNA.^[50] A more comprehensive presentation of miRNAs and their biological mechanism will be given in Chapter 5. In particular, during cancer initiation, development and metastasis, tumors show distinct and fingerprinting miRNA expression profiles, thus providing novel targets for cancer diagnosis and classification, as well indeed as potential therapeutic targets.^[51-52] Among the others, miR-210 has been found overexpressed in different tumor cells, related with the hypoxia pathway and associated with the cell cycle regulation.^[53-55] MiR-221 is also known to be a cancer-related miRNA involved in angiogenesis, cell migration and proliferation, targeting for example the p27Kip1 gene involved in cell cycle inhibition and tumor suppression.^[56-58] Therefore, these two miRNAs represent suitable candidates for a therapeutic antisense-antimiR approach. Full complementary PNA sequences to miR-210 and miR-221 were thus synthesized and mounted on zeolite nanocrystals according to the procedure reported above (paragraph 4.2). In the case of antimiR-210 probes, two PNAs were used, i.e. an unmodified one H-CCGCTGTCACACGCACAG-NH₂ and one containing a C5 modified PNA monomer bearing a lysine side chain, to which two spacer units were attached, capped at N-terminal with an acetyl group: Ac-CGCTGTT(OO)CACAC-Gly-NH₂ (where T is the monomer bearing the lysine modification and O is 2-(2-aminoethoxy)ethoxyacetyl spacer). For targeting the miR-221, a PNA bearing the same type of modified monomer was used: the sequence in this case was Ac-GACAATT(OO)GTAGC-Gly-NH₂.

After PNA attachment, the final system has been coated with a PLL layer as described previously. These hybrid antimiR tools were fabricated for being tested *in vitro* to study the potential antisense activity on knocking down target miRNA and the related effect on cells with ad hoc measurements. The antimiR activity experiments and all the necessary biological test are presently being carried out by Prof. Gambari's group at the Department of Biochemistry and Molecular Biology, University of Ferrara, Ferrara, Italy.

5- H-RRRRRRRR-CCGCTGTACACGCACAG-NH₂, where R stands for an arginine residue conjugated to the sequence during the solid phase synthesis (R₈-PNA)

All the above PNA sequences have been covalently bound to the zeolite surface following the same procedure described throughout this Chapter. Differently from the former PNA-zeolite conjugates, no PLL has been used for these new particles, in order to test their ability to be uptaken without the help of the polymer coating.

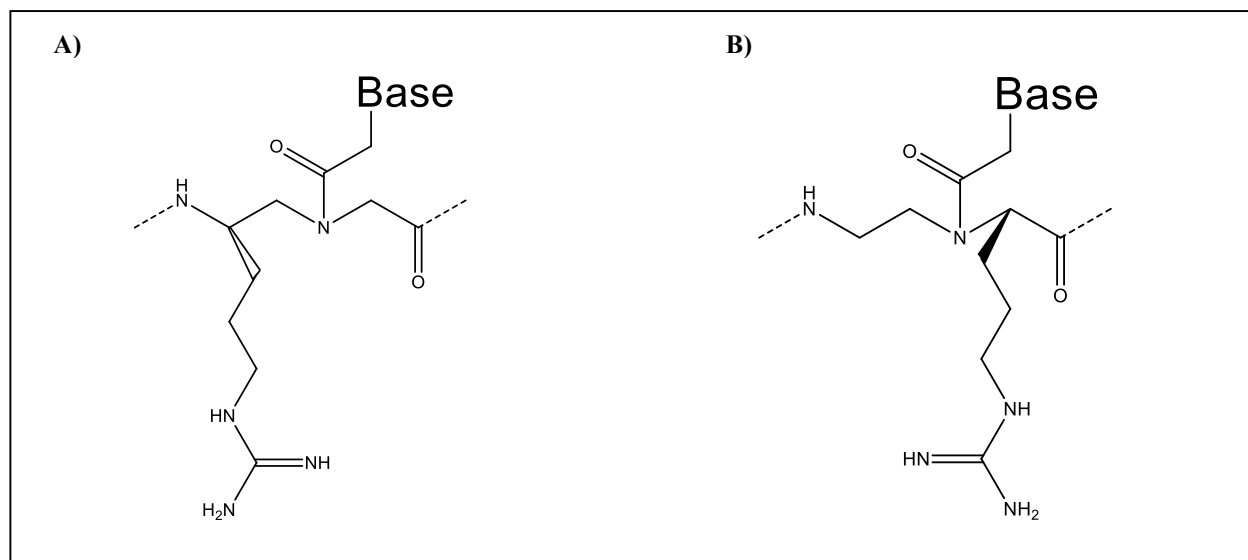


Fig. 4.10 Molecular structure of the modified 5L-Arg (A) and 2D-Arg (B) PNA monomers.

Hence, cellular uptake experiments were carried out using HeLa cells (50000 per well). Incubation was done from 1 hour up to 5 hours, using a particle concentration of 0.01 mg/mL. After the incubation, the cells were washed, fixed and analyzed by confocal microscopy. Once again, to visualize the particle inside the cells and to estimate the internalization efficiency, zeolites were at first filled with the hydrophobic green dye DXP. DAPI was used to stain the cell nuclei after fixation. Figure 4.11 reports the confocal micrographs after 1 hour of incubation, while in figure 4.12 the same micrographs after 4 hours are displayed.

As it can be seen from figure 4.11, in all cases only a very low cellular uptake could be achieved after 1 hour of incubation at the working concentration of 0.01 mg/mL, suggesting that this time is not sufficient for the cationic PNA-zeolites to be efficiently internalized, except in the case of 5L-Arg-PNA1 and 5L-Arg-PNA2. However, the scenario drastically changed after 4 hours of incubation (figure 4.12), since in that case a very high particle concentration could be detected for all the samples analyzed. In both case, i.e. after 1 and 4 hours of incubation, no significant differences in the internalization behavior could be noticed, even though, at the resolution offered

by the instrumentation, a very slight better uptake could be seen for the 5L-Arg-PNAs and for the R₈-PNA, suggesting that the molecular structure of the PNA probes might partially influence the internalization pathway. Though a direct comparison with the PLL coated system described in paragraph 4.2 is not possible, since data have been obtained in separate experiments, the PLL-coated particles clearly display an efficient uptake after 1 hour, whereas only 5L-Arg modified PNA seem to have some, though lower, uptake at the same concentration; it is worth noticing that at 4 hours incubation time, when using the cationic PNA-zeolites a very efficient and satisfying uptake can be achieved in only 4 hours, without the need of a polymer coating and presenting the benefit of delivering high-performance-targeting cationic agents for the anti-miR strategy.

It is interesting that cellular uptake does indeed depend not only on the total charges of the PNA coating, which is the same for all PNA showed in figures 4.11 and 4.12, but also from the position of the substituent, with 5L-Arg PNA model being the most effective. The 5L-Arg-PNA2 (alone) was incidentally also found from previous studies to be also the most effective anti-miR agent, together with R₈-PNA, in experiments carried out on K562 leukemic cells. **Errore. Il segnalibro non è definito.** It is also of outmost importance that polyarginine R₈-peptide carriers, unlike polylysine, have been shown to be specifically delivered *in vivo* to tumor tissues, in particular those exposing glycosaminoglucones on the cell surface.^[63]

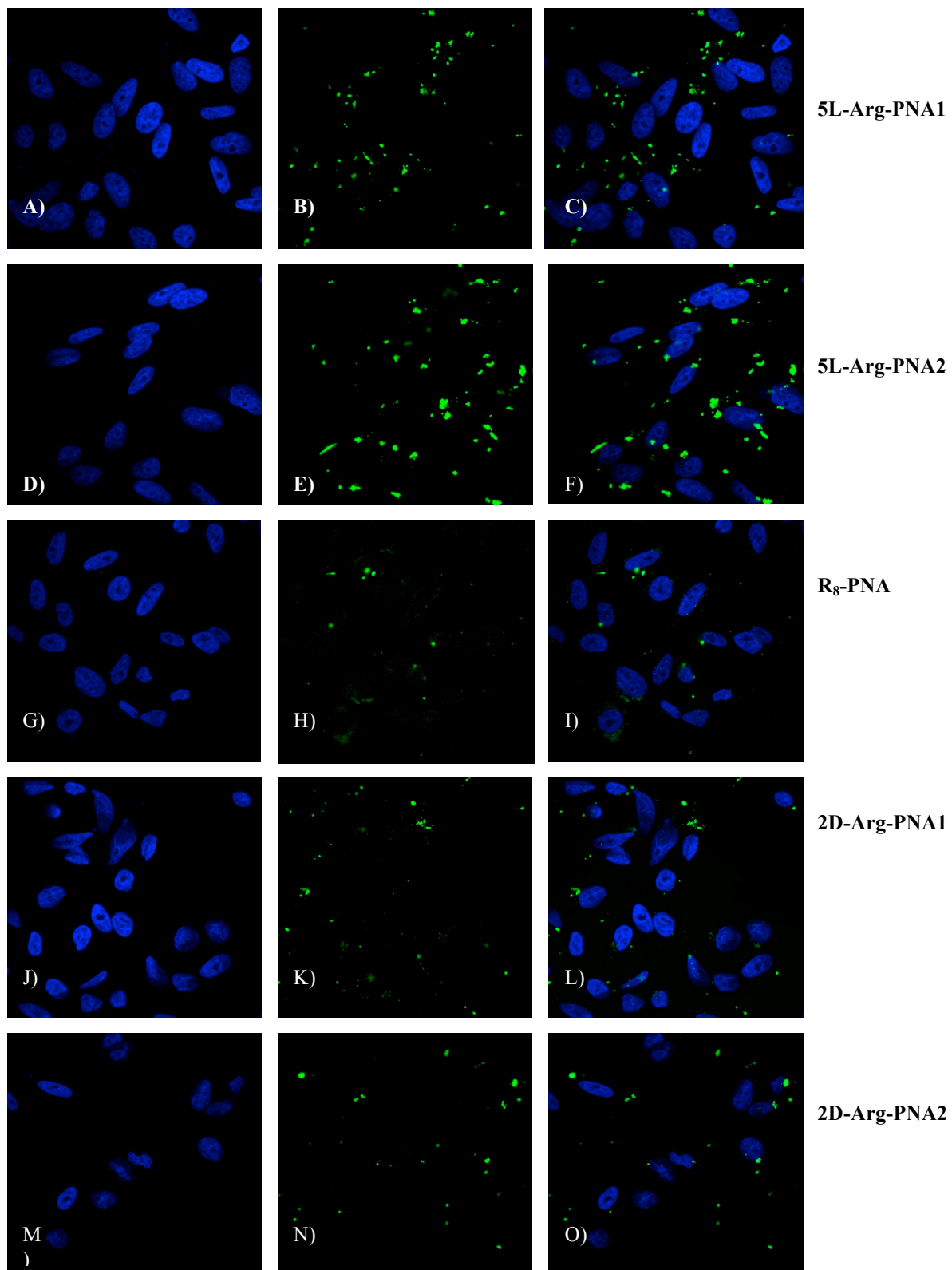


Fig. 4.11 Confocal micrographs of HeLa Cells incubated with a 0.01 mg/ml dispersion of cationic PNA-zeolites for 1 hour (A, D, G, J, M) fluorescent image of cell nuclei stained with DAPI; B, E, H, K, N) fluorescent image of DXP, showing the presence of the nanoparticles inside cells; C, F, I, L, O) overlay of the previous pictures. The respective samples are reported aside.

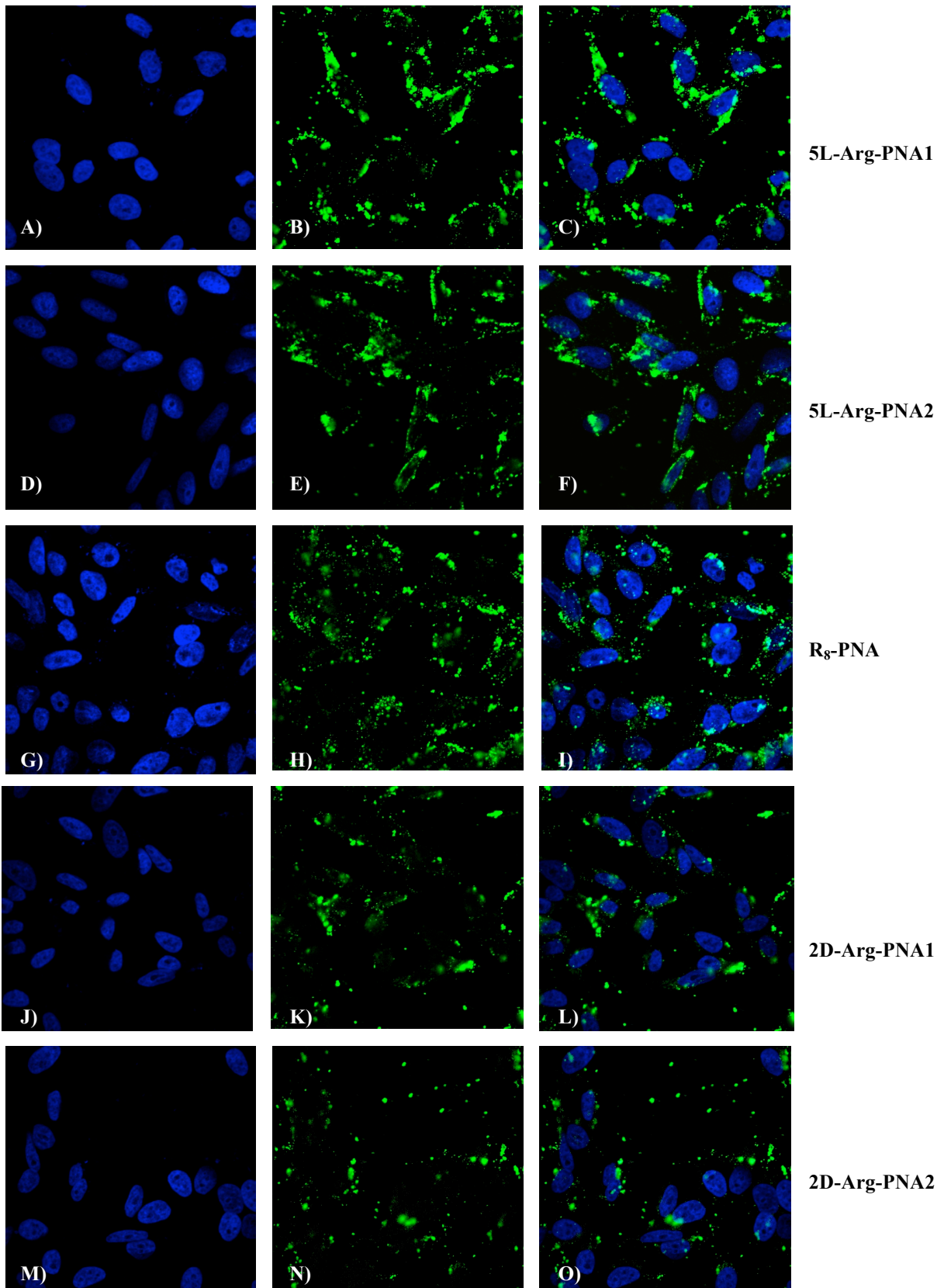


Fig. 4.12 Confocal micrographs of HeLa Cells incubated with a 0.01 mg/ml dispersion of cationic PNA-zeolites for 4 hours. (A, D, G, J, M) fluorescent image of cell nuclei stained with DAPI; B, E, H, K, N) fluorescent image of DXP, showing the presence of the nanoparticles

4.7 PNA-gated multifunctional zeolite nanocarriers for miRNA-responsive controlled drug delivery

As reported in the introduction, advanced nanoscale systems for drug delivery have recently received tremendous attention in the field of nanomedicine. A broad range of nanocarriers with diverse sizes, composition, architectures, and surface properties have been indeed designed. Nevertheless, the leakage of the drug from the carriers is in most cases governed by the Fickian diffusion, which is not specific to cells, tissues or organs. Thus, release of a drug from a nanocarrier which is slowly degrades would give rise to treatment of each cell to the same extent, thus generating unwanted side-effects, whereas ideally only cells showing tumor geno- or phenotypes should be treated. In view of a possible more specific and controlled delivery of the drugs to living organism to reduce the systemic toxicity, properly molecularly-tailored engineered strategies are needed. One of the best alternatives involves on-demand processes that become feasible through the design of stimuli-responsive systems that recognize their microenvironment and react in a dynamic way. This approach is indeed not trivial, since it requires the use of biocompatible materials that are able to undergo a specific processes such as protonation, hydrolytic cleavage, conformational change or molecular displacement in response to a desired stimulus, or that are susceptible to specific physical stimulation.^[64] Triggered drug release can be for example achieved by externally applied stimuli, including temperature changes, magnetic fields, ultrasounds, light, and electric fields.^[65-74] For instance, when a permanent magnetic field is applied to a ferrogel composed of Pluronic-F127 micelles encapsulating superparamagnetic iron oxide nanoparticles and a hydrophobic drug, the drug is released as iron oxide nanoparticles approach each other and squeeze the micelles.^[75] In a light-driven strategy, doxorubicin-loaded hollow gold nanospheres have shown accelerated drug release when irradiated in the NIR region, allowing enhanced anticancer activity and reduced systematic toxicity.^[76]

Even more interestingly, nanoscale stimuli-responsive devices may be directly sensitive to specific cell endogenous stimuli, such as a lowered intracellular pH, a higher glutathione concentration or an increased level of certain enzymes.^[77-83] Among the others, MSNPs with β -cyclodextrin nanovalves responsive to the endosomal acidification,^[84] or pH-sensitive liposomes that undergo conformational transitions triggering the drug release^[85] have been, for example, reported. Complexation of nucleic acids with reducible disulphide-containing polymers in the glutathione-rich tumor environment has been shown to improve transfection and gene silencing.^[86] MSNPs scaffolds grafted with polysaccharide derivatives have been reported to enable the specific delivery of doxorubicin after lysosomal enzyme-mediate cleavage of the glycoside bonds and reduction of

the polysaccharide chain lengths.^[87]

The concept of stimuli-responsive carriers can be also pushed to the challenge of a further personalized nanomedicine, designing advanced nanomaterials that exploit target-responsive release systems triggered by the intracellular presence of a specific genetic expression. Few examples have been reported so far in the literature of nanoparticles able to deliver a payload when triggered by the presence of a specific target nucleic acid,^[88] and *in vitro* experiments are still rare.^[89] A pioneering work has been very recently released by Zhang *et al.* on the use of DNA-hybrid-gated multifunctional MSNPs for dual targeted and miRNA-responsive controlled drug delivery, and it constitutes the only example in which a target miRNA is actually used as triggering delivery agent.^[90] Herein, the preliminary results on developing a miRNA-responsive drug delivery platform based on PNA-functionalized nanozeolites are discussed. The design of the system has been based on fabricating zeolite-L nanocrystals bearing PNA probes targeting miR-221 that were partially hybridized with a short dendrimer-modified-PNA, which has been thought to act as a stopper for the channels due to its steric hindrance (figure 4.13). The presence of the full complementary target miR-221 should enable the stopper-PNA displacement because of the higher affinity and duplex stability with the PNA anchored to the zeolites, which may lead to the opening of the pores and the subsequent release of the guest molecules.

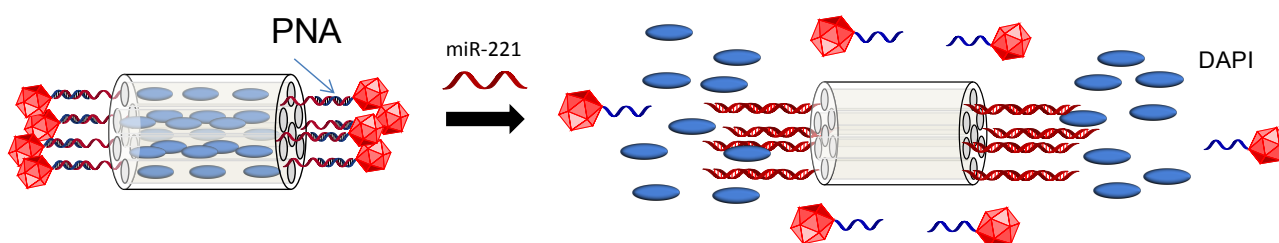


Fig. 4.13 Representative picture of the PNA-gated-zeolite-L system. The channels of the PNA-functionalized nanoparticles are blocked by a short dendrimer-PNA stopper that hybridizes with the PNA probes present on the zeolite surface. The upcoming target miR-221, which is full complementary to the PNA probes, leads to the stopper strand displacement and the formation of a miRNA/PNA duplex that does not impede the release of guest molecules.

In order to fabricate the gated nanozeolites, the diverse pieces of the systems were synthesized. At first, the anti-miR-221 PNA sequence H-(AEEA)-GCAGACAATGTAGCT-NH₂ and its cationic arginine-conjugated version H-RRRRRRRRR-GCAGACAATGTAGCT-NH₂ were synthesized accordingly to solid phase synthesis protocols. Both the PNA sequences were then used to produce the respective PNA-functionalized zeolites as described in section 4.2. All the zeolites were previously filled with DAPI, which is an ideal model guest molecule to investigate the delivery properties of the system. The dendrimer-conjugated-PNA was then synthesized. An 8-mer PNA

(N')-AGCTACAT-Gly-(C') was bound via solid phase acyl coupling reaction with a third-generation-branched acetonide-capped dendron carboxylic acid (Figure 4.14); after cleavage from the solid-support with TFA, a further step was needed to remove trifluoroacetyl esters formed during the final treatment, by incubation of the PNA at low temperature for several days; the final dendrimer-PNA was thus obtained with all hydroxyl groups exposed (see experimental section), which increased the hydrophilic nature to the conjugate.

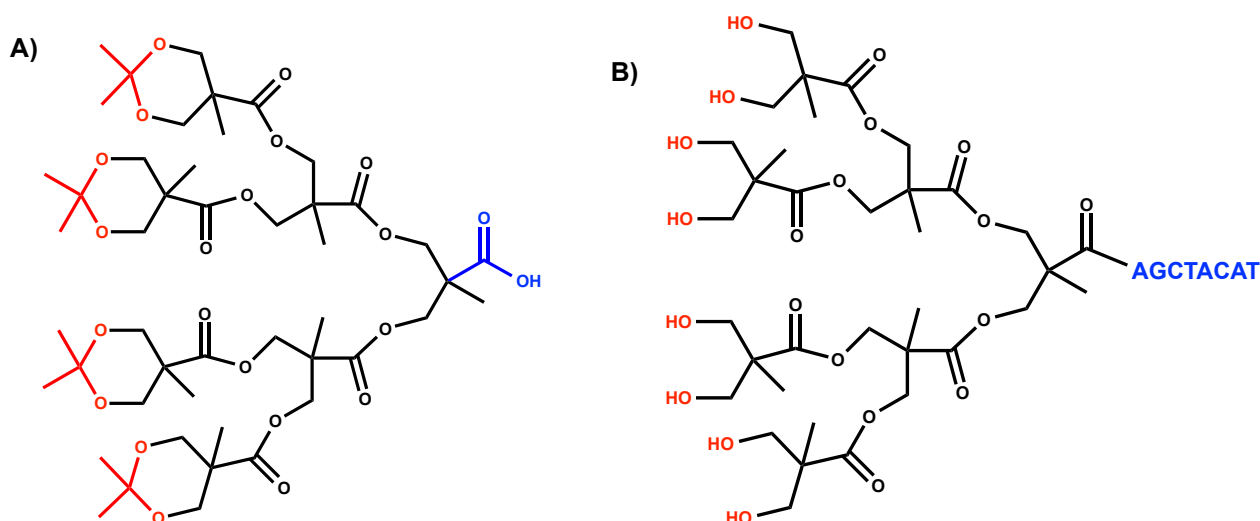


Fig. 4.14 A) Molecular structure of the third-generation-branched acetonide-capped dendron carboxylic acid. The carboxylic moiety of the dendron enables the acyl coupling reaction with the amine terminus of the PNA; B) final structure of the dendrimer-PNA after cleavage from the resin and hydrolysis of the acetonide groups.

In order to evaluate the relative stability of the PNA probes with the stopper dendrimer-PNA and the target miR-221, which is a key point for the potential well functioning of the closing-opening system, a full set of UV-Vis thermodynamic data on melting temperature was obtained.

In particular, the anti-miR-221 PNA/miR-221 DNA-ON (used as a model for miR-221) duplex showed a higher stability ($T_m = 74,8^\circ\text{C}$) than that of anti-miR-221 PNA/dendrimer-PNA ($T_m = 60,2^\circ\text{C}$), which is even a little bit less stable than the duplex between the anti-miR-211 PNA probe and a single mismatch target sequence ($T_m = 69,3^\circ\text{C}$). The same behavior was observed also for the cationic arginine-conjugated anti-miR-221 (R_8)-PNA, with a melting temperature of the duplex with the stopper dendrimer PNA ($T_m = 61,2^\circ\text{C}$) less than both the one of the duplex with a single mismatch sequence ($T_m = 74,6^\circ\text{C}$) and of the duplex with the full complementary target sequence ($T_m = 81,5^\circ\text{C}$). The thermodynamic data therefore demonstrated the potential applicability of the designed system, since the presence of the target miR-221 could favour the displacement of the dendrimer-PNA stopper from the PNA probes on the zeolite surface, thus leading to a less steric hindrance allowing for the drug release.

At this stage, hybridization studies were conducted at the material level, to assess the ability of forming the duplex between the PNA probes and the stopper at the when the first are anchored to the zeolite surface. After incubation of the PNA-functionalized zeolites with a 10 μM aqueous solution of the dendrimer-PNA, DLS and zeta potential measurements were carried out to check possible variation of the properties of the material due to the formation of the PNA/stopper duplex. Very interestingly, a significant shift in the DLS distribution graph of the particles was observed, since the average size of the antimiR-221 PNA-zeolites shifted from 102 ± 16 nm to the higher value of 163 ± 59 nm. The same behavior was obtained also when using the cationic antimiR-221 (R_8)-PNA-zeolites, with a change in the average size from 108 ± 16 nm to 162 ± 33 nm. This could be indeed ascribed to the formation of the duplex between the PNA probes and the dendrimer-PNA stopper. As expected, no changes in the zeta potential values were detected in both cases, due to the neutral nature of the stopper PNA.

To have a further proof of the duplex formation, UV-Vis spectroscopy was used recording the absorbance of a 5 μM dendrimer-PNA solution ($\lambda = 260$) before and after the incubation with the PNA-zeolites. The UV-Vis spectra reported in figure 4.15 clearly showed the decrease of the absorption peak after the incubation, which was due to the sequestering of the dendrimer-PNAs by the PNA-zeolites for the hybridization event.

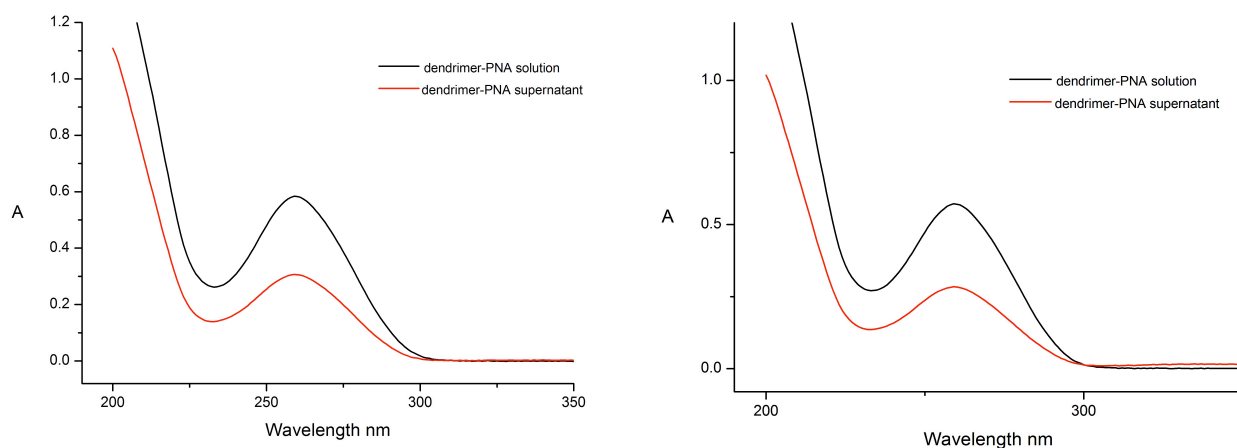


Fig. 4.15 Left) UV-Vis spectra before and after incubation of the dendrimer-PNA solution with antimiR-221-PNA-zeolites; Right) UV-Vis spectra before and after incubation of the dendrimer-PNA solution with cationic antimiR-221-(8R)-PNA-zeolites.

Preliminary cell experiments were done at this point to investigate the properties of the gated system and its ability to retain the guest molecules in absence of a triggering stimulus. Cell experiments were done using HeLa cells (approximately 50000 cells per well) and incubation was done over 5 hours using a particle concentration of 0.01 mg/mL in culture media. The cells were

incubated respectively with the mentioned anti-miR-221-PNA-zeolite/dendrimer-PNA stopper, both the neutral and the R₈-cationic version, and with the analog particles without the dendrimer-PNA stopcock, thus simulating the “closed” and “open” zeolite nanocarriers respectively. All the particles contained DAPI as a model releasable guest molecule. The incubation time was chosen on the base of previous results showing that after 4 hours PNA-(DAPI)-zeolites are able to deliver an amount DAPI clearly detectable by the nucleus stain. Additionally, the actin filaments of the cells were stained with Alexa Fluor® 647 Phalloidin, to better visualize the cells. The results are shown in figure 4.16 and 4.17.

Figures 4.16A and 4.17A report the results obtained when incubating the cells with PNA-(DAPI)-zeolites, and indeed the DAPI delivery effect, as expected, was the same as the one shown previously (Figure 4.8D). Figures 4.16E and 4.17E show instead the effect when incubating the cells with the hybridized PNA-zeolite/dendrimer-PNA particles. In this case, a significantly higher fraction of extranuclear DAPI fluorescence was observed, due to the fluorophore trapped within the nanoparticles, but a significant nuclear staining was also present. The leakage from the gated system could be due to the effect of miR221, which was shown being expressed in HeLa cells (especially during S and G2/M phases),^[91] or it might indicate that both the designed gated-systems were not able to completely keep the DAPI molecules caged in the channels. Since the nanoparticles have the same charge and slightly different shapes, a similar uptake is expected. In figure 4.16A and 4.17A the amount of particles might look drastically reduced when compared to figure 4.16E and 4.17E because nanoparticles that have released DAPI are no longer detected. Very interestingly, the blue emissions of the internalized particles in the case of the dendrimer-gated systems were significantly higher, thus indicating that a kinetically slower release of DAPI from the nanoparticles was indeed observed.

Although still not a yes-or-not closing/opening-system, these gated-PNA-zeolite platforms represent a very important proof-of-principle since at least different release rates could be modulated by the stopper unit once delivered to the cells. Further experiments are indeed envisaged to accurately investigate the release behavior in solution and when in presence of different levels of the target miR-221, and to check the potentiality of this approach for a target-dependent-triggered drug delivery.

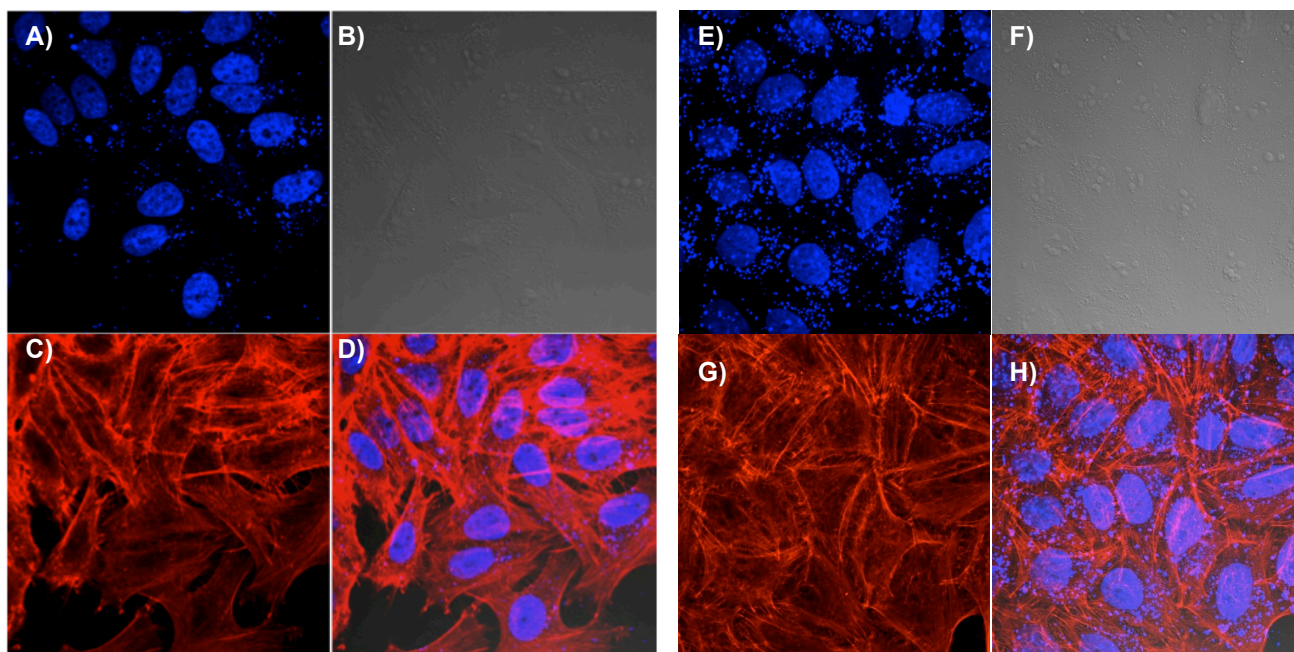


Fig. 4.16 Left) Confocal micrographs of HeLa Cells incubated with a 0.01 mg/ml dispersion of anti-miR-221-PNA-(DAPI)-zeolites for 5 hours. A) Fluorescent image recorded monitoring DAPI signal; B) brightfield image; C) Alexa Fluor® 647 Phalloidin; D) overlay of the previous images. Right) Confocal micrographs of HeLa Cells incubated with a 0.01 mg/ml dispersion of anti-miR-221-PNA-(DAPI)-zeolites hybridized with the dendrimer-PNA stopper for 5 hours. E) DAPI emission signal; F) brightfield image; G) Alexa Fluor® 647 Phalloidin; H) overlay.

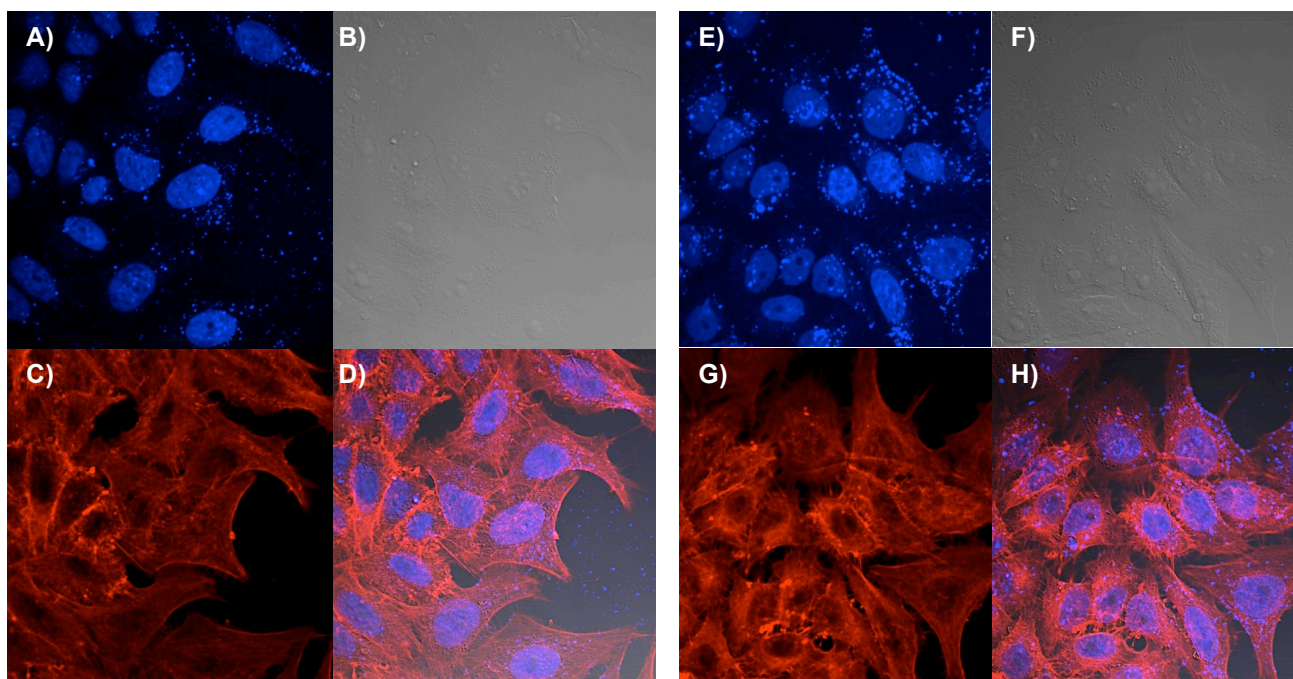


Fig. 4.17 Left) Confocal micrographs of HeLa Cells incubated with a 0.01 mg/ml dispersion of cationic anti-miR-221-(8R)-PNA-(DAPI)-zeolites for 5 hours. A) Fluorescent image recorded monitoring DAPI signal; B) brightfield image; C) Alexa Fluor® 647 Phalloidin; D) overlay of the previous images. Right) Confocal micrographs of HeLa Cells incubated with a 0.01 mg/ml dispersion of anti-miR-221-(8R)-PNA-(DAPI)-zeolites hybridized with the dendrimer-PNA stopper for 5 hours. E) DAPI emission signal; F) brightfield image; G) Alexa Fluor® 647 Phalloidin; H) overlay.

4.8 Conclusion

A novel multifunctional hybrid nanoparticle system to deliver simultaneous PNA and organic molecules into the cells has been developed. For the first time, an inorganic vector was armed with the RNA targeting potential of PNA, thus switching from an inert container to a bio-functional nanomaterial. Several strategies to obtain cellular uptake have been tested, with a thin layer of biodegradable PLL as coating being the most effective. Most importantly, it has been shown that the PNA-zeolite system remains intact even after the cell internalization, and a model drug, DAPI, can be slowly released from the carrier and delivered to the cell nuclei. This system can be further engineered in its components, as shown by the variety of dyes and coating PNA used. Cationic-PNA-zeolites have been alternatively proposed as suitable platforms for efficient internalization and PNA-based gene therapy targeting of specific microRNAs involved in tumor proliferation. Finally, PNA-gated multifunctional zeolite nanocarriers for miRNA-responsive controlled drug delivery have been also fabricated and showed encouraging preliminary results. The results are therefore opening interesting paths to the delivery of specific sequences of PNAs and to targeted-release of drugs, with a potential synergistic effect.

4.9 Experimental section

PNA Oligomer synthesis

The solid-phase synthesis of PNA sequence H-(AEEA)-CTTTCCTTCACTGTT-NH₂ was performed as reported in [36] and that of labeled PNA sequence H-TAMRA-(D-Lys)-GTAGATGA-NH₂ was carried out as reported in [92].^[92]

Modified cationic versions of anti-miR-210 PNAs were synthesized as reported in [10].

Anti-miR-221 PNA H-(AEEA)₂-GCAGACAATGTAGCT-Gly-NH₂ and its cationic version H-RRRRRRRRR-GCAGACAATGTAGCT-Gly-NH₂ (where R is an arginine residue) were synthesized with standard manual Boc-based chemistry using commercially available monomers, with HBTU/DIPEA coupling as described in the literature.^[93] The synthesis was carried out in a 20 μmol scale using MBHA resin. The AEEA spacer and the R₈ cationic arginine tail were introduced using the same coupling procedures after splitting the resin with the growing PNA into two batches. PNA purification was performed by RP-HPLC with UV detection at 260 nm using a semi-prep column C18 (10 μm, 7.8x300 mm, Xterra Waters), eluting with water containing 0.1% TFA (eluent A) and acetonitrile containing 0.1% TFA (eluent B); elution gradient: from 100% A to 50% B in 30 min, flow: 4 mL/min. The resulting pure PNA oligomers were characterized by ESI-MS, which gave positive ions consistent with the final products. For H-RRRRRRRRR-

GCAGACAATGTAGCT-Gly-NH₂, m/z found (calcd) 1084.5 (1084.5) [M+5H]⁵⁺, 903.7 (903.9) [M+6H]⁶⁺, 774.7 (774.9) [M+7H]⁷⁺, 678.0 (678.2) [M+8H]⁸⁺, 602.9 (602.9) [M+9H]⁹⁺, 542.4 (542.7), [M+10H]¹⁰⁺. For H-(AEEA)-GCAGACAATGTAGCT-Gly-NH₂, m/z found (calcd) 1438.5 (1438.7) [M+3H]³⁺, 1079.1 (1079.3) [M+4H]⁴⁺, 863.6 (863.3) [M+5H]⁵⁺, 719.7 (719.8) [M+6H]⁶⁺, 617.2 (617.2) [M+7H]⁷⁺, 540.1 (540.1), [M+8H]⁸⁺.

The dendrimer-PNA stopper sequence was synthesized as following. A first 8-mer PNA (N')-AGCTACAT-Gly-(C') was made by standard manual Boc-based chemistry using commercially available monomers, with HBTU/DIPEA coupling. The dendrimer head was then conjugated to the PNA in solid phase using the dendron PFd-G3-carboxyl-acetonide (Polymer Factory, Sweden), which was coupled to the 8-mer PNA with the same HBTU/DIPEA protocol. After cleavage and purification as described above, a series of trifluoroacetylated products were observed in the mass spectrum; thus the dendrimer-PNA was left at pH = 6 for 2 days at 4°C. After this time, which was needed to hydrolyze the TFA ester moieties produced during the cleavage (but not the dendron ester groups), the PNA was stored as a powder. Characterization by ESI-MS showed m/z found (calcd) 609 (608.6) [M+5H]⁵⁺, 760.8 (760.5) [M+4H]⁴⁺, 1014.1 (1013.8) [M+3H]³⁺. HRMS-Orbitrap analysis showed an exact mass of 3037.23646 [M+H]⁺ for the final product.

Nanozeolite surface modification with PNA

Amine-modified zeolites were first prepared by sonication of the particles (80 mg) in toluene (10 ml) for 30 minutes to form a good dispersion. APTES (50 µL, 0.2 mmol) was added to the suspension in presence of a catalytic amount of TEA and the mixture was stirred at room temperature overnight. The particles were then recovered by centrifugation and washed three times with ethanol to remove impurities. To obtain carboxylic acid-functionalized nanoparticles, 70 mg of the former amino-modified ones were dispersed in a succinic anhydride solution in DMSO (0.1 M in 10 mL) and, after 30 minutes of sonication to get a good dispersion, the mixture was stirred overnight at room temperature. The material was then centrifuged and washed three times with DMSO. After that, NHS-ester-functionalized nanozeolites were obtained by reaction of the former material (50 mg) with a solution of DIC and NHS (both 0.25 M) in dry DMSO. The nanoparticles were dispersed in 10 ml of the reactant solution and stirred overnight at room temperature under nitrogen inert atmosphere. The final material was again recovered by centrifugation washing with DMSO. PNA attachment was subsequently carried out by dispersing 5 mg of the activated-ester-modified-zeolites in 500 µL of a PNA solution 30 µM in a 100 mM carbonate buffer, H₂O:Acetonitrile 9:1, pH = 9. The dispersion was stirred overnight at room temperature, and PNA-zeolites were finally obtained centrifuging and washing three times with water. The final quenching

step was performed by stirring overnight at room temperature the PNA-zeolites with a 100 mM solution of ethanolamine in Tris buffer (100 mM, pH = 9). The final material was recovered by centrifugation and washed three times with water.

Poly-L-lysine coating

Poly-L-lysine coating was carried out by dispersing 1 mg of PNA-zeolites in a 1% w/v solution of poly-L-lysine hydrobromide in water and stirring the mixture at room temperature for 1 hour. The final material was recovered by centrifugation and washed with water.

DNA:PNA-zeolites hybridization test

PNA-zeolites-L were incubated at RT for 1 hour respectively with 500 μ L of 2 μ M solutions of a Cy3-labelled full-match DNA-ON sequence, a single mismatch sequence and a three-mismatch sequence (1 mg of material per each sample). After the incubation, the material was recovered by centrifugation and washed 5 times with water (30 min, 6000 rpm). Every sample was then dissolved in 200 μ L of HF and diluted to a final volume of 2.2 mL in water. The UV/Vis spectrum was eventually recorded for each sample, to check the intensity of the Cy3 signal coming from the hybridized DNA-ON sequence. All the sequences are reported in Table 4.1 in the text.

Quantification of PNA molecules on zeolite surface

TAMRA-PNA, whose sequence is reported above, and bearing a lysine amino group as middle attachment moiety, was linked to the zeolite-L crystals by following the procedure described previously for the unlabeled PNA. Then, 1 mg of PNA-zeolite-L were dissolved in 200 μ L HF and the sample was diluted with water to a final volume of 2.2 ml. Eventually the sample was analyzed by UV/Vis spectroscopy and the amount of PNA was calculated by the absorbance value of TAMRA dye ($\epsilon_{555} = 65000 \text{ M}^{-1} \text{ cm}^{-1}$). A rough estimation of the number of PNA molecules linked was obtained by the following reported calculations. From $\text{Abs}_{555} = 0.027$, the concentration of TAMRA resulted 0.42 μ M; from this, the number of PNA molecules attached to 1 mg zeolites was evaluated to be 5.6×10^{14} . The following average dimensions were used for the Zeolite-L: diameter \approx 50 nm; radius \approx 25 nm; length \approx 60 nm; mass = 0.001 g. The number of parallel channels was estimated by using the formula:

$$n_{\text{ch}} = \frac{(r)(r)^2\pi}{|a|^2 \sin 60} = \frac{\pi}{2\sqrt{3}} \left(\frac{2r}{|a|} \right)^2 \quad (1)$$

with

a: primitive vector perpendicular to the c-axis; r: zeolite-L diameter radius in nm

Equation (1) can be approximated as

$$n_{ch} = 1.104 r^2 \quad (2)$$

Thus a zeolite-L crystal with a radius of 25 nm contains about 690 parallel channels.

The number (mol) of unit cells in one crystal was calculated from :

$$N_{ch} = n_{ch} \left(\frac{1}{N_A |c|} \right) \text{ with} \quad (3)$$

l: length of zeolite crystal

|c|: primitive c-vector (0.75 nm)

Thus a zeolite L crystal with a length of 60 nm has 9.17×10^{-20} mol unit cells.

Weight of one crystal:

$$m_{Zeo} = N_{ch} M_{u.c.} \text{ with} \quad (4)$$

Mu.c. being the molecular weight of one unit cell (2880 g/mol)

Thus the weight of one zeolite-L crystal is about 2.64×10^{-16} g.

Number of crystals in 1 mg:

$$N_{Zeo} = \frac{\text{Sample mass}}{m_{Zeo}} \quad (5)$$

Thus in 1 mg of zeolites there are 3.79×10^{12} single crystals.

PNA molecules attached to one zeolite crystal:

$$\frac{5.6E14}{3.79E12} \approx 148 \quad (6)$$

Cell Culture

HeLa cells were cultured inside media which contain 88 % Dulbecco's Modified Eagle Medium (DMEM), 10 % Fetal Bovine Serum, 1 % Penicillin-Streptomycin and 1 % L-Glutamine 200 mM (all material was purchased from Gibco) under 37°C and 5% of CO₂ conditioning for 48 hours until 70 to 80 % cell confluency was reached. Subsequently, the cells were washed twice with Phosphate

Buffer Solution (PBS, Gibco) and treated with trypsin, then approximately 50,000 cells were reseeded on the monolayer glass cover slip inside 6 well plate culture dish. New culture media (2 ml) were added gently and the cells were grown overnight.

Cell Incubation with nanoparticles

Working solutions of culture medium containing PNA-zeolites in 0.01 mg/mL concentration were added gently to the cells. After 1, 4 and 24 hours of incubation, the media were removed and cells were washed with PBS twice. Cells were fixed with 4% paraformaldehyde (PFA) and, subsequently, the cell nuclei were stained with DAPI (4',6-diamidino-2-phenylindole). After staining, cells were washed once with PBS and then with water. Cells were removed from the well and mounted onto the rectangular glass cover for microscopy experiments.

Cell Viability Study

The cell viability after particle incubation was measured by means of an automatic cell counter (CASY, Roche Innovatis AG, Bielefeld, Germany). Approximately 50,000 cells were grown on 24 well plates overnight. The media were removed and replaced with 0.01 mg/ml of zeolite-PNA dispersion. The cells were incubated for 24 hours at 37°C under a 5% CO₂ atmosphere. After the incubation, the media were removed and put in an eppendorf tube and the cells were gently washed with PBS twice. The cells were detached by incubating with 500 µl of a trypsin solution for 5 minutes. Afterwards, 500 µl of culture media were added to the cells in order to block the trypsin activity. The solution was removed to the same eppendorf tube. Cell suspension inside the eppendorf tube was centrifuged at 1000 rpm for 5 minutes and the supernatant was removed. The pellet was resuspended in 1 mL of new culture media and 10 µL of the cell suspension was dissolved in 10 mL of CASY ton electrolyte solution, and measurement was performed with CASY. To compare the viability, the same setup was performed by incubating the cells with 30 % of DMSO in culture media (negative control) and without any particles (positive control).

REFERENCES

- [1] J.C. Hanvey, N.J. Peffer, J.E. Bisi, S.A. Thomson, R. Cadilla, J.A. Josey, et al. *Science* **1992**, 358, 1481-1485.
- [2] M.A. Shamma, C.G. Simmons, D.R. Corey, R.R. Shmookler, *Oncogene* **1999**, 18, 6191-6200.
- [3] J.G. Karras, M.A. Maier, T. Lu, A. Watt, M. Manoharan, *Biochemistry* **2001**, 40, 7853-7859.
- [4] U. Koppelhus, P.E. Nielsen, *Adv. Drug Deliver. Rev.* **2003**, 55, 267-280.

- [5] T. Ljungström, H. Knudsen, P.E. Nielsen, *Bioconjugate Chem.* **1999**, *10*, 965-972.
- [6] P.E. Nielsen, *Chem. Biodivers.* **2010**, *7*, 786-804.
- [7] E. Rozners, *J. Nucleic acids*, **2012**.
- [8] P. Zhou, A. Dragulescu-Andrasi, B. Bhattacharya, H. O'Keefe, P. Vatta, J.J. Hyldig-Nielsen, D.H. Ly, *Bioorg. Med. Chem. Lett.* **2006**, *16*, 4931-4935.
- [9] P. Zhou, M. Wang, L. Du, G.W. Fisher, A. Waggoner, D.H. *J. Am. Chem. Soc.* **2003**, *125*, 6878-6879.
- [10] A. Manicardi, E. Fabbri, T. Tedeschi, S. Sforza, N. Bianchi, E. Brognara, R. Gambari, R. Marchelli, R. Corradini, *ChemBioChem* **2012**, *13*, 1327-1337.
- [11] R. Mitra, K.N. Ganesh, *J. Org. Chem.* **2012**, *77*, 5696-5704.
- [12] D.R. Jain, V.L. Anandi, M. Lahiri, K.N. Ganesh, *J. Org. Chem.* **2014**, DOI: 10.1021/jo501639m
- [13] A. Dragulescu-Andrasi, S. Rapireddy, B.M. Frezza, C. Gayathri, R.R. Gil, D.H. Ly, *J. Am. Chem. Soc.* **2006**, *128*, 10258-10267.
- [14] B. Sahu, V. Chenna, K.L. Lathrop, S.M. Thomas, G. Zon, K.J. Livak, D.H. Ly, *J. Org. Chem.* **2009**, *74*, 1509-1516.
- [15] L. Good, S.K. Awasthi, R. Dryselius, O. Larsson, P.E. Nielsen, *Nat. Biotech.* **2001**, *19*, 360-364.
- [16] W.L. Munyendo, H. Lv, H. Benza-Ingoula, L.D. Baraza, J. Zhou, *Biomolecules* **2012**, *2*, 187-202.
- [17] T. Shiraishi, P.E. Nielsen, *Artif. DNA PNA XNA* **2011**, *2*, 90-99.
- [18] Y. Wolf, S. Pritz, S. Abes, M. Bienert, B. Lebleu, J. Oehlke, *Biochemistry* **2006**, *45*, 14944-14954.
- [19] N. Bendifallah, F.W. Rasmussen, V. Zachar, P. Ebbesen, P.E. Nielsen, U. Koppelhus, *Bioconjugate Chem.* **2006** *17*, 750-758.
- [20] J.J. Turner, G.D. Ivanova, B. Verbeure, D. Williams, A.A. Arzumanov, S. Abes, M.J. Gait, *Nucleic acids Res.* **2005**, *33*, 6837-6849.
- [21] P.N. Brown, H. Yin, *Chem. Commun.* **2013**, *49*, 4415-4417.
- [22] C. Cordier, F. Boutimah, M. Bourdeloux, F. Dupuy, E. Met, et al. *PLoS ONE* **2014**, *9*, e104999.
- [23] F. Marlin, P. Simon, S. Bonneau, P. Alberti, C. Cordier, C. Boix, C. Giovannangeli, *ChemBioChem* **2012**, *13*, 2593-2598.
- [24] S. Abes, D. Williams, P. Prevot, A. Thierry, M.J. Gait, B. Lebleu, *J. Control. Release* **2006**, *110*, 595-604.
- [25] T. Shiraishi, P.E. Nielsen, *Nat. Protocols* **2006**, *1*, 633-636.
- [26] A. Muratovska, R.N. Lightowlers, R.W. Taylor, D.M. Turnbull, R.A. Smith, J.A. Wilce, M.P. Murphy, *Nucleic acids Res.* **2001**, *29*, 1852-1863.
- [27] U. Koppelhus, T. Shiraishi, V. Zachar, S. Pankratova, P.E. Nielsen, *Bioconjugate Chem.* **2008**, *19*, 1526-1534.
- [28] T. Shiraishi, P.E. Nielsen, *Bioconjugate Chem.* **2012**, *23*, 196-202.
- [29] T. Ljungström, H. Knudsen, P.E. Nielsen, *Bioconjugate Chem.* **1999**, *10*, 965-972.
- [30] A. Füssl, A. Schleifenbaum, M. Göritz, A. Riddell, C. Schultz, R. Krämer, *J. Am. Chem. Soc.* **2006**, *128*, 5986-5987.
- [31] H. Fang, K. Zhang, G. Shen, K. L. Wooley, J.S.A. Taylor, *Mol. Pharm.* **2009**, *6*, 615-626.
- [32] N.A. McNeer, E.B. Schleifman, A. Cuthbert, M. Brehm, A. Jackson, C. Cheng, et al. *Gene Ther.* **2012**, 1-12.
- [33] P. Anstaett, Y. Zheng, T. Thai, A.M. Funston, U. Bach, G. Gasser, *Angew. Chem.* **2013**, *125*, 4311-4314.
- [34] S.R. Ryoo, J. Lee, J. Yeo, H. Na, Y.K. Kim, H. Jang, D.H. Min, *ACS nano* **2013**, *7*, 5882-5891.
- [35] A. Ruiz, D. Bruehwiler, T. Ban, G. Calzaferri, *Monatshefte fuer Chemie* **2005**, *136*, 77-89.

- [36] A. Candiani, A. Bertucci, S. Giannetti, M. Konstantaki, A. Manicardi, S. Pissadakis, A. Cucinotta, R. Corradini, S. Selleri, *J. Biomed. Opt.* **2013**, *18*, 057004.
- [37] A. Lesniak, A. Salvati, M.J. Santos-Martinez, M.W. Radomski, K.A. Dawson, C. Aberg, *J. Am. Chem. Soc.* **2013**, *135*, 1438-1444.
- [38] E. Bilensoy, *Expert Opin. Drug Deliver.* **2010**, *7*, 795-809.
- [39] L. Thiele, B. Rothen-Rutishauser, S. Jilek, H. Wunderli-Allenspach, H. P. Merkle, E. Walter, *J. Control. Release* **2001**, *76*, 59-71.
- [40] M. Liang, I.C. Ling, M.R. Whittaker, R.F. Minchin, M.J. Monteiro, I. Toth, *ACS Nano* **2010**, *4*, 403-413.
- [41] J.F. Stefanick, J.D. Ashley, T. Kiziltepe, B. Bilgicer, *ACS Nano* **2013**, *7*, 2935-2947.
- [42] D. Hühn, K. Kantner, C. Geidel, S. Brandholt, I. De Cock, S. J. H. Soenen, P. Rivera Gil, J.M. Montenegro, K. Braeckmans, K. Müllen, et al., *ACS Nano* **2013**, *7*, 3253-63.
- [43] H.J.P. Ryser, W. Shen, *P. Natl. Acad. Sci. USA* **1978**, *75*, 3867-3870.
- [44] T. Yoshida, T. Nagasawa, *Appl. Microbiol. Biot.* **2003**, *62*, 21-6.
- [45] F. Hudecz, S. Kutassi-Kowacs, G. Mezo, M. Szexerke, *Biol.Chem.* **1989**, *370*, 1019-1026.
- [46] M. Westwood, D. Roberts, R. Parker, *Carbohydrate Polymers* **2011**, *84*, 960-969.
- [47] D. Zheng, D.A. Giljohann, D.L. Chen, M.D. Massich, X.Q. Wang, H. Iordanov, A.S. Paller, *Proc. Nat. Ac. Sci.* **2012**, *109*, 11975-11980.
- [48] Y. Li, X. Duan, L. Jing, C. Yang, R. Qiao, M. Gao, *Biomaterials* **2011**, *32*, 1923-1931.
- [49] K.L. Young, A.W. Scott, L. Hao, S.E. Mirkin, G. Liu, C.A. Mirkin, *Nano lett.* **2012**, *12*, 3867-3871.
- [50] L. He, G.J. Hannon, *Nat. Rev. Genetics* **2004**, *5*, 522-531.
- [51] J. Lu, G. Getz, E.A. Miska, E. Alvarez-Saavedra, J. Lamb, D. Peck, T.R. Golub, *Nature* **2005**, *435*, 834-838.
- [52] R. Kuner, J.C. Brase, H. Sülthmann, D. Wuttig, *Methods* **2013**, *59*, 132-137.
- [53] C. Camps, F. Buffa, S. Colella, J. Moore, C. Sotiriou, H. Sheldon, J. Ragoussis, *Clin. Cancer Res.* **2008**, *14*, 1340-1348.
- [54] X. Huang, L. Ding, K.L. Bennewith, R.T. Tong, S.M. Welford, K.K. Ang, A.J. Giaccia, *Mol. Cell* **2009**, *35*, 856-867.
- [55] A. Giannakakis, R. Sandaltzopoulos, J. Greshock, S. Liang, J. Huang, K. Hasegawa, L. Zhang, *Cancer Biol. Ther.* **2008**, *7*, 255.
- [56] C. le Sage, R. Nagel, D.A. Egan, M. Schrier, E. Mesman, A. Mangiola, R. Agami, *EMBO J.* **2007**, *26*, 3699-3708.
- [57] P. Pineau, S. Volinia, K. McJunkin, A. Marchio, C. Battiston, B. Terris, A. Dejean, *Proc. Nat. Ac. Sci* **2010**, *107*, 264-269.
- [58] S. Galardi, N. Mercatelli, E. Giorda, S. Massalini, G.V. Frajese, S.A. Ciafrè, M.G. Farace, *J. Biol.Chem.* **2007**, *282*, 23716-23724.
- [59] F.M. Kievit, O. Veiseh, N. Bhattarai, C. Fang, J.W. Gunn, D. Lee, M. Zhang, *Adv. Funct. Mater.* **2009**, *19*, 2244-2251.
- [60] T. Xia, M. Kovoichich, M. Liang, H. Meng, S. Kabehie, S. George, J.I. Zink, A.E. Nel, *ACS nano*, *3*, 3273-3286.
- [61] J.E. Fuller, G.T. Zugates, L.S. Ferreira, H.S. Ow, N.N. Nguyen, U.B. Wiesner, R.S. Langer, *Biomaterials* **2008**, *29*, 1526-1532.
- [62] H. Otsuka, Y. Nagasaki, K. Kataoka, *Adv. Drug Deliver. Rev.* **2003**, *55*, 403-419.
- [63] I. Nakase, Y. Konishi, M. Ueda, H. Saji, S. Futaki, *J. Control. Release* **2012**, *159*, 181-188.
- [64] S. Mura, J. Nicolas, P. Couvreur, *Nat. Mater.* **2013**, *12*, 991-1003.
- [65] K.J. Chen, H.F. Liang, H.L. Chen, Y. Wang, P.Y. Cheng, H.L. Liu, H.W. Sung, *ACS nano* **2012**, *7*, 438-446.
- [66] Y. Cheng, J. Hao, L.A. Lee, M.C. Biewer, Q. Wang, M.C. Stefan, *Biomacromol.* **2012**, *13*, 2163-2173.

- [67] M.Y. Hua, H.L. Liu, H.W. Yang, P.Y. Chen, R.Y. Tsai, C.Y. Huang, K.C. Wei, *Biomaterials* **2011**, *32*, 516-527.
- [68] K. Cai, Z. Luo, Y. Hu, X. Chen, Y. Liao, L. Yang, L. Deng, *Adv. Mater.* **2009**, *21*, 4045-4049.
- [69] F.N. Al-Deen, J. Ho, C. Selomulya, C. Ma, R. Coppel, *Langmuir* **2011**, *27*, 3703-3712.
- [70] N.Y. Rapoport, A.M. Kennedy, J.E. Shea, C.L. Scaife, K.H. Nam, *J. Control. Rel.* **2009**, *138*, 268-276.
- [71] M. Javadi, W.G. Pitt, D.M. Belnap, N.H. Tsosie, J.M. Hartley, *Langmuir* **2012**, *28*, 14720-14729.
- [72] T. Tagami, W.D. Foltz, M.J. Ernsting, C.M. Lee, I.F. Tannock, J.P. May, S.D. Li *Biomaterials* **2011**, *32*, 6570-6578.
- [73] Q. Yuan, Y. Zhang, T. Chen, D. Lu, Z. Zhao, X. Zhang, W. Tan, *ACS nano* **2012**, *6*, 6337-6344.
- [74] H. Yan, C. Teh, S. Sreejith, L. Zhu, A. Kwok, W. Fang, Y. Zhao, *Angew. Chem. Int. Ed.* **2012**, *51*, 8373-8377.
- [75] J. Qin, I. Asempah, S. Laurent, A. Fornara, R.N. Muller, M. Muhammed, *Adv. Mater.* **2009**, *21*, 1354-1357.
- [76] J. You, R. Zhang, C. Xiong, M. Zhong, M. Melancon, S. Gupta, C. Li, *Cancer Res.* **2012**, *72*, 4777-4786.
- [77] J.Z. Du, X.J. Du, C.Q. Mao, J. Wang, *J. Am. Chem. Soc.* **2011**, *133*, 17560-17563.
- [78] C.H. Lee, S.H. Cheng, I. Huang, J.S. Souris, C.S. Yang, C.Y. Mou, L.W. Lo, *Angew. Chem.* **2010**, *122*, 8390-8395.
- [79] K.H. Min, J.H. Kim, S.M. Bae, H. Shin, M.S. Kim, S. Park, D.S. Lee, *J. Control. Rel.* **2010**, *144*, 259-266.
- [80] Y.E. Kurtoglu, R.S. Navath, B. Wang, S. Kannan, R. Romero, R.M. Kannan, *Biomaterials* **2009**, *30*, 2112-2121.
- [81] W. Ong, Y. Yang, A.C. Cruciano, R.L. McCarley, *J. Am. Chem. Soc.* **2008**, *130*, 14739-14744.
- [82] H. Hatakeyama, H. Akita, E. Ito, Y. Hayashi, M. Oishi, Y. Nagasaki, H. Harashima, *Biomaterials* **2011**, *32*, 4306-4316.
- [83] N. Singh, A. Karambelkar, L. Gu, K. Lin, J.S. Miller, C.S. Chen, S.N. Bhatia, S. N. *J. Am. Chem. Soc.* **2011**, *133*, 19582-19585.
- [84] H. Meng, M. Xue, T. Xia, Y.L. Zhao, F. Tamanoi, J.F. Stoddart, J.I. Zink, A.E. Nel, *J. Am. Chem. Soc.* **2010**, *132*, 12690-12697.
- [85] S. Han, Y. Liu, X. Nie, Q. Xu, F. Jiao, W. Li, C. Chen, *Small* **2012**, *8*, 1596-1606.
- [86] P. Vader, L.J. van der Aa, J.F. Engbersen, G. Storm, R.M. Schiffelers, *Pharm. Res.* **2011**, *28*, 1013-1022.
- [87] A. Bernardos, L. Mondragon, E. Aznar, M.D. Marcos, R. Martínez-Máñez, F. Sancenón, J. Soto,
- [88] E. Climent, R. Martínez-Máñez, F. Sancenón, M.D. Marcos, J. Soto, A. Maquieira, P. Amorós, *Angew. Chem.* **2010**, *122*, 7439-7441.
- [89] Z. Zhang, D. Balogh, F. Wang, S.Y. Sung, R. Nechushtai, I. Willner, *ACS nano* **2013**, *7*, 8455-8468.
- [90] P. Zhang, F. Cheng, R. Zhou, J. Cao, J. Li, C. Burda, Q. Min, J.J. Zhu, *Angew. Chem. Int. Ed.* **2014**, *53*, 2371-2375.
- [91] J.Y. Zhou, W.L. Ma, S. Liang, Y. Zeng, R. Shi, H.L. Yu, W.W. Xiao, W.L. Zheng, *BMB Rep.* **2009**, *42*, 593-598.
- [92] F. Totsingan, R. Marchelli, R. Corradini, *Artif. DNA PNA XNA* **2011**, *2*, 16-22.
- [93] A. Manicardi, A. Calabretta, M. Bencivenni, T. Tedeschi, S. Sforza, R. Corradini, R. Marchelli, *Chirality* **2010**, *22*, E161-E172.

5

Mesoporous silica nanoparticles for simultaneous delivery of temozolomide and microRNA-targeting PNA in glioma cancer treatment

Abstract

The administration of an efficient cancer therapy still remains a substantial goal, since the ability of cancer cells to adapt and develop new resistance pathways to the traditional use of a single therapeutic strategy. Thus, a very interesting and promising strategy for an efficient cancer treatment relies on the combination of two or more therapeutic approaches with diverse mechanisms, which can synergistically cooperate to provide an enhanced final anticancer effect. In this chapter, the use of multifunctional MSNPs for the simultaneous delivery of anti-miR-221 PNA probes and the chemotherapeutic drug temozolomide to drug resistant glioma cells is presented, demonstrating the synergistic effect of the two agents in inducing apoptosis. This represents the first example of combining miRNA-targeting PNAs to nanoparticle platforms loaded with a chemotherapy agent, being also the first time temozolomide has been delivered to glioma cells by means of a porous nanoparticle carrier. The successful results propose the TMZ-PNA-MSN system as a suitable tool for the development of novel approaches to tackle drug-resistance in glioblastoma, which represents indeed a key issue, since after surgery and radiotherapy, the chemotherapy protocol still suffers from the highly frequency of growth of drug-resistant cells.

This work has been carried out in collaboration with Professor Roberto Gambari's group, at the Department of Life Sciences and Biotechnology of the University of Ferrara (Italy), and in particular with Dr. Eleonora Brognara who took care of the biological experiments on human glioblastoma T98G cells.

5.1 MicroRNAs as gene therapy targets

Very recently, great attention and expectations have been raised by the possibility to use non-coding RNAs as either drugs or targets for therapies based on the regulation of gene expression.^[1] MicroRNAs (miRNAs or miRs) are a family of short non-coding RNAs (21-25 nucleotides) that are

involved in the regulation of the gene expression at the post-transcriptional level through the RNA interference pathway.^[2-3] In the general mechanism, two processing events lead to mature miRNA formation in animals. In the first, the newborn miRNA transcripts (pri-miRNA) are processed into c.a. 70-nucleotide precursors (pre-miRNA); in the second event that follows, this precursor is cleaved to generate shorter mature miRNAs.^[4] The sequential cleavages involved in miRNA maturation are catalyzed by two RNase-III enzymes, namely Drosha and Dicer.^[3,5] The first one is predominantly localized in the nucleus and cleaves the pri-miRNAs into stem-loop structured pre-miRNAs. These pre-miRNAs are exported from the nucleus into the cytoplasm by Exportin 5 (Exp5); at this stage, these hairpin precursors are cleaved by the Dicer into small, imperfect dsRNA duplexes (miRNA:miRNA), that contain both the mature miRNA strand and its complementary sequence. The mature ds-miRNA is then rapidly unwound since one of the two strands associates to Argonaute and other proteins to form the active miRISC complex.^[6-7] Then, the miRISC complex specifically recognizes and regulates particular mRNAs through pairing of the miR strand incorporated to a specific mRNA sequence. MiRNA-binding sites in animal mRNAs lie generally in the 3' UTR and a key feature of the recognition process involves Watson-Crick base pairing of miRNA nucleotides 2–8, representing the so-called seed region.^[8-10] Depending on the degree of complementary, strong interactions (perfect or near perfect matching) between the miRNA and its target mRNA lead to catalyzed degradation of the mRNA strand, while weak interactions (partial matching) exclude cleavage and promote repression of mRNA translation, via a different mechanism.^[11-13] A schematic view of the whole biological miRNA pathway is reported in Figure 5.1.

Since a single 3'UTR region of a given mRNA contains signal sequences for several microRNAs, and a single microRNA may exhibit multiple silencing on different mRNAs, the interference at the level of this complex biological pathway might pave the way to the achievement of strong biological effects.^[14-16]

It is nowadays established that microRNAs play a pivotal role in cancer, and the literature on this specific issue has become more and more comprehensive.^[17-22] MicroRNAs can play a double role in cancer, behaving both as oncogenes^[23-25] or tumor suppressor genes.^[26-27] In general, miRNAs promoting cancer target mRNA coding for tumor-suppression proteins, while microRNAs exhibiting tumor-suppression properties usually silence mRNAs coding oncoproteins. MicroRNAs that have been demonstrated to be involved in the initiation and progression of human cancer are defined as oncogenic miRNAs (oncomiRs).^[28-29] For all these reasons, miRNAs have been pointed out as eligible and powerful targets for gene therapy, since a strategy involving the knock down of selected miRNAs may provide significant anticancer therapeutic effects.^[30-34]

As one of the possible oncogenic miRNAs, miR-221 has been found upregulated in several tumor forms,^[35-37] and especially in gliomas.^[38-40] Among miR-221 targets, p27Kip1 mRNA appears to be one of the most interesting, since implicated in the inhibition of cell proliferation; hence, it represents a good candidate for a gene therapy strategy based on the upregulation of its expression by miR-221 knock down.^[41-43] Interestingly, the downregulation of miR-221 has been also shown to sensitize glioma cells to temozolomide, which is one of the most common antineoplastic agents for malignant glial tumors.^[44-47]

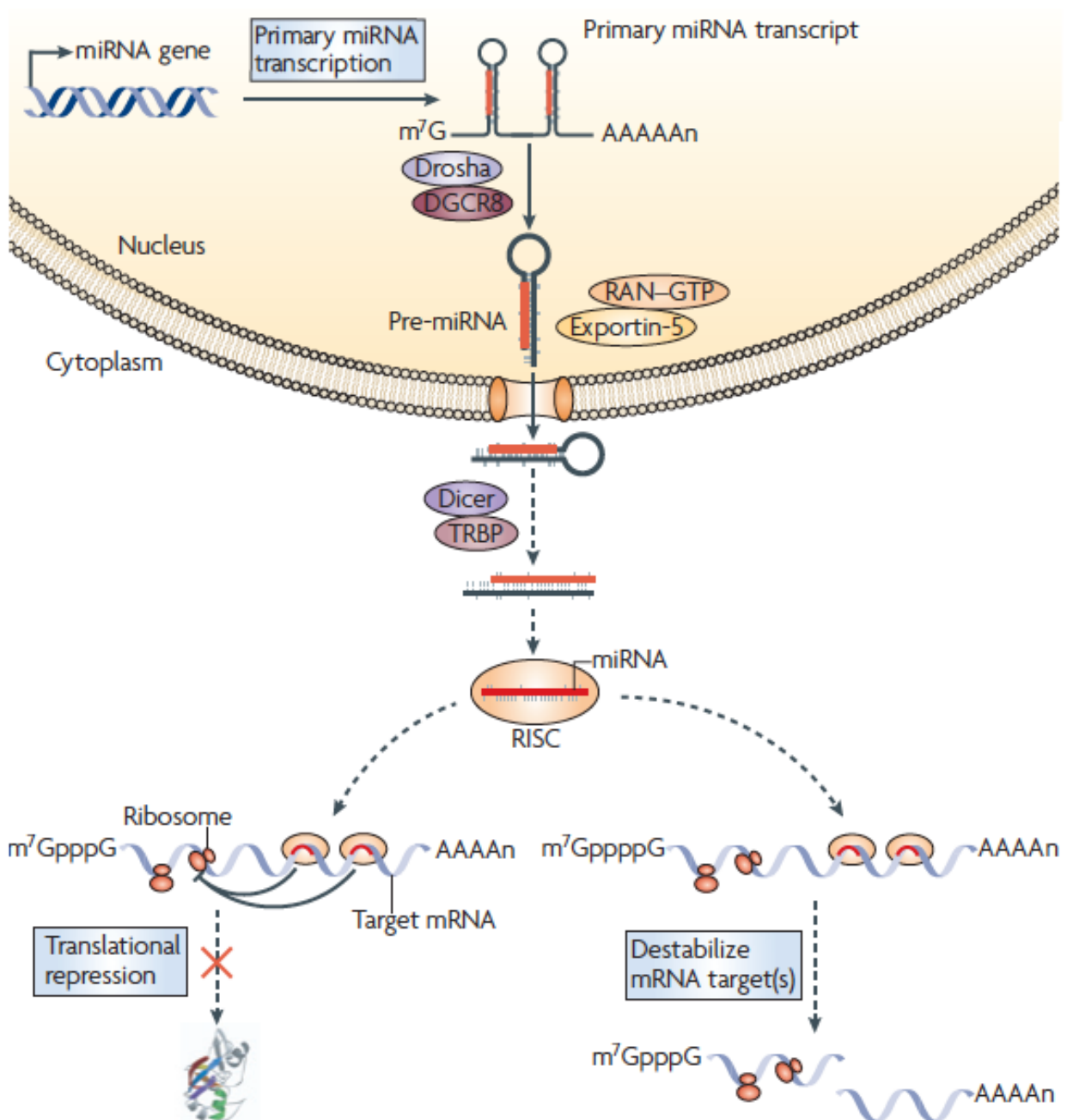


Fig. 5.1 Schematic model for the biogenesis and post-transcriptional activity of miRNAs. Reprinted by permission from Macmillan Publishers Ltd: Nature Reviews Immunology, advance online publication, 1 February 2008, doi:10.1038/nri2252, H.F. Lodish, B. Zhou, G. Liu, C.Z. Chen, *Nat. Rev. Immunol.* **2008**, 8, 120-130.

Among the possible available tools for anti-miR targeting, peptide nucleic acids (PNAs) represent an excellent choice, due to their properties described in the previous chapters, and they have been already shown being able to efficiently target miRNAs in anti-miR strategies.^[48-52]

In this chapter, the use of multifunctional MSNPs for the simultaneous delivery of anti-miR-221 PNA probes and temozolomide to drug resistant glioma cells will be discussed, demonstrating the synergistic therapeutic effect of the two agents. No reports have been given by far on the coupling of miRNA-targeting PNAs to nanoparticle platforms loaded with a chemotherapy agent, as well as their use on growing cancer cells. This has been also the first time temozolomide has been delivered to glioma cells by means of a porous nanoparticle carrier.

5.2 Synthesis and characterization of MSNPs

MSNPs of 100 nm in diameter were synthesized as described in Chapter 2. The size range of the particles represents a good regime for efficient cellular uptake and further cell experiments.^[53-55] In order to have fluorescent particles suitable for cellular tracking and localization studies, the red dye cyanine 5 was directly grafted to the silica network, thus introducing the first functionality of the nanomaterial already at the scaffold level. A one-pot synthesis was carried out using a Cy5-NHS-ester and a little amount of APTES, which made it possible to covalently embed the dye to the silica structure. This red dye was selected since its emission does not overlap with all the other signals used in the cellular uptake experiments and the biological tests. The particles have been extensively characterized with SEM, TEM, SAXS (see Chapter 2), fluorescence spectroscopy, and confocal microscopy (Figure 5.2 and 5.3 respectively)

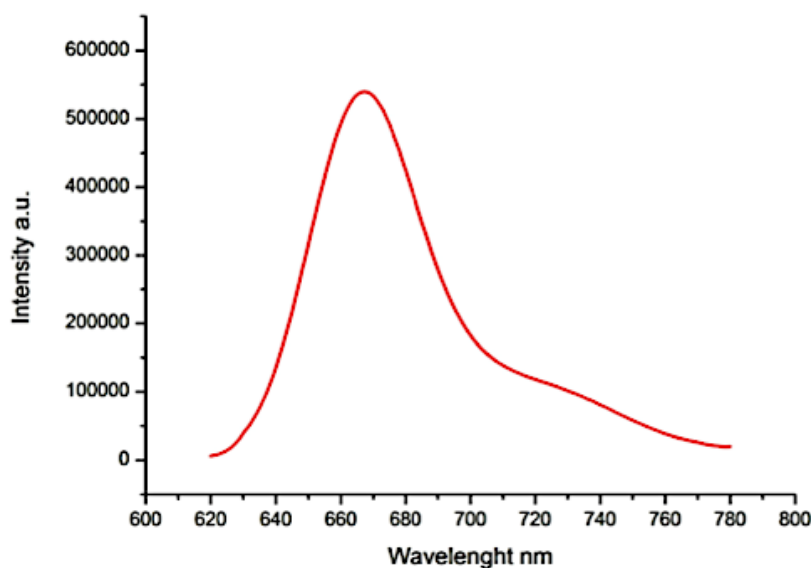


Fig. 5.2 Emission spectrum of the particle dispersion in ethanol ($\lambda_{exc} = 600$ nm).

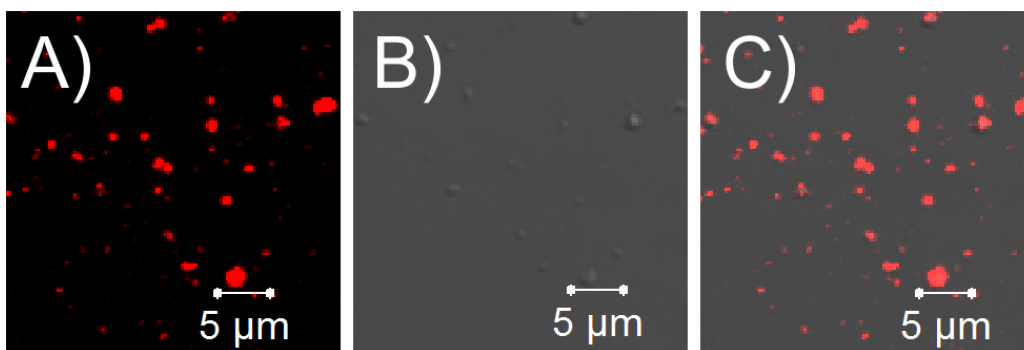


Fig. 5.3 Confocal micrographs showing Cy5-MSNPs. A) Cy5 emission; B) brightfield image; C) Overlay. The particles were excited using $\lambda_{\text{exc}} = 633$ nm.

5.3 Multi-functionalization of MSNPs

Fluorescent Cy5-MSNPs were obtained as described above, still containing the templating surfactant CTAB in the pore system. The zeta potential value of +8.94 mV registered for this particle is indeed due to the cationic heads of the CTAB still entrapped in the mesoporous structure. However, an extra small contribution can be also ascribed to some unreacted APTES molecules present in the scaffold. The persistent presence of the surfactant in the pores actually plays a crucial role for the following external surface functionalization with amine groups, preventing the silane to react also with the -OH groups of the inner surface of the pores, which may lead to an obstruction of the empty channels. APDMS was thus used to provide amine-functionalization of the particle surface by silane chemistry. At this point, CTAB could be totally removed by an overnight treatment with acidic ethanol. The final zeta potential value of +7.96 mV obtained at this step clearly indicated the presence of the amine functional groups on the outer surface of the particles, due to protonated amino groups in PBS medium, as well as a positive ninhydrin test. Subsequently, the amine groups were converted into carboxylic acids by reaction with succinic anhydride, which was confirmed by a zeta potential shift to -32.26 mV. The presence of a total net negative charge on the particle surface is indeed crucial for the final binding of the cationic anti-miR221 PNA probes. Before that, the chemotherapeutic agent temozolomide was loaded into the particle pores. Due to the low molecular weight of the drug and its neutral charge, an impregnation strategy was performed, as described in the experimental section, which allowed for achieving a final loading of 17% (*wt/wt*). This value was calculated by means of UV-Vis spectroscopy, following residual temozolomide absorption in the UV region after the loading procedure. The washing solutions were collected and the residual drug content was calculated by UV-Vis measurements at the wavelength $\lambda = 328$ nm. A calibration curve by standard solutions of temozolomide in methanol was built up to

allow for quantification, whose equation is $y = 56.343x$ (See Figure 5.4). The linear model has been validated by Mandel test.

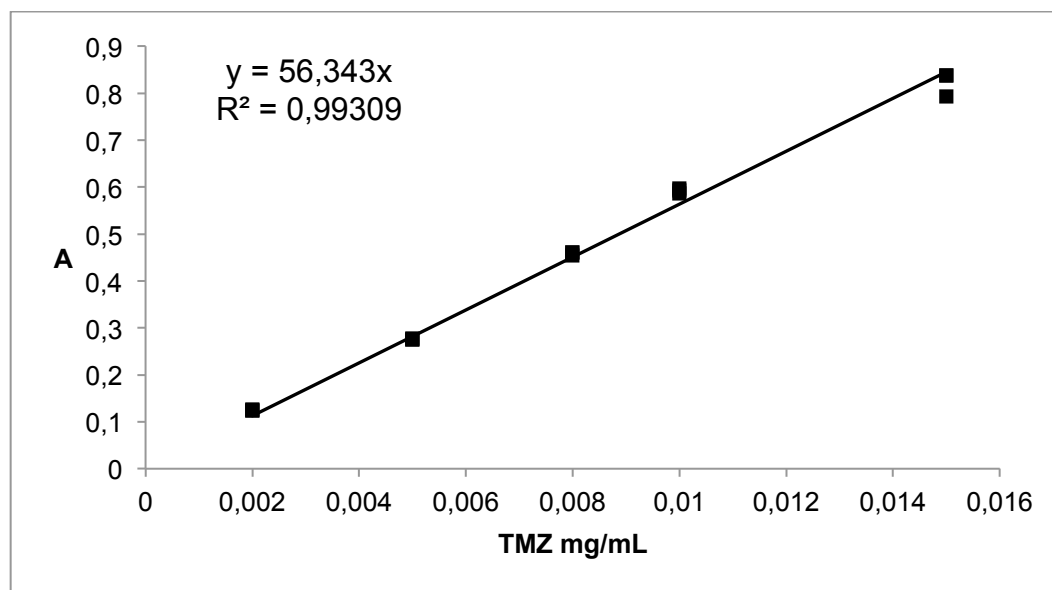


Fig. 5.4 Calibration curve for temozolomide in methanol.

Once MSNPs were filled up with the drug, cationic R_8 -PNA221 H-RRRRRRRRR-GCAGACAATGTAGCT-NH₂ (conjugated with eight D-arginine residues, R) could finally be uploaded to the nanocarriers. Due to their cationic nature, the arginine-modified PNA probes were electrostatically adsorbed on the negatively charged surface of carboxylic-functionalized MSNPs, by dispersing the particles in the aqueous PNA solution. From a targeting point of view, the adoption of cationic PNAs helps to enhance the hybridization properties of the probes by additionally exploiting electrostatic interaction.^[48,56] Moreover, the presence of cationic species on the particle surface directly improves the cellular uptake of the nanosystem, without further need of cationic polymer coatings.^[57] Furthermore, the use of cationic PNAs allows for reducing the number of steps otherwise required for a covalent binding of the probes to the particle surface, which may cause a progressive unwanted release of the drug. After R_8 -PNA221 adsorption, the zeta potential of the particles considerably shifted to + 0.34 mV, which indeed proved the successful binding of the PNAs to MSNPs. PNA loading was evaluated by UV-Vis spectroscopy monitoring the absorption peak at 260 nm before and after incubation with the negatively charged particles, and was found to be 3.6 nanomoles per mg of material (which, in weight, means 15 μ g PNA/mg MSNP). The extinction molar coefficient for PNA at 260 nm is reported elsewhere.^[58] The schematic view of the whole functionalization procedure is reported in Figure 5.5.

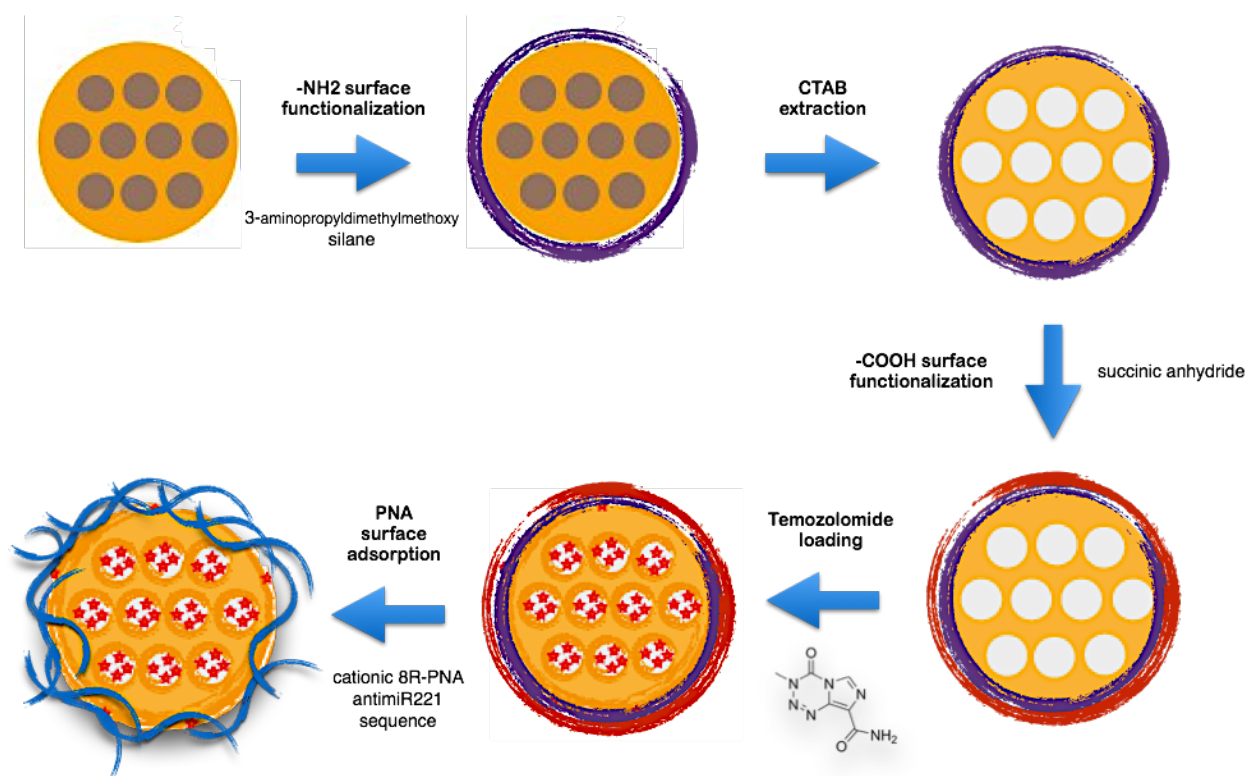


Fig. 5.5 Functionalization procedure for PNA-TMZ-(Cy5)-MSNPs. After the surfactant-templated synthesis of MSNPs, amine groups were first introduced to the particle surface. After that, CTAB extraction was performed. Amine groups were thus converted into carboxylic groups, and temozolomide loading in the pore system was carried out. Eventually, cationic R₈-PNA221 were adsorbed on the particle outer surface.

5.4 Cellular uptake studies

To address the interaction between the hybrid nanosystem and live cells, it was indeed necessary to check out the effective cellular uptake of the particles. For this purpose, a C6 glioma cell line was used. Visualization and tracking of the nanoparticles inside the cells was possible thanks to the cyanine 5 red emitting dye inserted in the silica scaffold during the sol-gel synthesis.

Additionally, for a better view of the cell shape, the actin filaments were stained with Alexa Fluor® 568 Phalloidin after cell fixation, whose emission does not overlap with that one of Cy5.

Cell experiments were done incubating C6 glioma cells (approximately 50,000 cells/plate) for 1, 4, and 24 hours, using a particle concentration of 0.05 mg/mL in culture media. After incubation, the cells were washed, fixed, and analyzed by confocal microscopy.

The results are shown in Figure 5.6. It is possible to notice that already after 1 hour a discrete number of nanoparticles could be visualized inside the cells, proving that the system is properly tailored for an efficient cellular uptake. An increase in incubation time then led to an increase in particle concentration in the cell cytoplasm. No particles, as expected, were internalized in the cell nucleus. Particle uptake was indeed proved by recording Z-stack images (Fig. 3D). Thus, though

PNAs generally show poor cell membrane permeability,^[59] the use of a cationic PNA on silica nanoparticle vector appears to efficiently overcome this limitation.

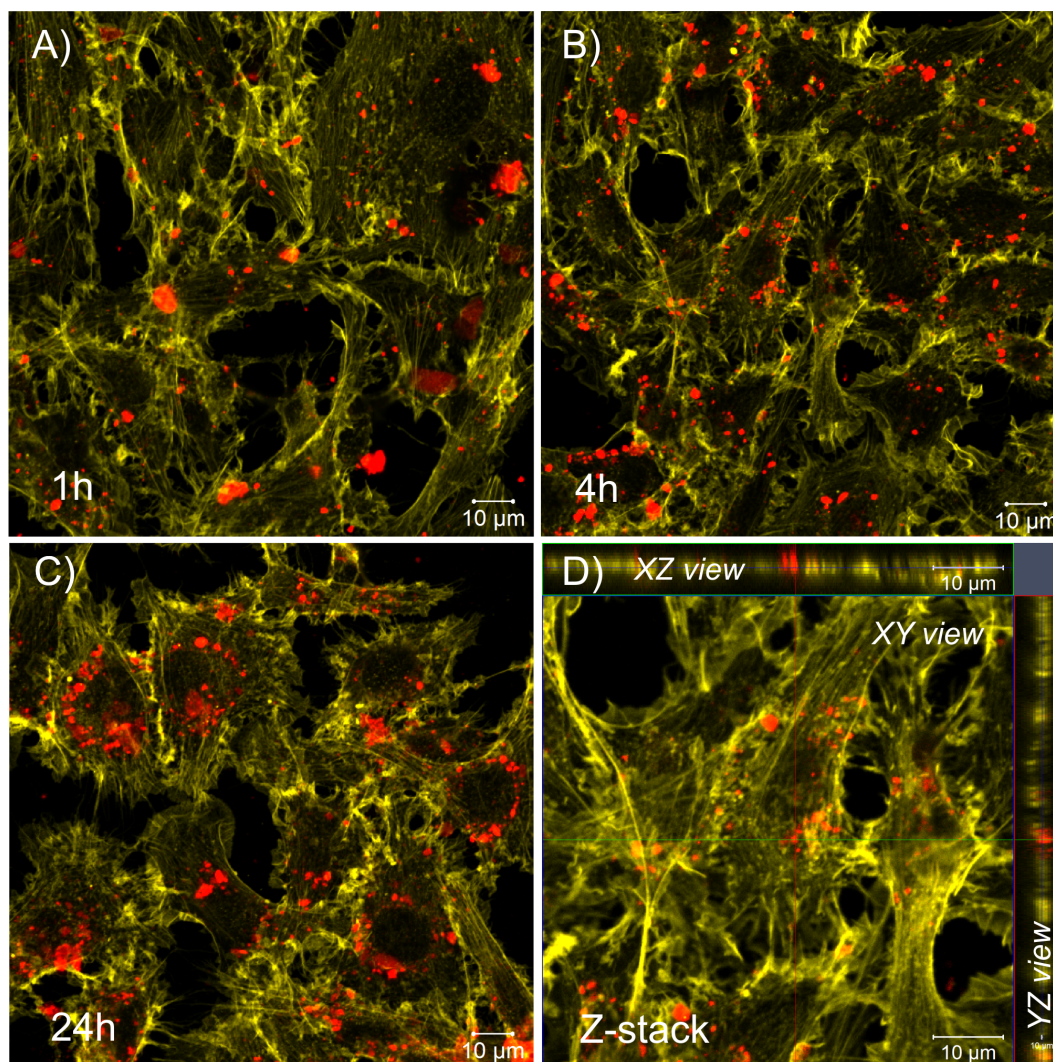


Fig. 5.6 Confocal micrographs of C6 glioma cells incubated with 0.05 mg/mL dispersion of PNA-TMZ-(Cy5)-MSNPs in culture media. A) 1 hour incubation; B) 4 hour incubation, C) 24 hour incubation, D) Z-stack showing 3D particle internalization. The red spots refer to the red emissive Cy5-MSNPs, while F-actin filaments are visualized in yellow after Alexa Fluor® 568 Phalloidin staining.

5.5 *In vitro* viability tests on C6 glioma cell line

As preliminary tests for studying the biological and possible cytotoxic activity of the PNA-temozolomide multimodal system, cell viability experiments were carried out on a C6 glioma cell line, incubating the live cells with different combinations of the material. It has been recently found that this C6 glioma cell line tends to overexpress the oncomiR-221, which is involved in the tumor proliferation.^[60-62] C6 glioma also represents a cell line resistant to temozolomide treatment, which makes it a suitable candidate for an early stage investigation of the therapeutic potentialities of the

PNA-TMZ-MSNPs system.^[63-65] A complete set of experiments was designed, incubating the cell for 24 and 48 hours with, respectively, MSNPs filled with temozolomide only (TMZ-MSNPs), MSNPs surface-modified with R₈-PNA221 only (PNA-MSNPs), and MSNPs loaded with temozolomide and coated with the R₈-PNA221 probes (PNA-TMZ-MSNPs). At the end of each of incubations, cells were trypsinized and cell pellets were harvested. The total cell viability was estimated and used as a direct indication of the cytotoxic effect of the material. The results are summarized in Figure 5.6 and 5.7.

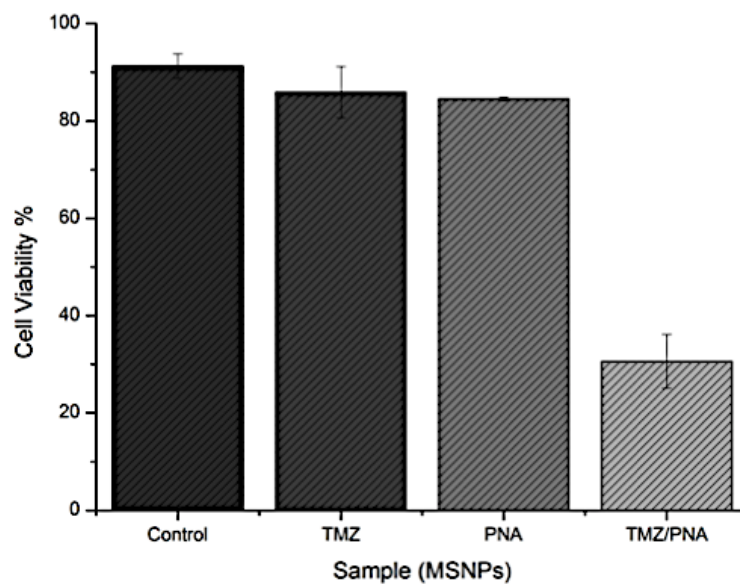


Fig. 5.6 Cell viability values measured after 24 hours of incubation for C6 rat glioma cells. Control (pure cell culture) 91.3% , TMZ-MSNPs 85.9%, PNA-MSNPs 84.6%, PNA-TMZ-MSNPs 30.6%. All experiments were reproduced in triplicate

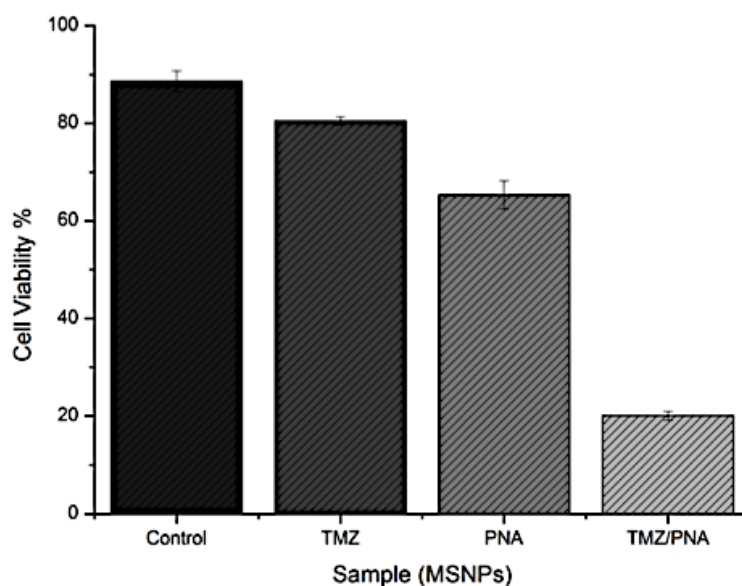


Fig. 5.7 Cell viability values measured after 48 hours of incubation for C6 rat glioma cells. Control (pure cell culture) 88.6%, TMZ-MSNPs 80.5%, PNA-MSNPs 65.3%, PNA-TMZ-MSNPs 20.1%. All experiments are reproduced in triplicate.

After 24 hours, TMZ-MSNPs and PNA-MSNPs showed a very small effect on cell viability, but very interestingly the dual delivery of the drug and the anti-miR-221 PNA probes (PNA-TMZ-MSNPs) determined a drastic reduction in the cell viability, up to a 30% value. After 48 hours, a visible reduction of cell viability was also observed for both TMZ-MSNPs and PNA-MSNPs, but a massive reduction was obtained for PNA-TMZ-MSNPs, which further decreased cell viability to 20% (Figure 5.7). This set of data suggests the combined delivery of temozolomide and anti-miR-221 PNAs can efficiently provide a synergistic cytotoxic effect to the C6 glioma cells, which is always higher than the mere sum of the contributions of the two mono-functionalized particles (TMZ-MSNPs and PNA-MSNPs).

Hence, due to the very promising results by far obtained, the system was tested on a TMZ-resistant T98G human glioma cell line, which will be described in the next paragraphs.

5.6 Effects of PNA-MSNPs on miR-221

Experiments on a human cell line were performed at the University of Ferrara by Professor Roberto Gambari's group. When the glioma cell line T98G was cultured in the presence of PNA-MSNPs a very reproducible effect was obtained, as shown in Figure 4.14. The results demonstrate that the miR-221 specific hybridization signal was reduced when RNA was isolated from T98G glioma cell lines cultured for 48 h in the presence of 0.25 mg/ml of PNA-MSNPs. As elsewhere published, no major effects have been obtained in these experiments using a neutral PNA anti-miR22.^[39] PNA-MSNPs (0.25 mg/ml, corresponding to 0.9 μ M concentration of R₈-PNA) induced a significant reduction in the miR221 bioavailability, as shown by the lower values obtained by qRT-PCR; the cationic PNA R₈-PNA221 at a comparable concentration (1 μ M) inhibited miR221 only slightly more efficiently (Figure 5.8). Since this test measures the competition of PNA and RT-PCR machinery for the target miR, this difference is probably due to delayed release of the PNA from the nanoparticles.

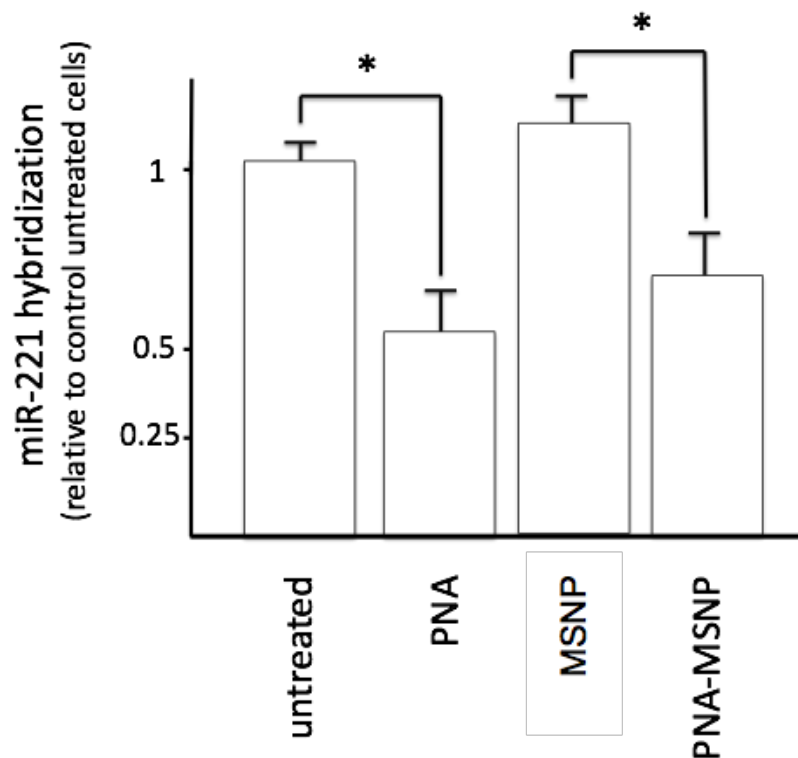


Fig. 5.8 Real time detection of miR-221 in T98G cells treated with PNA-MSNPs. T98G cells were cultured for 48 hours in the presence of 0.25 mg/ml MSNP, 0.25 mg/ml PNA-MSNP or 1 μ M R₈-PNA221, the RNA extracted and qRT-PCR identifying miR221 performed and compared to control untreated cells.

5.7 Effects of PNA-TMZ-MSNPs on apoptosis of glioma T98G cells

In the experiments described in Figure 5.9 (performed in triplicate) the TMZ-resistant T98G cell line was used and exposed to 0.1 and 0.5 mg/ml MSNPs either empty or carrying TMZ, R₈-PNA221 (PNA-MSNPs) and both TMZ and R₈-PNA221 (PNA-TMZ-MSNPs). The FACS analysis shown in Figure 4.15 suggests that a concentration-dependent uptake is obtained when T98G cells are treated for 24 hours with MSNPs, TMZ-MSNPs, PNA-MSNPs and TMZ-PNA-MSNPs. This analysis clearly indicates that almost all of the cells interact with the different MSNP-based formulations.

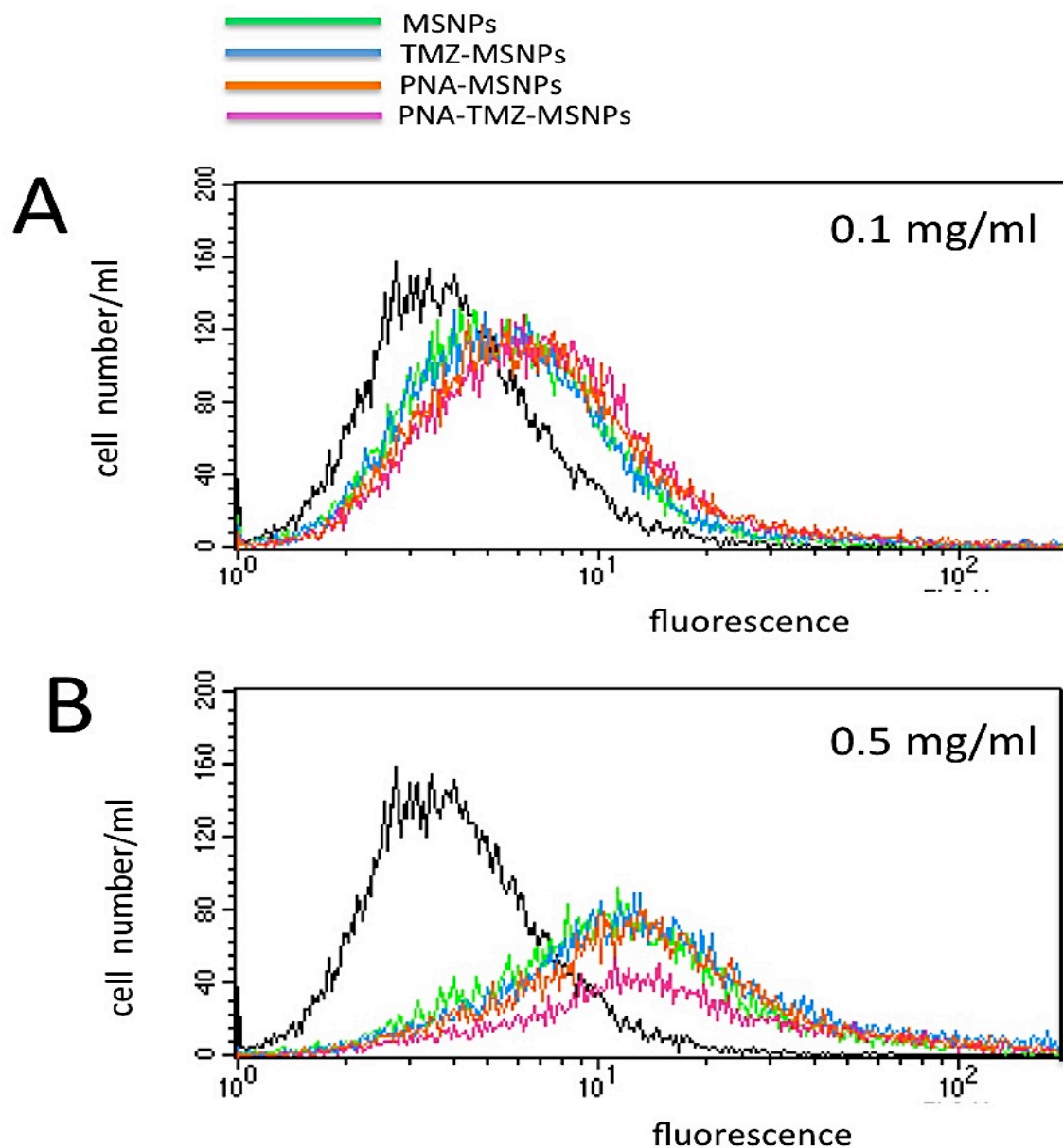


Fig. 5.9 FACS analysis on T98G cells cultured with MSNP-based formulations. T98G cells were cultured for 24 hours in the absence of treatments (black lines), with 0.1 (A) and 0.5 (B) mg/ml MSNPs (green lines), TMZ-MSNPs (blue lines), PNA-TMZ (orange lines) or TMZ-PNA-MSNPs (purple lines).

The glioma cell line T98G was cultured in the presence of TMZ. These cells are temozolomide resistant since a dramatic difference is observed when TMZ effects on T98G are compared to those obtained on TMZ-sensitive cell lines (such as glioma U251 cells) (6.22% apoptotic cells were obtained when 100 μ M TMZ was used, while 400 μ M TMZ caused highly cytotoxic and growth-suppression effects). The result shown in Figure 5.10 demonstrated that, as expected, TMZ was unable to induce high levels of apoptosis (see the summary results in Figure 5.10 and compare figure 5.10C with panels 5.10A and B). On the contrary, as elsewhere reported when

using a longer PNA sequence,^[39] R₈-PNA221 was able to induce apoptosis, as shown in Figure 6, panel D, leading to a significant increase of late apoptotic cells. It should be underlined that, at least in this cell line, a slight increase of apoptosis could be detected after exposure to unloaded MSNPs, either used at 0.1 mg/ml or 0.5 mg/ml (Figure 5.10 E, F and O). However, a further significant increase of apoptosis in T98G cells cultured in the presence of TMZ-MSNPs, PNA-MSNPs and PNA-TMZ-MSNPs was observed (see representative data shown in panels A-N, and the summary shown in panel O). In the case of delivery of the R₈-PNA221, the data conclusively show that MSNPs complexation does not interfere with R₈-PNA221 activity in intact cells. In the case of TMZ delivery, the conversion of T98G cells from TMZ-resistant to TMZ-sensitive was observed; in fact it is remarkable to have obtained 49.1% of apoptotic cells in TMZ-MSNPs treated T98G cells, a value significantly higher than the combined background levels of apoptosis observed in untreated and free-MSNPs treated cells (compare panel H with panels A and F). In any case, the induction of T98G apoptosis is particularly evident in the case of 0.5 mg/ml PNA-TMZ-MSNPs, which induced 70.86% total apoptotic cells, with an increase of 50.39% with respect to unloaded MSNPs. The summary of the MSNPs mediated effects are reported in Figure 5.10, panel O, for 0.5 mg/ml MSNPs, since this MSNP concentration approaches the reference concentrations of TMZ (400 μM, panel C of Figure 5.10) and R₈-PNA221 (2 μM, panel D of Figure 5.10). However, the effects of PNA-TMZ-MSNPs were also evident when the 0.1 concentration set was comparatively examined. In fact, 0.1 mg/ml PNA-TMZ-MSNPs induced a total of 26.92% apoptotic cells, with an increase of 15.60% with respect to unloaded MSNPs. The full set of data obtained indicate several remarkable effects: i) the MSNP alone showed a slight apoptosis induction, in line with earlier studies,^[66] which were attributed to the induction of oxidative response; ii) TMZ-MSNPs increase the proportion of apoptotic cells in respect to control MSNPs, whereas, as expected considering that the T98G cells are TMZ-resistant, 400 μM TMZ induces apoptosis with very low efficiency; this is attributed to the sustained release of TMZ, which is protected from clearance by the MSNP platform and slowly released over time within cells; iii) the PNA-MSNP have a pro-apoptotic effect slightly higher than that of R₈-PNA at comparable concentrations; iv) the multifunctional system displaying more efficiency in induction of apoptosis of T98G cells was PNA-TMZ-MSNPs, strongly suggesting a role of MSNP-delivered TMZ and PNA. The data also show that sustained release of TMZ was not contrasted by the combination of anti-miR221 PNA, but rather that an additional effect could be obtained, the combined delivery of these two agents having a massive effect on the induction of cell apoptosis in the tumor cell line.

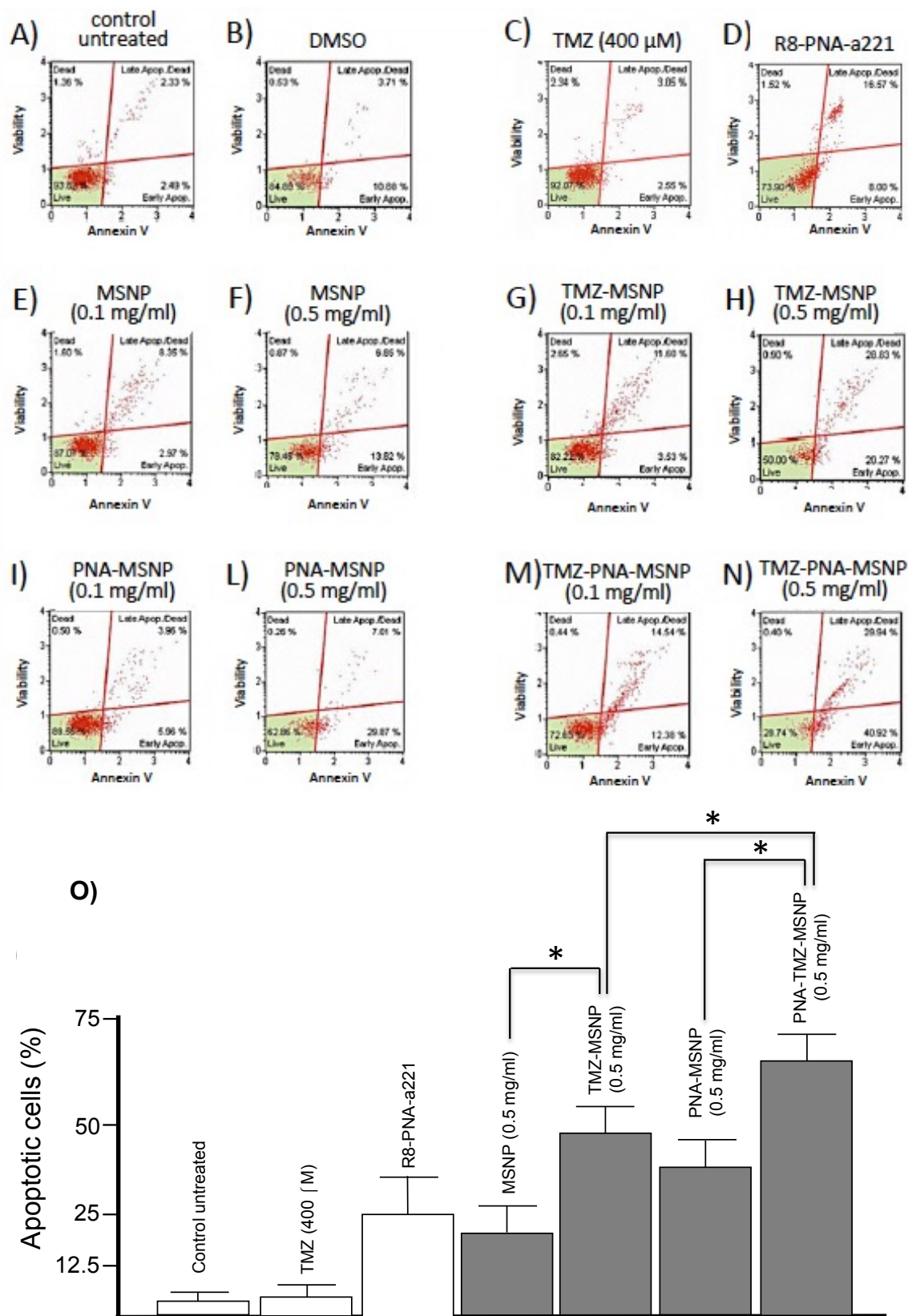


Fig. 5.10 TMZ-PNA-MSNPs induce apoptosis of glioma T98G cells. T98G cells were cultured for 48 hours in the absence of treatments (A), with 12.5 μ l DMSO (B), 400 μ M TMZ (C), 2 μ M R₈-PNA221 (D), 0.1 (E) and 0.5 (F) mg/ml MSNPs, 0.1 (G) and 0.5 (H) mg/ml TMZ-MSNPs, 0.1 (I) and 0.5 (L) mg/ml PNA-MSNPs, or 0.1 (M) and 0.5 (N) mg/ml PNA-TMZ-MSNPs. Cells were isolated and apoptosis was determined using Annexin V exclusion test, as described in the Materials and Methods section.

5.8 Conclusion

Although TMZ offers some hope to glioma patients, presently only low 5-year survival rate are achieved.^[67-68] The anti-miR approach is thus a possible alternative as it is now a major focus in translational research: clinical trials are being carried out for several anti-miR drugs, and, most notably, one clinical trial on humans is currently underway.^[69] Though nanocarriers such as mesoporous silica have been extensively used to enhance the efficiency of drugs by delayed release and protection from clearance (sustained drug release), and artificial DNA analogues such as LNA and PNA have been used as anti-miR drug candidates, the combination of mesoporous silica nanocarriers and anti-miR agents like PNA has not been explored so far.

The nanocarrier synthesized in the present work has multiple-purpose effects: it can protect and deliver the TMZ included; once internalized it can slowly release the TMZ, thus preventing clearance of the drug; at the same time it can allow intracellular delivery of the anti-mR221 PNA, thus acting downstream on important cell-cycle regulatory proteins. The combined delivery of these two systems has a massive effect on the induction of apoptosis. Therefore TMZ-PNA-MSNPs can be proposed as a novel approach to tackle drug-resistance in gliomas. This is a key issue, since after surgery and radiotherapy, the chemotherapy protocol commonly suffers from the development of drug-resistant glioma cells, as in the case of the usage of TMZ. Since strategies for the delivery of inorganic nanoparticle through the blood-brain-barrier (BBB) have been described, and since MSNP have been reported to accumulate into tumor tissues, the present strategy can be further exploited for the multiple-target treatment of gliomas, highly recurrent, frequently drug resistant, and life-threatening tumors.

5.9 Experimental section

Synthesis of cationic anti-miR-211 PNA (8R-PNA221)

The cationic anti-miR-221 PNA H-RRRRRRRRR-GCAGACAATGTAGCT-Gly-NH₂ (where R is an arginine residue) was synthesized with standard manual Boc-based chemistry using commercially available PNA monomers, with HBTU/DIPEA coupling as described elsewhere.^[70] The synthesis was carried out in a 10 μmol scale using MBHA resin loaded with Fmoc-Gly as a first monomer. The R8 cationic arginine tail was introduced using the same coupling procedures utilizing Boc-D-Arg(Tos)-OH residues. PNA purification was performed by RP-HPLC with UV detection at 260 nm using a semi-prep column C18 (10 μm, 7.8x300 mm, Xterra Waters), eluting with water containing 0.1% TFA (eluent A) and acetonitrile containing 0.1% TFA (eluent B); elution gradient: from 100% A to 50% B in 30 min, flow: 4 mL/min. The resulting pure PNA

oligomer was characterized by ESI-MS, which gave positive ions consistent with the final products: m/z found (calcd) 1084.5 (1084.5) $[M+5H]^{5+}$, 903.7 (903.9) $[M+6H]^{6+}$, 774.7 (774.9) $[M+7H]^{7+}$, 678.0 (678.2) $[M+8H]^{8+}$, 602.9 (602.9) $[M+9H]^{9+}$, 542.4 (542.7), $[M+10H]^{10+}$.

Amine-functionalization of MSNPs

(3-Aminopropyl)dimethylmethoxysilane (APDMS) (150 μ L) was added to a dispersion of 400 mg of MSNPs in ethanol, in presence of a catalytic amount of triethylamine (TEA). The mixture was then stirred overnight at room temperature. The particles were recovered by centrifugation and washed several times with ethanol.

Removal of CTAB from MSNP pores

CTAB was removed from MSNP pores by shaking the particles overnight in ethanol containing few drops of HCl 37%. Afterwards, they were recovered by centrifuging and washed several times with ethanol and water.

Carboxylate-functionalization of MSNPs (COOH-MSNPs)

MSNPs (80 mg) were dispersed in DMSO (10 mL), then succinic anhydride (100 mg) was added, and the mixture was stirred overnight at room temperature. The material was then recovered by centrifuging and washed three times with DMSO and twice with water.

Temozolomide loading (TMZ-MSNPs)

COOH-MSNPs (20 mg) were dispersed in 5 mL of methanol and 15 mg of temozolomide (TMZ) were added. The mixture was thoroughly sonicated to get a homogenous dispersion and then stirred overnight at room temperature. Methanol was then directly evaporated under vacuum, and the particles were washed with methanol and water to remove the non-internalized drug.

PNA-functionalization of MSNPs (PNA-MSNPs)

TMZ-MSNPs or COOH-MSNPs (10 mg) were dispersed in 1 mL of a 90 μ M aqueous solution of R₈-PNA221, and the mixture was stirred at room temperature for 4 hours. Afterwards, the material was recovered by centrifugation and washed with water.

Cell culture

Rattus norvegicus brain glioma (C6 glioma) cells were cultured inside media containing 88% Dulbecco's Modified Eagle Medium (DMEM), 10% Fetal Bovine Serum (FBS), 1% Penicillin-

Streptomycin and 1% L-Glutamine 200mM (all materials for cell culture were purchased from Gibco), under 37°C and 5% of CO₂ condition for 48 hours until reaching 80 to 90% cell confluency. Successively, the cells were washed twice with Phosphate Buffer Solution (PBS), trypsinated and approximately 50,000 cells were reseeded on the rectangular glass cover slip (VWR) inside six-well plate culture dish. 2 ml of fresh culture media was added gently and cells were grown overnight.

Human glioblastoma multiforme T98G cell line was cultured in humidified atmosphere of 5% CO₂/air in RPMI 1640 medium (Life Technologies, Monza, Italy) supplemented with 10% fetal bovine serum (FBS, Celbio, Milan, Italy), 100 units/ml penicillin and 100 mg/ml streptomycin.

Nanoparticle incubation for cell uptake recording and cell staining

Growth serum was removed and 1 mL of nanoparticle dispersion was gently added onto cells. Incubation period was done for 1, 4, and 24 hours. After incubation at 37°C and 5% of CO₂, the media was removed and the cell layer on glass cover slips was gently washed (three times) with PBS and fixed with 4% paraformaldehyde (PFA) solution for 10 minutes. Next, cell layer was washed twice with PBS and kept in 0.1% Triton X-100 in PBS for 5 minutes and afterwards in 1% bovine serum albumin, BSA (Sigma Aldrich), in PBS for 20 minutes. The cell layer on glass cover slip was stained with Phalloidin Alexa Fluor® 568 (Invitrogen), for F-actin/membrane staining, for 20 minutes, in the dark at room temperature, and washed twice with PBS and one time with water. The cover slips were mounted onto glass slides for microscopy measurements.

Fluorescence confocal microscopy experiments

All depicted fluorescence microscopy images were acquired by using Zeiss LSM 710 confocal microscope system with 63 times magnification, numerical aperture 1.3 of Zeiss LCI Plan-NEOFLUAR water immersion objective lens (Zeiss GmbH). The CY5 modified particles inside the cells were excited by a continuous wave (cw) laser at 633 nm while for the cells priorly co-stained with Alexa Fluor® 568 Phalloidin dye (excitation/emission wavelength: 578 nm/600 nm) were excited independently at 543 nm, respectively. The emission of the particles and Alexa Fluor® 568 Phalloidin were collected using their corresponding emission filter. All image processing was proceeded by ZEN software (Zeiss GmbH). False colour images were adjusted to better distinguish the particles and cellular organelles (F-actin).

Cell viability test

Cell viability test on C6 glioma cells was conducted based on non-invasive Electrical Current Exclusion (ECE) principle using an automatic CASY cell counting (Roche Innovatis AG). Approximately 50,000 cells were grown in 2 ml of fresh media inside 6 well plates at 37°C, 5% CO₂ environment overnight. The serum was removed and replaced independently with 1 ml of the nanoparticle dispersion respectively, namely TMZ-MSNPs, PNA-MSNPs, and PNA-TMZ-MSNPs (concentration 0.17 mg/mL). Subsequently, after 24 and 48 hours of incubation, the nanoparticle solutions were removed to Eppendorf tubes and 0.5 ml of trypsin-EDTA 0.25% (Invitrogen) were added. Cells were detached from the surface by rinsing for 5 minutes in the same condition explained before. Next, 0.5 ml of pure medium was added to neutralize trypsin. Cell suspensions were collected into the same Eppendorf tube and gently mixed. 100 µl of the cell suspension was dissolved in 10 ml of CASY-ton solution (Roche Innovatis AG) and measurement was performed.

Quantitative analyses of miRNAs

Reverse transcriptase (RT) reactions were performed using the TaqMan® MicroRNA Reverse Transcription Kit (Applied Biosystems, Foster City, CA, USA); real-time PCR was performed according to the manufacturer's protocols. Twenty ng per sample were used for the assays. All RT reactions, including no-template controls and RT-minus controls, were performed in duplicate using the CFX96 Touch™ Real-Time PCR Detection System (Bio-Rad Laboratories, Milan, Italy). The relative expression was calculated using the comparative cycle threshold method and as reference U6 snRNA was used to normalize all RNA samples, since it remains constant in the assayed samples by miR-profiling and quantitative RT-PCR analysis, as previously reported⁵⁰.

Analysis of apoptosis

Annexin V and Dead Cell assay on T98G cell line, untreated and treated for 48 h with different concentrations of temozolomide, R8-PNA-a221 and MSNPs, were performed with “Muse”™ (Millipore Corporation, Billerica, MA, USA) method, according to the instructions supplied by the manufacturer. This procedure utilizes Annexin V to detect PS (Phosphatidyl Serine) on the external membrane of apoptotic cells. A dead cell marker is also used as an indicator of cell membrane structural integrity. It is excluded from live, healthy cells, as well as early apoptotic cells. Four populations of cells can be distinguished in this assay. Cells were washed with sterile PBS 1X, trypsinized, suspended and diluted (1:2) with the one step addition of the Muse™ Annexin V & Dead Cell reagent. After incubation of 20 min at room temperature in the dark, samples were analyzed. Data from prepared samples are acquired and recorded utilizing the Annexin V and Dead

Cell Software Module (Millipore).

Cellular uptake by FACS analysis

T98G cells were culture in presence of MSNPs at 0.1 and 0.5 mg/ml concentrations for 24 hours. After incubation, for the determination of the cellular fluorescence intensity a FACScan (Becton Dickinson) was used. Cells were harvested and washed; then 20000 cells were analyzed using the FL2 channel to detect red fluorescence and the Cell Quest Pro software to analyze the data. The results were expressed as median fold, the ratio between the median of fluorescence intensity values obtained by cells in the presence and in the absence of treatment, respectively; also the MPF% (Median Peak Fluorescence %), expressing the increase % of the fluorescence value caused by the inducer molecule, could be used. A graphic presentation of data was finally obtained both by histograms, showing the number of cells versus the fluorescence intensity expressed (FL2), and cytograms, showing the sideward light scatter (SSC) versus either the forward light scatter (FSC) or the fluorescence intensity (FL2).

REFERENCES

- [1] H. Ling, M. Fabbri, G.A. Calin, *Nat. Rev. Drug Discover.* **2013**, *12*, 847-865.
- [2] L. He, G.J. Hannon, *Nat. Rev. Genet.* **2004**, *5*, 522-531.
- [3] D.P. Bartel, *Cell* **2004**, *116*, 281-297.
- [4] Y. Lee, K. Jeon, J.T. Lee, S. Kim, V.N. Kim, *EMBO J.* **2002**, *21*, 4663-4670.
- [5] G. Hutvagner, J. McLachlan, A.E. Pasquinelli, E. Bálint, T. Tuschl, P.D. Zamore, *Science* **2001**, *693*, 834-838.
- [6] R.W. Carthew, E.J. Sontheimer, *Cell* **2009**, *136*, 642-655.
- [7] M. Tijsterman, R.H. Plasterk, *Cell* **2004**, *117*, 1-3.
- [8] S. Obad, C.O. Dos Santos, A. Petri, M. Heidenblad, O. Broom, C. Ruse, S. Kauppinen, *Nat. Genet.* **2011**, *43*, 371-378.
- [9] N. Bushati, S.M. Cohen, *Annu. Rev. Cell Dev. Biol.* **2007**, *23*, 175-205.
- [10] P. Maziere, A.J. Enright, *Drug Discov. Today* **2007**, *12*, 452-458.
- [11] J. Brennecke, A. Stark, R.B. Russell, S.M. Cohen, *PLoS Biol.* **2005**, *3*, e85.
- [12] P. Brodersen, O. Voinnet, *Nat. Rev. Mol. Cell Biol.* **2009**, *10*, 141-148.
- [13] H.F. Lodish, B. Zhou, G. Liu, C.Z. Chen, *Nat. Rev. Immunol.* **2008**, *8*, 120-130.
- [14] S.K. Kota, S. Balasubramanian, *Drug Discov. Today* **2010**, *15*, 733-740.
- [15] A.G. Bader, D. Brown, M. Winkler, *Cancer Res.* **2010**, *70*, 7027-7030.
- [16] C.R. Sibley, Y. Seow, M.J. Wood, *Mol. Ther.* **2010**, *18*, 466-476.
- [17] R. Gambari, E. Fabbri, M. Borgatti, I. Lampronti, A. Finotti, E., *et al. Biochem. Pharm.* **2011**, *82*, 1416-1429.
- [18] S. Volinia, G.A. Calin, C.G. Liu, S. Ambs, A. Cimmino, F. Petrocca, *et al. Proc. Natl. Acad. Sci. USA* **2006**, *103*, 2257-2261.
- [19] D.M. Pereira, P.M. Rodrigues, P.M. Borralho, C.M. Rodrigues, *Drug Discov. Today* **2013**, *18*, 282-289.
- [20] B. Xie, Q. Ding, H. Han, D. Wu, *Bioinformatics* **2013**, btt014.
- [21] D.R. Hurst, M.D. Edmonds, D.R. Welch, *Cancer Res.* **2009**, *69*, 7495-7498.

- [22] T.A. Farazi, J.I. Spitzer, P. Morozov, T. Tuschl, *J. Pathol.* **2011**, *223*, 102-115.
- [23] J.K. Björk, A. Sandqvist, A.N. Elsing, N. Kotaja, L. Sistonen, *Development* **2010**, *137*, 3177–3184.
- [24] P.P. Medina, M. Nolde, F.J. Slack, *Nature* **2010**, *467*, 86-90.
- [25] S.D. Selcuklu, M.A. Donoghue, C. Spillane, *Biochem. Soc. Trans.* **2009**, *37*, 918.
- [26] M. Kano, N. Seki, N. Kikkawa, L. Fujimura, I. Hoshino, Y. Akutsu, *et al. Int. J. Cancer.* **2010**, *127*, 2804–2814.
- [27] N. Nohata, Y. Sone, T. Hanazawa, M. Fuse, N. Kikkawa, H. Yoshino, *et al. Oncotarget* **2011**, *2*, 29–42.
- [28] M.D. Edmonds, D.R. Hurst, D.R. Welch, *Cell Cycle* **2009**, *8*, 2673–2675.
- [29] S. Jiang, H.W. Zhang, M.H. Lu, X.H. He, Y. Li, H. Gu, *et al. Cancer Res.* **2010**, *70*, 3119–3127.
- [30] C.L. Esposito, L. Cerchia, S. Catuogno, G. De Vita, J.P. Dassie, G. Santamaria, V. de Franciscis, *Mol. Ther.* **2014**, doi:10.1038/mt.2014.5.
- [31] P. Trang, J.F. Wiggins, C.L. Daige, C. Cho, M. Omotola, D., Brown, F.J. Slack, *Mol. Ther.* **2011**, *19*, 1116-1122.
- [32] I.A. Babar, C.J. Cheng, C.J. Booth, X. Liang, J.B. Weidhaas, W.M. Saltzman, F.J. Slack, *Proc. Natl. Acad. Sci. U.S.A.* **2012**, *109*, 1695-1704.
- [33] H.L. Janssen, H.W. Reesink, E.J. Lawitz, S. Zeuzem, M. Rodriguez-Torres, K. Patel, *et al. N. Engl. J. Med.* **2013**, *368*, 1685-1694.
- [34] A. Tivnan, W.S. Orr, V. Gubala, R. Nooney, D.E. Williams, C. McDonagh, *et al. PloS one* **2012**, *7*, e38129.
- [35] P. Pineau, S. Volinia, K. McJunkin, A. Marchio, C. Battiston, B. Terris, *et al. Proc. Natl. Acad. Sci. U.S.A.* **2010**, *107*, 264-269.
- [36] J. Radojicic, A. Zaravinos, T. Vrekoussis, M. Kafousi, A.D. Spandidos, E.N. Stathopoulos, *Cell Cycle* **2011**, *10*, 507-517.
- [37] H. He, K. Jazdzewski, W. Li, S. Liyanarachchi, R. Nagy, S. Volinia, G.A. Calin, C.G. Liu, K. Franssila, S. Suster, *et al. Proc. Natl. Acad. Sci. U.S.A.* **2005**, *102*, 19075-80.
- [38] J. Zhang, L. Han, Y. Ge, X. Zhou, A. Zhang, C. Zhang, *et al. Int. J. Oncol.* **2010**, *36*, 913-920.
- [39] E. Brognara, E. Fabbri, E. Bazzoli, G. Montagner, C. Ghimenton, A. Eccher, *et al. J. Neuro-Oncol.* **2014**, *118*, 19-28.
- [40] C.Z. Zhang, J.X. Zhang, A.L. Zhang, Z.D. Shi, L. Han, Z.F. Jia, *et al. Mol. Cancer* **2010**, *9*, 229.
- [41] C. Zhang, C. Kang, Y. You, P. Pu, W. Yang, P. Zhao, *et al. Int. J. Oncol.* **2009**, *34*, 1653-1660.
- [42] J.K. Gillies, I.A. Lorimer, *Cell Cycle* **2007**, *6*, 2005.
- [43] T.E. Miller, K. Ghoshal, B. Ramaswamy, S. Roy, J. Datta, C.L. Shapiro, *et al. J. Biol. Chem.* **2008**, *283*, 29897-29903.
- [44] L. Chen, J. Zhang, L. Han, A. Zhang, C. Zhang, Y. Zheng, *et al. Oncol. Reports* **2012**, *27*, 854.
- [45] C. Quintavalle, D. Mangani, G. Roscigno, G. Romano, A. Diaz-Lagares, M. Iaboni, *et al. PLoS One* **2013**, *8*, e74466.
- [46] T.C. Hirst, H.M. Vesterinen, E.S. Sena, K.J. Egan, M.R. MacLeod, I.R. Whittle, *Br. J. Cancer* **2013**, *108*, 64-71.
- [47] H.M. Strik, C. Marosi, B. Kaina, B. Neyns, *Curr. Neurol. Neurosci. Rep.* **2012**, *12*, 286-293.
- [48] M.M. Fabani, C. Abreu-Goodger, D. Williams, P.A. Lyons, A.G. Torres, K.G. Smith, *et al. Nucleic acids Res.* **2010**, gkq160.
- [49] E. Fabbri, A. Manicardi, T. Tedeschi, S. Sforza, N. Bianchi, E. Brognara, *et al. ChemMedChem* **2011**, *6*, 2192-2202.
- [50] S.R. Ryoo, J. Lee, J. Yeo, H.K. Na, Y.K. Kim, H. Jang, *et al. ACS Nano* **2013**, *7*, 5882-5891.
- [51] E. Brognara, E. Fabbri, F. Aimi, A. Manicardi, N. Bianchi, A. Finotti, *et al. Int. J. Oncol.* **2012**, *41*, 2119-2127.

- [52] E. Fabbri, E. Brognara, M. Borgatti, I. Lampronti, A. Finotti, N. Bianchi, *et al. Epigenomics* **2011**, *3*, 733-745.
- [53] F. Torney, B.G. Trewyn, V.S.Y. Lin, K. Wang, *Nat. Nanotech.* **2007**, *2*, 295-300.
- [54] C.H. Lee, S.H. Cheng, Y.J. Wang, Y.C. Chen, N.T. Chen, J. Souris, *et al. Adv. Funct. Mater.* **2009**, *19*, 215-222.
- [55] F. Lu, S.H. Wu, Y. Hung, C.Y. Mou, *Small* **2009**, *5*, 1408-1413.
- [56] U. Koppelhus, T. Shiraishi, V. Zachar, S. Pankratova, P.E. Nielsen, *Bioconjugate Chem.* **2008**, *19*, 1526-1534.
- [57] A. Albanese, P.S. Tang, W. Chan, *Annu. Rev. Biomed. Eng.* **2012**, *14*, 1-16.
- [58] A. Candiani, A. Bertucci, S. Giannetti, M. Konstantaki, A. Manicardi, S. Pissadakis, *et al. J. Biomed. Opt.* **2013**, *18*, 057004.
- [59] U. Koppelhus, P.E. Nielsen, *Adv. Drug Deliver. Rev.* **2003**, *55*, 267-280.
- [60] J. Zhang, L. Han, Y. Ge, X. Zhou, A. Zhang, C. Zhang, *et al. Int. J. Oncol.* **2010**, *36*, 913-920.
- [61] Y. Wang, X. Wang, J. Zhang, G. Sun, H. Luo, C. Kang, Y. You *J. Neuro-Oncol.* **2012**, *106*, 217-224.
- [62] J.K. Kim, K.J. Choi, M. Lee, M.H. Jo, S. Kim *Biomaterials* **2012**, *33*, 207-217.
- [63] T. Kato, A. Natsume, H. Toda, H. Iwamizu, T. Sugita, R. Hachisu, *et al. Gene Ther.* **2010**, *17*, 1363-1371.
- [64] H. Zhang, S. Gao, *Int. J. Pharm.* **2007**, *329*, 122-128.
- [65] S. Ni, X. Fan, J. Wang, H. Qi, X. Li, *Ann. Biomed. Eng.* **2014**, *42*, 214-221.
- [66] X. Li, Q. He, J. Shi, *ACS nano* **2014**, *8*, 1309-1320.
- [67] Z. Lwin, d. MacFadden, A. Al.Zahrani, E. Atenafu, B.A. Miller, A. Sahgal, C. Menard, N. Laperriere, W.P. Mason, *J. Neurooncol.* **2013**, *115*, 303-310.
- [68] R. Stupp, M.E. Hegi, W.P. Mason, M.J. van den Bent, M.J. Taphoorn, R.C. Janzer, *et al. Lancet Oncol.* **2009**, *10*, 459-466.
- [69] H.L. Janssen, H.W. Reesink, E. Lawitz, S. Zeuzem, M. Rodriguez-Torres, K. Patel, *et al. New Engl. J. Med.* **2013**, *386*, 1685-1694.
- [70] A. Manicardi, A. Calabretta, M. Bencivenni, T. Tedeschi, S. Sforza, R. Corradini, R. Marchelli, *Chirality* **2010**, *22*, E161-E172.

6

Biodegradable hybrid core/shell silica nanospheres for protein encapsulation and intracellular delivery

Abstract

The direct delivery of specific proteins to live cells promises a tremendous impact in biological and medical application, from therapeutics strategies to engineered cell behavior reprogramming. This chapter describes the approach followed to create a breakable hybrid organo-silica nanoshell encapsulating protein molecules. The silica-based nature of the structure is modified with the introduction of disulfide moieties for triggering the breakdown of the shell and the consequent release of the protein cargo under reductive conditions. The breaking and release phenomena have been studied in details using Cytochrome C as a model protein cargo. The system has been then tested for the intracellular delivery, in cancer cells, of highly cytotoxic proteins demonstrating the therapeutic effect provided by the released enzymes. In addition a full investigation on the distribution and the biodegradation/release kinetics in live cells has been carried out using encapsulated Green Fluorescent Protein, which allowed for monitoring the system behavior by its fluorescence properties. The designed architecture may shine a new light on the delivery of biomacromolecules in living organisms to tackle different forms of diseases, since its biocompatible and biodegradable nature.

L. De Cola, E. A. Prasetyanto, A. Bertucci, D. Septiadi, *Disintegratable core/shell silica particles for encapsulating and releasing bioactive macromolecules*, **EP14305905**, Filed

6.1 Protein encapsulation and intracellular delivery

Several diseases are caused by the lack or low expression of important enzymes, proteins, and other biomolecules. The direct delivery of specific proteins to the cytoplasm thus holds tremendous potential in biological and medical application, from restoring the function of interest to introducing recombinant species that can regulate gene expression leading to a reprogramming of the cell behavior.^[1-5] The possible intracellular delivery of fragile, cytotoxic, or cell membrane-impermeable bioactive molecules, has to overcome serious obstacles to provide an effective therapy in live organisms though. In case of biomacromolecules such as proteins or enzymes, a further

hurdle in the release strategy is the difficulty of delivering the unmodified, functional protein or enzyme in an active conformation to the necessary site of action. In this respect, suitable delivery systems must be able to shield and protect the bioactive molecules in order to preserve their functional nature.^[6-7] Innovations in biotechnology and nanomedicine have led to a significant increase in the number of protein- and peptide-based therapeutics and other macromolecular drugs. Furthermore, recent advances in genomic and proteomic technologies are expected to continue to increase the pipeline of macromolecular therapeutic candidates.^[8-11] Nevertheless, when working with macromolecules one should take into account all the challenges that must be accomplished in order to successfully develop safe and effective therapeutics.^[12] For example, proteins and peptides tend to be degraded by proteolytic enzymes or, in the case of the higher molecular weight proteins, may be recognized by neutralizing antibodies.^[13-14] Moreover, such molecules can exhibit low solubility or poor serum stability, leading to short shelf lives.^[15-17] As a result, macromolecule-based therapeutic strategies often quickly lose their effectiveness or require frequent dosing. These factors have an impact not only on the cost of therapy, but also on patient acceptance and compliance, thus affecting the final usefulness. Hence, protein/enzyme stabilization is of great interest to a variety of applications including medical diagnostics, biocatalysis, and protein delivery. Especially for protein delivery applications, the nanocarriers or stabilizers have to fulfill stringent requirements. An ideal platform has to be not only non-toxic and non-immunogenic, but also must be able to protect labile proteins from natural deterioration, as said before. Moreover, it should be capable of providing long-term blood circulation of proteins and drugs, which can endow numerous advantages such as enhancing the efficiency of drug controlled-release, providing site specific protein delivery, as well as reducing the need for repetitive injections.^[18-19] Currently, protein stabilization for delivery purposes has mainly been achieved by micro- and nano-encapsulation (e.g. within liposomes, polymeric or inorganic structures)^[20-25] and bioconjugation (i.e. covalently linking proteins with water-soluble polymers or simply crosslinking proteins to form stable particles).^[26-30] The bioconjugation approach is however very labor intensive, and, in some cases, the process can cause the denaturation of the proteins into a conformation that results in significant activity loss.^[30-32] The encapsulation strategy has thus gained more and more attention in the past years since its promising results, and several examples of diverse host structures are reported in the literature. For instance, liposome-based nanocarriers have been recently used for intracellular release of antigenic ovalbumin.^[33] Among the polymeric structures used for protein encapsulation, PLGA nanoparticles have been reported several times as suitable platforms.^[34-36] A very useful feature that characterizes polymeric structures is the possibility of having biodegradable or, even better, stimuli-responsive networks for a controlled release.^[37-42] A unique example is also provided

by Hilvert's group, reporting the use of an engineered protein container to encapsulate GFP within a protein-protein core/shell architecture.^[43]

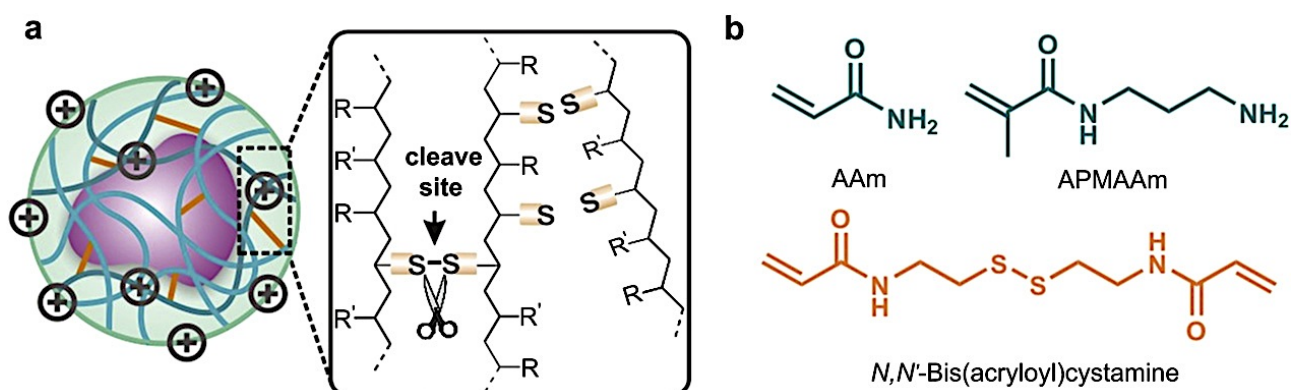


Fig. 6.1 Formation of redox-responsive protein nanocapsules. A) Schematic picture of protein nanocapsules with redox-responsive polymeric matrix (R and R' represent different monomer moieties); B) Chemical structures of monomers and crosslinker for S-S nanocapsules. Reprinted from M. Zhao, A. Biswas, B. Hu, K.I. Joo, P. Wang, Z. Gu, Y. Tang, *Biomaterials* **2011**, 32, 5223-5230. Copyright (2011), with permission from Elsevier.

The strategy based on polymer-based encapsulation may however suffer some lack of stability since only physical interactions are present between the polymer framework and the proteins, which can lead to a dismantling of the system before reaching the target area.^[44-45] Besides organic, the use of inorganic platforms for fabricating hybrid structures has been also shown, and silica particles have been proposed as attractive candidates.^[46-49] For instance, GFP has been encapsulated within a silica shell to create robust fluorescent bio-probes,^[50] and very recently the intracellular implantation of enzymes in hollow silica nanospheres for biocatalysis has been reported.^[51]

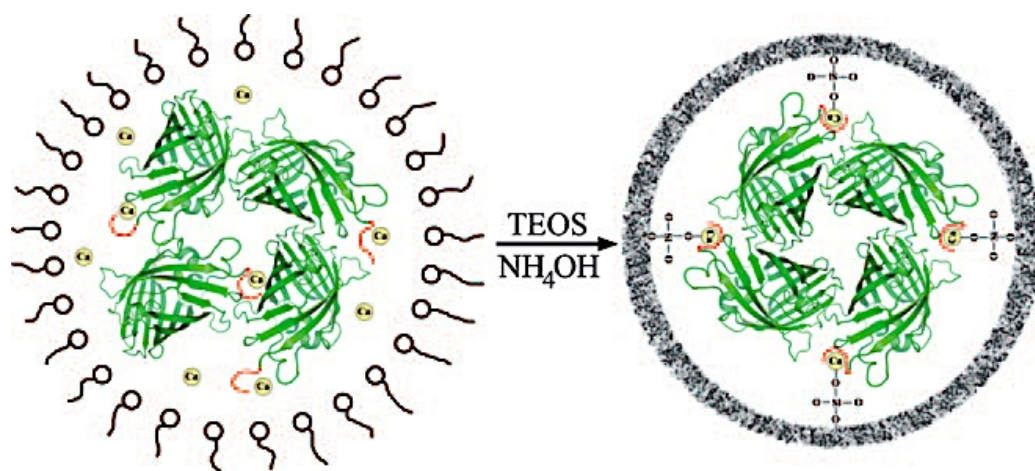


Fig. 6.2 Encapsulation of His-tagged EGFP (green) within a silica shell in presence of calcium ions acting as coordinating agents between the His-tags and the silica framework. Reprinted from A. Cao, Z. Ye, Z. Cai, E. Dong, X. Yang, G. Liu, *et al. Angew. Chem. Int. Ed.* **2010**, 49, 3022-3025. Copyright © 2010 WILEY-VCH Verlag GmbH & Co. KGaA, Weinheim

Nevertheless, therapeutic *in vitro* or *in vivo* applications using silica-protein hybrid architectures have not been demonstrated yet, as the release from an integer silica shells still remains a limit to overcome.

In this context, the development of an innovative system able to encapsulate bioactive macromolecules having improved stability properties, engineered in order to break into pieces for an efficient *in vitro* and *in vivo* delivery, but to survive the harsh environmental biological conditions to preserve the protein active folding, would represent a massive breakthrough. In this chapter, the realization of hybrid organic/inorganic core/shell nanoparticles in which diverse proteins are encapsulated within a biodegradable silica-based shell for the enzyme delivery into living cells, will be presented. The novel material represents an exceptional striking approach towards a safe and smart enzyme and protein delivery to live cells, in *in vivo*, and ultimately to cure diseases.

6.2 Core/shell capsules fabrication and characterization

The design for the realization of a breakable shell able to encapsulate a protein in its native folding and avoiding its denaturation must include some key elements: 1. A first protecting layer must be built around the protein in order to encapsulate the system in water and to maintain an “organic” environment before the silica shell is wrapped around. 2. The silica shell in order to be breakable must contain degradable groups that upon rupture will lead to the fragmentation of the entire capsule. We have therefore devised a methodology to implement all the required features. A hybrid organo-silica shell was built up directly around the protein cargo following a reverse nanoemulsion technique. The possibility of creating a biodegradable material involves the introduction into the silica network of organic elements whose rupture is triggered by a chemical reaction stimulus. Hence, the hybrid shell was synthesized using a mixture 40:60 of tetraethyl orthosilicate (TEOS) and bis[3-(triethoxysilyl)propyl]disulfide, which allowed for creating a silica-based structure containing disulfide bridges as hybrid elements. The disulfide group is indeed the responsive unit of the organosilica shell. The silica provides important properties such as: particle homogeneity, chemical stability and resistance, biocompatibility, while the disulfide bridge displays the unique feature of a reversible covalent bond: breakable, when a reducing agent is added, due to the reduction of the disulfide to thiol groups and, as a consequence, leading to the deformation and finally breakdown of the structure. Upon the destruction of the capsule, the protein cargo is indeed free to be delivered, leaving behind the small pieces of the wrecked shells. The choice of using disulfide bridges is based on the possibility of exploiting the reductive environment present in the

cells, and especially the one of the cancer cells overproducing the reductive agent glutathione. Glutathione is an abundant natural highly reactive tripeptide found within almost all cells. With respect to cancer, glutathione is found in elevated levels in tumor cells and its metabolism is able to play both protective and pathogenic roles.^[52-53] It is worth saying that the commercial availability of the disulfide silane favors indeed a quicker and less laborious experimental procedure, which is important when thinking on real applications on a larger scale.

The actual realization of the shell was performed following the reverse nanoemulsion procedure described in the experimental section, which is based on the formation of protein containing water drops in an organic medium, in presence of surfactants helping the construction of the silica layer around the drops. The first attempt on developing such a system was then carried out using Cytochrome C p450 as a model protein, since its absorption in the visible range favors the immediate visualization of the formation of the protein containing particles and enables an easy design of the following release experiments. In this way, very well defined nanospheres presenting a diameter around 40-50 nm were obtained (CyC@BS-NP), as shown by the SEM and TEM pictures reported in Figure 6.4.

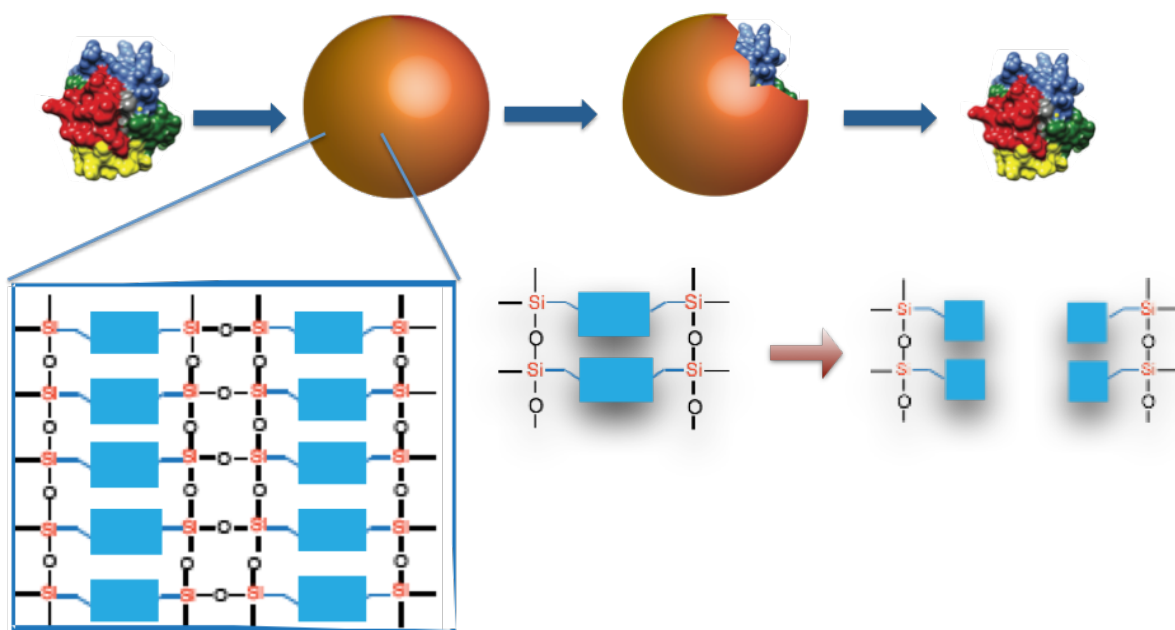


Fig. 6.3 Schematic view of the designed system. The protein cargo is encapsulated within a biodegradable hybrid shell, whose network is a silica-based disulfide bridges containing structure. The nanocapsules can release the content upon wrecking of the shell when in presence of a reducing agent.

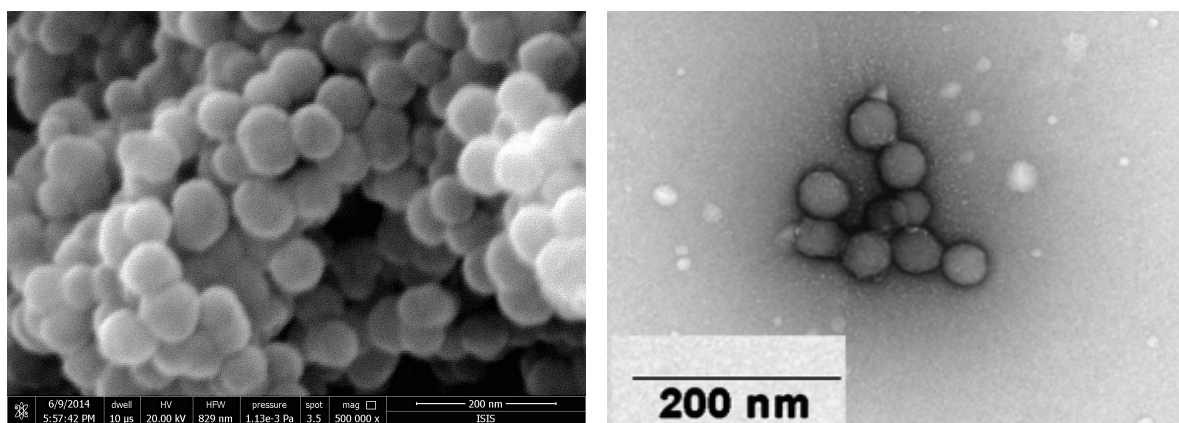


Fig. 6.4 SEM (left) and TEM (right) picture of CyC@BS-NP, revealing the average size of the particles.

In order to have a better characterization of the particles, and thus further hints about the effective core/shell structure, HR-TEM measurements were performed. Figure 6.5 displays the final image recorded, which shows the presence of a lighter organo-silica shell encapsulating a darker protein core (Cytochrome C hosts an iron-containing heme group), with a shell thickness estimable roughly to 15-20 nm, in accordance with the theoretical calculations reported in the following.

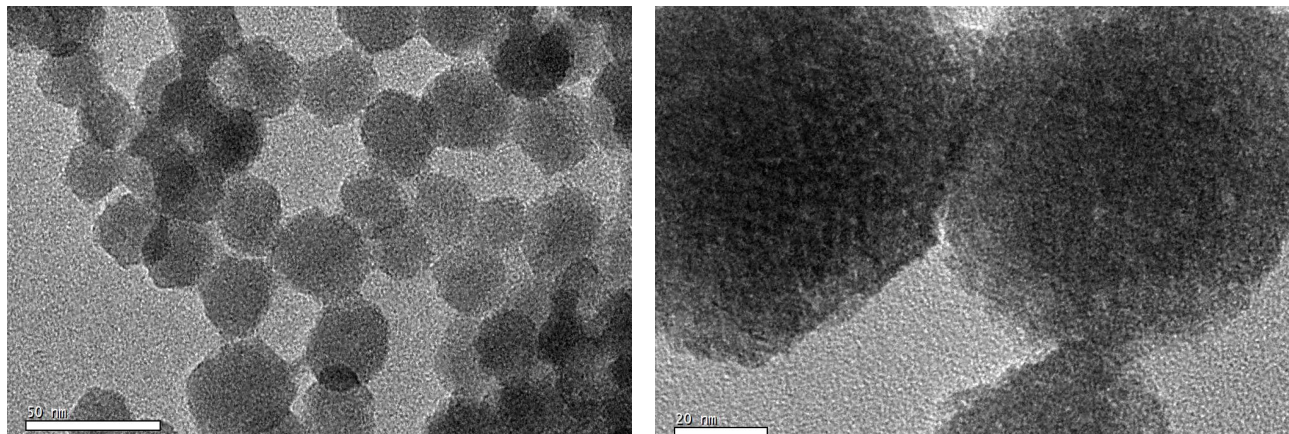


Fig. 6.5 HR-TEM pictures of CyC@BS-NP. The right panel especially offers a zoom showing in details the core/shell structure of the nanoparticles.

A further evidence of the actual encapsulation of the proteins within the shell was given by zeta potential measurements, showing an overall negative value of -17.67 mV in PBS medium (pH 7.0), which indeed excludes the hypothesis that protein molecules might be only adsorbed on the particle surface (CyC $pI = 10.5$). Indeed a more negative value is obtained when the capsules are formed without the disulfide bridge (see below) and it is consistent with the hypothesis that the silica incorporating a neutral group overall decreases the negative charge of the pure silica particles. The

encapsulation procedure can be applied to obtain non-breakable nanoshells, using TEOS only during the reverse emulsion synthesis (CyC@NonBS-NP).

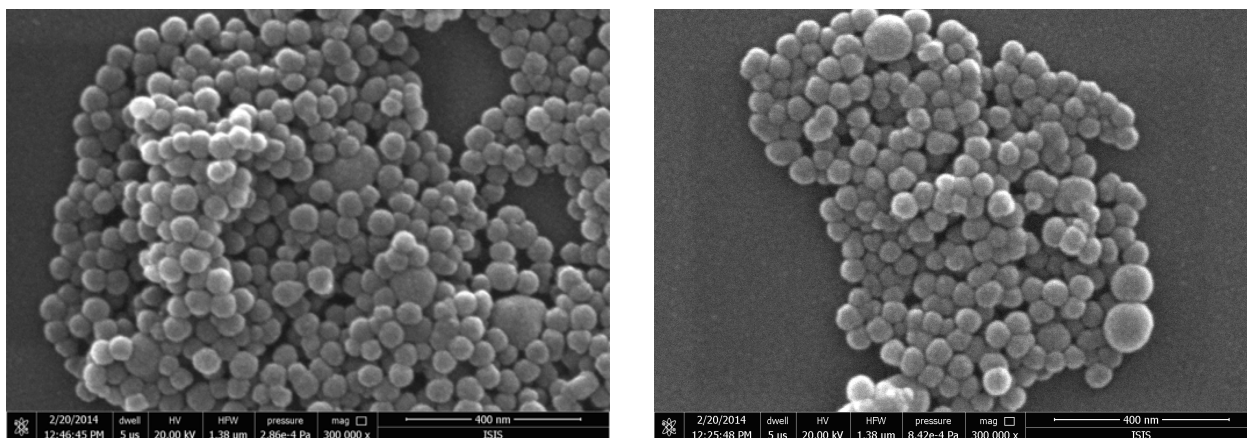


Fig. 6.6 SEM pictures of CyC@NonBrNP.

The non-breakable particles are of particular importance in order to have a quantitative evaluation of the breakability and of the release mechanism in live cell experiments. The use of TEOS only does not affect the final shape of the particles, which were obtained with the same aspect ratio of the breakable ones (Fig 6.6). A more negative zeta potential value of -20.00 mV was then registered for these particles.

Following this strategy, the same process was used to encapsulate diverse type of proteins, and, in particular, similar nanocapsules were fabricated using Human TRAIL APO2 Ligand (TRAIL@BS-NP), Onconase (Onconase@BS-NP), and Green Fluorescent protein (GFP@BS-NP) as proteinaceous cargo. These proteins were chosen depending on their nature and their functions for testing different aspects of the system, as will be described in the next paragraphs. The slight difference registered in the particle diameters depended on the size of the different proteins, as well as on the different concentration used during the encapsulation processes, since a bunch of macromolecules always played the role of templating substrate (see experimental section).

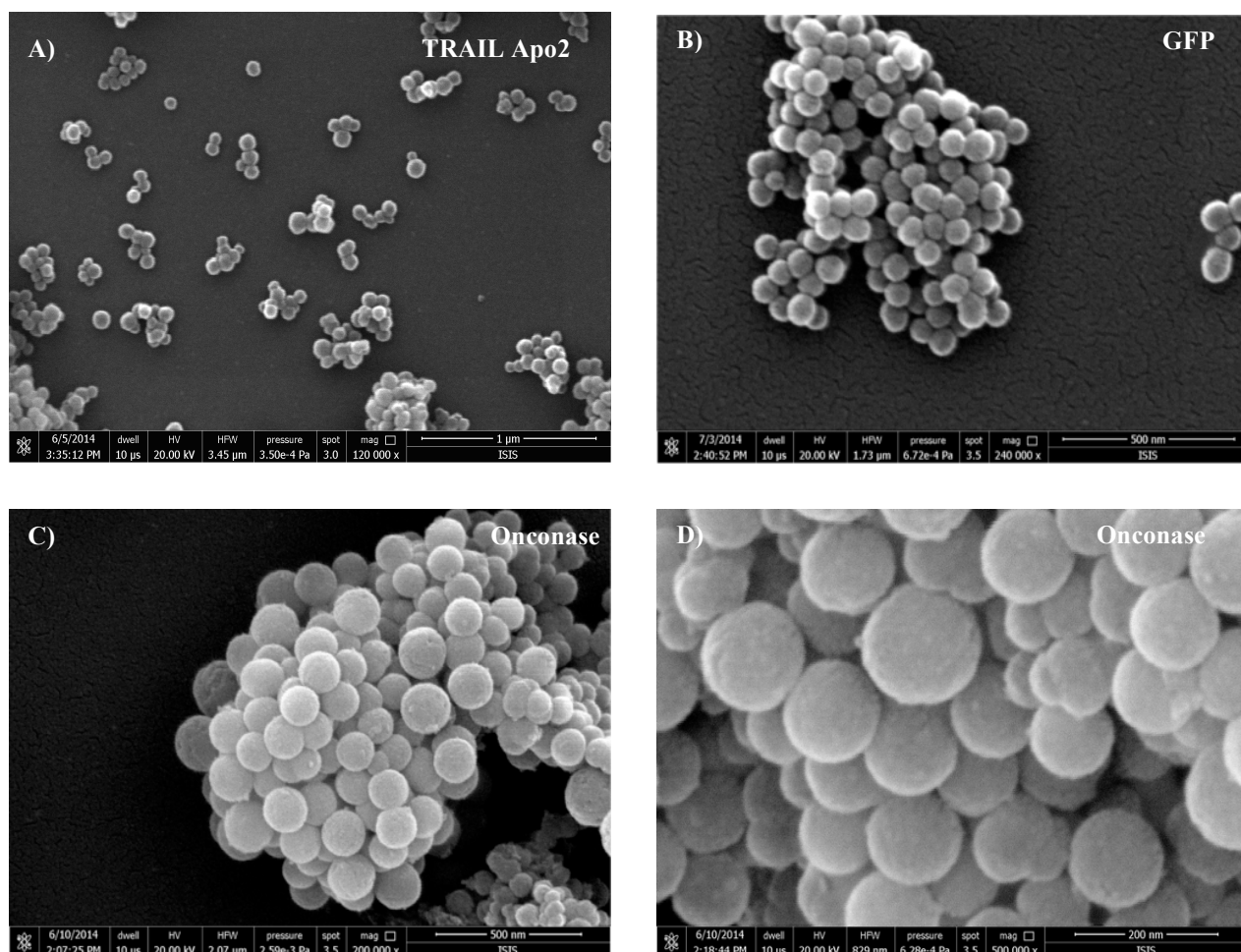


Fig. 6.7 SEM pictures of TRAIL@BS-NP (A); GFP@BS-NP (B), and Onconase@BS-NP (C, D)

6.3 Breaking the shell: kinetics and delivery properties

The possibility of delivering the protein cargo was investigated treating the designed core/shell particles under reducing environment, which should trigger the reduction of the disulfide bridges leading to a breakdown of the shell structure. CyC@BS-NPs were used as case study, since the wide availability of the starting material and the possibility of easily following the cargo release exploiting the absorption of the protein in the visible region. Therefore, three batches of CyC@BS-NPs were respectively left in water only, and treated with sodium borohydride NaBH_4 or glutathione as reducing agents. Sodium borohydride was used since being an efficient and irreversible reducing agent, not forming residual byproducts, which may interfere in the evaluation of the efficacy of the reduction. Glutathione was chosen in order to mimic the reducing environment that may operate at the live cell level. After incubating the particles under the above conditions for 24 hours, the supernatant was in every case recovered and analyzed via UV-Vis spectroscopy (Fig. 6.8). Due to the presence of particles, or their broken fragments, a scattering

phenomenon was always observed, thus a novel baseline considering this effect was produced and subtracted from the final data, giving scattering-free spectra. This consideration is valid also for all the following UV spectra.

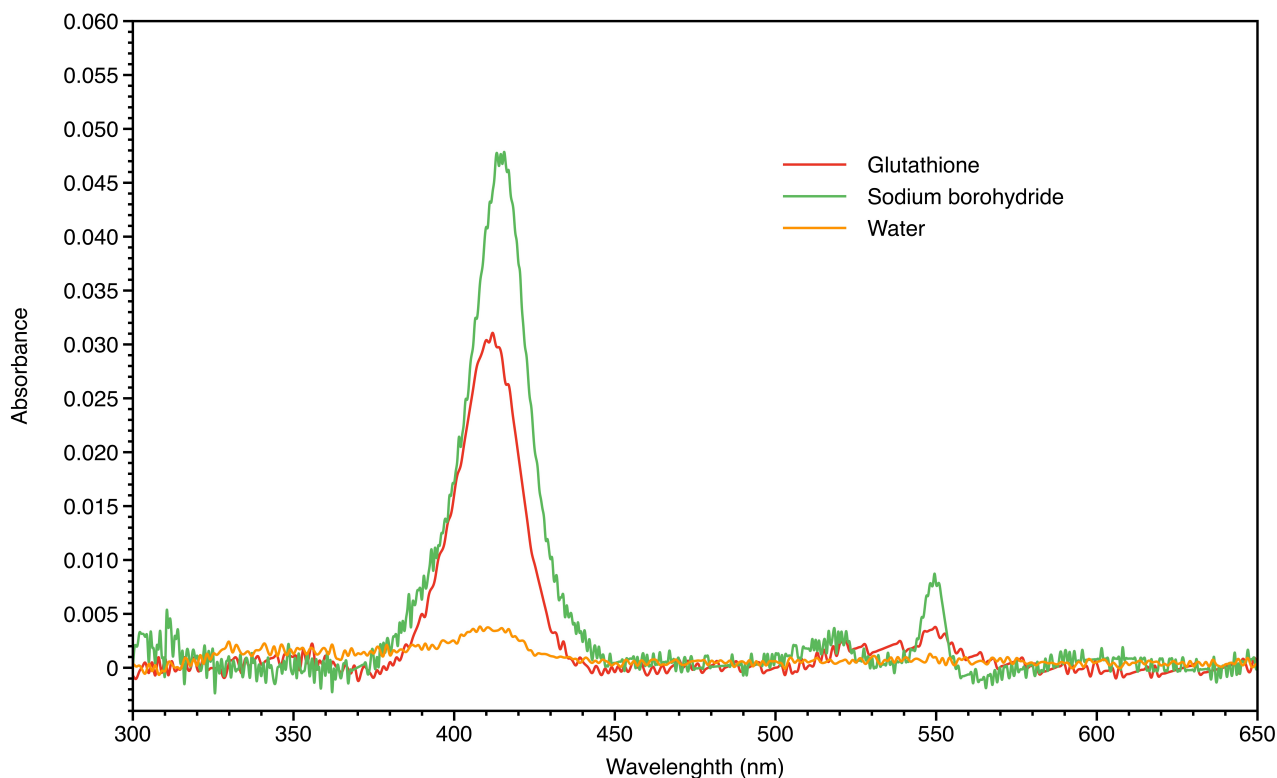


Fig. 6.8 UV-Vis spectra of the supernatants recovered after treating 0.5 mg/ml CyC@BS-NPs with water only (orange line), NaBH₄ (green line), and glutathione (red line) for 24 h.

From the UV-Vis spectra reported in Figure 6.8, it results evident that the control experiment show almost no absorption of the cytochrome due to the stable encapsulation while in the presence of the reducing agents the appearance of the absorption profile of the Cytochrome C in solution confirms the release of the protein in the water solution. This is a clear proof that the reductive environment actually had an effect on the shell structure, provoking its breakdown and thus leading to the release of the protein cargo into the solution only for the redox responsive particles. It is worth noticing that treatment with NaBH₄ seems to provide a higher release of the protein, which is to ascribe to the stronger reducing effect than the one of the glutathione.

A theoretical calculation was then performed for the case of CyC@BS-NPs treated with NaBH₄, which, on the basis of the protein released into the solution, can roughly give the minimum number of proteins encapsulated per particle.

At first, a calibration curve for standard solutions of Cytochrome C was built up, whose equation was $y = 0.0909(\pm 0.0008)x$ ($R^2 = 0.9954$, $n = 18$). The linear model was validated through Mandel

test. This curve endowed a rough quantification of the proteins encapsulated within the hybrid shell by the absorption peak at $\lambda = 410$ nm. The total number of moles of Cytochrome C encapsulated was estimated by Lambert-Beer equation, then, using an average density between the silica value and the Cytochrome C one, the minimum number of protein molecules per particle could be roughly estimated to be around 32. Taking into account the volume size of Cytochrome C,^[54-55] this leads to a theoretical thickness of the organo-silica shell around 19 nm and a protein core of 12 nm in diameter (considering a model nanosphere of 50 nm diameter, see experimental section for details).

To have a further evidence of the breaking/releasing phenomenon, glutathione was used to incubate the same batch of CyC@BS-NPs and a sample of non-biodegradable CyC@NonBS-NPs. The UV-Vis profile registered for the two recovered supernatants undoubtedly showed the appearance of the Cytochrome C absorption peaks only for the CyC@BS-NP sample, while nothing happened when using the total silica shell (Figure 6.9).

The presence of the released Cytochrome C in the solution when reducing the biodegradable shell was also assessed by ESI-TOF-MS, which gave the typical mass spectrum profile of the enzyme in aqueous solution (Fig. 6.10).

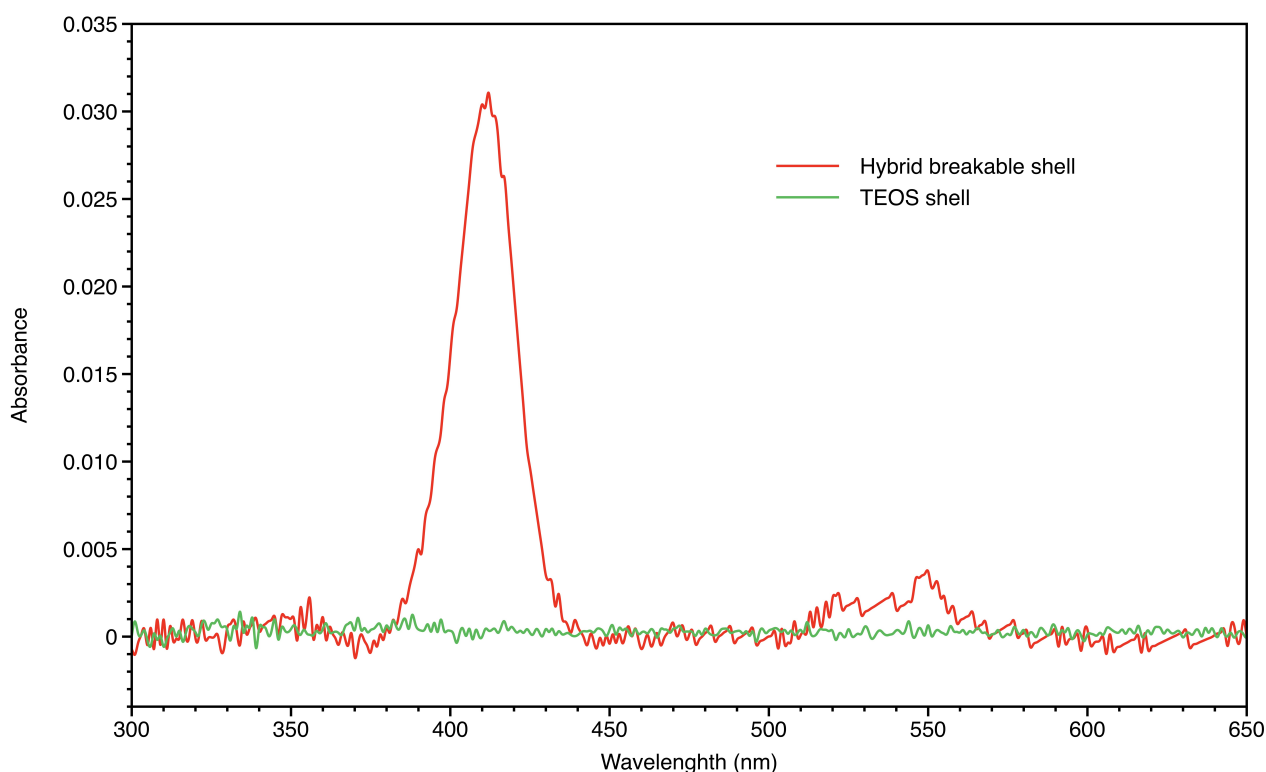


Fig. 6.9 UV-Vis spectra of the supernatants recovered after treating 0.5 mg/ml CyC@BS-NPs and an identical concentration of CyC@NonBS-NPs with glutathione for 24 h

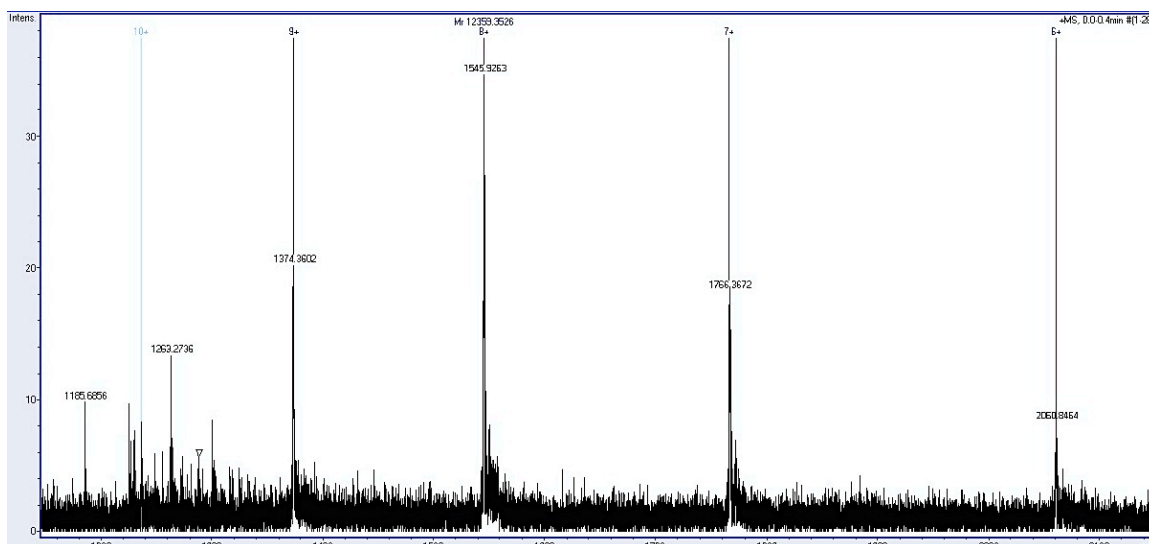


Fig. 6.10 ESI-TOF-MS spectrum of the supernatant recovered after treating CyC@BS-NPs with glutathione for 24 h, showing the typical charge distribution of the Cytochrome C.

UV-Vis spectroscopy was then utilized to study the release kinetics of the protein into solution, monitoring the Cytochrome C signal over time. Spectra were collected after 0, 1, 2, 4, 24, 48 hours of incubation with glutathione 5 mM. The release profile is shown in Figure 6.11. Glutathione is used for this study since it serves to mimic the intracellular environment.

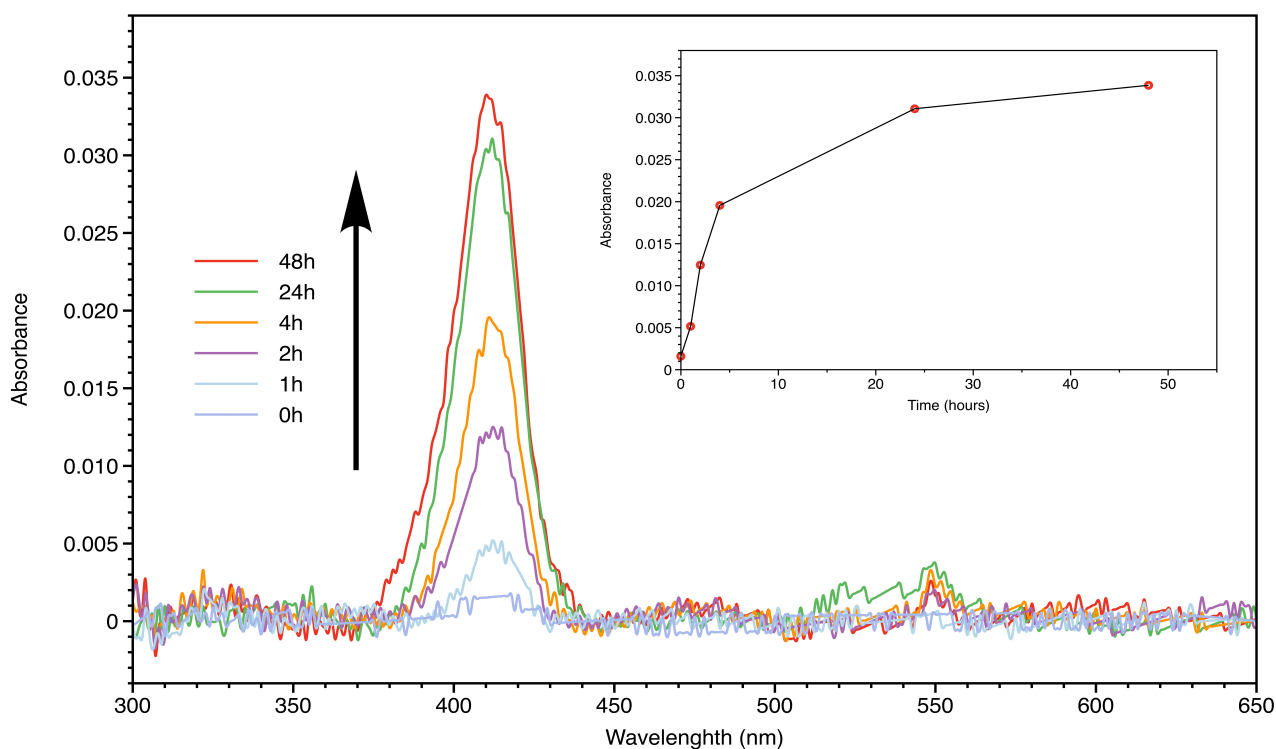


Fig. 6.11 UV-Vis spectra of the supernatants recovered after treating CyC@BS-NPs with glutathione over time. In the inset, release profile over time at fixed wavelength ($\lambda = 410$ nm)

From the UV-Vis spectra, one can notice that at time 0 (before adding glutathione) there is no enzyme signal, as expected. After adding the glutathione, already after 1 hour a small peak can be individuated centered around 400 nm. The concentration of the released protein into solution then increased over time, the absorption peak of the cytochrome becoming clearer and sharper. After 24 hours the signal appeared definitely well defined. It is worth to notice that the absorption intensity only slightly changed between 24 and 48 hours, suggesting most of the effective release took place in one day. The amount of protein released in this case can be estimated around 50%, as can be easily calculated comparing the spectrum (red line) after 48 hours of the breakable particles in glutathione (0.05 mg/mL) with the spectrum (black line) of the particle dispersion (1 mg/mL) in water (Fig. 6.12). As seen before, the percentage release can be notably increased when using a stronger reducing agent as NaBH₄.

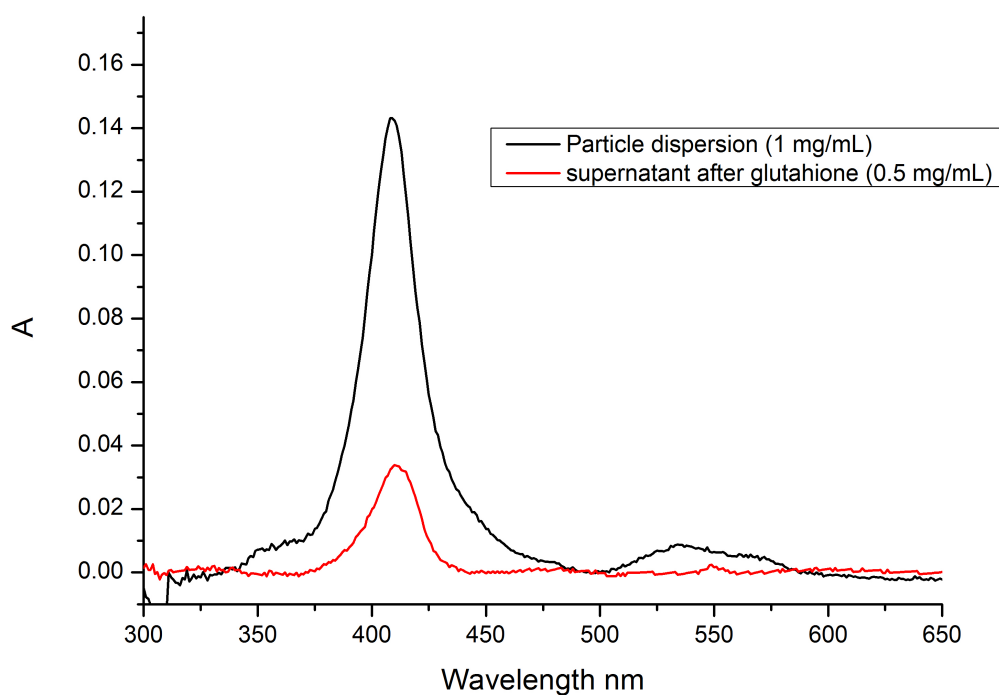


Fig. 6.12 UV-Vis spectra of the supernatant recovered after treating 0.5 mg/ml CyC@BS-NPs with glutathione for 48 h (red line), and of 1 mg/mL intact particle dispersion in water.

In order to study and visualize the associated breaking phenomenon at the single particle level, HR-TEM was used to follow the degradation of the hybrid structure when treated with reducing agent. Hence, cysteine was used since it resulted to give the best images under the TEM conditions. The degradation effect caused by the reduction treatment is displayed in the TEM pictures reported in Figure 6.13.

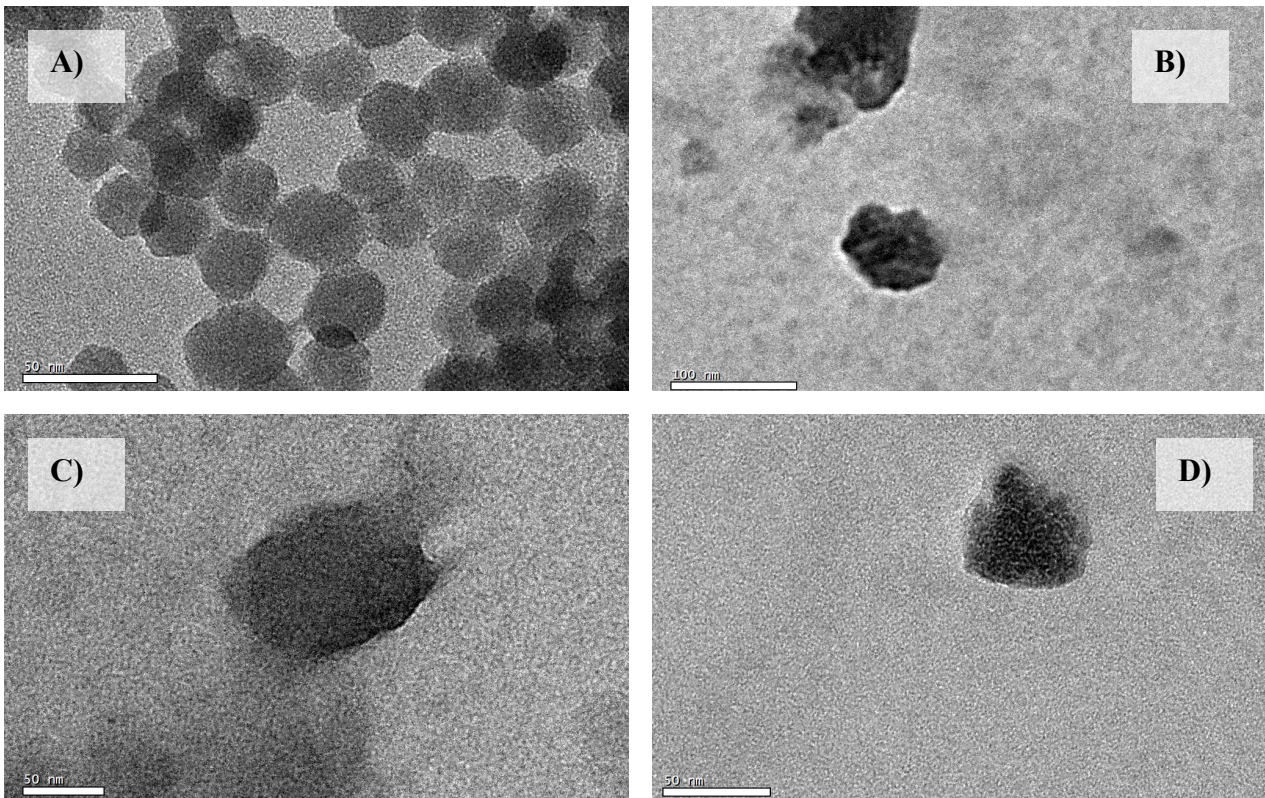


Fig. 6.13 HR-TEM pictures of CyC@BS-NPs (A) and of the same particles treated with cysteine (B, C, D), showing the effective degradation of the shell structure under reducing conditions.

In Fig. 6.13A the nanocapsules are shown before the addition of the breaking chemical. After 3 hours it was already difficult to find well defined spherical nanoparticles in the solution, meaning that cysteine worked effectively. Some completely deformed/wrecked nanoparticles were detected as reported in panels B-D. Looking at the top particle in panel B, one could even see "dynamically" the disruption of the shell structure. SEM was used to monitor the breaking phenomenon when using glutathione, and some single degraded particles could actually be found, as reported in Figure 6.14

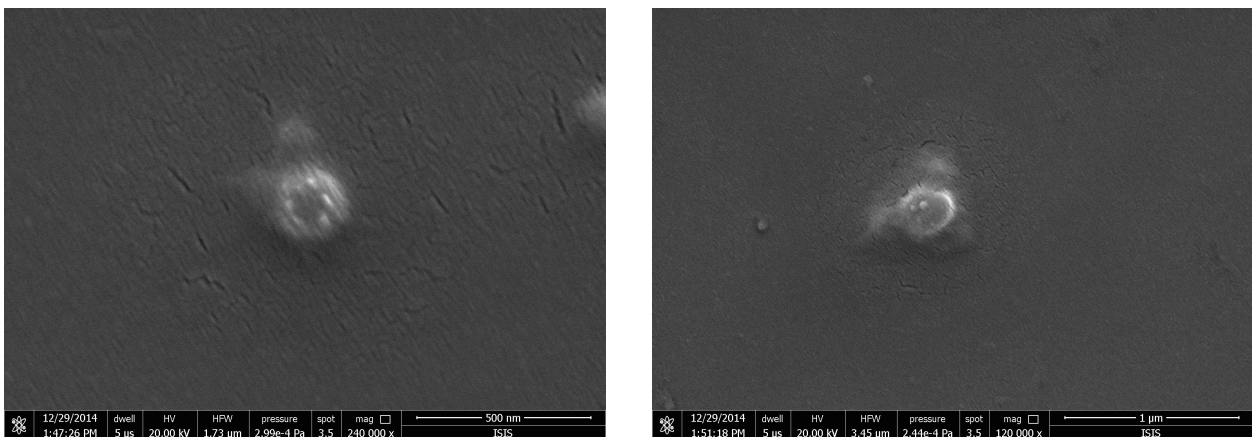


Fig. 6.14 SEM pictures of CyC@BS-NPs treated with glutathione for 24 hours, showing the degradation of the silica shell.

In addition, SEM was used to monitor the breaking kinetics in presence of glutathione in parallel to the UV-Vis experiment, which gave images at a lower magnification revealing the actual dynamic process on a larger scale.

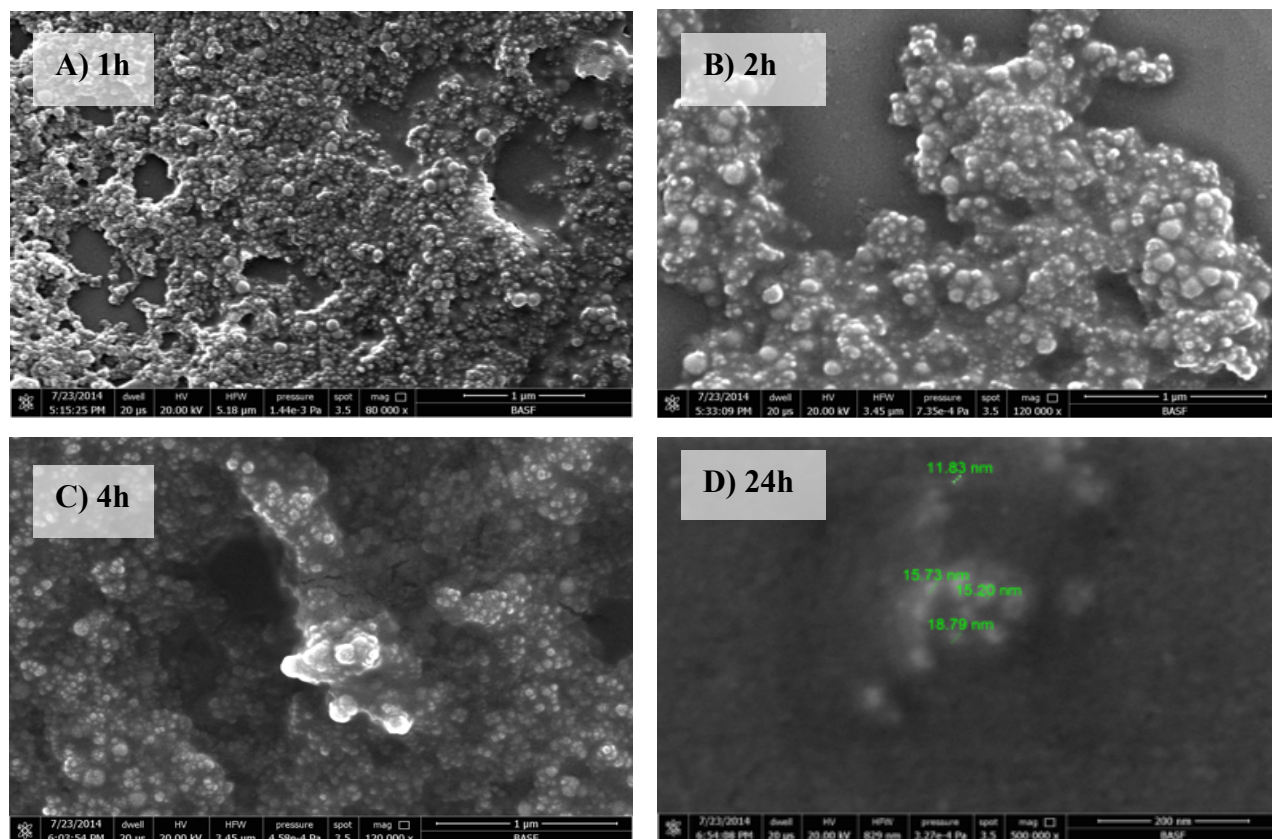


Fig. 6.15 SEM pictures of CyC@BS-NP treated with glutathione recorded over time. A) After 1 hour in reducing environment, B) 2 hours, C) 4 hours, D) 24 hours.

After 1 h, the majority of the particles still looked in a good shape, even though some areas could be found in which the material seemed “melting” and degrading. The breaking phenomenon resulted then much more evident after 2 hours, when the particles seemed definitely on the way to melt down and degrade. It is interesting to notice that some smaller pieces (between 15 and 25 nm) than the normal average size of the particles (50-60 nm) could be detected, which could be identified as broken pieces coming from the degradation of the material. After 24 hours, the environment looked totally amorphous and no nanoparticles could be observed but only some small random fragments could be visualized (Fig. 6.15D).

The SEM analysis allowed as well for carrying out EDX measurements, to map the percentage of the elements at the surface of the nanospheres. A comparison between the mapped elemental distribution for a sample of intact CyC@BS-NP and for one of the same particles treated with

NaBH₄ (which did not give any organic elemental contamination) was thus achieved through EDX analysis (Figure 6.16).

EDS Quantitative Results			EDS Quantitative Results		
Element	Wt%	At%	Element	Wt%	At%
NK	4.84	9.28	NK	48.21	65.51
SiK	92.63	88.60	SiK	44.52	30.17
SK	2.53	2.12	SK	7.27	4.32

CyC@BS-NP **CyC@BS-NP after reduction**

Fig. 6.16 Results of the EDX mapping performed for a sample of CyC@BS-NP (left) and for the same batch after treatment with NaBH₄ (right). The analysis gave the recorded weight percentage (Wt%) and atomic percentage (At%) for each element monitored, namely Nitrogen, Silicon, and Sulfur.

As expected, the intact nanospheres showed at the surface level a drastic abundance of silicon, which forms indeed the shell scaffold. The sulfur signal came indeed from the disulfide bridges embedded in the network, while the small nitrogen contribution could be probably ascribed to some sample contamination or to some shelled protein molecule reached anyhow by the electron beam. Interestingly, after the reductive agent treatment, one could notice the dramatic increase of the nitrogen abundance on the material surface, which can be ascribed to the enhanced exposure of the cytochrome C to the EDX beam caused by the degradation of the outer shell. The sulfur signal was found increased as well after the NaBH₄ treatment, possibly for the same effect of disruption of the shell structure, leading to the exposure of a higher number of sulfur atoms to the X-ray beam.

6.4 Live cell distribution

Live cell distribution experiments could be carried out by means of confocal microscopy, at the condition of having at hand an easily available and proper protein substrate to be encapsulated in the designed capsules. Green fluorescent protein (GFP) was indeed selected as suitable species for its bright luminescence properties. GFP was thus encapsulated within the hybrid breakable shell (GFP@BS-NP) following the procedure already described, and characterized as above (see Fig. 6.7B). Preliminary tests in solution to check the effective delivery of the GFP upon degradation of the shell were conducted, similarly to what already shown for CyC@BS-NPs. After treating the particles with a reducing agent, SEM images showed the same melting-breaking effect previously reported for the Cytochrome C case (see Figure 6.17B,C and Figure 6.15), and fluorescence spectroscopy analysis of the recovered supernatant registered the appearance of the typical GFP emission band in solution (Figure 6.17C).

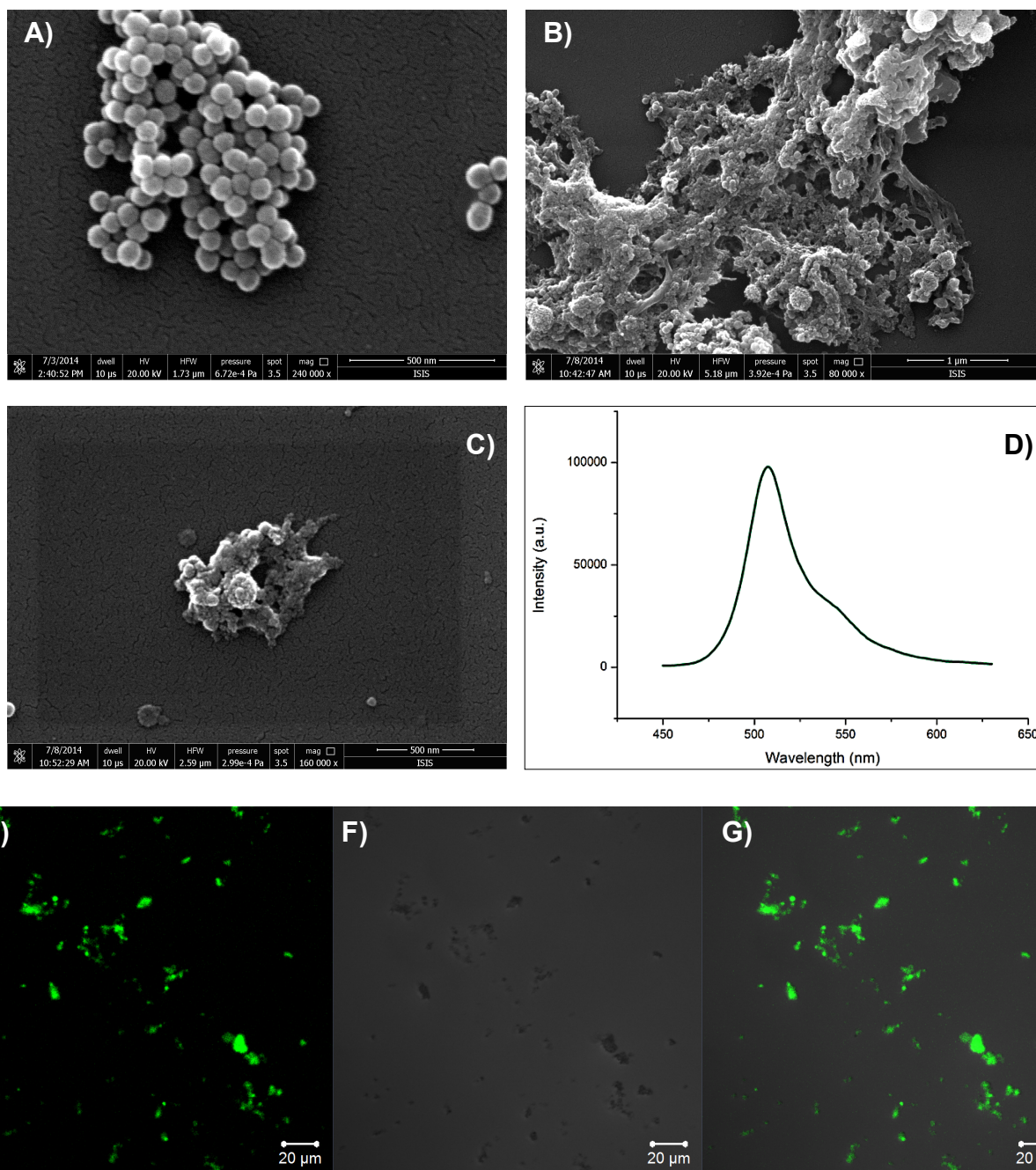


Fig. 6.17 A-D) SEM pictures of A) GFP@BS-NPs, and B,C) GFP@BS-NPs treated with NaBH₄ for 24 h. Panel D) shows the fluorescence emission spectrum recorded for the supernatant in reducing environment. E-G) Confocal micrographs of GFP@BS-NPs. E) GFP signal ($\lambda_{exc} = 488$ nm); F) brightfield image of the particle dispersion; G) merged

To prove that the NPs can also be broken by the glutathione of the cancer cells we have performed cell experiments on a C6 glioma cell line with incubation times of 1, 4, and 24 hours using a particle concentration of 0.05 mg/mL GFP@BS-NP per mL culture media. After fixation, the cells were analyzed via confocal microscopy following the GFP fluorescent signal. As can be seen from the confocal micrographs reported in Figure 6.18, cellular internalization of GFP@BS-NPs could

be observed already after 1 hour (taking into account the low concentration used) and, as expected, the number of particles internalized increased linearly over time, with a remarkable intracellular distribution at the final time of 24 hours.

Interestingly, a pale (low intensity) green staining was found as a diffused signal in the cytoplasmic region after 24h of incubation (see fluorescence image, 3rd row, Fig. 6.18), although the presence of big aggregates could not be neglected.

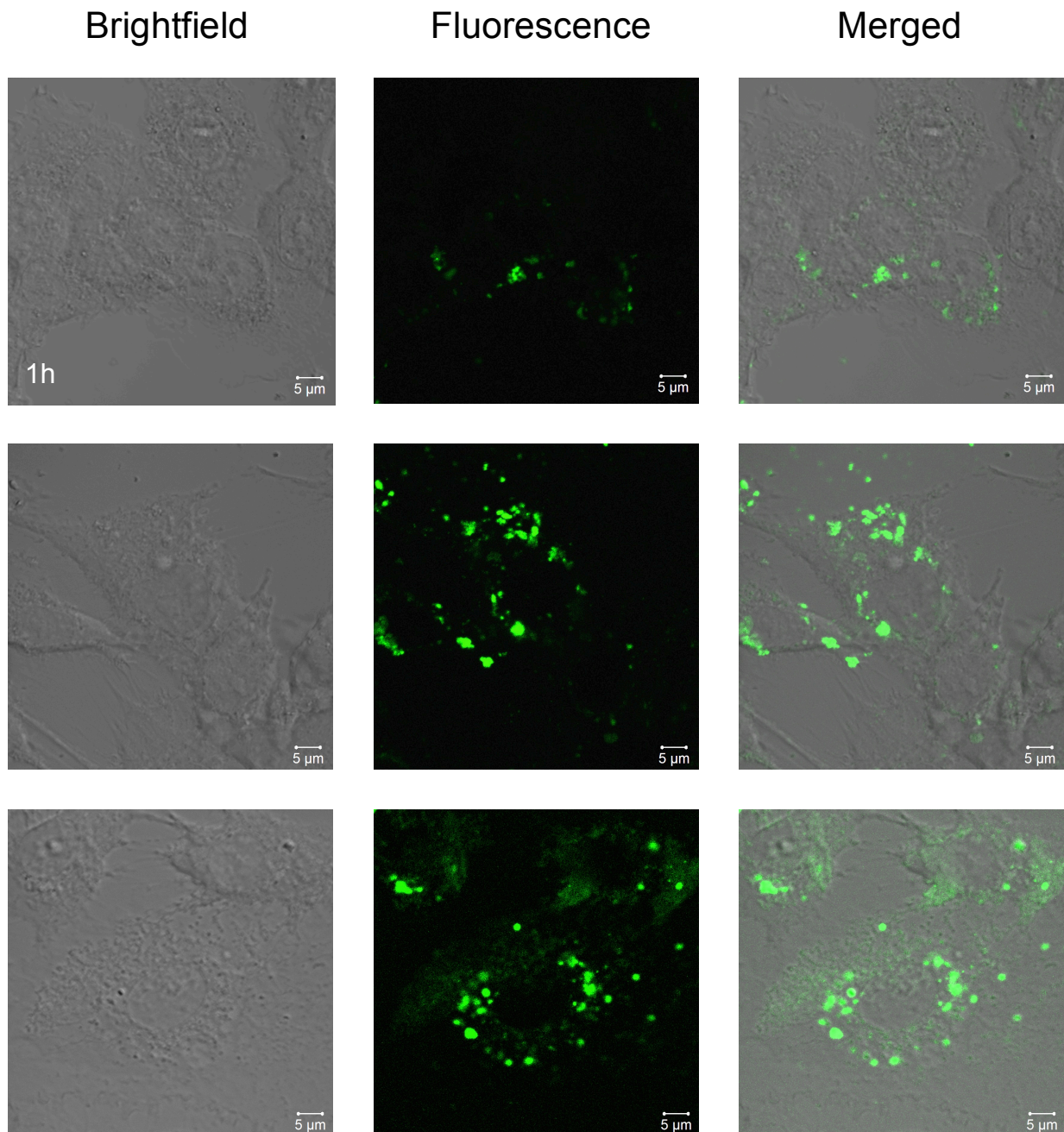


Fig. 6.18 Confocal microscopy images showing cellular uptake of GFP@BS-Nps in C6 Glioma cells. The cells were incubated for 1 (1st row), 4 (2nd row), and 24 hours (3rd row), with 0.05 mg particles in 1 ml of culture medium. The green signal corresponds to GFP emission. Excitation wavelength is 488 nm for GFP and the emissions was recorded in the range of GFP emission band.

To accurately investigate the fluorescence distribution inside the cells, which could give some hints on the breaking and release phenomenon, co-localization experiments were thus carried out. C6 glioma cells were incubated with GFP@BS-NPs (0.05 mg/mL, 24h), and lysosomes were labeled with the red fluorescent dye LysoTracker® Red, in order to check the overlap of this emission with the one of the GFP. As shown in Figure 6.19, most of the green big aggregates were found located in the lysosomes (co-localization coefficient 0.87), suggesting these are GFP@BS-NPs still integer and entrapped in these cellular vesicles. Interestingly, a green GFP signal was detected as diffused in the cytoplasm, without any specific co-localization with the lysosomes; some of this areas are highlighted with yellow circles in Fig. 6.19A and all of them are clearly distinguishable in Fig 6.19D. This spread “non co-localized” emission might indeed suggest the finding that the signal probably come both from very few particles that escaped from the endosomes before being entrapped in the lysosomes, and, more likely, from GFP that was actually released from both particles and lysosomes upon degradation of the protective shell, and subsequently distributed in the cytoplasm.

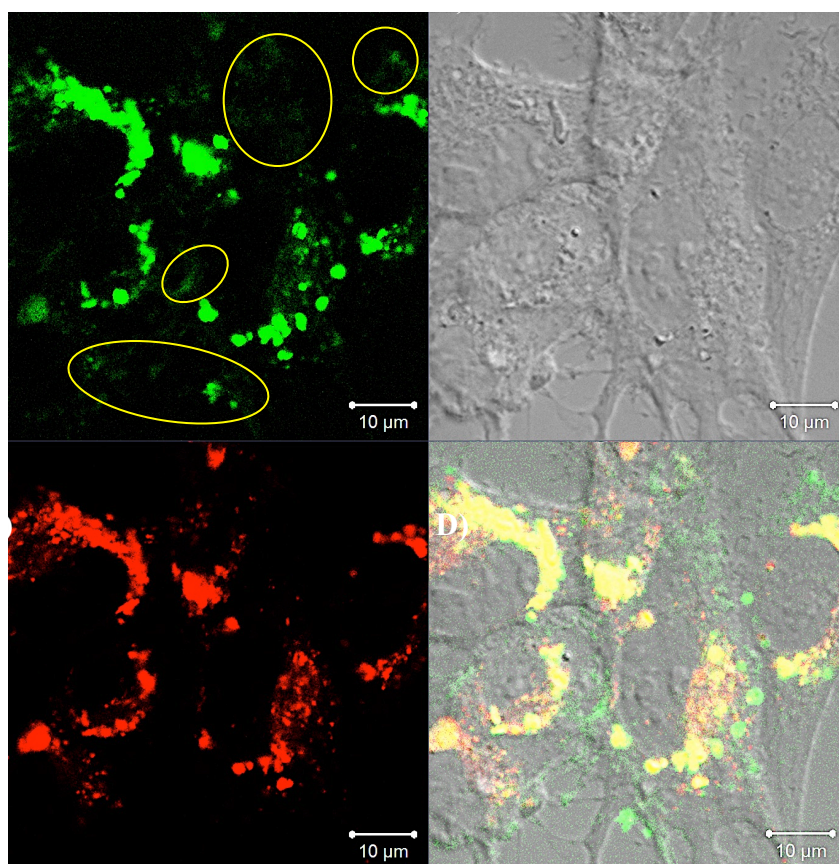


Fig. 6.19 Confocal micrographs showing the localization of the particles in C6 Glioma cells. A) GFP fluorescence emission; B) brightfield image; C) lysosome stain; D) merged. Excitation wavelengths are 488 and 594 nm for GFP and LysoTracker® Red, respectively. The yellow circles in panel A) underline the non co-localized GFP areas.

In order to have a better understanding of the release kinetics of GFP from the hybrid nanocapsules, despite the cell proliferation that reduces the number of particles during each cell cycle, a cell experiments was done in which the intracellular particle concentration was kept constant and the fluorescence signal distribution after 2 or 4 hours of incubation with a high concentration of particles (ca. 0.2 mg/mL) was investigated. In the first case, after 2 hours of incubation, the cells were extensively washed with PBS buffer to remove loosely bound particles from the cell surfaces. Then, cells were cultured and live-cell imaging was done directly after incubation for 1, 2, 4, 6, 20, 24, and 48 h, recording the GFP signal. Cell nuclei were stained with Hoechst 33342 to better visualize the cells and enhance the contrast.

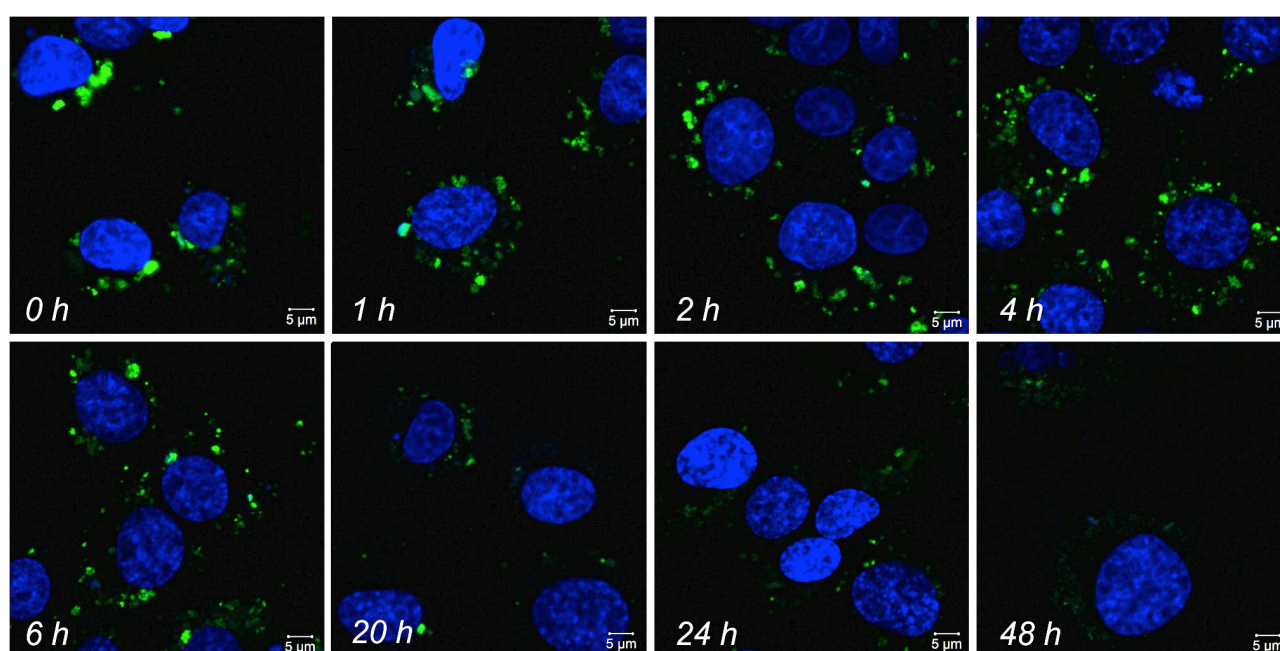


Fig. 6.20 Confocal microscopy images showing the kinetics of biodegradation and distribution of GFP@BS-NPs in C6 Glioma cells. The cells were incubated with the particles for 2 hours (0.2 mg/mL) and live imaging experiments were done directly after incubation, and subsequently after 1, 2, 4, 6, 20, 24, and 48 h. Blue color indicates the signal from Hoechst 33342 staining cell nuclei, while green corresponds to GFP fluorescence. Excitation wavelengths are 405 and 488 nm for Hoechst 33342 and GFP, respectively. Emissions were recorded with a Hoechst 33342 emission filter and GFP emission filter, respectively. The time reported for each panels refers to the one monitored starting right after the 2h incubation.

As can be seen from Figure 6.20, a remarkable distribution could be recorded inside the cells until 6 hours past the end of the incubation, which consisted of both large aggregates and diffused green signal. After 20 h, only very few aggregates could be found, followed by the presence of a pale (low intensity) green staining diffused in the cytoplasm. Moreover, the intensity value profile recorded for the cytoplasmic region (see Figure 6.21) indicated the GFP signals were fairly low after 20 h of culture time, indicating the constant loss of rather big aggregate (responsible instead for the higher intensities when monitoring from 0h to 6h past the end of incubation), replaced by a

diffused cytoplasmic green emission, which might indeed be due to the degradation of the nanocapsules releasing the protein cargo.

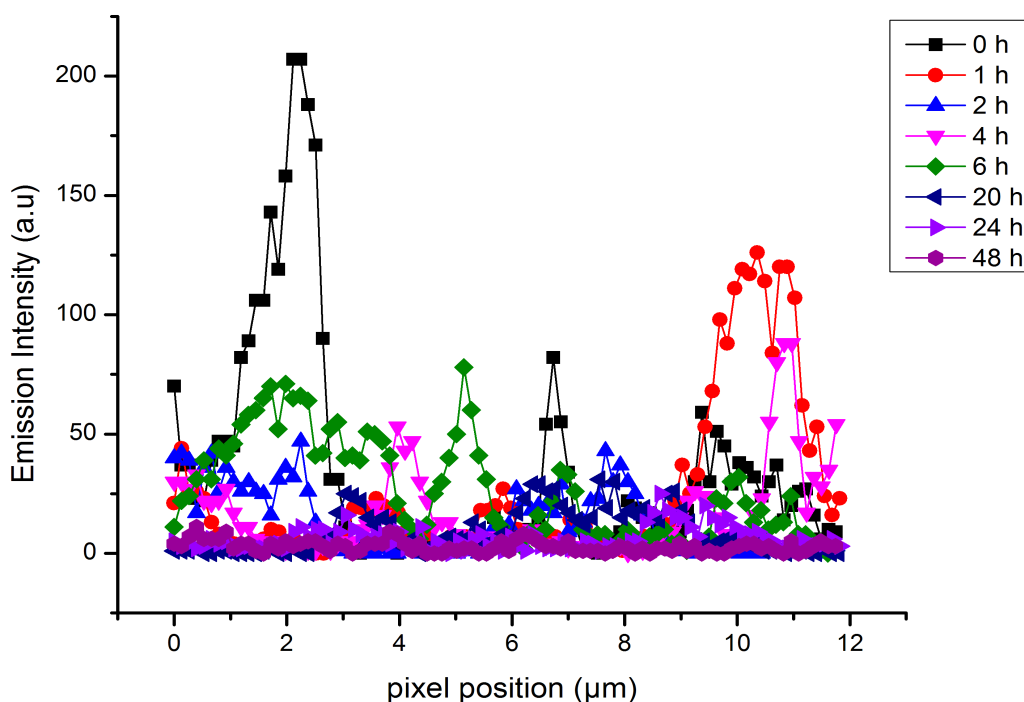


Fig. 6.21 Intensity profile recorded for GFP distributed in cytoplasmic region. The drop of the intensity values over time can be followed and it possibly suggests that the degradation of very big particles inside lysosomes started effectively 6h after stopping the incubation, leading to the GFP diffusion into the cytoplasm.

When the incubation time was increased from 2 to 4 hours (the particle concentration was still kept constant, e.g. 0.2 mg/mL), a higher number of particles were indeed found uptaken and distributed inside the cells (see Figure 6.22, after imaging at 0 hour).

As expected, the presence of discrete aggregates of particles in the cytoplasm was clearly observed right after 4 hours of incubation time, due to the longer time cells were kept in contact with the concentrated particle dispersion. The cells were subsequently grown in free particle-media for the next 24 hours, and big particle aggregates could still be detected, but interestingly a diffused widespread staining of GFP was clearly recorded in the cytoplasm, indicating the presence of free delivered protein. The cells were cultured in free particle-media up to 3 days, and no significant phenomena were registered, since the size of the aggregate inside the cells only slightly contracted, and the overall emission intensity generally shrank because of the cell proliferation cycles.

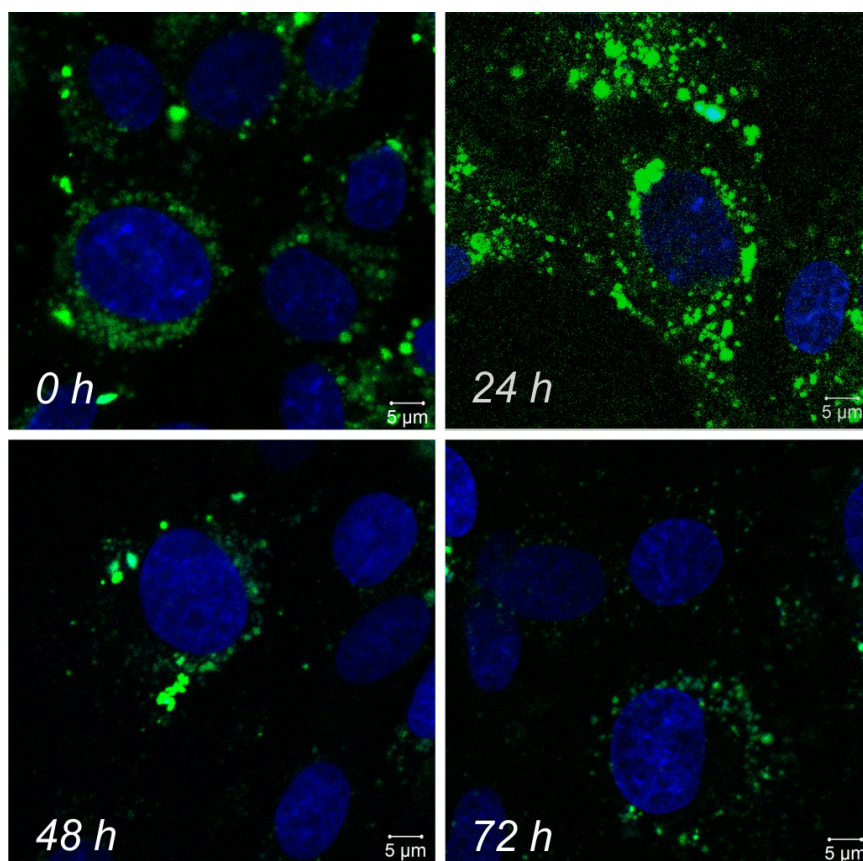


Fig. 6.22 Confocal microscopy images showing the kinetics of biodegradation and distribution of GFP@BS-NPs in C6 Glioma cells. The cells were incubated with the particles for 4 hours (concentration 0.2 mg/mL), followed by 10x washing treatment using PBS buffer. Imaging experiments were done directly after incubation, and subsequently after 1, 2, and 3 days. Blue color indicates the signal of Hoechst 33342 staining cell nuclei, while green corresponds to GFP emission. Excitation wavelengths are 405 and 488 nm for Hoechst 33342 and eGFP, respectively. Emissions were recorded with a Hoechst 33342 and a GFP emission filter, respectively

6.5 Intracellular delivery: anticancer activity

Once the material was deeply characterized, it was tested for delivering active and functional proteins to live cells. The reductive environment of the cytoplasm (especially related to the glutathione expression) is supposed to act as the trigger agent for the degradation of the outer shell, thus leading to the release of the protein cargo. A crucial point is indeed that the released biomolecules were still capable to carry on their supposed activity, therefore special proteins able to provide an anticancer effect were selected and used as cargo, to study the possible effect provided upon the release. For this reason, TRAIL Apo2 Ligand and Onconase were chosen as suitable encapsulated species, since their ability to induce apoptosis only in tumor mammalian cells. TRAIL Apo2 Ligand is a protein that belongs to the tumor necrosis factor (TNF) family of death ligands and can be used to overcome resistance to conventional chemotherapeutic drugs.^[56-58] Amongst the various proteins in the TNF family, TRAIL has been the subject of investigation as an anti-tumor agent since it selectively induces cell death in cancer cells with little or no toxicity to normal

tissues. Many studies involving preclinical models have shown that TRAIL is able to hamper the growth of human tumor xenografts *in vivo*.^[59-60] In addition, unlike many conventional anti-cancer agents, TRAIL can induce apoptosis independently from the p53 tumor suppressor gene status of cancer cells.^[61] Onconase® is a unique ribonuclease selectively cytotoxic to transformed cells, possessing potent *in vivo* antitumor activity.^[62-64] Onconase toxicity essentially results from its ability to degrade tRNAs,^[65] although some recent studies highlighted its possible activity in targeting also microRNAs.^[66] The unique targets and novel mechanism of action, together with lack of immunogenicity after repeated administration have pointed out Onconase to be a promising chemotherapeutics agent.^[67-68] Nevertheless, in both TRAIL and Onconase case, an efficient cellular uptake and a safe delivery platform still represent limiting aspects on the way of their real widespread use as chemotherapy tools. Hence, TRAIL and Onconase were encapsulated within the hybrid organo-silica shell following the so far described procedure, and the final material characterized as shown in the paragraph 6.2. TRAIL@BS-NP was thus initially tested on a C6 glioma cell line, which should be sensitive to the presence of the protein once delivered into the cytosol. To have a full series of data, the same cell line and number of cells were also incubated with CyC@BS-NP and CyC@BS-NPs, which were useful to individuate any possible undesired cytotoxic effect caused by the material itself. C6 glioma cells were incubated with the different materials (0.15 mg/ mL each) over 24 hours, then cells were trypsinized and the resulting cell pellets harvested. The total cell viability was measured as direct indicator of the cytotoxic/anticancer effect provided by the hybrid particles.

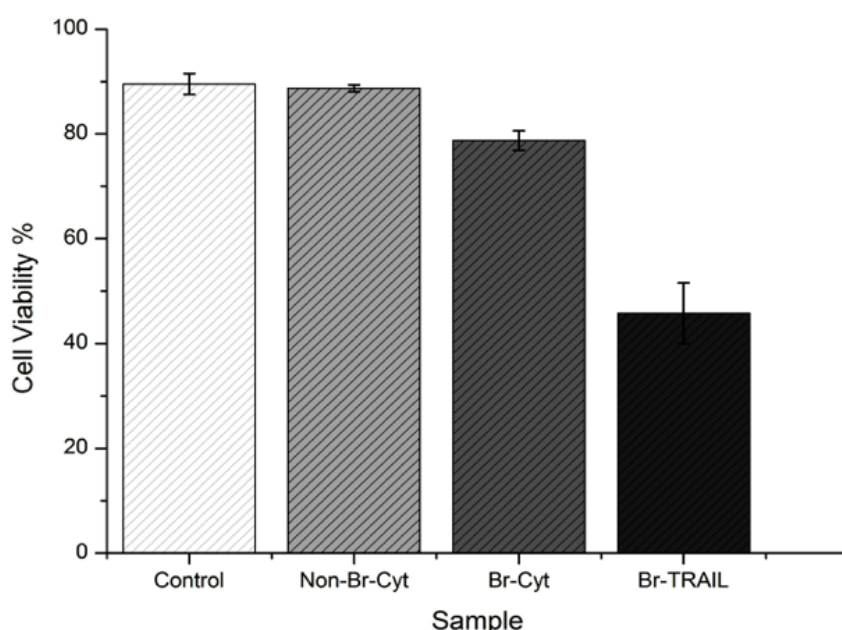


Fig. 6.23 Cell viability values obtained after 24 hours of incubation for C6 glioma cells. Control (pure cell culture) 89.5%, CyC@NonBS-NP 88.7%, CyC@BS-NP 78.7%, TRAIL@BS-NP 45.8%. All experiments were reproduced in triplicate.

From the graph displayed in Fig. 6.23, one can see that CyC@NonBS-NPs, as expected, did not influence the total cell viability with respect to the control culture, meaning that the core/shell system is absolutely biocompatible and non-cytotoxic. In the case of CyC@BS-NPs, a slight reduction of the viability was registered (78.7% vs 89.5% control), which can be possibly ascribed to an interference effect in the normal biological metabolism due to an excess of cytochrome C present in the cell after the delivery, being the mitochondrial release of cytochrome C a pathway for inducing apoptosis.^[69-71] It must be said that at this stage no biological evidences are available to support this hypothesis and work is in progress. Nevertheless, the main result appearing from the graph is the cell viability percentage obtained when treating the C6 Glioma cells with TRAIL@BS-NP, which induced a drastic reduction of the value up to 45% with respect to the control sample. This indeed might point out the effective role of the nanosphere system, which leads to the cellular internalization of the protein in the shelled form and subsequently to its release upon degradation of the outer structure. The released TRAIL is thus supposed to be still in an active conformation to carry on its apoptosis inducing effect, as suggested by the overall viability reduction. To further investigate this outcome, the same TRAIL@BS-NPs were used to incubate glioma cells under the same conditions, which were eventually analyzed through Trypan blue cell mortality test, to visualize the possible provided anticancer effect. Trypan blue is a dye able to selectively stain only dead cells, depending on the rupture of the cell membrane that enables its cell penetration, while live healthy cells are completely impermeable.^[72] The results are reported in Figure 6.24.

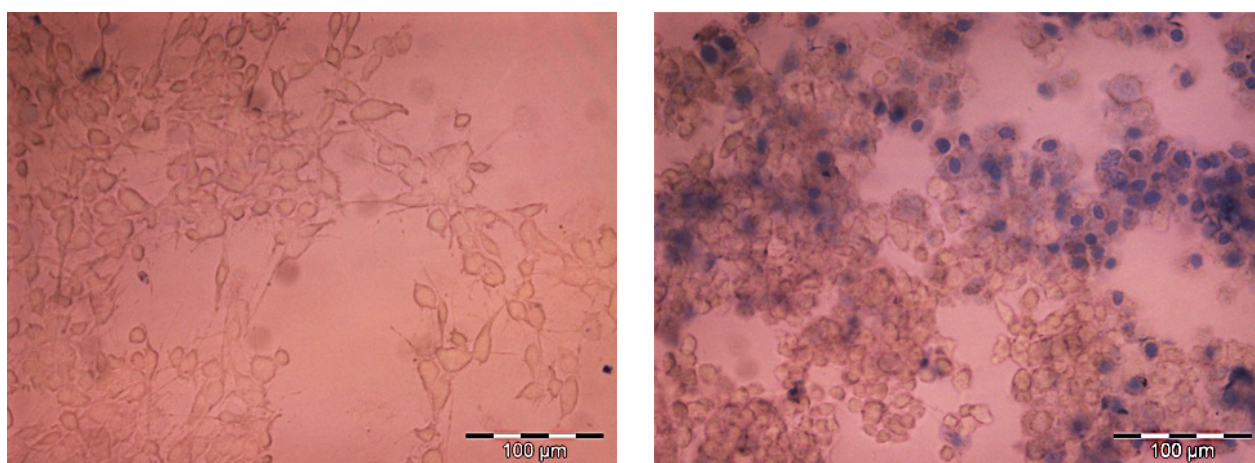


Fig. 6.24 Trypan blue cell mortality test performed after 24 hours of incubation for C6 glioma cells. Left) Control sample (pure cell culture), which shows the dye does not stain healthy cells; right) sample treated with 0.15 mg/ml TRAIL@BS-NP. Dead cells are visualized in blue after interaction with trypan blue.

As depicted in the fluorescence microscopy imaged shown in Figure 6.24, TRAIL@BS-NPs actually induced an apoptosis effect on C6 glioma cells, which is visualized through the trypan blue stain of dead cells. Although this test represents a qualitative one, it can be seen that the statistic

distribution of the blue stained dead cells seems to match the 45% cell viability percentage estimated before, proving the reproducibility of the TRAIL effect.

To further investigate the live cell delivery properties of the system and its potentiality as chemotherapeutic tool, similar viability experiments were conducted on the same cell line using Onconase@BS-NP. In this case, also Onconase@NonBS-NP were synthesized and used to incubate the cells, in order to have better hints on the effective role played by the biodegradable disulfide architecture. The cell experiments were then performed as above, and once again the cell viability was eventually evaluated as indicator of the induced cell apoptosis.

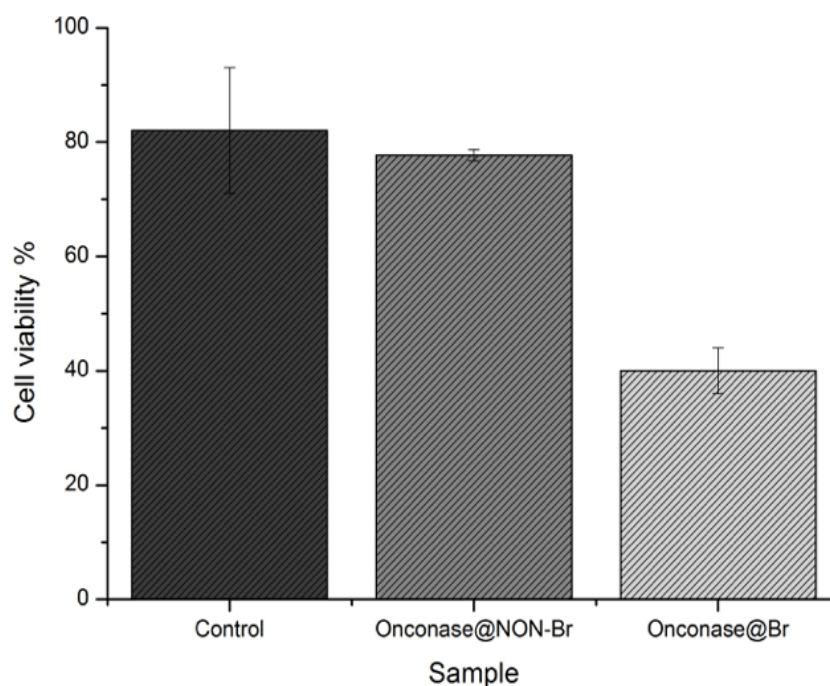


Fig. 6.25 Cell viability values obtained after 24 hours of incubation for C6 glioma cells. Control (pure cell culture) 82.5%, Onconase@NonBS-NP 77.7%, Onconase@BS-NP 40.6%. All experiments were reproduced in triplicate.

From the graph reported in Figure 6.25, one can first notice that the use of Onconase@NonBS-NP did not affect the cell viability, as no significant change could be registered with respect to the control sample. Still, this is a good indication of the biocompatibility of the material, as well as a proof that the protein cargo cannot leak out when the nanocapsule shell is made entirely of silica. On the other hand, when treating the cells with Onconase@BS-NP (0.15 mg/mL, 24 h), a dramatic drop of the viability percentage was obtained, up to 40%. This is indeed explained with the delivery of Onconase upon degradation of the breakable encapsulating shell. The data strongly suggest that the Onconase was thus released and it is still in its active conformation, able to carry on its related anti-tumor effect.

6.6 Conclusion

A general method for the encapsulation of proteins and enzymes within a biodegradable hybrid organo-silica shell has been performed. The inclusion of disulfide moieties in the silica network of the constructed shell allowed for triggering the breakdown of the shell and the consequent release of the protein cargo under reductive conditions. The designed system has been then tested for the intracellular delivery of highly cytotoxic proteins as TRAIL Apo2 Ligand or Onconase to glioblastoma cells, proving the therapeutic effect when the enzymes were delivered upon breaking of the protective shell, demonstrating the proteins were maintained in an active form during the encapsulation process. A full investigation on the live cell distribution and the biodegradation/release kinetics has been carried out by means of encapsulated GFP, which allows for following the system behavior by fluorescence confocal microscopy. On account of the properties of the nanocapsule architecture, the designed system may have a huge impact on a safe, controlled, and sustainable delivery of biomacromolecules in living organisms, taking into account that several diseases are caused by the lack or low expression of important enzymes, proteins, and other biomolecules. The possible direct delivery of specific proteins through the presented strategy thus might express tremendous potential in biological and medical application, and the future transfer to *in vivo* experiments is strongly envisaged.

6.7 Experimental section

CyC@BS-NP

Synthesis Breakable particles

Triton X-100 (1.77 mL) and n-hexanol (1.8 mL) were dissolved in Cyclohexane (7.5 mL). Separately, 300 μ L of a 2.5 mg/mL aqueous solution of Cytochrome C from equine heart were mixed with 40 μ L of tetraethyl orthosilicate (TEOS) and 60 μ L of bis[3-(triethoxysilyl)propyl]disulfide. After shaking, this mixture was added to the former organic medium. Eventually, 50 μ L of 30% ammonia aqueous solution were added and the water-oil emulsion was stirred overnight at room temperature.

After that, 20 mL of pure acetone were added in order to precipitate the CyC@BS-NPs and the material was recovered by means of centrifugation, washing twice with ethanol and three times with water.

Synthesis of Non-Breakable particles

The above described synthetic procedure was followed using only TEOS (100 μ L) as silica agent, instead of a mixture of TEOS and bis[3-(triethoxysilyl)propyl]disulfide.

Chemical biodegradability test and simulation of protein delivery

Reduction of the S-S bond was first performed with sodium borohydride (NaBH_4). NaBH_4 (1 mg) was added to 1 mL of a 0.5 mg/mL dispersion in water of CyC@BS-NPs. The mixture was stirred overnight at room temperature. After that, the sample was centrifuged and the supernatant was recovered in view of being analyzed by means of UV-Vis spectroscopy, to check out the presence of the delivered protein.

Reduction of the S-S bond was also performed with glutathione mimicking the process occurring inside of live cells. Glutathione (5 mM) was added to 1 mL of a 0.5 mg/mL dispersion in water of CyC@BS-NPs. The mixture was stirred overnight at room temperature. After that, the sample was centrifuged and the supernatant was recovered for being analyzed via UV-Vis spectroscopy, to check out the presence of the delivered protein.

The same glutathione test was performed under the same conditions for a sample of non-breakable particles, in order to compare the two results.

Breakdown/Release kinetics of Cytochrome C

Samples of 600 μ L of 0.5 mg/mL particle dispersion in water were incubated with 5 mM glutathione. The breaking/release kinetics was followed by centrifuging the samples and by analyzing the supernatant at the UV-Vis spectrometer, monitoring the absorption peak of released Cytochrome C. Sampling was done after 0, 1, 2, 4, 12, 24, 48 hours of incubation with glutathione. In the meantime, at every incubation stage, the residual material found stuck on the vial walls after centrifugation was rescued and analyzed by SEM.

Calculation of the number of proteins encapsulated in a single shell

From the UV-Vis spectrum of 1 mL of a 0.5 mg/mL dispersion of Cytochrome@BS-NP treated with NaBH_4 as model model reducing agent:

$$A = 0.04091 \text{ at } \lambda = 410$$

From the calibration curve of Cytochrome C in water: $y = 0.0909x$ (concentration in μM)

$$C = A/x = 0.04091/0.0909 = 0.4500 \mu\text{M}$$

$$MW_{\text{CytC}} = 12359.3526 \text{ g/mol}$$

$$n = CV = 0.4500E^{-6} \cdot 0.01 = 4.5E^{-9} = 4.5 \text{ nanomoles (V = 10 mL)}$$

$$\text{diameter (particle)} = \text{average } 50 \text{ nm}$$

$$\text{density}_{\text{CytC}} = 1.35 \text{ g/cm}^3$$

$$\text{density}_{\text{SiO}_2} = 0.445 \text{ g/cm}^3$$

$$\text{average considered density} = 0.9 \text{ g/cm}^3$$

$$V = 4/3\pi r^3 = 6.55E^{-17} \text{ cm}^3$$

$$m_{\text{single particle}} = dV = 0.9 \cdot 6.55E^{-17} = 5.9E^{-17} \text{ g}$$

$$\text{number}_{\text{particles}} = \text{total mass} / \text{mass 1 particle} = 0.005 \text{ g} / 5.9E^{-17} \text{ g} = 8.5E^{13}$$

$$\text{number}_{\text{CytochromeC molecules}} = \text{moles} \cdot \text{Avogadro } n = 4.5E^{-9} \cdot 6.023E^{23} = 27.1035E^{14}$$

$$\text{Number protein/particle} = 27.1035E^{14} / 8.5E^{13} = 31.886$$

$$\text{Cytochrome C size} = 2.6\text{nm} \times 3.2\text{nm} \times 3.3\text{nm} \text{ (from literature [54,55])} = 27.457 \text{ nm}^3$$

$$V \text{ (total protein encapsulated in 1 particle)} = 27.457 \cdot 31.886 = 875.49 \text{ nm}^3$$

$$V \text{ (1 particle)} = 6.55E^{-17} \text{ cm}^3 = 65449.85 \text{ nm}^3$$

$$V \text{ (spherical corona)} = 64574.36 \text{ nm}^3$$

$$\text{From } V \text{ (total protein encapsulated in 1 particle)} = 27.457 \cdot 31.886 = 875.49 \text{ nm}^3$$

$$R = \sqrt[3]{(3V)/(4\pi)} = 5.93 \text{ nm} \text{ (radius of supposed protein core),}$$

Which means $d \approx 12 \text{ nm}$, and $\approx 19 \text{ nm}$ thickness of the silica shell.

Cytotoxicity study

Cell viability was measured by an automatic cell counter CASY (Roche Innovatis 30 AG, Bielefeld, Germany). Around 50000 C6 Glioma cells from rat brain were grown in 2 ml of culture media inside 6 well plates at 37° C, 5% CO₂ environment, for 24 hours. Culture media were removed and replaced with a 0.15 mg/mL dispersion of CyC@BS-NP, followed by cell incubation. After 24 hours, the culture media were removed to an eppendorf tube and 0.5 mL of trypsin was added. In order to detach the cell from the surface of the plate, cells were incubated for the next 5 minutes.

Subsequently, 1.5 mL of new culture media was added to neutralize trypsin. Cell suspension together with the first solution collected were removed into a 10 mL eppendorf tube and centrifuged at 1000 rpm for 5 minutes. Supernatant was removed and cell pellets were suspended into 1 ml of new culture media. 100 μ L of the cell suspension were dissolved in 10 mL of CASYton solution and measurement was performed.

TRAIL@BS-NP

Synthesis

Triton X-100 (1.77 mL) and n-hexanol (1.8 mL) were dissolved in Cyclohexane (7.5 mL). Separately, 100 μ L of a 0.5 mg/mL aqueous solution of Human TRAIL (APO2 Ligand) were mixed with 40 μ L of tetraethyl orthosilicate (TEOS) and 60 μ L of bis[3-(triethoxysilyl)propyl]disulfide. After shaking, this mixture was added to the previous organic medium. Eventually, 50 μ L of 30% ammonia aqueous solution were added and the water-oil emulsion was stirred overnight at room temperature. After that, 20 mL of pure acetone were added in order to precipitate the TRAIL@BS-NP particles and the material was recovered by means of centrifugation, washing with ethanol twice and with water 3 times.

Cell viability experiments

Cell viability was measured by an automatic cell counter CASY (Roche Innovatis 30 AG, Bielefeld, Germany). Around 50000 C6 Glioma cells from rat brain were grown in 2 ml of culture media inside 6 well plates at 37° C, 5% CO₂ environment, for 24 hours. Culture media were removed and replaced with a 0.15 mg/mL dispersion of TRAIL@BS-NP, followed by cell incubation. After 24 hours, the culture media were removed to an eppendorf tube and 0.5 mL of trypsin was added. In order to detach the cell from the surface of the plate, cells were incubated for the next 5 minutes. Subsequently, 1.5 mL of new culture media was added to neutralize trypsin. Cell suspension together with the first solution collected were removed into a 10 mL eppendorf tube and centrifuged at 1000 rpm for 5 minutes. Supernatant was removed and cell pellets were suspended into 1 ml of new culture media. 100 μ L of the cell suspension were dissolved in 10 mL of CASYton solution and measurement was performed.

Toxicity assay via Trypan Blue

Culture media were removed from cell well plates and replaced with 0.15 mg/ml of TRAIL@BS-NP dispersion. The cells were incubated for the next 24 hours at 37°C and 5% CO₂ condition. After

the incubation, the medium was removed and the cells were gently washed with PBS three times to remove the excess of non-uptaken material. Subsequently, 10 ml of 0.4% trypan blue dye (Bio-Rad) were added and cells were incubated for the next 2 minutes. Cells were imaged without performing washing steps, using Olympus BX51M fluorescence microscope coupled to Olympus XC10 digital camera (Olympus Corporation).

Onconase@BS-NP

Synthesis

Synthesis of the breakable nanospheres was carried out following the same protocol already described for Cytochrome C and TRAIL. In this case, 300 μ L of a 1.66 mg/mL solution of Onconase (20 mM Tris buffer with 0.25 M NaCl) was used, together with TEOS (40 μ L) and bis[3-(triethoxysilyl)propyl]disulfide (60 μ L).

Onconase samples were kindly provided by Prof. Donald Hilvert's group, ETH, Zurich (CH).

Synthesis of non-breakable Onconase particles

The above described synthetic procedure was followed using only TEOS (100 μ L) as silica agent, instead of a mixture of TEOS and bis[3-(triethoxysilyl)propyl]disulfide.

Cytotoxicity study

Cell viability tests were done according to the same procedure already reported for Cytochrome and TRAIL particles.

Nanoparticle incubation

Culture media were removed from cell well plates and 1 mL of nanoparticles dispersion containing Atto565-labeled Onconase@BS-NP was gently added onto cells (concentration 0.1 mg/ml). Cells were incubated at 37°C and 5% of CO₂ for 1, 4, and 24 hours and after each of the incubation is finished, the media was removed and the cell layer on glass cover slips was gently washed three times with fresh PBS. Cell layer was fixed with 4% paraformaldehyde (PFA) solution for 10 minutes. The layer was washed twice with PBS and kept in 0.1% Triton X-100 in PBS for 5 minutes, washed twice with PBS and followed in 1% bovine serum albumin, BSA (Sigma Aldrich), in PBS for 20 minutes. Cells were gently washed with PBS twice. PBS was removed and the cell layer on glass cover slip was directly stained with Phalloidin Alexa Fluor® 647 (Invitrogen), for F-actin/membrane staining, for 20 minutes, in the dark at room temperature, and washed again twice

with PBS and once with water. The cover slips were mounted onto glass slides for confocal microscopy measurements.

Confocal microscopy experiment

Fluorescence microscopy experiments were carried using Zeiss LSM 710 confocal microscope system equipped with 63 times magnification, numerical aperture 1.3 of Zeiss LCI Plan-NEOFLUAR water immersion objective lens (Zeiss GmbH). The Atto565-labeled Onconase@BS-NPs were excited by a continuous wave (cw) laser at 543 nm, while the cells previously co-stained with DAPI (excitation/emission wavelength: 358 nm/461 nm) and Alexa Fluor® 647 Phalloidin dye (excitation/emission wavelength: 650 nm/668 nm) were excited independently at 405 and 633 nm, respectively. The emissions of the particles, DAPI, and Alexa Fluor® 647 Phalloidin were collected using their corresponding emission filter. All image processing was done by ZEN software (Zeiss GmbH). False colour images were adjusted to better distinguish the particles and cellular organelles.

GFP@BS-NP

Synthesis

The synthesis of the breakable nanospheres was carried out following the same protocol already described. In this case, 300 μ L of a 1 mg/mL PBS solution of GFP was used, mixed together with TEOS (40 μ L) and bis[3-(triethoxysilyl)propyl]disulfide (60 μ L).

Chemical biodegradability test and simulation of protein delivery

The breakdown of the silica shell was induced by reduction of the S-S bond with NaBH₄ or glutathione following the same procedure already reported for Cytochrome@BS-NPs.

After centrifugation, the supernatant was analyzed by fluorescence microscopy to assess the presence of the released GFP ($\lambda_{exc} = 430$ nm).

Confocal microscopy experiment

Fluorescence microscopy experiments were carried using Zeiss LSM 710 confocal microscope system equipped with 63 times magnification, numerical aperture 1.3 of Zeiss LCI Plan-NEOFLUAR water immersion objective lens (Zeiss GmbH). GFP emission was induced by exciting with a continuous wave (cw) laser at 488 nm, while the cells previously co-stained with Hoechst 33342 and LysoTracker® red were excited independently at 405 and 594 nm, respectively. The emissions of GFP, Hoechst 33342, and LysoTracker® red were collected using their

corresponding emission filter. All image processing was done by ZEN software (Zeiss GmbH). False colour images were adjusted to better distinguish the particles and cellular organelles.

C6 Glioma Cell culture

Animal cells, *Rattus norvegicus* brain glioma (C6 glioma) cells were grown inside culture media containing 88% Dulbecco's Modified Eagle Medium (DMEM), 10% Fetal Bovine Serum (FBS), 1% Penicillin-Streptomycin, and 1% L-Glutamine 200mM (all materials were purchased from Gibco), under 37°C and 5% CO₂ condition, until reaching 80 to 90% cell confluency. The cells were washed twice with Phosphate Buffer Solution (PBS, Gibco), trypsinated, and 50,000 cells were seeded on the rectangular glass cover slip (VWR) inside six-well plate culture dish and glass bottom dishes (MatTek). Fresh culture medium (2 mL) was added gently and cells were grown overnight.

REFERENCES

- [1] H. Zhou, S. Wu, J.Y. Joo, S. Zhu, D.W. Han, T. Lin, *et al.* *Cell stem cell* **2009**, *4*, 381-384.
- [2] D. Kim, C.H. Kim, J.I. Moon, Y.G. Chung, M.Y. Chang, B.S. Han, *et al.*. *Cell stem cell* **2009**, *4*, 472.
- [3] S.R. Schwarze, A. Ho, A. Vocero-Akbani, S.F. Dowdy, *Science* **1999**, *285*, 1569-1572.
- [4] T. Gaj, J. Guo, Y. Kato, S.J. Sirk, C.F. Barbas III, *Nat. Methods* **2012**, *9*, 805-807.
- [5] S. Amsellem, F. Pflumio, D. Bardin, B. Izac, P. Charneau, P.H. Romeo, S. Fichelson, *Nat. Med.* **2003**, *9*, 1423-1427.
- [6] J.R. Heath, M.E. Davis, *Annu. Rev. Med.* **2008**, *59*, 251.
- [7] V.R. Sinha, A. Trehan, *J. Control. Release* **2003**, *90*, 261-280.
- [8] Cancer Genome Atlas Network, *Nature* **2012**, *490*, 61-70.
- [9] A.M. Shah, D.L. Mann, *The Lancet*, **2011** *378*, 704-712.
- [10] K.M. Heffner, D.B. Hizal, A. Kumar, J. Shiloach, J. Zhu, M.A. Bowen, M.J. Betenbaugh, *Curr. Opin. Biotech.* **2014**, *30*, 80-86.
- [11] M. Tyers, M. Mann, *Nature* **2003**, *422*, 193-197.
- [12] S. Mitragotri, P.A. Burke, R. Langer, *Nat. Rev. Drug Discover.* **2014**, *13*, 655-672.
- [13] K. Fu, A.M. Klibanov, R. Langer, *Nat. Biotech.* **2000**, *18*, 24-25.
- [14] W. Jiskoot, T.W. Randolph, D.B. Volkin, C.R. Middaugh, C. Schöneich, G. Winter, *et al.* *J. Pharm. Sci.* **2012**, *101*, 946-954.
- [15] M.C. Manning, D.K. Chou, B.M. Murphy, R.W. Payne, D.S. Katayama, *Pharm. Res.* **2010**, *27*, 544-575.

- [16] S. Salmaso, S. Bersani, A. Semenzato, P. Caliceti, *J. Nanosci. Nanotech.* **2006**, *6*, 9-10.
- [17] M. Ye, S. Kim, K. Park, *J. Control. Release* **2010**, *146*, 241-260.
- [18] Z. Gu, A. Biswas, M. Zhao, Y. Tang, *Chem. Soc. Rev.* **2011**, *40*, 3638-3655.
- [19] J. Du, J. Jin, M. Yan, Y. Lu, *Curr. Drug Metab.* **2012**, *13*, 82-92.
- [20] M. Rao, C.R. Alving, *Adv. Drug Deliver. Rev.* **2000**, *41*, 171-188.
- [21] M.L. Tan, P.F. Choong, C.R. Dass, *Peptides* **2010**, *31*, 184-193.
- [22] G. Zhu, S.R. Mallery, S.P. Schwendeman, *Nat. Biotech.* **2000**, *18*, 52-57.
- [23] P. Tanner, P. Baumann, R. Enea, O. Onaca, C. Palivan, W. Meier, *Accounts Chem. Res.* **2011**, *44*, 1039-1049.
- [24] R. Ravindra, S. Zhao, H. Gies, R. Winter, *J. Am. Chem. Soc.* **2004**, *126*, 12224-12225.
- [25] R. Wang, Y. Zhang, D. Lu, J. Ge, Z. Liu, R.N. Zare, *Wiley Interdisciplinary Reviews: Nanomedicine and Nanobiotechnology* **2013**, *5*, 320-328.
- [26] A. Lees, G. Sen, A. Lopez-Acosta, *Vaccine* **2006**, *24*, 716-729.
- [27] M.J. Roberts, M.D. Bentley, J.M. Harris, *Adv. Drug Deliver. Rev.* **2012**, *64*, 116-127.
- [28] Y. Abe, H. Shibata, H. Kamada, S.I. Tsunoda, Y. Tsutsumi, S. Nakagawa, *Anti-Cancer Agents in Medicinal Chemistry* **2006**, *6*, 251-258.
- [29] S.E. Averick, E. Paredes, D. Grahacharya, B.F. Woodman, S.J. Miyake-Stoner, R.A. Mehl, *et al. Langmuir* **2012**, *28*, 1954-1958.
- [30] G. Pasut, F.M. Veronese, *Polymer Therapeutics I, Advances in Polymer Sciences*, Springer Berlin Heidelberg **2006**, 95-134
- [31] A.K. Shakya, H. Sami, A. Srivastava, A. Kumar, *Prog. Polym. Sci.* **2010**, *35*, 459-486.
- [32] S.I. Lim, Y. Mizuta, A. Takasu, Y.H. Kim, I. Kwon, *PloS one* **2014**, *9*, e98403.
- [33] E. Yuba, A. Harada, Y. Sakanishi, S. Watarai, K. Kono., *Biomaterials* **2013**, *34*, 3042-3052.
- [34] T. Feczko, J. Toth, G. Dósa, J. Gyenis, *Chem. Eng. Process.* **2011**, *50*, 757-765.
- [35] V.T. Tran, J.P. Karam, X. Garric, J. Coudane, J.P. Benoît, C.N. Montero-Menei, M.C. Venier-Julienne, *Eur. J. Pharm. Sci.* **2012**, *45*, 128-137.
- [36] Y.P. Li, Y.Y. Pei, X.Y. Zhang, Z.H. Gu, Z.H. Zhou, W.F. Yuan, *et al. J. Control. Release* **2001**, *71*, 203-211.
- [37] N. Rescignano, L. Tarpani, R. Tiribuzi, S. Montesano, S. Martino, L. Latterini, *et al. Macromol. Biosci.* **2013**, *13*, 1204-1212.
- [38] M. Zhao, A. Biswas, B. Hu, K.I. Joo, P. Wang, Z. Gu, Y. Tang, *Biomaterials* **2011**, *32*, 5223-5230.
- [39] S.Y. Choh, D. Cross, C. Wang, *Biomacromolecules* **2011**, *12*, 1126-1136.
- [40] N. Bhuchar, R. Sunasee, K. Ishihara, T. Thundat, R. Narain, *Bioconjugate Chem.* **2011**, *23*, 75-83.
- [41] D. Vasquez, R. Milusheva, P. Baumann, D. Constantin, M. Chami, C.G. Palivan, *Langmuir* **2014**, *30*, 965-975.
- [42] T. Akagi, Y. Zhu, F. Shima, M. Akashi, *Biomater. Sci.* **2014**, *2*, 530-537.
- [43] B. Wörsdörfer, Z. Pianowski, D. Hilvert, *J. Am. Chem. Soc.* **2012**, *134*, 909-911.
- [44] R. Gaudana, V. Khurana, A. Parenky, A.K. Mitra, *J. Drug. Deliver.* **2011**, Article ID 458128.
- [45] M. van de Weert, W.E. Hennink, W. Jiskoot, *Pharm. Res.* **2000**, *17*, 1159-1167.
- [46] Y. Wang, F. Caruso, *Chem. Mater.* **2005**, *17*, 953-961.
- [47] D. Ma, M. Li, A.J. Patil, S. Mann, *Adv. Mater.* **2004**, *16*, 1838-1841.
- [48] J.M. Wallace, J.K. Rice, J.J. Pietron, R.M. Stroud, J.W. Long, D.R. Rolison, *Nano Lett.* **2003**, *3*, 1463-1467.
- [49] A. Chaudhari, L. Vanmellaert, M. Bauwens, P. Vermaelen, C.M. Deroose, I. Naert, *et al. BioMed Res. Int.* **2013**.
- [50] A. Cao, Z. Ye, Z. Cai, E. Dong, X. Yang, G. Liu, *et al. Angew. Chem. Int. Ed.* **2010**, *49*, 3022-3025.
- [51] F.P. Chang, Y.P. Chen, C.Y. Mou, *Small* **2014**.
- [52] G.K. Balendiran, R. Dabur, D. Fraser, *Cell Biochem. Funct.* **2004**, *22*, 343-352.

- [53] J.M. Estrela, A. Ortega, E. Obrador, *Crit. Rev. Cl. Lab. Sci.* **2006**, *43*, 143-181.
- [54] M. Hartmann, *Chem. Mater.* **2005**, *17*, 4577-4593.
- [55] I. I. Slowing, B.G. Trewyn, V.S.Y. Lin, *J. Am. Chem. Soc.* **2007**, *129*, 8845-8849.
- [56] A.L. Lee, S.H. Dhillon, Y. Wang, S. Pervaiz, W. Fan, Y.Y. Yang, *Mol. Biosyst.* **2011**, *7*, 1512-1522.
- [57] L. Xu, S. Yin, S. Banerjee, F. Sarkar, K.B. Reddy, *Mol. Cancer Ther.* **2011**, *10*, 550-557.
- [58] K. Shah, Y. Tang, X. Breakefield, R. Weissleder, *Oncogene* **2003**, *22*, 6865-6872.
- [59] R. W. Johnstone, A. J. Frew, M. J. Smyth, *Nat. Rev. Cancer* **2008**, *8*, 782-798.
- [60] E. G. de Vries, M. N. de Hooge, J. A. Gietema, S. de Jong, *Clin. Cancer Res.* **2003**, *9*, 912-913.
- [61] G. Bossi, E. Lapi, S. Strano, C. Rinaldo, G. Blandino, A. Sacchi, *Oncogene* **2006**, *25*, 304-309
- [62] Z. Darzynkiewicz, S.P. Carter, S.M. Mikulski, W.J. Ardelt, K. Shogen, *Cell Tissue Kinet.* **1988**, *21*, 169-182.
- [63] W. Ardelt, K. Shogen, Z. Darzynkiewicz, *Curr. Pharm. Biotech.* **2008**, *9*, 215.
- [64] Y. Wu, S.M. Mikulski, W. Ardelt, S.M. Rybak, R.J. Youle, *J. Biol. Chem.* **1993**, *268*, 10686-10693.
- [65] S.K. Saxena, R. Sirdeshmukh, W. Ardelt, S.M. Mikulski, K. Shogen, R.J. Youle, *J. Biol. Chem.* **2002**, *277*, 15142-15146.
- [66] M. Qiao, L.D. Zu, X.H. He, R.L. Shen, Q.C. Wang, M.F. Liu, *Cell Res.* **2012**, *22*, 1199.
- [67] H.L. Zhao, C. Xue, J.L. Du, M. Ren, S. Xia, Y.G. Cheng, Z.M. Liu, *J. Control. Release* **2012** *159*, 346-352.
- [68] P.A. Leland, R.T. Raines, *Chem. Biol.* **2011**, *8*, 405-413.
- [69] S.H. Kaufmann, W.C. Earnshaw, *Exp. Cell Res.* **2000**, *256*, 42-49.
- [70] C. Garrido, L. Galluzzi, M. Brunet, P.E. Puig, C. Didelot, G. Kroemer, *Cell Death Differ.* **2006**, *13*, 1423-1433.
- [71] Kluck, R. M., Bossy-Wetzel, E., Green, D. R., & Newmeyer, D. D. (1997). The release of cytochrome c from mitochondria: a primary site for Bcl-2 regulation of apoptosis. *Science*, *275*(5303), 1132-1136.
- [72] Strober, W. (2001). Trypan blue exclusion test of cell viability. *Current protocols in immunology*, A-3B.

7

PNA-modified photonic crystal fibers as label-free DNA biosensors for the detection of single-point genetic mutations

Abstract

This chapter reports the development of methods for ultra-sensitive DNA detection and describes a novel biophotonics approach based on PNA-functionalized microstructured optical fiber for the analysis of specific DNA target sequences. The inner surface of a photonic crystal fiber, where a Bragg grating had been previously inscribed, has been functionalized by covalent linking of a PNA probe targeting a DNA sequence bearing a single point mutation related to cystic fibrosis disease. In order to achieve a final enhancement of the optical signal, oligonucleotide-functionalized gold nanoparticles were used to form a sandwich-like format, thus giving a notable change in the refractive index of the system, which allowed for optical signal amplification. Experimental measurements showed a clear shift of the reflected high order mode of the Bragg grating for a 100 nM DNA solution with a good reproducibility. The use of a single-mismatched DNA solution, corresponding to the wild-type gene, has proved the high selectivity of the sensor, whose format may be implemented for diverse sensing applications.

This work has been carried out in collaboration with Professor Stefano Selleri's group, at the Information Engineering Department of the University of Parma, and in particular with Dr. Alessandro Candiani and Sara Giannetti, using fibers produced by the group of Dr. Stavros Pissadakis at the Foundation for Research and Technology—Hellas FORTH, Institute of Electronic Structure and Laser IESL, Heraklion, Crete (Greece).

A. Candiani, A. Bertucci, S. Giannetti, M. Konstantaki, A. Manicardi, S. Pissadakis, A. Cucinotta, R. Corradini, S. Selleri, Label-free DNA biosensor based on a peptide nucleic acid-functionalized microstructured optical fiber-Bragg grating, *J. Biomed. Opt.* **2013**, *18* (5), 057004

7.1 Photonic crystal fibers for sensing applications

Standard optical fibers are well known for being able to guide light by total internal reflection,

which operates only if the fiber core has a higher refractive index than the encircling cladding. In the 90s' a novel idea emerged, though, that light could be trapped inside fibers characterized by the presence of a periodic wavelength-scale lattice of microscopic holes in the cladding, mimicking the behavior of a photonic crystal. Photonic crystal fibers (PCFs), known also as microstructured optical fibers (MOFs), thus have been developed and have become powerful devices implemented for various information and communication technologies.^[1-3]

The cross-section of such fibers is defined by an array of air holes, running throughout the whole length, in a matrix of dielectric material. This makes PCFs be unique devices in which the light-guiding properties can be excellently tailored by properly designing size, shape, and relative position of the air holes. PCFs can be divided into two main categories, hollow-core fibers and solid-core fibers, based on the different physics exploited for carrying the light.

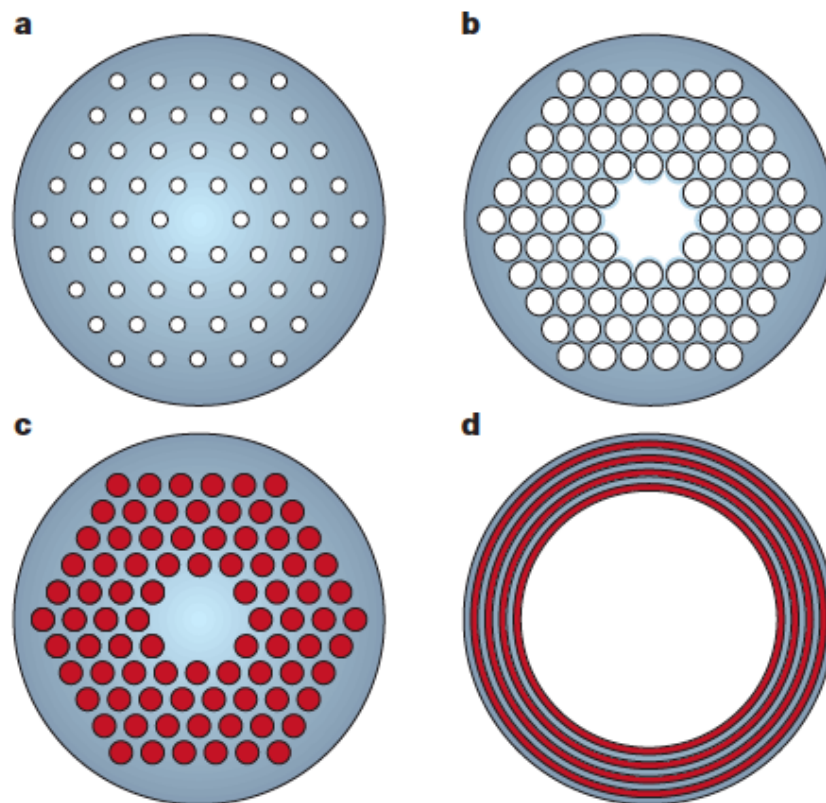


Fig. 7.1 Different designs of PCF waveguides. A) PCF with a pure silica core surrounded by a reduced-index photonic crystal cladding material. The guidance is achieved by modified total internal reflection. B) Air-guiding PCF in which light is confined into a hollow core by the bandgap of the 2D air–glass photonic crystal cladding. C) PCF in which light is confined to a low-index region by a photonic bandgap, but the core is made of pure silica while the holes in the cladding are filled with a high-index liquid. D) Hollow cylindrical multilayer fiber with an all-solid cladding. In every picture, white represents air, grey represents a low-index solid such as silica and red represents a high-index material. Reprinted by permission from Macmillan Publishers Ltd: Nature, advance online publication, 14 August 2003 (doi:10.1038/nature01940); *Nature* **424**, 847–851.

In hollow-core PCFs, the light confinement in a low-refractive-index core is obtained exploiting the

photonic bandgap mechanism, which is achieved by the introduction of the periodic lattice of holes in the cladding. Solid-core PCFs instead can guide light either in a high-refractive-index core, through a modified total internal reflection mechanism, or in a low-refractive-index core, again relying on the photonic bandgap provided by the microstructured pattern.^[4-5]

Fabrication of PCFs relies on manual assembly of glass capillaries and rods into an appropriate preform stack, whose structure corresponds approximately to the desired final fiber structure.^[6] Microstructured preforms are formed by stacking a number of capillary silica tubes and rods to form the desired air/silica pattern, fusing the stack into a preform, and then pulling the preform to a fiber at a sufficiently low temperature to avoid collapsing of the hole. The final step involves drawing the preform into a fiber with the desired dimensions. By tuning the process parameters one can define the size of the air-holes and their regularity, which allows for a high level of design flexibility and for a control over the core size and shape, as well over the index profile throughout the cladding region.

Both kinds of PCFs have undergone extensive research, with the aim of exploiting their unique characteristics to produce highly sensitive physical, chemical, and biological sensing devices.^[7-10] PCFs have opened up new fascinating possibilities in fiber-based sensor field, as their air-holes can be easily infiltrated with gases or liquids^[11-13] without compromising the fiber robustness, thus allowing for a very long interaction length, even when using very limited quantity of sample in the nanoliter range. In this view, PCF-based optical sensors based can be classified as true intrinsic sensors, where the interaction with the analyte takes place within the fiber itself, differently from extrinsic sensors, in which the optical fiber is used only as a signal transmission medium to couple light to and from the region where the sensing event occurs.

More in details, sensing performed in solid-core fibers, which is the topic of this and next chapters, is based on the evanescent tails of the guided mode field. The light propagating through a fiber is usually mostly confined into the core, but due to the evanescent component of the electromagnetic wave, the tail of the electromagnetic field penetrates into the holes of the microstructured cladding and thereby probes any sample sited there.^[14-17] The larger the fraction of the field that propagates as evanescent wave, the stronger the interaction between the light and the samples placed in the air holes. Solid-core fibers provide a lower field-sample interaction if compared to the hollow-core ones, but their much lower confinement losses on a broader wavelength range make them powerful sensing devices as well. Different solid-core PCF structures have been considered for sensing, and some examples are shown in Figure 7.2.

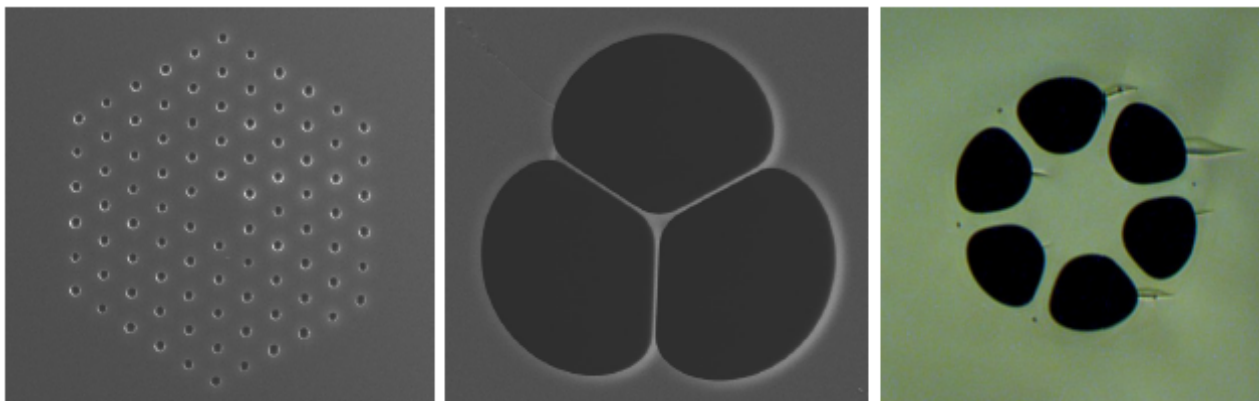


Fig. 7.2. Photonic crystal fibers with a hexagonal pattern of air holes forming the microstructured cladding (left), air-suspended core fiber (center), and hole assisted fiber (right). Adapted from R. Corradini, S. Selleri, *Photonic Crystal Fiber for Physical, Chemical and Biological Sensing in Photonic Bandgap Structures*, Bentham Publisher, **2010**, 80-84.^[18]

There is also an immense number of different working formats when using optical fiber sensors, which can be based on procedures exploiting fluorescent markers, or on the change in the refractive index after the infiltration of the target analyte, or the spectral response in transmission or reflection, or even that one given by Bragg, long period and relief gratings which can be inscribed into the fiber core or capillary surface.^[10,19]

PCFs are indeed very attractive and promising for bio-sensing applications. The simultaneously confinement of the liquid phase samples and the optical guided modes on the surface or within the holes of PCFs endows strong light- sample interaction over an extended length, which is crucial for the development of highly sensitive biological sensing in liquids. Among the reported applications of PCFs as biosensors, one of the pioneering work has been the one presented by Jensen *et al.* describing the detection of Cyanine 5 labeled-DNA strands in aqueous solution using a solid-core MOF^[12]. Ruan *et al.* used soft glass PCFs to detect quantum dot-labeled proteins, achieving a detection limit of 1 nM^[20]; Afshar *et al.* developed a generic model of excitation and fluorescence recapturing within filled solid-core MOFs.^[21] Polymeric MOFs, which have attractive material and biochemical properties, have also been successfully used in biophotonic sensing applications, and, for instance, a polymethylmethacrylate microstructured fiber has been utilized for fluorescence-based selective detection of the antibodies.^[22] In order to develop label-free detection schemes, Markos *et al.* realized a dual-core fiber biosensor able to detect changes in the layer thickness of antibody-antigene couples on the inner surfaces of the fiber holes by monitoring the change in the coupling length between the two cores.^[23] Long period gratings (LPGs) in microstructured fibers have been used by Rindorf *et al.* to measure the thickness of a monolayer of poly-L-lysine and dsDNA by observing the shift of the resonant LPG peak.^[24]

It is worth noticing that, differently from sensing of physical properties such as temperature and strain where the changes in intrinsic characteristic of the fibers can be exploited,^[25] chemical and especially biological sensing normally require modification of the outer or inner surfaces of the fibers with layers of capturing molecules.^[26] The possibility of chemically modifying the fiber surfaces indeed paves the way towards a variety of applications, tuning the properties of the device for the detection of specific biological targets. This is particularly evident when thinking on the development of PCF-based biosensors for DNA detection, enabling the selective capture and analysis of selected desired target sequences. The feasibility of this approach was demonstrated in the case of DNA capture for the first time by Coscelli *et al.* using PNA probes.^[27]

In this chapter, a novel DNA sensing approach based on a PNA-functionalized Bragg-grating-inscribed-PCF is reported. The use of a Bragg grating inscribed in the fiber allows to monitor the signal in reflection mode; in this way, a design of the sensor having both the light source and the detector at the same end of the fiber is made possible, thus leaving the opposite fiber end available for sample infiltration. The inner surface of a grapefruit geometry MOF has been functionalized with PNA probes to selectively capture a target DNA oligonucleotide related to the cystic fibrosis disease. An important novelty of the present work compared to previous ones has been the use of oligonucleotide-functionalized gold nanoparticles (ON-AuNPs) to form a sandwich-like system inside the fiber channels for optical signal amplification. A demonstration about the feasibility of such a biophotonic approach is presented in this Chapter. Most of this work has been published in the *Journal of Biomedical Optics*.^[28]

7.2 Fabrication of PNA-modified Photonic Crystal Fibers

The PFC used in this work was 25.8 cm long with grapefruit geometry, having five holes of 20.8 μm diameter each, forming an outer core of 16.1 μm . The Bragg grating was inscribed in the fiber as described in the experimental section. It reflects two major modes in the IR region, located at 1546 nm (fundamental) and 1541.6 nm (first order). $2\Lambda n_{\text{eff}}$, where n_{eff} is the effective refractive index at the location of the grating, and Λ is the Bragg grating period. The dependence of λ_{Bragg} on n_{eff} allows for detecting the hybridization event by exploiting ultra-small wavelength shifts of this band, in the IR spectral range, due to variation of the total refractive index.

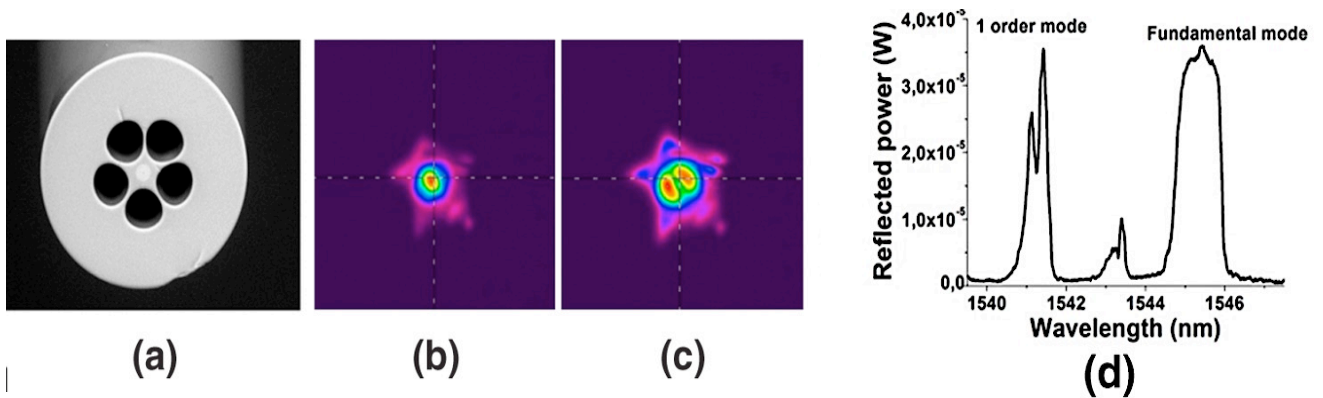


Fig. 7.3 A) SEM picture of the 5 hole-microstructured optical fiber; B) Fundamental and C) first order beam profiles. D) Reflection spectrum of the PCF, showing the fundamental and the first order modes. The double peak effect visible in the first order band is due to a slight birefringence of the fiber.

PNA-functionalization of the inner surface of the fiber holes was achieved by tethering the probes through a silanization procedure. After activation with acidic methanol, the silica surface was first functionalized with APTES by silane chemistry. The amine groups so introduced were then converted into carboxylic acid groups by reaction with succinic anhydride. Eventually, after the formation of activated NHS-ester moieties, the PNA probes were covalently attached to the surface via acyl coupling reaction. The PNA probe chosen H-(AEEA)₂-CTTTCCTTCACTGTT-NH₂ is full complementary to a DNA sequence bearing a single-point mutation (W1282X) implicated in cystic fibrosis disease (CF), which is the most common genetic mutation present on 50% to 60% of CF chromosomes in the Ashkenazy Jewish population.^[29-30] The PNA probe used is targeted to the mutant sequence and ideally should give low or no response to the wild type DNA, thus revealing only the presence of the disease-related sequence. After PNA attachment, the remaining NHS esters were quenched with ethanolamine.

To verify the ability of the PNA-modified surface to capture complementary DNA, the modified PCF and a non-functionalized one were infiltrated with a solution of fluorescently labeled Cy3-DNA, whose sequence was full complementary to the PNA sequence used for the surface functionalization (Cy3-GCAACAGTGAAGGAAAGCC). The two fibers were infiltrated for 50 minutes via a syringe pump with a DNA aqueous solution 100 nM, then dried with a nitrogen flow, washed with excess PBS and finally dried again. The two fibers were fixed on a glass slide and a fluorescent image was recorded by means of a microarray fluorescence reader, using a laser source of 543 nm for the excitation of the Cy3 label. By evaluating the fluorescence intensity from the Scan Array image through the instrument software, the signal-to-noise ratio, with respect to the

background of the plane glass slide, was found to be almost 140 in the case of the PNA-modified fiber, with a resulting signal that ensued to be almost nine folds more intense than that obtained for non-modified one. The Scan Array images are shown in Figure 7.4, demonstrating the actual success of the PNA functionalization procedure and the retained ability of the probes to bind to the complementary DNA full match target sequence.

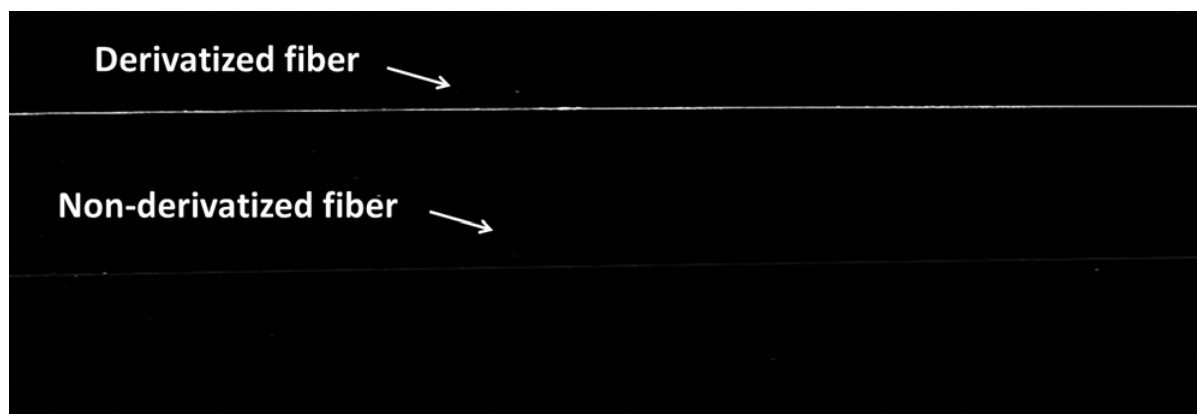


Fig. 7.4 Scan Array Express image of an unmodified PCF (below) and a PNA-functionalized one (above) after infiltration of the fluorescently Cy3-labeled full complementary DNA oligonucleotide.

Table 7.1 Sequences of the PNA probe and DNA strands used in this work. In underlined bold, the base corresponding to the W1282X CF mutation, in italics the target region for ON-AuNPs.

Oligo	Sequence	Role
PNA	H-spacer-CTTTCCTTCACTGTT-NH ₂	Probe
DNA	5'-ATCGATGGTGTGTCTT-GGGATTCAATAACTTTGC-AACAGTGA <u>A</u> AGGAAAG-3'	Full-match target
DNA	5'-ATCGATGGTGTGTCTT-GGGATTCAATAACTTTGC-AACAGTGG <u>G</u> AGGAAAG-3'	Single mismatch
DNA	5'-AAGACACACCATCGAT-3'-Biotin	AuNP-ON

The more intense fluorescence signal in the modified fiber is indeed due to the capture of the target DNA by the PNA probes attached on the inner fiber surface, whereas the residual fluorescence in the unmodified fiber is ascribed to a non-specific adsorption on the silica surface. Although in some protocols bovine serum albumin (BSA) can be used as blocking agent to reduce non-specific interaction with the substrate, in this case, due to the further use of ON-AuNPs for the optical signal enhancement, an unspecific gold nanoparticle-BSA interaction may produce unwanted binding during the final step of the analytic procedure, thus giving false positive results. Hence, only

passivation of the active sites with ethanolamine was used as reported above.

7.3 Nanoparticle-enhanced DNA detection

In the label-free detection experiment, a DNA strand bearing the CF point mutation in the PNA-target region and presenting a flanking region for further AuNP-ON binding was used, whose sequence is reported in Table 6.1. The fundamental design of the working scheme was based on the formation of a sandwich-like system PNA-DNA-(DNA-AuNP) in order to increase the sensitivity of the method through an optical signal enhancement. A schematic view of the designed system is displayed in Figure 7.5.

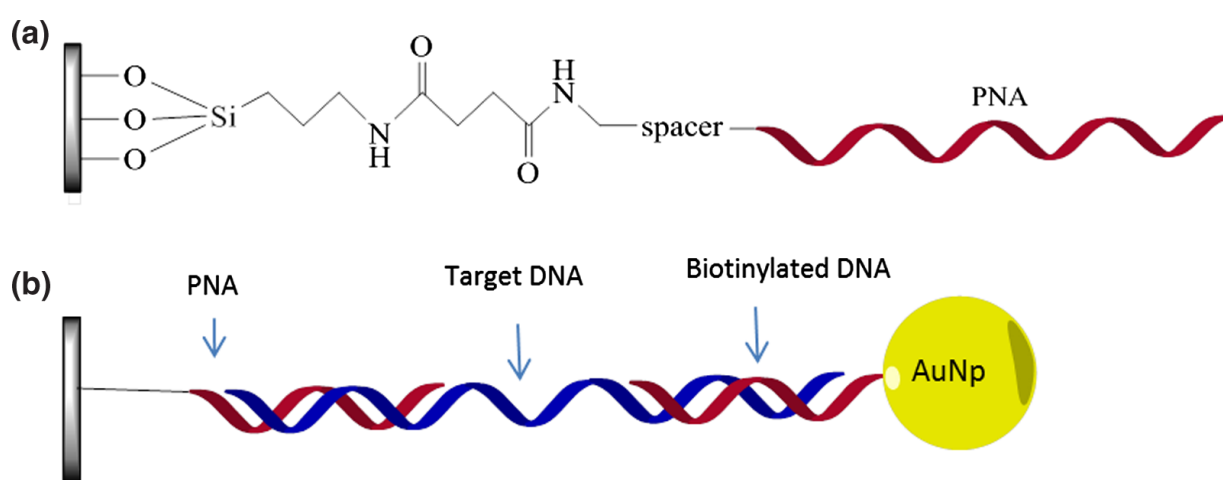


Fig. 7.5 A) Scheme of the covalent linkage of the PNA probe to the inner surface of the fiber holes; B) schematic view of the sandwich-like system used for DNA detection.

Nanoparticle and sub-wavelength structured material can lead to significant improvements in the detection limit of some optical-based analytical techniques, at the same time simplifying sensing devices and the protocols based on DNA and DNA-like probes^[31-35], especially in those in which the analytical response depends on an event taking place at the nanometer scale on the sensor surface. Accordingly to that, a great change in the refractive index can be achieved using gold nanoparticles (AuNPs) targeting the DNA already captured by specific PNA probes, as shown for other optical techniques.^[36-40] Thus, streptavidin-coated AuNPs were prepared and further loaded with a biotinylated DNA oligonucleotide complementary to the target DNA region flanking the PNA target sequence (Fig. 7.5 B), which is common to both the full-match and mutated sequence, and corresponding to the actual gene tract flanking the target mutation. Synthesis, characterization,

and functionalization of the gold nanoparticles are described in the experimental section.

The measurements were done through a customized optical setup, which is reported in Figure 7.6.

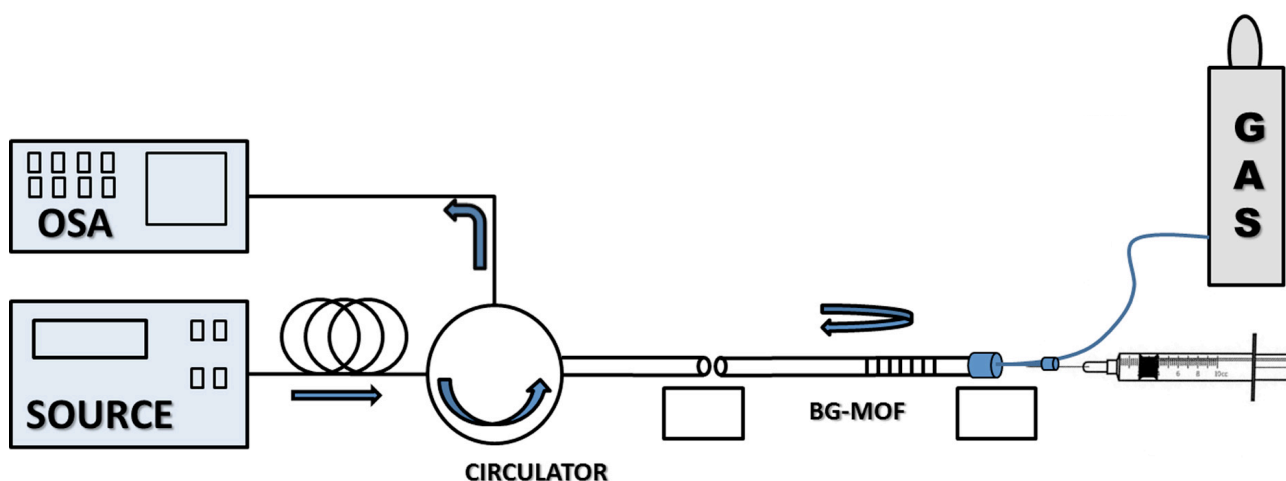


Fig. 7.6 Schematic of the optical setup implemented for the analysis. The light beam from ASE source is guided through the fiber core and is then reflected due to the Bragg grating; the reflected light is collected through a circulator and sent to a OSA detector. All the samples and reagents are infiltrated through the fiber channels by a syringe pump. The fiber is kept at constant tension (measured by a dynamometer) in order to avoid stretching of the Bragg grating.

The syringe pump was used for the infiltration of all samples at a fixed flow rate of $0.25 \mu\text{L}/\text{min}$, ensuring a continuous renewal of the DNA solution in contact with the surface. A 100 nM target full match DNA solution (Table 7.1) was thus infiltrated through the fiber capillaries for 1 hour; then the fiber was emptied by a nitrogen flow generated by a 5 atm line. The reflected signal after the first DNA pumping gave a small wavelength shift of 0.05 nm for the higher order, as illustrated in the red dash line in Fig 7.7 A. When the DNA binds to the PNA, it forms a duplex within a few nanometers from the surface of the fiber, resulting in a refractive-index change near the sensor surface. At this low DNA concentration, the captured DNA layer is not thick enough to be optically detected, in accordance with results obtained for other optical biosensors based on fiber gratings and on a similar functionalization.^[41-42] Therefore, to enhance the measured shift, the ON-AuNP solution was pumped for 1 hour under the same conditions, after which the fiber was washed with PBS and emptied again under nitrogen flow. The last process enables the AuPs to bind to the DNA target in a sandwich-like scheme, which leads to an efficient change of the effective refractive index of the system. Indeed, a much bigger wavelength shift was observed for the reflected high order band in this experiment, which was around 0.27 nm . No significant changes were instead observed for the fundamental mode, as reported in Fig 7.7 B.

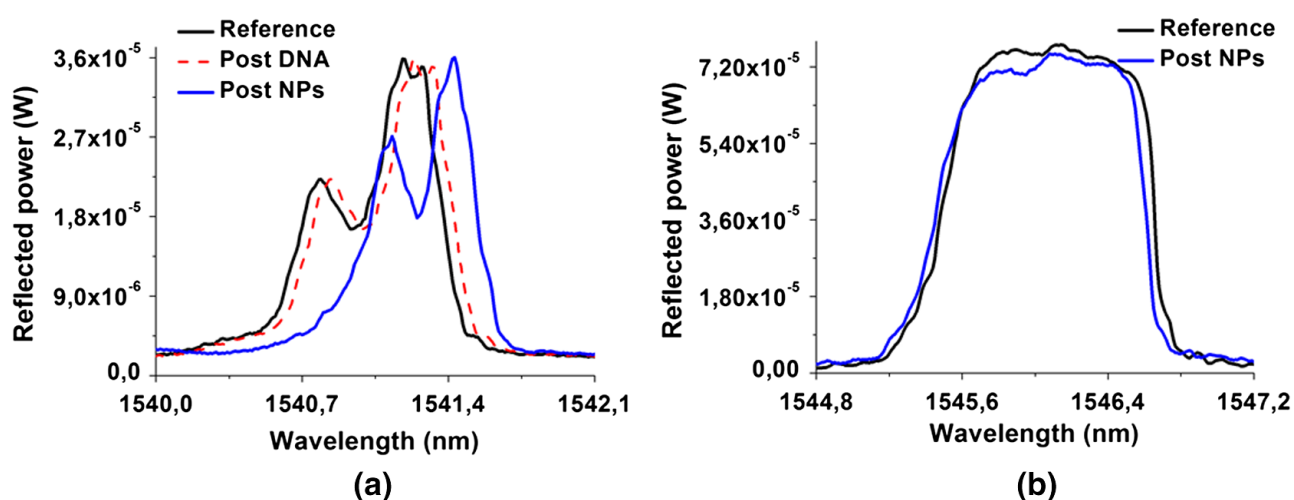


Fig. 7.7 Spectral measurements after the hybridization process with 100 nM full-match DNA solution (dashed red line) and after ON-AuNPs flow (blue line). A) A clear wavelength shift was recorded for the higher order mode, in the range of 0.27 nm; B) The fundamental mode did not show any significant change in the peak position.

The binding of the gold nanoparticles to their target on the DNA captured on the fiber successfully amplified the response of the device, increasing the effective refractive index of the fiber, n_{eff} . This effect was translated into a significant shift of the reflected high order Bragg peak, as described by the Bragg condition. The discrepancy between the two modes was supported by previous experiments on the spectral sensitivity of the two Bragg grating modes where liquids of different refractive indices were infiltrated in the capillaries. Measurements revealed that the high order mode is one order of magnitude more sensitive to refractive index changes with respect to the fundamental mode, supporting the theoretical calculations of beam profiles illustrated in Fig. 7.3 (B, C). Multiple measurements were then carried out using the same functionalized fiber, in order to evaluate the reproducibility of the sensing method. To do that, the fiber capillaries were washed with PBS for approximately 24 h with a pressure of 10 atm after each measurement. The removal of AuNPs and DNA target was confirmed spectrally by the reflected signal shifted back to its initial reference position. Two more hybridization processes were done under the same conditions showing very similar results, except for a small memory effect⁴⁰, which tends to slightly decrease the amplitude modulation with the number of tests carried out. The average wavelength shift of the high order mode was 0.04 ± 0.02 nm after first DNA hybridization, and 0.19 ± 0.06 nm ($n = 3$, RSD% = 35%) after AuNPs hybridization, as reported in Fig. 7.8.

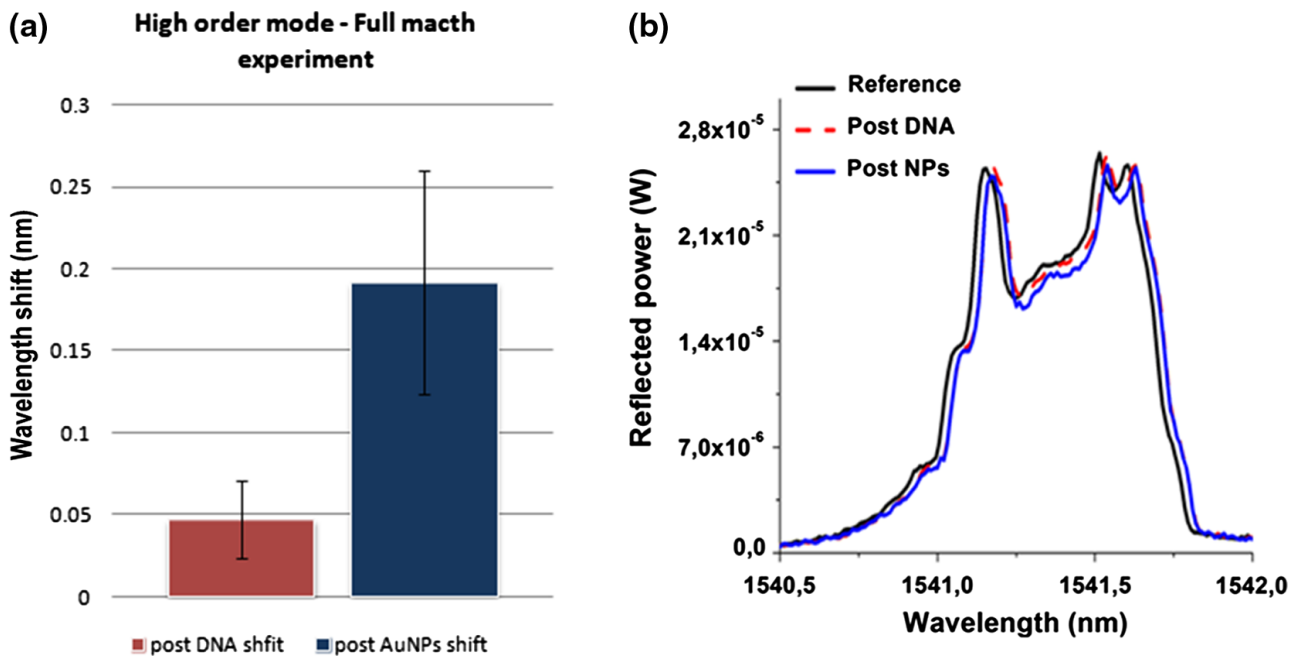


Fig. 7.8 A) Mean values of the high order wavelength shift after target DNA infiltration (red) and after ON-AuNPs (blue). Vertical bars represent sample standard deviation; a small memory effect decreases the modulation observed for each experiment performed on the same fiber. B) Spectral measurements after the hybridization process using 100 nM mismatch DNA solution and ON-AuNPs.

Eventually, the sequence-selectivity of the fiber was tested using the mismatched ON (DNA-MM), corresponding to the healthy wild type DNA, differing of only one base from the target full match DNA in the PNA targeting region, but bearing exactly the same sequence for ON-AuNP recognition. A 100 nM mismatch DNA solution was thus analyzed under the same conditions, after which a spectral measurement was recorded. The experiments showed a very weak total shift of 0.025 nm (Fig. 7.8 B), much lower than that obtained for the full match CF-DNA. After this measurement, the same fiber was washed with PBS, dried, and the hybridization experiment was repeated using the full match target DNA; the response was a final shift of 0.11 nm, consistent with the former ones, thus confirming the sequence-selectivity of the analytical method.

7.4 Conclusion

A novel DNA sensing device based on the optical response of Bragg grating inscribed-PCFs has been presented for the first time. The use of PNA probes allowed to attain sequence discrimination at the single-base level. Though the wavelength shift of the reflected high order Bragg mode was small when DNA was captured, a significant signal was achieved when using ON-AuNPs, thus indicating that these nano-tools can efficiently induce a change in effective refractive index of the

system. It has been also proved that the device is able to efficiently discriminate between a full match target DNA and a single mismatch one, thus confirming the high specificity of PNA-based methods.

This first demonstration proves the feasibility of realizing a sensor for biological measurements monitoring the wavelength of the light band reflected by a Bragg grating, utilizing the fiber both as a sensing element and as a microfluidic probe. The fiber used in this work shows a good compromise between size of the holes, sensitivity and relative ease of inscription of the grating. The approach can be extended to different versions of PCFs, with improved sensitivity to local refractive index changes, thus increasing signal modulation and sensitivity. Other recognition elements able to bind target analytes, such as proteins or contaminants, may be introduced following a similar strategy, thus making this technology suitable for powerful, compact, and versatile biosensing platforms.

7.5 Experimental section

PNA synthesis

The synthesis of the PNA probes was performed on a Syro I fully automated peptide synthesizer (Biotage, Uppsala, Sweden) in a 5 μmol scale following Fmoc chemistry, using two equivalent/double coupling protocol, with HBTU/DIPEA coupling and a Rink amide resin, loaded with Fmoc-PNA-T-OH as first monomer. The crude PNA oligomer was then purified by RP-HPLC with UV detection at 260 nm, with use of a semi-preparative XTerra Prep RP18 column (7.8 \AA ~ 300 mm, 10 μm , Waters), with a gradient elution from 100% A (0.1% TFA in water) to 100% B (0.1% TFA in acetonitrile) in 30 min; flow rate was 4 mL/min. The resulting pure PNA was characterized by ESI-MS: m/z found (calcd) 533.7 (533.8) $[\text{M}+8\text{H}]^{8+}$, 609.9 (610.0) $[\text{M}+7\text{H}]^{7+}$, 711.4 (711.5) $[\text{M}+6\text{H}]^{6+}$, 853.7 (853.6) $[\text{M}+5\text{H}]^{5+}$. The purified PNA was quantified by UV-Vis spectroscopy by UV absorbance using the following $\epsilon_{260} \text{ M}^{-1} \text{ cm}^{-1}$ for the nucleobases: T 8600, C 6600, A 13700, G 11700. The final concentration of 971.6 μM for a 1 mL sample corresponded to 971.6 nmol of product (19% yield).

Synthesis of Oligonucleotide-functionalized-gold nanoparticles

The procedure used for derivatization of gold nanoparticles was adapted from that reported by D'Agata et al.^[43] Gold nanoparticles (AuNPs) were synthesized by citrate reduction of HAuCl_4 . HAuCl_4 (20 mL, 1 mM aqueous solution) was heated up to boiling, then 2 mL of sodium citrate (38.8 mM in H_2O) were quickly added by a syringe. The solution was stirred vigorously for 10 min

under reflux. After that, the gold colloidal solution was stirred at room temperature till the flask was totally cooled down. At this stage, the purple solution was filtered through an RC filter (0.45 μM), to obtain particles in the sub-20 nm range. The AuNPs were then characterized by UV-vis spectroscopy^[44] and a mean diameter of 13 ± 3 nm was found. In order to obtain the final conjugation with a 16-mer biotinylated ON, AuNPs were initially coated with streptavidin using the following procedure: 1 ml of a diluted colloidal solution of AuNPs (plasmonic absorbance 0.2) was incubated for 1 h at 4°C with 20 μL of a 1 mg/mL streptavidin aqueous solution, then pH was adjusted to 8.5 with NaOH and an overnight incubation at 4°C was carried out. Then, a purple pellet was obtained by centrifuging the sample (3390 rcf, 30 min), which was resuspended in 500 μL H_2O . Conjugation with the biotinylated DNA sequence was carried out by adding 20 μL of a 100 μM aqueous solution of the biotinylated ON to the streptavidin coated-AuNPs. After 30 min of incubation at room temperature, the solution was centrifuged (845 rcf, 30 min) and the resulting pellet was resuspended in 100 μL PBS, pH = 7.

Bragg grating inscribed- Photonic Crystal Fiber

The PCF used in this work is 25.8 cm long with 5 hole-grapefruit geometry, with every hole of 20.8 μm diameter, forming an outer core of 16.1 μm , which includes a 3.5% wt Ge doped socket of diameter 8.5 μm . The fiber has been provided by Acreo Fiberlab (Acreo AB, Sweden). A 22 mm-long Bragg grating was inscribed in the fiber using a 1067.73 nm phase mask and a 193 nm excimer laser, with 10 ns laser radiation at the FORTH laboratory.^[45] The grating reflects two major modes, located at 1546 nm (fundamental) and 1541.6 nm (high), with strengths of 25 and 12 dB, respectively. Profile beam measurements showed that the fundamental mode is confined into the Ge-doped core, while the 1st order mode is defined by the surrounding capillary structure, extending to a greater area. The inscription of the grating causes a slight birefringence effect in the fiber, and this is observed in the high order mode spectrum, which shows a double peak profile. The Bragg grating inscription has been performed at Foundation for Research and Technology (FORTH), Heraklion, Greece.

PNA functionalization

The protocol used for PNA functionalization of the inner surface of the fiber channels is described as following:

1. Cleaning and activation of the silica surface with treatment with HCl:Methanol 1:1 for 30 min.
2. Silanization with APTES 5% in ethanol, overnight.
3. Reaction of the amine group with succinic anhydride 0.25 M in DMF.

4. Activation of the carboxylic function with DIC and NHS in DMF dry as solvent, 0.25 M both, overnight.
5. Reaction of the activated ester with the terminal amine group of the PNA probe, 30 μ M in 100 mM carbonate buffer, H₂O:ACN 9:1, 0.001% sodium dodecylsulfate, pH = 9, overnight.
6. Quenching with ethanolamine, 50 mM in aqueous Tris buffer, pH = 9, for 3 h.

Internal modification was obtained by applying a nitrogen pressure of 2 atm to an in-house built apparatus comprised by a PTFE tubing reservoir containing the solutions, connected to the end of the fiber through a HPLC-PEEK ferrule junction. After each treatment, the fiber was washed with the corresponding solvent, and the liquid was completely removed under nitrogen flow.

Optical Set-up

An amplified stimulated emission (ASE) source (ASE 1600, NTT Electronics), used as a broadband IR light source, was connected to a fiber optic circulator 1 λ ~ 2 (1530 to 1570 nm bandwidth), as shown in Figure 7.6. The light was coupled to the functionalized PCF through the port2 of the circulator, and the reflected signal was analyzed through the port3 using an optical spectrum analyzer (Ando AQ-6315A). Sample infiltration process was performed pumping the solutions in the holes of the MOF by a syringe pump. The system was connected to a high-pressure micro-filtered nitrogen line, to empty and dry the fiber after sample flowing. In order to make the setup more stable and reliable, a high precision dynamometer was used to keep the fiber always under the same tension. The measurements were made in a clean room environment with a temperature control system. Spectral measurements of the reflected signal have been recorded at the beginning and at the end of every hybridization phase.

Measurement protocol

After the light beam from the Amplified Stimulated Emission (ASE) source was coupled to the PCF and to the Optical spectrum analyzer (OSA), a syringe pump was used to pump all the samples through the fiber at a fixed flow rate of 0.25 mL/min. Some tens of microliters of the DNA solution were sucked and used for the infiltration over 1 hour; then the fiber was emptied under a nitrogen flow generated by a 5 atm line. The reflected signal after the first DNA pumping was recorded by means of the OSA. The infiltration of ON-AuNPs solution was then carried out under the same conditions; after 1 hour, the new spectrum was registered by means of the OSA, and the fiber was eventually thoroughly washed with PBS for approximately 24 h with a pressure of 10 atm.

REFERENCES

- [1] J.C. Knight, T.A. Birks, P.S.J. Russell, D.M. Atkin, *Opt. Lett.* **1996**, *21*, 1547-1549.
- [2] J. Broeng, D. Mogilevstev, S.E. Barkou, A. Bjarklev, *Opt. Fiber Technol.* **1999**, *5*, 305-330.
- [3] P. Russell, *Science* **2003**, *299*, 358-362.
- [4] J.C. Knight, *Nature* **2003**, *424*, 847-851.
- [5] F. Luan, A.K. George, T.D. Hedley, G.J. Pearce, D.M. Bird, J.C. Knight, P.S.J. Russell, *Opt. Lett.* **2004**, *29*, 2369-2371.
- [6] P.S.J. Russell, *J. Lightwave Technol.* **2006**, *24*, 4729-4749.
- [7] L. Rindorf, P.E. Høiby, J.B. Jensen, L.H. Pedersen, O. Bang, O. Geschke, *Anal. Bioanal. Chem.* **2006**, *385*, 1370-1375.
- [8] J.R. Ott, M. Heuck, C. Agger, P.D. Rasmussen, O. Bang, *Opt. Express* **2008**, *16*, 20834-47.
- [9] D. Passaro, M. Foroni, F. Poli, A. Cucinotta, S. Selleri, J. Lægsgaard, A. Bjarklev, *IEEE Sensors J.* **2008**, *8*, 1280-1286.
- [10] A.M. Cubillas, S. Unterkofler, T.G. Euser, B.J. Etzold, A.C. Jones, P.J. Sadler, *et al. Chem. Soc. Rev.* **2013**, *42*, 8629-8648.
- [11] C.M.B. Cordeiro, C.J.S. de Matos, E.M. dos Santos, A. Bozolan, J.S.K. Ong, T. Facincani, G. Chesini, A.R. Vaz, C.H.B. Cruz, *Meas. Sci. Technol.* **2007**, *18*, 3075-3081.
- [12] J.B. Jensen, L.H. Pedersen, P.E. Hoiby, L.B. Nielsen, T.P. Hansen, J.R. Folkenberg, J. Riishede, D. Noordegraaf, K. Nielsen, A. Carlsen, A. Bjarklev, *Opt. Lett.* **2004**, *29*, 1974-1976.
- [13] Z. He, F. Tian, Y. Zhu, N. Lavlinskaia, H. Du, *Biosens. Bioelectron.* **2011**, *26*, 4774-4778.
- [14] Z. Yinian, H. Du, R. Bise, *Opt. Express* **2006**, *14*, 3541-3546.
- [15] C.M.B. Cordeiro, M.A.R. Franco, G. Chesini, E.C.S. Barretto, R. Lwin, C.H.B. Cruz, *Opt. Express* **2006**, *14*, 13057-13066.
- [16] A.V. Shahraam, S.C. Warren-Smith, T.M. Monro, *Opt. Express* **2007**, *15*, 17891-17901.
- [17] D. Yong, W.L. Ng, X. Yu, C.C. Chan, *Sensor. Actuat. A-Phys.* **2013**, *191*, 22-26.
- [18] R. Corradini, S. Selleri, *Photonic Crystal Fiber for Physical, Chemical and Biological Sensing in Photonic Bandgap Structures*, Bentham Publisher, **2010**, 80-84.
- [19] R. Narayanaswamy, O.S. Wolfbeis, *Optical Sensors*, Springer, New York, **2004**.
- [20] Y. Ruan, E.P. Schartner, H. Ebendorff-Heidepriem, P. Hoffmann, T.M. Monro, *Opt. Express* **2007**, *15*, 17819-17826.
- [21] V.S. Afshar, S.C. Warren-Smith, T.M. Monro, *Opt. Express* **2007**, *15*, 17891-17901.
- [22] J. Jensen, P. Hoiby, G. Emiljanov, O. Bang, L. Pedersen, A. Bjarklev, *Opt. Express* **2005**, *13*, 5883-5889.
- [23] C. Markos, W. Yuan, K. Vlachos, G.E. Town, O. Bang, *Opt. Express* **2011**, *19*, 7790-7798.
- [24] L. Rindorf, J.B. Jensen, M. Dufva, L.H. Pedersen, O. Bang, *Opt. Express* **2006**, *14*, 8224-8231.
- [25] L. Rindorf, O. Bang, *J. Opt. Soc. Am. B* **2008**, *25*, 310-324.
- [26] S. Smolka, M. Bart, O. Benson, *Opt. Express* **2007**, *15*, 12783-12791.
- [27] E. Coscelli, M. Sozzi, F. Poli, D. Passaro, A. Cucinotta, S. Selleri, R. Corradini, R. Marchelli, *IEEE J. Sel. Top Quant.* **2010**, *16*, 967-972.
- [28] A. Candiani, A. Bertucci, S. Giannetti, M. Konstantaki, A. Manicardi, S. Pissadakis, A. Cucinotta, R. Corradini, S. Selleri *J. Biomed. Optics* **2013**, *18*, Article Number: 057004.
- [29] T. Shoshani, A. Augarten, E. Gazit, N. Bashan, Y. Yahav, Y. Rivlin, *et al. Am. J. Hum. Genet.* **1992**, *50*, 222-228.
- [30] B. kerem, O. Chiba-Falek, E. Kerem, *Genetic testing* **1997**, *1*, 35-39.
- [31] C.A. Mirkin, R.L. Letsinger, R.C. Mucic, J.J. Storhoff, *Nature* **1996**, *382*, 607-609.
- [32] R. Elghanian, J.J. Storhoff, R.C. Mucic, R.L. Letsinger, C.A. Mirkin, *Science* **1997**, *277*, 1078-1081.
- [33] N.L. Rosi, C.A. Mirkin, *Chem. Rev.* **2005**, *105*, 1547-1562.
- [34] A. Merkoçi, *Biosens. Bioelectron.* **2010**, *26*, 1164-1177.

- [35] L.M. Zanolì, R. D'Agata, G. Spoto, *Anal. Bioanal. Chem.* **2012**, 402, 1759-1771.
- [36] S.K. Kim, H. Cho, J. Jeong, J.N. Kwon, Y. Jung, B.H. Chung, *Chem. Commun.* **2010**, 46, 3315-3317.
- [37] J.K. Pokorski, J.M. Nam, R.A. Vega, C.A. Mirkin, D.H. Appella, *Chem. Commun.* **2005**, 16, 2101-2103.
- [38] R. D'Agata, R. Corradini, G. Grasso, R. Marchelli, G. Spoto, *ChemBioChem* **2008**, 9, 2067-2070.
- [39] R. D'Agata, G. Breveglieri, L.M. Zanolì, M. Borgatti, G. Spoto, R. Gambari, *Anal. Chem.* **2011**, 83, 8711-8717.
- [40] J. Sun, Y. Xianyu, X. Jiang, *Chem. Soc. Rev.* **2014**, 43, 6239-6253.
- [41] A. Candiani, M. Sozzi, A. Cucinotta, S. Selleri, R. Veneziano, R. Corradini, *et al. IEEE J. Sel. Top. Quant. Electron.* **2012**, 18, 1176-1183.
- [42] M. Sozzi, A. Cucinotta, R. Corradini, R. Marchelli, M. Konstantaki, S. Pissadakis, S. Selleri, *Proc. SPIE* **2011**, 7894-7820.
- [43] R. D'Agata, R. Corradini, C. Ferretti, L. Zanolì, M. Gatti, R. Marchelli, G. Spoto, *Biosens. Bioelectron.* **2010**, 25, 2095-2100.
- [44] W. Haiss, N.T. Thanh, J. Aveyard, D.G. Fernig, *Anal. Chem.* **2007**, 79, 4215-4221.
- [45] S. Pissadakis, M. Livitziis, G. D. Tsibidis, *J. Eur. Opt. Soc. Rap. Public.* **2009**, 4, 09049.

8

Detection of unamplified genomic DNA by a PNA-modified photonic crystal fiber optofluidic system

Abstract

In Chapter 6, it has been shown how PNA-functionalized microstructured optical fibers with Bragg grating inscribed could emerge as powerful biosensors for the detection of selected target DNA sequences. In this chapter, the same technology has been implemented for the further goal of achieving an ultra-sensitive PCR-free detection directly on genomic DNA, targeting a gene tract of the genetically modified Roundup Ready soy. Large mode area (LMA-10) photonic crystal fibers have been used as optofluidic devices for the detection of DNA by measuring the shift in the wavelength of the reflected IR light. Enhancement of optical read-out was obtained using streptavidin coated gold-nanoparticles interacting with the genomic DNA captured in the fiber channels (0%, 0.1%, 1% and 10% RR-Soy). Significant, label-free, and amplification-free detection of target DNA in ultra-low concentrations, low percentages, and with very low sample consumption was achieved. Computer simulations of the fiber optics based on the finite element method (FEM) has been done to study the deposit of the material in the fiber channel, which revealed the formation of a multi-layer of DNA and nanoparticles with an average thickness of 39 nm for the highest percentage (10% RR soy) analyzed.

This work has been carried out in collaboration with Professor Stefano Selleri's group, at the Information Engineering Department of the University of Parma, and in particular with Dr. Alessandro Candiani and Sara Giannetti, using fibers produced by the group of Dr. Stavros Pissadakis at the Foundation for Research and Technology—Hellas FORTH, Institute of Electronic Structure and Laser IESL, Heraklion, Crete (Greece).

A. Bertucci, A. Candiani, S. Giannetti, A. Manicardi, A. M. Cucinotta, G. Spoto, M. Konstantaki, S. Pissadakis, S. Selleri, R. Corradini, Detection of Unamplified Genomic DNA by a PNA-based Microstructured Optical Fiber (MOF) Bragg-grating Optofluidic system, *Biosensor. Bioelectron.* **2015**, *63*, 248–254

8.1 PNA-functionalized Large Mode Area Photonic Crystal Fibers

In the previous chapter, a hybrid optical fiber bearing specific PNA probes for DNA detection has been described as an advanced tool in which the sensing element can be integrated in a microfluidic device for the generation of optical signals. Label-free ON-DNA detection could be performed through this approach, but PCR-free detection of genomic DNA should be an ultimate goal for rapid and point-of-care diagnostics.^[1-4] Indeed, PCR-based techniques are still the golden standard in the DNA analysis field, but they show drawbacks as the difficulty in amplifying large target DNA molecules (more than about 10000 bases) or as the possible amplification of DNA sequences different from the target ones resulting in non-specific signals.^[5] Thus, a growing interest on the possibility of directly analyzing non-amplified genomic DNA has emerged, which would be an efficient strategy reducing the extra labor and costs derived from the amplification step. The very high sensitivity required when non-amplified DNA is the target of the analysis has led research towards the development of novel sensor designs, often showing a combination of advanced materials with specific detection probes.^[6-10] A general overview about PCR-free detection with different techniques has been given in the Introduction of this thesis, and it has been the subject of a Book,^[11] in a chapter of which we summarized the literature about the use of advanced probes.^[11]

Among the possible sensor formats, the formerly presented PNA-modified PCFs might be optimal candidates to perform nanoparticle-enhanced detection of unamplified genomic DNA, with optical read-out in the IR region and with consumption of very small sample volumes. Hence, this detection system has been tested on genomic DNA extracted from a complex matrix (soy flour), directly diluted and analyzed without any amplification steps.

The fiber used in this work was a silica glass PCF LMA-10 (Large Mode Area), reported in figures 8.1a,b. It has a $\sim 10\ \mu\text{m}$ core, while the cladding region is formed by 60 holes of $2.85\ \mu\text{m}$ diameter each and an inter-hole distance of $6.4\ \mu\text{m}$. The geometry of such a fiber should let the evanescent waves strongly interact with the samples placed in the holes, thus offering a very high sensitivity. As for the 5-hole fiber described in the previous chapter, the sensing has been performed in a reflection mode, which is made possible thanks to the presence of a Bragg grating inscribed. For the inscription of the grating, a standard $1073.2\ \text{nm}$ period phase mask setup was used,^[12] with a $193\ \text{nm}$ high coherence, $10\ \text{ns}$ pulse duration excimer laser. Under these conditions, a Bragg grating pitch of $536.6\ \text{nm}$ was obtained, with back scattered light in the $1550\ \text{nm}$ spectral region (Fig. 8.1).

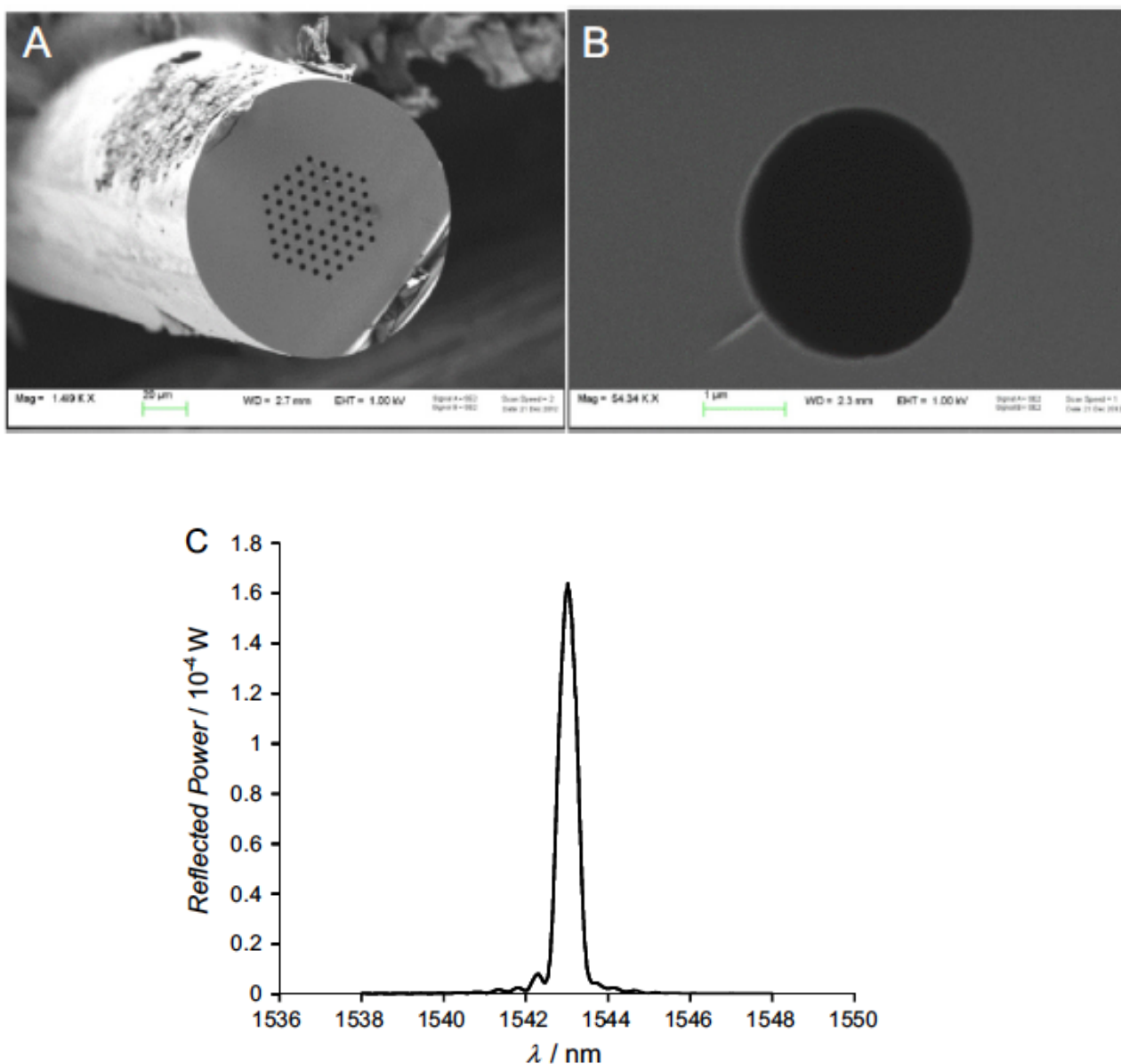


Fig. 8.1. LMA-10 fiber structure and Bragg-grating reflection. (A) SEM image of the LMA-10 fiber, showing the hexagonal geometry of the channels. (B) Magnification of a single hole. (C) Spectrum of the reflected light of the LMA-10 PCF with Bragg grating inscribed.

For this fiber, as for those described in chapter 7, the reflected wavelength (Bragg wavelength) depends on the effective refractive index of the system, which allows for detecting the DNA capture event exploiting ultra-low wavelength shifts of this band accordingly to variation of the index itself (see Chapter 7).

The PNA binding to the inner surface of the microchannels was performed by amide bond formation, following exactly the same strategy described in the previous chapter, which ensures a stable covalent link between the probes and the silica surface. The PNA probes bear a sequence full complementary to a specific tract of Roundup Ready (RR) soy (8.2). The RR soy was selected as a target DNA model because of its relevance in food control and because samples of certified DNA

content of the target sequence are available and unambiguous for this substrate (genomic DNA from soy flour).^[13] Additionally, D'Agata *et al.* previously reported the use of the same certified material tested in SPR biosensing devices.^[2] The detection scheme, following what already described in Chapter 6, relies on a significant optical signal enhancement achieved by the formation of a sandwich-like system PNA/DNA/ON-AuNPs, with the presence of the modified nanoparticles leading to a functional change of the effective refractive index. The DNA and PNA sequences selected for the hybridization processes are reported in Figure 8.2.

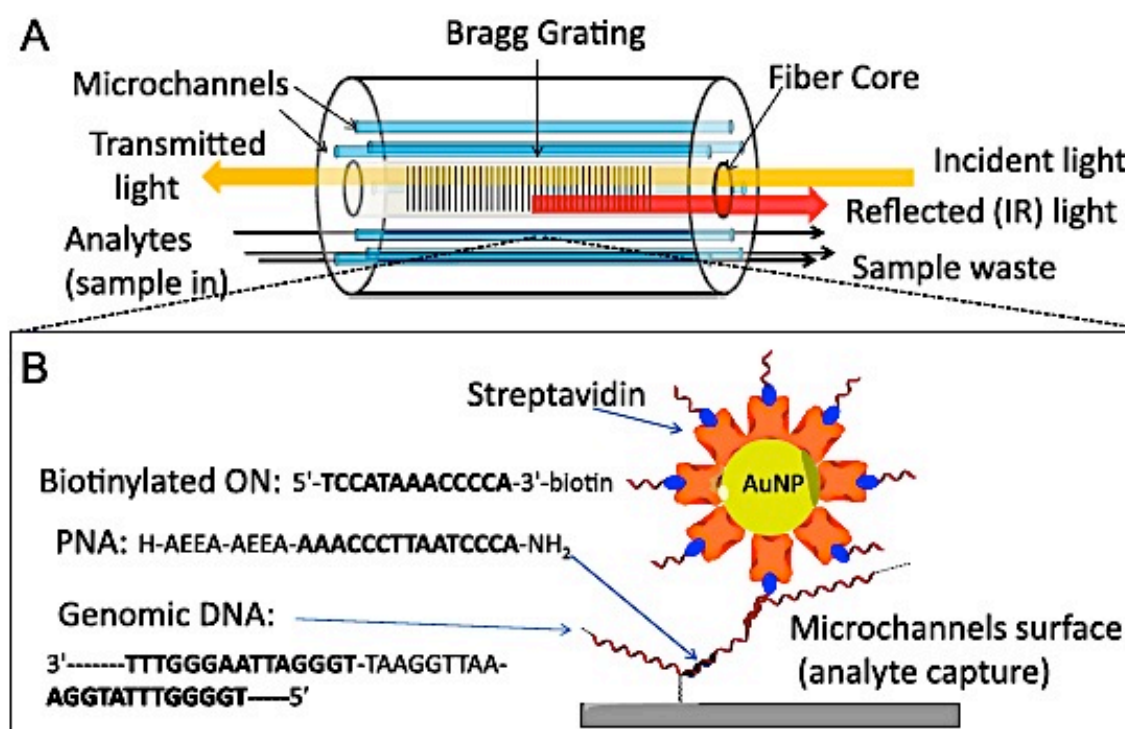


Fig. 8.2 Biosensing with modified LMA-10 fiber. A) Schematic of the optical procedure implemented for biosensing using LMA-10 PCF: analytes are pumped from one end into the fiber capillaries surrounding the core; the light beam is coupled at the opposite end to the fiber core and the reflected light from the Bragg grating is collected at the same side (see Fig. 8.3 for instrumental setup). B) Sequences of PNA, target DNA tract, and oligonucleotide loaded on the AuNPs, together with the scheme of the hybridization events taking place on the surface of the fiber channels. The PNA probes recognize the target tract of genomic DNA, whose flanking region captures the streptavidin-coated AuNPs bearing a matched biotinylated oligonucleotide tail.

8.2 Optical detection of genomic DNA and statistics analysis

Having prepared the PNA-modified PCFs, the possibility of obtaining significant reproducible wavelength shift using non-amplified genomic DNA was investigated. The DNA was extracted from samples of reference flour material (GMO material content certified by Institute for Reference Materials and Measurements, IRMM) containing 0%, 1%, and 10% of transgenic soybean flour,

using a commercial kit and standard procedures. The concentration of each DNA solution was evaluated with a Pico200 Picodrop Spectrophotometer and standard samples of 30 ng/mL were produced by dilution. Before every optical measurement, the DNA was thermally denatured at 95 °C and rapidly cooled (1–2 min) in an ice bath, in order to prevent dsDNA re-annealing, which competes with hybridization on the PNA probes.

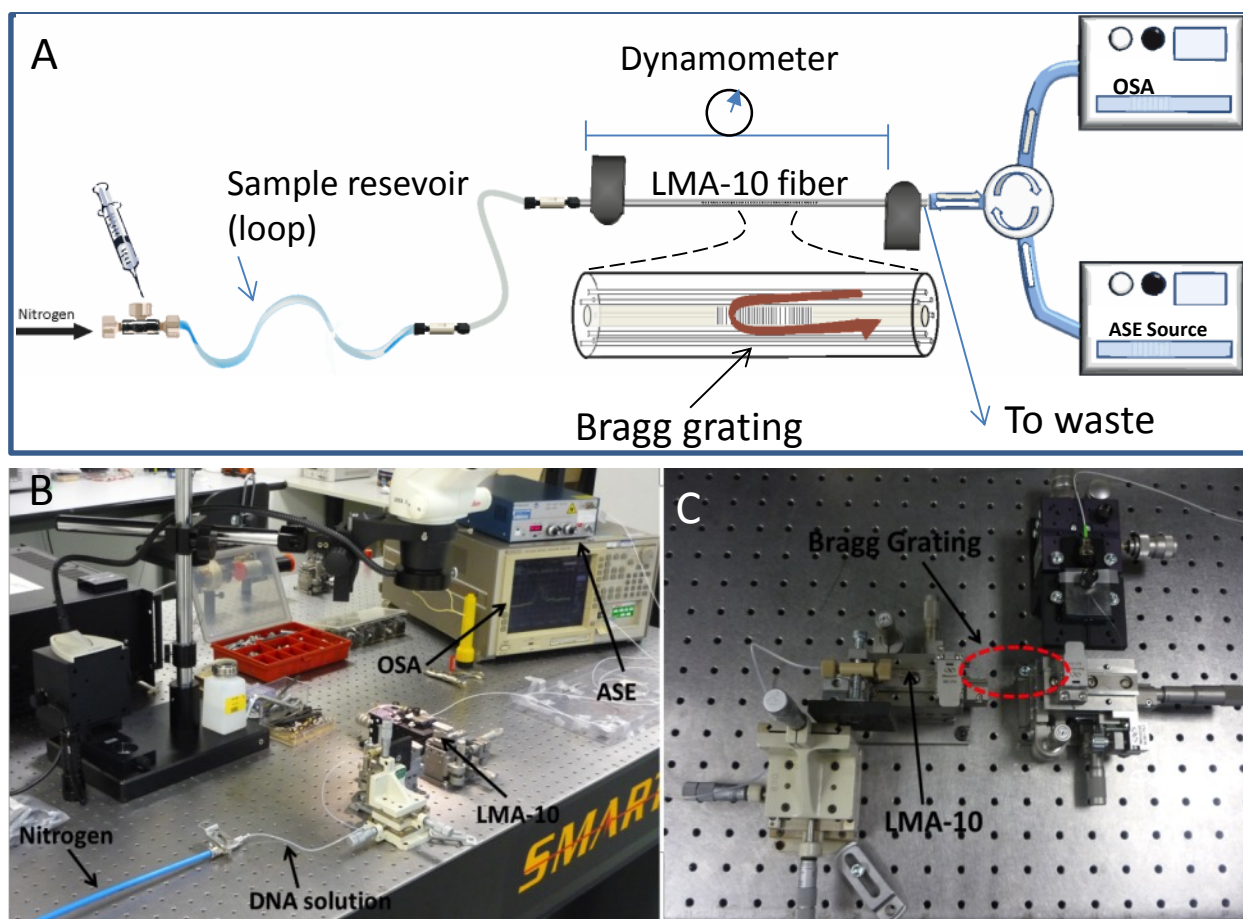


Fig. 8.3 The experimental optical setup. A) Schematic of the optical setup: a light beam from ASE source is sent through the fiber core and is then reflected due to the Bragg grating; the reflected light is collected through a circulator and sent to a OSA detector. All the samples and reagents are pumped through the fiber channels by pressure from a nitrogen line. The fiber is kept at constant tension (measured by a dynamometer) in order to avoid uncontrolled stretching of the Bragg grating. B) Photograph of the setup on optical breadboard. C) Closer view of the setup area with the LMA-10 fiber.

The detection scheme of the PCF biosensor was therefore that displayed in Figure 8.2. The customized optical setup implemented for the measurements is shown in Figure 8.3.

The frozen samples were melted just before their use and the corresponding solutions were pumped through the fiber holes for 50 min (total volume of sample was 100 μ L, corresponding to 3 ng of DNA). The fibers were subsequently emptied and dried under a nitrogen flow, since it has been

shown that the sensitivity of grating sensors is around three times higher when measurements are carried out in air rather than in liquid media.^[14] The position of the reflection band generated by the Bragg grating was at first monitored after infiltration of DNA but no significant shift was observed (Fig. 8.4 A, Student's *t*, $n = 4$, $\alpha = 0.05$).

Thus, a 0.3 nM ON-AuNP solution was infiltrated in the LMA-10 PCF after the target DNA flow, accordingly to the sandwich-type scheme shown in Figure 8.2, in view of nanoparticle-mediated optical signal amplification.^[15-19] The ON-AuNPs were synthesized and characterized as described in the experimental section. After data collection, fibers were washed with PBS to restore initial conditions. Each fiber, after emptying, was reused for subsequent measurements.

Quadruplicate measurements were performed alternating the solutions with different target contents, in order to avoid systematic errors, and statistical significance analysis was carried out (Fig. 8.4 B and Table 8.1). A significant shift of the Bragg reflection band was observed when using the 10% RR content sample (Fig. 8.4 A), whereas a weaker shift was recorded in the case of 1% RR sample, and, notably, no statistically significant shift was obtained for the sample containing no RR DNA (Fig. 8.4 B and Table 8.1).

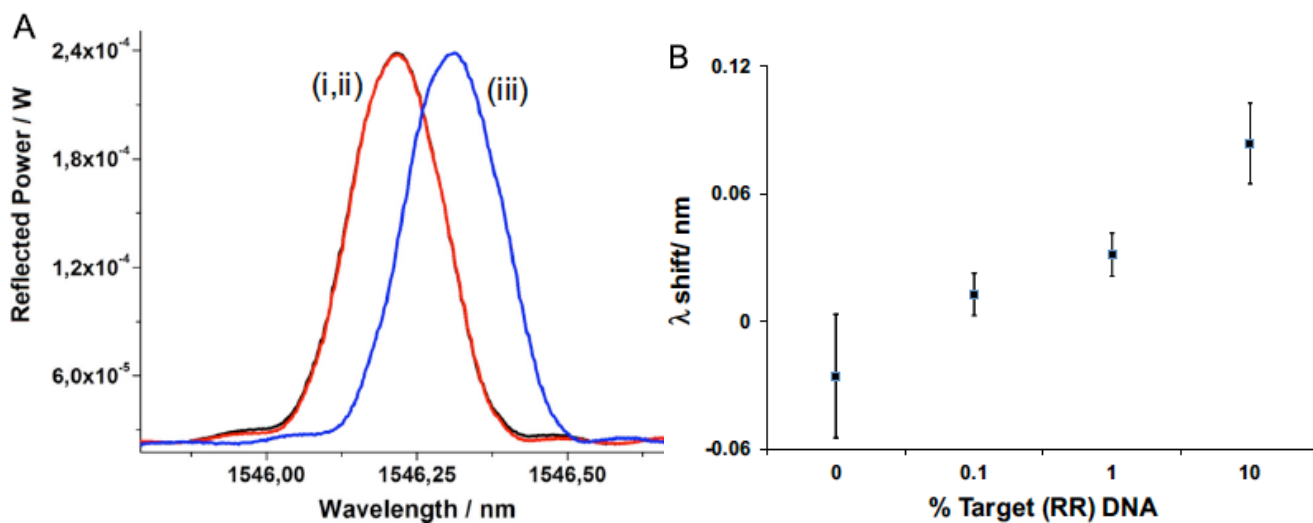


Fig. 8.4 A) Wavelength shift in the reflection mode obtained for the PNA-LMA10 fibers (i) before (black line), (ii) after genomic DNA (red line), and (iii) after ON-AuNPs infiltration (blue line), using 10% RR DNA sample, leading to an average shift of 0.08 nm (RSD 27%). B) Optical shifts obtained using DNA at the same concentration (30 ng/mL), but with different RR % (vertical bars represent sample standard deviation). ANOVA evaluation (Table 7.2) showed significant differences between each pair of percentage levels, except 0-0.1% and 0.1-1%.

ANOVA test (Table 8.2) was then applied to check out statistically significant difference ($\alpha = 0.05$) proved a statistically significant difference among the mean values obtained for each sample (0%, 0.1 %, 1%, and 10%). Hartley test was first done to assess homoscedasticity among the four levels

($q = 4, n = 3, \alpha = 0.05$), giving a negative response ($p > \alpha, F_{\text{calc}} = 24.91$ vs. $F_{\text{tab}} = 3.49$, Table 7.2). ANOVA test was performed giving a positive response ($p < \alpha$). Bonferroni test was therefore carried out for each couple of mean values (0-0.1%, 0-1%, 0-10%, 0.1-1%, 1-10%, and 0.1-10%). Every mean value was found significantly different from each other ($\alpha = 0.05$, Table 7.2), except for the couples 0-0.1% and 0.1-1%.

Table 8.1 Observed Bragg wavelength shifts after infiltration of target DNA and ON-AuNPs in the LMA-10. Mean values, standard deviation, and RSD% are reported for each sample.

Sample	λ shift (nm)	Average	SD ^a	RSD %
<i>Calf Thymus</i>	-0.019	0.01	0.03	- ^b
	0.017			
	0.045			
0% RR soy	-0.030	-0.025	0.03	- ^b
	-0.047			
	-0.042			
	0.016			
0.1% RR soy	0.000	0.013	0.01	76
	0.022			
	0.020			
	0.009			
1% RR soy	0.029	0.03	0.01	33
	0.030			
	0.045			
	0.023			
10% RR soy	0.055	0.08	0.02	25
	0.094			
	0.094			
	0.091			

^a Standard Deviation

^b Not applicable (values oscillating around zero)

Table 8.2 ANOVA evaluation of significance and Bonferroni values.

ANOVA		
F_{calc}		$F_{\text{tab}}(0.05, 3, 12)$
24.91		3.49
Bonferroni test		
Couple	t_B	$t_{\text{tab}}(0.05, 6, 12)$
0% - 1%	4.37	
1% - 10%	3.92	
0% - 10%	8.29	3.15
0.1% - 0%	2.91	
0.1% - 1%	1.46	
0.1% - 10%	5.38	

This is a very interesting result taking into account the extremely low quantity of total DNA used (3 ng in total), which corresponds to few thousands (about 2500) copies,^[2] of which only small percentages contain the target sequence. A non-significant shift was registered for the 0.1% RR soy sample (Fig. 8.4 B, Table 8.1 and 8.2). According to these data, the minimal concentration of the unamplified target GMO DNA that could be significantly distinguished from the blank has been that of the 1% sample, i.e. 0.3 ng/mL, corresponding to an estimated 410 zM concentration.^[2] Eventually, an unrelated genomic DNA (DNA from calf thymus) was used to check possible effects of unspecific binding; also in this case no significant shift was registered (Table 8.1).

8.3 Finite element method simulation

In order to accurately investigate the modulation of the reflected signal with respect to the growth of the hybrid bio-layer inside the fiber channels, finite element method (FEM) solver has been used to simulate the field distribution inside the fiber core. The effective refractive index n_{eff} has been

evaluated for both a reference and a hybridized fiber.^[20] Based on the refractive index measured in analogous experiments in the IR region,^[21] several simulations were conducted at different thickness of the bio-layer, having refractive index of 1.502, corresponding to the organic material deposited on the nanoparticles^[14] and covering the surface of the fiber capillaries. Numerical results under these conditions showed an increase of the n_{eff} of 7.5×10^{-5} around 1550 nm, which is consistent with the observed average shift of 0.08 nm for the 10% RR sample, for a layer thickness of 39 nm (Fig. 8.5 and 8.6).

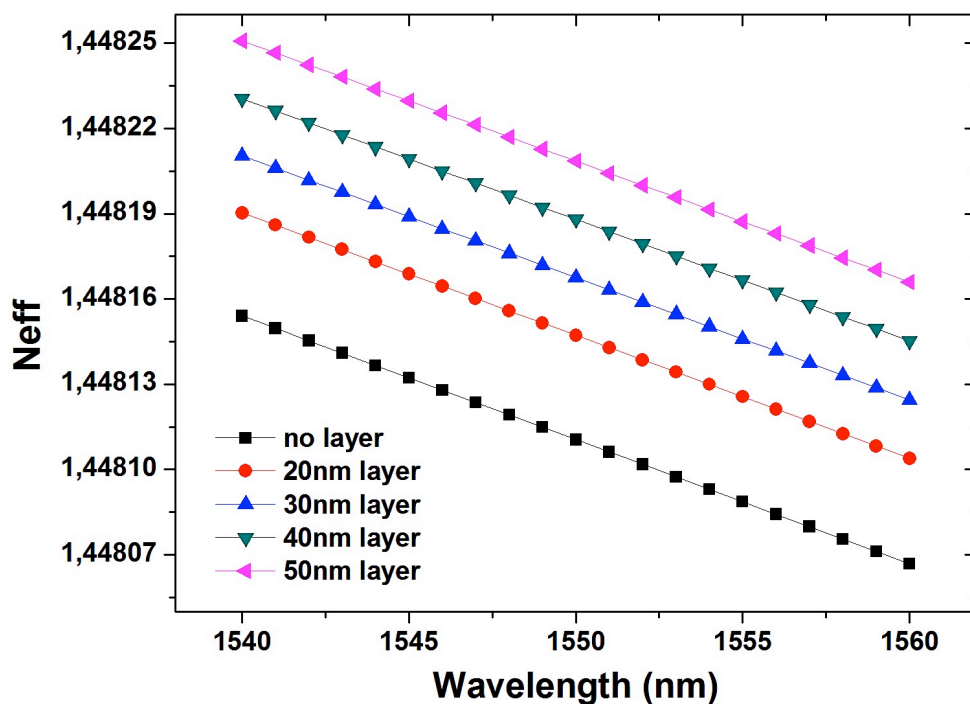


Fig. 8.5 Results of finite element calculations carried out for different wavelengths and different thickness of the biolayer on the channel surface.

Since the size of the gold nanoparticles was measured by the Mie model^[22-23] to be 13 ± 3 nm, while the streptavidin coating could be evaluated having thickness in the range 3.5-5 nm^[24-26] all around the NP, the value obtained for the biolayer is consistent with the average deposition of more than one layer of nanoparticle/streptavidin material on the fiber surface. This is in line with the increased sensitivity observed for genomic DNA detection in other optical techniques using a similar AuNP capture scheme.^[2-3]

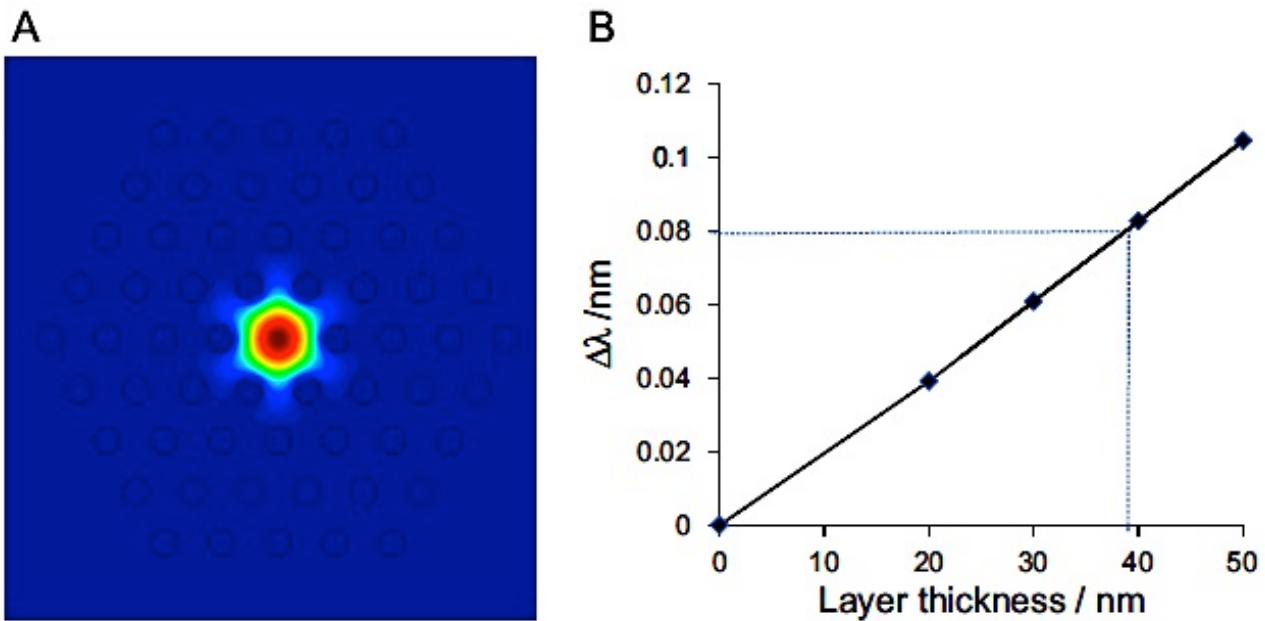


Fig. 8.6 Modelling of the LMA-10 sensing process. A) Finite element method (FEM) simulations show the field distribution inside the microstructured optical fiber. B) Calculated wavelength shift vs. thickness of the biolayer created upon the functionalization and hybridization processes. The dashed lines represent the observed shift for the 10% RR sample and the corresponding calculated thickness.

8.4 Conclusion

It has been for the time demonstrated that direct detection of genomic DNA, without PCR or other amplification reactions, can be obtained using IR light reflection, by combining Bragg-Grating microstructured optical fibers and PNA probes, using streptavidin-coated gold-nanoparticles for signal enhancement. Such a sensing scheme allowed for clearly distinguishing between materials containing a small percentage of targets (10% and 1%), in the presence of a large excess of non-target-DNA. The signal position was demonstrated not to depend on excess DNA (see unrelated calf thymus or non-GMO soy) or traces of protein contaminants, but specifically on the target sequence concentration in the sub-attomolar range.

These results parallel those obtained with SPR-based biosensors,^[2,27-29] which already rely on well-established and optimized techniques and instrumentation, while the presented approach is instead the first example of direct genomic DNA sensing using MOF-based sensors and can be further optimized. Both techniques have the advantage of being sensitive to local changes in the surface refractive index, and thus of being less prone to interference from bulk solution, requiring no labeling of the target DNA with chromophores or fluorophores as other conventional techniques. The PCF device has the rewarding features of presenting a compact format in which the optical fiber can act at the same time as a sensing unit, a microfluidic device and transmitter of data obtained. Furthermore, the very low concentrations, the small volumes of sample and of ON-AuNP

used, and, even more, the very small volume circulating in the inner channels of LMA-10 (60 nL for a 15 cm fiber tract) allow to envisage that a negligible consumption of the sample and of the nanoparticles can be attained in future studies. The presented PCF sensing format has an extremely small effective sensing area, coupled with an intrinsically efficient sample delivery system, showing the advantage of easily allowing a flow-through delivery of analytes directly to the Bragg-grating sensing unit by infiltration of small sample volumes within the fiber.^[30]

This technology can thus be implemented for the realization of portable instrumentation suitable for an on-site detection and with ultra-low sample concentration and very low consumption of reagents, and further development can take advantage of the advanced technology available for information and communication technologies, e.g. by using flexible bundles of optical fibers for multi-channel sensor development.

8.5 Experimental section

PNA synthesis

The sequence of the PNA was chosen on the basis of previous results using microarrays and SPRI devices and synthesized as reported.^[2,31] ESI-MS was used to identify the product and characterization was consistent with that previously reported. PNA probe H-AEEA-AEEA-AAACCCTTAATCCCA-NH₂ calcd. 853.6 [MH₅]⁵⁺, 711.5 [MH₆]⁶⁺, 610.0 [MH₇]⁷⁺, 533.8 [MH₈]⁸⁺; found *m/z* 853.7, 711.4, 609.9, 533.7.

Bragg Grating Inscription in LMA-10 fibers

The photonic crystal fiber LMA-10 manufactured by NKT Photonics was treated as described previously for Bragg-grating inscription¹¹, using a standard 1073.2 nm period phase mask setup, with a 193 nm high coherence, 10 ns pulse duration excimer laser. The energy density of the inscription beam was 200 mJ/cm² and the repetition rate of the laser 40 Hz while the laser beam length on the fiber was 5 mm. For an exposure of approximately 2 h in the aforementioned conditions, FBGs of up to 1 dB strength are inscribed, back scattering in the 1550 nm spectral region.

Optical setup

An amplified stimulated emission (ASE) source (ASE 1600, NTT Electronics) was used as a broadband light source; this was connected to a fiber optic circulator 1×2 (1530–1570 nm bandwidth). The light was coupled to the functionalized LMA-10 through the port2 of the

circulator, and the reflected signal was analyzed through the port3 using an optical spectrum analyzer (Ando AQ-6315A). The functionalization of the microcapillaries and the sample flowing were realized by introducing the reagents in a reservoir PTFE tubing, and then pumping them in the holes of the MOF using a micro-filtered nitrogen flow at a 5 atm pressure. Optical microscopy was used to check in real time the liquid flowing within the fiber. The measurements were carried out in a temperature-controlled cleanroom, and a high precision dynamometer was also used to keep the fiber always with the same tension. Spectral measurements of the reflected power have been recorded at the beginning and at the end of every hybridization phase.

Conjugation of PNA to fiber channel surface

PNA functionalization of the inner silica surface of the fiber channels was performed following the same procedure described in the experimental section of Chapter 6. Briefly, after silanization of the surface with APTES (5% in ethanol), amine groups were turned into carboxylic functions (succinic anhydride 0.25 M in DMF) and eventually in activated ester forms (DIC and NHS 0.25 M both in dry DMF). Coupling reaction with the terminal amine group of the PNA gave a covalent link between the surface and the probes through the formation of an amide bond (PNA 30 μ M in carbonate buffer 100 mM, pH = 9, H₂O:ACN 9:1). Final quenching was realized with ethanolamine (50 mM in TRIS buffer, pH = 9).

Synthesis of oligonucleotide-modified gold nanoparticles

ON-AuNPs were obtained through the same procedure described in Chapter 6. Briefly, naked gold nanoparticles were synthesized by citrate reduction of HAuCl₄ and characterized by UV–Vis spectroscopy (diameter 13 ± 3 nm). Surface coating with streptavidin was done incubating 1 mL of the colloidal solution of AuNps (absorbance 0.2, $\lambda=520$ nm) for 1 h at 4 °C with a streptavidin aqueous solution (20 μ l of 1 mg/mL mother solution); the pH was then adjusted to 8.5 and an overnight incubation at 4 °C was carried out. Final ON-AuNPs were obtained adding the biotin-ON-DNA solution (20 μ L of a 100 μ M mother solution) and incubating for 30 min at room temperature. Once the final product was recovered, it was resuspended in PBS buffer. The concentration of the final ON-AuNP solution was evaluated with UV–Vis spectroscopy and 0.3 nM working solutions were obtained by dilution.

DNA extraction and analysis

Genomic DNA was extracted from each Roundup Ready GMO certified reference material (0%, 1%, 10%), using the IonForce kit (Generon, Italy), according to the manufacturer's protocol. Samples of 400 mg of soy flour were always used as starting material. The concentration of the total DNA in the final extracted samples was quantified using a Pico200 Picodrop Spectrophotometer (Picodrop Limited, Hinxton, UK) accordingly to the manufacturer's procedure. For the following optical analysis, all the samples were diluted to a final concentration of 30 ng/mL in PBS buffer; genomic DNA was then fragmented by sonication for 2 min and by vortexing for 1 min. Immediately before the optical analysis, all samples were heated up to 95 °C for 5 min in order to separate the two DNA strands; strand re-association was prevented by ice cooling the samples for 1 min before the introduction into the optical apparatus. About 100 μ L of sample were transferred into a PTFE tube reservoir coupled to the optical fiber and a nitrogen flow was used to inject the sample into the MOF at a constant rate, ensuring a continuous renewal of the solution in contact with the modified surface of the channels. The DNA solution was allowed to flow through the fiber for 50 min, which was then dried under nitrogen pressure. After optical data had been collected, a 0.3 nM solution (10 μ L) of ON-AuNPs was injected into the fiber under the same conditions, and the measurement was performed in the same way.

Finite element method simulations

A full-vector modal solver has been applied, based on finite element method (FEM) magnetic field modulation. The symmetry of the fiber section was considered, and thus one quarter of the optical fiber was modeled; after drawing the model, the materials have been defined with their relative refractive indices. The whole domain was then divided into 125998 triangles, which are ideal to render such cross-section, with increasing density in the most sensitive areas, such as in the microcapillaries of the fiber, and decreasing one in remote areas, where the field tends not to propagate. This division corresponds to a number of nodes equal to 252683, in which the equations of the FEM have been resolved. The effective refractive index n_{eff} , which is directly proportional to the reflected Bragg wavelength ($\lambda_{\text{B}} = 2n_{\text{eff}}\Lambda$), has been evaluated for the reference fiber and for different bio-layer thickness of the hybridized fiber. The fiber LMA-10 used is entirely made of silica, but one must consider that the effective refractive index n_{eff} is the result of the hybrid nature of the microstructure pattern, which is made of silica and air. Since the refractive index of the silica part can slightly vary depending on the manufacturing process, the actual value for the LMA-10 fiber was calculated by FEM solver, using a backward process, exploiting the Bragg formula (see above) and Sellmeier equations, and adjusting the material refractive index (n_{mat}) in order to obtain

an n_{eff} value calculated corresponding to the experimental one; a value of n_{mat} of 1.451 was obtained for by this approach. Starting from this value, the effect of coating with a bio-layer having a refractive index of 1.502, corresponding to organic material deposited on the functionalized nanoparticle and captured on the capillary channels within the fiber, was simulated using possible layers of 20, 30, 40, and 50 nm.

REFERENCES

- [1] G. Spoto, R. Corradini (Eds.), *Detection of Non-amplified Genomic DNA*, Springer, Dordrecht, **2012**.
- [2] R. D'Agata, R. Corradini, C. Ferretti, L. Zanolì, M. Gatti, R. Marchelli, G. Spoto, *Biosens. Bioelectron.* **2010**, *25*, 2095-2100.
- [3] R. D'Agata, G. Breveglieri, L. Zanolì, M. Borgatti, G. Spoto, R. Gambari, *Anal. Chem.* **2011**, *83*, 8711-8717.
- [4] X. Zhou, D. Xing, Y. Tang, W.R. Chen, *PLoS one* **2009**, *4*, e8074.
- [5] C. Zhang, D. Xing, *Chem. Rev.* **2010**, *110*, 4910-4947.
- [6] S. Dubus, J.F. Gravel, B. Le Drogoff, P. Nobert, T. Veres, D. Boudreau, *Anal. Chem.* **2006**, *78*, 4457-4464.
- [7] M. Minunni, S. Tombelli, J. Fonti, M.M. Spiriti, M. Mascini, P. Bogani, M. Buiatti, *J. Am. Chem. Soc.* **2005**, *127*, 7966-7967.
- [8] W. Zhu, X. Su, X. Gao, Z. Dai, X. Zou, *Biosens. Bioelectron.* **2014**, *53*, 414-419.
- [9] Y. Wen, H. Pei, Y. Shen, J. Xi, M. Lin, N. Lu, et al. *Sci. Rep.* **2012**, *2*, 867.
- [10] H.T. Ngo, H.N. Wang, A.M. Fales, T. Vo-Dinh, *Anal. Chem.* **2013**, *85*, 6378-6383.
- [11] A. Bertucci, A. Manicardi, R. Corradini in *Detection of non-amplified Genomic DNA* (Eds. G. Spoto, R. Corradini) Springer, Dordrecht, The Netherlands, **2012**, 89-124.
- [12] S. Pissadakis, M. Livitziis, G.D. Tsibidis, *J. Eur. Opt. Soc. Rap. Public* **2009**, *4*, 09049
- [13] V.N. Njiti, O. Myers, D. Schroeder, D.A. Lightfoot, *Agron. J.* **2003**, *95*, 1140-1145.
- [14] A.K. Mudraboyina, J. Sabarinathan, *Sensors* **2011**, *11*, 11295-11304.
- [15] I.E. Sendroiu, L.K. Gifford, A. Lupták, R.M. Corn, *J. Am. Chem. Soc.* **2011**, *133*, 4271-4273.
- [16] J.K. Pokorski, J.M. Nam, R.A. Vega, C.A. Mirkin, D.H. Appella, *Chem. Commun.* **2005**, *16*, 2101-2103.
- [17] G. Spoto, *Anal Bioanal. Chem.* **2013**, *405*, 573-584.
- [18] A.R. Halpern, J.B. Wood, Y. Wang, R.M. Corn, *ACS Nano* **2013**, *8*, 1022-1030.
- [19] L.K. Gifford, I.E. Sendroiu, R.M. Corn, A. Lupták, *J. Am. Chem. Soc.* **2010**, *132*, 9265-9267.
- [20] M. Konstantaki, P. Childs, M. Sozzi, S. Pissadakis, *Laser Photonic Rev.* **2013**, *7*, 439-443.
- [21] Z. Wang, J.R. Heflin, K. van Cott, R.H. Stolen, S. Ramachandran, S. Ghalmi, *Sens. Actuators B*, **2009**, *139*, 618-623.
- [22] W. Haiss, N.T.K. Thanh, J. Aveyard, D.G. Fernig, *Anal. Chem.* **2007**, *79*, 4215-4221.
- [23] N.G. Khlebtsov, *Anal. Chem.* **2008**, *80*, 6620-6625.
- [24] K. Kaur, J.A. Forrest, *Langmuir* **2010**, *28*, 2736-2744.
- [25] J. Liu, S. Tian, L. Tiefenauer, P.E. Nielsen, W. Knoll, *Anal. Chem.* **2005**, *77*, 2756-2761.
- [26] T. Liebermann, W. Knoll, P. Sluka, R. Hermann, *Colloids Surf. A* **2000**, *169*, 337-350.

- [27] H. Sipova, J. Homola, *Anal. Chim. Acta* **2013**, 773, 9-23.
- [28] S. Scarano, M. Mascini, A.P.F. Turner, M. Minunni, *Biosens. Bioelectron.* **2010**, 25, 957-966.
- [29] L.M. Zanolì, R. D'Agata, G. Spoto, *Anal. Bioanal. Chem.* **2012**, 402, 1759-1771.
- [30] X. Fan, I.M. White, *Nat. Photonics* **2011**, 5, 591-597.
- [31] A. Germini, S. Rossi, A. Zanetti, R. Corradini, C. Fogher, R. Marchelli, *J. Agric. Food Chem.* **2005**, 53, 3958-3962.

9

Tweezer-like Dual-Pyrene PNA as fluorescent switching probe for selective nucleic acid detection

Abstract

Nucleic acids structures can be chemically tailored to create self-reporting molecular probes that exploit selective recognition of target sequences to provide an analytical response. The excellent hybridization properties combined with high chemical and biological stability, indeed make PNA oligomers suitable for the realization of specific probes for diagnostic applications. The PNA scaffold can serve as a model for the design of new compounds able to perform nucleic acid recognition and detection, exploiting the introduction of proper chemical modifications to the basic structure. In this chapter, a PNA-based switching probe is presented, which is synthesized introducing two pyrene groups onto the same monomer unit, in a novel tweezer-like geometry. The detection scheme is thus based on the pyrene excimer-monomer switching, which reverses the more typical monomer-to-excimer mechanism. Preliminary studies on the fluorescence properties of the single synthesized monomer have paved the way to the realization of anti-miR 221 PNA switching probe, whose final fluorescence performances makes it a suitable and efficient tool for specific target nucleic acid detection. The synthesis of the designed probe also highlights the feasibility of creating complex multifunctional molecules by introducing cross-talking modifications to a PNA sequence both at the backbone and the nucleobase level on the same monomeric unit.

9.1 Molecular probes for analytical nucleic acid recognition

Though the biosensor technologies described in the previous chapters have reached outstanding performances, thanks to the availability of nanostructured materials, for *in vivo* application a very important point is to obtain nucleic acid probes tailored in such a way to give a detectable analytical signal in solution. This would allow to trace the nucleic acid levels directly in cellular systems, and can be useful to provide new insights in the mechanism of action of nanocarriers and nano-container targeting DNA or RNA.

Two main different kinds of nucleic acid-based probes can be generally realized, which are hybridization probes that are based on the formation of complementary base pairs with the target

sequence, and aptamer probes that exploit selective recognition of non-nucleic acid analytes to provide an analytical response. With the recent efforts on DNA probe technology, a variety of fluorescent bioprobes that exploit nucleic acids as bioreceptors have been engineered. The development of sensitive and selective sensing schemes based on nucleic acid fragments has lately become a very productive research field, because of their numerous applications including detection and visualization of DNA and RNA in genomic analyses, monitoring amplification progress in quantitative PCR (QPCR) assays, and detection of non-nucleic acid analytes (proteins, small molecules, metal ions) with aptamer-based sensors.^[1-5]

In this Chapter, the design and construction of switching probes for nucleic acid detection will be discussed. In general, these probes are synthetic DNA or RNA molecules (with a sequence designed for a specific target molecule) containing a reporter group that can be monitored using fluorescence spectroscopy. A simple probe of this kind labels its target by binding, because of specific probe–target hybridization, then the alteration of the fluorescence characteristics of reporter group(s) is exploited as an analytical signal. Oligonucleotide-based fluorescent probes can be thus seen as molecular biosensors consisting of a biologically relevant molecular recognition element integrated to a signal-transduction element.

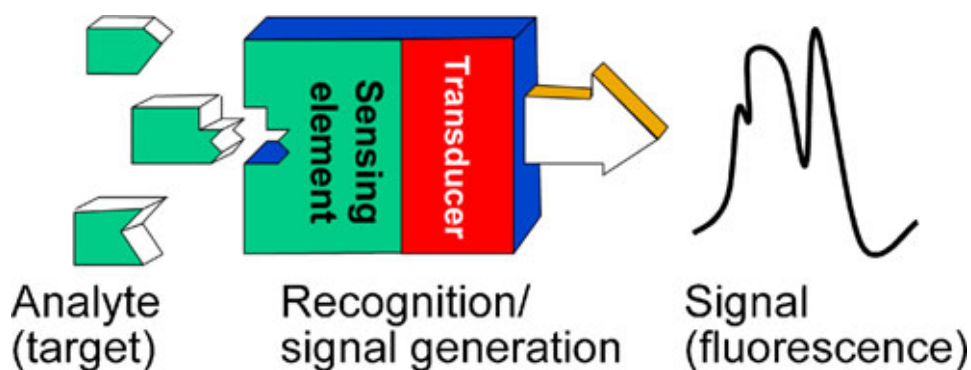


Fig. 9.1 Schematic layout of a fluorescent biosensor. Springer, *Analytical and Bioanalytical Chemistry*, 399, 2011, 3157, Nucleic acid-based fluorescent probes and their analytical potential B. Juskowiak, Figure 1, with kind permission from Springer Science and Business Media.

Natural nucleic acids (DNA, RNA) have been generally used as recognition elements, but some of their synthetic analogues, for example peptide nucleic acids (PNA), locked nucleic acids (LNA)^[6-7] or morpholino phosphoroamidate oligonucleotides (MO) have recently been proposed as excellent alternatives.^[8-13] A detailed overview on PNA properties can be found in the Introduction of this

thesis (Chapter 1.5); the use of PNA, LNA, and MO as advanced probes for nucleic acid detection has been described by us in a book chapter.^[14]

The fluorescence reporter moiety is generally covalently bound to the oligonucleotide of interest, and the fluorophores used can be divided into two main classes: (1) dyes that change their fluorescence properties on binding nucleic acids, mainly used in single-labeled probes, and (2) fluorophores with intrinsically strong fluorescence, for example fluorescein and rhodamine derivatives, which are brought into contact with each other or with a quencher molecule through proper structural design. The mechanism of signal transduction for single-labeled probes may rely on several different processes including the electron transfer quenching with the participation of nucleobases, fluorescence enhancement as result of energy transfer from nucleobases to the acceptor^[15] or steric restrictions imposed on the fluorophore, a mechanism that was shown for light-up probes.

Transduction processes responsible for the performance of probes bearing two dyes may be based on fluorescence quenching, fluorescence resonance energy transfer (FRET) and monomer–excimer emission switching.^[16-17] All the processes are distance-dependent, thus structural rearrangement of the probe upon binding to the target should result in an alteration of the fluorescence characteristics of the system. In a typical FRET experiment, a biopolymer is labeled with two different fluorophores, a donor and an acceptor, covalently attached at different locations. Interactions between the electronic excited states of these dye molecules lead to the transfer of excitation energy in a non-radiative process from the donor molecule to the acceptor molecule. The occurrence of FRET strictly depends upon conditions as the distance between the donor and acceptor fluorophores (typically 10–80 Å), the spectral overlap between the donor emission and acceptor absorption spectra, and the orientation of transition moments of both fluorophores.^[18-19] The efficiency of FRET can thus be measured by looking at the decrease in the fluorescence (or lifetime) of the donor or at the increase in the fluorescence of the acceptor. Two design strategies are commonly used, which involve the use of molecular beacon in which both energy transfer partners are attached to the same oligonucleotide at the 3' and 5' termini, and of dual probes, in which two short oligonucleotides are single-labeled with the donor and acceptor fluorophores.^[20-24]

The monomer–excimer switching approach exploits the fact that an excited fluorophore (e.g. pyrene) molecule can form an excited-state weak association complex with another ground-state fluorophore, forming an excimer.^[16,25] In the case of pyrene, this excimer has a broad red-shifted emission band near 480 nm, compared with the structured emission of the pyrene monomer at 400 nm. A properly designed oligonucleotide probe thus switches between excimer and monomer emissions depending on the presence of analyte target (free and bound states of the probe), and

various formats of suitable probes have been reported in the literature (see Figure 9.3).^[26-30]

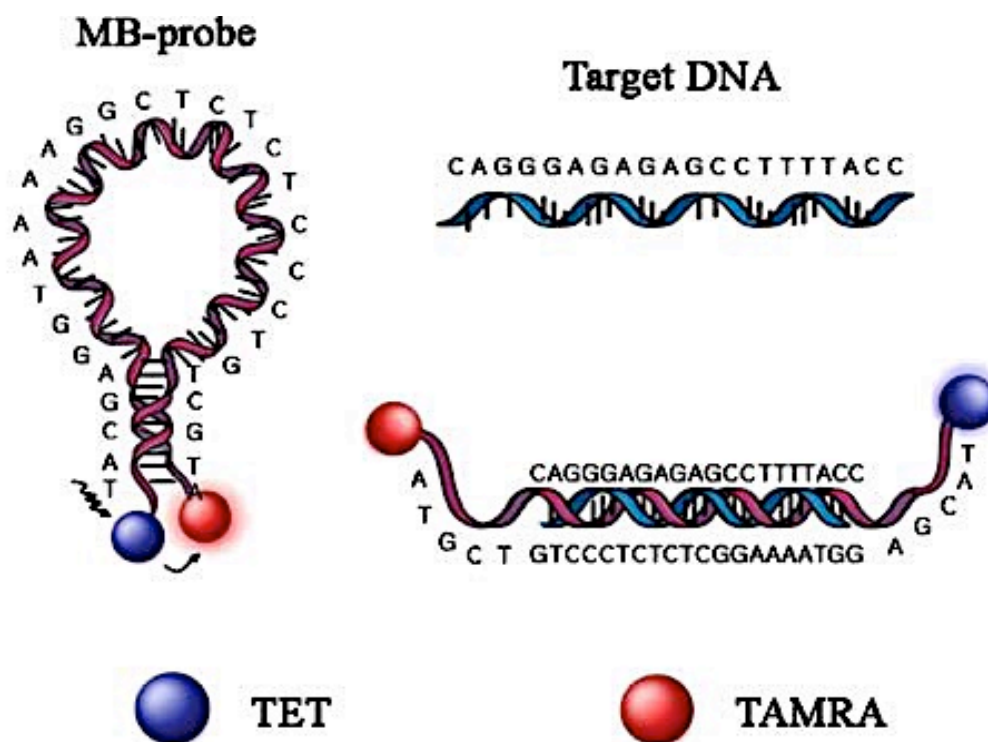


Fig. 9.2 The hairpin structure of a molecular beacon probe, labeled with TET and TAMRA. In the stem-closed structure, the distance between TET (tetrachlorofluorescein) and TAMRA (tetramethyl-6-carboxyrhodamine) is close enough that FRET occurs; after hybridization with the target, the structure opens preventing FRET to occur, which allow for monitoring the fluorescence intensity of the former donor (TET). Springer, *Analytical and Bioanalytical Chemistry*, 387, 2007, 2609, Fast and sensitive DNA analysis using changes in the FRET signals of molecular beacons in a PDMS microfluidic channel, Jung, L. Chen, S. Lee, S. Kim, G.H. Seong, J. Choo, *et al.* Figure 2, with kind permission from Springer Science and Business Media.

A third type is based on the changes in fluorophore properties upon hybridization, and can be obtained through probe-intercalator conjugation, forced intercalation, or using specific probes which interact with the grooves of probe:nucleic acid duplex; in this class fall light-up probes, which consist of a thiazole orange derivative linked to a PNA oligomer.^[31-32] Upon hybridization with a target sequence, a duplex structure is formed in which the thiazole orange moiety intercalates and the probe is triggered to become brightly fluorescent.^[33-36] Because of their PNA backbone, light-up probes are highly specific: a single base mismatch in the target sequence is sufficient to prevent probe binding, as indicated by the lack of fluorescence increase.^[37]

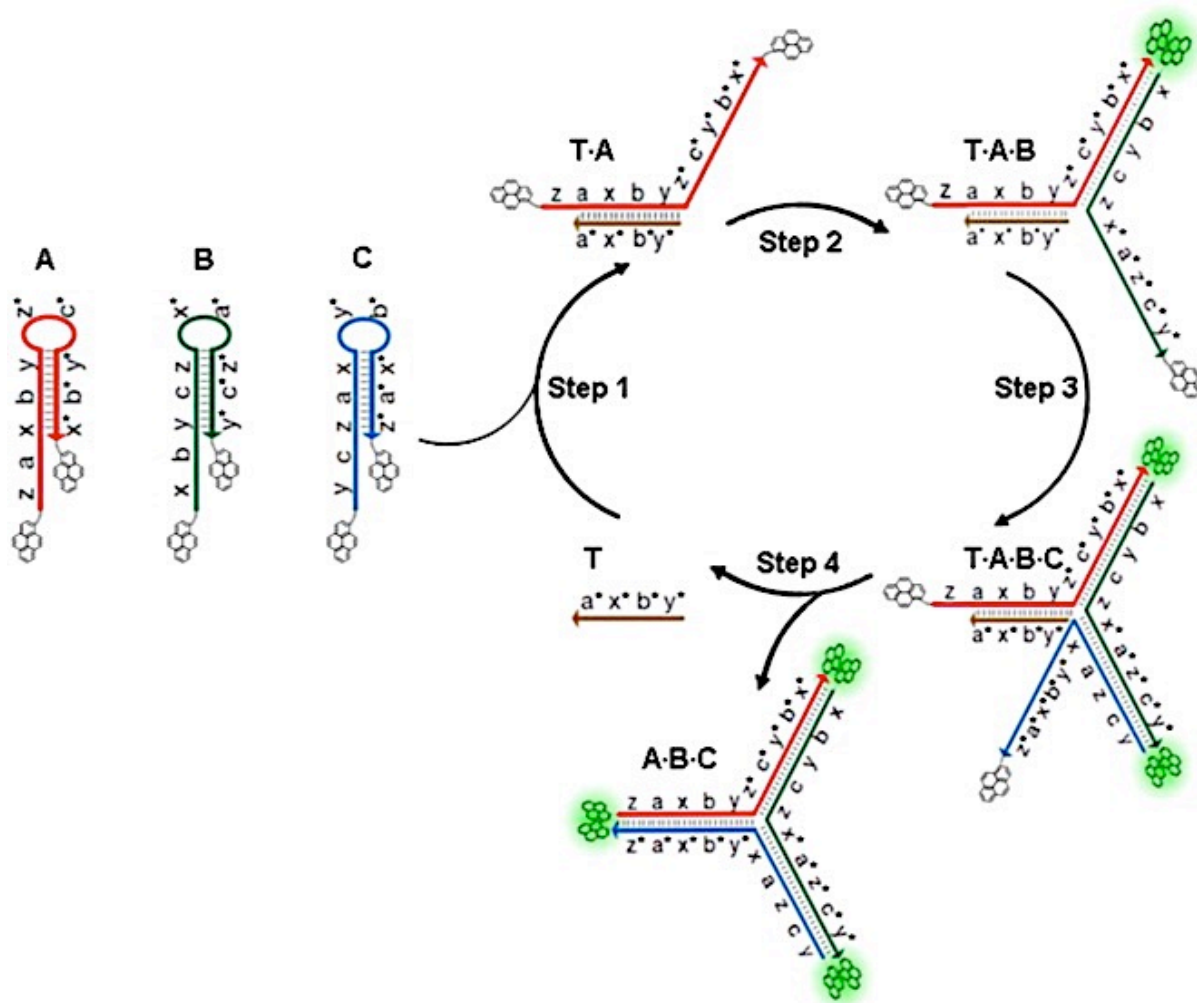


Fig. 9.3 Schematic representation of an enzyme-free nucleic acid amplified detection (T = Target DNA, A = Probe A, B = Probe B, C = Probe C). The presence of target catalyzes the formation of hybridized structures that lead to the formation of pyrene excimer couples, whose fluorescence signal is detected. Reprinted with permission from Z. Qing, X. He, J. Huang, K. Wang, Z. Zou, T. Qing, *et al. Anal. Chem.* **2014**, *86*, 4934-4939. Copyright (2014) American Chemical Society.

Nevertheless, as mentioned before, thanks to their high affinity for DNA and RNA, their high sequence selectivity, and their stability towards degradation induced by both peptidases and nucleases, PNA oligomers have been successfully used as scaffold for many other different formats of designed fluorescent probes. PNA-based molecular beacons using the fluorophore-quencher scheme have been for example proposed by Frank-Kamenetskii^[38] or by Corradini and co-workers,^[39-40] who also reported the highly selective single nucleotide polymorphism recognition by using a chiral-modified (5S) PNA beacon.^[41] Among the others, the use of a PNA hybridization probe-based FRET technique has been proposed by Gaylord *et al.* in combination with emissive cationic polymers,^[42] by Karadag *et al.* for the quantification of genotype mutations in fibrous dysplasia,^[43]

and very recently by Wang *et al.* for mRNA imaging in live cells through a soft nanoparticle-mediated intracellular delivery.^[44] Modifications of PNA with pyrene moieties have been reported for studying the stacking interactions and excimer emission in PNA₂DNA triplex structures,^[45] for the realization of single-modified pyrenyl-PNA probes for nucleic acid recognition,^[46] and for developing dual pyrene-labeled pyrrolidinyI PNA strands.^[47]

In this chapter the synthesis of a self-reporting PNA probe doubly modified with pyrene moieties is reported. The design was based on the conformational change that PNA monomers must experience when forming a PNA:DNA duplex (figure 9.4); thus a novel tweezer-like arrangement of pyrene units was used to achieve an excimer-to-monomer switching. Studies on melting temperatures and fluorescence essays have provided the proof-of-principle that the pyrene-tweezer PNA probe is indeed switching state upon hybridization, thus demonstrating that this design is suitable for the development of efficient probes for specific target nucleic acid detection.

9.2 Design and Synthesis of a double-pyrene-modified PNA monomer

The typical molecular beacon scheme is based on reporter groups placed at the two termini of the probes and one of the most common approach, when using pyrene moieties, involves the switch from the monomer to the excimer form to give the detectable signal. For PNA probes, another possibility is provided by the relatively flexible backbone of the probe itself, and by the possibility to introduce different moieties both on the backbone and on the nucleobase. By inspecting the available crystal structures of PNA:DNA duplex,^[48] it is possible to predict that a nucleobase-linked moiety will protrude into the major groove, whereas a substituent on C5 carbon, with S-stereochemistry, will be directed either outwards or in the minor groove. Thus, the interactions between two moieties placed respectively in these positions would be prevented by hybridization with DNA, whereas it would be permitted in the single strand. Thus the conformational change imposed by hybridization with DNA can be used to induce a switch in the photophysical or chemical properties of the two residues.

In this work, as a proof-of-principle, two pyrene groups were placed on the same monomer of the probe sequence, thus allowing to follow the designed conformational change through the switch between excimer and monomer pyrene fluorescence emission.

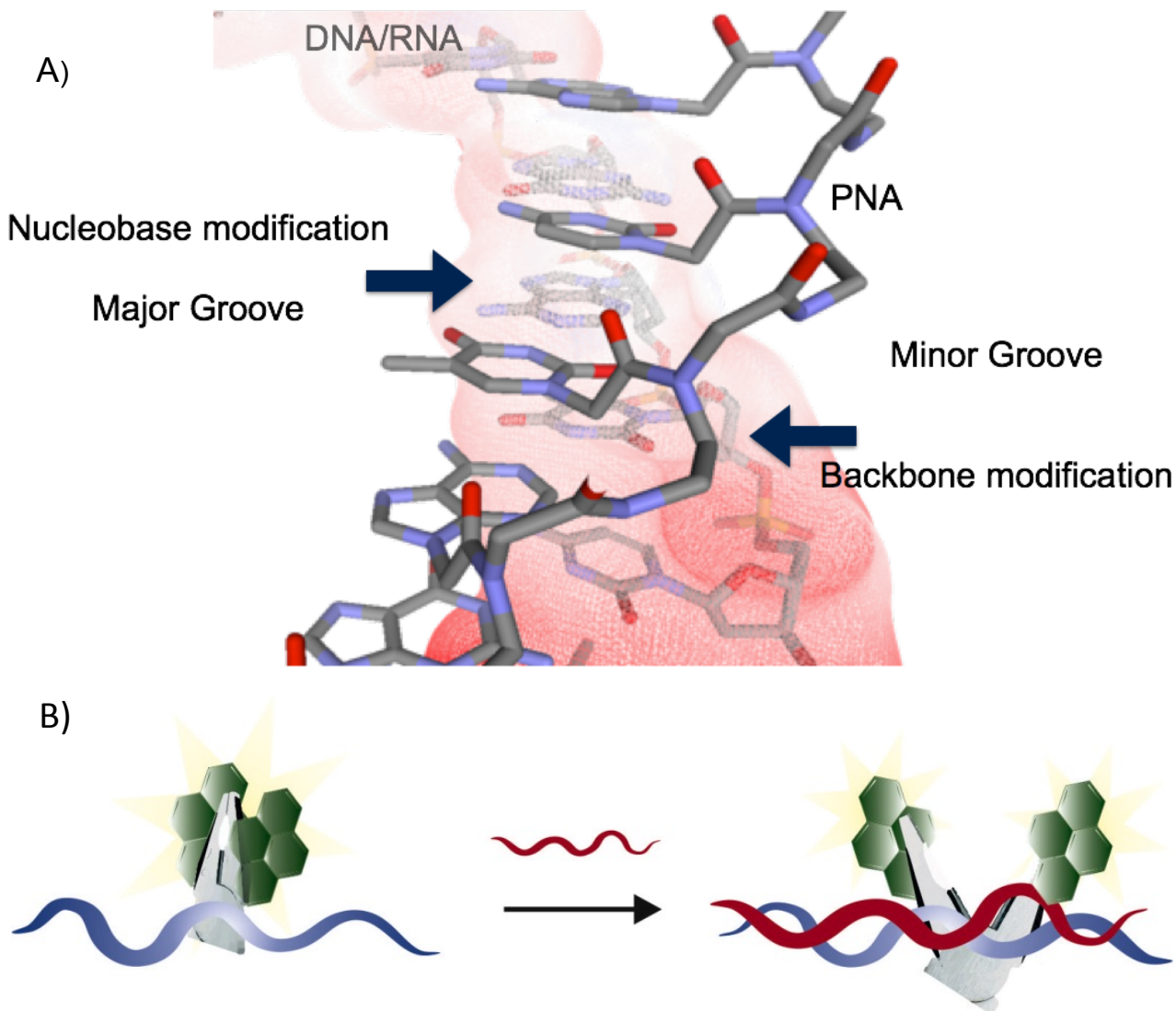


Fig. 9.4 A) Crystal structure of a PNA:DNA duplex showing the positioning of nucleobase-appended or C5-backbone substituents; B) schematic drawing of the proposed system. The PNA probe has an initial flexible conformation that enables two pyrene units to interact giving excimer emission (left); after hybridization with the target sequence (red strand), the two pyrene branches are forced to open resulting in the monomer species emission (right), thus providing a switching-based mechanism suitable for detection purposes.

In view of realizing such a probe, at first the synthesis of a dual-modified single PNA monomer was carried out, to check out whether whose fluorescence properties were suitable for the next proper working of the entire probe. The molecular structure of the dual-pyrene-modified PNA monomer is reported in Figure 9.5.

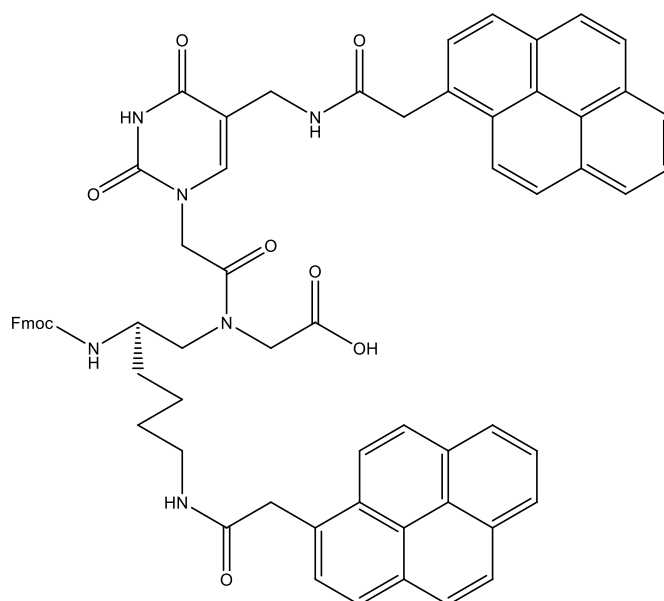
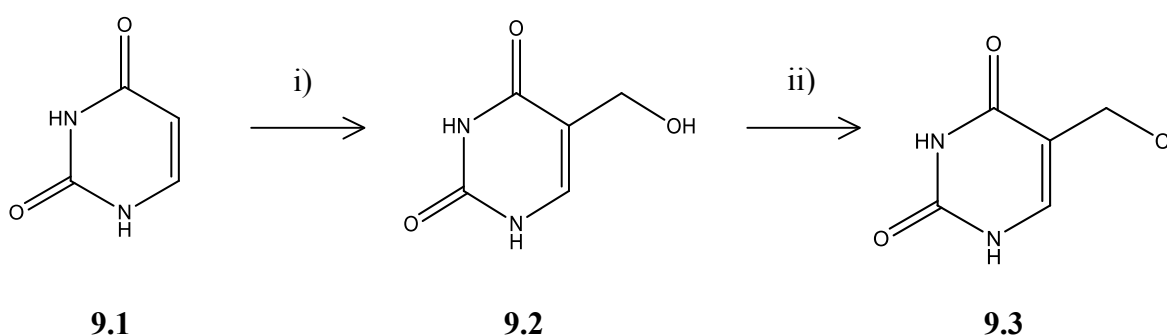


Fig. 9.5 Molecular structure of the dual-pyrene-modified PNA monomer. One group is linked to the nucleobase moiety, while the other is bound to the backbone through a lysine chain linker, in a tweezer-like geometry.

The synthetic pathway has been developed based on four main stages: 1-Synthesis of the modified nucleobase (uracil) bearing a pyrene group via functionalization of the atom position 5 of the ring; 2- Synthesis of the PNA backbone modified at the C5 position with a lysine chain, to introduce a reactive amine group; 3-synthesis of the entire monomer through coupling reaction between the pyrene-functionalized nucleobase (1) and the lysine-modified PNA backbone (2); 4-insertion of the second pyrene moiety on the C5 lysine chain via formation of a new amide bond.

Accordingly to this retrosynthetic pathway, the synthesis of the pyrene-modified uracil nucleobase was initially carried out (figure 9.6). As first step, commercial uracil (**9.1**) was hydroxymethylated at the 5-carbon following a literature procedure^[49] to obtain 5-(hydroxymethyl)uracil (**9.2**), which was then rapidly converted into the corresponding azide (**9.4**), after activation of the leaving group by substitution of the hydroxyl group with chloride under acidic conditions. The N-1 position was then alkylated with ethyl 2-bromoacetate to produce **9.5**, bearing the linker for connecting the nucleobase to the PNA backbone.



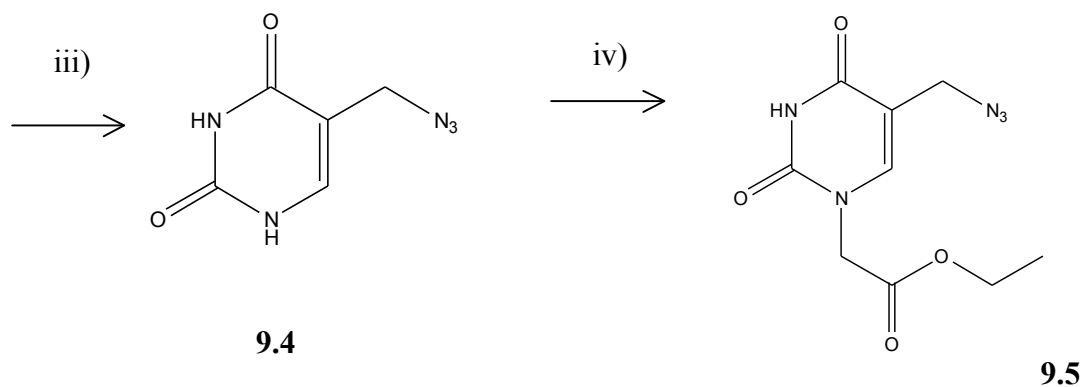


Fig. 9.6 Synthesis of ethyl 2-(5-azidomethyluracil-1-yl)acetate. i) CH_2O , Et_3N in H_2O , 74%; ii) HCl 37%, quantitative; iii) NaN_3 in DMF , 86%; iv) $\text{BrCH}_2\text{COOEt}$, K_2CO_3 in DMF , 20%.

For the insertion of pyrene on the monomer, the azide (**9.5**) was first converted with Staudinger reduction to the corresponding amine **9.6**, on which 1-pyreneacetic acid was bound using HBTU/DIPEA as coupling agent. The ester **9.7** was then hydrolyzed to the acid **9.8**, which is the form finally needed for the following linking to the PNA backbone (figure 9.7).

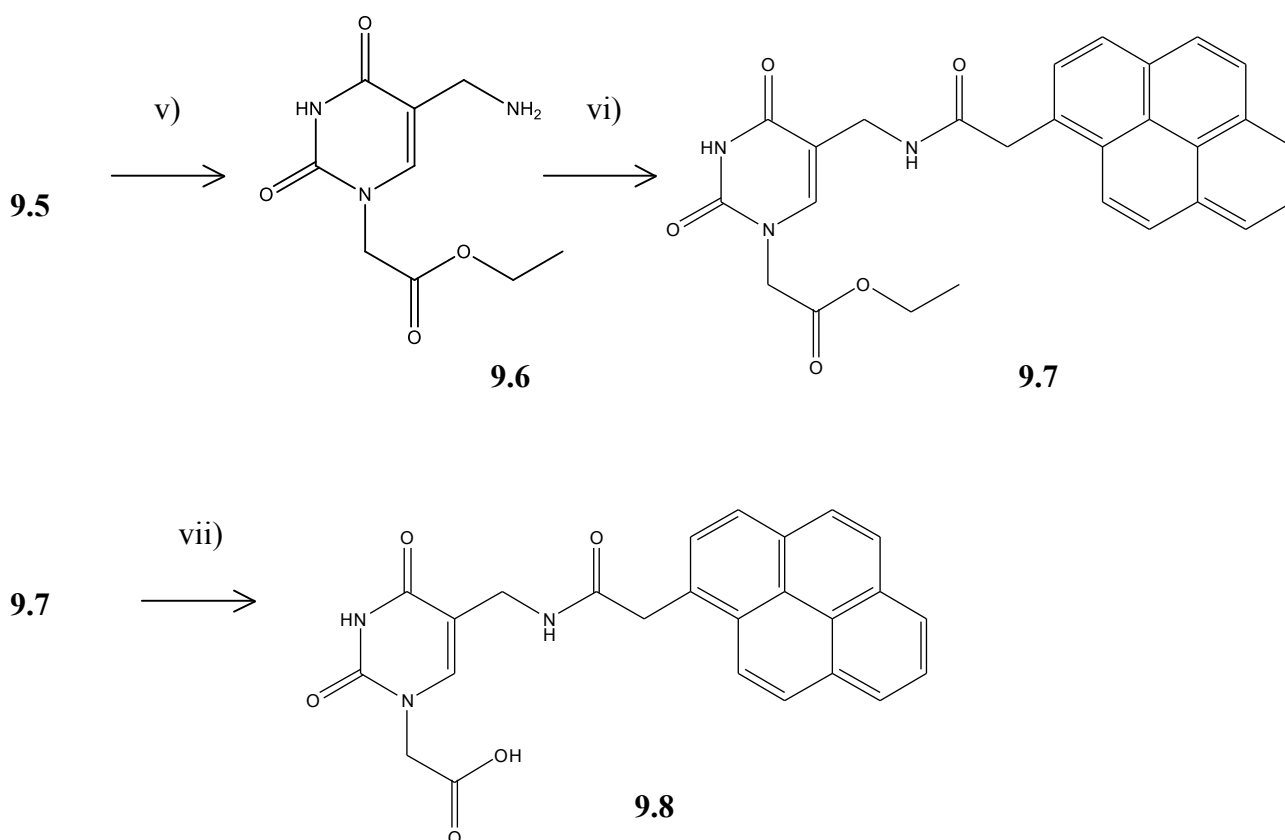


Fig. 9.7 Synthesis of 2-(5-(2-(pyren-1-yl)acetamido)methyluracil-1-yl)acetic acid. v) PPh_3 , H_2O in THF , 76%; vi) 1-pyreneacetic acid, HBTU, DIPEA, in DMF , 73%; vii) NaOH in MeOH , 74%.

In parallel, the synthesis of the modified PNA backbone was carried out. Recent studies have shown that the substitution of the achiral PNA backbone with chiral units derived from amino acids can affect the DNA binding ability, depending on the position and the stereochemistry of the stereogenic centers introduced.^[50] Monosubstitution at the 5-carbon of the backbone with a S-configuration turned out to induce a strong preference for right-handed helical structures, leading to strong DNA binding, while the R-configuration gave unfavorable intra-strand interactions hampering DNA hybridization. Hence, a 5-substituted Fmoc-PNA backbone monomer with a lysine side chain in S-configuration was synthesized.^[39,51-52]

Starting from the commercially available Fmoc-L-Lys(Boc)-OH (**9.9**), the corresponding *N*-methoxy-*N*-methyl amide **9.10** (Weinreb amide) was obtained by treatment with *N*-methoxy-methylamine hydrochloride using HBTU/DIPEA as coupling agents (figure 9.8). The amide **9.10** was then reduced to the corresponding aldehyde **9.11** with LiAlH₄. The Weinreb amide form was chosen since its ability to prevent the further reduction of the newly formed aldehyde to alcohol, thanks to the formation of a stable intermediary Li-metal complex that hampers the second addition of a hydride ion to the carbonyl group.^[53-54] This synthetic way also makes it possible to preserve the optical purity of the product, which could otherwise undergoes racemization under the reduction conditions.^[55] Eventually, reductive amination with glycine methyl ester was performed to yield the lysine-modified PNA methyl ester backbone.

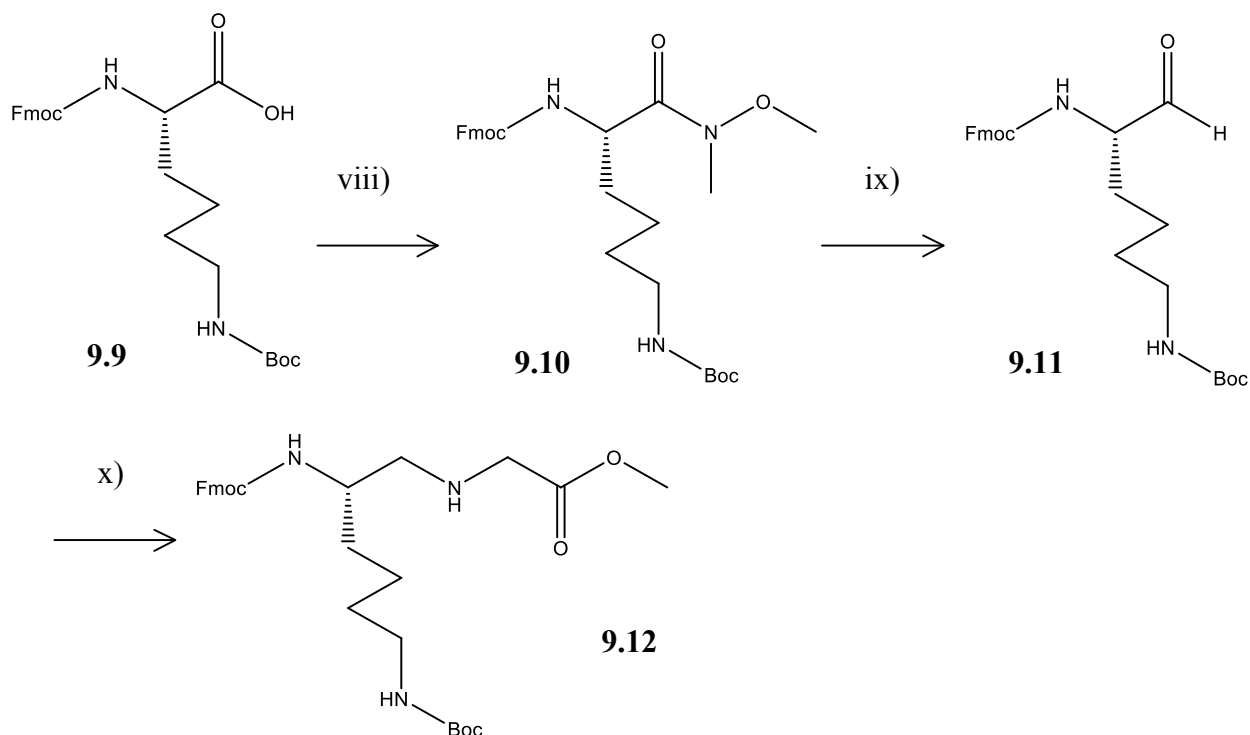
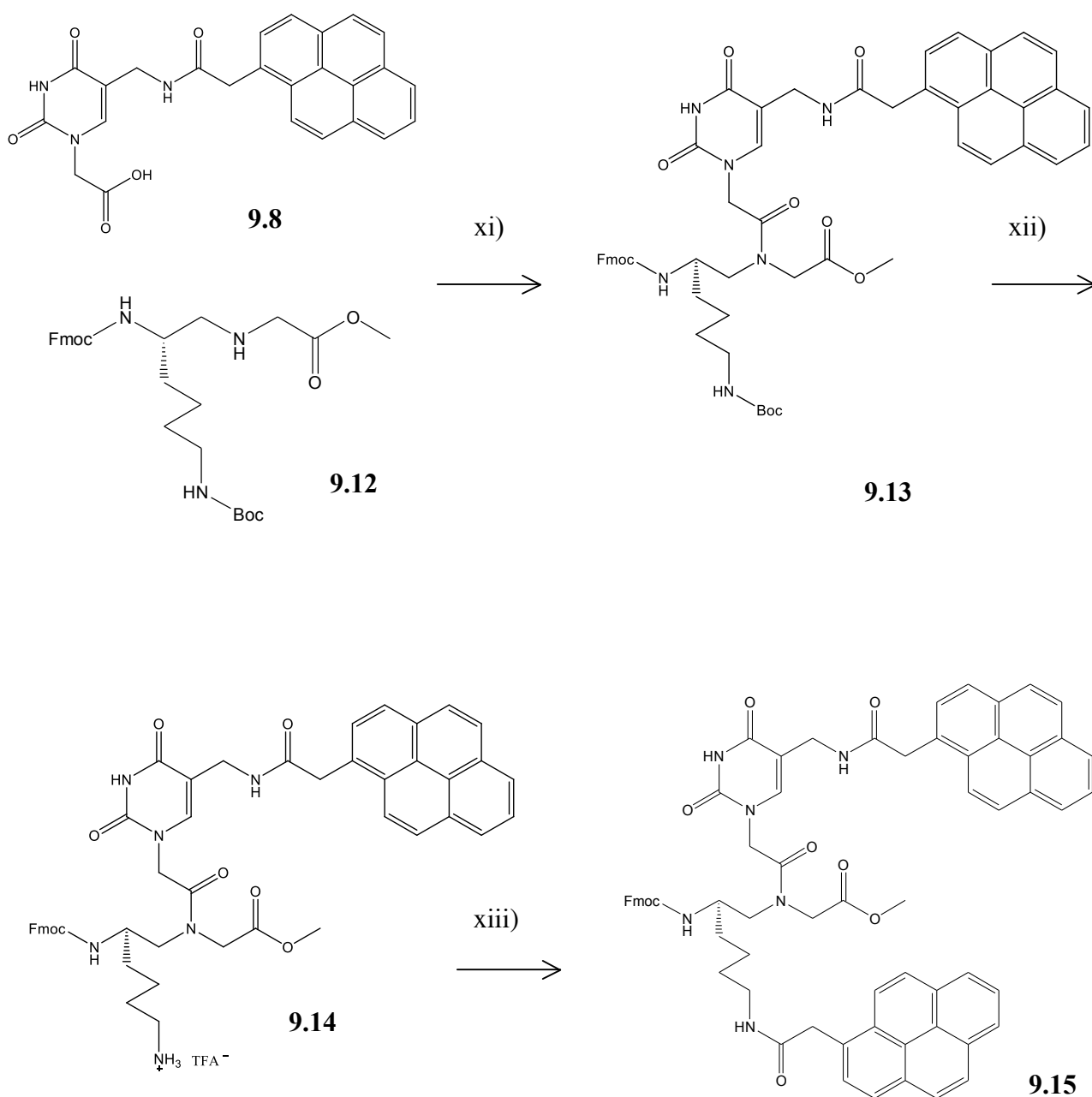


Fig. 9.8 Synthesis of Fmoc-Lys(Boc)-PNA backbone methyl ester. viii) (MeO)MeNH·HCl, HBTU/DIPEA in DMF, 92%; ix) LiAlH₄ in THF, 70%; x) H₂NCH₂CO₂Me, NaBH₃CN, CH₃COOH in MeOH, 56%.

At this stage, the coupling between the pyrene-modified uracil unit **9.8** and the PNA backbone **9.12** was carried out in view of realizing the whole final monomer, using EDC/DHBtOH as activating agents, thus obtaining the methyl ester PNA monomer **9.13**. After Boc deprotection with TFA, which afforded **9.14** in quantitative yield, 1-pyreneacetic acid was used to insert the second pyrene moiety into the lysine side chain through the same HBTU/DIPEA coupling protocol seen for reaction *vii*). Hydrolysis of **9.15** in basic conditions yielded the final dual-pyrene functionalized chiral monomer **9.16** (Figure 9.9).



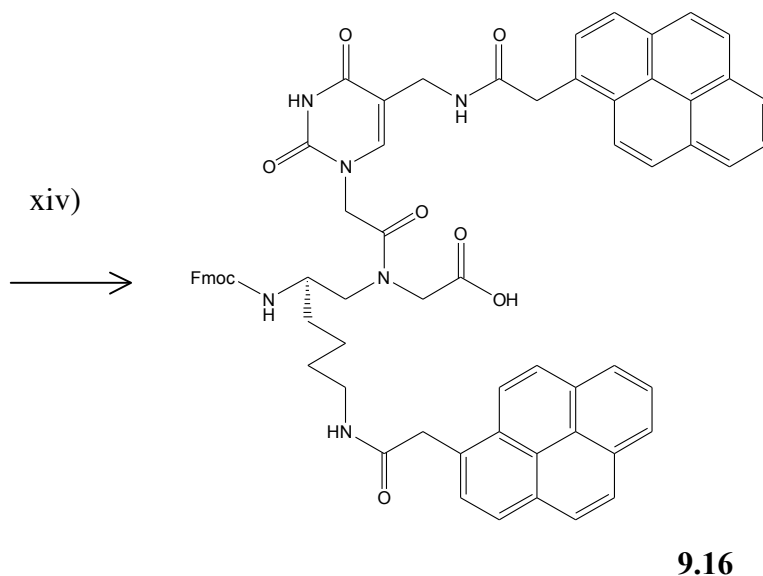


Fig. 9.9 Synthesis of Fmoc-Lys(Pyr)-PNA-(U-Pyr)-OH. xi) EDC·HCl, DhBtOH, DIPEA in DMF, 30%; xii) CH₂Cl₂/TFA 1:1, quantitative; xiii) 1-pyreneacetic acid, HBTU, DIPEA in DMF, 26%; xiv) Ba(OH)₂·8H₂O in THF/H₂O 1:1, 35%.

9.3 Studies on fluorescence properties

Fluorescence studies were carried out in order to assess whether the designed structure of the monomer could effectively enable the formation of a pyrene excimer, which is the pre-requisite for the excimer-monomer switching mechanism. Thus, the fluorescence emission spectrum of solutions of 1-pyreneacetic acid as reference and the above synthesized PNA monomer at the same concentration were recorded under the same conditions. The typical emission spectrum of the pyrene as a monomer is centered in the spectral region around 380-410 nm, while the excimer band is supposed to appear around 480 nm. An excitation wavelength $\lambda_{\text{exc}} = 345$ nm was always used.

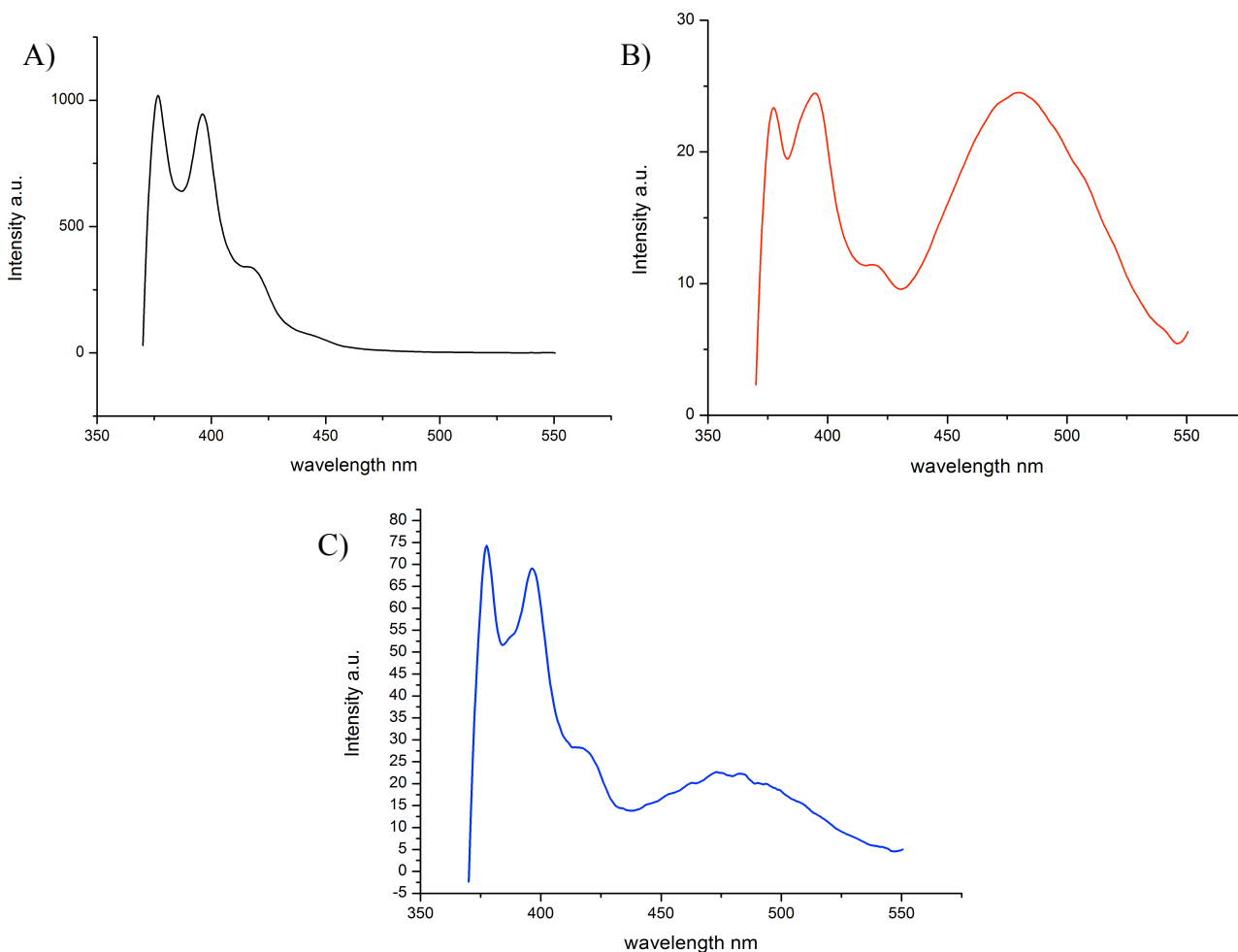


Fig. 9.10 A) fluorescence emission spectrum of a 1 μM aqueous solution of 1-pyreneacetic acid (0.09% DMSO) ($\lambda_{\text{ex}}=345$ nm). The typical bands of the monomer emission are visible in the region 380-410 nm; B) emission spectrum recorded for a 1 μM aqueous solution of the dual-pyrene modified PNA monomer (0.09% DMSO), which shows a huge band at 480 nm typical of the excimer formation; C) emission spectrum recorded for a 1 μM aqueous solution of the dual-pyrene modified PNA monomer in 10% DMSO, which still shows the excimer band, but reduced when compared to the former case.

As shown in the spectra reported in Figure 9.10 A-B, a pyrene excimer band was observed in the case of the modified PNA monomer, suggesting that the monomer displays sufficient degrees of freedom to allow the interaction between the two pyrene moieties.

To further verify the formation of the excimer, the same measurement was carried out in a solution 1 μM in 10% DMSO, to minimize the trend of the monomer to precipitate in water and to evaluate how a less polar environment could affect the π -stacking interactions (Fig. 9.10 C). The presence of the excimer band is still clearly distinguishable, although it is worth to notice its reduced intensity, which is ascribed to the fact the π -stacking interaction leading to the excimer formation is a hydrophobic one, and then better stabilized in a more polar environment^[56] (see Fig. 9.10 B).

9.4 Synthesis of a PNA-based switching probe

Once verified the feasibility of using such a design for the dual-pyrene modified PNA monomer as actual sensing element, a whole PNA probe was synthesized. The sequence chosen H-GCAGACAATTGTAGCT-NH₂ is full complementary to the microRNA 221, which indeed represents a very interesting target in cancer diagnostics (see Chapter 5 for details). The underlined T in the sequence indicates the position of dual-pyrene modified monomer.

Due to difficulties in directly coupling the modified monomer synthesized above to the growing sequence because of a hampering steric hindrance (results not shown), the synthesis of this switching PNA probe was performed by introduction of the pyrene moieties on a precursor PNA monomer during solid phase synthesis, thus overcoming the steric hurdles in an elegant and effective way. The solid phase synthesis of the PNA probe was initially carried out following normal Boc procedure, until the insertion of a doubly modified thymine PNA monomer **9.22**. The precursor doubly branched unit bearing an azide group linked to the thymine and a side lysine chain conjugated to the backbone was obtained by coupling of the modified nucleobase **9.21** to the functionalized PNA backbone monomer **9.20** (Figure 9.11). The ester moiety was then hydrolyzed to give the corresponding carboxylic acid (**9.23**) to be used in the solid phase synthesis. This dual-modified unit allows for a next on-resin functionalization, being the azide and the Fmoc protecting group orthogonal to the Boc one. This is necessary for carrying on the Boc synthesis of the remaining PNA sequence, maintaining two groups prone to a further insertion of other functional moieties in a final stage. The synthetic pathway followed for the introduction of the double on-resin modification is depicted in Figure 9.12.

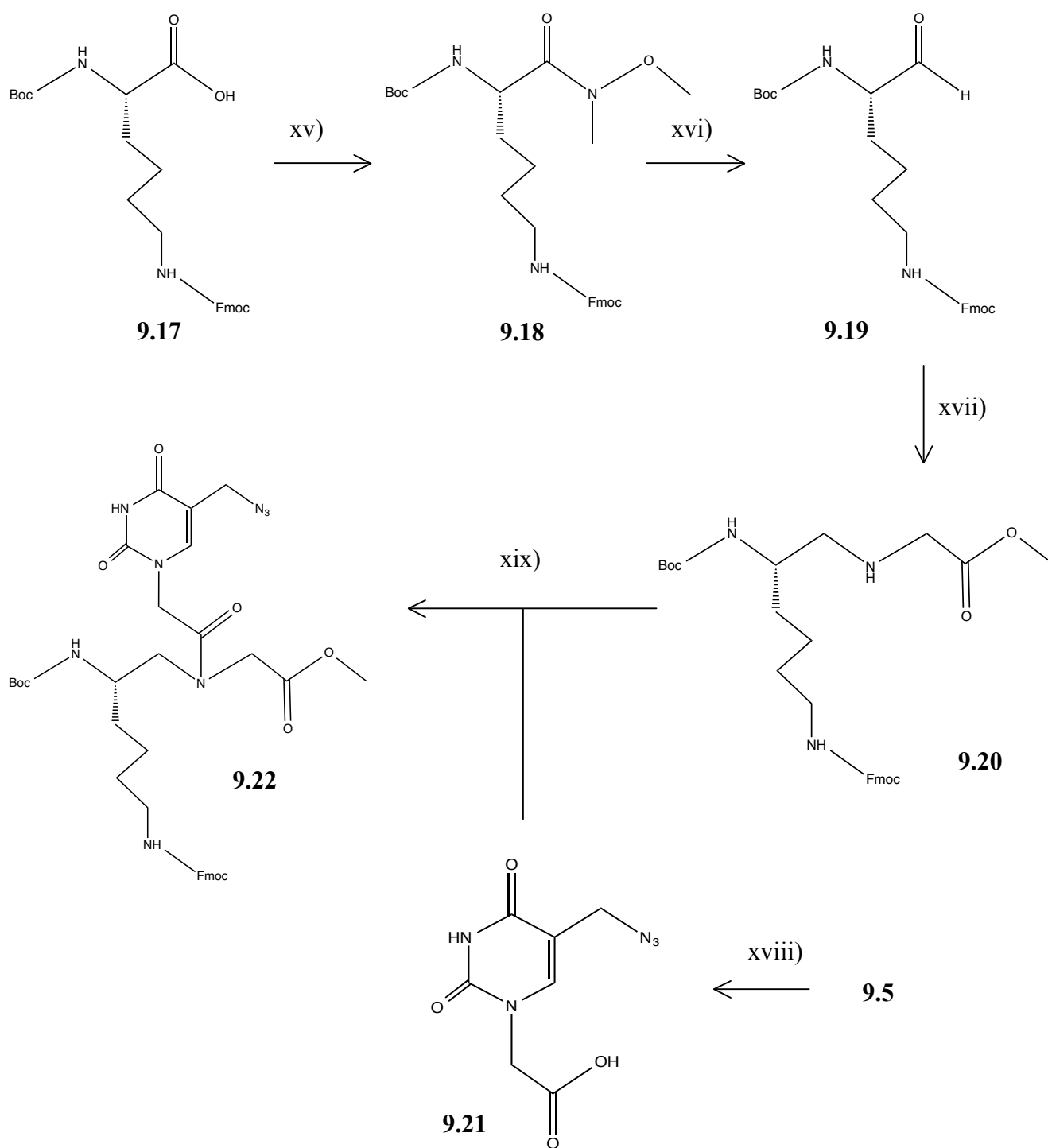
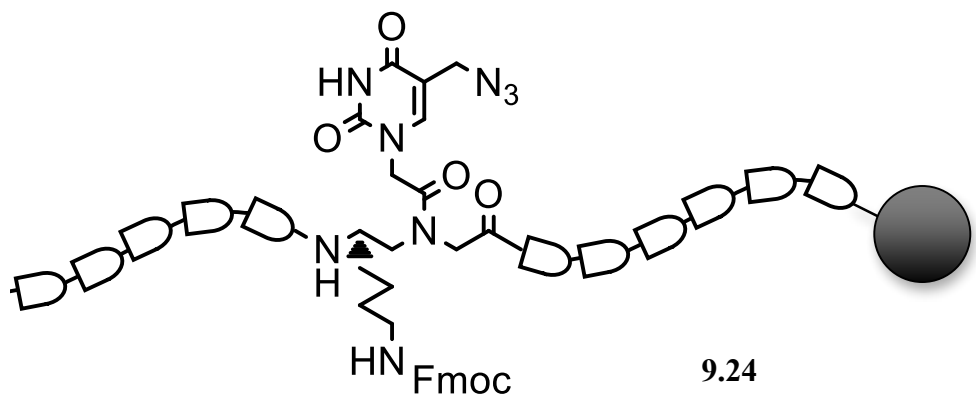
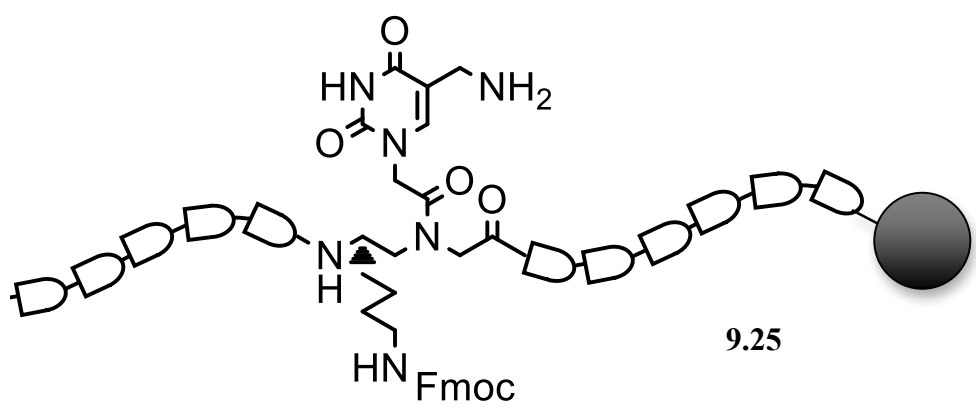


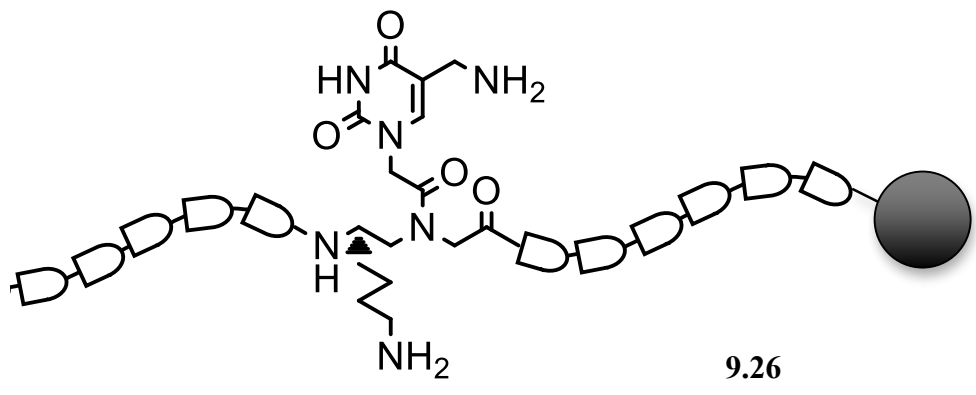
Fig. 9.11 Synthesis of Boc-Lys(Fmoc)-PNA-(U-N₃)-OMe. xv) (MeO)MeNH·HCl, HBTU/DIPEA in DMF, 94%; xvi) LiAlH₄ in THF, 75%; xvii) H₂NCH₂CO₂Me, NaBH₃CN, CH₃COOH in MeOH, 57%; xviii) NaOH in MeOH, 96%; xix) EDC·HCl, DhBtOH, DIPEA in DMF, 81%.



xx)



xxi)



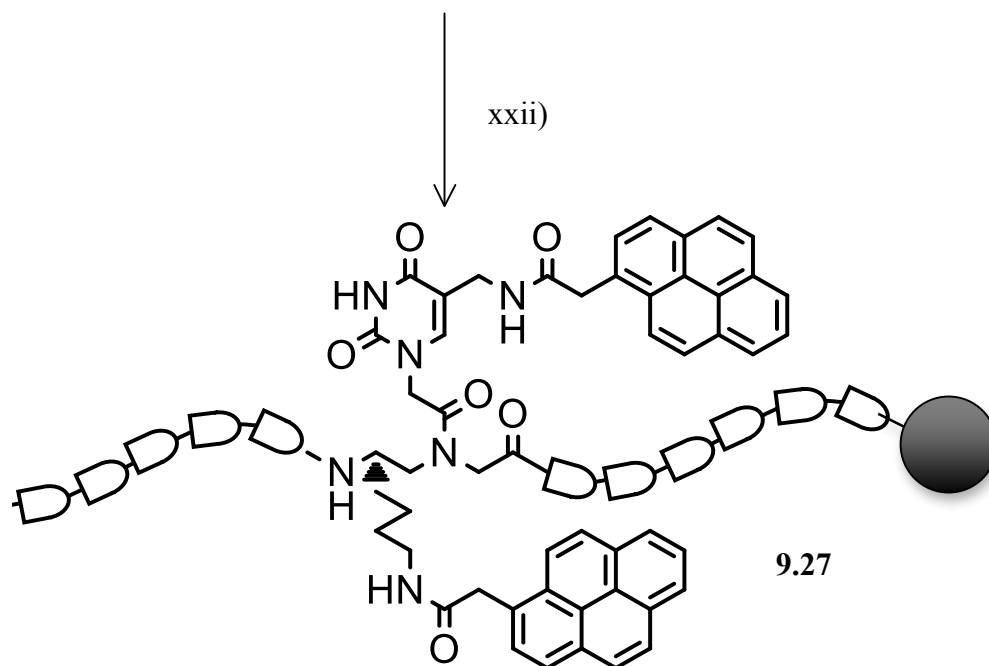


Fig. 9.12 Solid phase synthesis of the dual-pyrene modified PNA probe. xx) PMe_3 in $\text{H}_2\text{O}/\text{THF}$; xxi) piperidine 20%; xxii) 1-pyreneacetic acid, HBTU, DIPEA in DMF.

Once the PNA sequence had been completed following a mixed Boc/Fmoc synthesis, the azide group of **9.24** was reduced to amine group under Staudinger conditions (**9.25**). At this point, deprotection of the side Fmoc group was performed in basic conditions in order to have two available amine groups at the two branches of the monomer (**9.26**). The final simultaneous introduction of two pyrene groups was carried out exploiting coupling reaction with HBTU/DIPEA in a large excess of 1-pyreneacetic acid through formation of two new amide bonds (**9.27**).

After purification by RP-HPLC, the final product was characterized by UPLC-MS and UV-Vis spectroscopy, as described in the experimental section.

9.5 Detection of target nucleic acid by fluorescence emission switching

The actual ability of the above-described PNA probe to hybridize with the target sequence, giving a detectable analytical fluorescent response, has been investigated. A DNA strand 5'-AGCTACATTGTCTGC-3' mimicking the ribonucleic sequence of the miR-221 was used as model target. As expected, the emission spectrum of a 5 μM aqueous solution of the dual-pyrene modified PNA showed a broad emission band centered around 470 nm, which is indeed due to the pyrene excimer (Fig. 9.13, left). Then, the effect of the addition of the DNA target sequence to the PNA probe was investigated, following the change in the fluorescence emission spectrum over time.

In Figure 9.13 (right) the emission spectra recorded at different times at room temperature are reported, which clearly show how the formation of PNA/DNA duplex causes a radical change in the

fluorescence signal. The excimer band drastically dropped upon the addition of the target sequence, with a simultaneous increase of the monomer bands.

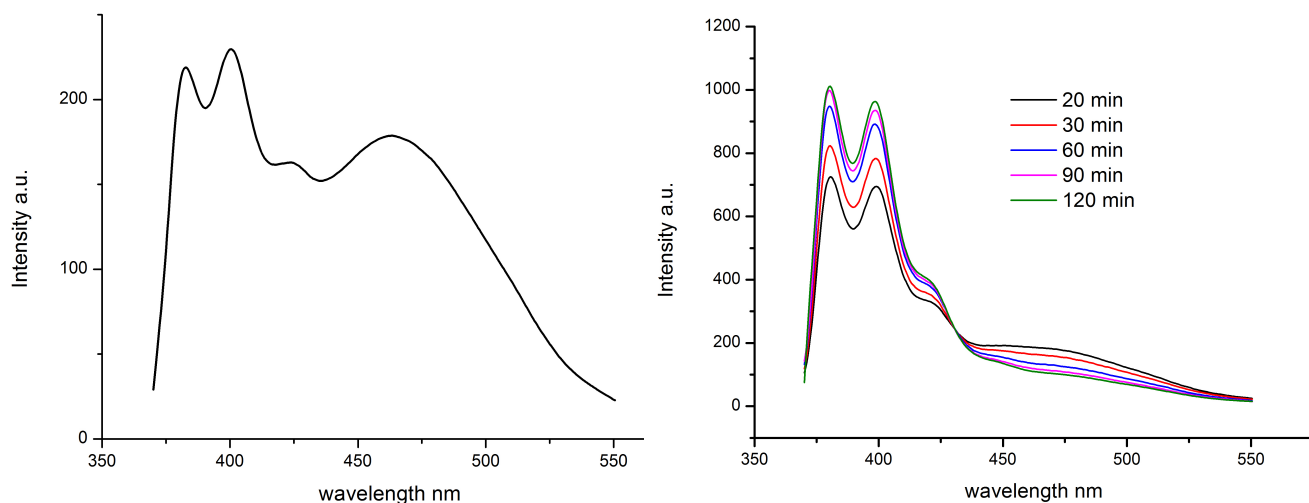


Fig. 9.13 Left) Fluorescence emission spectrum of a 5 μ M aqueous solution of the dual-pyrene modified PNA probe, before addition of the target DNA. Right) Kinetics of the interaction between the PNA probe and the target sequence, which cause the drop of the excimer band and the increase of the monomer peaks ($T = 25^\circ\text{C}$).

In order to quantify this effect, the intensity ratio excimer/monomer was monitored; from this, it could be calculated that, already after 20 minutes of incubation at room temperature, the initial excimer/monomer ratio underwent a dramatic reduction of 69% (see the green line “20 min” in Fig. 9.13, right, compared to the spectrum in Fig. 9.13, left). Time passing by, the ratio underwent a constant decrease to 76% (30 min), 83% (60 min), and 86% (90min). After 120 min, the reduction eventually stabilized on an almost plateau value of 87%. A kinetic curve based on this ratio is reported in Figure 9.14 (right). All these data suggests the effective a conformational change of the probe upon hybridization, which can provide detection of the target sequence by the drastic change in the emission spectrum.

In order to study the selectivity of the probe, the same hybridization test was carried out using a single mismatch sequence 5'-ACGTACGTTGTCTCG-3', bearing the mismatched base in correspondence of the pyrene-clamping unit of the PNA probe. The results are reported in Figure 9.14. As it can be seen from the emission spectrum profiles in Fig. 9.14 (left), a slight reduction effect over time of the excimer band is observed, which is however less dramatic than the one obtained for the full match experiment. Converting this effect in percentage values, a reduction of 44% of the excimer/monomer signal ratio was obtained after 20 minutes of incubation, when a 69%

was recorded when using the full match target sequence. The ratio then dropped of 50% (30 min), 62% (60 min), 68% (90 min), and eventually of 73% after 120 minutes.

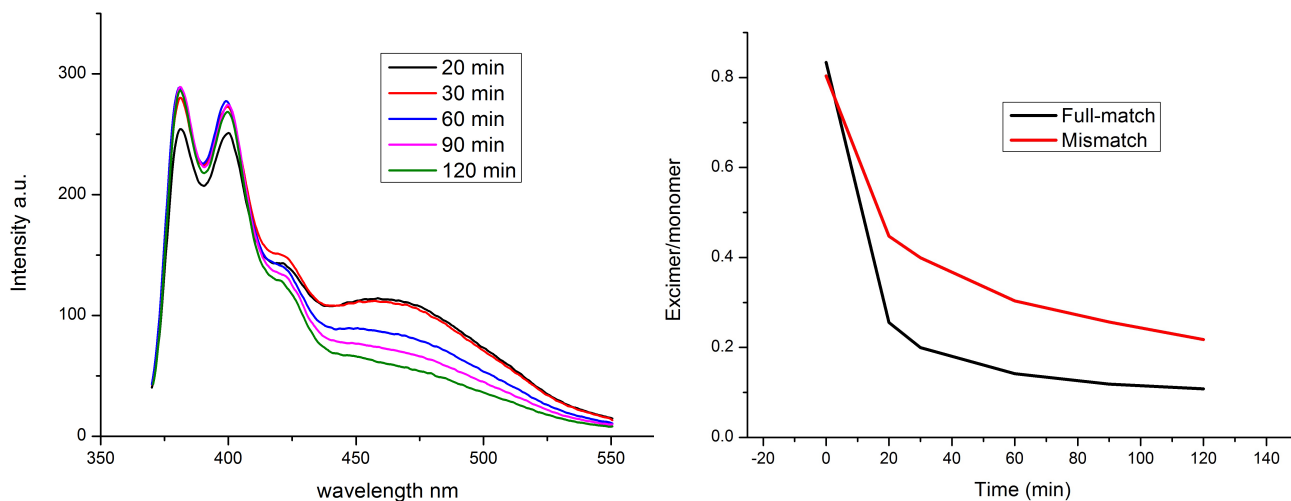


Fig. 9.14 Left) Emission spectrum profiles over time when adding a single mismatch sequence to the PNA switching probe. Right) Kinetics of the interaction between the PNA probe and the DNA sequences (black line = full match, red line = mismatch), expressed as the excimer/monomer intensity ratio as function of time ($T = 25^{\circ}\text{C}$).

As it can be seen from the kinetics of the excimer/monomer ratio (Fig. 9.14 right panel), a more significant effect was obtained when the PNA probe targeted the full match sequence, and pointed out the selectivity of the switching probe at least kinetically. Being the mismatched base in correspondence of the pyrene-clamping unit, this is a very good model to study the kinetics of the hybridization with the target sequence that triggers the opening of the initially paired pyrene branches.

The same experiments were then conducted varying the incubation temperature, to investigate how this parameter could influence the detection system. Hence, measurements at 40°C were firstly carried out. In this case, the concentration of the solutions analyzed was additionally shrunk to $1\ \mu\text{M}$, to create highly diluted conditions to prevent any concentration-driven stacking effect.

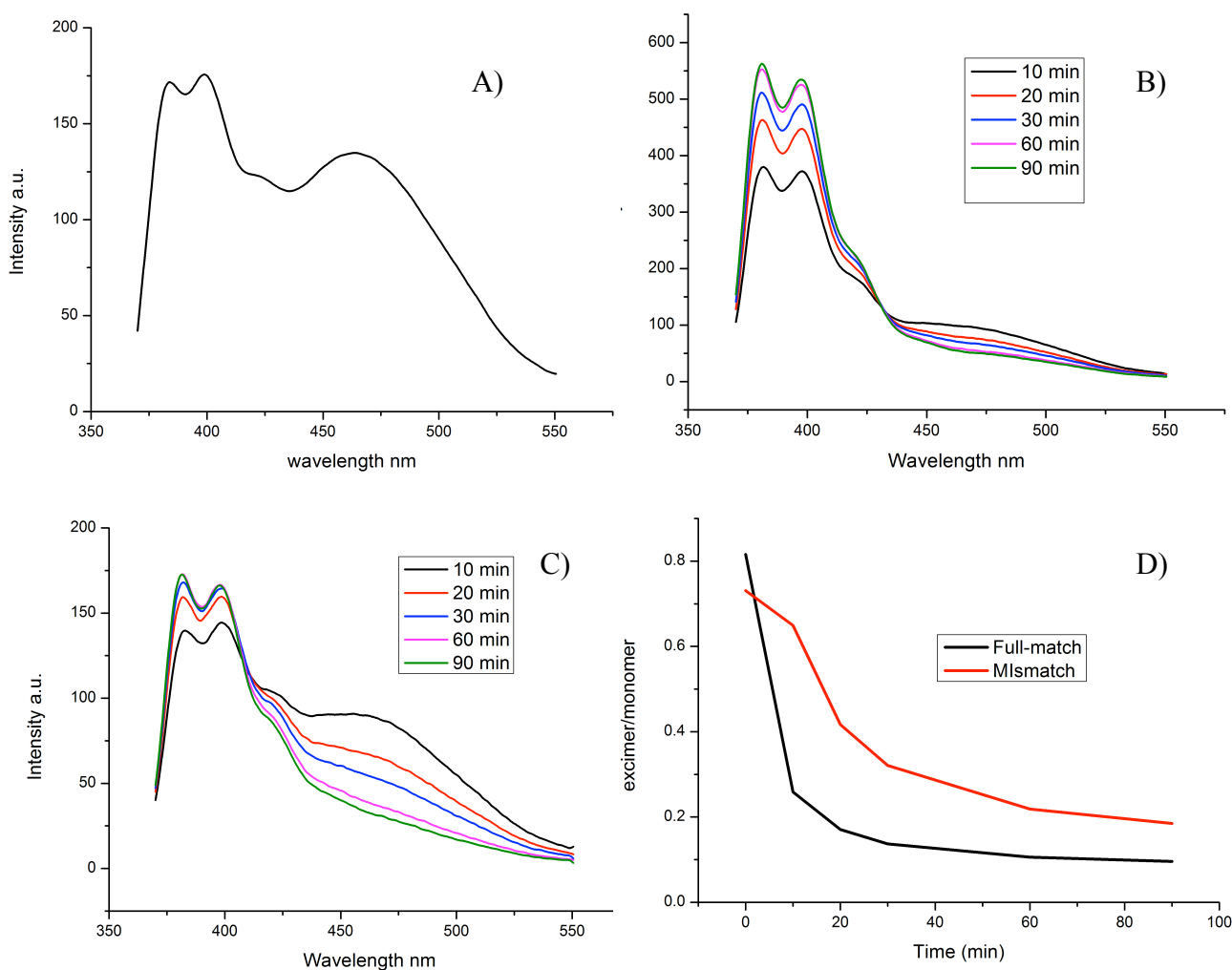


Fig. 9.15 A) Fluorescence emission spectrum of a 1 μM aqueous solution of the dual-pyrene modified PNA probe, before addition of the target DNA, 40 $^{\circ}$ C. B) Emission spectrum profiles over time when adding the full match sequence to the PNA switching probe solution at 40 $^{\circ}$ C. C) Same emission profile over time in presence of a single mismatch sequence. D) Kinetics of the interaction between the PNA probe and the DNA sequences (black line = full match, red line = mismatch), expressed as the excimer/monomer intensity ratio as function of time.

Looking at the graphs reported in Figure 9.15A and 9.15B, the effect of the interaction of the PNA probe with the full match target sequence or the single mismatch one was found to be absolutely comparable to the one obtained at room temperature, providing the same switch in the emission spectrum of the pyrene units. With respect to the RT curves, the plateau was here reached in a reduced time, which is in accordance with the influence of the temperature on the hybridization process. Still, the interaction with the full match sequence gave a reduction of the excimer/monomer intensity ratio always higher than that obtainable when using the single mismatch sequence (from 68% vs. 11% after 10 min and 79% vs. 41% after 20 min, to 88% vs.

75% after 90 minutes in the plateau area). Differences in the kinetic curves of the full match and the mismatched sequence are depicted in Figure 9.15D.

Furthermore, the kinetics of the process was studied at 50° C as well, to understand the effect of an even higher temperature on the hybridization processes. The same experiments were then carried out, but in this case also a random DNA sequence 5'-GGTGAATGAGTAAC-3' was also used, to have a more detailed view on the sensing phenomenon by an additional comparison. The results are reported in Figure 9.16.

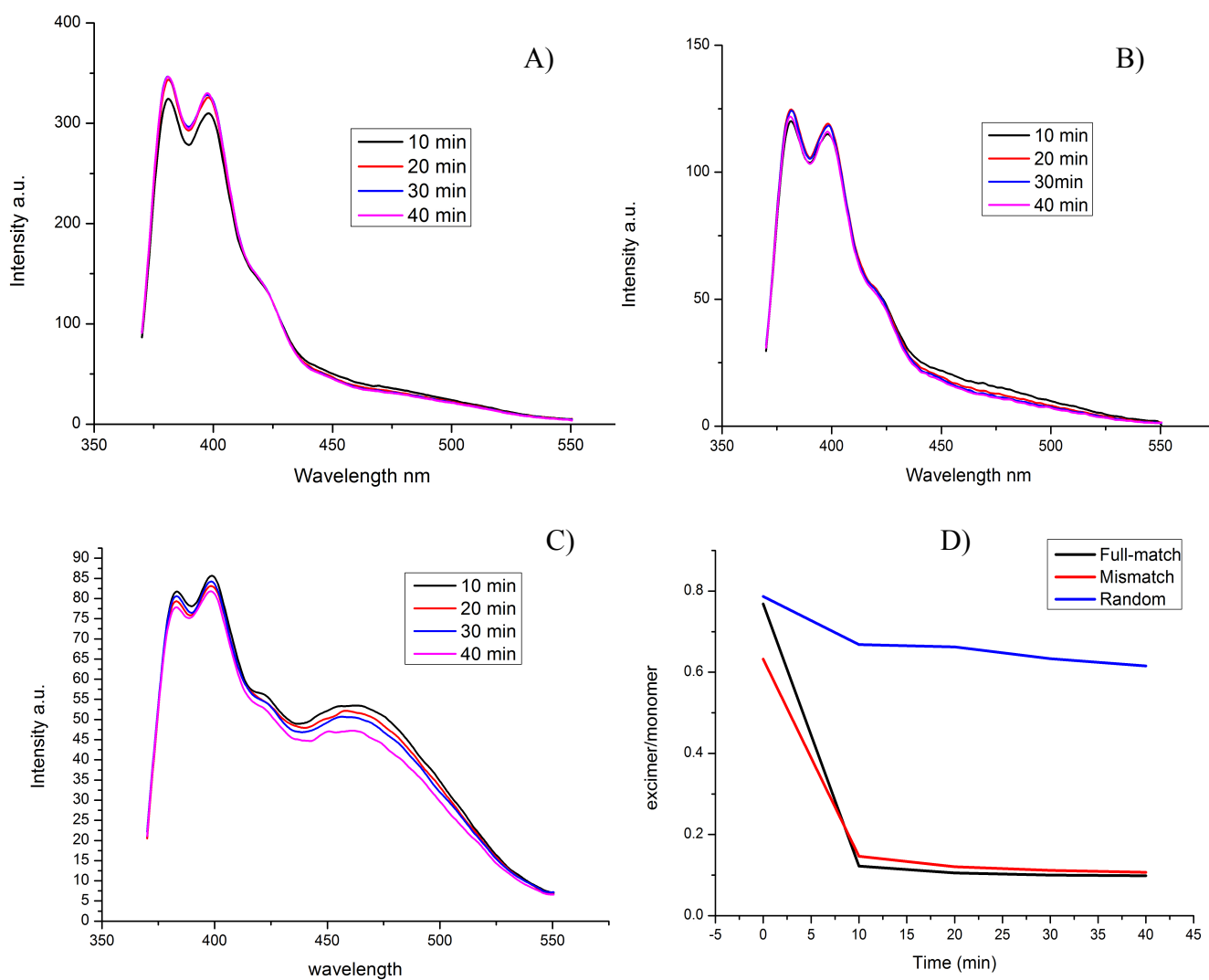


Fig. 9.16 A) Emission spectrum profiles over time when adding the full match sequence to the PNA switching probe solution at 50° C. B) Same emission profiles over time in presence of a single mismatch sequence. C) Emission spectrum profiles over time when adding a random DNA sequence to the PNA switching probe. D) Kinetics of the interaction between the PNA probe and the DNA sequences (black line = full match, red line = mismatch, blue line = random sequence), expressed as the excimer/monomer intensity ratio as function of time.

Still in this case, the interaction of the PNA probe with the full match target sequence gave the typical switch in the emission spectrum from the excimer to the monomer signal. Nevertheless, comparing with the previous corresponding curves, working at 50° C made the plateau be reached already after 20 minutes of incubation (86% excimer/monomer intensity ratio reduction, and 87% after 40 minutes), which is in accordance with the influence of the higher temperature in favoring the hybridization event. Interestingly, at this temperature, also the hybridization of the probe with the single mismatched sequence resulted drastically magnified, as it can be seen from the emission spectrum profiles in Figure 9.16B. A difference was still found between the reduction percentages for the two cases (86% vs. 76% after 10 minutes, 87% vs. 83% after 40 minutes), but greatly reduced, thus suggesting that the kinetic effect was predominant in determining the selectivity observed at lower temperature. However, the scenario completely changed when adding the random DNA sequence to the PNA probe, which led to an almost negligible switch from the excimer to monomer emission (15% excimer/monomer intensity ratio reduction after 10 minutes and 22% after 40 minutes) ascribed to non-specific interactions between the two strands (Fig. 9.16C). The minimal effect registered in this case provided a further proof on the sequence selectivity of the detection scheme. The kinetics profiles are eventually reported in Figure 9.15D.

9.6 Studies on stability of PNA(py-py):DNA duplexes

Melting temperatures (T_m) of the different PNA:DNA duplexes were measured and used as indicators of the complex stability, which might give complementary information to the fluorescence behavior presented above. Solutions of PNA and DNA in PBS (1 μ M) were used for the analysis at the UV-Vis spectrophotometer; the melting temperatures were then calculated for PNA:DNA_{FM} (full-match sequence), PNA:DNA_{MM} (single mismatch sequence), and PNA:DNA_{RM} (random sequence), as reported in Table 8.1.

Table 9.1 Melting temperatures of the diverse PNA:DNA duplexes analyzed and PNA:PNA self-melting

Duplex	Melting temperature
PNA:DNA _{FM}	71.3° C
PNA:DNA _{MM}	65.9° C
PNA:DNA _{RM}	62.9° C
PNA:PNA _(self-melting)	63.9° C

As expected, the highest duplex stability (i.e. the highest T_m) has been found for the PNA:DNA_{FM} complex, according to the full base pairing between the probe and the target sequence.

The insertion of a single mismatch into the sequence caused a notable reduction of the duplex stability (PNA:DNA_{MM}), as pointed out by the lower T_m (65.9° C vs. 71.3° C). The melting temperature for the PNA:DNA_{RM} complex was eventually registered at an even lower value (62.9° C), but this value is most probably due to self-melting of the probe (63.9°C), undergoing spontaneously a conformational transition at this temperature, since no stable base pairing is expected from the random sequence. A conformational transition, and not self-association of the probes, is supposed to occur, since progressive dilutions of the PNA probe solution did not lead to any change in the fluorescence emission spectrum (see Figure 9.13 and 9.15).

9.7 Conclusion

A novel PNA-based switching probe that is able to undergo a change in the disposition of two pyrene moieties upon complexation with the target nucleic acid has been designed and synthesized; the conformational change can be revealed through the change in the fluorescence emission as analytical response. Flexibility of the PNA structure (both at the monomer and at the oligomer level) allowed for arranging the substituents in an appropriate geometry leading to the excimer fluorescent emission. It was possible to obtain the doubly pyrene-functionalized PNA through solid phase synthesis and on-resin modification, which enabled to overcome the limitations due to the steric hindrance of the modified monomer. Studies on fluorescence properties when in presence of the model target miR-221-mimicking DNA sequence have pointed out the effectiveness of the switching mechanism, thus demonstrating the feasibility of this approach, which can be extended to other fluorophores or reactive moieties. This mechanism was found to be sequence-specific, and hence mediated by recognition of the DNA strand by PNA. Thus, it will be possible to exploit this strategy in order to produce a predefined motion of functional group in a controlled way, depending on the presence of a specific target DNA, both for diagnostic and for therapeutic purposes.

9.8 Experimental section

5-hydroxymethyluracil (9.2)

In a Shlenk tube, uracil (10 g, 89.5 mmol) was dispersed together with paraformaldehyde (8.5 g, 283 mmol) in 200 ml H₂O, then triethylamine (17.5 ml, 125.9 mmol) was added and the reaction mixture was stirred overnight at 60° C. The excess formaldehyde was then purged with nitrogen in a 15% solution of sodium hypochlorite and the reaction solution was concentrated under vacuum to give an oil that was mixed with 30 ml H₂O; the product was precipitated adding 25 ml ethanol, collected through sintered glass filter and washed with cold ethanol. Subsequently, aliquots of

product were collected repeating the concentration-precipitation process to give **8.2** as white solid (9.2 g, 74%). **Rf** = 0.68 (MeOH); **¹H NMR** (DMSO-d₆, 300MHz) δ 11.05 (s, 1H), 10.71 (s, 1H), 7.24 (s, 1H), 4.85 (br s, 1H), 4.10 (s, 2H); **¹³C NMR** (DMSO-d₆, 75MHz) δ 163.8, 151.3, 138.2, 112.7, 55.8; **MS** (ESI, MeOH) m/z calcd for C₅H₆N₂O₃ [M]: 142.0378, found: 165 [M+Na]⁺, 307 [2M+Na]⁺; **FT-IR** (KBr) 3369, 3189, 3038, 2865, 1704, 1672 cm⁻¹.

5-chloromethyluracil (9.3)

In a round bottom flask, **9.2** (4 g, 10.6 mmol) was dissolved in HCl 37% (60 ml) and the solution stirred overnight at RT. A white precipitate was formed, which was recovered as white solid by drying under vacuum (4.5 g, quantitative yield). **Rf** = 0.62 (MeOH), **¹H NMR** (DMSO-d₆, 300MHz) δ 11.28 (s, 1H), 11.06 (d, J = 5.9 Hz, 1H), 7.75 (d, J = 5.9 Hz, 1H), 4.42 (s, 2H); **¹³C NMR** (DMSO-d₆, 75MHz) δ 162.8, 151.0, 142.4, 108.8, 39.8; **MS** (ESI, MeOH) m/z calcd for C₅H₅ClN₂O₂ [M]: 160.0040, found: 199 [M+K]⁺, **FT-IR** (KBr) 3305, 3125, 3044, 2829, 1759, 1697, 1656, 1178, 738 cm⁻¹.

5-azidomethyluracil (9.4)

Sodium azide (1.9 g, 29 mmol) was dispersed in 10 ml dry DMF, meanwhile **9.3** (4.1 g, 25.3 mmol) was dissolved in 50 ml dry DMF. This latter solution was then slowly added dropwise to the azide solution. After stirring overnight at RT, the reaction was quenched adding HCl 37% and the resulting white suspension was concentrated under vacuum. The product was thoroughly sonicated in 50 ml DCM/H₂O 1:1 and the suspension then filtered through sintered glass funnel, obtaining **9.4** as white-yellowish solid (3.6 g, 86%). **Rf** = 0.73 (MeOH), **¹H NMR** (DMSO-d₆, 300MHz) δ 11.32 (d, J = 5.7 Hz, 1H), 11.04 (s, 1H), 7.66 (d, J = 5.7 Hz, 1H), 4.06 (s, 2H); **¹³C NMR** (DMSO-d₆, 75MHz) δ 163.8, 151.0, 141.9, 106.4, 46.3; **MS** (ESI, MeOH): m/z calcd for C₅H₅N₅O₂ [M]: 167.0443, found: 191 [M+Na]⁺; **FT-IR** (KBr) 3219, 3079, 3026, 2825, 2132, 1757, 1689, 1667 cm⁻¹.

Ethyl 2-(5-azidomethyluracil-1-yl)acetate (9.5)

In a round bottom flask **9.4** (2.1 g, 12.8 mmol) and K₂CO₃ (1.77 g, 12.8 mmol) were dispersed in 50 ml dry DMF and cooled down to 0° C with an ice bath. Ethyl 2-bromoacetate (1.42 ml, 12.8 mmol) was diluted in 5 ml dry DMF and added dropwise to the former solution. The reaction was then warmed to RT and stirred overnight. The solvent was evaporated under vacuum and the resulting oil was partitioned between EtOAc (60 ml) and water (60 ml). Once transferred into a separatory funnel, the aqueous phase was re-extracted with EtOAc (3 x 60ml). The organic

fractions were combined, dried over Na₂SO₄, and concentrated under vacuum. Purification was accomplished by flash column chromatography eluting with EtOAc:hexane 1:1. The fractions containing the product were combined and dried under vacuum to yield **9.5** as white solid (0.53 g, 17%). **Rf** = 0.66 (EtOAc), ¹H NMR (DMSO-d₆, 400 MHz) δ 11.67 (s, 1H) 7.85 (s, 1H), 4.54 (s, 2H), 4.17 (q, J = 6.9 Hz, 2H), 4.07 (s, 2H), 1.22 (t, J = 7.1 Hz, 3H); ¹³C NMR (DMSO-d₆, 75MHz) δ 167.1, 162.4, 150.2, 142.4, 110.0, 62.4, 48.8, 46.9, 14.0; **MS** (ESI, MeOH) m/z calcd for C₉H₁₁N₅O₄ [M]: 253.0811, found: 276 [M+Na]⁺, 292.1 [M+K]⁺; **FT-IR** (KBr) 3160, 3036, 2841, 2109, 2082, 1739, 1701, 1647 cm⁻¹.

Ethyl 2-(5-aminomethyluracil-1-yl)acetate trifluoroacetate salt (9.6)

In a round bottom flask **9.5** (0.4 g, 1.57 mmol) was solubilized in 15 ml distilled THF, then water (72 μl) was added, and the reaction mixture was cooled to 0° C with an ice bath. Triphenylphosphine (0.85 g, 3.25 mmol) was thus added to the flask. The reaction was warmed to RT and stirred overnight. The solvent was then evaporated under reduced pressure, the crude was dissolved in the minimum amount of TFA, then precipitated with Et₂O (30 ml). The solid was recovered by centrifugation and washed with DCM (3 times), to yield **8.6** as white solid (trifluoroacetate salt) (0.41 g, 76%). **Rf** = 0.4 (EtOAc/MeOH/NH₃(aq. 30%) 5:4:1); ¹H NMR (DMSO-d₆, 400 MHz) δ 11.84 (s, 1H), 7.96 (br s, 3H), 7.88 (1s, H), 4.57 (s, 2H), 4.17 (q, J = 7.1 Hz, 2H), 3.65 (br d, J = 5.0 Hz, 2H), 1.23 (t, J = 7.1 Hz, 3H); ¹³C NMR (DMSO-d₆, 75MHz) δ 167.7, 163.2, 158.2 (q, J = 33 Hz), 150.4, 146.1, 116.3 (q, J = 294 Hz), 105.7, 61.1, 48.8, 35.1, 13.8; **MS** (ESI, MeOH) m/z calcd for C₉H₁₃N₃O₄ [M]: 227.0906, found: 228 [M+H]⁺, 455 [2M+H]⁺; **FT-IR** (KBr) 3566, 3446, 3200, 2998, 2829, 1728, 1713, 1667 cm⁻¹.

Ethyl 2-(5-(2-(pyren-1-yl)acetamido)methyluracil-1-yl)acetate (9.7)

In a round bottom flask, 1-pyreneacetic acid (383 mg, 1.46 mmol) and HBTU (354 mg, 1.41 mmol) were dissolved in 5 ml dry DMF. The solution was then cooled down to 0° C with an ice bath, and DIPEA was added (673 μl, 3.66 mmol). The mixture was first stirred for 30 minutes at 0° C, then kept stirred while warming to RT. At this point, **9.6** (250 mg, 0.73 mmol) was added and the mixture was stirred overnight at RT. **9.7** was then collected as a pale brown solid through Büchner funnel filtration, after precipitation from the reaction mixture with 20 ml EtOAc and 20 ml H₂O (3 h, 4° C). A second aliquot of product was collected by precipitation with 90 ml hexane of the organic phase (3 h, 4° C), washed with saturated KHSO₄ (2 x 30 ml), saturated NaHCO₃ (2 x 30 ml) and brine (30ml). The whole procedure yielded **9.6** as a brownish solid (252 mg, 73%). **Rf** = 0.87 (EtOAc/MeOH/NH₃(aq. 30%) 5:4:1); ¹H NMR (DMSO-d₆, 400 MHz) δ 11.56 (s, 1H), 8.52 (t, J =

5.5 Hz, 1H), 8.41 (d, J = 9.3 Hz, 1H), 8.29 (d, J = 7.4 Hz, 2H), 8.24 (d, J = 7.9 Hz, 1H), 8.20 (d, J = 9.3 Hz, 1H), 8.16 (m, 2H), 8.07 (d, J = 7.6 Hz, 1H), 8.02 (d, J = 7.9 Hz, 1H), 7.52 (s, 1H), 4.46 (s, 2H), 4.24 (s, 2H), 4.10 (q, J = 7.1 Hz, 2H), 3.92 (d, J = 5.5 Hz, 2H), 1.18 (t, J = 7.1 Hz, 3H); ^{13}C NMR* (DMSO-d₆, 75 MHz) δ 170.7, 168.4, 163.9, 151.2, 143.5, 131.3, 131.4, 130.8, 130.2, 129.5, 129.1, 127.8, 127.7, 127.3, 126.6, 125.6, 125.4, 125.2, 124.6, 124.4, 110.7, 61.6, 49.2, 40.4, 35.7, 14.4; MS (ESI, MeOH) m/z calcd for C₂₇H₂₃N₃O₅ [M]: 469.16377, found: 470 [M+H]⁺, 492 [M+Na]⁺, 508 [M+K]⁺; HRMS (ESI-Orbitrap, MeOH) m/z found: 470.17075 [M+H]⁺; FT-IR (KBr) 3041, 1670, 1684, 1472 cm⁻¹.

2-(5-(2-(pyren-1-yl)acetamido)methyluracil-1-yl)acetic acid (9.8)

In a round bottom flask **9.7** (179 mg, 0.38 mmol) was dissolved in 10 ml MeOH, then 5 ml NaOH 1 M were added, and the mixture was stirred overnight. The organic solvent was then evaporated under vacuum, the pH was lowered to 3 with HCl 37% and **9.8** was collected over Büchner funnel as a brown-red solid (124 mg, 74%). R_f = 0.00 (EtOAc), ^1H NMR (DMSO-d₆, 400 MHz) δ 11.47 (s, 1H), 8.50 (t, J = 5.4 Hz, 1H), 8.36 (d, J = 9.3 Hz, 1H), 8.26 (d, J = 7.6 Hz, 2H), 8.22 (d, J = 8.1 Hz, 1H), 8.18 (d, J = 9.3 Hz, 1H), 8.13 (m, 2H), 8.05 (d, J = 7.6 Hz, 1H), 8.00 (d, J = 7.8 Hz, 1H), 7.54 (s, 1H), 4.37 (s, 2H), 4.23 (s, 2H), 3.89 (d, J = 5.3 Hz, 2H); ^{13}C NMR* (DMSO-d₆, 75 MHz) δ 170.7, 169.9, 164.0, 151.2, 143.7, 131.4, 131.3, 130.8, 130.2, 129.5, 129.1, 127.8, 127.7, 127.3, 126.6, 125.5, 125.4, 125.2, 124.6, 124.4, 110.5, 49.3, 49.2, 35.8; MS (ESI, MeOH) m/z calcd for C₂₅H₁₉N₃O₅ [M]: 441.13247, found: 442 [M+H]⁺, 464 [M+Na]⁺, 480 [M+K]⁺; HRMS (ESI(-)-Orbitrap, MeOH) m/z found: 440.12518 [M-H]⁻; FT-IR (KBr) 3041, 1700, 1684, 1472 cm⁻¹.

Fmoc-Lys(Boc)-N(Me)OMe (9.10), Fmoc-Lys(Boc)-H (9.11), Fmoc-Lys(Boc)-PNA Backbone (9.12)

The products **9.10**, **9.11** and **9.12** have been synthesized and fully characterized according to the procedures reported by Totsingan *et al.*^[39]

Fmoc-Lys(Boc)-PNA-(U-Pyr)-OMe (9.13)

In a round bottom flask **9.8** (107 mg, 0.243 mmol) was dissolved in 5 ml dry DMF and cooled to 0° C with an ice bath. *N*-(3-Dimethylaminopropyl)-*N'*-ethylcarbodiimide hydrochloride (EDC·HCl) (48 mg, 0.25 mmol), 3-Hydroxy-1,2,3-benzotriazin-4(3H)-one (DhBtOH) (41 mg, 0.25 mmol), and DIPEA (101 μl , 0.58 mmol) were added, and the mixture was stirred for 15 minutes before warming up to RT. After 20 minutes, **8.12** (127 mg, 0.243 mmol) was added and the mixture was stirred overnight at RT. The solvent was then evaporated under vacuum; the crude product was re-

dissolved in 1 ml DMF, diluted in 100 ml EtOAc, and washed with saturated KHSO₄ (2 x 100 ml), saturated NaHCO₃ (2 x 100 ml) and brine (2 x 100 ml). The organic phase was recovered, dried over Na₂SO₄ and concentrated under vacuum. Purification was accomplished by flash column chromatography with gradient elution (EtOAc to EtOAc:MeOH 9:1). The fractions containing the product were combined and dried under vacuum to yield **9.13** as pale brown solid (69.3 mg, 30%).

Rf = 0.60 (EtOAc:MeOH 7:3), **¹H NMR** (CDCl₃, 400 MHz) δ 8.58 (s, 1H), 8.09-8.18 (m, 5H), 7.97-8.03 (m, 4H), 7.88 (d, J = 7.7 Hz, 2H), 7.75 (d, J = 7.3 Hz, 2H), 7.53-7.61 (m, 2H), 7.39 (t, J = 7.4 Hz, 2H), 7.25-7.32 (m, 2H), 7.19 (s, 1H), 4.25 (t, J = 5.6 Hz, 2H), 4.09-4.23 (m, 6H), 4.08 (br s, 1H), 3.95 (m, 4H), 3.80 (s, 3H), 3.71 (s, 2H), 3.07 (m, 2H), 1.45 (s, 9H), 1.27-1.70 (m, 6H); **¹³C NMR*** (CDCl₃, 100 MHz) δ 10.95, 22.97, 23.77, 25.45, 28.93, 30.38, 38.76, 41.86, 47.03, 48.01, 49.50, 49.88, 50.84, 66.43, 68.18, 110.62, 119.97, 123.05, 123.09, 124.63, 125.10, 125.27, 125.39, 126.11, 127.07, 127.37, 127.69, 128.17, 128.45, 128.80, 129.50, 130.76, 130.85, 130.98, 131.25, 141.32, 143.75, 156.34, 163.26, 169.27, 171.54; **MS** (ESI, MeOH) m/z calcd for C₅₄H₅₆N₆O₁₀ [M] 948.40579, found: 972 [M+Na]⁺, 988 [M+K]⁺; **HRMS** (ESI-Orbitrap, MeOH) m/z found: 949.41333 [M+H]⁺, 971.3950 [M+Na]⁺; **ATR-FTIR** 2929, 1748, 1679, 1541, 1458, 1389, 1172, 743 cm⁻¹.

Fmoc-Lys-PNA-(U-Pyr)-OMe trifluoroacetate salt (9.14)

9.13 (66 mg, 0.069 mmol) was dissolved in CH₂Cl₂/TFA 1:1 (2 ml), cooling down to 0° C with an ice bath and stirring for 30 minutes. The solvent was then evaporated under vacuum and the product was washed three times with CH₂Cl₂, yielding a pale brown solid **9.14** (73 mg, quantitative yield) as trifluoroacetate salt. **Rf** = 0.69 (EtOAc:MeOH 1:1), **¹H NMR** (DMSO-d₆, 400 MHz) δ 11.43 (s, 1H), 8.48-8.55 (m, 1H), 8.38 (d, J = 8.6 Hz, 1H), 8.12-8.31 (m, 6H), 8.03-8.12 (m, 1H), 7.99-8.03 (m, 1H), 7.88 (m, 2H), 7.65 (m, 3H), 7.23-7.43 (m, 5H), 5.24 (br s, 3H), 4.50 (s, 2H), 4.30-4.37 (m, 2H), 4.29 (m, 1H), 4.22 (d, J = 6.4 Hz, 4H), 3.91 (m, 3H), 3.70 (s, 2H), 3.63 (s, 3H), 2.75 (m, 2H), 1.12-1.60 (m, 6H); **¹³C NMR*** (DMSO-d₆, 100 MHz) δ 22.87, 27.17, 29.46, 31.34, 35.71, 47.31, 48.65, 49.97, 51.59, 52.00, 52.31, 52.70, 65.61, 110.36, 114.83, 116.08 (q, J = 280 Hz), 117.78, 120.54, 124.30, 124.49, 125.10, 125.32, 125.52, 126.62, 127.25, 127.45, 127.77, 127.85, 128.06, 129.08, 129.47, 130.21, 130.82, 131.21, 131.41, 141.29, 144.05, 144.24, 151.25, 158.66 (q, J = 35.7 Hz), 164.07, 167.89, 170.70; **MS** (ESI, MeOH) m/z calcd for C₄₉H₄₈N₆O₈ [M] 848.35336, found: 850 [M+H]⁺, 872 [M+Na]⁺; **HRMS** (ESI-Orbitrap, MeOH) m/z found: 849.36035 [M+H]⁺, 871.3426 [M+Na]⁺; **ATR-FTIR** 3000, 1678, 1518, 1466, 1161 cm⁻¹.

Fmoc-Lys(Pyr)-PNA-(U-Pyr)-OMe (9.15)

In a round bottom flask, 1-pyreneacetic acid (117 mg, 0.13 mmol) was dissolved in 1 ml dry DMF together with HBTU (46 mg, 0.12 mmol), then the solution was cooled down to 0° C with an ice bath, and DIPEA (56 µl) was added. The mixture was stirred for 30 minutes at 0° C, then 30 minutes more while warming up to RT. At this point **9.14** (62 mg, 0.064 mmol) was added and the mixture was allowed to react overnight. Subsequently, the reaction mixture was diluted with 200 ml EtOAc and washed with saturated KHSO₄ (2 x 200 ml), saturated NaHCO₃ (2 x 200 ml) and brine (2 x 200 ml). The organic phase was recovered, dried over Na₂SO₄ and concentrated under vacuum. Purification was accomplished by flash column chromatography with gradient elution (EtOAc to EtOAc:MeOH 1:1). The product containing fractions were combined and dried under vacuum to yield **8.15** as pale brown solid (18 mg, 26%). **Rf** = 1.00 (EtOAc/MeOH/NH_{3(aq)} 30%) 5:4:1); **¹H NMR** (DMSO-d₆, 400 MHz) δ 11.43 (s, 1H), 8.50 (m, 1H), 8.33-8.38 (m, 2H), 8.10-8.27 (m, 12H), 7.93-8.06 (m, 4H), 7.83 (t, J = 8 Hz, 2H), 7.59-7.71 (m, 3H), 7.24-7.41 (m, 5H), 4.46 (m, 2H), 4.21-4.12 (m, 7H), 3.98-4.05 (m, 2H), 3.88 (m, 4H), 3.66 (s, 2H), 3.58 (s, 3H), 3.06 (m, 2H), 1.23-1.61 (m, 6H); **¹³C NMR*** (DMSO-d₆, 100 MHz) δ 11.7, 14.35, 22.85, 23.70, 28.81, 29.39, 30.29, 38.52, 47.23, 65.73, 66.21, 67.86, 79.08, 79.73, 110.26, 120.51, 124.39, 124.54, 125.18, 125.31, 126.56, 127.24, 127.45, 127.61, 127.82, 129.11, 129.46, 130.12, 130.77, 131.24, 131.54, 132.01, 141.14, 143.19, 144.05, 144.26, 164.01, 167.45, 169.80, 170.30, 170.63; **MS** (ESI, MeOH) m/z calcd for C₆₇H₆₀N₆O₉ [M] 1090.42653, found: 1114 [M+Na]⁺, 569 [M+2Na]²⁺; **HRMS** (ESI-Orbitrap, MeOH) m/z found: 1091.43323 [M+H]⁺, 1108.4604 [M+NH₄]⁺, 1113.4157 [M+Na]⁺, 1129.3897 [M+K]⁺; **ATR-FTIR** 3291, 3039, 2926, 1665, 1530, 1447, 1183 cm⁻¹.

Fmoc-Lys(Pyr)-PNA-(U-Pyr)-OH (9.16)

Ba(OH)₂·8H₂O (10 mg, 0.033 mmol) was added to a suspension of **9.15** (17 mg, 0.016 mmol) in THF:H₂O 1:1 and the mixture was allowed to react overnight at RT. The pH was then lowered to 2.5 with HCl 37%, the solvent was evaporated under vacuum, and the residual product was dissolved in the minimum amount of DMF. A crude solid was precipitated as with 40 ml water and purification was accomplished by flash column chromatography (CH₂Cl₂/MeOH 9:1). The product containing fractions were combined and dried under vacuum to yield **8.16** as pale brown solid (6.0 mg, 35%). **Rf** = 0.15 (CH₂Cl₂:MeOH 9:1); **¹H NMR** (DMSO-d₆, 400 MHz) δ 14.94 (s, 1H), 11.37 (s, 1H), 8.49 (br m, 1H), 8.35 (m, 2H), 8.07-8.26 (m, 12H), 7.95-8.03 (m, 4H), 7.83 (t, J = 7.1 Hz, 2H), 7.66 (m, 3H), 7.24-7.41 (m, 5H), 5.40 (s, 1H), 4.47 (m, 2H), 4.23-4.30 (m, 2H), 4.12-4.23 (m, 6H), 3.87 (m, 4H), 3.72 (s, 2H), 3.02 (m, 2H), 1.21-1.54 (m, 6H); **¹³C NMR*** (DMSO-d₆,

100 MHz) δ 29.46, 30.35, 30.44, 30.64, 30.70, 30.89, 31.08, 31.14, 38.60, 39.35, 41.60, 41.81, 110.22, 120.40, 120.50, 121.85, 124.31, 124.39, 124.56, 125.22, 125.41, 126.62, 126.87, 127.25, 125.66, 127.76, 127.85, 128.49, 129.11, 129.40, 130.16, 130.84, 131.28, 131.65, 137.89, 139.88, 143.04, 145.93, 151.22, 164.00; **MS** (ESI, MeOH) m/z calcd for $C_{66}H_{56}N_6O_9$ [M] 1076.41088, found: 1100 $[M+Na]^+$, 1122 $[M-H+2Na]^+$; **HRMS** (ESI(-) Orbitrap, MeOH) m/z found: 853.3365 $[M-Fmoc]^-$.

Boc-Lys(Fmoc)-N(Me)OMe (9.18)

In a round bottom flask, commercial available Boc-Lys(Fmoc) **9.17** (3.78 g, 8.07 mmol) was solubilized in DMF (38 ml) and cooled to 0°C with an ice bath. HBTU (3.37 g, 8.88 mmol) and DIPEA (4.2 ml, 24.11 mmol) were subsequently added to the solution, which was stirred for 15 minutes at 0°C and further 15 minutes at RT. Then, *N,O*-dimethylhydroxylamine hydrochloride (1.58 g, 16.20 mmol) was added. After 3 hours the solvent was evaporated under reduced pressure and the resulting oil was taken up with EtOAc (200 ml), transferred in a separatory funnel and washed with saturated $KHSO_4$ (2 x 400 ml), saturated $NaHCO_3$ (2 x 400 ml) and brine (2 x 200 ml). The organic layer was dried over Na_2SO_4 and the solvent removed under reduced pressure to yield **9.18** (4.25 g, 94%) as a white foamy solid. **Rf** = 0.51 (EtOAc); **1H NMR** ($CDCl_3$, 400 MHz) δ 1.45 (11H, m), 1.54 (2H, m), 1.63 (2H, m), 3.21 (5H, br s), 3.77 (3H, s), 4.22 (1H, t, J = 6.7 Hz), 4.39 (2H, d, J = 6.8 Hz), 4.69 (1H, s), 5.04 (1H, s), 5.30 (1H, d, J = 8 Hz), 7.30 (2H, t, J = 6.8 Hz), 7.41 (2H, t, J = 7.4 Hz), 7.62 (2H, d, J = 7.2 Hz), 7.78 (2H, d, J = 7.4 Hz); **^{13}C NMR** ($CDCl_3$, 100 MHz) δ 22.5, 28.4, 29.3, 32.1, 32.6, 40.8, 47.3, 50.1, 61.6, 66.5, 79.6, 119.9, 125.1, 127.0, 127.7, 141.3, 144.0, 155.7, 156.5, 173.1; **MS** (ESI, MeOH) m/z calcd for $[C_{28}H_{37}N_3O_6]$ 511.28824, found: 534 $[M+Na]^+$, 550 $[M+K]^+$; **HRMS** (ESI-Orbitrap, MeOH) found 534.2569 for $[M+Na]^+$; **FT-IR** (KBr) 742, 760, 1169, 1248, 1366, 1390, 1523, 1655, 1707, 2975, 2864, 3007, 3342 cm^{-1} .

Boc-Lys(Fmoc)-H (9.19)

In a round bottom flask the amide **9.18** (2.52 g, 4.93 mmol) was solubilized in THF (100 ml) and cooled down to 0° C with an ice bath. Under vigorous stirring, a 1M solution of $LiAlH_4$ in THF (6 mL, 5.91 mmol) was added dropwise over 10 minutes and the reaction was periodically checked to control the disappearing of the starting material. After 40 minutes the reaction was quenched by adding saturated $KHSO_4$ (65 ml), the organic layer was then removed under reduced pressure and the aqueous phase was extracted with EtOAc (200 ml). The organic phase was washed with saturated $KHSO_4$ (2 x 200 ml), saturated $NaHCO_3$ (2 x 200 ml) and brine (200 ml). The organic phase was dried over Na_2SO_4 and the solvent removed under reduced pressure to yield **8.19** (1.68 g,

75%) as a white foamy solid. **Rf** = 0.60 (EtOAc); **¹H NMR** (CDCl₃, 400 MHz) δ 1.45 (14H, m), 1.61 (1H, m), 3.15 (2H, m), 4.15 (2H, m), 4.40 (2H, d, *J* = 5.4 Hz), 5.22 (1H, br s), 5.42 (1H, d, *J* = 6.2 Hz), 7.27 (2H, t, *J* = 7.2 Hz), 7.30 (2H, t, *J* = 6.3 Hz), 7.52 (2H, d, *J* = 7.4 Hz), 7.73 (2H, d, *J* = 7.4 Hz), 9.53 (1H, s); **¹³C NMR** (CDCl₃, 100 MHz) δ 22.2, 28.2, 28.7, 29.6, 40.4, 47.3, 59.6, 66.6, 80.2, 119.9, 125.0, 127.1, 127.7, 141.3, 143.9, 155.7, 156.6, 199.9; **MS** (ESI, MeOH) *m/z* calcd for [C₂₆H₃₂N₂O₅]: 452.23112, found: 507 [M+Na+CH₃OH]⁺, 523 [M+K+CH₃OH]⁺; **HRMS** (ESI-Orbitrap, MeOH) found: 475.24554 for [M+Na]⁺.

Boc-Lys(Fmoc)-PNA Backbone (9.20)

In a round bottom flask the aldehyde **9.19** (1.60 g, 3.53 mmol) and glycine methyl ester hydrochloride (1.33 g, 10.60 mmol) were solubilized in MeOH (40 ml) and cooled to 0° C with an ice bath. After 20 minutes NaBH₃CN (266 mg, 4.24 mmol) and acetic acid (0.24 mL, 4.24 mmol) were added and the reaction mixture was allowed to react for further 3 hours before evaporating the solvent under reduced pressure. The resulting solid was dissolved in EtOAc (250 ml), transferred in a separatory funnel and washed with saturated NaHCO₃ (2 x 150 ml) and brine (150 ml). The organic layer was dried over Na₂SO₄, the solvent was removed under reduced pressure and the residue was purified by flash chromatography (from EtOAc/hexane 7:3 to EtOAc) to give **8.20** (1.05 g, 57%) as a yellowish foamy solid. **Rf** = 0.28 (EtOAc); **¹H NMR** (CDCl₃, 400 MHz) δ 1.44 (15H, m), 2.02 (1H, m), 2.63 (2H, m), 3.18 (2H, m), 3.39 (1H, d, *J* = 17.5 Hz), 3.44 (1H, d, *J* = 17.3 Hz), 3.66 (1H, m), 3.70 (3H, s), 4.21 (1H, t, *J* = 6.6 Hz), 4.38 (2H, d, *J* = 6.9 Hz), 4.85 (1H, s), 5.13 (1H, s), 7.31 (2H, t, *J* = 7.4 Hz), 7.39 (2H, t, *J* = 7.3 Hz), 7.59 (2H, d, *J* = 7.2 Hz), 7.75 (2H, d, *J* = 7.4 Hz); **¹³C NMR*** (CDCl₃, 100 MHz) δ 22.9, 28.4, 29.6, 32.8, 40.7, 47.3, 50.1, 50.7, 51.8, 52.9, 66.5, 79.2, 119.2, 125.0, 127.0, 127.7, 141.3, 144.0, 156.3, 155.9, 172.9; **MS** (ESI, MeOH) *m/z* calcd for [C₂₉H₃₉N₃O₆]: 525.28389, found 526 [M+H]⁺, 548 [M+Na]⁺.

2-(5-azidomethyluracil-1-yl)acetic acid (9.21)

The product **9.21** has been synthesized and fully characterized according to what already reported by Manicardi *et al.*^[57]

Boc-Lys(Fmoc)-PNA-(U-N₃)-OMe (9.22)

In a round bottom flask the acid **9.21** (398 mg, 1.77 mmol), EDC·HCl (338 mg, 1.77 mmol), DhBtOH (288 mg, 1.77 mmol) and DIPEA (308 μL, 1.77 mmol) were solubilized in dry DMF (5 ml) and cooled down to 0° C with an ice bath. Then **9.20** was added to the mixture, which was

stirred for 30 minutes, then warmed to RT and allowed to react overnight. The solvent was then evaporated under reduced pressure. The resulting solid was dissolved in EtOAc (250 ml), transferred in a separatory funnel and washed with saturated KHSO₄ (2 x 250 ml), saturated NaHCO₃ (2 x 250 ml) and brine (250 mL). The organic phase was dried over Na₂SO₄, the solvent removed under reduced pressure and purification was accomplished by flash chromatography (gradient elution from EtOAc/hexane 9:1 to EtOAc), to yield **9.22** (874 mg, 81%) as a yellowish foamy solid. **Rf** = 0.30 (EtOAc); **¹H NMR** (CDCl₃, 400 MHz) δ 1.35-1.1.63 (15H, m), 3.20 (2H, d, *J*= 6.5 Hz), 3.37 (2H, m), 3.49 (1H, m), 3.47 (3H, s), 4.04 (2H, m), 4.14 (1H, t, *J*= 7.0 Hz) 4.23 (2H, m), 4.40-4.89 (4H, m), 6.74 (2H, br s), 7.27 (1H, s), 7.33 (2H, t, *J*= 7.2 Hz), 7.42 (2H, t, *J*= 7.5 Hz), 7.61 (2H, d, *J*= 7.5 Hz), 7.78 (2H, d, *J*= 7.6 Hz), 9.12 (1H, s); **¹³C NMR*** (CDCl₃, 100 MHz) δ 22.8, 28.3, 29.4, 31.5, 40.2, 47.1, 47.3, 47.8, 49.3, 52.4, 53.0, 66.6, 80.0, 109.4, 120.0, 125.0, 127.1, 127.7, 141.3, 143.3, 144.0, 150.6, 156.0, 156.6, 162.7, 167.2, 169.5; **MS** (ESI, MeOH) *m/z* calcd for [C₃₆H₄₄N₈O₉]: 732,32313, found 755 [M+Na]⁺, 771 [M+K]⁺.

Boc-Lys(Fmoc)-PNA-(U-N₃)-OH (9.23)

A solution of Ba(OH)₂·8H₂O (412 mg, 1.30 mmol) in water (45 ml) was added to a solution of the ester **9.22** (863 mg, 1.18 mmol) in THF (45 ml) at 0° C. The reaction was periodically controlled with TLC until disappearing of the starting material. After 30 minutes the reaction was quenched with 1M HCl (2.7 ml), the solvent was removed under reduced pressure and the pH was adjusted to 2.5. The solution was then cooled to 4°C and aged for 2 hours; the product **9.23** (874 mg, 88%) was then collected by Büchner filtration. **Rf** = 0.35 (EtOAc:MeOH 9:1); **¹H NMR** (DMSO-d₆, 400 MHz) δ 1.35-1.1.63 (15H, m), 2.97 (2H, m), 3.2-3.6 (3H,m)[°], 3.92 (2H, m), 4.07 (2H, s), 4.21-4.30 (3H, m), 4.52-4.83 (2H, m), 6.80 (1H, d, *J*= 8.8 Hz), 7.27 (1H, br s), 7.34 (2H, t, *J*= 7.4 Hz), 7.42 (2H, t, *J*= 7.4 Hz), 7.59 (1H, s), 7.69 (2H, d, *J*= 7.3 Hz), 7.89 (2H, d, *J*= 7.6 Hz), 11.56 (1H, br s); **¹³C NMR*** (CDCl₃, 100 MHz) δ 23.3, 28.7, 29.7, 31.6, 41.2, 47.1, 47.2, 48.5, 49.2, 50.5, 51.9, 65.6, 78.3, 107.7, 120.6, 125.4, 127.5, 128.0, 141.2, 144.4, 145.9, 151.2, 156.1, 156.5, 163.9, 167.5, 170.9; **MS** (ESI, MeOH) *m/z* calcd for [C₃₅H₄₂N₈O₉]: 718,30747, found 741 [M+Na]⁺, 757 [M+K]⁺.

[°] Integral is not defined due to signal overlap with water peak.

* Overlapping ¹³C signals

PNA synthesis

The PNA chain **9.24** was synthesized following standard manual Boc-based solid-phase synthesis with HBTU/DIPEA as coupling agents, using the preformed monomer **9.23** in addition to commercially available Boc-PNA monomers on a MBHA resin loaded with Fmoc-Gly-OH as first monomer (0.2 mmol/g). After the conjugation of monomer **9.23**, washing and capping were done accordingly to Fmoc procedure, in order to preserve intact the modified unit. Once the entire sequence was synthesized, **9.25** was obtained in 1 μmol scale by reduction of the azide group according to an established solid phase Staudinger reaction using a solution $\text{H}_2\text{O}:\text{THF}:\text{trimethylphosphine}$ (1M in THF) 3:2:1 (2 x 10 min). Fmoc protective group on the lysine side chain was removed to give a second free amine function (**9.26**) using a 20% piperidine solution in DMF (8 minutes, twice). The dual-pyrene functionalized PNA **9.27** was obtained by subsequent coupling of 1-pyreneacetic acid using standard HBTU/DIPEA strategy (2.6 mg 1-pyreneacetic acid, 3.79 mg HBTU, 3.5 μl DIPEA). PNA purification was performed by RP-HPLC with UV detection at 260 nm using a semi-prep column C18 (10 μm , 7.8x300 mm, Xterra Waters), eluting with water containing 0.1% TFA (eluent A) and acetonitrile containing 0.1% TFA (eluent B); elution gradient: from 100% A to 50% B in 30 min, flow: 4 mL/min. The resulting pure PNA oligomer was dissolved in $\text{H}_2\text{O}:\text{ACN}$ 1:1 and characterized by ESI-MS, which gave positive ions consistent with the final products: m/z found (calcd) 949 (948.75) $[\text{M}+5\text{H}]^{5+}$, 791 (790,79) $[\text{M}+6\text{H}]^{6+}$, 678 (677,96) $[\text{M}+7\text{H}]^{7+}$. Quantification by UV-Vis spectroscopy (ϵ_{260} $\text{M}^{-1}\text{cm}^{-1}$ T 8600, C 6600, A 13700, G11700) gave a concentration of 71.97 μM for a 1 ml sample, corresponding to 71.9 nmol (7.2 % yield).

REFERENCES

- [1] A.A. Marti, S. Jockusch, N. Stevens, J. Ju, N.J. Turro, *Acc. Chem. Res.* **2007**, *40*, 402-409.
- [2] J. Liu, Z. Cao, Y. Lu, *Chem. Rev.* **2009**, *109*, 1948-1998.
- [3] A.Z. Wang, O.C. Farokhzad, *J. Nucl. Med.* **2014**, *55*, 353-356.
- [4] D.M. Kolpashchikov, *Chem. Rev.* **2010**, *110*, 4709-4723.
- [5] B. Juskowiak, *Anal. Bioanal. Chem.* **2011**, *399*, 3157-3176.
- [6] S. Singh, A. Koshkin, *Chem. Commun.* **1998**, *4*, 455-456.
- [7] M. Petersen, C.B. Nielsen, K.E. Nielsen, G.A. Jensen, K. Bondensgaard, S.K. Singh, *et al. J. Mol. Recognit.* **2000**, *13*, 44-53.
- [8] V.V. Demidov, *Trends Biotechnol.* **2003**, *21*, 4-7.
- [9] N. Svanvik, G. Westman, D. Wang, M. Kubista, *Anal. Biochem.* **2000**, *28*, 26-35.
- [10] W.P. Kloosterman, E. Wienholds, E. de Bruijn, S. Kauppinen, R.H. Plasterk, *Nat. Methods* **2005**, *3*, 27-29.
- [11] Y. Kam, A. Rubinstein, A. Nissan, D. Halle, E. Yavin, *Mol. Pharm.* **2012**, *9*, 685-693.

- [12] S. Kummer, A. Knoll, E. Socher, L. Bethge, A. Herrmann, O. Seitz, *Bioconjugate Chem.* **2012**, *23*, 2051-2060.
- [13] I.E. Catrina, S.A. Marras, D.P. Bratu, *ACS Chem. Biol.* **2012**, *7*, 1586-1595.
- [14] A. Bertucci, A. Manicardi, R. Corradini in *Detection of non-amplified Genomic DNA* (Eds. G. Spoto, R. Corradini) Springer, Dordrecht, The Netherlands, **2012**, 89-124.
- [15] S. Sueda, T. Ihara, B. Juskowiak, M. Takagi, *Anal. Chim. Acta* **1998**, *365*, 27-34.
- [16] J.R. Lakowicz, C.D. Geddes, Eds. *Topics in fluorescence spectroscopy* **1991**, New York: Plenum press.
- [17] H. Huang, A.A. Martí, *Anal. Bioanal. Chem.* **2012**, *402*, 3091-3102.
- [18] R.M. Clegg, *Meth. Enzymol.* **1992**, *211*, 353-388.
- [19] J.R. Lakowicz, *Principles of fluorescence spectroscopy*, **2006**, 3rd edn. Springer, New York
- [20] H. Abe, E.T. Kool, *Proc. Nat. Ac. Sci. USA* **2006**, *103*, 263-268.
- [21] D. Zhou, L. Ying, X. Hong, E.A. Hall, C. Abell, D. Klenerman, *Langmuir* **2008**, *24*, 1659-1664.
- [22] J. Jung, L. Chen, S. Lee, S. Kim, G.H. Seong, J. Choo, *et al. Anal. Bioanal. Chem.* **2007**, *387*, 2609-2615.
- [23] C. Xu, R. Zhou, R. Zhang, L. Yang, G. Wang, *ACS Macro Lett.* **2014**, *3*, 845-848.
- [24] P. Jothikumar, V. Hill, J. Narayanan, *Biotechniques* **2009**, *46*, 519.
- [25] F.M. Winnik, *Chem. Rev.* **1993**, *93*, 587-614.
- [26] M. Kosuge, M. Kubota, A. Ono, *Tetrahedron Lett.* **2004**, *45*, 3945-3947.
- [27] A. Okamoto, T. Ichiba, I. Saito, *J. Am. Chem. Soc.* **2004**, *126*, 8364-8365.
- [28] J. Huang, Y. Wu, Y. Chen, Z. Zhu, X. Yang, C.J. Yang, *et al. Angew. Chem. Int. Ed.* **2011**, *50*, 401-404.
- [29] R. Häner, S.M. Biner, S.M. Langenegger, T. Meng, V.L. Malinovskii, *Angew. Chem. Int. Ed.* **2010**, *49*, 1227-1230.
- [30] Z. Qing, X. He, J. Huang, K. Wang, Z. Zou, T. Qing, *et al. Anal. Chem.* **2014**, *86*, 4934-4939.
- [31] N. Svanvik, A. Stahlberg, U. Sehlstedt, R. Sjoback, M. Kubista, *Anal. Biochem.* **2000**, *287*, 179-182.
- [32] O. Köhler, O. Seitz, *Chem. Commun.* **2003**, *23*, 2938-2939.
- [33] N. Svanvik, J. Nygren, G. Westman, M. Kubista, *J. Am. Chem. Soc.* **2001**, *123*, 803-809.
- [34] P. Wolffs, R. Knutsson, R. Sjöback, P. Rådström, *Biotechniques* **2001**, *31*, 766-769.
- [35] A. Tonelli, T. Tedeschi, A. Germini, S. Sforza, R. Corradini, M.C. Medici, *et al. Mol. BioSystems* **2011**, *7*, 1684-1692.
- [36] Y. Kam, A. Rubinstein, S. Naik, I. Djavsarov, D. Halle, I. Ariel, *et al. Cancer Lett.* **2014**, *352*, 90-96.
- [37] J. Isacson, H. Cao, L. Ohlsson, S. Nordgren, N. Svanvik, G. Westman, M. Kubista, R. Sjoback, U. Sehlstedt, *Mol. Cell Probes* **2000**, *14*, 321-328.
- [38] H. Kuhn, V.V. Demidov, J.M. Coull, M.J. Fiandaca, B.D. Gildea, M.D. Frank-Kamenetskii, *J. Am. Chem. Soc.* **2002**, *124*, 1097-1103.
- [39] F. Totsingan, S. Rossi, R. Corradini, T. Tedeschi, S. Sforza, A. Juris, E. Scaravelli, R. Marchelli. *Org. Biomol. Chem.* **2008**, *6*, 1232 – 1237.
- [40] L.M. Zanolli, M. Licciardello, R. D'Agata, C. Lantano, A. Calabretta, R. Corradini, *et al. Anal. Bioanal. Chem.* **2013**, *405*, 615-624.
- [41] F. Totsingan, T. Tedeschi, S. Sforza, R. Corradini, R. Marchelli, *Chirality* **2009**, *21*, 245-253.
- [42] B.S. Gaylord, A.J. Heeger, G.C. Bazan, *Proc. Nat. Ac. Sci USA* **2002**, *99*, 10954-10957.
- [43] A. Karadag, M. Riminucci, P. Bianco, N. Cherman, S.A. Kuznetsov, N. Nguyen, *et al. Nucleic Acids Res.* **2004**, *32*, e63.
- [44] Z. Wang, K. Zhang, Y. Shen, J. Smith, S. Bloch, S. Achilefu, *et al. Org. Biomol. Chem.* **2013**, *11*, 3159-3167.
- [45] A. Manicardi, L. Guidi, A. Ghidini, R. Corradini, *Beilstein J. Org. Chem.* **2014**, *10*, 1495-1503.

- [46] T. Tedeschi, A. Tonelli, S. Sforza, R. Corradini, R. Marchelli, *Artif. DNA, PNA & XNA* **2010**, *1*, 83-89.
- [47] N. Maneelun, T. Vilaivan, *Tetrahedron* **2013**, *69*, 10805-10810.
- [48] V. Menchise, G. De Simone, T. Tedeschi, R. Corradini, S., Sforza, R. Marchelli, D. Capasso, M. Saviano, C. Pedone, *Proc. Nat. Acad. Sci.* **2003**, *100*, 12021-12026.
- [49] R.H.E. Hudson, X. Liu, F. Wojciechowski, *Can. J. Chem.* **2007**, *85*, 302-312.
- [50] S. Sforza, T. Tedeschi, R. Corradini, R. Marchelli, *Eur. J. Org. Chem.* **2007**, 5879-5885.
- [51] E.A. Englund, D.H. Appella, *Angew. Chem. Int. Ed.* **2007**, *46*, 1414-1418.
- [52] S. Rapireddy, G. He, S. Roy, B.A. Armitage, D.H. Ly, *J. Am. Chem. Soc.* **2007**, *129*, 15596-15600.
- [53] M. Mentzel, H.M.R. Hoffmann, *J. Prak. Chem-Chem. Ztg.* **1997**, *339*, 517-524.
- [54] D.A. Evans, L. Kværnø, T.B. Dunn, A. Beauchemin, B. Raymer, J.A. Mulder *et al.* *J. Am. Chem. Soc.* **2008**, *130*, 16295-16309.
- [55] H. Hu, J. Goon Ho, R.C. Sung, N.K. Su, T.K. Yong, S.P. Hwang, K.K. Sung, *et al.* *Arch. Pharm. Res.* **2012**, *35*, 517-522.
- [56] Y. Zheng, A. Hashidzume, Y. Takashima, H. Yamaguchi, A. Harada, *Nat. Commun.* **2012**, *3*, 831.
- [57] A. Manicardi, A. Accetta, T. Tedeschi, S. Sforza, R. Marchelli, R. Corradini, *Artif. DNA PNA XNA* **2012**, *3*, 53-62.

10

Instrumental techniques

Abstract

This chapter gives a short general overview on the most important instrumental methods used throughout this thesis. The corresponding experimental details can be found in the dedicated section of each Chapter. Basic spectroscopic (such as UV-Vis, IR, and NMR) techniques are not here discussed.

10.1. Scanning electron microscopy (SEM)

The SEM is a type of microscope that uses electrons to create high resolved images of the sample. Since their development in the early 1950's, scanning electron microscopes have developed new areas of study in the medical and physical science communities.^[1] The SEM uses a focused beam of high-energy electrons to generate a range of signals at the surface of solid specimens. The signals that come from electron-sample interactions give especially information about the external morphology of the sample and its chemical composition. In most applications, data are collected over a selected area of the surface of the specimen, and a 2-dimensional image is generated that displays spatial variations in the sample properties with respect to the interaction with the electron beam. Areas ranging from approximately 1 cm to few microns in width can be imaged in a scanning mode using conventional SEM techniques, having magnification up to more than 500000x and resolution of few nanometers. The SEM is also capable of performing analyses of selected point locations on the sample; this approach is especially useful in qualitatively or semi-quantitatively analysis in determining the chemical composition of the surface (EDX mode).

When speaking about the fundamental principles of SEM, accelerated electrons in an SEM carry significant amounts of kinetic energy, and this energy is dissipated as a variety of signals produced by electron-sample interactions when the incident electrons are decelerated in the solid sample. The electron beam is generated at the electron source, which is placed at the top of the electron column. Two types of electron sources are generally used in SEM-instruments, i.e. Thermoionic-Sources and Field-Emission-Sources. Thermoionic-Sources are based on a thin conductive wire (usually tungsten), which is heated to temperatures where the energy of the weakest bounded electrons exceeds the work function of the material, thus allowing for the electron emission. Field-Emission-

Sources use high electric fields between a cathode and an anode, in a way that if the applied electric field is big enough, the work function of the cathode dramatically decreases and electron emission is possible even at room temperature.

In any case, an anode is then placed right under the source to provide the acceleration of the electrons down the column, whose voltage can be modulated by the user between +1 and +50 kV.

A defined electron beam is then created by means of several condenser lenses, which cause a repulsive electric field and a condensation of the electrons, focusing them on the following aperture. After passing through the condenser lens, the beam is divergent and must be refocused on the sample. This is done by means of the focusing lens, which are located just above the sample.

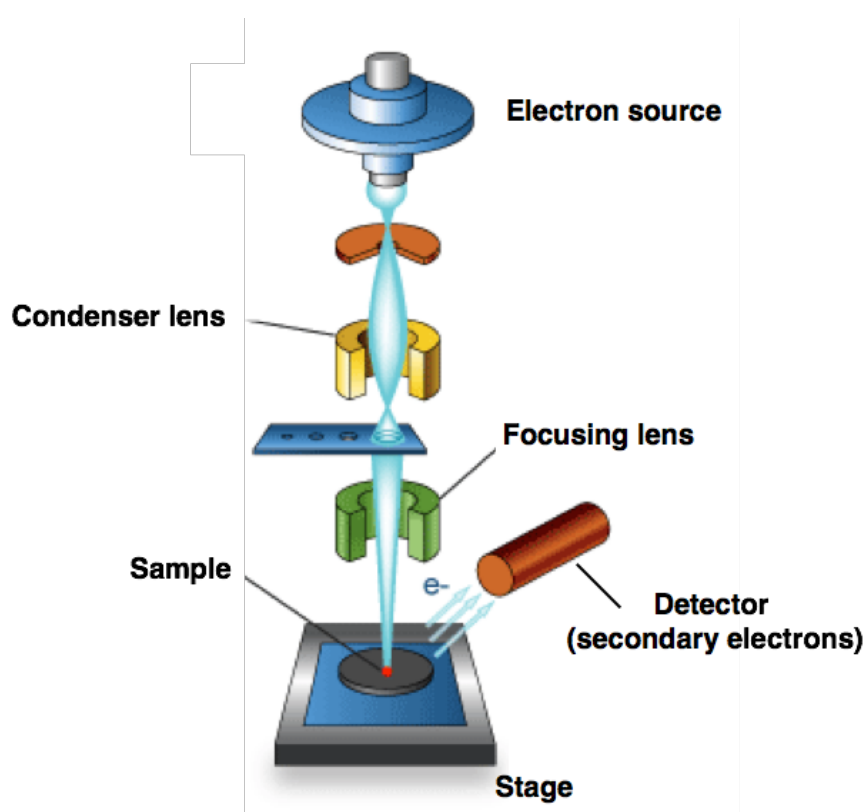


Fig 10.1 Schematic draw showing the components of a SEM instrument.

Upon interaction of the electron beam with the sample, diverse signal can be recorded. These signals include secondary electrons which are used to produce the typical SEM image, backscattered electrons (also used for imaging purposes), diffracted backscattered electrons (that can be used to gain information on the crystal structures and orientations of minerals), X-ray photons that are used for elemental analysis, and heat. The Secondary electrons are commonly used for imaging samples since are the most valuable for showing morphology and topography. Secondary electrons originate when the incident electron beam excites an electron in the sample,

which then migrates to the surfaces and escapes from the sample, depending on its energy. Due to the very low energy, only secondary electrons near the surface can leave the sample and produce the output signal. The Volume in which secondary electrons are produced is relatively small, which leads to a high axial resolution (a few nm). The final image is thus a map of the secondary electron density depending on the properties of the sample.

X-ray generation is instead produced when the excited electrons of specific orbitals return to lower energy states, yielding X photons that are of a fixed wavelength related to the difference in electronic energy levels for a given element. Thus, characteristic X-rays are produced for each element, allowing for a chemical composition mapping of the sample surface.

10.2 Transmission electron microscopy (TEM)

Transmission electron microscopy is used to produce images from a specimen by illuminating the sample with high energetic electrons within a high vacuum, and detecting the electrons that are transmitted through the sample. The word “transmission” means that, in TEM configuration, the electron beam is directly pointed towards the detector, with the sample being placed in between the electron source and detector itself. The electrons that pass through the sample without being scattered then cause bright areas in the image, while the sample regions that stop or hamper the electron beam give rise to darker spots. The range of final greys visualized in the image thus depends on the way the electrons interact with and are scattered by the sample.^[2]

TEM offers the advantage of pushing the limit of resolution down to 50 pm, with possible magnification in the order of 10000000x, making it possible to work at the atomic level.

A schematically view of the electron path in a TEM instrument is shown in figure 10.2

The electron source works similarly to those used for SEM, but TEM uses significantly higher accelerating voltages, typically between 80 kV and 400 kV (depending on the application and on sample nature).

The condenser lens is then located before the object and plays the role of forming the beam. The main purpose of the condenser lens is to focus the light onto the sample, also controlling the diameter of the electron beam. For lower magnification the beam is spread onto the object to illuminate a larger area, whereas, when high magnification is desired, the beam is strongly condensed onto the object.

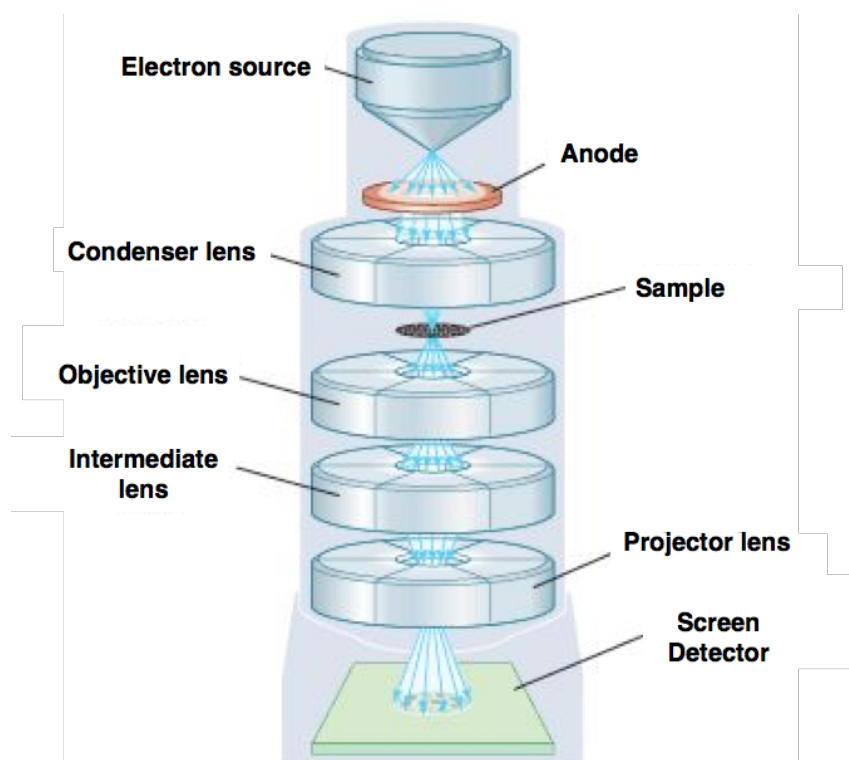


Figure 10.2 Schematic draw showing the components of a TEM instrument.

Once the electron beam passes through the specimen, it reaches the objective lens, which generates the first intermediate image of the sample, the quality of which determines the resolution of the final image. The intermediate image is an inverted initial one, which then is subsequently magnified by the intermediate lens, and produces a second intermediate image. This second intermediate image is collected by the projector lens, which forms the final image onto a fluorescent screen or a recording device.

10.3 Dynamic light scattering (DLS)

Dynamic light scattering (DLS), also called photon correlation spectroscopy, is a widespread technique used to determine the size of particles in dispersion. Particles suspended in liquids are in Brownian motion due to random collisions with solvent molecules. This motion causes the particles to diffuse through the medium. The diffusion coefficient, D , is inversely proportional to the particle size according to the Stokes-Einstein equation:

$$D = \frac{k_B T}{3\pi\eta_0 d}$$

D : diffusion coefficient; k_B : Boltzmann's constant; T : absolute temperature; η_0 : viscosity; d : hydrodynamic diameter.

This equation shows that, for large particles, D will be relatively small, and, thus, the particles will move slowly, while for smaller particles, D will be larger and the particles will move more rapidly. Therefore, by observing the motion and determining the diffusion coefficient of particles in liquid media, it is possible to determine their size.

When a laser light is focused onto the particles, light is scattered in all directions. The scattered light that is observed comes from a collection of scattering elements, so that the observed intensity of the scattered light at any instant is a result of the interference of light scattered by each element. Hence, it will depend on the relative positions of the elements. If the particles are in motion, the relative positions of particles will change in time; and thus, fluctuations in time of the scattered light intensity will be observed. Because particles in Brownian motion move about randomly, the scattered intensity fluctuations are random. The intensity fluctuates faster for smaller particles and slower for bigger particles. The fluctuations of the scattered light are analyzed using the autocorrelation function (ACF).

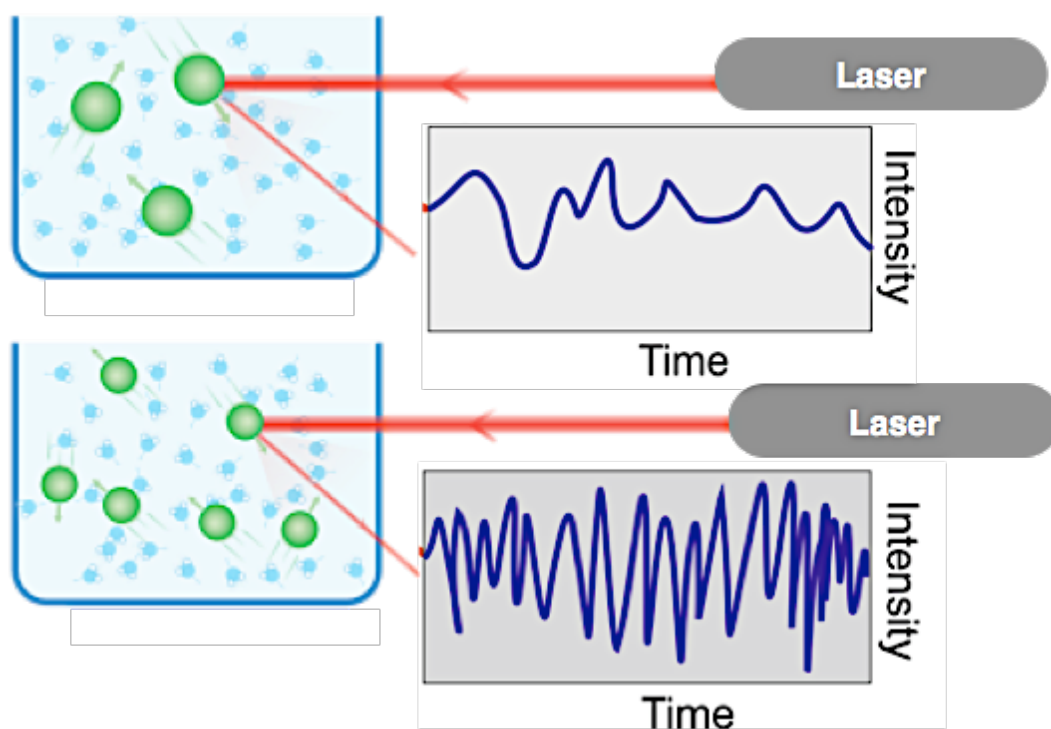


Figure 10.3. Representation of the random intensity fluctuations of the scattered laser obtained from a dispersion of bigger particles (top) and smaller particles (bottom).

The ACF is a function that decays as a function of delay time. For small particles with rapid motion and rapid intensity fluctuations, the autocorrelation function is a rapidly decaying exponential function with a large decay constant, while for large particles the exponential decays more slowly with a smaller decay constant. The ACF is then used to calculate the diffusion coefficient and

therefore the size of the particles. The particle size is eventually given in the form of a statistical distribution sorted by scattering intensity, volume or number of particles. The directly measured (and thus more reliable) parameter is always the intensity distribution, while the volume and the number distributions are subsequently calculated via software from the intensity distribution by using Mie theory. The intensity distribution is thus the general and most common way used to show DLS data.

10.4 Zeta potential

Most particles dispersed in a liquid have positive or negative surface charge. In a liquid, the ions that have opposite charge to the particle surface gather close to the particle to keep an electric neutrality. Thus, ionized layers with opposite charge tend to surround the surface of a particle. The concentration of the counter ions will be high in the area near the particle's surface and will gradually decrease with distance from the surface. Equal numbers of positive and negative ions exist in the area far from the particle's surface so that electric neutrality is maintained. This ion distribution is called a “diffuse electrical double layer.” The diffuse electrical double layer can be divided into two main layers:

- the layer of ions close the particle surface is called the “Stern layer.” The ions in the Stern layer are strongly attracted to the surface of the particle;
- the layer outside the Stern layer is called the diffuse layer. In this layer, the ions are diffused.

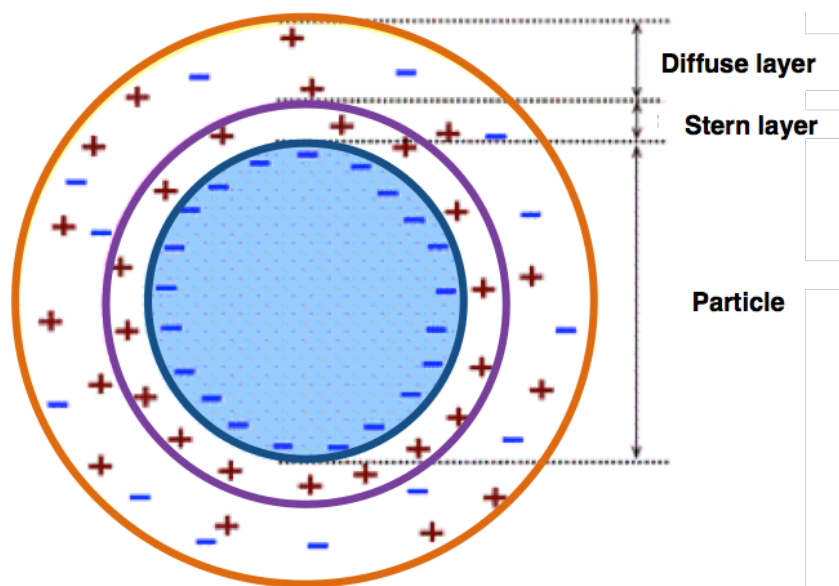


Figure 10.4 Stern and Diffusive layer surrounding a particle dispersed in a medium.

When the particles undergo Brownian motion in a medium, they move together with the Stern layer

and a part of the diffused layer. The interface between moving and non-moving ions in the diffused layer is called the slipping plane. The zeta potential is then defined as the potential at the slipping plane versus a point far away from the particle. If zeta potential is high, the particles are stable due to high electrostatic repulsion between them. On the contrary, a low zeta potential value (approaching zero) increases the probability of particles colliding; therefore, forming particle aggregates. Thus, zeta potential is generally used as an index of the dispersion stability of particles, i.e. how much they tend to aggregate in the medium. Indeed, the zeta potential allows also for studying the changes in the net surface particle charge upon functionalization or modification.

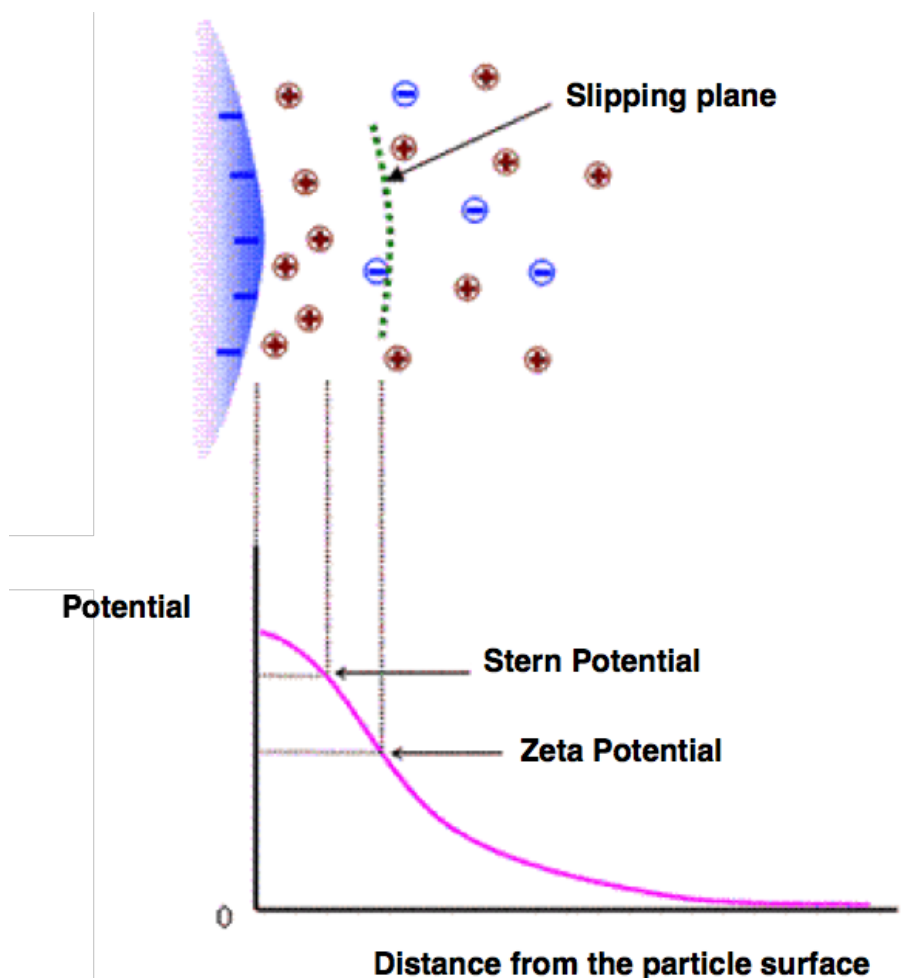


Figure 10.5 Concept of zeta potential

When an electric field is applied to a dispersion of surface charged particles, these are moving towards the oppositely charged electrode. The velocity the particles are moving with is proportional to the surface charge, and the zeta potential can be therefore determined by measuring the speed of particles in an electric field. Electrophoretic light scattering is the method most generally used to determine the speed of the particles. To do this, the particles are irradiated with a laser light, and the

scattered light emitted from the particles is detected. Because the frequency of the scattered light is shifted from the incident light in proportion to the speed of the particles movement, the electrophoretic mobility of the particles can be measured from the frequency shift of the scattered light. This method is based on the Doppler effect; therefore, it is also called the “Laser Doppler Method.”

The frequency shift v_D is related to the mobility of particles, U :

$$v_D = \frac{Uq}{2\pi} \cos \frac{\theta}{2} = \frac{Un}{\lambda} \sin \theta$$

where q is the scattering vector ($q=4\pi n \sin(\theta/2)/\lambda$); λ is the wavelength; n is the refractive index of the medium, and θ is the scattering angle.

The zeta potential measurement is then performed in a glass cell resembling the electrophoresis scheme; thus, it is worth noticing that the movement of the particles is directed by the electroosmotic flow occurring in the measure cell, and the typical parabolic profile of the final flow, which is the sum of the electroosmotic one and the particle true mobility, is expected and taken as a good indicator of reliability of the measurement.

10.5 Confocal Microscopy

Confocal microscopy offers many advantages over conventional optical epifluorescence microscopy, including the ability to control depth of field, elimination or reduction of background information away from the focal plane, and the capability to collect serial optical sections from thick sample. The basic key to the confocal strategy is the use of spatial filtering techniques to eliminate out-of-focus light.

The confocal principle in fluorescence laser scanning microscopy is schematically shown in Figure 10.6. Coherent light emitted by the laser system (excitation source) passes through an excitation pinhole aperture that is placed in a conjugate plane (confocal) with a scanning point on the specimen and a second pinhole aperture located in front of the detector. When the laser is reflected by a dichromatic mirror and scanned across the specimen in a defined focal plane through the objective, secondary fluorescence emitted from points on the sample (in the same focal plane) pass back through the dichromatic mirror and are focused as a confocal point at the detector pinhole aperture.

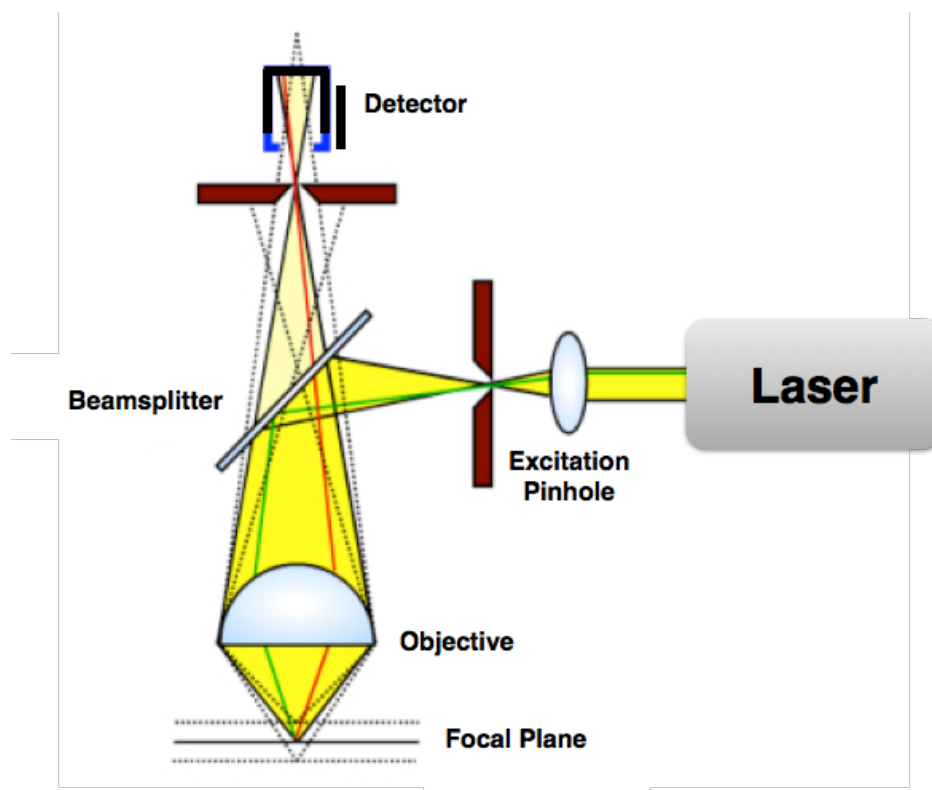


Figure 10.6 Schematic picture showing the principle of confocal microscopy.

The amount of fluorescence emission that occurs at points above and below the objective focal plane is not confocal with the pinhole. Since only a small fraction of the out-of-focus fluorescence emission is delivered through the pinhole aperture, most of this extraneous light is not detected by the photomultiplier and does not contribute to the resulting image. The dichromatic mirror, barrier filter, and excitation filter perform similar functions to the analog components in an epifluorescence microscope. Refocusing the objective in a confocal microscope shifts the excitation and emission points on a specimen to a new plane that becomes confocal with the pinhole apertures of the light source and detector.

In traditional fluorescence microscopy, the entire sample is exposed to intense illumination from the source lamp, and the resulting image of secondary fluorescence emission is generally projected onto the surface of an electronic array detector. In contrast, the mechanism of image formation in a confocal microscope is essentially different. The confocal fluorescence microscope consists of multiple laser excitation sources, a scan head with optical and electronic components, electronic detectors (usually photomultipliers), and a computer for acquisition, processing, analysis, and display of images. These properties actually allow the user to record 3D-images using different combinations of excitation and emission wavelengths as long as the emission spectra of the diverse species do not completely overlap, which is a key tool when analyzing bio-samples that require the use of multiple labels.

10.6 Electrospray-Mass Spectrometry (ESI-MS)

The ESI (electrospray ionization) source belongs to the category of API (atmospheric pressure ionization) ion sources, which ionize the sample at atmospheric pressure and then transfer the ions into the mass analyzer. The first work that recognized the possibility to generate gas-phase ions from macromolecules by formation of a spray at the exit of an electrically charged capillary was delivered by Dole in 1968^[3]; however, the worldwide success of the ESI source began when Fenn and his collaborators developed the electrospray ionization technique, proposing it as a real interface for mass spectrometry^[4], and then showing the possibility of obtaining multiply charged ions from biological macromolecules.^[5] Fenn was awarded the Nobel Prize for Chemistry in 2002. The ESI process is nowadays among the key methods for the analysis of macromolecules and biopolymers through the determination of the molecular weight. In particular, it is worth noticing that the ESI source, in addition to provide a soft ionization of the selected species, is able to distribute on the molecule, if this is suitable, a very high number of charges. Mass spectrometry measures the mass/charge ratio (m/z) of the ions: this means that an ion of mass 10000 Da displaying 10 charges will be detected at m/z 1000. This is extremely important since allows the detection of high molecular weight molecules such as peptides, proteins, oligonucleotides, even in the case of analyzers with low limits of nominal mass, through an extension of the effective range. ESI is produced by applying a strong electric field, under atmospheric pressure, to a liquid passing through a capillary tube with a weak flow. The electric field is obtained by inducing a potential difference of 3-6 kV between this capillary and the counter electrode; this induces a charge accumulation at the liquid surface located at the end of the capillary, which breaks to form highly charged droplets.

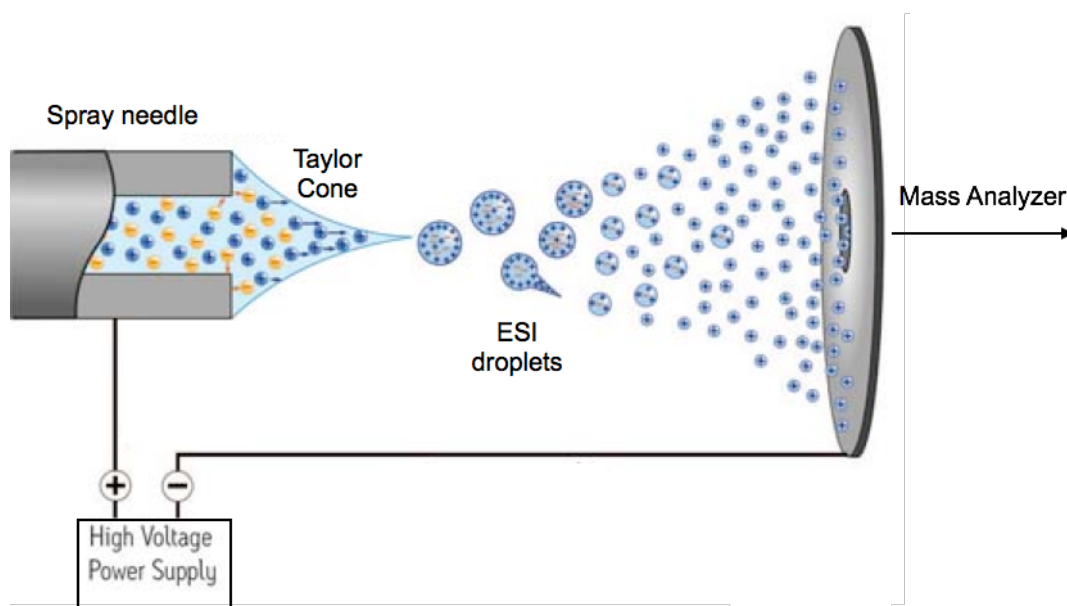


Figure 10.7 Schematic diagram of ESI source.

Under the pressure of the accumulating charges at the tip of the needle, the nascent drop tends to elongate till the surface tension is broken and the shape of the profile changes to the so-called “Taylor cone”, with the appearance of the spray. A gas injected coaxially at a low flow rate helps the dispersion of the spray to be limited in space. The droplets then pass through a heated capillary transfer to remove the last solvent molecules, producing the gas phase ions that will be guided to the mass analyzer. A fair range of possible mass analyzers can be found in modern instruments depending on the users’ needs, the most common being single and triple quadrupoles, ion traps, time-of-flight (TOF) analyzers, and advanced combination of these. A particular and very recently developed mass analyzer, the electrostatic trap “Orbitrap”, will be described in the next paragraph. Working at atmospheric pressure and being able to ionize liquid sample, ESI source also represents the keystone that makes it possible to interface a liquid chromatography system with mass spectrometry (LC-MS), thus allowing for introducing a separation technique at the early stage. This indeed plays a crucial role offering the possibility to analyze complex mixtures by separating the different composing species, and then to identify and to characterize each of them by recording the mass spectrum, offering excellent sensitivity and selectivity.

10.7 Electrostatic Trap “Orbitrap”

The Orbitrap is an electrostatic ion trap that uses the Fourier transform to convert the acquired signals into the mass spectra. This analyzer is based on a completely new concept, proposed by Aleksandr Makarov and described in details first in patents^[6] and then in a famous article published on *Analytical Chemistry*.^[7] The first commercial instrument was launched by Thermo Electron Corporation in June 2005.

The outer part of the analyzer consists of an electrode having the shape of a barrel, within which is located a second electrode shaped as a spindle. The maximum diameter of the central electrode is 8 mm and of the outer one 20 mm. In this central zone, for positive ions, is applied a negative voltage of several kiloVolts, while the outer electrode is at ground potential. The ions are injected into the trap through a narrow cut on the outer electrode, being perpendicular to the direction of the main axis (z-axis). Once inside the trap, the ions begin to oscillate around the spindle following intricate spirals, under the influence of an electrostatic field with a peculiar distribution of potential, obtained by DC voltage and the unique geometry of the trap.

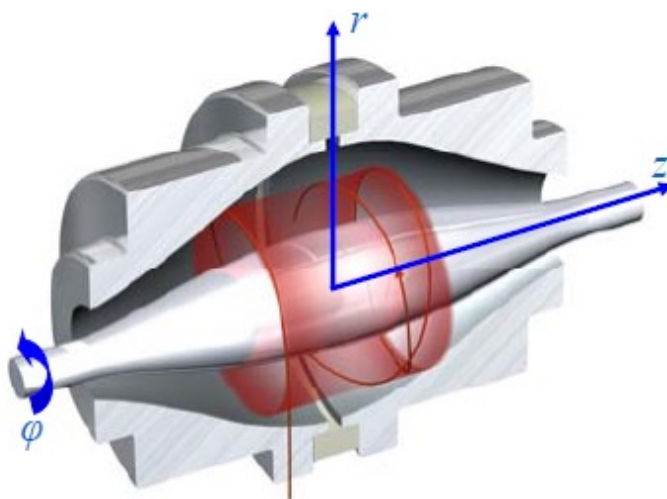


Figure 10.8 Pictorial section view of an Orbitrap. The spiral trajectory of an ion spinning around the central spindle is highlighted in red.

The trajectory inside the trap is rationalized with the motion of an ion such as that of a ring (generated by the rotation around the spindle) which moves back and forth along the z axis, almost equal to a pendulum. The frequency of the harmonic oscillation is directly related to the ratio m/z and it is independent from the kinetic energy of the incoming ion. The induced current caused by the oscillation of the ions is then measured and converted by means of a Fourier transform in the individual frequencies and intensities, leading to the generation of the mass spectrum.

The Orbitrap has extremely high mass accuracy (1-2 ppm) and resolution ($R = 100000$, according to the definition FWHM with m/z 1000), taking into account, however, that the latter is inversely to the square root of the ratio m/z .

A possible geometry of the whole instrument available on the market is shown in Figure 10.9.

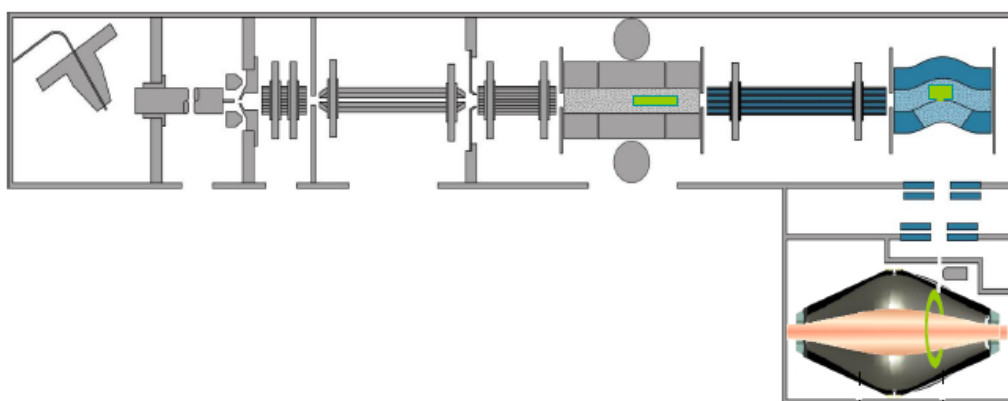


Figure 10.9 Scheme of a LTQ Orbitrap instrument (Thermo Electron Corporation).

After the ion source, a series of focus lenses and quadrupoles guide the ions through the core of the instrument, then a linear ion trap is used as first mass analyzer, allowing for selection of specific ions to analyze or performing MSⁿ experiments. A second trap, called "C-trap", is then placed just before of the Orbitrap, and serves to accumulate ions and to control the direct injection into the Orbitrap, in which, finally, the HR-MS measurement will take place.

REFERENCES

- [1] J.J. Bozzola, L.D. Russell, *Electron microscopy: principles and techniques for biologists*, **1999** Jones & Bartlett Learning.
- [2] D.B. Williams, C.B. Carter, *The Transmission Electron Microscope* **1996**, Springer Us.
- [3] M. Dole, L.L. Mack, R.L. Hines, R.C. Mobley, L.D. Ferguson, M.B. Alice, *J. Chem. Phys.* **1968**, *49*, 2240.
- [4] C.M. Whitehouse, R.N. Dreyer, M. Yamashita, J.B. Fenn, *Anal. Chem.* **1985**, *57*, 675–679.
- [5] J.B. Fenn, M. Mann, C.K. Meng, *Science*, **1989**, *246*, 64
- [6] A. Makarov, Mass spectrometer, **1999**, US Patent, 5886346
- [7] A. Makarov, *Anal. Chem.* **2000**, *72*, 1156-1162.

11

Summary

The general aim of this thesis titled “Hybrid organic-inorganic interfaces for biomedical applications” is the synthesis, functionalization and implementation of different kinds of hybrid nanostructured materials and devices for applications in nanomedicine and diagnostics.

The thesis unfolds through 10 chapters describing each a different aspect of the research work.

Chapter 1 starts with giving a general overview about the main themes and subjects the whole work refers to. Hence, nanotechnology and its applications to the medical field are firstly presented, highlighting the crucial role nanomaterials play in the development of novel fundamental tools. The concept of using nanocontainers in biomedicine is pointed out. In the following, general concepts about the realization of hybrid bioorganic-inorganic advanced architectures are given. A special focus is then dedicated to Zeolite-L and Mesoporous silica nanoparticles (MSNPs), these being the porous materials used in this thesis. Peptide Nucleic Acid (PNA) is then introduced as one of the key elements applied for the development of some of the hybrid systems proposed. Related to this, an overview on the state of the art of nucleic acid detection techniques is eventually reported, pointing out currently available technology and new challenges.

Chapter 2 presents the preparation of the essential tools used in this thesis. At first, zeolite-L synthesis, guest molecule loading, and surface functionalization are described, together with the strategies available for the characterization of the material. The analog information is reported for the case of MSNPs, giving details on the synthesis, characterization, surface modification, and cargo loading. A brief overview about the chemistry the synthesis of PNA is based on is then presented, highlighting the most common synthetic strategies and the characterization procedures.

Chapter 3 opens the section dedicated to the realization of tailored hybrid nanomaterials. It describes the use of zeolite-L as a multifunctional DNA and drug release systems in live cells. After an introduction unfolding the zeolite-L structure, functionalization, and assembly into functional

materials, it is shown that DNA functionalized zeolites can be effectively used to transfect cells with foreign genetic material, combining the release of guest organic molecules. The double delivery of DNA and a model drug (DAPI) in HeLa cells is demonstrated; the particle uptake and the intracellular release kinetics of the DNA and DAPI are investigated in details. Eventually, it is shown that the particles are localized in the lysosomes, while the detached DNA is found collected by the mitochondria.

Chapter 4 discusses the use of zeolite-L nanocrystals for an efficient PNA delivery into living cells. Being the PNA rather cell membrane impermeable, the linkage of probes to an inorganic nanocarrier is pointed out as a possible strategy to perform an efficient cellular internalization. It is shown that high amounts of PNAs can be internalized into live cells by covalently binding them to the zeolite surface forming a hybrid concrete and coating the particles with a thin layer of biodegradable poly-L-lysine. Furthermore the pore system can be filled with a model drug, which is then released from the crystals after cell uptake. A variation of the general concept is achieved using cationic PNAs coupled to the zeolites, which do not require the use of poly-L-lysine to enhance the cellular uptake. Preliminary results about the possibility of creating a stimulus responsive PNA-gated system targeting selected microRNAs are eventually reported.

Chapter 5 deals with another strategy implemented in the field of nanomedicine, involving the use of mesoporous silica nanoparticles (MSNPs) as multifunctional carriers for the treatment of glioblastoma. Fluorescent MSNPs are synthesized and then functionalized in such a way to host a specific chemotherapy agent as a payload, temozolomide, and to adsorb cationic PNA probes on the surface. These probes are designed to target miR-221, which is overexpressed in this cancer form and related to the tumor proliferation and its resistance to temozolomide treatment. Biological test carried out on Human glioma T98G cells demonstrate the anti-miR activity displayed by the released PNA and the overall enhanced effect of induction of apoptosis provided by the multifunctional system, suggesting the synergistic therapeutic benefit achieved by the combination of gene therapy and sustainable drug administration.

Chapter 6 presents a breakthrough in the field of protein delivery, facing the hurdles and the challenges of conceiving a proper system to efficiently protect and deliver fragile biomacromolecules. Diverse proteins and enzymes are encapsulated within a hybrid biodegradable

organo-silica shell, allowing for the fabrication of advanced structured core/shell nanoparticles. The presence of disulfide bridges embedded in the silica network let the degradation of the shell possible when in presence of reducing agents, as the one also available in the cell cytoplasm. Deep studies on the breaking/release phenomenon are especially presented using Cytochrome C as model protein cargo, then the enzymatic activity of the released species is investigated through the use of high cytotoxic proteins as TRAIL APO2 ligand or Onconase. Live cell distribution experiments are eventually described by means of encapsulated GFP, which allows for tracking and studying the systems inside the cells.

Chapter 7 moves to the section of thesis dedicated to ultra-sensitive nucleic acid detection, in which the concept of making hybrid bioorganic-inorganic interfaces is exploited for generating advanced analytical devices and biosensors. A novel biophotonics approach based on PNA-functionalized microstructured optical fibers for the analysis of specific DNA target sequences is presented. Photonic crystal fibers (PCF) are unique optical platforms characterized by an array of holes running along the whole length of the fiber. The inner surface of a PCF, where a Bragg grating has been additionally inscribed, is functionalized by covalently linking PNA probes targeting a DNA sequence containing the single point mutation W1282X related to cystic fibrosis disease. In order to achieve a final enhanced optical signal, oligonucleotide-functionalized gold nanoparticles are used following a sandwich-like detection scheme, which allows for the amplification of the optical signal. Experimental measurements show a clear shift of the reflected high order mode of the Bragg grating for a 100 nM DNA solution with good reproducibility. The use of a single-mismatched DNA solution, corresponding to the wild-type gene, proves the high selectivity of the sensor, whose format may be suitable for diverse sensing applications.

Chapter 8 gives an additional and further account on the implementation of the same PCF technology in view of performing ultra-sensitive PCR-free detection of genomic DNA, targeting a gene tract of the genetically modified Roundup Ready soy. Large mode area (LMA-10) photonic crystal fibers are functionalized with PNA probes and used as optofluidic devices for the detection of DNA by measuring the wavelength shift of the reflected light in the IR region upon the hybridization event. Enhancement of optical read-out is obtained using streptavidin coated gold-nanoparticles interacting with the genomic DNA captured in the fiber channels (0%, 0.1%, 1% and 10% RR-Soy). Statistical analysis proves the achievement of significant, label-free, and

amplification-free detection of target DNA in ultra-low concentrations, low percentages, and with very low sample consumption. Computer simulations of the fiber optics based on the finite element method (FEM) reveal the formation of a multi-layer of DNA and nanoparticles, which gives the enhanced sensitivity of the technique.

Chapter 9 shifts the concept of targeted nucleic acid detection from the device level to a molecular one, giving an example of synthetic organic chemistry applied to the realization of self-reporting molecular probes for diagnostics purposes. The excellent hybridization properties combined with high chemical and biological stability indeed point out PNA oligomers as suitable scaffolds to be tailored modified in view of producing specific probes. The PNA skeleton serves as a platform for the design of a switching probe able to perform nucleic acid recognition and detection, exploiting the introduction of two pyrene groups onto the same monomer unit, giving a novel clamping-like geometry. The detection scheme is thus based on the pyrene excimer-monomer switching mechanism, triggered by the hybridization of the probe with the target sequence. The final anti-miR 221 PNA switching probe is totally synthesized on solid phase and fluorescence spectroscopy experiments show the system gives the desired performances upon recognition of the target, making it a suitable and efficient tool for specific nucleic acid detection.

Chapter 10 summarizes the main instrumental techniques used throughout this thesis. A special focus is given to microscopy techniques (SEM, TEM, Confocal Microscopy), dynamic light scattering (DLS) and zeta potential, and mass spectrometry (ESI-MS).

ACKNOWLEDGMENTS

I wish to begin this acknowledgment section thanking Prof. Roberto Corradini for giving me the unique opportunity of undertaking this PhD and for being such a great supervisor. You picked me up as your candidate, betting on this unknown analytical chemist, and I can now say how lucky I was that you noticed me. During these three years I learnt so many things from you that made my scientific knowledge better and better, and I could appreciate the way you run your group and the incredible passion that you put on your work. You have been always kind, helpful, and willing to listen to me.

Indeed, I want to thank Prof. Luisa De Cola for the same reasons. It is definitely countless the amount of things I could learn from you, which I am sure they will be fundamental for my career. Although you run such a big group, you always found time to meet and discuss with me, giving me precious advices. Since the very first time, you made me feel like part of your group, which I can define as a family, and you have always been so kind and caring for me.

I want also to thank the French Embassy in Italy that actually allowed me to undertake this joint PhD through its scholarship, and gave me the opportunity to make this wonderful experience.

My biggest “thank you” goes to you, Milio, since without you and what you have done for me, everything would probably be different today. There are no words to describe how much I am fond of you, and I feel so lucky that I found you on my way and I could share all these PhD years with you. Io lo so benissimo chi siamo.

Thank you Elena, because you made these three years something special, from the everyday life at the University to all our “serate vizio”. You are so precious, and you brought the smile to my face every given day. Even our daily complaining has been a moment to enjoy with you. Grazie davvero. Thank you Federico, because you also made these years unforgettable, all those Monday Nights will be always on my mind. As you told me, we should always live our life a little bit above our possibilities. Well, I think we did.

Thank you Manici, no matter if you are far away and I am such a stone-hearted guy, every time you were here for our Chinese dinner it was always a special moment, and all our weird awkward conversations are still something unique to me. You are so out of the common way, that’s why I like you. In any case, I can find you on Tinder.

Thanks to Anastasia, for welcoming me all the times I was over Zurich. You are still somebody that I know I can always lean on.

Thanks you Irene, because you are just wonderful. You deserved all those T-rexing of mine, as I can’t get enough of your boccolo.

Thanks Gardo, you are a great man. You showed me how you can get older, build up a family, have kids, without losing the energy to live your own life and follow your passions. Sei un grande. Come le nostre trasferte.

Thank you Carola, because especially after I got back to Italy, you definitely turned my mood from grey to good. Thanks for the morning coffee, for the nights out, and for making me feel one “ometto” of yours.

Thanks to all the Monday Night crew, to Daniele, Giacomo, Fonta, Francesco, Dario. It was so amazingly weird to tell people that I needed the weekend to rest in view of the Monday night party.

Thanks to Bigna, Corrado, Menozzi, for rendering the Department a unique place to stay. It has always been like being in a big family. Or in an MTV trashy show.

Thanks to Alex and Massi for sharing the life in the lab. And thanks to Costanza for being always so helpful.

I wanna thank also Ale C. and Sara, it has been nice working with you, and I think in the end we did a really good job.

Thank you so much, Henning, for all the time we have spent together in Strasbourg. I learned several things from you at work, and, most of all, I found a great friend. All those beers, the parties, the trips, everything we did together have made my first experience abroad the best I could have ever imagined.

And exactly the same goes for you Dedy. Working with you was definitely a pleasure, and for all the rest, for all the time that we shared together, you made my staying in Strasbourg such a wonderful time. I am so happy that I have met you. You just need to improve your gambling skills, but, well, nobody's perfect.

Thank you Eko, because you are a unique person. I think that having the opportunity to work together with you has been one of the most valuable of my life; I learned so many things from you, ranging from pure science to the way to work problems out. And the way you are so kind and helpful with everybody is something rare to find.

Thank you Longhi, for your continuous attempt to mess up my super organized life. It is true that you never got me bored, because, somehow, your innate clumsiness and chaos render you a special girl. You are indeed one of the best pieces of my Strasbourg puzzle.

Thanks Pengkun for sharing the lab life this last year, you are a wise guy and deserve to be the new king of the lab.

Thank you Etienne, for helping me with the French part of this thesis. I miss our wild nights at Jimmy's and our great moments of high-class football. Allez-les-Bleus.

Thanks to all the members of the group that rendered my Strasbourg time so rich, Fede, Ricardo, Youssef, Stephan, Etienne, Nadia, Laura, Amparo, Ingrid, Ale, Ines, Mia, Deanne, and all the others. You are special, guys.

Thank you Giulia, for keeping on listening to my boring stories. Our “working” breakfasts and dinners are priceless to me.

Thanks Anita, come what may.

Thanks to Maio, Zivo, Monta, Camu, Lollo, Macchia, and all my closest friends. Because the more I was working on this piece of science, the more I needed somebody like you to bring me back to “reality”. Thanks for being always at my side. I think you will never ever understand what writing a paper or doing research mean, and that’s why, somehow, you are so precious to me.

Thank you Lolly, for being the special person you are. Per quella boccia di Champagne che, nonostante tutto e tutti, tu continui sempre ad aprire insieme a me.

Thanks to my parents, for their support during all these years and for always letting me free to decide upon my life, which I think is the most important fact. I feel somehow lucky that I was playing my Dad’s music while working in the lab, which is not definitely a usual thing.

Thanks to my grandparents for always being present in my life. You are so important, And thanks to you, nonno, that you would have been so proud of me today. Thank you for still being the best person I have ever met in my life.

CURRICULUM VITAE

PERSONAL INFORMATION

First name: ALESSANDRO

Surname: BERTUCCI

Nationality: Italian

Birthplace: Parma, Italy

Date of birth: 26/04/1987

Current Address: Strada Casa Bianca 33, 43123 Parma, Italy

Phone: +39 3491595548

Email: bertucci@unistra.fr, alessandro.bertucci@nemo.unipr.it,



EDUCATION

- Period: January 2012 – March 2015

Institute: Department of Chemistry, University of Parma, Italy – Institut de Science et d'Ingénierie Supramoléculaires (ISIS), University of Strasbourg, France

Status: Ph.D. Student in Chemical Sciences

Supervisors: Prof. Roberto Corradini, Prof. Luisa De Cola

- Period: October 2009 – October 2011

Institute: University of Parma, Italy

Level Classification: *Laurea Magistrale in Chimica* (Master Degree in Chemistry)

Specialization: Analytical Chemistry

Supervisors: Prof. M. Careri, Dr. L. Elviri

Final Score: 110/110 *cum laude*

- Period: October 2006 – September 2009

Institute: University of Parma, Italy

Level Classification: *Laurea in Scienze e Tecnologie Chimiche* (Bachelor Degree in Chemical Science and Technology)

Supervisor: Prof. C. Mucchino

Final Score: 110/110 *cum laude*

-Period: 2001-2006

Institute: Liceo Scientifico G. Marconi, Parma, Italy

Level Classification: Maturità scientifica (High School degree, studies on arts and sciences)

Final score: 100/100

PUBLICATIONS

A. Bertucci, A. Candiani, S. Giannetti, A. Manicardi, A. M. Cucinotta, G. Spoto, M. Konstantaki, S. Pissadakis, S. Selleri, R. Corradini, *Detection of Unamplified Genomic DNA by a PNA-based Microstructured Optical Fiber (MOF) Optofluidic system with Bragg-Grating*, Biosensor and Bioelectronics, **2015**, 63, 248–254

A. Bertucci, H. Lülff, D. Septiadi, A. Manicardi, R. Corradini, L. De Cola, *Intracellular delivery of Peptide Nucleic Acid and organic molecules using zeolite-L nanocrystals*, Adv. Health. Mat, **2014**, 3, 1812-1817.

H. Lülff, A. Bertucci, D. Septiadi, R. Corradini, L. De Cola, *Multifunctional inorganic nanocontainer for DNA and drug delivery into living cells*, Chem-Eur. J. **2014**, 20, 10900-10904.

A. Candiani; A. Bertucci; S. Giannetti; M. Konstantaki; A. Manicardi; S. Pissadakis; A. Cucinotta; R. Corradini; S. Selleri; *Label-free DNA biosensor based on a peptide nucleic acid-functionalized microstructured optical fiber-Bragg grating*, J. Biomed. Opt. **2013**, 18 (5), 057004

A. Bertucci, A. Manicardi, E. Cavatorta, A. Candiani, M. Sozzi, A. Cucinotta, S. Giannetti, S. Selleri, R. Corradini, *Development of new tools for highly specific nucleic acid detection: PNA-modified photonic crystal fibers and PNA-based switching probes*, La Chimica e l'Industria, **2013**, 4, 110-111.

Bertucci, A.; Manicardi, A.; Corradini, R.; *Advanced Molecular Probes for Sequence-Specific DNA Recognition*, in: *Detection of non-amplified Genomic DNA*, Spoto, G.; Corradini, R. Eds. Springer, Dordrecht, The Netherlands **2012**.

A. Bertucci, E.A. Prasetyanto, D. Septiadi, A. Manicardi, E. Brognara, R. Gambari, R. Corradini, L. De Cola, *Concomitant delivery of Temozolomide and MicroRNA-targeting PNA using mesoporous silica nanoparticles induces apoptosis in drug resistant glioma cancer cells*, **Submitted**.

PATENTS

L. De Cola, E. A. Prasetyanto, A. Bertucci, D. Septiadi, *Disintegratable core/shell silica particles for encapsulating and releasing bioactive macromolecules*, EP14305905, **Filed**.

Hybrid organic-inorganic interfaces for biomedical applications

Résumé

Le travail de recherche de cette thèse consiste en le développement de nouveaux matériaux hybrides organiques-inorganiques pour des applications en nanotechnologie, nanomédecine et diagnostic. Dans ce contexte, des cristaux poreux de zéolite-L ont été utilisés comme nano-vecteur pour faire de la transfection d'ADN et d'ANP, en combinaison avec le relargage de molécules hôtes placées dans les pores. Des nanoparticules de silice mesoporeuses multifonctionnelles ont été utilisées pour traiter le glioblastome, en combinant la thérapie génique avec l'administration durable d'un principe actif. Des nano-coquilles hybrides biodégradables ont été encore développés pour encapsuler des protéines et les relâcher dans les cellules vivantes. Dans le domaine de la détection d'acides nucléiques, des fibres optiques à cristal photonique, fonctionnalisées avec des sondes d'ANP, ont été exploitées comme plateformes optiques pour faire de la détection ultra-sensible d'oligonucléotides ou d'ADN génomique. Enfin, la squelette de l'ANP a été modifié à créer des sondes fluorescentes pour reconnaître et détecter la présence des séquences cibles spécifiques.

Résumé en anglais

The research work presented throughout this thesis focuses on the development of novel organic-inorganic hybrid materials for applications in nanotechnology, nanomedicine and diagnostics. In such a context, porous zeolite-L crystals have been used as nanocarriers to deliver either DNA or PNA in live cells, in combination with the release of guest molecules placed into the pores. Multifunctional mesoporous silica nanoparticles have been designed to treat glioblastoma, combining gene therapy with the sustained delivery of a chemotherapy agent. Biodegradable hybrid nano-shells have been furthermore created to encapsulate proteins and release them in living cells upon degradation of the outer structure in reductive environment. In the field of nucleic acid detection, photonic crystal fibers, functionalized with specific PNA probes, have been exploited as optical sensing devices to perform ultra-sensitive detection of DNA oligonucleotides or genomic DNA. Eventually, the PNA backbone has served as scaffold to synthesize fluorescent switching probes able to recognize and to detect the presence of specific target sequences.